

41 Published Works on Crystal structures

B.T.M Willis

Ph.D.

1968

ProQuest Number: 10107341

All rights reserved

INFORMATION TO ALL USERS

The quality of this reproduction is dependent upon the quality of the copy submitted.

In the unlikely event that the author did not send a complete manuscript and there are missing pages, these will be noted. Also, if material had to be removed, a note will indicate the deletion.



ProQuest 10107341

Published by ProQuest LLC(2016). Copyright of the Dissertation is held by the Author.

All rights reserved.

This work is protected against unauthorized copying under Title 17, United States Code.
Microform Edition © ProQuest LLC.

ProQuest LLC
789 East Eisenhower Parkway
P.O. Box 1346
Ann Arbor, MI 48106-1346

B. T. M. Willis: List of Publications

The publications are divided between four different fields of crystallography, and for this reason are not listed in strict chronological order. A few reports of the United Kingdom Atomic Energy Authority are included: these are available from H.M. Stationery Office. Joint publications are marked with an asterisk.

1. Crystal structures of magnetic materials

- (1) *"Crystal structure and antiferromagnetism in haematite"
(1952) Proceedings of Physical Society (London), vol. 65B, p.950.
- (2) *"Change of structure of ferrous oxide at low temperature"
(1953) Acta Crystallographica, vol. 6, p.827.
- (3) "Crystal structure and antiferromagnetism of chromium antimonide"
(1953) Acta Crystallographica, vol. 6, p.425.
- (4) *"The low-temperature crystal structure of magnetite"
(1953) Acta Crystallographica, vol. 6, p.565.
- (5) *"Crystal structure and magnetic properties of cobalt ferrite at low temperatures"
(1953) Nature, vol. 172, p.1054.
- (6) *"Magnetic transitions and structural changes in hexagonal manganese compounds"
(1954) Proceedings of Physical Society (London) vol. 67 A, p.290.

2. Crystal defects

- (7) "Screw dislocations in quartz"
(1952) Nature, vol. 170, p.115.
- (8) *"Diffraction from dislocations"
(1956) Nature, vol. 177, p.712.
- (9) *"An X-ray study of neutron-irradiated lithium fluoride"
(1957) Philosophic Magazine, vol. 2, p.1018.
- (10) "An optical method of studying the diffraction from imperfect crystals. I. Modulated Structures"
(1957) Proceedings of Royal Society (London), vol. 239, p.189.
- (11) "An optical method of studying the diffraction from imperfect crystals II. Crystals with dislocations"
(1957) Proceedings of Royal Society (London), vol. 239, p.191.
- (12) "An optical method of studying the diffraction from imperfect crystals III. Layer structures with stacking faults"
(1959) Proceedings of Royal Society (London), vol. 248, p.183.
- (13) "Application of X-ray diffraction techniques to irradiation damage problems"
(1958) U.K.A.E.A. Report, M-2751.

- (14) "The effect of segregation on the diffraction from a face-centred cubic alloy with deformation faults"
(1959) Acta Crystallographica, vol. 12, p.683.
- (15) "Positions of the oxygen atoms in $UO_2 \cdot 13$ "
(1963) Nature, vol. 197, p.775.
- (16) "Point defects in uranium oxides"
(1964) Proceedings of British Ceramic Society, vol. 1, p.9.
- (17) "Neutron diffraction studies of non-stoichiometric compounds"
(1965) Proceedings of International Conference on Electron Diffraction and Crystal Defects, Melbourne. Published by Australian Academy of Science
- (18) "Thermodynamic and transport properties of uranium dioxide and related phases"
(1965) Chapter 2 of book published by the International Atomic Energy Agency, Vienna.

3. Single crystal diffractometry

- (19) "Sometheoretical properties of the double-crystal spectrometer used in neutron diffraction"
(1960) Acta Crystallographica, vol. 13, p.763.
- (20) "Use of a two-circle device to obtain three-dimensional diffraction data"
(1961) Acta Crystallographica, vol. 14, p.90.
- (21) "Single-crystal neutron diffraction instruments at the DIDO reactor"
(1962) Jour. Sci. Instrum., vol. 39, p.590.
- (22) "Use of a three-circle goniometer for diffraction measurements"
(1962) Brit. Jour. Applied Physics, vol. 13, p.548.
- (23) *"The Harwell Mark I Automatic Neutron Diffractometer"
(1962) U.K.A.E.A. Report, R-4143.
Also published, in revised form, as
*"Automatic neutron diffractometer for three-dimensional structure-factor determination"
(1963) Rev. Sci. Instrum., vol. 34, p.224.
- (24) *"The Harwell Mark II automatic neutron diffractometer installation"
(1962) U.K.A.E.A. Report, R-4162.
Also published, in revised form, as
*"A programmed multi-channel neutron diffractometer installation"
(1963) Nuclear Instruments and Methods, vol. 24, p.115.
- (25) "Diffractometria con cristallo singolo"
(1965) Published by the Centro Nazionale di Strutturistica Roentgenografica del CNR, Italy.
- (26) *"Single-crystal diffractometry"
(1966) Book published by the Cambridge University Press, in the series "Cambridge Monographs on Physics".

- (27) "A note on Burbank's paper on 'Intrinsic and systematic multiple diffraction'"
(1966) Acta Crystallographica, vol. 21, p.175.

4. Neutron Crystallography

- (28) "A three-dimensional neutron diffraction study of ferrocene"
U.K.A.E.A. Report R-3708; Acta Crystallographica
(1960), vol. 13, P.1088.
- (29) "The interpretation of integrated intensity measurements in X-ray and neutron diffraction"
(1962) U.K.A.E.A. Report, R-3818.
- (30) "Secondary extinction and neutron diffraction"
(1962) Contribution to the book "Pile neutron research in physics"
published by the International Atomic Energy Agency, Vienna.
- (31) *"Double-Bragg scattering of thermal neutrons by ThO_2 and UO_2 "
(1962) U.K.A.E.A. Report, R-3959.
- (32) "Neutron diffraction studies of the actinide oxides. I Uranium dioxide and thorium dioxide at room temperature"
(1963) Proceedings of Royal Society (London), vol. 274, p.122.
- (33) "Neutron diffraction studies of the actinide oxides. II. Thermal motions of the atoms in uranium dioxide and thorium dioxide between 20°C and 1100°C "
(1963) Proceedings of Royal Society (London), vol. 274, p.134
- (34) *"A neutron diffraction study of cerium dioxide at room temperature"
(1963) U.K.A.E.A. Report, R-4939.
- (35) "Structures of UO_2 , UO_{2+x} and U_4O_9 by neutron diffraction"
(1964) Journal de Physique, vol. 25, p.431.
- (36) "The anomalous behaviour of the neutron reflexions of fluorite"
(1965) Acta Crystallographica, vol. 18, p.75.
- (37) *"Neutron diffraction study of antiferromagnetism in UO_2 "
(1965) Physics Letters, vol. 17, p.118.
- (38) *"Structure of a monocarboxylic acid derivative of vitamin B_{12} . Crystal and molecular structure from neutron diffraction analysis"
(1967) Nature, vol. 214, p.130.
- (39) *"Anharmonic vibration and forbidden reflexions in silicon and germanium"
(1967) Proceedings of Royal Society (London) A298, p.307.
- (40) *"Solution of the phase problem in neutron diffraction by the anomalous dispersion method"
(1966) U.K.A.E.A. Report R-5195.
- (41) *"Anharmonic contributions to the Debye-Waller factors of UO_2 "
(1967) Acta Crystallographica, vol. 23A.

B. E. W. Willis
Dr. B. E. W. Willis

Papers 1-6

1. Crystal Structures of Magnetic Materials (1-6)

This is a group of papers describing X-ray diffraction studies of anti-ferromagnetic and ferrimagnetic materials, examined above and below the magnetic transition temperature. The aim of the work was to determine changes of crystal symmetry or of unit cell dimensions associated with changes of magnetic properties. The work was carried out in a two-year period when the candidate was a member of the research staff of the General Electric Co. Ltd., Wembley.

Crystal Structure and Antiferromagnetism in Haematite

By B. T. M. WILLIS AND H. P. ROOKSBY

Research Laboratories, The General Electric Company, Limited, Wembley, Middlesex

MS. received 7th July 1952

ABSTRACT. The crystal structure of haematite has been investigated by x-ray analysis in the temperature range 20°C to 950°C. On cooling through a temperature of approximately 675°C the rhombohedral unit cell undergoes a sudden expansion along the triad axis direction. The results are interpreted in terms of an antiferromagnetic behaviour of pure haematite, with a Curie point at approximately 675°C. It is shown that the behaviour is analogous to that of the cubic oxides FeO and Fe₃O₄, which exhibit structure cell deformations on cooling through certain critical temperatures.

§1. INTRODUCTION

THE magnetic properties of haematite, α -Fe₂O₃, undergo certain changes in the neighbourhood of 675°C, which have been discussed in detail by Chevallier (1951). At this same temperature a thermal expansion abnormality has been reported by Chaudron and Forestier (1924), and Roth and Bertram (1929) have observed an anomaly in the specific heat-temperature curve. Thus a second-order change takes place at 675°C, and Néel (1949) has suggested that this change comprises a transition from an antiferromagnetic to a paramagnetic state. Recent neutron diffraction work on haematite by Shull *et al.* (1951) has given some support to Néel's hypothesis.

In view of the absence of information concerning the precise behaviour of the structure cell of haematite near the critical point of 675°C, it was decided to investigate the change of the lattice parameters of the material over the temperature range 20°C to 950°C. The results prove that the structure cell of α -Fe₂O₃

undergoes a deformation resembling those exhibited by FeO and Fe₂O₄ at certain critical temperatures, and it is concluded that this is consistent with the view that haematite assumes an antiferromagnetic state below 675° c.

§ 2. APPARATUS AND SPECIMENS

The x-ray camera used for the investigation was a high temperature 19 cm Debye-Scherrer camera of the design previously described by Owen (1943). The temperature of the sample could be varied from room temperature to 950° c, and maintained constant to $\pm 1^\circ$ c. An earlier calibration of the instrument against the melting points of several metals had shown that the temperatures recorded by the thermocouples were within a few degrees of the temperature of the irradiated part of the specimen. Further accuracy in measuring the temperature was not attempted, since, as will become apparent in the discussion, a possible small error in our scale of temperatures has no important bearing on the results.

Throughout the experiment the air inside the camera was maintained at a pressure of 1 cm of mercury. This pressure was sufficiently low to obtain reproducible performance from the furnaces within the high temperature enclosure, and also to reduce background fogging on the x-ray powder photographs. All the photographs were obtained with Co K α radiation.

Samples from several different sources were studied. The chief samples comprised a natural haematite from Sweden, a natural micaceous haematite from East Africa, and a red synthetic oxide, prepared by firing a precipitated hydrated oxide (goethite) in air at 400° c and then for several hours in air at 1300° c. In the preparation of specimens from the hard natural materials care was taken in powdering to avoid introducing lattice strains. All the specimens investigated gave satisfactory powder photographs exhibiting no appreciable line broadening.

§ 3. X-RAY EXAMINATION

At room temperatures haematite is rhombohedral, with the oxygen atoms in approximately hexagonal close packing and the iron atoms occupying two-thirds of the octahedral holes in the oxygen lattice (Wells 1950). It will be convenient to describe the results with reference to a hexagonal, rather than a rhombohedral, structure cell.

A preliminary exploration of the thermal changes in the lattice was made without recourse to detailed measurements at every temperature. Powder lines were sought whose relative positions were particularly sensitive to any change of shape of the structure cell, i.e. change of c/a . It so happens that the adjacent high-order lines 10(14) and 410 are very favourably placed for this purpose.

The relative positions of these two lines at different temperatures in the range 20° c to 950° c are shown in the photographs (actual size) in fig. 1. It can be seen that the separation of the lines Δ changes in a non-uniform manner with temperature. From 20° c to 300° c the change of Δ is relatively small, but from 300° c to 680° c Δ decreases more rapidly, and at a rate which increases with temperature. Above 680° c Δ is again almost independent of temperature.

The general shape of the (Δ , temperature) curve was closely similar to that of the (c/a , temperature) curve, and the latter is shown in fig. 2. This curve possesses a point of inflection at approximately 675° c, which is the critical temperature for the second-order change. Within the accuracy of measurement

of c/a (± 0.0002) it was found that the value of c/a for a given sample in the temperature range 20°C to 950°C was independent of the previous heat treatment in this range.

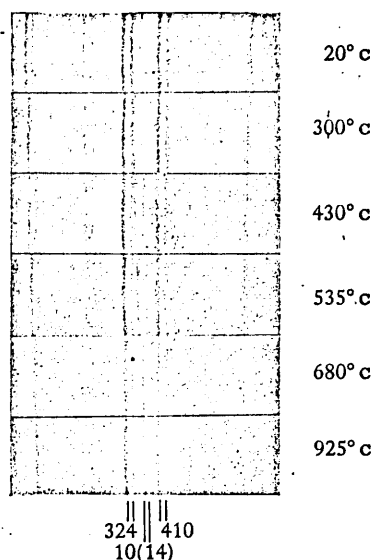


Fig. 1. Parts of x-ray powder photographs of haematite at successively increasing temperatures showing relative displacements of 324, 10(14) and 410 reflections.

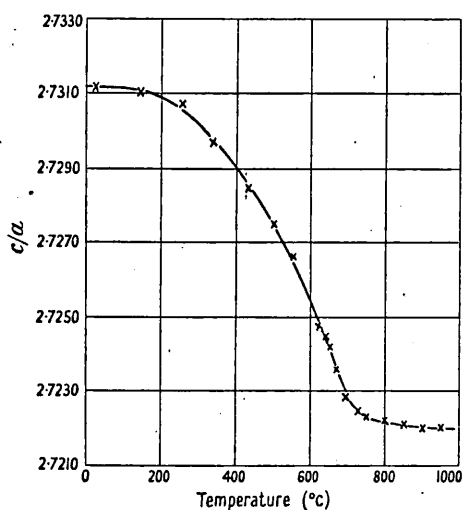


Fig. 2. Curve showing change with temperature of axial ratio c/a of structure cell of haematite.

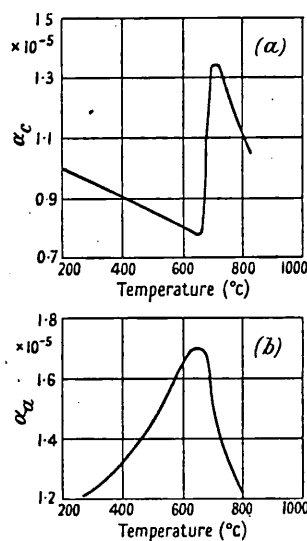


Fig. 3. Curves showing variations with temperature of expansion coefficients of haematite along (a) c direction, (b) a direction.

Several other synthetic oxides were examined, and all gave substantially the same curve as fig. 2. Some slight differences in the room temperature value of c/a were observed for certain specimens, and in particular for synthetic oxides fired at relatively low temperatures the measured value was 2.7305 instead of

2.7311. Subsequent heat treatment of such specimens in air at 1300° c, however, led to an increase of the room temperature value of c/a to 2.7311. Thus fig. 2 represents the general character of the (c/a , temperature) curve for all the samples of haematite examined.

The expansion coefficient-temperature curves for the directions parallel and perpendicular to the triad axis were determined from the slopes of the lattice parameter-temperature ((c, T) and (a, T)) curves. The results are shown in figs. 3(a) and 3(b). α_c refers to the expansion coefficient parallel to the triad axis, and α_a to the expansion coefficient perpendicular to this axis. α_c falls gradually from room temperature to 670° c, and then rises almost discontinuously to nearly twice its value. It then falls again from 700° c to 950° c. The behaviour of α_a is less noteworthy; it simply rises to a maximum at approximately 675° c.

These results are to be contrasted with those obtained by Chaudron and Forestier (1924) on polycrystalline compressed blocks of the oxide powder. Chaudron observed a maximum, rather than a discontinuity, in the (α, T) curve, and his (α, T) curve was not reversible but showed considerable thermal hysteresis. The differences between our curves and those given by Chaudron are not surprising in view of the fact that the x-ray measurements give the precise behaviour of the structure cell. The dilatometric measurements on the oxide powder are influenced by the state of subdivision of the powder, and can disclose no information concerning the anisotropic behaviour of the lattice.

§ 4. DISCUSSION

Our results indicate that the rhombohedral structure cell of haematite undergoes an abnormal change on cooling through the critical temperature of 675° c. The change comprises a sudden relative expansion along the triad axis, involving a change of the rhombohedral angle from the approximately constant value of 55° 24' above the critical temperature to a value which decreases with decreasing temperature below 675° c, and attains a value of 55° 16' at room temperature (see table).

Crystal Structure Data for α -Fe₂O₃

Temp (°c)	Hexagonal system			Rhombohedral system	
	a_H (Å)	c_H (Å)	c/a	a_R (Å)	α
20	5.0345	13.749	2.7311	5.4271	55° 15.8'
750	5.0856	13.845	2.7223	5.4698	55° 24.3'

This behaviour is analogous to that of the other iron oxides, FeO and Fe₃O₄, which undergo slight structural changes from cubic to rhombohedral symmetry by a relative expansion along a triad axis on cooling through certain temperatures. In the case of FeO the deformation first appears below -80° c (Rooksby and Tombs 1951), which is the critical temperature for the appearance of antiferromagnetism in that material. Fe₃O₄ exhibits the deformation (Tombs and Rooksby 1951) below the antiferromagnetic critical temperature of -160° c.

In α -Fe₂O₃ the atomic arrangement perpendicular to the triad axis resembles that perpendicular to a triad axis in the cubic structures of FeO and Fe₃O₄. In particular, sheets of iron atoms alternate with sheets of oxygen atoms, although the iron atom sheets are puckered in α -Fe₂O₃, and in FeO and Fe₃O₄ the oxygen atoms are in cubic instead of hexagonal close packing. Thus all three structures exhibit the same kind of abnormal lattice dilatation, in which the spacing between

the iron atom sheets suddenly increases on cooling through certain critical temperatures of magnetic transformations. As the magnetic transformation involves the onset of the antiferromagnetic condition in FeO and Fe₃O₄, it appears that the structure cell behaviour of α -Fe₂O₃ is consistent with the view that haematite is also an antiferromagnetic oxide, with a critical temperature at approximately 675°C. The expansion coefficient-temperature curves in figs. 3(a) and 3(b) indicate that the exchange forces, which lead to the antiferromagnetic orientation of the electron spins, are directed mainly along the triad axis direction. This is in general agreement with the views of Néel (1949) and Shull *et al.* (1951) that the electron spins are parallel within a given iron atom sheet and antiparallel with respect to neighbouring sheets.

There is a close resemblance between the present observations on haematite and those made by Greenwald (1951) on the isomorphous chromium sesquioxide Cr₂O₃. In the case of Cr₂O₃, however, the dilatation on cooling through the antiferromagnetic critical temperature of 45°C comprises a relative contraction instead of expansion along the triad axis direction.

The existence of a lower transition point in haematite at -70°C has recently been reported by Guillaud (1951), who has shown that certain magnetic and thermal expansion abnormalities occur at this temperature. Shull *et al.* (1951) have suggested, on the basis of neutron diffraction observations, that a 90° rotation of the magnetic dipoles occurs at this transition point. Apart from single observations at -180°C and -70°C we have not studied the behaviour of the structure cell below room temperature. These observations showed, however, that there is no phase change between room temperature and -180°C, and that the rhombohedral angle is approximately the same at -180°C, -70°C and room temperature. In combination with the conception of a 90° rotation of magnetic dipoles this indicates that the exchange forces between the dipoles are independent of their orientation.

REFERENCES

- CHAUDRON, G., and FORESTIER, H., 1924, *C. R. Acad. Sci., Paris*, **179**, 63.
 CHEVALLIER, R., 1951, *J. Phys. Radium*, **12**, 172.
 GREENWALD, S., 1951, *Nature, Lond.*, **168**, 397.
 GUILLAUD, C., 1951, *J. Phys. Radium*, **12**, 489.
 NÉEL, L., 1949, *Ann. Phys., Paris*, **12**, 249.
 OWEN, E. A., 1943, *J. Sci. Instrum.*, **20**, 190.
 ROOKSBY, H. P., and TOMBS, N. C., 1951, *Nature, Lond.*, **167**, 364.
 ROTH, W. A., and BERTRAM, W., 1929, *Z. Elektrochem.*, **35**, 306.
 SHULL, C. G., STRAUSER, W. A., and WOLLAN, E. O., 1951, *Phys. Rev.*, **83**, 333.
 TOMBS, N. C., and ROOKSBY, H. P., 1951, *Acta Crystallogr.*, **4**, 474.
 WELLS, A. F., 1950, *Structural Inorganic Chemistry* (Oxford: University Press), 2nd edn., p. 379.

Change of Structure of Ferrous Oxide at Low Temperature*

By B. T. M. WILLIS AND H. P. ROOKSBY

Research Laboratories of The General Electric Company Limited, Wembley, England

(Received 28 May 1953)

The structure of ferrous oxide has been studied between room temperature and liquid-air temperature (90° K.) by X-ray powder photography. The results support the conclusion of Jette & Foote that at room temperature the structure is of the NaCl-type with a small and variable number of the Fe²⁺ sites vacant, so that the stoichiometric composition FeO is never attained.

At low temperature (below 200° K.) the structure is rhombohedral, the new structure cell being derived from the originally cubic cell by an extension along one of the triad-axis directions. This is a change of the second order and appears to be directly connected with the transition from the paramagnetic to the antiferromagnetic state on cooling through 198° K. The magnitude of the change, as measured at liquid-air temperature, is very sensitive to the concentration of iron in the oxide. Thus, for the oxide of minimum iron content the rhombohedral angle α at 90° K. is within one minute of the value (60°) which corresponds to cubic symmetry, whereas α is 59° 23' for the least iron-deficient oxide.

It is shown that the powder photograph taken at liquid-air temperature provides a much more sensitive indication of the degree of homogeneity of the sample than that taken at room temperature.

1: Introduction

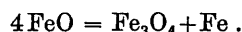
The variable composition of ferrous oxide has been known for some time, but the origin of this variation has received various interpretations from different authors. From an investigation of the chemical composition, room-temperature lattice parameter, and density of oxides of different composition, Jette & Foote (1933*a, b*) concluded that at room temperature the structure is of the NaCl-type with a small and variable number of the Fe²⁺ sites vacant. Bénard (1937, 1939), however, measured the lattice parameters of various oxide preparations and obtained quite different results (the two sets of results are discussed below in § 3). He concluded that oxides of minimum iron content correspond to stoichiometric FeO, and that oxides of higher iron content contain the excess iron in interstitial solid solution. The present state of our knowledge has been recently reviewed by Wyckoff (1952), who says: 'When ferrous oxide is heated with an excess of iron and quenched from a series of temperatures, the lattice parameter is greater the higher the quenching temperature. This has been interpreted to mean that at elevated temperatures iron dissolves in and swells the ferrous oxide structure: it could also represent an attempt to complete the lattice by approaching the 1:1 composition ratio.'

The main part of the present investigation is concerned with the low-temperature structure of ferrous oxide. In addition, certain observations on the room-

temperature structure are given, as they have an important bearing on the discussion of the low-temperature measurements, and, moreover, help to resolve the disagreement between the results of Bénard and of Jette & Foote.

2. Preparation of oxides of different composition

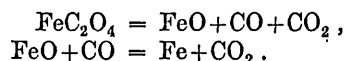
Ferrous oxide is unstable below 570° C. and decomposes according to the equation



The velocity of this reaction attains a maximum at 500° C. (Bénard & Chaudron, 1936), but is very small at room temperature. Consequently, ferrous oxide samples must be prepared above 570° C. and then rapidly quenched to room temperature. It is desirable to carry out X-ray examinations soon after the quenching process, in order to avoid ambiguities arising from partial decomposition of the metastable ferrous oxide preparations.

Approximately 20 g. of ferrous oxide, used as the basic material (A) for subsequent preparations, were prepared by decomposition of ferrous oxalate at 800° C. in a stream of nitrogen. The product obtained after heating for 3 hr. gave an X-ray powder photograph showing lines of the ferrous oxide structure only. The preparation of the oxide from the oxalate was not used by Jette & Foote (1933*a*), because they found that the product obtained by decomposition *in vacuo* gave lines of free iron as well as ferrous oxide on the powder photograph. In their work, the formation of free iron may have been due to reduction of the oxide by carbon monoxide according to the equations

* Communication No. 554 from the Staff of the Research Laboratories of The General Electric Company Limited, Wembley, England.



We avoided this difficulty by carrying away the carbon monoxide and carbon dioxide gases in a stream of nitrogen.

The material (*A*) was then divided into two equal portions. One portion was mixed with a small excess of iron (mixture *B*) and the other portion with a small excess of Fe_3O_4 (mixture *C*). The mixture *B* was further subdivided into several quantities weighing approximately 1 g. each, and each quantity was separately enclosed in a small platinum thimble and sealed in an evacuated quartz tube. The individual tubes were heated at a given temperature in the range 600–1200° C. The duration of the heat treatment was from 2 hr. to 60 hr., depending on the temperature, and after this time the tube was quenched by rapid immersion in cold water. In this way several different samples were obtained, corresponding to ferrous oxide in equilibrium with iron at different temperatures from 600° C. to 1200° C.

Samples of ferrous oxide in equilibrium with Fe_3O_4 were prepared in exactly the same way from mixture *C*.

3. Room-temperature structure

X-ray powder photographs of each sample were taken at room temperature and liquid-air temperature (90° K.) with a 19 cm. camera using $\text{Co } K\alpha$ radiation. For sintered specimens care was taken in powdering to avoid introducing excessive lattice distortion. X-ray photographs of these specimens gave sharp high-order lines.

The room-temperature lattice parameter (a_0) of each sample was determined to an accuracy of $\pm 0.0003 \text{ \AA}$

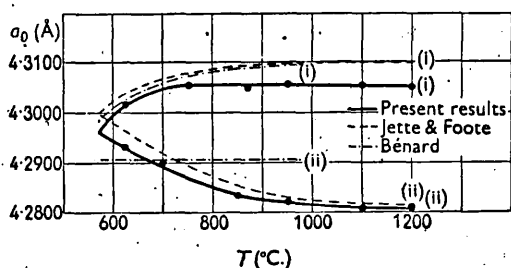


Fig. 1. Curves showing relation between a_0 and the quenching temperature, T , for ferrous oxide heated in presence of (i) Fe, (ii) Fe_3O_4 , according to different authors.

by means of the usual extrapolation methods, and the results are given in Fig. 1, in which a_0 is plotted against T , the temperature from which the sample was quenched. Curve (i) refers to the samples of ferrous oxide heated in the presence of free iron and curve (ii) to the samples heated with Fe_3O_4 . Determinations of the a_0 versus T curve have also been carried out by Jette & Foote (1933*b*) and Bénard (1939). Their results are also included in the figure after the values of a_0

have been multiplied by the factor 1.00202, in order to express them on the same absolute scale ($\text{Co } K\alpha_1 = 1.78890 \text{ \AA}$) as the present results.

Fig. 1 shows that our results are in much closer accord with the previous observations of Jette & Foote than with those of Bénard. In particular, we have confirmed that a_0 decreases rapidly with the increasing quenching temperature T for the oxide heated in the presence of Fe_3O_4 , whereas Bénard found that a_0 is independent of T in the temperature range 575–975° C. It was this observation that led him to conclude that ferrous oxide in equilibrium with Fe_3O_4 corresponds to stoichiometric FeO.

It is difficult to account for the apparently anomalous results of Bénard, except on the basis of incorrect heat treatment. Unfortunately, there is no reference in his papers to the details of heat treatment of the oxide in the presence of Fe_3O_4 , and only three experimental points were included on his curve (ii) (Fig. 1) referring to such oxides. We have found that, for temperatures below 900° C., heating for a few hours only is not sufficient to give samples with a value of a_0 which corresponds to ferrous oxide in equilibrium with Fe_3O_4 .

4. Structure at liquid-air temperature

The low-temperature structure of ferrous oxide has been previously investigated by Ellefson & Taylor (1934), who reported that the structure remained cubic down to 160° K. We have observed, however, a decisive structure change in ferrous oxides when cooled below *c.* 200° K., and this has been briefly reported in an earlier communication (Tombs & Rooksby, 1950).

Fig. 2(*a*) is a photograph of the room-temperature powder pattern ($\text{Co } K\alpha$ radiation) of the original oxide (*A*), and Fig. 2(*b*) is the corresponding photograph taken at liquid-air temperature. The 220, 311 and 420 lines are slightly broader in (*b*) than in (*a*), whereas the definition of the 400 line remains unchanged. This suggests that at low temperatures the cubic structure cell is deformed very slightly along a [111] direction to give a rhombohedral cell, and this interpretation is completely verified by observations on oxide samples in which the iron concentration is higher.

The X-ray photographs of Fig. 2(*c*) and (*d*) represent results on a specimen of ferrous oxide obtained by heat treatment of oxide (*A*) in the presence of free iron at 900° C. It will be seen that the 220 and 420 lines of Fig. 2(*c*) have each been split into two lines of approximately the same intensity in Fig. 2(*d*), and the 331 line into three lines of which the two lower-angle lines are relatively weak. The 400 line remains unsplit. This form of powder pattern is that expected for a change from a cubic to a rhombohedral structure cell by extending the cubic cell along a [111] direction.

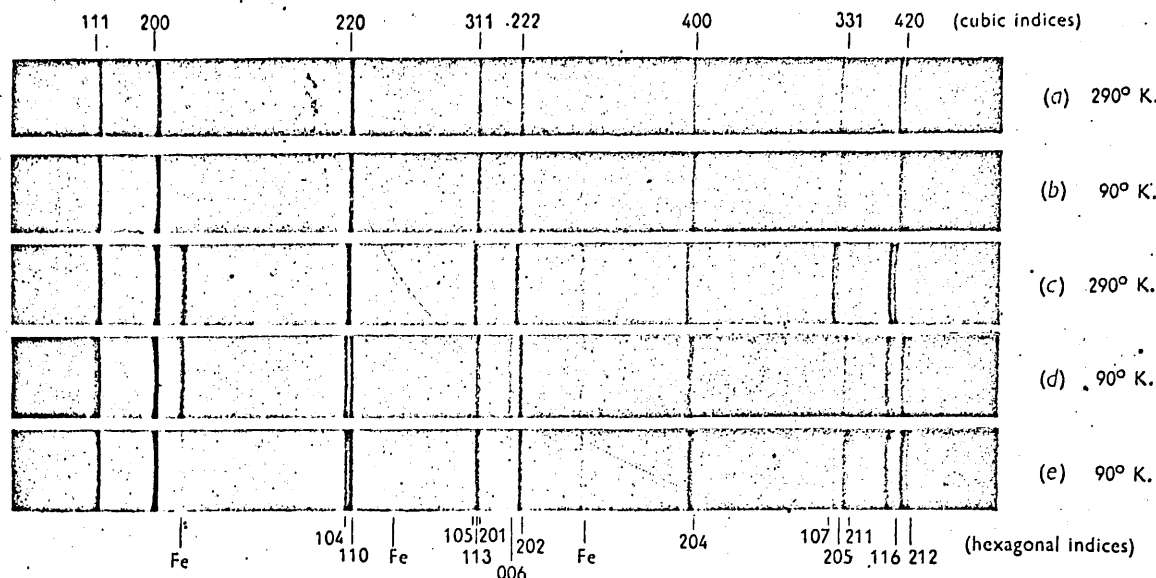


Fig. 2. X-ray powder photographs of different samples of ferrous oxide taken at liquid-air and room temperatures.

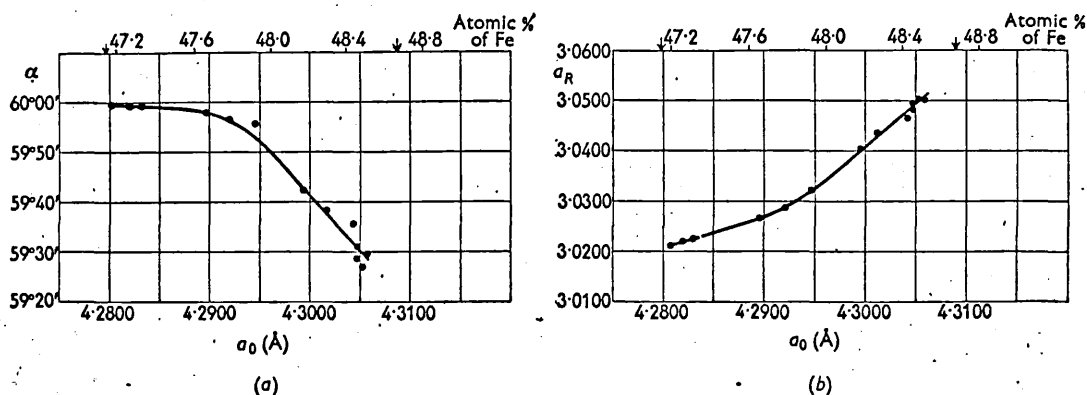


Fig. 3. (a) Relation between α at 90° K. and the room-temperature value of a_0 .
(b) Relation between a_R at 90° K. and the room-temperature value of a_0 .

The rhombohedral angle α is therefore less than the 60° required by cubic symmetry.

The observed spacings and intensities taken from the low-temperature powder pattern (Fig. 2(d)) are listed in Table 1, and compared with the values calculated by assuming a rhombohedral structure cell with lattice parameters

$$a_R = 3.0499 \text{ \AA}, \alpha = 59^\circ 27.5'$$

and with atomic parameters equivalent to those for the room-temperature face-centred cubic structure. Agreement between calculated and observed figures is extremely good.

Values of the rhombohedral lattice parameters a_R , α have been determined for many samples of different iron content from appropriate 90° K. powder photographs. The results are given in the curves Fig. 3(a) and (b), in which the room-temperature structure cell dimension, a_0 , is plotted against α and a_R , respectively.

According to Jette & Foote (1933a), a_0 increases with iron content in an approximately linear fashion, and their data have been used in Fig. 3 to express a_0 in terms of the atomic percentage of iron in the ferrous oxide structure. The two arrows on each abscissa axis indicate the limits of homogeneity of ferrous oxide as determined by the same authors (Jette & Foote, 1933b). We see from the figure that the magnitude of the cubic/rhombohedral change is relatively small for oxides containing up to 47.8 atomic% of iron, but that for oxides of higher iron content the magnitude of the change increases more rapidly. The lattice parameters of ferrous oxide at its limits of homogeneity are listed in Table 2. These values are derived from extrapolation of the curves in Fig. 3(a) and (b).

The two lines 116 and 212 in Fig. 2(d) are of approximately the same density. However, in Fig. 2(e), which is a photograph taken at liquid-air temperature of a different sample, 116 appears to be distinctly

Table 1. Observed and calculated spacings and intensities (Co $K\alpha_1$) for ferrous oxide (48.5 atomic% Fe) at 90° K.

hkl (hexagonal indices)	Corresponding room- temperature cubic indices	d_o (Å)	d_c (Å)†	I_o	I_c †
104 } 110 }	220	1.5246 1.5122	1.5248 1.5124	<i>s</i> <i>s</i>	97 95
105 } 113 } 201 }	311	1.3014 1.2941 1.2908	1.3018 1.2941 1.2903	<i>w</i> <i>m</i> <i>m</i>	21 42 21(+21*)
006 } 202 }	222	1.2497 1.2366	1.2501 1.2365	<i>w</i> <i>m</i>	16 46
204	400	1.0738	1.0738	<i>m</i>	38
107 } 205 } 211 }	331	0.99179 0.98663 0.98157	0.99180 0.98665 0.98159	<i>w</i> <i>w</i> <i>m</i>	20 20 40
116 } 212 }	420	0.96364 0.95733	0.96358 0.95730	<i>s</i> <i>s</i>	95 100

s = strong, *m* = medium, *w* = weak.

* Coincidence with $113\alpha_2$.

† Calculated using lattice parameters (hexagonal cell): $a_H = 3.0248$, $c_H = 7.5010$ Å, and intensities normalized to $I_{212} = 100$.

weaker than 212, and the apparent densities of the lower-angle components of the other groups of lines are correspondingly reduced. This apparent weakening of the lower-angle components also occurred in varying degrees in low-temperature photographs of other samples.

Table 2. Lattice parameters for ferrous oxides of limiting compositions

Composition	Cubic cell (290° K.) a_c	Rhombohedral cell (90° K.)	
		a_R	α
Maximum iron	4.3088 Å	3.0550 Å	59° 23.0'
Minimum iron	4.2800 Å	3.0210 Å	59° 59.5'

This effect can be explained as follows. If we consider the cubic 420 line, splitting occurs at low-temperatures into the components 116 and 212, whose displacements from the 420 line (after correcting for thermal contraction) differ considerably. The displacement of 116 is approximately nine times that of 212, as the structure change on cooling takes place by an extension parallel to the rhombohedral triad axis with only a relatively small contraction normal to this axis. Thus any slight inhomogeneity of the sample, involving small local variations of lattice spacing, results in a broadening of 116 relative to 212, and this broadening is apparent as a reduction of the peak density of the line. For the same reason an apparent reduction in density of the lower-angle components of the other groups of lines takes place. It should be emphasised that it is the apparent densities of the lower-angle components that show this anomalous behaviour. If integrated intensities had been evaluated, the anomalies would in all probability have disappeared, but no confirmatory measurements have been carried out.

The relative peak densities between components of

split lines in the low-temperature powder photograph are of some practical interest. The density relationships provide a very sensitive indication of the degree of homogeneity of any given sample, an indication which is not apparent in the room-temperature photographs.

X-ray powder photographs of an oxide of high iron content were taken at the intermediate temperatures 160° K. and 200° K. The splitting of the cubic lines could be clearly seen at 160° K., whereas no splitting was observable at 200° K.

5. Discussion of results

It is clear from the X-ray photographs taken at different temperatures below room temperature that the change of structure of ferrous oxide, which develops on cooling through a certain transition temperature T_1 , is a change of the 'second order'. The change develops over an extended range of temperatures, and involves no re-arrangement of the ions within the structure cell. Similar structure changes have been observed in MnO and NiO below the temperatures 160° K. and 470° K. respectively (Tombs & Rooksby, 1950; Rooksby, 1948). It must be noted, however, that the deformation on cooling ferrous oxide takes place in an opposite sense from the changes in MnO and NiO, so that the rhombohedral angle is less than 60° for ferrous oxide and greater than 60° for MnO and NiO.

The X-ray results indicate that for ferrous oxide of high iron content T_1 lies between 160° K. and 200° K. According to Bizette (1946), the antiferromagnetic transition temperature of ferrous oxide is 198° K., and there is strong reason for believing (Smart & Greenwald, 1950) that the structure change is directly connected with the development of the antiferromagnetic state below this temperature. Moreover, Shull, Strauser & Wollan (1951) have shown by neu-

iron-diffraction observations on powdered ferrous oxide at 80° K. that the magnetic moments of the Fe²⁺ ions are parallel within a given (111) sheet of Fe²⁺ ions and antiparallel between adjacent sheets. This picture is consistent with the X-ray observations, which indicate the development of a unique triad axis normal to a set of (111) planes.

The reason for the marked difference in the magnitude of the crystal structure change at low temperatures of ferrous oxide samples of different iron content (see Table 2) is not clear. It is unlikely that the difference is due to a variation of the transition temperature T_1 between the different samples. Such an explanation would require a change of T_1 of approximately 100° K. when the iron content of the sample increases from 47.5 to 48.5 atomic%, whereas the actual change in T_1 for this range is probably much less. Thus Bizette (1946) found that T_1 was 198° K. for a sample of maximum iron content, and Millar (1929) that T_1 was 185° K. for a sample which was probably of minimum iron content. Further, Bizette compared the variation of T_1 as a function of composition in the solid solution system FeO-MgO, and found that on lowering the atomic concentration of Fe by 1% (by replacement of Fe²⁺ with the non-magnetic ion Mg²⁺) a reduction in T_1 of 5° K. only took place.

It appears reasonable to expect the magnitude of deformation below T_1 , which takes place in a direction normal to (111) ionic sheets, to increase as

the number of vacant sites and Fe³⁺ ions within the sheets is reduced, i.e. as the stoichiometric composition is approached. However, on Bénard's interpretation of the room-temperature structure, the deformation is extremely small for stoichiometric FeO and increases rapidly as the proportion of dissolved Fe²⁺ ions increases. We believe that this is therefore additional evidence in favour of the interpretation of Jette & Foote.

References

- BÉNARD, J. (1937). *C. R. Acad. Sci., Paris*, 205, 912.
 BÉNARD, J. (1939). *Ann. Chim.* (11), 12, 5.
 BÉNARD, J. & CHAUDRON, G. (1936). *C. R. Acad. Sci., Paris*, 202, 1336.
 BIZETTE, H. (1946). *Ann. Phys., Paris*, (12), 1, 295.
 ELLEFSON, B. S. & TAYLOR, N. W. (1934). *J. Chem. Phys.* 2, 58.
 JETTE, E. R. & FOOTE, F. (1933a). *J. Chem. Phys.* 1, 29.
 JETTE, E. R. & FOOTE, F. (1933b). *Trans. Amer. Inst. Min. (Metall.) Engrs.* 105, 276.
 MILLAR, R. W. (1929). *J. Amer. Chem. Soc.* 51, 215.
 ROOKSBY, H. P. (1948). *Acta Cryst.* 1, 226.
 SHULL, C. G., STRAUSSER, W. A. & WOLLAN, E. O. (1951). *Phys. Rev.* 83, 333.
 SMART, J. S. & GREENWALD, S. (1950). *Nature, Lond.* 166, 523.
 TOMBS, N. C. & ROOKSBY, H. P. (1950). *Nature, Lond.* 165, 442.
 WYCKOFF, R. W. G. (1952). *Crystal Structures*, vol. 1. New York: Interscience Publishers.

Cryst. (1953). 6, 831

The Structure of Dimethyl Oxalate

BY MARYON W. DOUGILL AND G. A. JEFFREY*

Department of Inorganic and Physical Chemistry, The University of Leeds, England

(Received 7 April 1953)

An X-ray analysis of the crystal structure of dimethyl oxalate shows that the molecule has a planar *trans-trans* configuration, which is the planar structure of least steric interference. The bond lengths and valency angles are C¹-C¹ 1.53±0.03, C¹-O¹ 1.19, C¹-O² 1.31, O²-C² 1.46±0.05 Å, C¹-C¹-O¹ 125°, C¹-C¹-O² 110°, O¹-C¹-O² 125°, C¹-O²-C² 118°±3°. The intramolecular methyl to carbonyl distance is 2.70 Å. Of the four intermolecular distances which are less than 3.95 Å, three at 3.35, 3.54 and 3.57 Å correspond to co-ordination of carbonyl oxygen atoms around a methyl group very approximately in the directions of the C-H bonds. It is suggested that there is weak association or polarization bonding between the carbonyl and the methyl groups which accounts for the anomalous melting point. This may also provide an explanation of the differences which have been reported in the Raman spectra of the solid and liquid.

Introduction

the recent crystal-structure analyses of α -anhydrous oxalic acid (Cox, Dougill & Jeffrey, 1952),

oxalic acid dihydrate (Ahmed & Cruickshank, 1953), ammonium oxalate hydrate (Jeffrey & Parry, 1952) and sodium oxalate (Jeffrey & Parry, 1953) it was found that the configuration of the (COO)₂ is planar in the acids but not necessarily so in the salts. In (NH₄)₂(COO)₂·H₂O the oxalate ion is non-planar with

* Now at Chemistry Department, University of Pittsburgh, S.A.

Acta Cryst. (1953). 6, 425**Crystal structure and antiferromagnetism of CrSb.*** By B. T. M. WILLIS, *Research Laboratories of The General Electric Company Limited, Wembley, England*

(Received 24 December 1952)

Introduction

Previous work (Rooksby, 1948; Rooksby & Tombs, 1951) on the crystal structures of the antiferromagnetic oxides MnO, FeO, CoO and NiO has shown that small lattice changes, involving a slight departure from cubic symmetry, take place in these compounds when they are cooled through their antiferromagnetic transition points. The bulk of the remaining known antiferromagnetic compounds have crystal structures, above their transition points, which do not belong to one of the cubic space groups. Nevertheless, it appears from recent studies on chromium sesquioxide (Greenwald, 1951) and α -ferric oxide (Willis & Rooksby, 1952) that non-cubic antiferromagnetic compounds also undergo lattice changes in the neighbourhood of their transition points. These changes are closely analogous to those displayed by the cubic oxides in that they comprise an anomalous expansion or contraction along a principal crystal axis. The changes in cubic crystals are inevitably accompanied by lowering of symmetry, whereas in hexagonal and rhombohedral crystals they can occur simply by an alteration of axial ratio without modification of symmetry.

The present investigation is concerned with the behaviour of the structure cell of the antiferromagnetic compound CrSb. Like MnTe, the subject of a recent study by Greenwald (see below), this crystallizes in the hexagonal system, and possesses the NiAs-type of crystal structure. The investigation has shown that the changes in the structure cell of CrSb in the neighbourhood of its transition point are those to be expected from the general picture outlined above.

Experimental

The compound was prepared by mixing chromium and antimony in the atomic ratio 0.45 Cr to 0.55 Sb, and heating in an evacuated quartz tube for 4 hr. at 650° C. One end of the quartz tube was then opened and attached to a diffusion pump, and the excess antimony was distilled off at 500° C. Homogenization of the product was achieved by reheating *in vacuo* for several hours at 550° C.

An X-ray powder photograph revealed only the presence of CrSb, with the NiAs-type structure. The room-temperature lattice parameters were:

$$a = 4.108, c = 5.440 \text{ \AA}, (\text{Cu } K\alpha_1 = 1.54050 \text{ \AA}).$$

These values are to be compared with those given by Wyckoff (1951):

$$a = 4.115, c = 5.479 \text{ \AA},$$

and by Snow (1952):

$$a = 4.127, c = 5.451 \text{ \AA}.$$

* Communication No. 536 from the Staff of the Research Laboratories of The General Electric Company Limited, Wembley, England.

Chemical analysis showed the preparation to contain 33.6% Cr and 66.3% Sb, compared with the theoretical 29.9% Cr and 70.1% Sb for stoichiometric CrSb.

A small quantity of the powder was sealed in an evacuated quartz capillary tube of 0.3 mm. bore, and X-ray powder photographs were taken at various temperatures between room temperature and 650° C., using a 19 cm. high-temperature camera of the Owen (1943) type. An X-ray photograph at -180° C. was also obtained, using the method described by Tombs (1952). Cu $K\alpha$ radiation was used throughout, no serious difficulties being encountered because of secondary fluorescence from the chromium in the specimen.

The above temperature range included the antiferromagnetic transition temperature, which is in the neighbourhood of 400° C. (Foëx & Graaf, 1939). The lattice parameters were calculated for each photograph to an accuracy of $\pm 0.001 \text{ \AA}$. The results are given in Fig. 1,

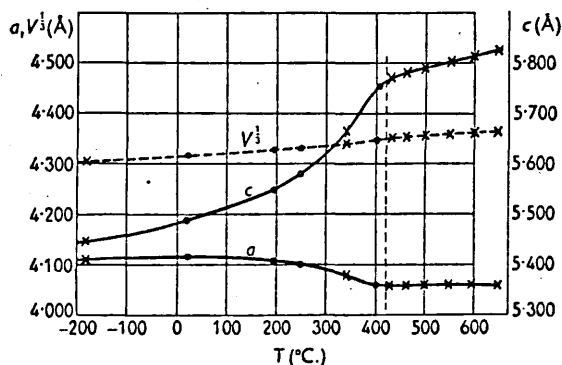


Fig. 1. Curves showing temperature variation of c , a and $V^{\frac{1}{2}}$ for structure cell of CrSb. The vertical broken line represents the magnetic transition temperature T_{λ} .

in which c and a are plotted against the temperature T . Another sample of CrSb was prepared using a similar technique to that described above, and the lattice parameter measurements for this sample are also included in Fig. 1.

Both (c, T) and (a, T) curves possess a point of inflexion in the neighbourhood of 400° C. Thus the curves are divided into two portions on either side of the antiferromagnetic transition temperature T_{λ} . Between -180° C. and T_{λ} , c and dc/dT increase steadily with temperature; above T_{λ} , c increases less rapidly with temperature and dc/dT is constant.

The value of the axial ratio c/a increases from 1.335 at room temperature to 1.422 at 420° C. Further, the linear expansion coefficient (α_c) along the c axis is exceptionally large between these two temperatures. Its value just below T_{λ} is approximately 3×10^4 per deg. C. It is remarkable that, whereas α_c is large and positive over the whole temperature range of -180° C. to 650° C., α_a is zero above T_{λ} and negative for several hundred deg. C. below T_{λ} .

In Fig. 1 the broken line represents the variation with temperature of $V^{1/3}$, where V ($= 0.866 ca^2$) is the structure cell volume. The slope of this curve is approximately uniform and the curve passes smoothly through the transition region in the neighbourhood of 400°C .

Discussion

In CrSb the magnetic atoms (Cr) are arranged in plane sheets perpendicular to [0001]. The results just described indicate that the distance between these sheets decreases anomalously as the temperature is lowered through the transition point. This effect takes place without any sudden change of structure cell volume or change of crystal symmetry. According to Snow (1952) the magnetic moments of the chromium atoms in a given (0001) plane are all parallel, but moments in neighbouring planes are antiparallel. Thus the antiferromagnetic exchange forces are directed predominantly along the [0001] direction, an interpretation which is strongly supported by the present work.

It is interesting to note that MnTe, which is also an antiferromagnetic compound with the NiAs-type structure, undergoes a similar decrease of c/a (Greenwald, 1952) on being cooled through the transition temperature near 35°C . The magnitude of the change for MnTe is, however, considerably smaller than in CrSb.

The transition temperature of CrSb has been variously reported as 400°C . (Foëx & Graaf, 1939) and 450°C . (Snow, 1952). It is not possible to obtain a more precise value from the shape of the magnetic susceptibility-temperature curve, as the maximum in this curve is exceptionally broad. If we assume that the lattice changes in CrSb appear as soon as the temperature falls below T_1 , we can determine the value of T_1 from Fig. 1 as $420 \pm 10^\circ\text{C}$.

References

- FOËX, G. & GRAAF, S. (1939). *C. R. Acad. Sci., Paris*, 209, 160.
GREENWALD, S. (1951). *Nature, Lond.* 168, 397.
GREENWALD, S. (1952). Private communication.
OWEN, E. A. (1943). *J. Sci. Instrum.* 20, 190.
ROOKSBY, H. P. (1948). *Acta Cryst.* 1, 226.
ROOKSBY, H. P. & TOMBS, N. C. (1951). *Nature, Lond.* 167, 364.
SNOW, A. I. (1952). *Phys. Rev.* 85, 365.
TOMBS, N. C. (1952). *J. Sci. Instrum.* 29, 364.
WILLIS, B. T. M. & ROOKSBY, H. P. (1952). *Proc. Phys. Soc. B*, 65, 950.
WYCKOFF, R. W. G. (1951). *Crystal Structures*, Vol. 1. New York: Interscience Publishers.

Acta Cryst. (1953). 6, 565

The low-temperature crystal structure of magnetite.* By H. P. ROOKSBY and B. T. M. WILLIS,
Research Laboratories of The General Electric Company Limited, Wembley, England

(Received 21 February 1953)

In a recent communication Abrahams & Calhoun (1953) have presented new evidence concerning the low-temperature structure of magnetite, Fe_3O_4 . They conclude that the structure cell deforms on cooling below 115°K . to give an orthorhombic arrangement rather than the rhombohedral arrangement previously proposed by Tombs & Rooksby (1951).

Since Tombs & Rooksby's paper was written we have obtained additional results that support a rhombohedral deformation. It is the purpose of this note to record these results, and to indicate the difficulties of reconciling them with an orthorhombic low-temperature structure for magnetite.

If Abrahams & Calhoun's evidence for an orthorhombic change is carefully studied, it is found to rely principally on the detection of a splitting of the cubic 800 line into two components at liquid-nitrogen temperature. This line should remain unsplit for a rhombohedral transition. Because the 800 doublet separation, measured by Abrahams & Calhoun with a Norelco spectrometer, was so small, viz. 4 min. of arc (Fe $K\alpha$ reflection), and the general fit of all our earlier data with the rhombohedral interpretation so close, we undertook further studies by photographic methods. Powder photographs were taken at liquid-air (95°K .) and liquid-nitrogen (80°K .) temperatures using Co K and Cr K radiations. In this way we examined the splitting of a wide range of reflexions,

including 440, 444 and 840, in addition to the 533, 731 and 800 lines studied by Abrahams & Calhoun.

Through the courtesy of Dr Abrahams we were able to examine a specimen of his magnetite powder. Results were in every respect similar to results obtained with our own preparations, so that possible ambiguities arising from use of materials of different origins are eliminated.

Planar spacing values for components of split reflexions gave in every instance the separations predicted by a rhombohedral structure cell with dimensions

$$a_R = 5.940 \text{ \AA}, \alpha = 59^\circ 47.5' \text{ at } 80^\circ \text{ K}.$$

Making the assumption that the atomic co-ordinates correspond with those in the cubic arrangement, the calculated and observed relative intensities of resolved components agree better with the rhombohedral than with the orthorhombic interpretation. The evidence on lines 440, 533, 444, 800 and 840 is summarized in Table 1.

It may be noted that we have not been able to detect any splitting of 800 photographically, though noticeable broadening might have been expected with a separation of the magnitude indicated by Abrahams & Calhoun. Attention, however, may be drawn particularly to the manner of splitting of 440. The splitting is disclosed clearly in either liquid-air or liquid-nitrogen temperature photographs taken with Cr radiation. Two equally strong components, with a separation of approximately 13 min., occur for the α doublet wave-length, and a corresponding splitting is seen with the β reflexion, in which any intensity ambiguity due to overlaps is naturally absent.

* Communication No. 543 from the Staff of the Research Laboratories of The General Electric Company Limited, Wembley, England.

Table 1.

Throughout the table lines are referred to in order of increasing θ

Cubic hkl	Form of splitting observed below transition temperature	Expected result for rhombohedral interpretation	Expected result for orthorhombic interpretation
440	Two components of approximately equal intensities	Split into two components, 208 and 220 (hexagonal indices). Ratio of multiplicity factors 1 : 1	Split into three components, 040, 224 and 400. Multiplicity factors 1 : 4 : 1
533	Three components, the two outer ones (highest θ values) being just resolved. Inner component considerably weaker than the combined outer components	Split into three components, 1,0,11, 315 and 401; the last two nearly coincide. Multiplicity factors 1 : 2 : 1	Split into four components, 143, 035, 305 and 413. Multiplicity factors 2 : 1 : 1 : 2
444	Two components, the inner one considerably weaker than the outer one	Split into two components, 0,0,12, and 404. Multiplicity factors 1 : 3	Split into two components, 044 and 404. Multiplicity factors 1 : 1
800	No splitting or broadening noticeable down to 80° K.	No splitting	Split into two components, 008 and 440. Multiplicity factors 1 : 2
840	Two components of approximately equal intensities	Split into two components, 2,2,12 and 244. Multiplicity factors 1 : 1	Split into four components, 260, 444, 228 and 620. Multiplicity factors 1 : 2 : 2 : 1

The relevant section of the photograph is reproduced in Fig. 1. (This photograph also contains the 511 α reflexion.

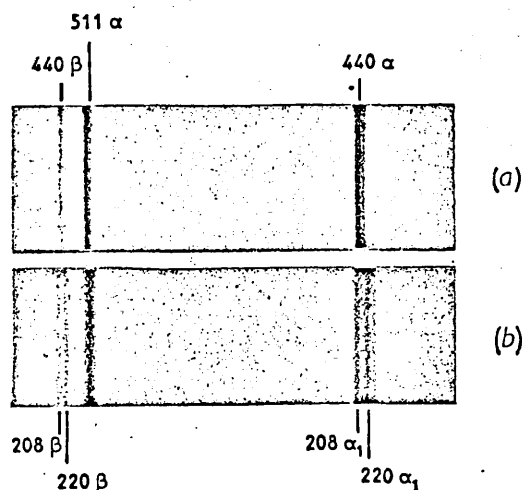


Fig. 1. Sections of powder photographs (19 cm. camera, Cr K radiation) at $\times 2$ magnification showing splitting of cubic 440 line into two components at 80° K. (a) 295° K.; (b) 80° K.

Since this line originates from planes making a relatively small angle with planes of the {100} form, separation between the components of the split reflexion at 80° K. is small and only slight broadening is noticeable.)

This simple splitting of 440 is exactly that to be expected for the rhombohedral deformation along [111]. For the orthorhombic change we expect three components with the middle one approximately four times as strong as the other two. We believe that the behaviour of 440 is thus of utmost importance when deciding between the two proposed low-temperature structures.

In this connexion it is perhaps relevant to mention

results on FeO, for which a substantial rhombohedral deformation at 95° K. has been observed (Rooksby & Tombs, 1951). Line-splitting effects in low-temperature powder photographs of FeO are closely analogous to those found for Fe₃O₄. Owing to the greater magnitude of the deformation of FeO, however, the separation of the two components of line 220 is much larger than in the case of the 440 line for Fe₃O₄, but line 400 remains unsplit. It is hoped to publish the results on FeO in more detail in the near future.

Summarizing, the additional experimental evidence obtained by photographic methods appears to provide adequate confirmation of the original interpretation of the transition in magnetite at low temperatures as a rhombohedral structural deformation. It is admitted that this interpretation does not explain the small splitting of 800 observed by Abrahams & Calhoun. On the other hand we have not been able to detect such splitting by photographic means.

Ultimately, when the structure change is studied in very precise detail, it may be found that the symmetry is lowered to monoclinic or triclinic, but a principal dilatation along [111] appears to be reasonably consistent with the present evidence. It will probably require investigations on single crystals at temperatures below 80° K. to settle the issue unequivocally.

We should like finally to express our thanks to Dr Abrahams for allowing us to see his paper before publication.

References

- ABRAHAMS, S. C. & CALHOUN, B. A. (1953). *Acta Cryst.* 6, 105.
 ROOKSBY, H. P. & TOMBS, N. C. (1951). *Nature, Lond.* 167, 364.
 TOMBS, N. C. & ROOKSBY, H. P. (1951). *Acta Cryst.* 4, 474.

(Reprinted from *Nature*, Vol. 172, p. 1054, December 5, 1953)

Crystal Structure and Magnetic Properties of Cobalt Ferrite at Low Temperatures

COBALT ferrite ($\text{CoO} \cdot \text{Fe}_2\text{O}_3$) and magnetite ($\text{FeO} \cdot \text{Fe}_2\text{O}_3$) both crystallize at room temperature with the inversed-spinel-type of structure¹. A magnetic transition consisting of an abrupt decrease of saturation magnetization takes place in magnetite² at 116° K., and is accompanied by a slight deformation of the structure cell from cubic symmetry above the transition to approximately rhombohedral symmetry below³. As cobalt ferrite⁴ undergoes a similar magnetic transition at 90° K., we might expect that, like magnetite, it is no longer cubic below its magnetic transition temperature. We have shown by means of X-ray powder photography that this is indeed true, but the departure from cubic symmetry is even smaller than in the case of magnetite. Our results indicate that the structure cell of cobalt ferrite at low temperatures is approximately tetragonal.

Powder photographs were taken at liquid nitrogen temperature (80° K.) with a 19-cm. camera; both cobalt $K\alpha$ and iron $K\alpha$ radiations were employed. Several different specimens were prepared by mixing appropriate proportions of pure CoO and $\alpha\text{Fe}_2\text{O}_3$, and firing the mixture in air for several hours at 1,100° C. The departure from cubic symmetry was revealed by splitting of some of the high-order, originally cubic lines. The cubic 840 and 800 reflexions were each split into two components with intensities approximately in the ratio 2:1, in order of increasing Bragg angle. No splitting of the high-order 444 (iron $K\alpha$) and 555 (cobalt $K\alpha$) reflexions could be detected.

This behaviour indicates that there is a principal dilatation along a [100] direction, so that the structure cell is approximately tetragonal with c/a slightly less than unity. This interpretation requires 840 to be split into three tetragonal components (840, 804 and 408); but the first two of these are too close together to be resolved. In the accompanying table we give several independent values of c/a , deduced from measurements on split cubic reflexions. These values are in fairly good mutual agreement. In view of the extreme smallness of the lattice deformation, it would be of interest to study the line splitting in more detail by means of a sensitive counter spectrometer.

Cubic reflexion	Tetragonal indices	Wave-length	Value of c/a
800	800, 008	Iron $K\alpha_1$	0.99368
800		Iron $K\alpha_2$	0.99870
840	840 $\left\{ \begin{array}{l} 804 \\ 408 \end{array} \right.$	Cobalt $K\alpha_1$	0.99885

We believe that the X-ray results on Fe_2O_4 and CoFe_2O_4 at low temperatures are relevant to the interpretation of the low-temperature magnetic transitions. The changes of symmetry take similar forms to those observed in FeO and CoO respectively, as these monoxides are cooled below their anti-ferromagnetic Curie temperatures⁵. Thus FeO and $\text{FeO}\cdot\text{Fe}_2\text{O}_3$ are both rhombohedral at low temperatures, with the rhombohedral angle α_R slightly less than 60° , and CoO and $\text{CoO}\cdot\text{Fe}_2\text{O}_3$ are both tetragonal with c/a slightly less than unity. Verwey's theory⁶ of the origin of the low-temperature transition in magnetite involves an ordering of the valency electrons in the octahedral sites. His model requires a low-temperature tetragonal symmetry, whereas the observed symmetry is more nearly rhombohedral. The observed low-temperature symmetry in cobalt ferrite is tetragonal, but Verwey's model cannot explain this as electronic interchange between Co^{2+} and Fe^{3+} is more or less inhibited. We conclude that Verwey's theory cannot explain the origin of the low-temperature transitions in either magnetite or cobalt ferrite. The correct solution may be found by considering the close similarity of their structural behaviour with that of the corresponding simple monoxides.

H. P. ROOKSBY
B. T. M. WILLIS

Research Laboratories,
The General Electric Co., Ltd.,
Wembley. Aug. 17.

¹ Verwey, E. J. W., and Heilmann, E. L., *J. Chem. Phys.*, **15**, 174 (1947).

² Weiss, P., and Forrer, R., *Ann. de Phys.*, (10), **12**, 279 (1929).

³ Rooksby, H. P., and Willis, B. T. M., *Acta Cryst.*, **6**, 565 (1953).
Abrahams, S. C., and Calhoun, B. A., *Acta Cryst.*, **6**, 105 (1953).

⁴ Guillaud, C., and Creveaux, H., *C.R. Acad. Sci., Paris*, **230**, 1256 (1950).

⁵ Tombs, N. C., and Rooksby, H. P., *Nature*, **165**, 442 (1950).

⁶ Verwey, E. J. W., Haayman, P. W., and Romelijn, F. C., *J. Chem. Phys.*, **15**, 181 (1947).

Magnetic Transitions and Structural Changes in Hexagonal Manganese Compounds

By B. T. M. WILLIS AND H. P. ROOKSBY

Research Laboratories of The General Electric Company, Limited, Wembley, England

MS. received 2nd December 1953, and in amended form 13th January 1954

Abstract. The lattice parameters of the isomorphous compounds MnAs, MnSb and MnBi have been measured over a temperature range which includes the temperatures at which certain magnetic transitions occur. Characteristic changes develop near the magnetic transition temperatures and are of two kinds: (a) discontinuous changes of lattice dimensions (MnAs at 40°C, MnBi at 320°C), which are associated with magnetic transitions of the first order, (b) discontinuous changes of the temperature derivatives of the lattice parameters (MnAs at 130°C, MnSb at 320°C), associated with second-order magnetic transitions.

Correlation of the results on MnAs and MnSb with those obtained by Greenwald on MnTe indicates that the magnetic exchange energy for manganese atoms at a distance r apart is a maximum for $r = 2.94 \text{ \AA}$.

The magnetic change which takes place in MnBi near 440°C is caused by decomposition of the material and is not a Curie point phenomenon.

§ 1. INTRODUCTION

ALL four manganese compounds, MnAs, MnSb, MnBi and MnTe, which crystallize at room temperature with the hexagonal NiAs type of structure (figure 4), show interesting magnetic changes between room temperature and 600°C. These changes consist of transitions between ferromagnetic, antiferromagnetic and paramagnetic states (see table 1), but there is some doubt concerning the precise nature of the transitions in MnAs and MnBi. For convenience we shall denote antiferromagnetic-ferromagnetic, antiferromagnetic-paramagnetic and ferromagnetic-paramagnetic changes by symbols, namely A-F, A-P and F-P respectively.

Table 1. Magnetic States of Hexagonal Manganese Compounds

	Ferromagnetic	Antiferromagnetic	Paramagnetic	Reference
MnAs	< 45°C	? 45-130°C	> 130°C	Guillaud (1951 a)
MnSb	< 313°C	↔	> 313°C	Serres (1947)
MnBi	< 360°C	? 360-445°C	> 445°C	Guillaud (1951 a)
MnTe	—	< 50°C	> 50°C	Serres (1947)

MnSb possesses a ferromagnetic Curie point at 313°C, MnTe an antiferromagnetic Néel point at 50°C. The magnetic changes shown by MnAs and MnBi, which are both ferromagnetic at room temperature, are more complex. In the case of MnAs the ferromagnetism disappears at 45°C on heating, but reappears at a lower temperature, 34°C, on cooling. Guillaud (1951 a) has

suggested that this magnetic change is a first-order F-A transition, and that MnAs does not become paramagnetic until a higher temperature, 130°C, is attained. He believes that the magnetic behaviour of MnBi, with corresponding changes at 360°C (or 340°C on cooling) and 445°C, can be similarly explained.

The present work comprises an investigation of the variation with temperature of the lattice parameters of MnAs, MnSb and MnBi. It is shown that characteristic changes of lattice dimensions but not of structure type occur in the neighbourhood of the magnetic transition temperatures. Further, these changes give some indication of the nature of the associated magnetic transitions.

Guillaud (1951 b) has previously reported discontinuous changes of lattice parameter at 45°C for MnAs and 360°C for MnBi, but there are certain significant differences between our results and his. We have also extended the measurements to include the higher temperatures at which the additional magnetic transitions in MnAs and MnBi occur. For MnTe a lattice dilatation at the antiferromagnetic Néel point has been recently noted by Greenwald (1953). All these results are considered in more detail in the discussion below.

§ 2. EXPERIMENTAL PROCEDURE

Powder photographs were taken between room temperature and 600°C using a 19-cm Unicam high-temperature camera and CuK α radiation. This is not the best choice of radiation for manganese compounds, because of secondary fluorescence effects. But since it was necessary to seal the specimens in evacuated silica capillaries, the employment of the softer iron radiation would have required unduly long exposures.

All compounds were prepared by mixing appropriate quantities of the constituent elements and heating in sealed evacuated silica tubes. The preparations of MnAs and MnSb were straightforward. In the case of MnAs, pure manganese and arsenic in the proportions 40:60 atomic per cent respectively were well ground together and heated for 20 hours at 800°C. With the exception of one end the tube was lagged, so that during cooling to room temperature the excess arsenic collected at the unlagged end. MnSb was prepared by heating equimolecular proportions of manganese and antimony for one hour at 800°C. Powder photographs of these preparations revealed only lines for compounds having the NiAs-type structure.

The preparation of MnBi presented certain difficulties. According to Adams, Hubbard and Syeles (1952), the formation of MnBi from manganese and bismuth takes place by means of a peritectic reaction. After numerous experiments the most satisfactory preparation was obtained as follows. Manganese and bismuth were mixed in the ratio 45:55 atomic per cent and heated *in vacuo* for one hour at 1000°C. The temperature was then lowered slowly to 440°C, held there for several hours, and finally reduced to room temperature. The powder photograph of the product showed the presence of MnBi (NiAs-type structure) and bismuth in roughly equal proportions. Further enrichment of the MnBi content was achieved by magnetic separation. Little confusion in interpretation was caused by residual bismuth in the specimen as the principal x-ray observations were made above the melting point of bismuth. We must emphasize, however, that the results on MnBi described below refer to the alloy in the presence of excess bismuth.

§ 3. RESULTS

The x-ray data are conveniently summarized in the lattice parameter-temperature curves, figures 1-3.

MnAs

As the temperature rises through 39°C (figure 1) a discontinuous decrease of a takes place, leading to a contraction of structure cell volume of 2%. No corresponding change takes place in the c -axis direction. The precise magnitudes of these lattice changes are recorded in table 2.

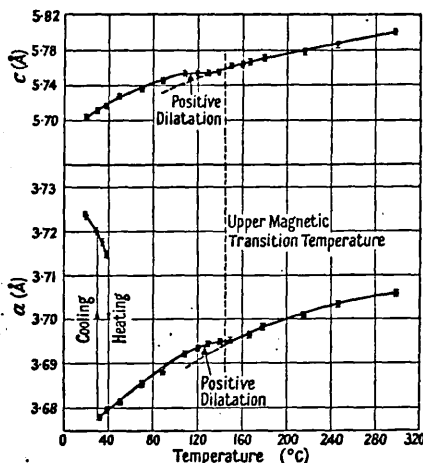


Figure 1. Curves showing variations with temperature of structure cell dimensions of MnAs.

Table 2. Lattice Dimensions of MnAs, MnSb and MnBi

Temp. (°C)	MnAs		MnSb	MnBi		
	Just below	Just above	20	20	Just below	Just above
	39	39			320	320
a (Å)	3.724	3.715	4.128	4.286	4.310	4.380
c (Å)	5.706	5.721	5.789	6.116	6.182	5.991
$V^{1/3}$ (Å)		4.090	4.064		4.634	4.634

By careful adjustment of the temperature of the two furnaces it was found possible to produce a temperature gradient of a few degrees across a specimen at the mean temperature of 39°C. In this way diffraction lines of both low- and high-temperature 'structures' were recorded on the same film. The two sets of lines could easily be distinguished, as they were inclined at a small angle to each other. All lines were sharp and clearly defined, showing that the lattice change was strictly discontinuous.

The change exhibited small thermal hysteresis. On cooling the material from above 39°C the lines of the low-temperature structure failed to re-appear until a temperature of 32°C was reached.

These results are in good agreement with those of Guillaud (1951 a), who measured the lattice parameters at two points on the heating curve, at 20°C and 45°C. Minor differences between the two sets of results, such as small differences in the absolute values of lattice dimensions and of transition.

temperatures, can probably be accounted for on the basis of a small difference of composition.

The second region of interest in figure 1 is in the neighbourhood of 140°C, where both the (a , T) and (c , T) curves show an inflection. The lattice dilatation involved here is characteristic of an A-P change. For other antiferromagnetic compounds with rhombohedral or hexagonal symmetry, e.g. Cr_2O_3 (Smart and Greenwald 1951), $\alpha\text{-Fe}_2\text{O}_3$ (Willis and Rooksby 1952) and CrSb (Willis 1953), the anomalous dilatation occurs principally along the c -axis direction. But there appears to be no reason in principle why the dilatation should not take place normal to this axis as in MnAs. Thus the x-ray data support the suggestion of Guillaud (1951 a), based on magnetic evidence, that an A-P change occurs at approximately 130°C.

MnSb

The (a , T) curve (figure 2) shows a pronounced inflection near 320°C, whereas the (c , T) curve is of nearly uniform slope throughout the entire range from room temperature to 600°C. The ferromagnetic Curie point is 314°C.

MnBi

There is a discontinuous change in both a and c at 320°C (figure 3), a increasing by 1.5% and c decreasing by 3% on heating through this temperature. The resulting change of cell volume is less than 0.1% (table 2).

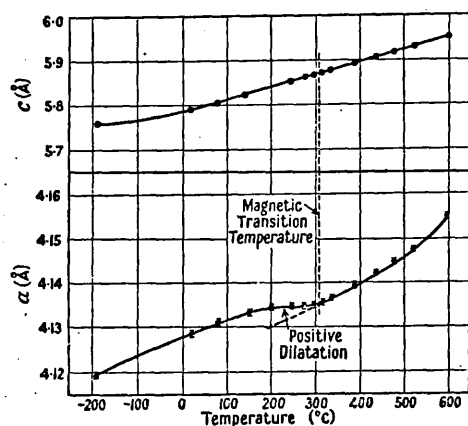


Figure 2. Curves showing variations with temperature of structure cell dimensions of MnSb.

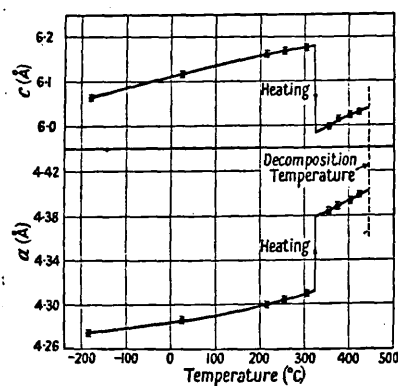


Figure 3. Curves showing variations with temperature of structure cell dimensions of MnBi.

We are unable to explain completely the differences between these results and those of Guillaud (1951 b), who was the first to observe this dilatation. Guillaud made x-ray measurements at room temperature on two samples, one of ferromagnetic MnBi cooled slowly from above the transition, and the other of non-ferromagnetic MnBi rapidly quenched from 400°C. He deduced that c decreases by 5% whilst a remained unchanged on heating through 360°C. There are thus differences both in the nature of the dilatation and the temperature at which it occurs. On the other hand, our results are in good agreement with the observations of Adams, Hubbard and Syeles (1952), who give $c = 5.87 \pm 0.02$ Å for MnBi rapidly quenched from 320°C.

On heating samples of MnBi beyond 320°C we observed an irreversible change of structure in the region of 435°C. The diffraction lines of the NiAs-type structure were replaced by lines of an unidentified phase, and this phase persisted on subsequent cooling below 435°C. The existence of a magnetic change at 440°C has been known for some time. Fürst and Halla (1938) attributed it to a Curie point change, whereas other authors (Bekier 1914, Siebe 1919) considered that a peritectic reaction takes place at 440°C. More recently Guillaud (1951 a) and Smart (1953) have lent support to the former point of view in suggesting that 440°C represents the antiferromagnetic Néel temperature of MnBi. The present results show clearly that decomposition of MnBi occurs before the Néel temperature, if it exists, is reached, and that there is therefore a fundamental difference between the behaviour of MnAs and MnBi at their upper magnetic transition points (130°C and 440°C respectively). The magnetic change in MnAs is an order-disorder effect, which involves no structural change apart from a small adjustment of lattice parameters; in MnBi the magnetic change is caused by decomposition.

§ 4. GENERAL DISCUSSION

Magnetic changes taking place without alteration of composition or phase can be broadly classified into transitions of the first or second order (Smart 1953). The former include F-A transitions and give rise to a discontinuous change of orientation of electron spins. Second-order transitions include F-P and A-P changes; in these an ordering of spin orientations develops gradually on cooling below the transition temperature.

The x-ray measurements on hexagonal manganese compounds demonstrate that characteristic lattice changes accompany these two kinds of magnetic change. Thus first-order magnetic transitions occur in MnAs at 40°C and in MnBi at 320°C, and are accompanied by discontinuous changes of lattice parameters. (By dilatometric measurements on polycrystalline compacts Smits, Gerding and Vermast (1931) observed a volume change in MnAs near 40°C. Investigation of MnBi by a similar method, however, would fail to indicate a first-order change since there is no overall alteration of structure cell volume.) The second-order magnetic transitions in MnAs at 130°C, in MnSb at 314°C, and in MnTe at 50°C (Greenwald 1953), are not characterized by abrupt changes in lattice dimensions but by discontinuous variations in the temperature derivatives of these dimensions. The lattice parameter-temperature curves are reversible for second-order changes; in the case of first-order changes there is thermal hysteresis in the transition region.

Occasionally it is even possible to distinguish between second order F-P and A-P changes by purely x-ray means. F-P transitions in cubic substances (e.g. α -Fe at 770°C) take place without change of lattice symmetry, whereas A-P transitions in materials which are cubic in the paramagnetic region (e.g. NiO, MnO, CoO) lead to a slight deformation to rhombohedral or tetragonal symmetry below the transition point. No change of symmetry occurs in non-cubic substances (e.g. MnSb, MnAs, MnTe) and the above distinction does not arise.

Smart (1953) has considered theoretically the dilatation accompanying first-order magnetic changes. He suggests that the magnetic atoms in the majority of antiferromagnetic materials are arranged in sheets of atoms of the

same spin, so that in an A-F change a dilatation takes place normal to these sheets. Thus in MnBi he considers the sheets to be normal to the c -axis, and in MnAs to contain the c -axis. Unfortunately, his model for MnBi fails to account for the abrupt change in both a and c ; moreover, for MnAs one would expect a symmetry lower than hexagonal in the antiferromagnetic region, whereas the x-ray results give no evidence of such an effect.

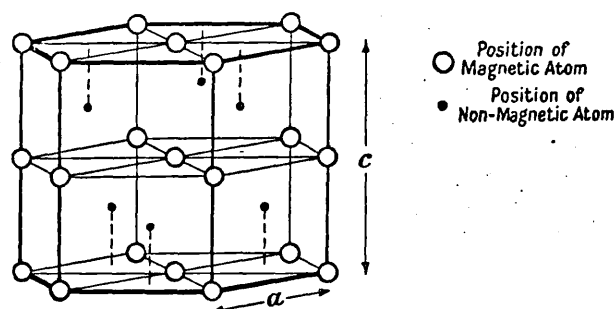


Figure 4. NiAs-type crystal structure: the magnetic atoms occur in plane sheets, normal to the c -axis and of spacing $c/2$.

Theoretical treatments of the thermal expansion associated with second-order changes have been given by Néel (1937), Shockley (1939), and Greenwald and Smart (1950). According to the latter authors the exchange interaction J between neighbouring magnetic atoms leads to a deepening of the magnetic energy levels by a factor $2Z|J|S^2$. S is the total spin quantum number of a single atom and Z is the number of nearest neighbours. As J is a function of the separation r of magnetic atoms, the exchange interactions will in general produce a change of r leading to an increase of J . In fact it is easy to show (Shockley 1939) that there is an increase or decrease of r according to whether $\partial J/\partial r$ is positive or negative. In the special case of $\partial J/\partial r = 0$ there is no change of r , i.e. no anomalous lattice dilatation.

The theory can be applied to magnetic materials of the NiAs type, noting that nearest magnetic neighbours to a given magnetic atom lie along the c axis and are at a distance away of $c/2$ (see figure 4). The observed sign of the dilatation in the c direction is given in table 3 for the Mn compounds MnAs, MnSb and MnTe. (The data for MnTe were taken from Greenwald 1953). The dilatation is zero for MnSb and we can conclude that $\partial J/\partial r = 0$ for $r = \frac{1}{2}c = 2.94\text{\AA}$, where J is the exchange interaction between neighbouring Mn atoms; $\partial J/\partial r$ is positive for $r = 2.88\text{\AA}$ and negative for $r = 3.36\text{\AA}$. From these data the curve in figure 5(a), relating J and r , has been constructed. J is given in arbitrary units and the ordinates corresponding to the points for MnAs and MnTe have been estimated roughly, assuming that $\partial J/\partial r$ is proportional to the observed magnitude of the dilatation.

It is of interest to compare figure 5(a) with figure 5(b), which represents the (J, r) curve for Mn as deduced by Guillaud (1943) using an independent method. Guillaud's method consisted of plotting the second-order transition temperature T_c against r . T_c can be taken as a measure of J (in arbitrary units), as T_c is related simply to J by the equation $T_c = Z|J|/2k$, where k is Boltzmann's constant. There is serious doubt as to the validity of including the point for MnBi in

figure 5(b). Guillaud assumed that MnBi possessed a second-order transition point at 440°C, whereas the present work indicates that there is instead a complete transformation. Figure 5(b) contains an additional point for MnTe, which was not included by Guillaud. The correspondence between figures 5(a) and (b)

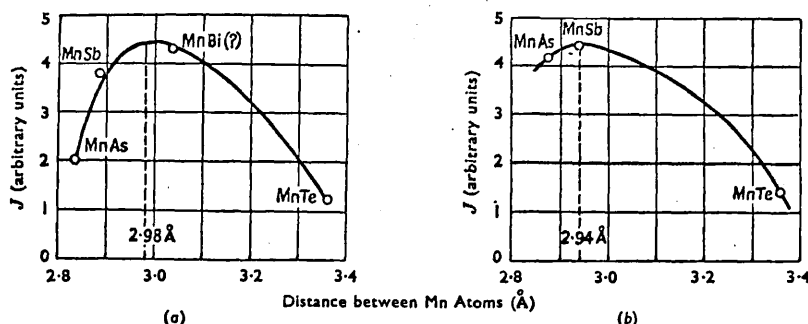


Figure 5. (J, r) curves: (a) from x-ray data, (b) from magnetic data, based on Guillaud (1943).

appears to be fairly good. Both curves indicate that J passes through a maximum value (in accordance with the theoretical considerations of Bethe, see Bozorth 1951), and the closeness of the two estimates, 2.94 Å and 2.98 Å, for the position of the maximum is noteworthy. Unfortunately the two curves possess too few points. Additional points could be obtained by taking observations on materials with different c parameters, and the preparation of solid solutions between the several compounds may well provide the required range of c values.

Table 3. Lattice Dilatation at Second-Order Transition

Compound	$r (=c/2)$	Obs. sign of dilatation	Sign of $\partial J/\partial r$
MnAs	2.88 Å	+ve (figure 1)	+ve
MnSb	2.94 Å	0 (figure 2)	0
MnTe	3.36 Å	-ve	-ve

REFERENCES

- ADAMS, E., HUBBARD, W. M., and SYELES, A. M., 1952, *J. Appl. Phys.*, **23**, 1207.
 BEKIER, E., 1914, *Intern. Z. Metallographie*, **7**, 83.
 BOZORTH, R. M., 1951, *Ferromagnetism* (New York: Van Nostrand).
 FÜRST, U., and HALLA, F., 1938, *Z. phys. Chem. B*, **40**, 285.
 GREENWALD, S., 1953, *Acta Cryst., Camb.*, **6**, 396.
 GREENWALD, S., and SMART, J. S., 1950, *Nature, Lond.*, **166**, 523.
 GUILLAUD, C., 1943, *Thesis*, University of Strasbourg.
 GUILLAUD, C., 1951 a, *J. Phys. Radium*, **12**, 223; 1951 b, *Ibid.*, **12**, 143.
 NÉEL, L., 1937, *Ann. Phys., Paris*, **11**, 8, 237.
 SERRES, A., 1947, *J. Phys. Radium*, **8**, 146.
 SHOCKLEY, W., 1939, *Tech. Publ. Bell Tel. Syst.*, **18**, 645.
 SIEBE, Z., 1919, *Z. anorg. Allgem. Chem.*, **108**, 161.
 SMART, J. S., 1953, *Phys. Rev.*, **90**, 55.
 SMART, J. S., and GREENWALD, S., 1951, *Phys. Rev.*, **82**, 113.
 SMITS, A., GERDING, H., and VERMAST, F., 1931, *Z. phys. Chem. (Bodenstein Festband)*, p. 357.
 WILLIS, B. T. M., 1953, *Acta Cryst., Camb.*, **6**, 425.
 WILLIS, B. T. M., and ROOKSBY, H. P., 1952, *Proc. Phys. Soc. B*, **65**, 950

Dr. Moreton Moore

For Use in the Library.



- ◆ Department of Physics
- ◆ Dr Moreton Moore
Reader in Crystallography
- ◆ Royal Holloway
University of London
Egham
Surrey TW20 0EX
- ◆ College 01784 434455
Direct Line 01784 443441
Fax 01784 472794

1996 May 16

To Barry Wintour
Librarian

Dear Barry,

The accompanying letter has been passed to me for action. As it happens, I know Terry Willis well and I'd like to help.

What is the situation regarding the borrowing of his Dsc Thesis?

With best wishes,

Moreton





ISIS FACILITY

Rutherford Appleton Laboratory
Chilton Didcot
Oxfordshire
OX11 0QX
Switchboard +44 (0)1235 821900

The Departmental Administrator
Department of Physics
Royal Holloway College
University of London
Egham
Surrey TW20 0EX

Phone +44 (0)1235 445684
Fax +44 (0)1235 445383
E-mail c.j.carlile@rutherford.ac.uk

15 April 1996

Dear Sir

reference
Professor B T M Willis, who graduated from Royal Holloway College with a PhD in ca 1952, was awarded a DSc degree some time in the 1970s. I am planning a scientific meeting to celebrate his 70th birthday in May 1997 and would like to see his DSc Thesis to assist me in assembling his publication list and early collaborators.

I would be most grateful for any help you could offer.

With thanks,
Yours sincerely

C J CARLILE

Head, ISIS Science Spectroscopy & Support Division

Brits index X

> GF. 24 MAY 1996

Hon Prof Physics Univ. Wales .

Consul X . Does not have a loan copy .

Univ. Wales Coll. Cardiff . X .

RHC

T
BPG
Wil.

Dsc. Depos.
1968 4 vols.
University of London .

Forty-one published works on crystallography
in 4 vols. 83.926-929 .

2. Crystal Defects (7-18)

These papers describe experimental studies (using various kinds of radiation) of the nature of the defects in crystals. Two principal types of problem were examined: radiation damage caused by fast neutron irradiation, and the oxygen defects associated with departures from stoichiometry in uranium dioxide. These problems are related to the research programme at Harwell, where the bulk of the work was carried out.

2

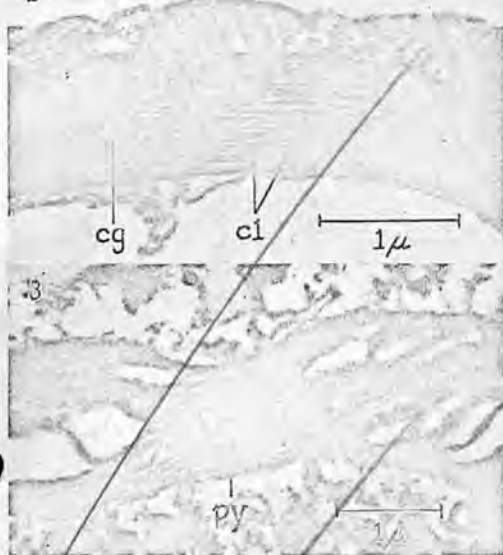


Fig. 2. Section through a chloroplast showing lamellae (cl), inter-lamellar spaces and some chloroplast granules (cg). $\times 20,000$
 Fig. 3. Section through a chloroplast showing the pyrenoid (py). $\times 16,000$

selves are below the limit of resolution of this instrument. Since the size of the chlorophyll molecule is below the limit of resolution of the electron microscope, nothing can be said at present about the location of chlorophyll in respect to the lamellae.

A dense body found in the centre of the chloroplasts in some of our electron micrographs is interpreted as the pyrenoid; it appears as a condensation of inter-lamellar material, with which it is frequently continuous. The lamellae can be followed, in some cases, through the pyrenoid and appear to be tightly held together in this region (Fig. 3). In other instances, namely, in very dense pyrenoids, the lamellar structure seems to disappear at this level. A large cytoplasmic vacuole is frequently present outside the chloroplast in contact with the pyrenoid.

Chloroplasts with structure and organization similar to those of *Euglena* were found in *P. stipitata*. Further studies on the light versus dark reaction in the formation and structure of the chloroplasts are in progress; a full account of this work will be reported and published elsewhere⁷.

J. J. WOLKEN*
 G. E. PALADE

Rockefeller Institute for Medical Research,
 New York 21, April 18.

* Fellow of the American Cancer Society on the recommendation of the Committee on Growth, National Research Council.

¹ Weier, T. E., and Stocking, C. R., *Bot. Rev.*, 18, 14 (1952). Granick, S., "Photosynthesis in Plants" (edit. Franck and Loomis, Iowa State College Press, 1949). Frey-Wyssling, A., "Submicroscopic Morphology of Protoplasm and its Derivatives" (Elsevier Publishing Co., 1948). Rabinowitch, E. I., "Photosynthesis," 1 (Interscience Publishers, 1945).

² Menke, W., *Protoplasma*, 22, 56 (1934).

³ Menke, W., *Naturwiss.*, 28, 158 (1940).

⁴ Kausche, G. A., and Ruska, H., *Naturwiss.*, 28, 303 (1940). Menke, W., *Protoplasma*, 35, 116 (1940). Thomas, J. B., Bustraan, M., and Paris, C. H., *Biochim. et Biophys. Acta*, 8, 90 (1952).

⁵ Hutner, S. H., *Trans. Amer. Phil. Soc.*, 94, 152 (1950). Hutner, S. H., Provasoli, L., and Filfus, J. (paper to be presented on "Growth of Protozoa", *Annals N.Y. Acad. Sci.*).

⁶ Palade, G., *J. Exp. Med.*, 95, 285 (1952).

⁷ Wolken, J. J., and Palade, G., paper to be presented along with paper in Ref. 5 above.

Screw Dislocations in Quartz

In a recent letter in *Nature*, Amelinckx¹ has given evidence for the existence of screw dislocations in mica. He observed a step, 140 Å. high, which terminated on the surface: the point of termination of the step defined the point of emergence of a screw dislocation of Burgers's vector 140 Å.

I have obtained similar evidence for the existence of screw dislocations in quartz. Fig. 1 is a photograph of the major rhombohedral face (1011) of a natural quartz crystal, showing the edges of growth sheets which have spread in two separate directions, denoted α and β in the figure. The α growth fronts are continuous, and parallel to the geographical contours of the face; but the β growth fronts are discontinuous along the diagonal black line. This line is terminated on the surface at both ends, and is parallel to the line of intersection of the face with an adjacent major rhombohedral plane. Fig. 2 is the corresponding two-beam interference picture ($\lambda = 5460 \text{ Å.}$) of the area shown in Fig. 1, and shows that the diagonal line represents a step the height of which varies between 0 and 950 Å.

It is well known² that the {1011} major rhombohedral planes of quartz are planes of 'partial cleavage'. We can conclude that the diagonal line in Fig. 1 is a slip line, partial slip having taken place parallel to the major rhombohedral plane. The points of termination of the slip line, and the points along its length where a change of height occurs, mark the points of emergence of screw dislocations.

The slip line in Fig. 1 is much more visible than the growth fronts, although the latter are approximately 3000 Å. high—that is, several times higher than the maximum height of the slip step. The reason for this reduced visibility of the growth fronts is that the risers of the growth fronts make a small angle (approximately 1°) with the plane surface of the growth sheets, whereas the slip line represents a sharp, vertical step.

I have observed a growth spiral on quartz, indicating that growth had taken place from a screw dislocation of Burgers's vector 220 Å. This is therefore additional evidence for the existence of dislocations in the quartz lattice. It is hoped to publish a fuller account of a study of the topography of quartz surfaces elsewhere.



Fig. 1. ($\times 7$)

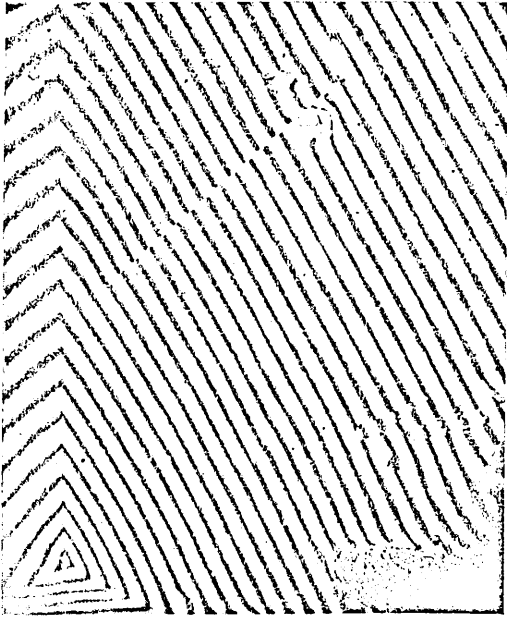


Fig. 2. ($\times 7$)

I wish to thank Prof. S. Tolansky for his continual interest in this work; the Director, Signals Research and Development Establishment, Christchurch, for the loan of the crystal; and the Chief Scientist, Ministry of Supply, for permission to publish this account.

B. T. M. WILLIS

Royal Holloway College,
(University of London),
Englefield Green,
Surrey.
May 7.

¹ Amelinckx, S., *Nature*, 169, 530 (1952).
² Nomoto, O., *Nature*, 164, 359 (1949).

The Energy Momentum Tensor in Dirac's New Electromagnetic Theory

DIRAC has recently¹ proposed a generalization of his new theory of electromagnetism so as to permit vortical streams of the electrical charge. The vortical motion has been introduced by redefining the potentials in a more general manner. Dirac has then framed two stationary principles, both of which lead back to the Lorentz equation of motion for an electric charge, with, however, the ratio, $m/e = k$, only occurring in it. The first of these stationary principles has for its action density

$$L = -\frac{1}{2} F_{\mu\nu} F_{\mu\nu} + \frac{1}{2} \lambda (v_\nu v_\nu - 1), \quad (1)$$

where the potentials are assumed to be of the form

$$A_\mu = kv_\mu + \xi \frac{\partial \eta}{\partial x_\mu}. \quad (2)$$

In these equations v_μ is the velocity vector, $v_\mu v_\mu = 1$, and ξ and η are two independent functions of the x_ν . λ is an arbitrary function of the x_ν . Varying the integral Lagrangian (1), one gets the equations,

$$v_\nu v_\nu = 1, \quad (3)$$

$$k \frac{\partial F_{\mu\nu}}{\partial x_\nu} = \lambda v_\mu \quad (4)$$

and

$$\frac{\partial F_{\mu\nu}}{\partial x_\nu} \frac{\partial \xi}{\partial x_\mu} = \frac{\partial F_{\mu\nu}}{\partial x_\nu} \frac{\partial \eta}{\partial x_\mu} = 0, \quad (5)$$

so that

$$v_\mu \frac{\partial \xi}{\partial x_\mu} = v_\mu \frac{\partial \eta}{\partial x_\mu} = 0. \quad (6)$$

(4) is the Maxwell equation, and (5) after reduction becomes the Lorentz equation

$$k \frac{dv_\mu}{ds} = v_\nu F_{\nu\mu}. \quad (7)$$

In making the variation, the A_μ , ξ , η and λ were treated as the independent field functions.

The canonical energy momentum tensor $T_{\rho\sigma}$ derived in the standard way from the Lagrangian (1) is

$$T_{\rho\sigma} = \frac{\partial kv_\lambda}{\partial x_\sigma} F_{\rho\lambda} + \frac{\partial \xi}{\partial x_\sigma} F_{\rho\nu} \frac{\partial \eta}{\partial x_\nu} + \frac{\partial \eta}{\partial x_\sigma} F_{\mu\rho} \frac{\partial \xi}{\partial x_\mu} + \delta_{\rho\sigma} L. \quad (8)$$

This tensor is not symmetrical and so with it angular momentum would not be conserved. To make it symmetrical we may proceed in the usual way (see, for example, Wentzel, "Quantum Theory of Fields", Appendix by Jauch) and add,

$$T'_{\rho\sigma} = -\frac{\partial}{\partial x_\lambda} (kv_\sigma F_{\rho\lambda}) = -\frac{\partial}{\partial x_\lambda} G_{\rho\lambda\sigma} \\ = \frac{\partial}{\partial x_\lambda} G_{\lambda\rho\sigma}. \quad (9)$$

$T'_{\rho\sigma}$ has the necessary properties of vanishing divergence and vanishing integrals of the energy and momentum components, for

$$\frac{\partial T'_{\rho\sigma}}{\partial x_\rho} = -\frac{\partial}{\partial x_\rho} \frac{\partial}{\partial x_\lambda} G_{\rho\lambda\sigma} = 0,$$

$$\int T'_{4\sigma} dx_1 dx_2 dx_3 = -\int \frac{\partial}{\partial x_\lambda} G_{4\lambda\sigma} dx_1 dx_2 dx_3 \\ = -\int \frac{\partial}{\partial x_k} G_{4k\sigma} dx_1 dx_2 dx_3 = 0.$$

Now by (4),

$$T'_{\rho\sigma} = -\frac{\partial kv_\sigma}{\partial x_\lambda} F_{\rho\lambda} - kv_\sigma \frac{\partial F_{\rho\lambda}}{\partial x_\lambda} = \frac{\partial kv_\sigma}{\partial x_\lambda} F_{\rho\lambda} - v_\sigma \lambda v_\rho. \quad (10)$$

So the symmetrical tensor, $\theta_{\rho\sigma} = \theta_{\sigma\rho}$, is

$$\theta_{\rho\sigma} = T_{\rho\sigma} + T'_{\rho\sigma} = F_{\sigma\lambda} F_{\rho\lambda} - v_\sigma \lambda v_\rho + \delta_{\rho\sigma} L. \quad (11)$$

The ξ and η variables do not appear explicitly in this formula, and the tensor is, apart from notation, of the same form as the tensor of the irrotational theory, the θ_{00} and θ_{0k} components of which have been given by Le Couteur².

I thank Prof. P. A. M. Dirac for suggesting this problem to me.

S. F. B. TYABJI

Christ's College,
Cambridge.
May 20.

¹ Dirac, P. A. M., *Proc. Roy. Soc., A*, 209, 291 (1951); *A*, 212, 303 (1952).
² Le Couteur, K. J., *Nature*, 169, 146 (1952).

(Reprinted from *Nature*, Vol. 177, p. 712 only, April 14, 1956)

Diffraction from Dislocations

WILSON¹ has calculated the nature of the diffraction from a cylindrical crystal with a single axial screw dislocation. Diffraction from an edge dislocation is more difficult to treat theoretically, because of the more complex nature of the elastic field surrounding the dislocation. An approximate treatment has been given by Wilson², who assumed that the displacements of the atoms were parallel to the Burgers vector. We have succeeded in solving the diffraction problem for a cylindrical crystal with an axial edge dislocation, in which the displacements correspond to isotropic elastic theory. Two independent methods were used: straightforward calculation (by T. S.), and direct observation in a Lipson diffractometer of the optical diffraction pattern of a two-dimensional grating representing the crystal (B. T. M. W.). In Fig. 1 we reproduce the optical diffraction pattern given by a grating representing (a) a perfect crystal (no dislocation) and (b) a simple-cubic crystal with an edge dislocation normal to the plane corresponding to the plane of the grating.

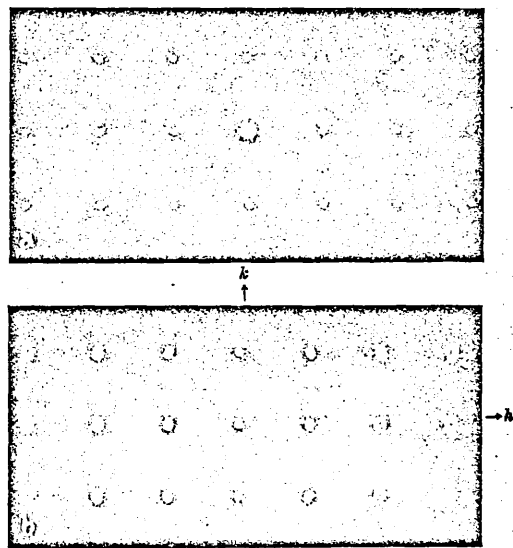


Fig. 1. Diffraction patterns from gratings representing (a) perfect crystal, (b) crystal with dislocation. The horizontal axis in (b) corresponds with the slip direction

Our results can be summarized as follows. The h -axis in reciprocal space is parallel to the slip direction (Burgers vector) and the l -axis to the axis of the dislocation. (1) Any spreading of the diffracted intensity in reciprocal space is confined to the planes $l = 0, \pm 1 \dots$, and the intensity within these planes is independent of l . (2) The $h0l$ reflexion is broader and weaker than the $0kl$ reflexion for equal values of h and k . (3) The maxima of the $h0l$ reflexion are displaced from the ideal reciprocal lattice point by an amount that increases linearly with h ; the maxima of the $0kl$ reflexion are also displaced, but the displacement is roughly independent of k for small k . (4) The intensity at the ideal $h0l$ and $0kl$ lattice points is zero for $h, k > 4$. (5) The form of the distribution of intensity around an ideal reciprocal lattice point depends on its co-ordinates in reciprocal space, on the strength of the dislocation and on the value of Poisson's ratio, but not otherwise on the crystal structure. In contrast with the case of a screw dislocation¹, the spread of intensity around the ideal reciprocal lattice point is not of circular symmetry.

These results were obtained using an average value of 0.3 for Poisson's ratio. It is clear that the diffraction pattern is quite different from that proposed by Wilson on the basis of the more approximate theory².

Our thanks are due to Prof. F. C. Frank for discussion of this problem, and to Dr. J. Thewlis, who suggested the use of the optical method for its solution.

T. SUZUKI

H. H. Wills Physical Laboratory,
Royal Fort,
Bristol 8.

B. T. M. WILLIS

Atomic Energy Research Establishment,
Harwell,
Nr. Didcot, Berks.
Dec. 13.

¹ Wilson, A. J. C., *Acta Cryst.*, 5, 318 (1952).

² Wilson, A. J. C., *Research*, 3, 387 (1950).

An X-Ray Study of Neutron Irradiated Lithium Fluoride†

By R. E. SMALLMAN and B. T. M. WILLIS
Metallurgy Division, A.E.R.E., Harwell, Nr. Didcot, England

[Received May 8, 1957]

ABSTRACT

The nature of the damage in neutron irradiated lithium fluoride has been examined by x-rays up to neutron doses at which the majority of the ions have been displaced from their lattice sites. The observations have been made by Debye-Scherrer powder photography, Laue photography and small-angle scattering. The results indicate that isolated defects predominate at low doses, but that these cluster to form large defects at doses higher than about 10^{17} neutrons/cm².

With the exception of some small-angle scattering all the x-ray effects anneal out in the range 400°–500° c. This residual scattering is interpreted as that associated with gas bubbles.

§ 1. INTRODUCTION

THE nature of the damage induced in lithium fluoride by reactor irradiation has been the subject of several recent x-ray investigations. The problem has doubtless owed its popularity to the simplicity of the unirradiated structure and, more important, to the ease with which the structure can be damaged.

Binder and Sturm (1954) showed that for a dose of 6×10^{16} neutrons/cm² the lattice expansion as measured from the change of lattice parameter was equivalent to that determined from density measurements. This indicated that the expansion was due to the production of isolated Frenkel defects, an interpretation which was later supported by annealing experiments (Binder and Sturm 1955). Keating (1955) measured the integral breadths of the 001 reflections of crystals irradiated at rather higher doses, 2.1 and 7.5×10^{17} n/cm². He observed considerable line broadening, which he interpreted in terms of a model of flat clusters of defects in the (001) plane separated by uniformly stressed material. Finally Mayer (1955) has reported measurements by Perio of the variation of lattice parameter with dose, and Brooks (1956) has reported some x-ray results of Guinier. Both these sets of results will be referred to below.

In the present work new x-ray results are reported on lithium fluoride irradiated in the range 3×10^{16} to 7×10^{18} n/cm².

† Communicated by A. H. Cottrell, F.R.S.

§ 2. IRRADIATION PROCEDURE

The standard samples were plates, $\frac{1}{2}$ mm thick, cleaved from larger single crystals obtained from Harshaw Chemical Co., U.S.A. These crystals were irradiated in the centre of BEPO, the graphite moderated reactor at Harwell, in a slow neutron flux of about 10^{12} n/cm²/sec and at a temperature of $55 \pm 15^\circ$ C.

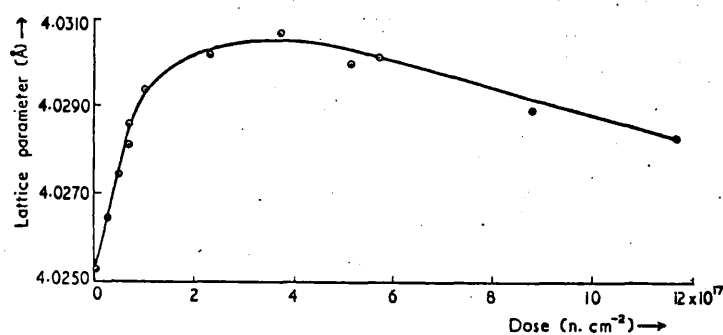
The doses were measured by determining the γ -activity of cobalt wire monitors placed with the samples. Owing to self-screening the mean dose received by a sample was less than the unscreened dose recorded by the monitor. Calculations based on the assumption of an infinite slab of $\frac{1}{2}$ mm thickness showed that the standard sample received a mean dose 80% of that recorded by the monitor. This correction has been applied to the dose figures quoted below. Self-screening also produced a variation of $\pm 3\%$ in the dose throughout a given sample; this variation is about half the error involved in estimating the relative doses.

§ 3. X-RAY RESULTS

3.1. Measurements of Lattice Parameter and Line Breadth

Debye-Scherrer photographs were taken of powders, which were prepared from fragments cleaved from irradiated single crystals. The lattice parameter a was obtained from the line positions on the photographs. Figure 1 shows the variation of a with dose. For small doses the change of a , $\Delta a/a$, is proportional to dose; at higher doses a increases to a maximum at 4×10^{17} n/cm² and then falls again. These results are in good agreement with those obtained by Perio (see Mayer 1955).

Fig. 1



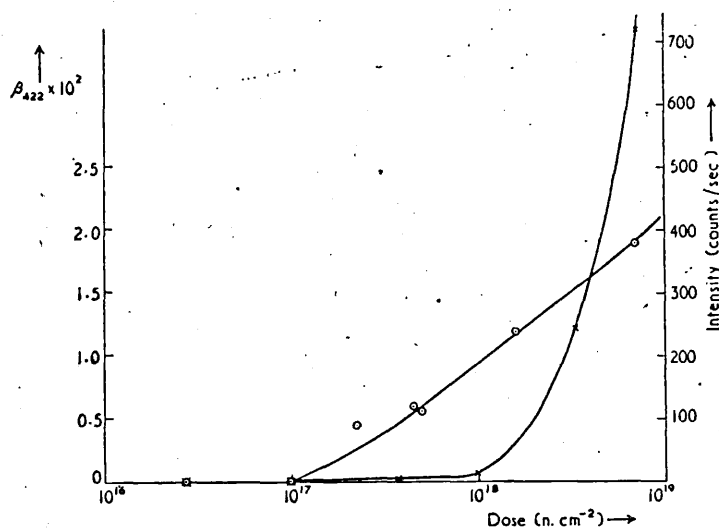
Lattice parameter of LiF as a function of slow neutron dose.

The integral breadths β_{hkl} of the powder lines were measured from line profiles obtained by microdensitometry. The instrumental broadening was corrected by the Jones (1938) method, and it was assumed that the breadth of the unirradiated crystal was entirely instrumental. A plot of $\beta \cos \theta/\lambda$ versus $2 \sin \theta/\lambda$ for the most heavily irradiated sample

(7.2×10^{18} n/cm²) was a straight line of slope 0.0042 through the origin. This showed that the line broadening was predominantly due to strain rather than crystallite size, and that the mean strain was 0.0042.

The integral breadth of the $422\alpha_1$ line as a function of dose is shown in fig. 2. β_{422} is the same as the unirradiated value up to 1×10^{17} n/cm²; above this β_{422} increases rapidly with dose and shows no sign of saturation.

Fig. 2



Integral breadth of $422\alpha_1$ line ○, and intensity of x-ray scattering at 1° x, as a function of slow neutron dose.

3.2. Laue Photographs

Transmission 'Laue' photographs, using both white and monochromatic MoK α radiation, have been taken of a number of irradiated single crystals. In the heavily irradiated (i.e. greater than 10^{18} n/cm²) samples narrow, well-defined streaks appear along the $\langle 100 \rangle$ directions. The streaks extend from the origin to the 200 reciprocal lattice points, and are produced by reflection of the characteristic MoK α radiation.

'Defect diffuse scattering' (Huang 1947), which arises from the distortion of the lattice around the individual point defects, has been carefully looked for. This scattering is difficult to observe experimentally, as it is concentrated near the strong Bragg reflections and is in a region where the thermal diffuse scattering is a maximum. However, extra diffuse scattering has been observed along the radial direction joining the reciprocal lattice point to the origin. Such a radial distribution of intensity is predicted by the theory of defect diffuse scattering (Huang 1947, Cochran 1956).

3.3. Small-angle X-Ray scattering

The apparatus used for these tests was that described by Smallman and Westmacott (1957) for the study of cold work and irradiation effects in metals. It consisted essentially of an asymmetric quartz monochromator limited with slits to give $\frac{1}{2}^\circ$ beam divergence. The sample to focus distance was 80 mm and the intensity of scattering recorded either on a film or directly using a Geiger counter.

A film taken with a crystal irradiated to 3×10^{18} n/cm² and oriented with the (100) and (001) planes respectively perpendicular and parallel to the x-ray beam, showed that the small angle scattering was approximately isotropic. It was therefore possible to use a Geiger counter (Mullard type MX118 with slit 0.3 mm \times 5 mm) to measure accurately the intensity distribution along the (100)-(001) zone. Figure 3 shows a plot of log (intensity) versus θ^2 (radians²) for six crystals irradiated with successively increasing doses of 5×10^{16} , 1.0×10^{17} , 1.0×10^{18} , 3.3×10^{18} and 7×10^{18} n/cm². The results (corrected for parasitic scattering but not for beam height) have been plotted in this way since it is known (Guinier and Fournet 1955) that for a collection of identical scattering groups the intensity scattered over an angle θ is given by

$$I = Mn^2I_e \exp(-4\pi^2K^2\theta^2/3\lambda^2). \quad \dots \dots (1)$$

Here I_e is the intensity scattered by an electron at small angles, M is the number of groups, n represents the difference between the number of electrons in one group and in an equal volume of surrounding matrix, and K is the radius of gyration of the groups.

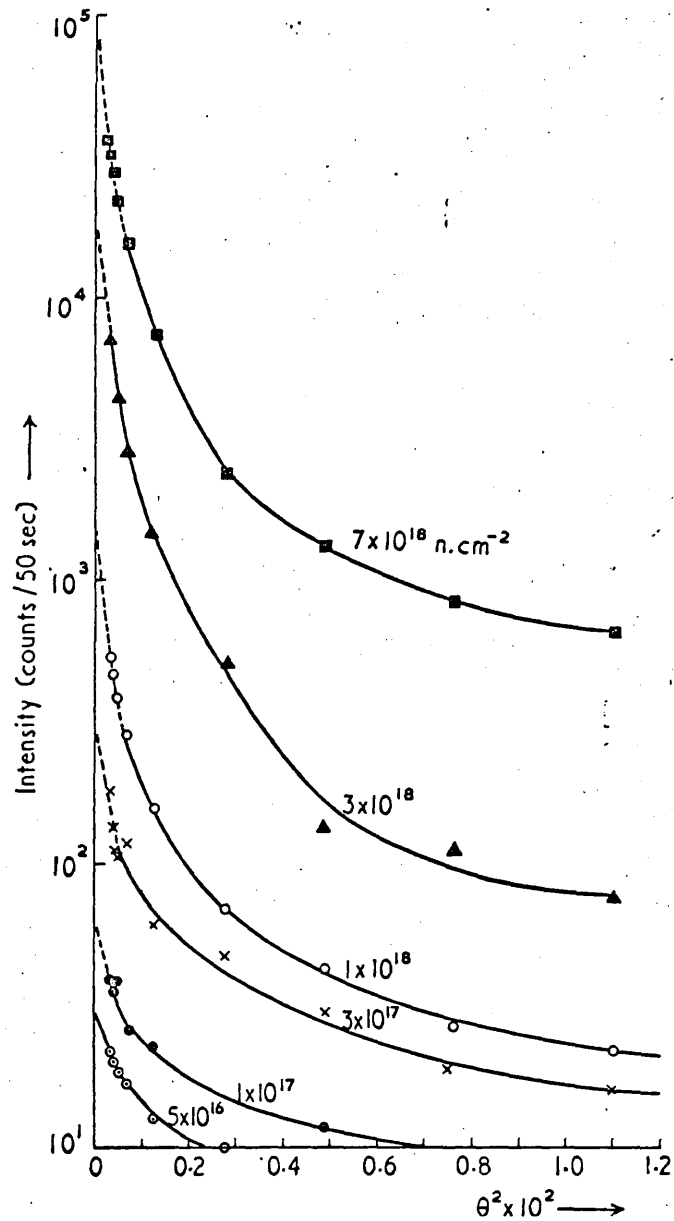
The amount of small angle scattering for irradiations less than 3×10^{17} n/cm² is extremely small but above this dose the scattering becomes appreciable. The intensity of scattering at 1° as a function of dose is shown in fig. 2 together with the line broadening results.

Accurate analysis of such a complex scattering system is difficult but an estimate of the maximum size of scattering region is of interest. The table shows the radius of gyration K for the various irradiated crystals calculated from the extreme low angle linear portion of the log I versus θ^2 curve.

Irradiation dose (n/cm ²)	Size K (Å)	Irradiation dose (n/cm ²)	Size K (Å)
5×10^{16}	10	1×10^{18}	23
1×10^{17}	15.5	3.3×10^{18}	22
3.7×10^{17}	18.5	7×10^{18}	22

It can be seen that the size of the scattering group increases with neutron dose up to about 10^{18} n/cm² and then remains approximately constant at 22 Å. The number of such regions also increases extremely rapidly with dose, as the intercept on the log I axis indicates,

Fig. 3



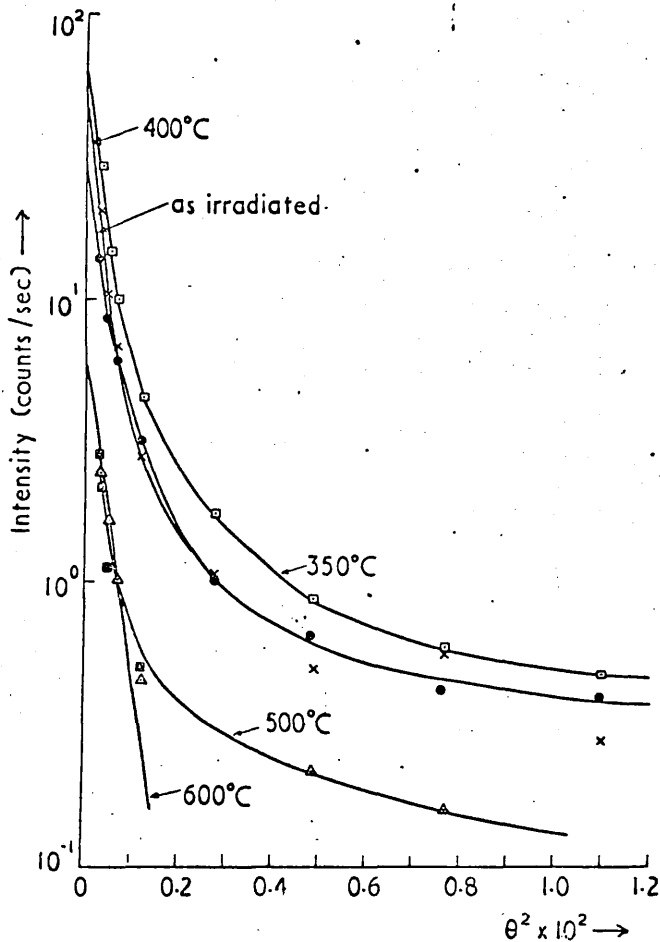
Log. (intensity) versus θ^2 for six crystals irradiated at successively increasing doses.

3.4. Annealing Experiments

Irradiated single crystals have been vacuum annealed for 1 hr periods at 50° and 100° c intervals in the range from room temperature to 700° c. After each anneal the crystals were examined by the three x-ray techniques mentioned above. The bulk of the damage annealed out between 400°

and 500° c., i.e. the lattice parameter reverted to its original value, the powder lines became sharp and the Laue streaks disappeared. The small angle scattering results showed that the annealing behaviour of the scattering group was extremely complex. Below 400° c there is a small increase in small angle scattering but a large decrease does occur

Fig. 4



Log (intensity) versus θ^2 for crystal irradiated to 10^{18} n/cm² and annealed for one hour at successively increasing temperatures. ● As irradiated, □ annealed at 350° c, × 400° c, △ 500° c, ■ 600° c.

in the range 400–500° c. Further annealing at temperatures above 500° c causes the log I versus θ^2 plot to become approximately linear but does not remove the scattering completely. The scattering curves for a crystal irradiated to 1×10^{18} n/cm² after various anneals are given in fig. 4. Substantial small angle scattering remains after high temperature annealing.

Irradiated lithium fluoride is dark red or black depending on the severity of the dose. On annealing the colour of all the samples changed. Crystals irradiated less than 10^{18} n/cm² become yellow-brown at low temperatures but finally colourless in the range 400–500° C. The crystals more heavily irradiated remained dark up to 400–500° C, then became white.

§ 4. DISCUSSION.

In the irradiation range below 10^{17} n/cm² the amount of small angle scattering and line broadening is extremely small whereas the lattice parameter increases linearly with dose. This initial linear portion of the lattice parameter *versus* dose curve (fig. 1) can be interpreted as being mainly due to isolated Frenkel defects distributed at random throughout the lattice. From the slope of this portion we can obtain, by assuming that the lattice expands by the molecular volume for each pair of Frenkel defects produced, an estimate of the number of defects per fission. This number is fairly close to the theoretical estimate of 1900 obtained by assuming that all the defects remain in the lattice during and after the irradiation (Seitz and Koehler 1956). We conclude therefore that the major part of the damage does not anneal out at room temperature.

We can interpret the saturation of the lattice parameter *versus* dose curve by using the rough criterion for saturation suggested by Pease (see Varley 1955). An upper limit to the concentration of Frenkel defects is that for which any additional interstitial introduced in the lattice is adjacent to a vacant lattice site. If the defects are immobile this will occur when the vacancy concentration is of the order of $1/N$, where N is the number of lattice sites surrounding an interstitial site. Now the cross section for thermal neutron absorption in LiF is 70 barns so that for the saturation dose of 3×10^{17} n/cm² a mole fraction $(70 \times 10^{-24})(3 \times 10^{17}) = 2.1 \times 10^{-5}$ of fissions occurs. The corresponding concentration of vacancies is $(2.1 \times 10^{-5})(\frac{1}{2})(1900) = 1/50$. This is rather less than $1/N$, but the difference can be accounted for by assuming interstitial-vacancy interactions over a few ionic distances.

We attribute the fall of the lattice parameter *versus* neutron dose curve to the coagulation of point defects. Evidence for coagulation is provided by the appearance of $\langle 100 \rangle$ streaks in Laue photographs and by small angle scattering. The streaks indicate a break-up of the periodicity in the $\langle 100 \rangle$ directions, as produced, for example, by the condensation of interstitial atoms in (100) planes. The small angle scatter curves show that the scattering system is more complex, being more sensitive to vacancy groups than interstitial aggregates. However it is expected that aggregates of lithium and fluorine atoms, together with groups of vacancies are present. Any variation in size of each of these scattering groups will give rise to a concave type of $\log(\text{intensity})$ *versus* θ^2 curve, as observed. Coagulation of defects also produces long range strain, as revealed by the line broadening measurements. The interpretation

of line broadening in terms of crystallite size is invalid (see § 3), although Varley (1956) reports that Pease has deduced thereby an estimate of the size of the region disordered by a single fission process.

On annealing, the Laue streaks, line broadening and changes in lattice parameter all completely disappear in the temperature range 400–500° c. However, some small angle scattering still remains even at 700° c. This residual scattering is believed to be due to the new atoms, ³H and ⁴He, formed by transmutation. The number of such atoms per group can be calculated from the x-ray measurements, since from eqn. (1) the number of scattering particles *M* is given by

$$M = NI(O)/n^2, \quad \dots \dots \dots (2)$$

where *I*(0) is the intercept intensity in electrons per atom and *N* is the number of atoms/cm³. The conversion of the intensity from counts/sec. to electrons/atom can be made, knowing the geometry of the apparatus and the main beam intensity (Smallman and Westmacott 1957). For our arrangement one count/sec. is equivalent to 20 electrons/atom. Thus in the 1 × 10¹⁸ n/cm² and high temperature annealed sample the number of groups is about 4 × 10¹⁵/cm³. However, the number of transmuted atoms formed during irradiation is 8 × 10¹³/cm³ so that the number of atoms per group is about 2000. If these small atoms fit interstitially in the lattice sites (½, ½, ½) or (½, 0, 0) then the volume occupied is about 500 unit cells. This is not in agreement with the observed size of the scattering group of 30 Å radius. The difference can be accounted for if it is assumed that gas atoms by capturing vacancies in their neighbourhood expand into gas bubbles forming a stable cavity. Such behaviour has been observed metallographically when irradiated uranium (Cottrell 1956) and beryllium (Barnes and Redding, private communication) is heated. An estimate of the size of cavity which this group of atoms would acquire at temperature *T*°K may be obtained since the pressure of a gas bubble of radius *R* is given by

$$P = 2\gamma/R \quad \dots \dots \dots (3)$$

where γ is the surface energy of the lithium fluoride. Since the volume of gas atoms at n.t.p. is

$$A_G/\rho_G N \quad \dots \dots \dots (4)$$

where ρ_G is the density of the gas at n.t.p. and *A_G* the atomic weight of the gas and *N* Avogadro's number, the number of gas atoms per bubble at pressure *P* and temperature *T*°K is given by

$$4\pi R^3 \rho_G N P / 273/3 A_G T. \quad \dots \dots \dots (5)$$

Taking the number of atoms per bubble as that given above (2 × 10³) and with $\gamma = 200$ ergs/cm² and $\rho_G/A_G = 4.5 \times 10^{-3}$ g/cm³ the size of the bubble is about 30 Å radius, in agreement with that observed at 600° c.

§ 5. CONCLUSIONS

Three principal x-ray techniques, Debye-Scherrer powder photography, Laue photography, small angle scattering, have been used to determine the effect of neutron irradiation on crystals of lithium fluoride. The results indicate that for low doses ($<10^{17}$ n/cm²) the defects are predominantly isolated. However at doses higher than about 10^{17} n/cm² clusters of defects such as interstitial platelets in (100) planes and groups of vacancies are formed. These defects anneal out in the temperature range 400°–500° c but above this temperature it is believed that the transmuted atoms ³H and ⁴He which remain form small gas bubbles.

ACKNOWLEDGMENTS

We would like to thank Mr. T. M. Valentine, Mr. K. Rouse and Mr. K. H. Westmacott for assistance in the experimental work.

Note added in proof.—The presence of gas pockets has been confirmed by microscopic examination of samples annealed for long periods just below the melting point. For example, bubbles six microns in size and of square cross section were observed after heating for 24 hours at 700° c.

REFERENCES

- BINDER, D., and STURM, W. J., 1954, *Phys. Rev.*, **96**, 1519; 1955, *Ibid.*, **99**, 603.
BROOKES, H., 1956, *Annual Review of Nuclear Science*, 215.
COCHRAN, W., 1956, *Acta cryst., Camb.*, **9**, 994.
COTTBELL, A. H., 1956, *Metallurg. Rev.*, **1**, 479.
GUINIER, A., and FOURNET, G., 1955, *Small-angle scattering of X-rays* (London: Chapman and Hall).
HUANG, K., 1947, *Proc. roy. Soc.*, **190**, 102.
JONES, F. W., 1938, *Proc. roy. Soc.*, **166**, 16.
KEATING, D. J., 1955, *Phys. Rev.*, **97**, 832.
MAYER, G., 1955, *International Conference on Peaceful Uses of Atomic Energy*, **7**, 686.
SEITZ, F., and KOEHLER, J. S., 1956, *Solid State Physics*, **2**, 443.
SMALLMAN, R. E., and WESTMACOTT, K. H., 1957 (to be published).
VARLEY, J. H. O., 1955, *International Conference on Peaceful Uses of Atomic Energy*, **7**, 644; 1956, *Progr. nucl. Energy*, **1**, 672.

Reprinted without change of pagination from the
Proceedings of the Royal Society, A, volume 239, pp. 184-191, 1957

An optical method of studying the diffraction from imperfect crystals

I. Modulated structures

By B. T. M. WILLIS

Atomic Energy Research Establishment, Harwell, Berks

(Communicated by A. H. Cottrell, F.R.S.—Received 17 July 1956)

[Plates 5 to 7]

The correspondence between the X-ray diffraction pattern of a crystal and the optical diffraction pattern of a two-dimensional grating has been used to determine the nature of the diffraction from imperfect crystals. A two-dimensional grating representing the structure of the imperfect crystal is prepared on a very fine-grained photographic plate by a technique which gives an error of less than 1μ in the positions of the elements of the grating. The grating is placed in a bath of cedar-wood oil between optically flat glass plates, and its Fraunhofer diffraction pattern is observed in a modified Lipson diffractometer. Illustrations are given of the application of the optical method to the study of the diffraction from modulated structures; such as the alloy Cu_3FeNi_3 with a periodic variation of lattice parameter, and the age-hardening aluminium-copper alloy with a variation of both lattice parameter and structure amplitude.

1. INTRODUCTION

The structure of an imperfect crystal is normally determined by the trial-and-error method. A given arrangement of atoms in the crystal is postulated, and the calculated X-ray diffraction pattern produced by this arrangement is compared with the observed pattern. This may involve a considerable amount of calculation, which can be reduced by the use of optical diffraction methods. A two-dimensional grating is prepared representing the projection on one plane of a large number of atoms of the proposed structure; the Fraunhofer diffraction pattern of this grating is then obtained with the aid of an 'X-ray microscope' (Bragg 1939), and compared with the observed X-ray pattern. Optical methods have been developed by Lipson and his school (see references in Hughes & Taylor 1953) primarily to help determine complex organic structures; but they may prove specially valuable in the field of imperfect structures, as satisfactory theories of diffraction from certain kinds of imperfect structure, for example a crystal with dislocations (Wilson 1955), are not available.

Bragg & Lipson (1943) and Taylor, Hinde & Lipson (1951) have carried out preliminary investigations of the use of optical methods in determining the nature of the diffraction from imperfect structures. Bragg & Lipson photographed the optical diffraction patterns of line gratings simulating the structures of various alloys, but the restriction to one-dimensional gratings severely limited the power of the method. Taylor *et al.* prepared two-dimensional gratings to illustrate the diffraction from (a) hexagonal cobalt containing stacking faults and (b) Cu_3Au at different stages of ordering; these gratings were made by punching holes in an opaque card with a pantograph punch. They found that the principal limitation of the optical method

was the difficulty of constructing suitable gratings. In the cobalt problem (*a*), for instance, only a small number of 'atoms' could be included in the gratings, and this limited the quantitative evaluation of the patterns. Further, for these two problems there was no need to locate the 'atoms' in the gratings very accurately, but, in general, imperfect structures contain a high proportion of atoms displaced by only small amounts from their ideal lattice sites. Taylor *et al.* concluded that a quicker and more accurate method of making the gratings should be devised.

In the present paper a method for preparing two-dimensional gratings is described. The method, which was designed to overcome the limitations mentioned above of the pantograph punch technique, has been used in a study of the diffraction effects from modulated structures. This study is also described in the paper. Other applications—to the study of the diffraction from crystals with dislocations and with stacking faults—will form the subjects of later papers.

2. CONSTRUCTION OF GRATINGS

A diagram of the 'grating machine' is shown in figure 1. The grating is prepared on a fine-grained photographic plate *P* (preferably a Lippmann plate with grain size less than $1\ \mu$), which rests on a floating carriage F_1 ; F_1 itself rests on a second floating carriage F_2 mounted on a surface plate *S*. The surface of *S* is accurately parallel to the planes of the carriages. Both carriages are seated kinematically on three steel balls, free to run in grooves, and this allows translational movements of the carriages in mutually perpendicular directions. These movements are controlled by micrometers M_1 , M_2 with non-rotating anvils and scales reading to $0.2\ \mu$. A constant thrust of the carriages on the micrometer anvils is obtained by slightly tilting the surface plate out of the horizontal plane.

Three vertical pillars fixed to the surface plate support a rectangular plate *R* which, in position, is just clear of the upper emulsion side of the photographic plate. In the centre of the rectangular plate is a narrow slit *N*, 2.5 cm long, and underneath the slit is attached a thin foil containing a round $10\ \mu$ pinhole. The pinhole can be made by passing a high-frequency discharge through a thin sheet of mica. This forms a round hole at the discharge point, and the remaining mica is then made opaque by evaporating aluminium on to it. On exposure to a parallel beam from a 'compact-source' mercury-vapour lamp, an image of the pinhole is recorded on the photographic plate. A photographic shutter at the focus of the light source controls the exposure time. To represent atoms of different sizes on the grating, the photographic plate is carefully over-exposed, causing image spread; in controlling the image size in this way it is essential to include a mains voltage stabilizer in the lamp circuit.

Certain types of imperfect structures, such as layer structures containing stacking faults and distorted crystals with modulation of lattice parameter and structure amplitude, can be represented by gratings prepared by repeating a whole row of 'atoms' at a time. In this case the single pinhole is replaced by a row of a hundred or more $10\ \mu$ pinholes, which are placed under the narrow slit *N*, and this row is then used as the repeat unit in 'ruling' the two-dimensional grating. The original row of pinholes is itself prepared by recording images of a $10\ \mu$ pinhole at regular intervals on a Lippmann plate, and by printing this on a second Lippmann plate.

The performance of this grating machine compares favourably with that of the pantograph punch machine of Lipson. The estimated error in the position of an element of a grating is less than 1μ (see §4), whereas it is 30μ (Hughes & Taylor 1953) for a punched-card grating. A grating of 1000×1000 elements can be prepared, photographing a row of elements at a time, in two hours; this is the time required

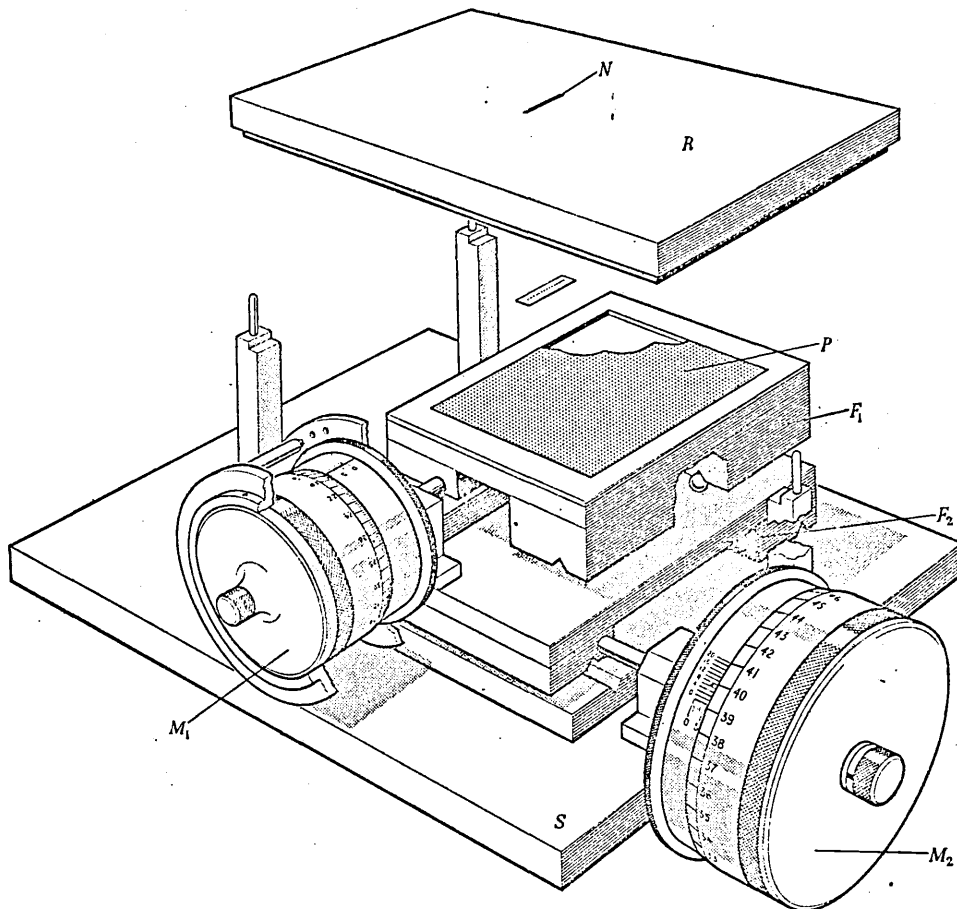


FIGURE 1. Diagram of the equipment used to make the two-dimensional gratings.

to make a 40×40 grating (Taylor *et al.* 1951) by the pantograph method. A further important advantage of the photographic technique is that the gratings can be made on a very small scale, with the repeat distance between the elements as small as 20μ , so that high-quality diffraction patterns can be obtained without using highly corrected lenses.

3. OBSERVATION OF THE DIFFRACTION PATTERNS

The patterns are photographed using an optical diffractometer similar to that described by Hughes & Taylor (1953). Light from a high-pressure mercury-vapour lamp is directed on a pinhole at the focus of a plano-convex lens of 1.5 m focal length. The grating is placed in the parallel beam emerging from this lens, and the diffracted

beams are brought to a focus by a second lens of the same focal length. The repeat distance in the gratings is 250μ or less, so that the diffraction spectra are well separated in the image plane; the diffraction patterns can therefore be photographed on fast quarter-plates, without recourse to the special fine-grain techniques devised by Hughes & Taylor.

The uneven optical thickness of the photographic plate on which the grating is made causes irregular variations in the path lengths of the diffracted beams, and a consequent deterioration in the quality of the diffraction pattern. To overcome this difficulty the grating is immersed in cedar-wood oil and sandwiched between a pair of optically flat glass plates (Bragg & Stokes 1945). This technique is not necessary if the repeat distance between the grating elements is sufficiently small.

A grating prepared photographically consists of opaque spots on a clear background. The area of the spots is small compared with the area of the background, and consequently the grating gives a dazzling zero order of diffraction, tending to mask the central portion of the pattern. This defect is avoided by using the complementary grating, prepared by printing on a second Lippmann plate. A number of gratings, which were photographic negatives of one another, were used to demonstrate Babinet's principle, which states that, except in the region of zero order, the distribution of illumination in the diffraction patterns of two complementary gratings are identical.

In addition to the lines of the mercury spectrum the source gives an appreciable white light continuum, which produces spurious radial streaks in the diffraction pattern. It is essential to remove these streaks by photographing the pattern with monochromatic light isolated by a filter of very small bandwidth. The photographs shown in figures 3 to 11 (plates 5 to 7) were taken using a nine-layer interference filter together with a gelatine filter, the combination passing a band of 20 \AA half-width, centred on the mercury green line ($\lambda 5461$).

4. DIFFRACTION FROM MODULATED STRUCTURES

(a) *One-dimensional modulation of lattice parameter and structure amplitude*

Wilson (1949) has given a summary of the theory of diffraction from modulated structures, in which the lattice parameter and structure amplitude vary periodically throughout the structure. The model he considered was a simple-cubic crystal distorted along one direction, the x axis, according to the equations

$$a_n = a \left(1 + b \sin \frac{2\pi n}{N} \right), \quad (1)$$

$$F_n = F \left(1 + g \sin \frac{2\pi n}{N} \right). \quad (2)$$

Here a_n is the spacing between the n th and $(n+1)$ th unit cells numbered along the x axis, F_n the structure amplitude of the n th cell, a and F respectively the lattice parameter and structure amplitude of the undistorted cell, b and g the amplitudes of the two modulations and Na their wavelength. Wilson derived expressions for the intensity of diffraction when the lattice parameter and structure amplitude varied

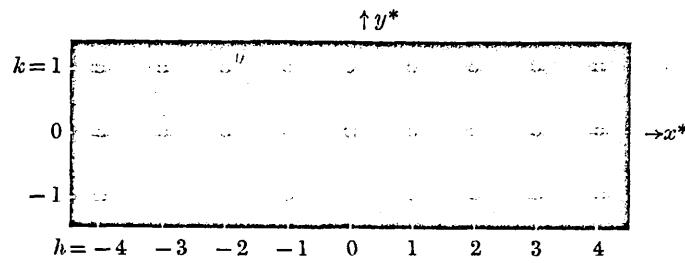


FIGURE 3. Diffraction pattern of a grating representing a simple cubic crystal with a sinusoidal modulation of lattice parameter along the x axis; small amplitude of modulation.

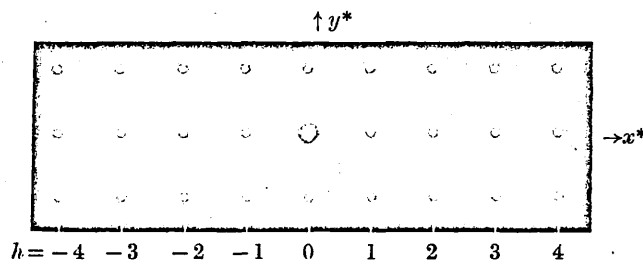


FIGURE 4. Diffraction pattern corresponding to an undistorted crystal.

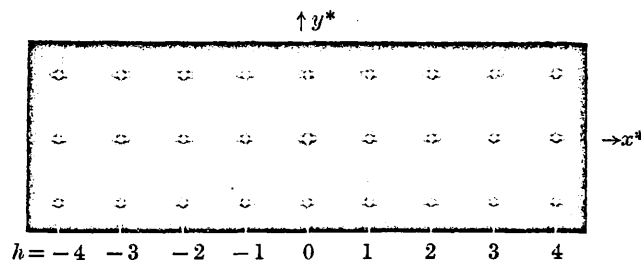


FIGURE 5. Diffraction pattern corresponding to a crystal with a sinusoidal modulation of structure amplitude along the x axis.

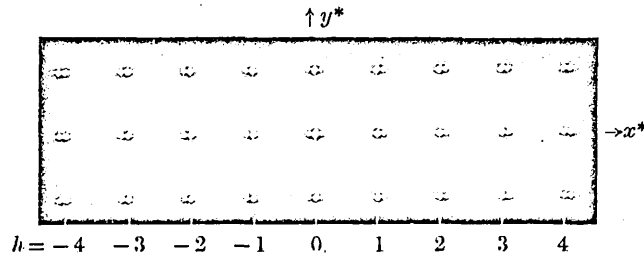


FIGURE 6. Diffraction pattern of a grating representing a simple cubic crystal with the modulations of figures 3 and 5 combined.

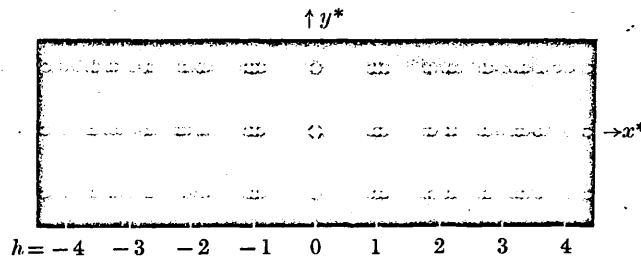


FIGURE 7. Diffraction pattern corresponding to a sinusoidal modulation of lattice parameter along the x axis; large amplitude of modulation.

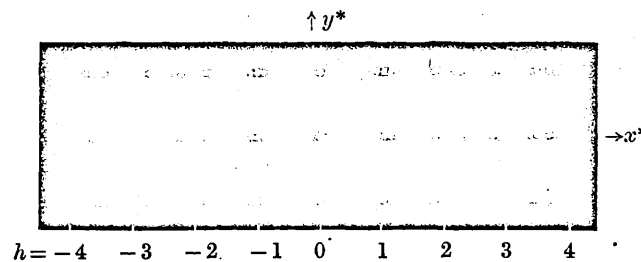


FIGURE 8. Diffraction pattern corresponding to a square-wave modulation of lattice parameter along the x axis; large amplitude of modulation.

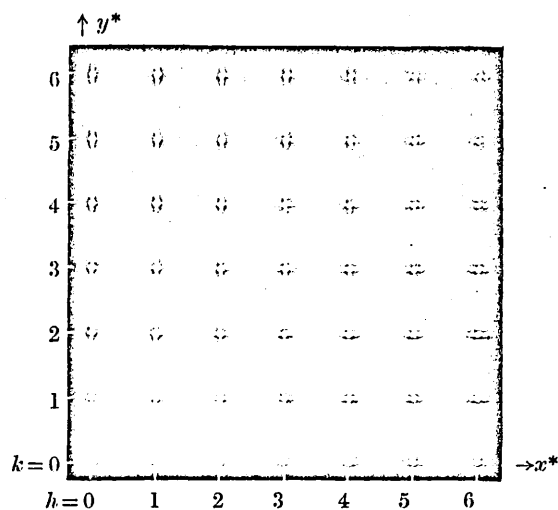


FIGURE 10. Diffraction pattern of a grating representing the one-dimensional model of the modulated structure of Cu_4FeNi_3 .

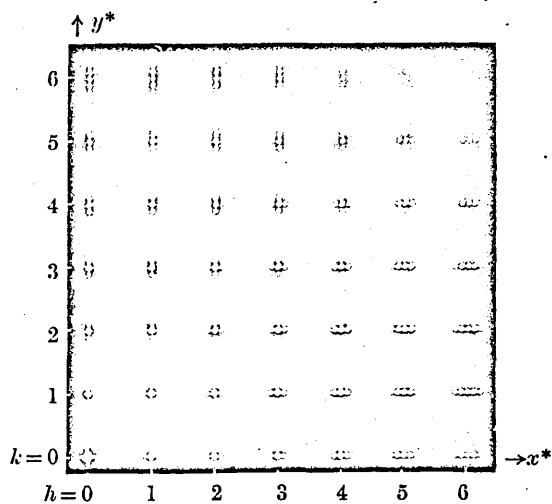


FIGURE 11. Diffraction pattern corresponding to the two-dimensional model of Cu_4FeNi_3 .

independently, and gave an approximate treatment for the case of simultaneous variation of lattice parameter and structure amplitude. Hargreaves (1951) has extended the theory to square-wave modulation; his treatment applies to a crystal with small amplitude of modulation of lattice parameter and for this case the diffraction is similar to that from a crystal with sinusoidal modulation. These theories are not necessarily valid for large amplitudes of lattice parameter modulation, or more exactly for large values of hNb , where h is the order of diffraction along the reciprocal x^* axis corresponding to the axis of modulation. The optical method can be used to determine the nature of the diffraction from modulated structures, when no restriction is placed on the amplitude or the wave form of the modulation, and when the modulation occurs along the x axis only or along the x and y axes simultaneously.

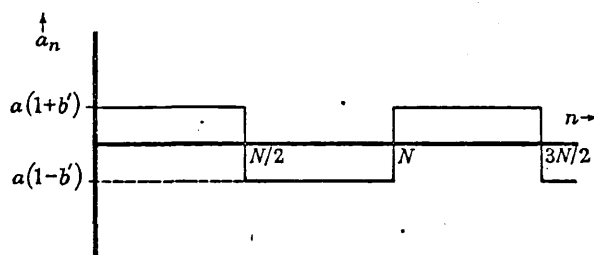


FIGURE 2. The spacing between adjacent elements along the modulation axis as a function of the number of the element, for square-wave modulation.

The optical diffraction pattern is shown first (figure 3, plate 5) of a two-dimensional grating with a periodic variation of spacing along the x axis in accordance with equation (1). The amplitude of the modulation, b , was 2% and its wavelength $10a$, where the repeat distance, a , was 250μ ; 100×100 elements were included in the grating. The co-ordinates in reciprocal space are denoted h, k , where h and k are integral for the diffraction spectra of the corresponding grating with $b = 0$. As the rows of spectra parallel to the x^* axis are identical, three rows only, for $k = 0$ and ± 1 , are shown in the photograph.

Figure 4 shows the diffraction pattern of an undistorted two-dimensional grating. Comparison of figures 3 and 4 shows that the modulation of lattice parameter introduces pairs of satellite reflexions, which flank the main reflexions and are displaced from them along the x^* axis by $\pm 0.1a^*$, where a^* is the repeat distance between the main reflexions. The components of each pair are equal in intensity, and this intensity increases with h , being zero for $h = 0$. Higher-order satellites, displaced from the main reflexions by $0.2a^*$, $0.3a^*$, ..., appear for $h \geq 4$. All these features are explained satisfactorily by the theory (Wilson 1949), which indicates that the intensity of a satellite associated with the h th-order main reflexion is $J_i^2(hNb)$, where i is the number of the satellite, counting from the main reflexion as $i = 0$, and J_i is the Bessel function of order i . For $hNb < 1$, which corresponds in our case to $h < 4$, J_i^2 is appreciable for $i = 0$ and 1 only.

Diffraction patterns of the same form as figure 3 were obtained from gratings with square-wave modulation of spacing along the x axis and amplitude of modulation, b' (see figure 2), equal to 2%. A number of gratings were prepared with the mean

repeat distance, a , varying between 250 and 25μ . The satellite reflexions were clearly resolved for all the gratings, including the one with smallest a , and this indicated that the error in the position of an element in a grating was probably less than 1μ .

Figure 5 shows the diffraction pattern of a grating representing a crystal with a uniform lattice parameter but with a sinusoidal modulation of structure amplitude in accordance with equation (2). The amplitude of the modulation, g , was 30 % and its wavelength $10a$. This grating was prepared by controlled over-exposure, as described in § 2. Each main reflexion in the pattern is accompanied by a pair of satellites displaced along the x^* axis by $\pm 0.1a^*$. All the satellites have the same intensity, independent of h . A grating with a square-wave variation of scattering power gave a similar pattern. These results are again in agreement with the theory (Hargreaves 1951).

Figure 6, plate 6, is the diffraction pattern of a grating representing a crystal with combined sinusoidal variation of lattice parameter and structure amplitude, with maximum lattice parameter coinciding with minimum structure amplitude. The modulations were equivalent to those possessed individually by the gratings whose diffraction patterns are shown in figures 3 and 5. Comparison of figure 6 with figure 3, the pattern for lattice parameter modulation only, shows that the effect of the additional structure amplitude modulation is to introduce a pair of weak satellites of equal intensity at $h = 0$, and to cause the components of the remaining pairs of satellites to be unequal in intensity, with the component of higher intensity lying on the higher-angle side of the main reflexion. This type of grating was used as a model by Preston (1938) to explain the origin of the asymmetrical streaks in X-ray photographs of an aluminium-copper alloy.

The diffraction patterns shown in figures 7 and 8 were given by gratings with spacing modulation of relatively large amplitude; the grating for figure 7 had a sinusoidal modulation of amplitude 10 %, and that for figure 8 a square-wave modulation of similar amplitude. For small values of h , up to $h = 2$, the two patterns are identical; as Nb is unity, this range of h is equivalent to the condition $hNb < 2$, the same condition given by Hargreaves (1951) for the validity of his theory for square-wave modulation of lattice parameter. There is no correspondence between the patterns for the higher orders of diffraction, but in both cases the satellites represent the predominant part of the diffracted intensity and the 'main' reflexions (corresponding to integral values of h) are either weak or absent.

(b) *Modulation of lattice parameter along both the x and y axes*

The investigations of Daniel & Lipson (1943, 1944) showed that the reciprocal lattice of the modulated structure of Cu_4FeNi_3 consists of integral hkl points, each accompanied by three pairs of satellite points; these satellites occur along the principal x^* , y^* , z^* directions through the hkl points, and their intensities are proportional to h^2 , k^2 , l^2 , respectively (see figure 9). Daniel & Lipson concluded that the lattice parameter was modulated sinusoidally along the [100] axes, but were unable to determine from their diffraction data whether the modulation was one-, two- or three-dimensional. (In the one-dimensional case the modulation within a given small region of the crystal occurs along one axis only, but in neighbouring regions

this axis lies along different [100] directions; in the three-dimensional case the modulation occurs everywhere along all three cubic axes.)

The optical method gives the form of the diffraction pattern for the one- and two-dimensional cases. Figure 10, plate 7, is the diffraction pattern from a grating consisting of two regions of equal size; the spacing in one region was modulated

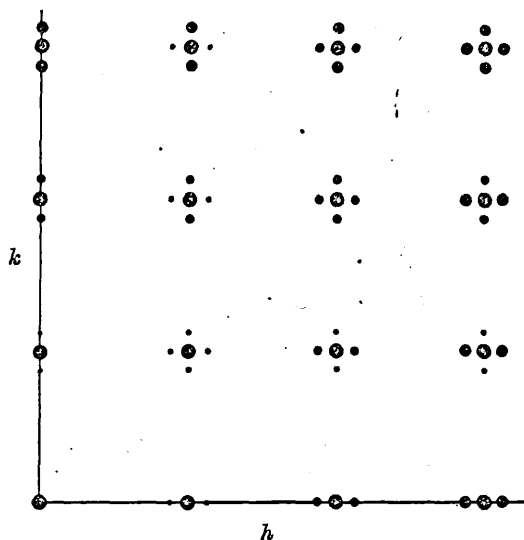


FIGURE 9. Reciprocal lattice of Cu_4FeNi_3 in the $l = 0$ plane.

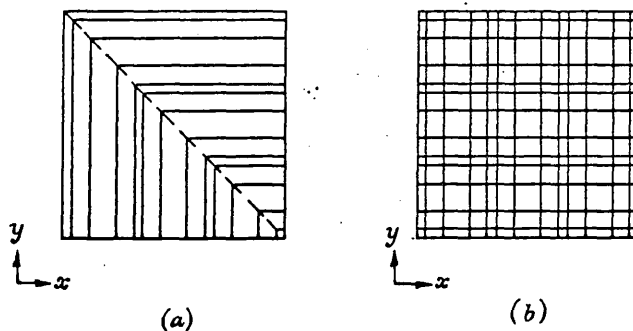


FIGURE 12. Schematic diagrams of a grating modulated along both x and y axes; (a) one-dimensional modulation, (b) two-dimensional modulation.

along x and in the other along y (figure 12 (a)). The amplitude of each modulation was 2% and the wavelength $10a$. Figure 11 is the corresponding portion of the diffraction pattern of a grating modulated throughout along both x and y (figure 12 (b)).

For low orders of diffraction ($h, k \leq 3$) the spectra in figures 10 and 11 are of similar form, but for higher orders additional reflexions appear in figure 11 which do not lie along the principal x^* , y^* directions through the ideal hk points. When h and k exceed 6, these additional reflexions constitute the most intense part of the hk spectrum, and for h and k greater than 8 there are no reflexions at all along the x^* ,

y^* directions. For these gratings Nb was equal to 0.2, so the condition for the patterns to be appreciably different is that hNb and kNb exceed about 0.6. Hargreaves (1951) studied the X-ray diffraction from a single crystal of a copper-iron-nickel alloy, for which Nb was approximately equal to 0.6, and he observed no satellite reflexions apart from those lying along the principal x^* , y^* , z^* directions through the ideal hkl points. It can be concluded therefore that the lattice parameter modulation was probably one-dimensional.

5. CONCLUSIONS

The optical method provides a rapid means of determining the nature of the diffraction from modulated structures, and the intensity distribution in the diffraction pattern agrees with the theory, where this is available.

The restriction of the method to two-dimensional problems is not a serious drawback in the field of imperfect structures. Certain types of defects, such as parallel edge dislocations and stacking faults in monolayer structures, disturb the periodicity along one or two dimensions only of the lattice, and the structures can be adequately represented by two-dimensional gratings. Other defects, for example isolated vacancies and interstitial atoms give rise to a lattice distortion in all directions, but certain features of the reciprocal lattice can still be obtained from gratings which simulate the arrangement of the atoms in a section of the crystal.

The author wishes to thank Dr H. M. Finnieston and Dr J. Thewlis for their helpful criticism of the manuscript and for their constant encouragement in the course of this research, and Mr J. Hicks who showed great skill in constructing the grating machine.

REFERENCES

- Bragg, W. L. 1939 *Nature, Lond.*, **143**, 678.
 Bragg, W. L. & Lipson, H. 1943 *J. Sci. Instrum.* **20**, 110.
 Bragg, W. L. & Stokes, A. R. 1945 *Nature, Lond.*, **156**, 332.
 Daniel, V. & Lipson, H. 1943 *Proc. Roy. Soc. A*, **181**, 368.
 Daniel, V. & Lipson, H. 1944 *Proc. Roy. Soc. A*, **182**, 378.
 Hargreaves, M. E. 1951 *Acta Cryst.* **4**, 301.
 Hughes, W. & Taylor, C. A. 1953 *J. Sci. Instrum.* **30**, 105.
 Preston, G. D. 1938 *Proc. Roy. Soc. A*, **167**, 526.
 Taylor, C. A., Hinde, R. M. & Lipson, H. 1951 *Acta Cryst.* **4**, 261.
 Wilson, A. J. C. 1949 *X-ray optics*. London: Methuen.
 Wilson, A. J. C. 1955 *Nuovo Cim.* (10), **1**, 277.

An optical method of studying the diffraction from imperfect crystals

II. Crystals with dislocations

BY B. T. M. WILLIS

Atomic Energy Research Establishment, Harwell, Berks

(Communicated by A. H. Cottrell, F.R.S.—Received 17 July 1956)

[Plates 8 and 9]

Lipson's optical diffractometer has been used to determine the diffraction patterns of gratings representing crystals with dislocations. The optical method lends itself readily to the solution of the two-dimensional problem of diffraction by a single edge dislocation. The intensity distribution near the ideal reciprocal lattice points is, in general, complex, but for certain special points it is relatively simple and in agreement with that deduced by a new theory of Suzuki. An earlier theory of Wilson's fails to explain the observed intensity distribution. Diffuse scattering, not predicted by Suzuki's theory, occurs in the form of streaks joining the reciprocal lattice points. The diffraction has also been studied from gratings consisting of photographs of dislocated bubble rafts, and from a grating whose diffraction pattern is related to that of a screw dislocation. A brief discussion is given of the expected diffraction patterns from crystals with various arrays of dislocations.

1. INTRODUCTION

In part I (Willis 1957), referred to below as I, the nature of the diffraction from modulated structures was studied by Lipson's optical diffractometer, which gives the diffraction pattern of a two-dimensional grating representing the crystal. This method, including the new photographic technique of constructing the gratings, has been used to study the nature of the diffraction from crystals with dislocations. The results, which are primarily concerned with the diffraction from single dislocations, are presented in this paper. A brief discussion is given of the application of these results to the problem of the diffraction from crystals containing various arrays of dislocations.

The theory of the diffraction from a cylindrical crystal with a single axial screw dislocation is comparatively straightforward and has been treated by Wilson (1949, 1952, 1955) and Frank (1949). It is difficult to apply the optical method to this problem, for the structure cannot be produced by repeating a two-dimensional configuration of atoms in a third direction, and so cannot be properly represented by a two-dimensional grating. However, as shown below (§ 3), this limitation can be partly overcome. On the other hand, the diffraction from a single edge dislocation is very difficult to treat theoretically, because of the complex nature of the elastic strain field surrounding the dislocation. A rough theoretical treatment has been given by Wilson (1950) using highly simplified equations for the displacements of the atoms, and a more satisfactory one by Suzuki (1956), who assumed displacements given by isotropic elastic theory. Suzuki derived the intensity distribution in the immediate neighbourhood of the $h0l$ and $0kl$ ideal reciprocal lattice points,

where the h axis refers to the Burgers vector direction and the l axis to the direction of the dislocation. Fortunately, the diffraction from a crystal with a single edge dislocation (or with a number of parallel edge dislocations) can be determined for all points in reciprocal space by the optical method, for the crystal is built from identical layers of atoms stacked normal to the dislocation axis and the problem is therefore essentially two-dimensional.

2. SINGLE EDGE DISLOCATION

A grating representing a monatomic simple-cubic crystal with a single edge dislocation was prepared by the photographic method described in I. The displacements of the elements ('atoms') of the grating from their positions in the undislocated grating were calculated from the equations given by isotropic elastic theory (Read 1953):

$$\left. \begin{aligned} u &= \frac{b}{2\pi} \left[\tan^{-1} \frac{y}{x} + \frac{1}{2(1-\nu)} \frac{xy}{x^2+y^2} \right], \\ v &= -\frac{b}{8\pi(1-\nu)} \left[(1-2\nu) \ln(x^2+y^2) + \frac{x^2-y^2}{x^2+y^2} \right]. \end{aligned} \right\} \quad (1)$$

Here x, y are rectangular co-ordinates in the plane of the grating, with the x axis parallel to the Burgers vector and the xy plane normal to the dislocation. u, v are the components in the x, y directions of the displacements produced by the dislocation, b the magnitude of the Burgers vector, and ν Poisson's ratio. In the present case b was taken as the repeat distance, a , in the undislocated grating and ν as 0.3, an average value for common metals. The magnitude of a was chosen as 250μ . This was sufficiently small to give adequate separation of the diffracted spectra, which were photographed on fast plates using the mercury green wavelength ($\lambda 5461$), and large enough to correspond to an error of less than 0.5% of a in the location of the individual elements of the grating. In order to observe clearly a large number of orders in the diffraction pattern, the diameter of the elements (approximately 10μ) was made much less than a . The central portion of this grating is shown in figure 1(a), plate 8. For clarity, the size of the elements has been deliberately increased by printing from an over-exposed negative.

Figure 2(a), plate 8, shows the diffraction pattern of a circular portion of this grating of radius $10a$, centred at the dislocation. The positive h and k axes in the photograph correspond to the positive x and y axes respectively in the grating. The reciprocal lattice of the corresponding cylindrical crystal of radius $10a$ and infinite length is equivalent to the pattern in figure 2(a) repeated at each integral l plane, $l = 0, \pm 1, \dots$

A number of other gratings were prepared of different radii (up to $20a$) and different Burgers vectors (a and $2a$), and with displacements given by the same equations (1) using $\nu = 0.3$. From the study of the diffraction patterns of all the gratings the following conclusions were drawn concerning the distribution of intensity around the ideal hkl points of a cylindrical crystal with an axial edge dislocation.

(a) The dislocation causes a spreading of the intensity in reciprocal space. This spreading is confined to the integral l planes and its form is independent of l . (For this reason the hkl point is referred to below as hk .)

(b) The intensity distribution in the neighbourhood of an hk point is, in general, complex and depends on both h and k . It is not of circular symmetry, unlike the case of the screw dislocation (see § 3).

(c) An $h0$ reflexion has roughly the shape of a figure of eight, while an $0k$ reflexion is in the form of a cross made by four points with an extra point at the centre for $k \leq 4$.

(d) The position of the peak intensity of an $h0$ reflexion is displaced from the ideal reciprocal lattice point by an amount that increases roughly linearly with h (see figure 5 (a)). The peak intensity of an $0k$ reflexion is also displaced, but the displacement tends, if anything, to decrease with increasing k (figure 5 (b)).

(e) The intensity at the ideal $h0$ point is zero except for $h = 0, 2, 4$; the intensity at the ideal $0k$ point is zero for $k \geq 5$ (figure 2 (b)).

(f) The spreading of intensity in the integral l plane increases linearly with the strength, b , of the dislocation and with the reciprocal of the radius of the crystal.

All these results (a) to (f) agree well with the theory of Suzuki (Suzuki 1957; Suzuki & Willis 1956), which gives the distribution of intensity around the ideal $h0$ and $0k$ points, assuming atomic displacements given by equations (1). To describe this distribution, polar co-ordinates ρ, ϕ are chosen in the integral l plane with the origin of co-ordinates at the ideal reciprocal lattice point and the line $\phi = 0$ parallel to the h axis (figure 3). Suzuki shows that the intensity $I_h(\rho, \phi)$ of the $h0$ reflexion at the point (ρ, ϕ) varies with ρ and ϕ in accordance with the equations

$$I_h(\rho, \phi) = GG^*,$$

$$G(\rho, \phi) = i^h \exp(ih\phi) \sum_{n=0}^{\infty} \left\{ \begin{aligned} & [(-\alpha_n^{(1)} + \alpha_n^{(2)}) \cos 2(2n+1)\phi \\ & + (\alpha_n^{(3)} + \alpha_n^{(4)}) \cos 4n\phi] + i \{ (-\alpha_n^{(1)} - \alpha_n^{(2)}) \sin 2(2n+1)\phi \\ & + (\alpha_n^{(3)} - \alpha_n^{(4)}) \sin 4n\phi \} \end{aligned} \right\} \quad (2)$$

where $\alpha_n^{(1)} = \epsilon_{2n+1} J_{2n+1}(p) s^{-2} \int_0^s \xi J_{h+2(2n+1)}(\xi) d\xi,$

$$\alpha_n^{(2)} = \epsilon_{2n+1} J_{2n+1}(p) s^{-2} \int_0^s \xi J_{h-2(2n+1)}(\xi) d\xi,$$

$$\alpha_n^{(3)} = \epsilon_{2n} J_{2n}(p) s^{-2} \int_0^s \xi J_{h+4n}(\xi) d\xi,$$

$$\alpha_n^{(4)} = \epsilon_{2n} J_{2n}(p) s^{-2} \int_0^s \xi J_{h-4n}(\xi) d\xi,$$

and $\epsilon_m = 1$ for $m = 0$
 $= 2$ for $m \neq 0$.

J_m is the Bessel function of order m , A is the radius of the crystal or grating, $g = 2\pi\rho A$ and $p = h/4(1-\nu)$. If a^* is the repeat distance between the main reflexions, the series in (2) converges rapidly for $\rho \ll a^*$ and I_h can be evaluated by considering

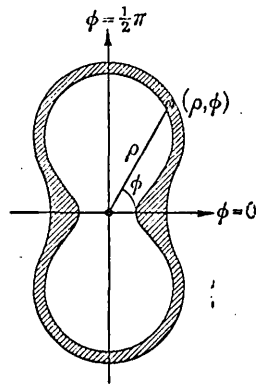


FIGURE 3. Schematic representation of observed $h0$ reflexion showing definition of co-ordinates ρ , ϕ .

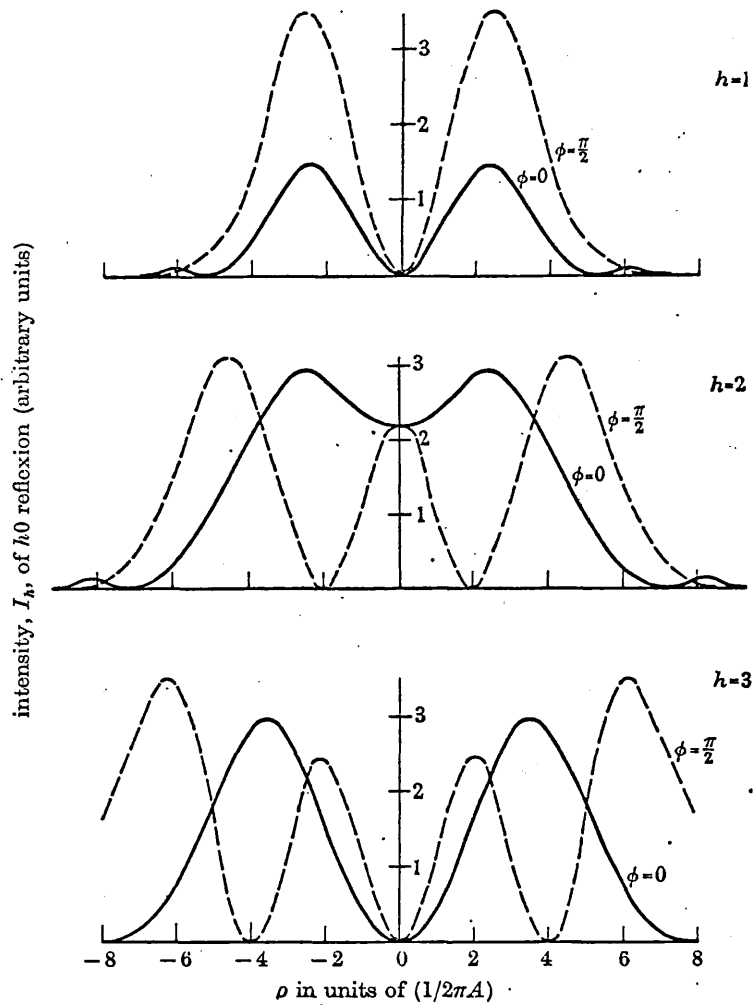


FIGURE 4. Theoretical curves for edge dislocation on elastic theory model showing I_{ϕ} as a function of ρ for $\phi = 0, \frac{1}{2}\pi$ and $h = 1, 2, 3$.

the first two or three terms only in the series. By this means I_h has been calculated as a function of ρ for the two directions $\phi = 0$ and $\phi = \frac{1}{2}\pi$, taking $\nu = 0.3$. The curves obtained for $h = 1, 2, 3$ are shown in figure 4. There is a striking qualitative agreement between these theoretical curves and the appearance of the $h0$ reflexions in figure 2(a); in particular, the number of prominent maxima in each curve in figure 4 is equal to the number observed.

A quantitative comparison between observation and theory has been obtained by considering the displacements of the positions of peak intensity of the $h0$

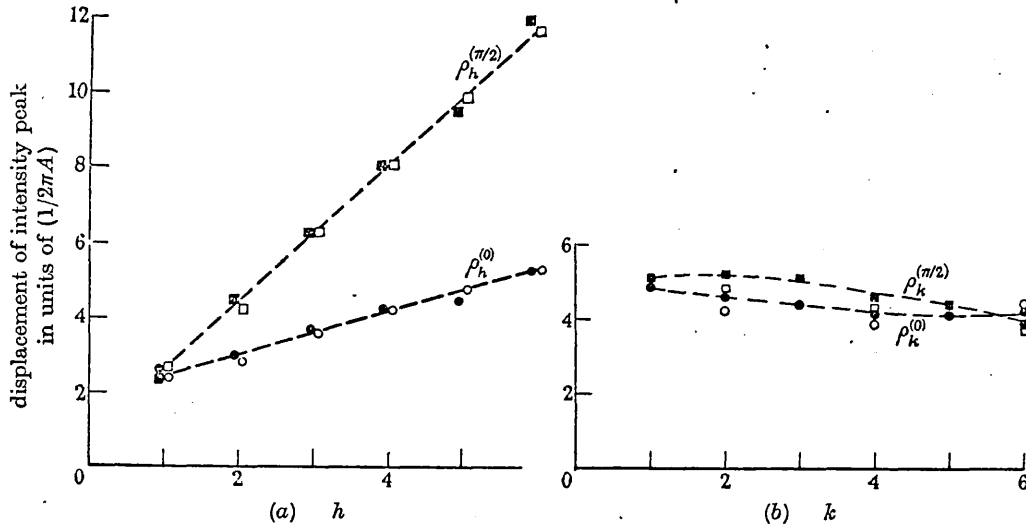


FIGURE 5. Observed (●, ■) and calculated (○, □) values of displacements of intensity peaks from ideal reciprocal lattice points, as measured along $\phi = 0$ and $\phi = \frac{1}{2}\pi$, and plotted against order. (a) $h0$ reflexions, (b) $0k$ reflexions. The points in (a) lie remarkably close to the straight lines:

$$\rho_h^{(0)} = (2\pi A)^{-1} (1.9 + 0.55h) \quad \text{and} \quad \rho_h^{(\pi/2)} = (2\pi A)^{-1} (0.8 + 1.80h).$$

reflexions from the ideal reciprocal lattice points. Let $\rho_h^{(0)}, \rho_h^{(\pi/2)}$, denote the magnitudes of these displacements as measured along the two directions $\phi = 0, \phi = \frac{1}{2}\pi$ respectively. In figure 5(a) the observed and calculated values of $\rho_h^{(0)}$ and $\rho_h^{(\pi/2)}$ are plotted against h ; the observed points represent average values measured from the diffraction patterns of several gratings with different radii and Burgers vectors, while the theoretical points were obtained from curves of the type shown in figure 4. The same procedure was used to obtain corresponding results for the $0k$ reflexion (figure 5(b)), the theoretical points being derived from equations of Suzuki of the same general form as equations (2). Agreement between observation and theory is good, particularly for the $h0$ reflexions.

In addition to the diffraction patterns from gratings prepared by the photographic method, patterns were also recorded from gratings consisting of reduced photographs of hexagonal bubble rafts (Bragg & Nye 1947). Figure 6, plate 9, is a photograph of the diffraction pattern from an edge dislocation in the centre of a bubble raft of radius $15a'$, where a' is the distance between adjacent bubbles at

a large distance from the dislocation. The h axis in figure 6 is along the Burgers vector direction. The bubbles in the raft were relatively large (1.9 mm in diameter), so that this grating represented a relatively 'soft' metal with a value of Poisson's ratio somewhat greater than 0.3 (Read 1953). The dislocation was therefore narrower than that considered above for the simple-cubic model. Nevertheless, apart from the modification due to the hexagonal symmetry, there is a definite similarity of figure 6 with figure 2 (*a*). Thus in both patterns the $h0$ reflexions are roughly in the form of a figure of eight, and the $0k$ reflexions in the form of a cross with zero intensity at its centre for $k \geq 3$ (figure 6) and $k \geq 5$ (figure 2 (*b*)). It appears that the distribution of intensity around an ideal reciprocal lattice point depends on its co-ordinates in reciprocal space, on the strength of the dislocation and on the value of Poisson's ratio, but not otherwise on the crystal structure.

3. EDGE DISLOCATION: HALL-WILSON APPROXIMATION

It was pointed out by Hall (1950) that to a first approximation the atomic displacements produced by an edge dislocation can be represented by the equations

$$\left. \begin{aligned} u &= \frac{b}{2\pi} \tan^{-1} \frac{y}{x}, \\ v &= 0. \end{aligned} \right\} \quad (3)$$

The xy plane is normal to the dislocation, u, v are the x, y components of the displacement of an atom with co-ordinates (x, y) and b is the magnitude of the Burgers vector. The net displacements given by (3) are approximately the same as those given by equations (1) (cf. figures 1 (*a*) and (*b*)), but equations (3) fail to satisfy the conditions for elastic equilibrium. The problem of the diffraction from a hypothetical crystal with an 'edge dislocation' described by (3) has been considered theoretically by Wilson (1950), but before discussing his results the solution of this problem by the optical method will be described.

A two-dimensional grating was prepared with the positions of the elements given by equations (3) taking b equal to the repeat distance, a , in the undislocated grating. Figure 1 (*b*) is a photograph of a small portion of the dislocated grating. The diffraction pattern of a circular portion of this grating of radius $15a$ and centred at the dislocation is shown in figure 7, plate 9. The $0k$ reflexions are unaffected by the dislocation, where the k axis refers to the direction normal to the Burgers vector, but the remaining hk spectra are drawn out into hollow rings with zero intensity at the centre. The diameters of the rings are independent of k but increase with h , so that the rings are of appreciable diameter for the higher values of h . The reciprocal lattice is therefore quite different from that corresponding to an edge dislocation in elastic equilibrium (cf. notes (*b*), (*c*) and (*e*) in §2), and there appears to be no justification for using the simplified equations (3) to obtain the approximate nature of the diffraction from an edge dislocation.

It is interesting, however, to compare the observed and calculated diffraction patterns of a two-dimensional grating deformed according to (3), as this pattern is closely related to that of a screw dislocation. According to Wilson (1950) the

dependence of the intensity $I_{hk}(\rho, \phi)$ of the hk reflexion on ρ and ϕ is described by the equations

$$\left. \begin{aligned} I_{hk}(\rho, \phi) &= GG^*, \\ G(\rho, \phi) &= i^h \exp(ih\phi) s^{-2} \int_0^s \xi J_h(\xi) d\xi. \end{aligned} \right\} \quad (4)$$

The symbols ρ, ϕ, A have the same meanings as previously defined for equations (2). In deriving (4) Wilson assumed that $\rho \ll a^*$. Equations (4) show immediately that I_{hk} is independent of k and has circular symmetry (i.e. is independent of ϕ), in agreement with the observed pattern in figure 7. The integral in (4) is readily evaluated by expressing it in the form of a series, as suggested by Wilson (1952),

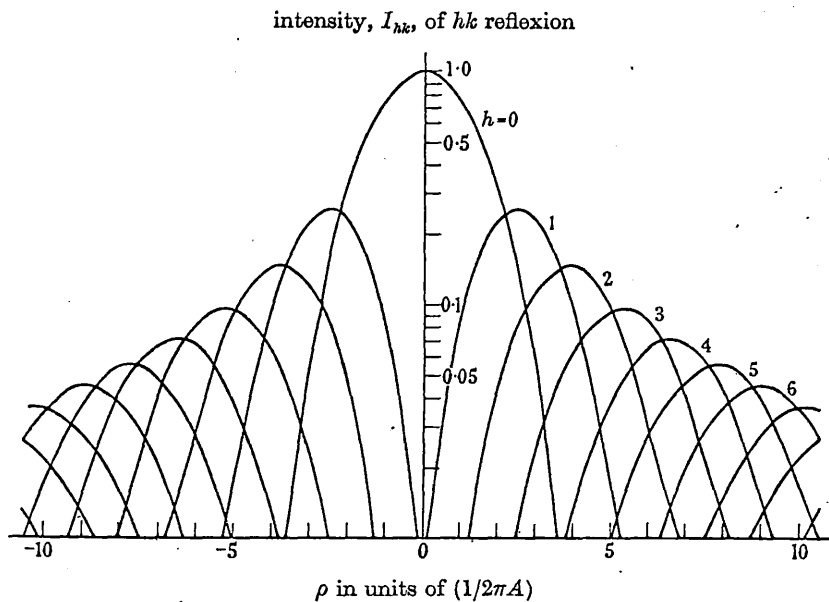


FIGURE 8. Theoretical curves for edge dislocation on Hall-Wilson model showing I_{hk} as a function of ρ for $h = 0, 1, 2, \dots$. I_{hk} is normalized to peak intensity of 00 reflexion.

and this leads to the series of curves in figure 8. These curves show I_{hk} as a function of ρ for the different orders of diffraction $h = 0, 1, 2, \dots$. For each value of h the intensity increases uniformly with ρ up to the position of peak intensity at $\rho = \rho_h$, and then falls away uniformly for $\rho > \rho_h$. Thus $2\rho_h$ corresponds with the diameter of the hk diffraction ring in figure 7. In figure 9 theoretical and observed values of ρ_h are plotted as a function of h . The theoretical points were obtained from figure 8 and the observed points by measuring the diameters of the diffraction rings in figure 7 between the positions of peak intensity. Theory and observation are in very good agreement up to the highest value of ρ_h , which corresponded to $\rho \approx 0.2a^*$. Thus equations (4) give an adequate representation of the diffraction from a dislocation with atomic displacements defined by (2), and they are still valid at a considerable distance from the ideal hkl point.

Apart from the factor $\exp(ih\phi)$, which affects the phase but not the intensity of diffraction, equations (4) describe the diffraction from a cylindrical crystal with an axial screw dislocation possessing displacements in accordance with elastic theory (Wilson 1952). The symbol h , however, now refers to the axis of the screw dislocation, so that the spreading of intensity is confined to the integral h planes perpendicular to the dislocation direction, and within these planes the intensity varies with the distance ρ from the hk point according to (4). The reciprocal lattice of a crystal with

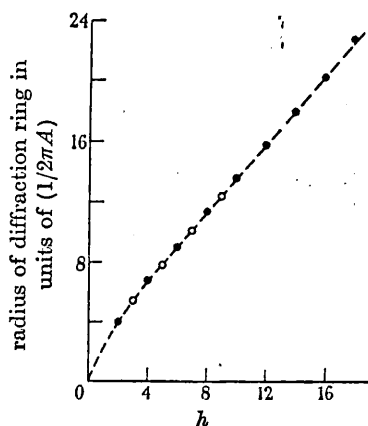


FIGURE 9. Observed (•) and calculated (o) values of radius of diffraction ring plotted against order, h .

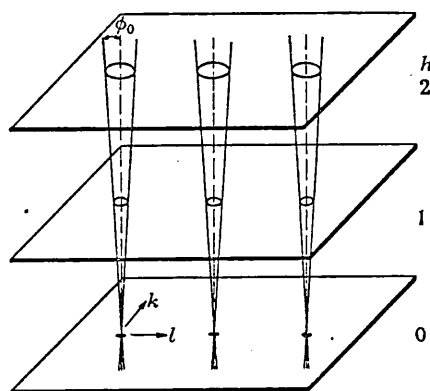


FIGURE 10. Portion of reciprocal lattice of screw dislocation. Regions of large diffracted intensity occur at intersections of integral h planes with cones of semi-angle ϕ_0 (after Frank 1949).

a single screw dislocation is therefore of the form shown in figure 10, in which the regions of large diffracted intensity are at the intersections of the integral h planes with cones of semi-angle ϕ_0 and of axes defined by $k, l = \text{integers}$ (Frank 1949). In the notation used above ϕ_0 is approximately equal to ρ_h/ha^* . Figure 10 may be considered to be derived from the diffraction pattern in figure 7 by rotating the individual diffraction rings in figure 7 through 90° about an axis through the centre of the ring and parallel to the k axis.

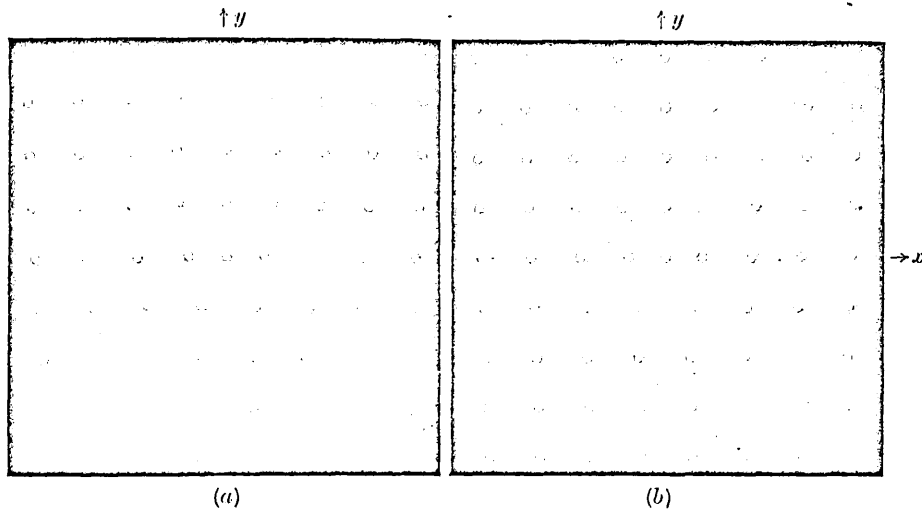


FIGURE 1. Enlarged prints of portions of gratings representing edge dislocation on (a) elastic theory model, (b) Hall-Wilson model. In (b) horizontal rows are straight.

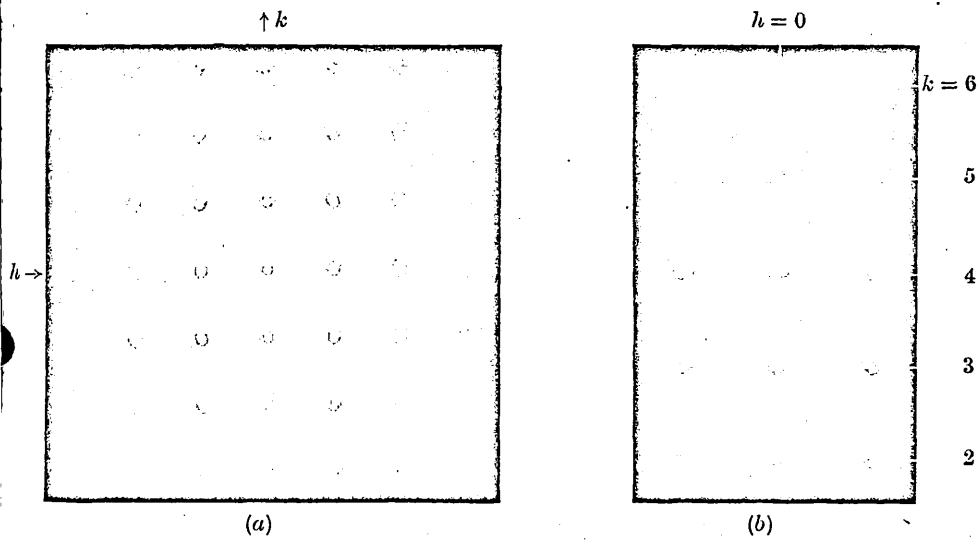


FIGURE 2. (a) Central portion of diffraction pattern of grating shown in figure 1(a). h axis parallel to Burgers vector. (b) $0k$ reflexions between $k = 2$ and $k = 6$.

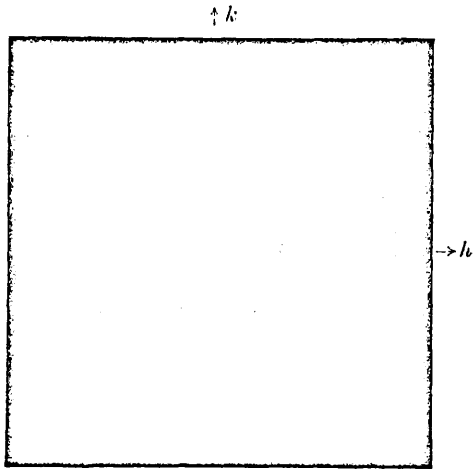


FIGURE 6. Diffraction pattern of edge dislocation at centre of bubble raft.

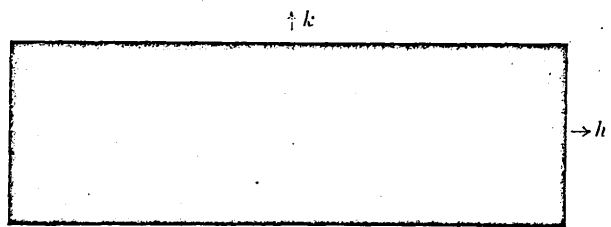


FIGURE 7. Diffraction pattern of grating shown in figure 1(b).

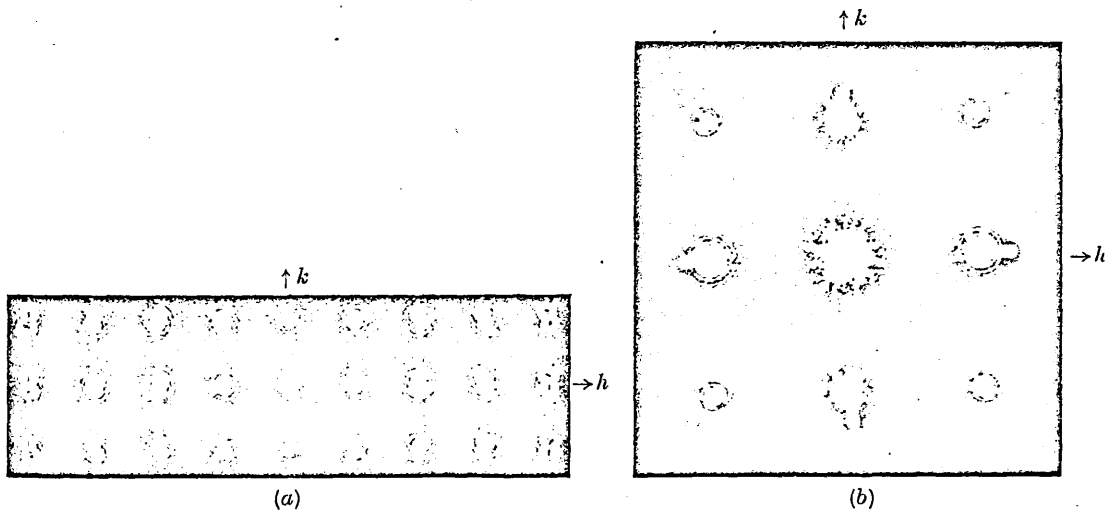


FIGURE 11. Diffraction patterns of edge dislocation showing diffuse scattering (a) between low-order reflexions, (b) around origin of reciprocal lattice.

Frank (1949) has shown that the radii ρ_h of the diffraction rings in figure 10 increase with order h according to the rough equation

$$\rho_h = \frac{1}{2\pi A} (1.5h).$$

A slightly different equation,

$$\rho_h = \frac{1}{2\pi A} (1 + 1.33h),$$

has been used by Williamson & Smallman (1956) to deduce dislocation densities from Debye-Scherrer spectra. Figure 9 shows that a more correct expression, valid for $h \geq 2$, is

$$\rho_h = \frac{1}{2\pi A} (1.8 + 1.16h).$$

4. DIFFUSE SCATTERING FROM AN EDGE DISLOCATION

Suzuki's theory discussed in § 2 can only be applied strictly in the immediate neighbourhood of the ideal reciprocal lattice points, where $\rho \ll a^*$. It was shown that the theory is in good agreement with the results obtained by the optical method up to a value of ρ of $0.1a^*$. However, for higher values of ρ it is to be expected that the correspondence between theory and observation is less satisfactory. For $\rho = 0.5a^*$ the theory breaks down completely, whereas the optical method gives an accurate representation of the diffracted intensity throughout the whole of reciprocal space.

For this reason the optical method was used to investigate the scattering between the principal reflexions. Figure 11 (a), plate 9, shows the diffraction pattern of an edge dislocation grating (elastic theory displacements) with the main reflexions considerably over-exposed in order to reveal the weak 'diffuse scattering', consisting of streaks joining the reciprocal lattice points in rows of constant h . The photograph also shows subsidiary maxima surrounding the main reflexions, and additional weak reflexions produced by a small amount of contamination of the mercury green line with the yellow doublet. The intensity of the streaks connecting reciprocal lattice points increases with order h , but the streaks still appear around the origin of reciprocal space, as shown in figure 11 (b) taken with an even longer exposure. It was found that as the radius of the grating increases the streaks become more clearly defined and more uniform in intensity, and move closer to the straight line connecting reciprocal lattice points in a given row of constant h . It appears therefore that in the case of a cylindrical crystal with a single axial edge dislocation the reciprocal lattice points in a row of constant h and l (where the l axis is along the dislocation) are joined by narrow well-defined streaks whose intensities vary little along their lengths.

5. DISCUSSION

The spreading of the main reflexions produced by a single dislocation is inversely proportional to the radius of the cylindrical crystal with its axis along the dislocation. To observe the diffraction effects listed in § 2 it is therefore necessary to use extremely fine X-ray beams which irradiate no more than a few microns of the

crystal. High-order reflexions must be studied. Using an X-ray diffractometer of sufficient resolution the intensity at the centre of the $h0$ and $0k$ reflexions should be zero for $h, k \geq 5$.

The displacements of the atoms near a wall of parallel equidistant edge dislocations in a small-angle tilt boundary are given to a good approximation by equations (1) (Burgers 1939). The diffraction is therefore approximately the same as for a single edge dislocation, apart from modification by an appropriate interference function of period $1/d$ ($\ll a^*$), where d is the separation of adjacent dislocations.

The application of the results to crystals containing other arrays of dislocations is a matter of some complexity. The distribution of intensity around the ideal reciprocal lattice points is independent of the structure type (§ 2), so that the results apply to structures other than simple-cubic. If, however, a face-centred cubic crystal is chosen, the Burgers vector of a total dislocation is parallel to $[110]$, so that a given crystal is expected to possess such dislocations lying along the six different $[110]$ directions. Consequently, the observed X-ray diffraction pattern will be considerably more complex than the pattern for a single dislocation. A more practical method of studying the diffraction from arrays of non-parallel dislocations may be the investigation of the diffuse scattering between reciprocal lattice points.

My thanks are due to Dr T. Suzuki and Professor F. C. Frank, F.R.S., for valuable discussions; Dr H. M. Finnieston, Dr J. Thewlis and Mr K. R. E. Smith for comments on the manuscript; and Dr W. M. Lomer for the loan of several photographs of bubble rafts.

REFERENCES

- Bragg, W. L. & Nye, J. F. 1947 *Proc. Roy. Soc. A*, **190**, 474.
 Burgers, J. M. 1939 *Acad. Sci. Amst.* **42**, 293, 378.
 Frank, F. C. 1949 *Research, Lond.*, **2**, 542.
 Hall, W. H. 1950 Ph.D. Thesis (Birmingham).
 Read, W. T. 1953 *Dislocations in crystals*. New York: McGraw-Hill.
 Suzuki, T. 1957 (In preparation.)
 Suzuki, T. & Willis, B. T. M. 1956 *Nature, Lond.*, **177**, 712.
 Williamson, G. K. & Smallman, R. E. 1956 *Phil. Mag.* (8), **1**, 34.
 Willis, B. T. M. 1957 *Proc. Roy. Soc. A*, **239**, 184 (part I).
 Wilson, A. J. C. 1949 *Research, Lond.*, **2**, 541.
 Wilson, A. J. C. 1950 *Research, Lond.*, **3**, 387.
 Wilson, A. J. C. 1952 *Acta Cryst.* **5**, 318.
 Wilson, A. J. C. 1955 *Nuovo Cim.* (10), **1**, 277.

J. A. White

12

*Reprinted without change of pagination from the
Proceedings of the Royal Society, A, volume 248, pp. 183-198, 1958*

An optical method of studying the diffraction from imperfect crystals

III. Layer structures with stacking faults

BY B. T. M. WILLIS

Atomic Energy Research Establishment, Harwell, Berks

(Communicated by A. H. Cottrell, F.R.S.—Received 2 April 1958)

[Plates 7 and 8]

The reciprocal lattice intensity distribution has been determined quantitatively using a photomultiplier to measure the optical diffraction intensities. The systems examined included the simple-cubic structure with 'wollastonite-type' stacking faults, the close-packed-hexagonal structure with growth faults, and the face-centred-cubic structure with deformation faults on one set and on two sets of {111} planes. It is shown that the Paterson (1952) analysis of the diffraction from deformation faulted f.c.c. crystals can be extended to intersecting faulted {111} planes, provided that the faulting parameter, α , is not greater than about 0.1.

The main limitation of the optical method concerns the restriction in the number of layers (10^3) which can be conveniently represented in one grating. This restriction gives rise to weak fluctuations in the observed intensity distribution and to an uncertainty of up to 0.03 in the determination of α from this distribution.

1. INTRODUCTION

The structure of many solids can be conceived as the stacking together of identical layers of atoms. These layer structures often contain 'stacking faults', or errors in the sequence of layers, where the order of two successive layers fails to conform with the regular stacking sequence. Stacking faults may arise in several ways: during crystal growth (as in graphite, silicon carbide), after phase transformation (cobalt, lithium), or by cold-work (gold, copper, α -brass).

X-ray diffraction provides the main experimental evidence for stacking faults. The effect of the faults on the reciprocal lattice is to draw out some of the hkl points into rods, whose long axis corresponds with the direction normal to the layers. A study of the intensity distribution along these rods in single-crystal X-ray patterns can lead to a determination of the kind and density of the faults; similar information can be obtained from powder photographs, where the faults produce a broadening, and in some cases a displacement, of the Debye-Scherrer lines. This kind of study assumes a knowledge of the theoretical intensity distribution for diffraction from the faulted layer system under investigation, but these theoretical treatments are restricted in a number of ways:

(a) They have been worked out for only a limited number of faulted layer systems: there are many possible systems which have not yet been theoretically examined.

(b) To simplify the theory it is normally assumed that the faults are distributed at random intervals along the stacking direction, i.e. there is no interaction between

faults, and that they extend over complete atomic layers. In some cases at least there is evidence that neither assumption is true (Christian & Spreadborough 1956; Barrett 1950).

(c) The diffraction treatments normally apply to faulting on one set of layer planes only. Thus in the case of stacking faults in deformed face-centred-cubic metals the diffraction theory has been developed for faulting on one set of close-packed planes only (Paterson 1952), whereas faults produced by heavy cold-work probably occur simultaneously on several intersecting sets of $\{111\}$ planes.

The optical method (Willis 1957) provides an alternative way of determining the distribution of diffracted intensity from a given faulted layer structure. The method can be applied to any layer structure in which an individual fault consists of a translation (not necessarily constant) of the layer in one fixed direction, or to any structure containing such faults on two different sets of intersecting layers. The most serious limitation to the optical method, at least as regards making quantitative predictions from the optical diffraction patterns, concerns the number of layers of the crystal that can be represented in one grating. If one row of the grating corresponds to one layer of the crystal, the maximum number of layers that can be conveniently represented is about 10^3 , whereas a typical single crystal for X-ray diffraction work may contain 10^5 to 10^7 layers. For randomly spaced stacking faults a strict representation of the structure must include all the layers. Taylor, Hinde & Lipson (1951) used 40-row gratings to study the diffraction from growth-faulted cobalt, but the number of rows was insufficient to allow quantitative evaluation of the diffraction pattern.

The preparation of gratings and the recording of their diffraction patterns are described in the following section, and in §3 the validity of the optical method is tested by comparing the observed and calculated intensity distributions along the diffraction streaks of 'wollastonite-type' faulted gratings. It is shown that the effect of the limited number of rows in the grating is to reduce the amount of detail which can be observed in the optical diffraction pattern, but that under carefully chosen conditions of observation close agreement is obtained between theory and observation. With these conditions established the diffraction from faulted close-packed structures is examined in §4; the cases considered are stacking faults in one set of planes for face-centred-cubic (f.c.c.) and for close-packed-hexagonal (c.p.h.) structures, and faults in two sets of intersecting planes for f.c.c.

2. EXPERIMENTAL METHOD

(a) Preparation of gratings

As a typical example the preparation will be described of gratings representing the structure illustrated in Figure 1 (a). This diagram is a projection in the ac plane of a faulted simple-cubic structure, in which a single fault consists of a displacement of the (001) plane of atoms in its own plane by $\frac{1}{2}\mathbf{a}$. In the complete structure these faults appear at random intervals in the [001] direction and with a density α . The faulting parameter, or faulting density, α , is defined as the probability that a given layer is faulted.

To prepare the corresponding gratings the grating machine described previously (Willis 1957) was used. A row of 5μ pinholes, spaced 50μ apart, was repeated photographically at intervals of 50μ perpendicular to its length; at the position of a fault an additional displacement was made of 25μ along the row. This latter displacement was made by means of a micrometer, which had an attachment allowing rapid rotation of the micrometer head between two fixed positions 25μ apart. The original row was repeated a thousand times, and so each grating represented the stacking of a thousand layers of atoms in a structure with a fixed faulting parameter, α . The time required to rule one grating was less than 1 h.

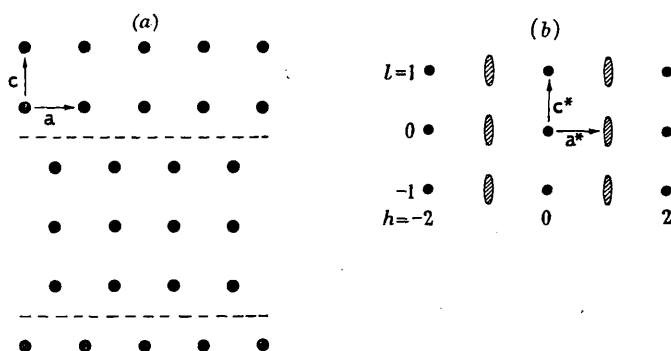


FIGURE 1. (a) Projection in ac plane of simple-cubic structure with faults consisting of a displacement of (001) planes by $\frac{1}{2}a$. The fault positions are indicated by broken lines. (b) Portion of corresponding reciprocal lattice.

Tables of random numbers (Kendall & Babington-Smith 1951) were used to obtain the positions of the faults in a particular grating. These tables contain sets of a thousand digits with each set consisting of the digits 0 to 9 in a random sequence. The sequence of digits in a given set was associated with the sequence of a thousand rows in a given grating; for a faulting parameter of, say, 0.2 two of the digits from 0 to 9 were chosen to denote the faulted positions and the remaining eight digits the unfaulted positions.

(b) Observation of diffraction patterns

The patterns were observed with a modified Lipson optical diffractometer (figure 2(a)). After reflexion at the mirror M , monochromatic light from the mercury-arc source L was focused on the entrance pinhole E , $\frac{1}{2}$ mm in diameter. The grating G was immersed in cedar-wood oil and placed between two optical flats, which in turn were located between two identical plano-convex lenses, L_1 and L_2 . These lenses were 11 cm in diameter, 150 cm in focal length and corrected for spherical aberration, which was the only serious form of aberration affecting the diffraction pattern. The diffracted beams were reflected in the optically flat mirror F and brought to a focus in the plane P conjugate with the horizontal plane through E .

To measure the intensity distribution in the diffraction pattern a photomultiplier PM was used, mounted on a platform Q shown in detail in figure 2(b).

At the centre of this platform and in the focusing plane of the diffracted beams was an adjustable slit S through which the light entered the multiplier. The diffraction pattern was scanned by moving the platform along rails R with the aid of a micrometer C . To photograph the pattern the whole assembly in figure 2(b) could be interchanged with a quarter-plate holder. Different magnifications of the pattern were achieved by placing the grating not only in the parallel beam between the two lenses, but also at the alternative positions G_1 , G_2 in the divergent beam above L_1 .

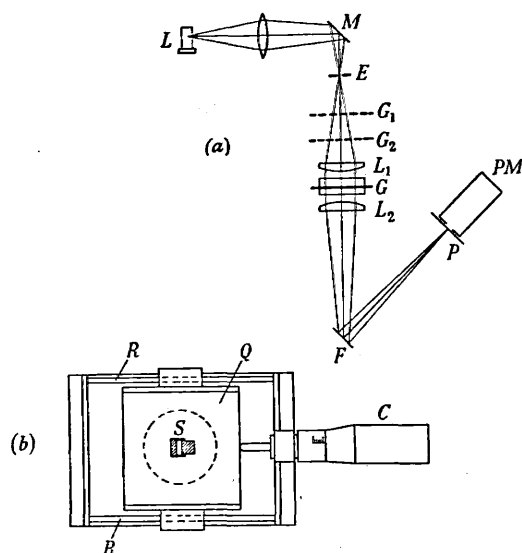


FIGURE 2. Apparatus for recording optical diffraction patterns: (a) diffractometer; (b) detail of multiplier assembly, with broken circle denoting position of multiplier.

3. WOLLASTONITE-TYPE FAULTS

The type of fault shown in figure 1(a), involving a displacement of a layer in its own plane by $\frac{1}{2}\mathbf{a}$, occurs in wollastonite (Jeffrey 1953), and the corresponding diffraction problem for a randomly spaced set of faults has been treated theoretically by Wilson (1949). In this section the results given by the theory and by the optical method are compared, and from this an estimate is obtained of the accuracy with which quantitative predictions can be made by the optical method. This particular faulted system was examined first because of its simplicity.

(a) Theory

A portion of the reciprocal lattice in the $\mathbf{a}^*\mathbf{c}^*$ plane, as given by Wilson's theory, is illustrated in figure 1(b). Columns of reflexions with h even are unaffected by the faults, but those with h odd are drawn out into streaks in the direction of the \mathbf{c}^* -axis. The intensity $I(l)$ at a point along the streak with co-ordinate l (not necessarily integral) is given by the series (Wilson 1949):

$$I(l) = NA_0 + 2(N-1)A_1 \cos 2\pi l + \dots + 2A_{N-1} \cos 2\pi(N-1)l. \quad (1)$$

Here N is the total number of layers in the crystal, or rows in the grating, and

$$A_n = F^2(1 - 2\alpha)^n,$$

where F is the structure factor of a unit cell in the unfaulted structure and α is the faulting parameter. Wilson summed (1) assuming $\alpha \ll 1$, but as we are going to study gratings for which this condition does not necessarily apply, the summation must be carried out for the complete range of α ($0 \leq \alpha \leq 1$). This is easily done by putting

$$\delta = (1 - 2\alpha) \exp 2\pi i l,$$

whence (1) becomes

$$I(l) = NF^2 + 2F^2 \Re \left[\frac{(N-1)\delta - \delta^N}{(1-\delta)} - \frac{\delta^2 - \delta^N}{(1-\delta)^2} \right], \quad (2)$$

where \Re denotes the real part of the term in square brackets. Each grating contained 1000 rows, i.e. $N = 10^3 \gg 1$, so that (2) is given very closely by

$$I(l) = \frac{2NF^2\alpha(1-\alpha)}{1-2\alpha+2\alpha^2-(1-2\alpha)\cos 2\pi l}. \quad (3)$$

Strictly speaking, formula (3) represents the average intensity from a large number of gratings, each containing 1000 rows, with the same faulting parameter α but with different sequences of randomly distributed faults. We require to investigate how closely the diffraction from any one of these individual gratings is represented by (3).

(b) *Observed intensity distribution*

Photographs of the diffraction patterns from gratings with different values of α are shown in figure 3, plate 7. In agreement with figure 1(b), columns of reflexions with h even consist of well-defined spots, whereas those with h odd are drawn out into streaks along the \mathbf{c}^* direction. For $\alpha = 0.1$ the streaks are quite short, but as α increases they elongate until, for $\alpha = 0.5$, they fuse together into one continuous band. The streaks contract again for $\alpha > 0.5$, but are now centred on points with half-integral values of l .

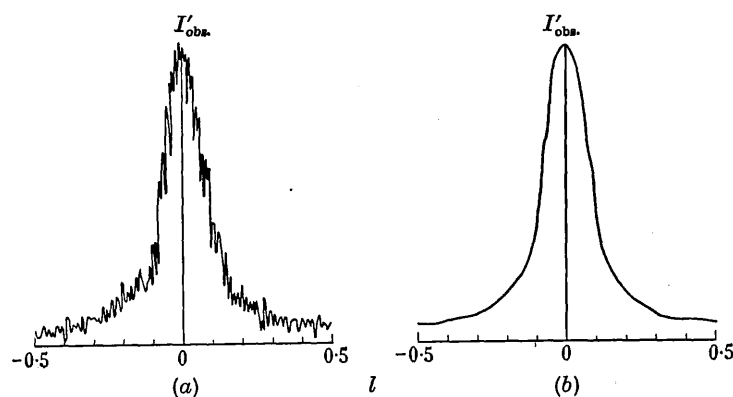


FIGURE 4. Intensity as a function of distance along diffraction streak of $\alpha = 0.2$ grating, as measured using a width t of multiplier slit of (a) 0.1 m, (b) 1 mm. The order separation is 17 mm.

Figure 4 shows the observed intensity as a function of l along the $h = 1$ column of the grating with faulting parameter of 0.2. The two curves refer to different values of the width t of the multiplier slit. For very small t (figure 4(a)) fluctuations appeared in the intensity distribution curve, but these were smoothed out by opening up the slit (figure 4(b)). It was found that by masking a portion of the grating, so as to reduce the number of rows in the grating contributing to the diffraction pattern, the fluctuations became more pronounced. This indicates that their origin is connected with the limited number of rows in the grating, and that they would disappear if this number was increased sufficiently. For our present purpose these fluctuations are undesirable, and must be removed by increasing the multiplier slit width, in spite of the loss of resolution in the measurement of the intensity distribution that this entails. The minimum value of t consistent with negligible fluctuations of intensity was found to be about a quarter of the half-width of the diffraction peak, a criterion for the magnitude of t which is used in all the intensity measurements described below. For any given faulted layer system adjacent diffraction peaks are normally separated by a whole order, or by a large fraction of an order, so that the loss of resolution imposed by the finite width of multiplier slit is not serious.

(c) *Correction of observed distribution*

Formula (3) refers to the intensity distribution from a grating with infinitely small scattering elements and for which the diffraction pattern is observed using infinitely small multiplier slit S and entrance pinhole E (figure 2). Before comparing observed and theoretical intensity distributions the influence on the observed distribution must be considered of the following three factors:

- (a) finite diameter d of the holes of the grating,
- (b) finite width t of the multiplier slit,
- (c) finite diameter a of the entrance pinhole.

The intensity distribution in the diffraction pattern of a grating with holes of diameter d is equivalent to the distribution for infinitely small holes after multiplication by the Airy modulation function $A(l)$. $A(l)$ is of the form

$$\frac{4J_1^2\{\beta\sqrt{(h^2+l^2)}\}}{\beta^2(h^2+l^2)}, \quad (4)$$

where J_1 is the Bessel function of first order, β is a constant proportional to the diameter of the holes and h is the order number of the column in which the reflexion occurs. The correction arising from (a) was made by plotting formula (4) as a function of l , choosing β so that $A(l)$ was reduced by the ratio of the corresponding observed intensities in passing from $l = 0$ to $l = 1$. The corrected intensity was then obtained by dividing the observed intensity by $A(l)$ (figure 5(a)).

The correction due to (b) was evaluated using the equation

$$I'_{\text{obs.}}(l) = \frac{1}{t} \int_{l-\frac{1}{2}t}^{l+\frac{1}{2}t} I_{\text{obs.}}(l) dl, \quad (5)$$

where $I'_{\text{obs.}}(l)$ is the observed intensity for a multiplier slit of width t , and $I_{\text{obs.}}(l)$ is the intensity which would have been measured *under the same conditions of*

resolution with an infinitely small slit. The difference between $I'_{\text{obs.}}$ and $I_{\text{obs.}}$ was relatively small, and for this reason $I_{\text{obs.}}$ was readily determined from (5) by a trial-and-error graphical procedure (figure 5(b)).

Finally, the observed distribution depends on the diameter a of the entrance pinhole E in figure 2(a), and must be corrected for the condition $a \rightarrow 0$. This correction was calculated assuming incoherent illumination at E . As the maximum value of a corresponded to $\frac{1}{30}$ th of the order separation, the correction proved to be negligible except for $\alpha \leq 0.1$.

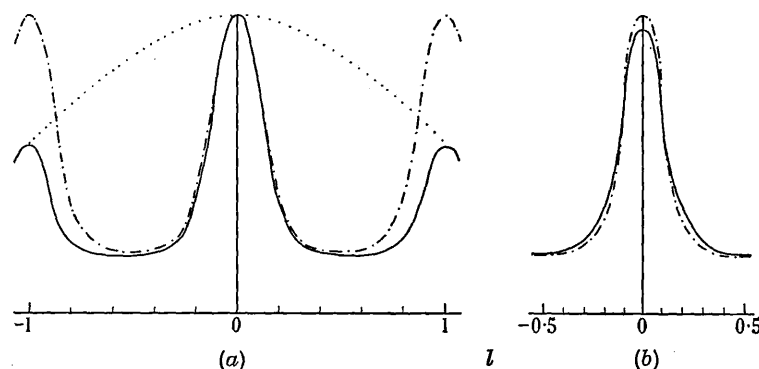


FIGURE 5. Correction of observed distribution curve for: (a) finite diameter of holes of grating, (b) finite width of multiplier slit. —, observed distribution; - - - - -, corrected observed distribution;, Airy function $A(l)$.

(d) Comparison between theory and observation

The observed intensity distribution curves for $\alpha = 0.1, 0.3, 0.5$, corrected in the manner indicated above, are shown in figure 6, together with the corresponding theoretical curves calculated from formula (3). The scale of intensity for each curve has been adjusted to give the same integrated intensity between adjacent orders. Agreement between observed and theoretical curves is good, and this is also borne out by table 1 which compares observed and theoretical values of $I_{\text{min.}}/I_{\text{max.}}$, the ratio of the minimum and maximum intensities along a diffraction streak. The table indicates that the faulting parameter of a grating can be deduced to within a factor of ± 0.02 from observations on the intensity distribution in its diffraction pattern.

TABLE 1. RATIO OF MINIMUM AND MAXIMUM INTENSITIES ALONG A DIFFRACTION STREAK

faulting parameter, α	$10^2 I_{\text{min.}}/I_{\text{max.}}$	
	observed	calculated
0.1	1.2	1.0
0.2	7.0	6.5
0.3	19.5	18.5
0.4	42.0	44.5
0.5	92.5	100.0

It is concluded that, in spite of the loss of resolution associated with using a multiplier slit of definite width, the optical method adequately reproduces the main features of the diffraction from layer structures with wollastonite-type stacking faults. In the next section we will see that the same kind of accuracy can be achieved with other faulted layer systems.

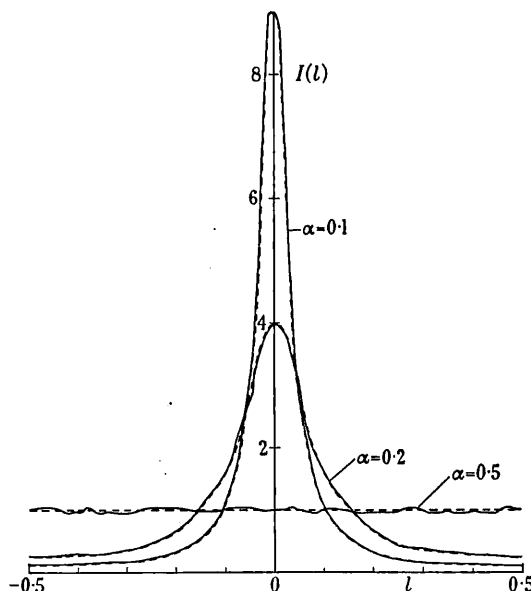


FIGURE 6. Observed intensity distribution curves along diffraction streaks of wollastonite-type faulted gratings with different values of α . Theoretical curves are shown dotted. $I(l)$ is in arbitrary units.

4. STACKING FAULTS IN FACE-CENTRED-CUBIC AND CLOSE-PACKED-HEXAGONAL STRUCTURES

There are three possible kinds of position, usually denoted A , B and C , for the atoms in a close-packed layer, and the sequence of packing of these layers is $ABCABC\dots$ for f.c.c. and $ABAB\dots$ (or $BCBC\dots$ or $CACA\dots$) for c.p.h. A stacking fault occurs when either of these regular sequences is interrupted, with the restriction that adjacent layers must be different. There are two possible positions for each layer, so that a very large number of stacking sequences are theoretically possible; however, we will only be concerned here with sequences of randomly spaced 'growth faults' and 'deformation faults', as most theoretical diffraction treatments have been devoted to these cases. The stacking rule for grown faults is that, at the position of each fault, the next nearest layers are the same for f.c.c. and different for c.p.h.; in faulting by deformation the original packing sequence is maintained on either side of the fault, but the crystal as a whole slips at the fault.

The three types of layer change into one another by slip along the $[2\bar{1}1]$ direction (cubic indices). The change in atomic positions produced by the different types of stacking fault is therefore seen most readily from a projection of the structure normal to $[01\bar{1}]$, i.e. normal to the plane containing $[2\bar{1}1]$ and the stacking

direction $[111]$. (The corresponding projection for the c.p.h. structure is normal to $[110]$ (hexagonal indices).) Figure 7 illustrates how disorder is introduced in this projection by a single deformation fault in f.c.c. and a single growth fault in c.p.h. It is clear that for stacking faults confined to a single set of close-packed planes the complete structure in three dimensions is obtained in each case by regularly repeating in two directions the row of atoms marked by the dotted line.

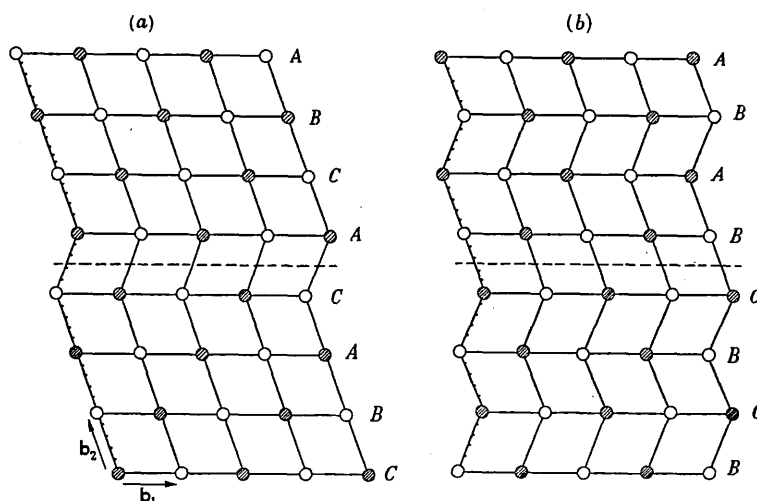


FIGURE 7. (a) Projection on a plane normal to $[01\bar{1}]$ of f.c.c. structure with single deformation fault; (b) projection on a plane normal to $[110]$ of c.p.h. structure with single growth fault. The unfaulted sequence is $ABCABC \dots$ in (a) and $ABAB \dots$ in (b). The open and closed circles represent atoms in different elevations.

If the number of such repetitions is large, the reciprocal lattice is confined to regions which spread out only in the direction corresponding to the normal to the close-packed planes. The theory of diffraction from faulted close-packed structures is concerned primarily with the variation of intensity of the diffraction streaks along this direction, but the intensity distribution can also be derived optically, using gratings which represent the projection of the structure normal to $[01\bar{1}]$. A minor difficulty here is that the atoms in the two different elevations (figure 7) cannot be distinguished in the grating; the effect of this on the reciprocal lattice is discussed below.

(a) Growth-faulted hexagonal cobalt

Cobalt can crystallize in either a f.c.c. or c.p.h. arrangement, but in the hexagonal form it is imperfect, giving a mixture of sharp and diffuse lines on an X-ray powder photograph (Edwards & Lipson 1942). Wilson (1942) has shown that the X-ray observations can be explained by postulating the development of randomly spaced growth faults, which give rise to a reciprocal lattice of the form shown in figure 8(a). The \mathbf{C}^* -axis in this figure is reciprocal to the hexagonal $[001]$ direction, and the indices corresponding to \mathbf{A}^* , \mathbf{C}^* are H , L . Columns of reflexions with H divisible by 3 consist of sharp spots, as in the unfaulted structure, but the remaining columns consist of alternating short and long streaks.

The layer sequence for 1000 layers of cobalt was determined using random number tables, and the corresponding gratings were prepared on the basis of figure 7(b) by using a uniform row of elements to represent a horizontal row of atoms, and repeating this along the direction of the dotted line. Figure 9, plate 7, is a photograph of the central portion of the diffraction pattern from such a grating; the pattern reproduces the main features of the reciprocal lattice in figure 8(a). The observed intensity distribution along the diffraction streaks of the

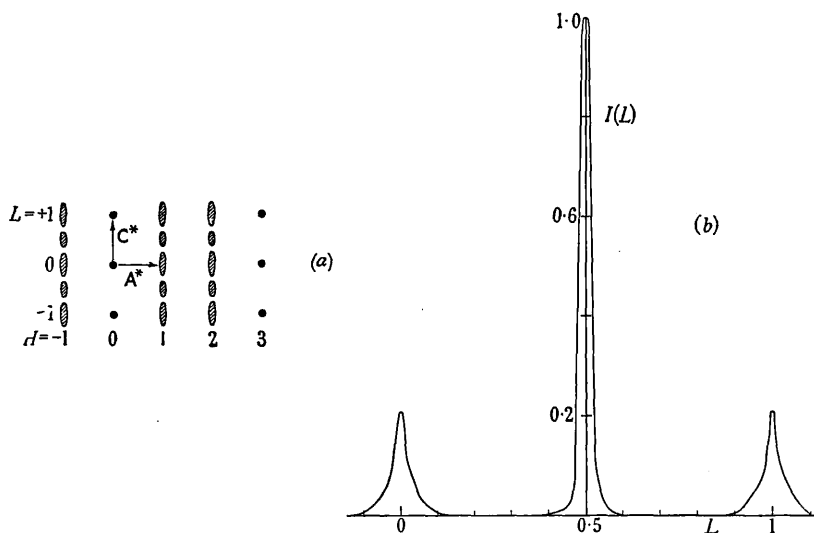


FIGURE 8. (a) Portion of reciprocal lattice of growth-faulted hexagonal cobalt (after Edwards & Lipson 1942). \mathbf{C}^* corresponds to the normal to the close-packed planes. (b) Intensity distribution along diffraction streaks of corresponding grating ($\alpha = 0.1$).

$\alpha = 0.1$ grating is given in figure 8(b). According to Wilson (1942) the faulting parameter for hexagonal cobalt is about 0.1, and the intensity distribution curve which he deduced theoretically for this value of α is virtually the same as that in figure 8(b).

(b) *Face-centred-cubic deformation faults on one set of close-packed planes*

The diffraction patterns of gratings with faulting densities of 0.1, 0.3 and 0.5, and prepared on the basis of the projection in figure 7(a), are shown in figure 10, plate 8. Figure 11 is a diagram based on these photographs and indicating the main features of the reciprocal lattice. The points of intersection of the broken lines mark the positions of the reciprocal lattice points of the unfaulted structure ($\alpha = 0$), and the axes \mathbf{b}_1^* , \mathbf{b}_2^* are reciprocal to the axes \mathbf{b}_1 , \mathbf{b}_2 in figure 7(a). If H_1 , H_2 are the indices, treated as continuous variables, corresponding to \mathbf{b}_1^* , \mathbf{b}_2^* , then reciprocal lattice points with $H_2 = 3n$ (n integral) are not affected by the faulting, but the remaining points ($H_2 = 3n \pm 1$) are drawn out into symmetrical streaks. The peaks of these streaks are displaced along \mathbf{b}_1^* by an amount $\pm \Delta H_1$ depending on α , and the sign of the displacement corresponds to the sign in $H_2 = 3n \pm 1$.

In table 2 the observed displacements ΔH_1 are given for different values of α . They are compared with the displacements calculated from the diffraction theory of Paterson (1952), which gives

$$|\Delta H_1| = \frac{1}{6} - (1/2\pi) \arctan [\sqrt{3} (1 - 2\alpha)]. \quad (6)$$

The difference between observed and calculated values of $|\Delta H_1|$ is equivalent to a difference in α of up to 0.03. Thus from observations of the optical diffraction pattern the faulting parameter can be estimated to about the same accuracy as that noted previously for wollastonite-type faults.

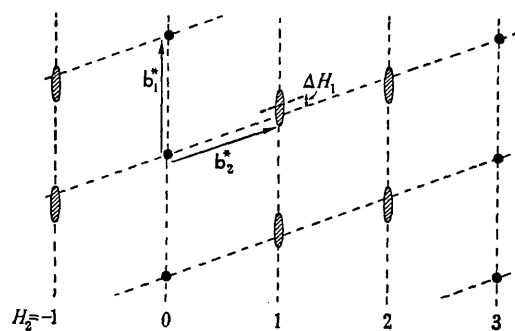


FIGURE 11. Diagram indicating main features of reciprocal lattice for f.c.c. deformation faults on $\{111\}$ planes.

TABLE 2. FACE-CENTRED-CUBIC DEFORMATION FAULTS ON ONE SET OF PLANES: DISPLACEMENT OF PEAK OF DIFFRACTION STREAK FROM IDEAL RECIPROCAL LATTICE POINT

faulting parameter, α	displacement $ \Delta H_1 $, expressed as percentage of $ b_1^* $	
	observed	calculated
0	0	0
0.1	1.7	1.6
0.2	3.7	3.9
0.3	6.8	7.1
0.4	10.5	11.4
0.5	17.6	16.7

The displacement of the peaks of the diffraction streaks and the dependence of this displacement on α form the basis of the determination by X-ray methods of the faulting parameters of heavily cold-worked f.c.c. metals and alloys (Warren & Warekois 1955; Christian & Spreadborough 1956; Smallman & Westmacott 1957). However, severe cold-work probably produces faulting on more than one set of $\{111\}$ planes, whereas the Paterson analysis applies to deformation faulting on one set only. Thus the physical significance of α , obtained by substituting the measured displacements into equation (6), is unknown. Warren & Warekois (1955) have suggested that it may be a good enough approximation to consider this value of α as the sum of the probabilities of faulting in the different sets of active $\{111\}$.

planes, but they gave no justification for this suggestion. We examine next the diffraction from gratings representing f.c.c. structures with deformation faults on two sets of close-packed planes, and show from the analysis of the results that Warren's suggestion is in fact correct provided that $\alpha \ll 1$.

(c) *Face-centred-cubic deformation faults on (111) and $(\bar{1}\bar{1}\bar{1})$ planes*

Figure 7(a) shows the atomic positions for a single stacking fault between close-packed (111) planes. Both sets of close-packed planes, (111) and $(\bar{1}\bar{1}\bar{1})$, are viewed on edge in this projection, so that a stacking fault between the $(\bar{1}\bar{1}\bar{1})$ planes could equally well have been shown. The atomic arrangement in figure 12 corresponds to faults occurring simultaneously on both sets of planes. The distortion is severe where the faults cross (indeed, this is a source of hardening for slip), and there will be a re-adjustment of the atomic positions in this region. Nevertheless, at least for relatively small faulting densities, figure 12 may be considered to be a good representation of the atomic positions for stacking faults on two sets of intersecting close-packed planes.

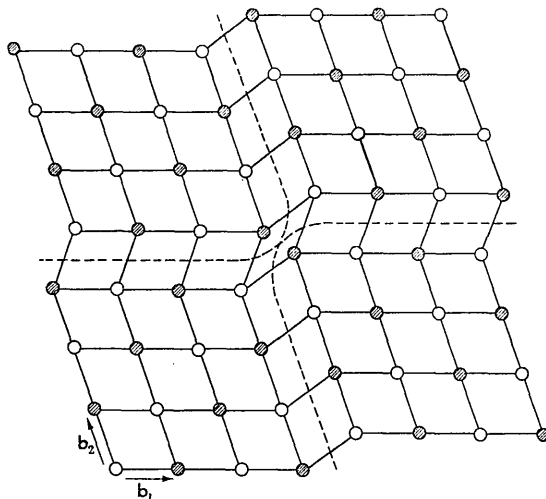


FIGURE 12. Projection normal to $[01\bar{1}]$ of f.c.c. structure with a single deformation fault on each of the (111) and $(\bar{1}\bar{1}\bar{1})$ sets of planes. The open and closed circles represent atoms in different elevations.

The corresponding gratings were prepared in two stages: one row of the grating, representing a row of atoms along the \mathbf{b}_1 direction (figure 12), was made first, and this row was then repeated in the \mathbf{b}_2 direction to give the final grating of 1000×1000 elements. The same faulting density α was given to each set of faults, but different sequences of random numbers were used in 'programming' each set.

Figure 13, plate 8, shows a photograph of the diffraction pattern for $\alpha = 0.15$, and figure 14 is a diagram based on this photograph and indicating the positions of the peaks of the reflexions. The points of intersection of the broken lines ($H_1, H_2 = \text{integers}$) define the positions of the ideal reciprocal lattice points. The section of the reciprocal lattice shown repeats in the $\mathbf{b}_1^* \mathbf{b}_2^*$ plane at intervals corresponding to multiples of 3 of H_1 and H_2 .

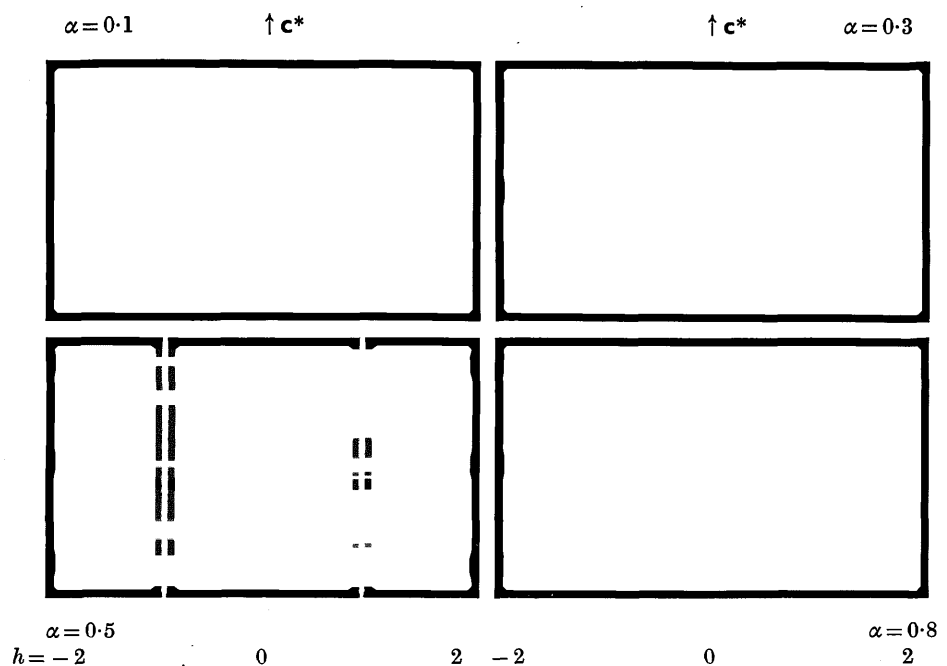


FIGURE 3. Diffraction patterns from gratings representing wollastonite-type faulted structures with different values of faulting parameter, α . Reflexions in the h -odd columns are drawn out into streaks along c^* .

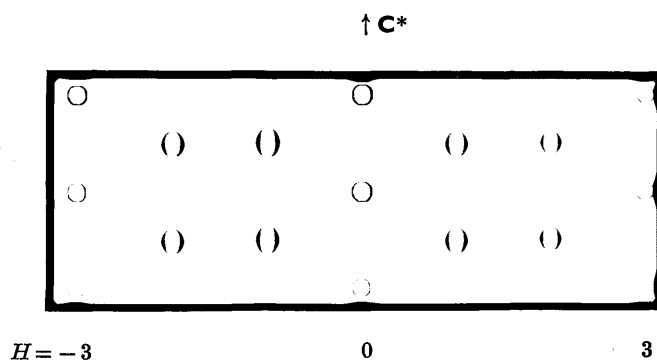


FIGURE 9. Diffraction pattern of grating representing growth-faulted hexagonal cobalt ($\alpha=0.3$), showing alternating strong and weak streaks in $H=3n \pm 1$ columns.

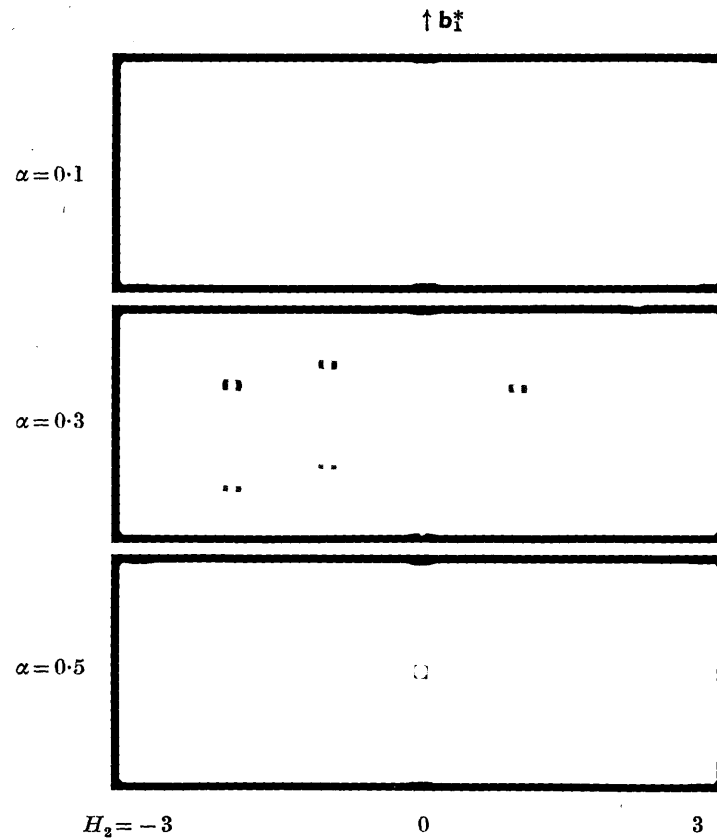


FIGURE 10. Diffraction patterns of gratings representing f.c.c. structure with deformation faults on one set of close-packed planes only. The peaks of the $H_2 = 3n \pm 1$ reflexions are progressively displaced along \mathbf{b}_1^* as α increases.

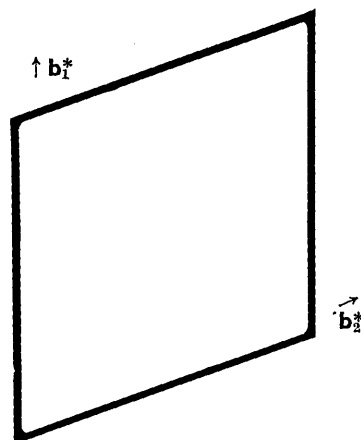


FIGURE 13. Diffraction pattern of grating representing f.c.c. structure with random deformation faults on both (111) and $(\bar{1}\bar{1}\bar{1})$ planes.

The reciprocal lattice in three dimensions is obtained by repeating the pattern in figure 14 in the planes $H_3 = 0, 2, 4, \dots$, where H_3 is the index defined in equation (8) below. However, as we cannot distinguish in the grating representation between the two kinds of atoms in the projection on to the $(0\bar{1}\bar{1})$ plane, the unit cell of the grating is smaller than the true cell. By consequence, the pattern in figure 14 is also repeated in the planes $H_3 = 1, 3, 5, \dots$, but is displaced so that the origin of the pattern is at $(H_1 H_2) = (\frac{3}{2} \frac{3}{2})$.

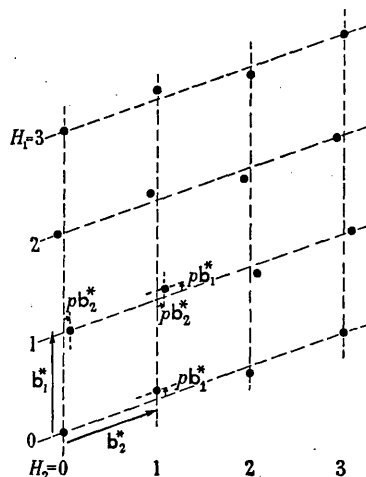


FIGURE 14. Diagram indicating main features of reciprocal lattice for f.c.c. deformation faults on both (111) and $(\bar{1}\bar{1}\bar{1})$ planes.

TABLE 3. CLASSIFICATION OF $H_1 H_2$ REFLEXIONS

	H_1	H_2	ΔH_1	ΔH_2
A-type	$3m$	$3n \pm 1$	0	$\pm p$
	$3m \pm 1$	$3n$	$\pm p$	0
B-type	$3m \pm 1$	$3n \pm 1$	$\pm p$	$\pm p$
C-type	$3m$	$3n$	0	0

The reflexions can be classified into three types according to the kind of displacement from the ideal reciprocal lattice points: *A*-type displaced along either \mathbf{b}_1^* or \mathbf{b}_2^* ; *B*-type displaced along both \mathbf{b}_1^* and \mathbf{b}_2^* ; and *C*-type undisplaced. If $\Delta H_1, \Delta H_2$ are the components of the displacement along $\mathbf{b}_1^*, \mathbf{b}_2^*$, the three types are characterized in the way indicated in table 3. For H_3 odd the number $\frac{3}{2}$ must be added to each entry in the first two columns. In this table m, n are integers and $\Delta H_1, \Delta H_2 = \pm p$ means a displacement of $\pm p\mathbf{b}_1^*, \pm p\mathbf{b}_2^*$, the choice of sign corresponding to $H_1, H_2 = 3m \pm 1$.

Figure 15 shows the measured variation of p with α . The broken line represents the peak displacement given by the Paterson equation (6); it is clear that p increases with α at a lower rate than for the one-dimensional case, but that the two curves coincide approximately for α less than 0.12. In the following we use this result to calculate the relative displacements of Debye-Scherrer lines, as produced by weak deformation faulting ($\alpha \ll 1$) in the (111) and $(\bar{1}\bar{1}\bar{1})$ planes.

The value of d^* ($= 2 \sin \theta/\lambda$) is given by

$$d^{*2} = |H_1 \mathbf{b}_1^* + H_2 \mathbf{b}_2^*|^2 + |H_3 \mathbf{b}_3^*|^2, \quad (7)$$

where $\mathbf{b}_1^* \mathbf{b}_2^* \mathbf{b}_3^*$ are reciprocal to $\mathbf{b}_1 \mathbf{b}_2 \mathbf{b}_3$ and $H_1 H_2 H_3$ are the corresponding indices. The axes $\mathbf{b}_1, \mathbf{b}_2$ are in the $(01\bar{1})$ plane and \mathbf{b}_3 normal to this plane; the three axes are related to the cubic axes $\mathbf{a}_1 \mathbf{a}_2 \mathbf{a}_3$ by the equations

$$\mathbf{b}_1 = \frac{1}{2}\mathbf{a}_1 + \frac{1}{4}\mathbf{a}_2 + \frac{1}{4}\mathbf{a}_3,$$

$$\mathbf{b}_2 = -\frac{1}{2}\mathbf{a}_1 + \frac{1}{4}\mathbf{a}_2 + \frac{1}{4}\mathbf{a}_3,$$

$$\mathbf{b}_3 = \frac{1}{2}\mathbf{a}_2 - \frac{1}{2}\mathbf{a}_3.$$

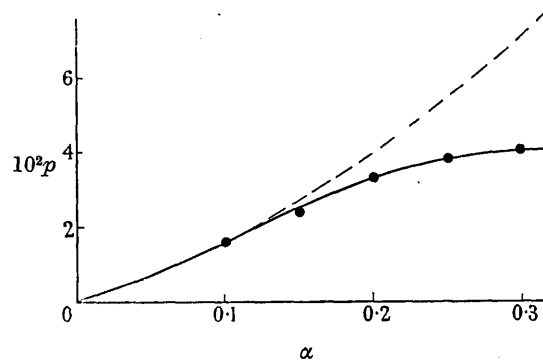


FIGURE 15. Peak displacements of two-dimensionally faulted gratings as a function of α .
— — —, Paterson curve corresponding to equation (6).

Similar equations relate $H_1 H_2 H_3$ and the cubic $h_1 h_2 h_3$ indices

$$\left. \begin{aligned} H_1 &= \frac{1}{2}h_1 + \frac{1}{4}h_2 + \frac{1}{4}h_3, \\ H_2 &= -\frac{1}{2}h_1 + \frac{1}{4}h_2 + \frac{1}{4}h_3, \\ H_3 &= \frac{1}{2}h_2 - \frac{1}{2}h_3. \end{aligned} \right\} \quad (8)$$

Putting $|\mathbf{b}_1^*| = |\mathbf{b}_2^*| = \sqrt{3}/a$, $|\mathbf{b}_3^*| = \sqrt{2}/a$ in (7), where a is the lattice parameter of the f.c.c. cell, we get

$$d^{*2} = \frac{1}{a^2} (3H_1^2 + 3H_2^2 + 2H_1H_2 + 2H_3^2).$$

Deformation faulting changes H_1, H_2 to $H_1 + \Delta H_1, H_2 + \Delta H_2$, and the corresponding change in d^* is Δd^* , where

$$\Delta d^* \cdot d^* = \frac{1}{a^2} [(3H_1 + H_2) \Delta H_1 + (H_1 + 3H_2) \Delta H_2].$$

But $\Delta d^*/d^* = \cot \theta \Delta \theta$, so that the change of Bragg angle $\Delta \theta_{H_1 H_2 H_3}$ of the $H_1 H_2 H_3$ component of a powder line is

$$\Delta \theta_{H_1 H_2 H_3} = \tan \theta \left[\frac{(3H_1 + H_2) \Delta H_1 + (H_1 + 3H_2) \Delta H_2}{3H_1^2 + 3H_2^2 + 2H_1H_2 + 2H_3^2} \right]. \quad (9)$$

Thus the value of $\Delta\theta$ is obtained by converting to $H_1H_2H_3$ indices using equation (8), determining ΔH_1 , ΔH_2 from table 3 and substituting in (9). The procedure is illustrated in table 4 for the $\{111\}$ and $\{200\}$ powder lines, as the relative displacements of these lines were measured in the experiments of Warren & Warekois (1955) and Smallman & Westmacott (1957).

TABLE 4. CHANGE IN BRAGG ANGLE OF COMPONENTS OF $\{111\}$ AND $\{200\}$

$h_1h_2h_3$	$H_1H_2H_3$	ΔH_1	ΔH_2	$\cot \theta \Delta \theta$
111	100	0	p	$\frac{1}{3}p$
$\bar{1}11$	010	p	0	$\frac{1}{3}p$
1 $\bar{1}$ 1	$\frac{1}{2}\bar{1}\bar{1}$	p	$-p$	$\frac{2}{3}p$
11 $\bar{1}$	$\frac{1}{2}\bar{1}1$	p	$-p$	$\frac{2}{3}p$
200	1 $\bar{1}$ 0	$-p$	p	$-p$
020	$\frac{1}{2}\bar{1}1$	$-p$	$-p$	$-p$
002	$\frac{1}{2}\bar{1}\bar{1}$	$-p$	$-p$	$-p$

According to figure 15, p is equal to $|\Delta H_1|$ in equation (6), provided that $\alpha < 0.1$. If we further assume that $\alpha \ll 1$ then (6) simplifies to

$$p = \sqrt{3} \alpha / 4\pi.$$

Table 4 therefore gives

$$\langle \Delta\theta_{111} \rangle_{av.} = \sqrt{3} \alpha \tan \theta / 8\pi$$

and

$$\langle \Delta\theta_{200} \rangle_{av.} = -\sqrt{3} \alpha \tan \theta / 4\pi,$$

so that finally we have $\langle \Delta(\theta_{111} - \theta_{200}) \rangle_{av.} = 3\sqrt{3} \alpha \tan \theta / 8\pi$.

This is exactly twice the value given by Paterson's theory applied to a faulting density α on only one set of planes. The result has been derived by assuming that for $\alpha \ll 1$ the components of the displacements of the reflexions along the close-packed directions $[111]$ and $[\bar{1}11]$ are given by equation (6). Using similar assumptions it is easy to generalize this result to the case of faulting on all four sets of close-packed planes; the conclusion is that, if the measured difference $\Delta(\theta_{111} - \theta_{200})$ is substituted in equation (9), then the resultant value of α must be interpreted as the sum of the faulting densities for the different sets of active $\{111\}$ planes.

5. CONCLUSION

It has been shown that the optical method can be used to determine the nature of the diffraction from layer structures with stacking faults on one or two sets of planes. The main limitation of the method lies in the restriction to the number of layers that can be represented in a single grating. In the present work this number was 1000. Any large increase above this number is impracticable, not only because of the excessive time required to make a grating of, say, 10^4 lines, but also because such a grating would be unsuitable for examination in the diffractometer in its present form. The effect of this limitation is to introduce intensity fluctuations in the observed intensity distribution, and these fluctuations can only be removed at the cost of loss of resolution.

If the number of lines in the grating is reduced to 300 or less, the intensity fluctuations become more pronounced and subsidiary maxima begin to appear along the diffraction streaks. It is possible that these are the origin of the weak diffuse maxima observed by Hirsch, Kelly & Menter (1955) in the diffraction streaks of beaten gold foil, as the estimated number of layers in the stack of (111) layers producing these streaks was only 70. These authors interpreted the displacements of the diffuse maxima from the ideal reciprocal lattice points by means of Paterson's theory, and obtained thereby very high values of α (up to 0.5), but this interpretation is not valid if the diffuse maxima are simply intensity fluctuations in the sense described above.

The author wishes to thank Dr H. M. Finnieston for his interest and encouragement, and Mr K. D. Rouse and Mr T. M. Valentine for experimental assistance.

REFERENCES

- Barrett, C. S. 1950 *Trans. Amer. Inst. Min. (Metall.) Engrs*, **188**, 123.
Christian, J. W. & Spreadborough, J. 1956 *Phil. Mag.* (8), **1**, 1069.
Edwards, O. S. & Lipson, H. 1942 *Proc. Roy. Soc. A*, **180**, 268.
Hirsch, P. B., Kelly, A. & Menter, J. W. 1955 *Proc. Phys. Soc. Lond. B*, **68**, 1132.
Jeffrey, J. W. 1953 *Acta Cryst.* **6**, 821.
Kendall, M. G. & Babington-Smith, B. 1951 *Tables of random sampling numbers*. Cambridge University Press.
Paterson, M. S. 1952 *J. Appl. Phys.* **23**, 805.
Smallman, R. E. & Westmacott, K. 1957 *Phil. Mag.* (8), **2**, 669.
Taylor, C. A., Hinde, R. M. & Lipson, H. 1951 *Acta Cryst.* **4**, 261.
Warren, B. E. & Warekois, E. P. 1955 *Acta Met.* **3**, 473.
Willis, B. T. M. 1957 *Proc. Roy. Soc. A*, **239**, 184 (part I; which is followed by part II).
Wilson, A. J. C. 1942 *Proc. Roy. Soc. A*, **180**, 277.
Wilson, A. J. C. 1949 *X-ray optics*. London: Methuen.

UNCLASSIFIED

A.E.R.E. M & C/R 2751

Approved for Sale

IRRADIATION DAMAGE

PAPERS PRESENTED AT THE FIRST COLLOQUIUM

OF THE

U.K.A.E.A. DIFFRACTION ANALYSIS CONFERENCE

HELD AT

A.W.R.E.

ON THE 2ND APRIL,

1958

EDITED BY J. THEWLIS

U.K.A.E.A. Research Group,
Atomic Energy Research Establishment,
HARWELL.

November, 1958

/AMT

HL.58/3164

* The only paper included here
is that given by the candidate

THE APPLICATION OF X-RAY DIFFRACTION TECHNIQUES TO

IRRADIATION DAMAGE PROBLEMS

by

B. T. M. WILLIS

The X-ray diffraction pattern of a crystal can undergo the following changes as a result of irradiation:

- (1) Displacement of the Bragg reflexions to lower θ values, indicating an expansion of the lattice.
- (2) Reduction of the integrated intensities of the Bragg reflexions.
- (3) Broadening of the Bragg reflexions.
- (4) Appearance of "diffuse scattering" between the Bragg peaks.
- (5) Appearance of low-angle scattering.

In this article various models for the damaged structure are considered. It is shown on the basis of these models how the diffraction effects listed above can arise, and what kind of information concerning the damage can be deduced from interpretations using these models. Experimental results to date are briefly described.

Isolated defects giving no lattice distortion (Model A)

The first model we consider is that of a crystal containing isolated vacancies and interstitial atoms. The defects are randomly distributed and of low concentration, and there is no distortion of the lattice around them (figure 1). A single interstitial scatters X-rays as an isolated atom of the same size and number of electrons, and by Babinet's Principle a vacancy scatters similarly (except at $\theta = 0$). Thus scattering takes place for all values of the scattering angle, θ , and falls off with θ in accordance with the f^2 curve, where f is the corresponding atomic scattering factor (figure 2). For randomly distributed defects there is no overall correlation of phase between the scattering from different particles, and the total intensity is the product of the number of defects and the scattering from one defect.

The existence of this type of diffuse scattering has been exploited by Antal (1) to determine the number of point defects produced by neutron irradiation of graphite. Neutron, rather than X-ray, scattering was employed, and the total scattering was measured by observing the attenuation of a direct beam of neutrons passing through a width t of sample. If I_0 , I_e are the incident and emergent intensities, then for the unirradiated sample

$$(I_e / I_0)_{\text{unirr}} = \exp(-\sigma Nt) , \quad (1)$$

where N is the number of atoms/c.c. and σ is the scattering cross-section for isotope, spin and inelastic scattering. Neutron wavelengths greater than $2d_{\max}$, where d_{\max} is the maximum graphite spacing, were used, so that σ does not include Bragg scattering. For the same sample after irradiation

$$(I_e / I_o)_{\text{irr}} = \exp \left[- (\sigma + f\sigma_d) Nt \right] . \quad (2)$$

Here σ_d is the cross-section for scattering by one defect, a quantity which is known accurately from nuclear scattering data, and f is the atomic fraction of defects. f is determined immediately from the division of (1) and (2).

The f value found for graphite was accurate to $\pm 10\%$: an important factor in this error was the neglect of lattice distortion in the simple model A.

Isolated defects with lattice relaxation Model B)

The theoretical problem of X-ray scattering from isolated defects, taking into account relaxation of the lattice around the defects, has been treated by Huang and others(2). For metals such as copper the radial displacement Δr of an atom at a distance r from a defect is taken as

$$\Delta r = c/r^2 , \quad (3)$$

where c is a factor determining the degree of relaxation around the defect (see figure 3).

There are three consequences of this relaxation from the point of view of X-ray diffraction.

(a) Overall lattice expansion

The lattice parameter, a , increases on average by Δa . Typical values of $\Delta a/a$ are:

$a/a = 10^{-4}$	for Mo	after a neutron irradiation of	$2 \cdot 10^{19}$	nvt.
10^{-3}	for MgO	"	"	$5 \cdot 10^{20}$ nvt.
10^{-2}	for diamond	"	"	$5 \cdot 10^{20}$ nvt.

(b) Defect diffuse scattering

The displacements of the atoms from their ideal positions can be described by a Fourier series of waves of different wave vectors \underline{k} and wave amplitudes $a_{\underline{k}}$. Let us consider one of these waves, say the wave of form $a_{\underline{k}} \cos 2\pi \underline{k} \cdot \underline{r}$, with wavelength $1/k$ and wave-normal directed along the x -axis. This wave gives rise to two satellite reflexions on either side of each principal reflexion. The satellites lie along the x^* axis through the main reflexion and are displaced from it by $\pm k$ (figure 4). The intensities of the satellites are proportional to $a_{\underline{k}}^2$. Clearly, the combined effect of all waves of different \underline{k} 's is to build up a 3-dimensional diffuse scattering region around each

reciprocal lattice point.

The treatment for defect diffuse scattering bears a strong formal resemblance with that for thermal diffuse scattering. Both types of scattering are present in a defect structure examined at normal temperatures, and this renders the experimental problem of isolating the defect diffuse scattering a matter of considerable difficulty. No convincing demonstration of this type of scattering in irradiated materials has yet been reported.

(c) Reduction of integrated intensity

The effect of thermal agitation is to give rise to diffuse scattering at the expense of Bragg scattering into the main reflexions. In the same way we expect a reduction of integrated intensity of the main reflexions after irradiation. The intensity in the Bragg peak is reduced by the factor $\exp(-2M')$ where M' is proportional to $fc^2 \sin^2 \theta/\lambda^2$. If the constant c in equation (3) is known, the defect concentration, f , can be found by measuring the reduction of integrated intensity produced by irradiation. This "artificial temperature" effect has been observed by Tucker and Senio⁽³⁾ in neutron irradiated B_4C , but a quantitative analysis of their results was not possible owing to the complex nature of the initial structure.

High density of defects. Clustering (Model C)

Hitherto our discussion has been limited to the case of low density of defects, i.e. $f \ll 1$. As the density increases, line broadening effects appear, indicating that the lattice is being strained and/or fragmented into smaller particles. The integral breadths due to strain and particle size respectively can be written

$$\beta_{\text{strain}} = 2 \xi \tan \theta, \quad \beta_{\text{particle size}} = \lambda \sec \theta / \epsilon. \quad (4)$$

ξ is the mean strain, θ the Bragg angle, λ the wavelength and ϵ the "apparent" particle size. Assuming that the total breadth β_{tot} is the sum of that due to strain and particle size, (4) gives

$$\beta_{\text{tot}} = 2 \xi \tan \theta + \lambda \sec \theta / \epsilon$$

or
$$\beta_{\text{tot}} (\cos \theta / \lambda) = 2 \xi \sin \theta / \lambda + 1 / \epsilon.$$

A plot of $\beta_{\text{tot}} (\cos \theta / \lambda)$ against $2 \sin \theta / \lambda$ is a straight line of slope ξ and intercept $1/\epsilon$.

Using this analysis Smallman and Willis⁽⁴⁾ showed that the line broadening in neutron irradiated LiF is primarily due to strain. On the other hand, Tucker⁽⁵⁾ concluded that grain fragmentation is responsible for the broadening in neutron irradiated U_3O_8 .

Under conditions of heavy irradiation clumps of atomic defects can form, and if the average electron density in these clumps is different from that of the matrix

small-angle X-ray scattering appears⁽⁴⁾. This scattering falls off to zero when the interference condition $\sin \theta \doteq \theta = \lambda/D$ is satisfied. An estimate of the average size D of the clumps can be found using this relation.

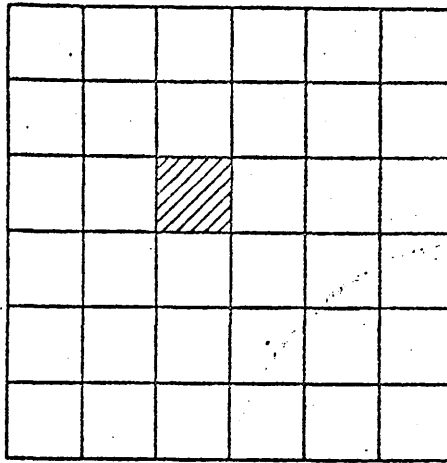
References

1. Antal, J. J. et al, Phys. Rev. 99, 1081 (1955).
2. Huang, K. Proc. Roy. Soc. A, 190, 102 (1947).
Cochran, W. Acta Cryst. 6, 259, 941, 944 (1956).
Borie, B. Acta Cryst. 10, 89 (1957).
3. Tucker, C. W. and Senio, P. Acta. Cryst. 8, 371 (1955).
4. Smallman, R. E. and Willis, B. T. M. Phil. Mag. 2, 1018 (1957).
5. Tucker, C. W. and Senio, P. "An X-ray study of the effect of fission on the crystal structure of solids" KAPL-749.

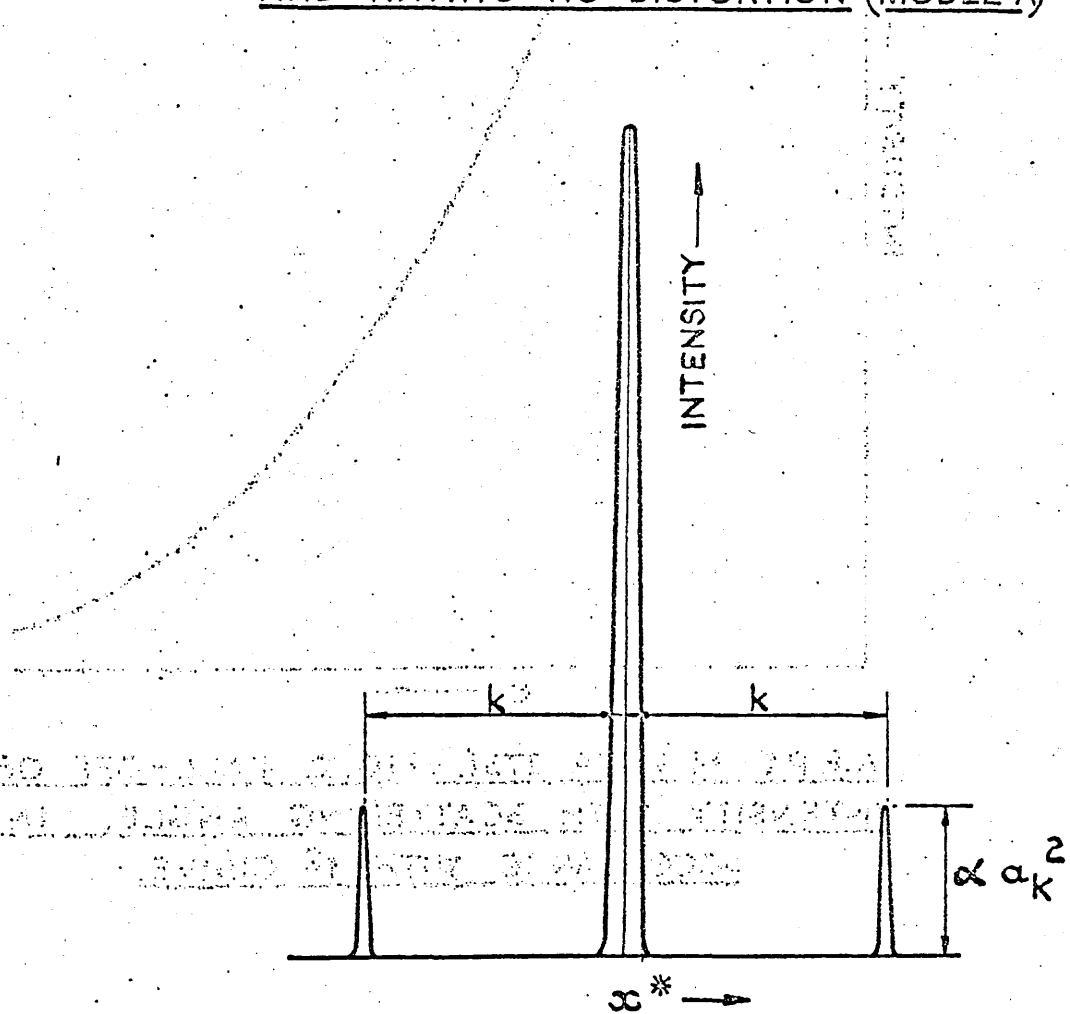
Illustrations

- Figure 1. Lattice containing isolated point defects and having no distortion (Model A).
- Figure 2. Fall-off of intensity with scattering angle, in accordance with f^2 curve.
- Figure 3. Lattice with relaxation around the point defects (Model B).
- Figure 4. Modulation of lattice by plane wave $a_c \cos 2\pi kr$ gives satellite reflexions flanking each main reflexion.

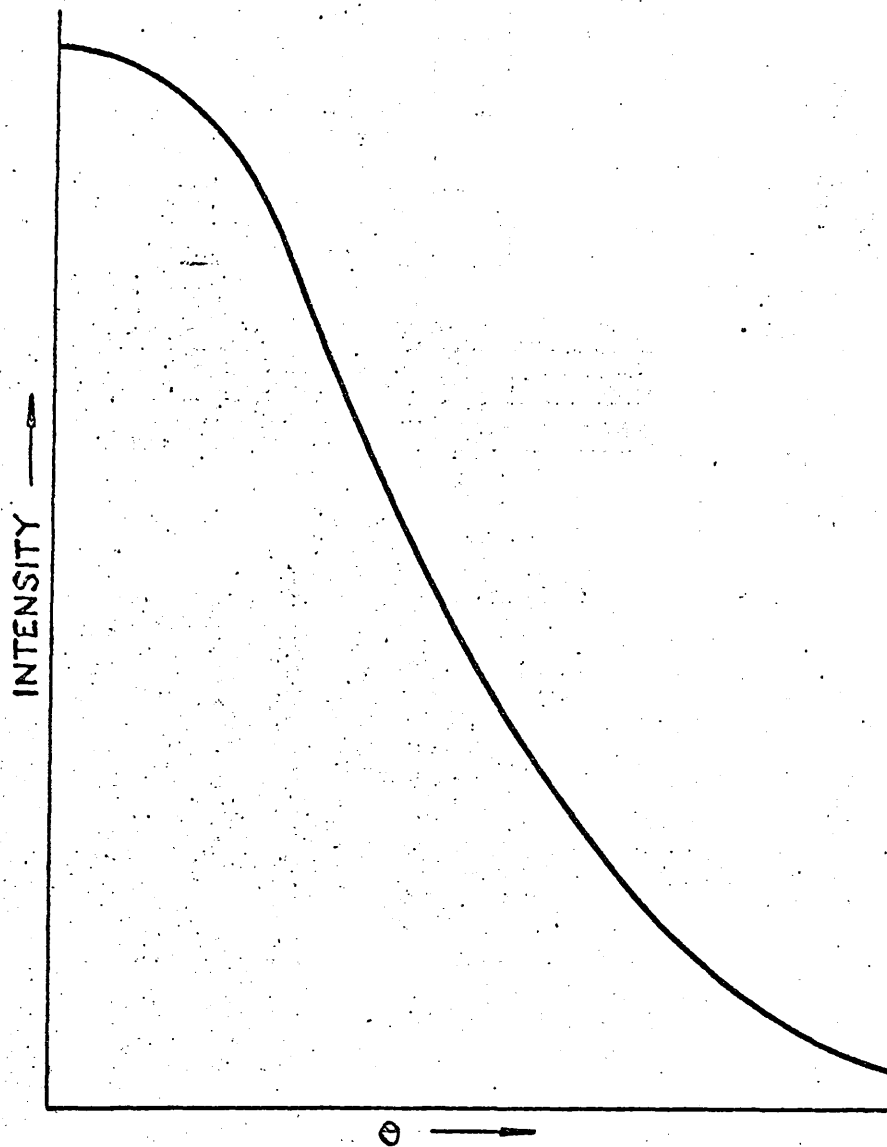
 POINT DEFECT



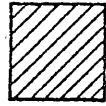
A.E.R.E. M & C/R 2751. FIG. I. LATTICE CONTAINING ISOLATED POINT DEFECTS AND HAVING NO DISTORTION (MODEL A)



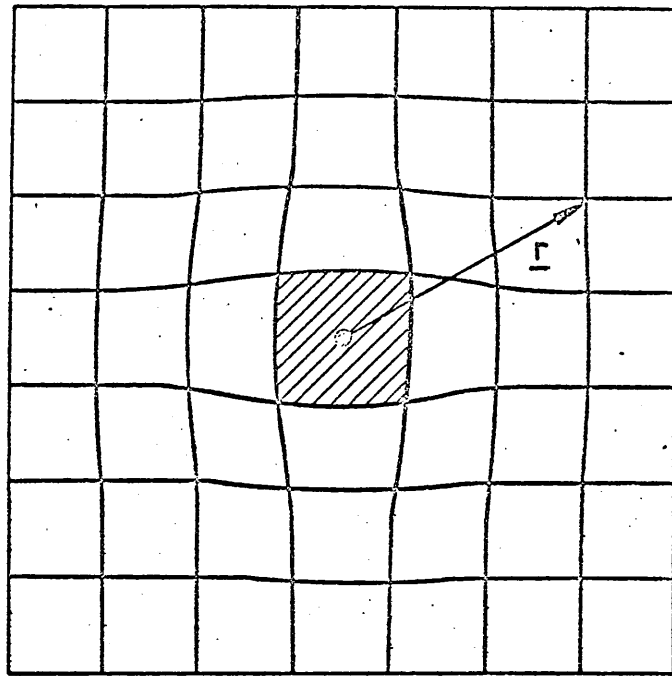
A.E.R.E. M & C/R 2751. FIG. 4. MODULATION OF LATTICE BY PLANE WAVE $a_k \cos. 2\pi kx$ GIVES SATELLITE REFLEXIONS FLANKING EACH MAIN REFLEXION.



A.E.R.E. M & C/R 2751. FIG. 2. FALL-OFF OF
INTENSITY WITH SCATTERING ANGLE, IN
ACCORDANCE WITH $\frac{1}{\theta^2}$ CURVE.



POINT DEFECT



A.E.R.E. M & C/R 2751. FIG. 3. LATTICE WITH RELAXATION AROUND THE POINT DEFECTS (MODEL B). THE RADIAL DISPLACEMENT OF THE LATTICE POINT WITH POSITION VECTOR \underline{r} IS $c|\underline{r}|^{-2}$.

Acta Cryst. (1959). 12, 683

The Effect of Segregation on the Diffraction from a Face-Centred Cubic Alloy with Deformation Faults

BY B. T. M. WILLIS

Atomic Energy Research Establishment, Harwell, Berks, England

(Received 9 October 1958 and in revised form 16 March 1959)

The Paterson theory of X-ray scattering from a face-centred cubic structure with deformation faults is extended to include the case of a f.c.c. alloy, in which segregation of the alloy components takes place at the faults. The principal effect of segregation is to make the reflexions asymmetrical. It is possible that this asymmetry could be detected in the powder lines of certain cold-worked alloys.

1. Introduction

Suzuki (1952) has suggested a hardening mechanism for face-centred cubic alloys, involving a segregation of solute atoms at deformation stacking faults. Segregation can occur because the crystal structure is close-packed hexagonal in a layer two atoms thick at the stacking fault; the concentration of solute atoms at the fault will therefore differ from the average, when the faulted region is in thermodynamic equilibrium with the surrounding cubic phase. Using this idea Suzuki has explained certain mechanical properties of alloys (see also Cottrell, 1954), but so far no direct evidence for segregation has been obtained. It is possible that such evidence could be provided by X-ray diffraction.

The purpose of this paper is to calculate the nature of the X-ray scattering from a deformation-faulted f.c.c. alloy, in which the alloy composition at the faults differs from that in the cubic matrix. We thus require to extend the treatment of Paterson (1952), dealing with the diffraction from a homogeneous, faulted f.c.c. crystal, to include the case of segregation.

2. Intensity distribution in reciprocal space

(a) General formula

Fig. 1(a) illustrates the stacking sequence of the close-packed (111) layers, with the faulted positions denoted by F , and f_1, f_2 representing the scattering powers averaged over the atoms in the two kinds of layer. When several faults occur in succession, the

c.p.h. structure is developed only at the boundaries of the set, so that segregation takes place only at the kinks in the 'stacking line'.

The theory developed in this section assumes that there is no change of layer spacing accompanying segregation. The extension of the theory to include both change of scattering power and of spacing is considered in the Appendix, but it is shown there that the simpler theory of this section is adequate for most cases.

We make the usual assumption that faulting is restricted to one set of (111) planes only: the limitations imposed by this assumption have been considered by Willis (1958).

At first, the treatment follows very closely that given by Warren & Warekois (1955) for the problem of deformation-faulting without segregation.

It is convenient to choose hexagonal axes A_1, A_2, A_3 , with A_1, A_2 in the (111) plane and A_3 normal to this plane. If a_1, a_2, a_3 are the cubic axes of the unfaulted structure, then

$$\left. \begin{aligned} A_1 &= -a_1/2 + a_2/2 \\ A_2 &= -a_2/2 + a_3/2 \\ A_3 &= a_1/3 + a_2/3 + a_3/3 \end{aligned} \right\} \quad (1)$$

Similar equations relate the corresponding hexagonal H_1, H_2, H_3 and cubic hkl indices:

$$\left. \begin{aligned} H_1 &= -h/2 + k/2 \\ H_2 &= -k/2 + l/2 \\ H_3 &= h/3 + k/3 + l/3 \end{aligned} \right\} \quad (1a)$$

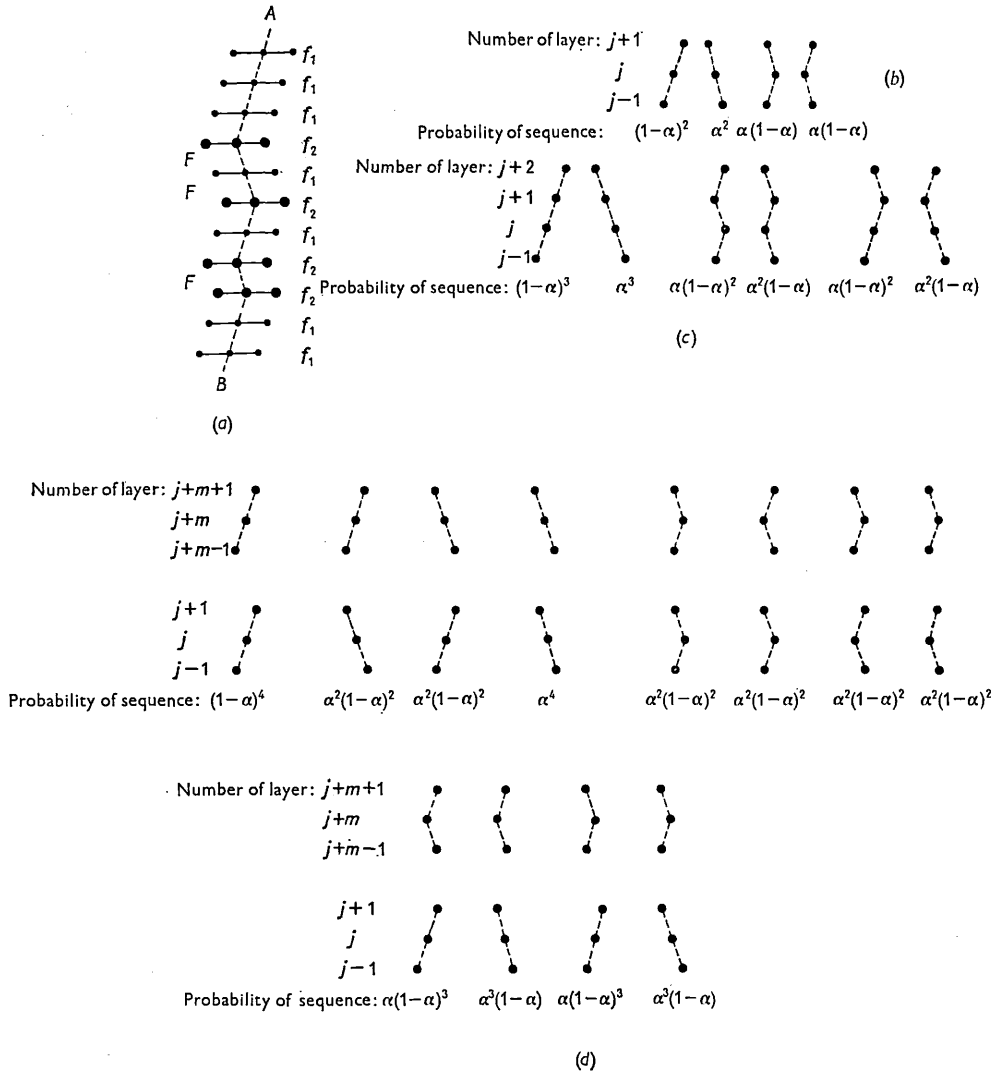


Fig. 1. (a) Diagram illustrating stacking sequence of (111) layers. Faulted positions are denoted F , and the average scattering powers of the atoms in the two kinds of layer are denoted f_1, f_2 . The 'stacking line' is the broken line AB . (b) Different types of sequence for three successive layers. (c) Different types of sequence for four successive layers. (d) Different types of sequence for the six layers $j-1, j, j+1, j+m-1, j+m, j+m+1$, where $m \geq 2$.

In the presence of faulting A_3 is not a repetition vector of the lattice, and so H_3 is not necessarily integral.

Let $\mathbf{r}_{m_1 m_2 m_3}$ be the position vector of the atom $m_1 m_2$ in layer m_3 , i.e.

$$\mathbf{r}_{m_1 m_2 m_3} = m_1 \mathbf{A}_1 + m_2 \mathbf{A}_2 + m_3 \mathbf{A}_3 + \delta_{m_3}, \quad (2)$$

where δ_{m_3} is a vector which depends on m_3 and gives the change in \mathbf{r} due to the presence of faults. (δ_{m_3} can be written $\frac{1}{3} n_{m_3} (\mathbf{A}_1 - \mathbf{A}_2)$, where n_{m_3} is an integer depending on m_3 .) The diffracted intensity I is then

$$I = I_e \sum_{m_1 m_2 m_3} \sum_{m_1' m_2' m_3'} f_{m_1 m_2 m_3} f_{m_1' m_2' m_3'} \times \exp \left\{ \frac{2\pi i}{\lambda} (\mathbf{S} - \mathbf{S}_0) \cdot (\mathbf{r}_{m_1' m_2' m_3'} - \mathbf{r}_{m_1 m_2 m_3}) \right\}, \quad (3)$$

where \mathbf{S}_0, \mathbf{S} are unit vectors along the incident and scattered directions, λ the incident wavelength and I_e the scattered intensity per electron. Substituting (2) into (3) gives:

$$I = I_e \sum_{m_1 m_2 m_3} \sum_{m_1' m_2' m_3'} f_{m_1 m_2 m_3} f_{m_1' m_2' m_3'} \times \exp \left\{ \frac{2\pi i}{\lambda} (\mathbf{S} - \mathbf{S}_0) \cdot [(m_1' - m_1) \mathbf{A}_1 + (m_2' - m_2) \mathbf{A}_2 + (m_3' - m_3) \mathbf{A}_3 + \delta_{m_3'} - \delta_{m_3}] \right\}. \quad (4)$$

The average scattering power of an atom depends on m_3 only and can be written f_{m_3} . Further if we consider the unfaulted crystal to be in the form of a parallelepiped, and neglect a small term corresponding to

weak diffuse scattering and arising from the disordered distribution of atoms in the (111) plane, (4) becomes:

$$I = I_e \frac{\sin^2 \left[\frac{\pi}{\lambda} (\mathbf{S} - \mathbf{S}_0) \cdot N_1 \mathbf{A}_1 \right] \sin^2 \left[\frac{\pi}{\lambda} (\mathbf{S} - \mathbf{S}_0) \cdot N_2 \mathbf{A}_2 \right]}{\sin^2 \left[\frac{\pi}{\lambda} (\mathbf{S} - \mathbf{S}_0) \cdot \mathbf{A}_1 \right] \sin^2 \left[\frac{\pi}{\lambda} (\mathbf{S} - \mathbf{S}_0) \cdot \mathbf{A}_2 \right]} \times \sum_{m_3} \sum_{m_3'} f_{m_3} f_{m_3'} \exp \left\{ \frac{2\pi i}{\lambda} (\mathbf{S} - \mathbf{S}_0) \cdot [(m_3' - m) \mathbf{A}_3 + \delta_{m_3'} - \delta_{m_3}] \right\}. \quad (5)$$

Here N_1, N_2 are the number of atoms along the $\mathbf{A}_1, \mathbf{A}_2$ directions. If the coefficient of the summation is denoted by Φ^2 and $\delta_{j+m} - \delta_j$ by Δ_m , where $j, j+m$ refer to the j th, $j+m$ th layers, then the summations can be separated and written as:

$$I = \Phi^2 \sum_{m=-N}^N N_m \langle f_j f_{j+m} \exp \left[\frac{2\pi i}{\lambda} (\mathbf{S} - \mathbf{S}_0) \cdot \Delta_m \right] \rangle_{av.} \times \exp \left[\frac{2\pi i}{\lambda} (\mathbf{S} - \mathbf{S}_0) \cdot m \mathbf{A}_3 \right].$$

N is the total number of layers and N_m the number of layers with an m th neighbouring layer (i.e. $N_m = N - |m|$). $(\mathbf{S} - \mathbf{S}_0)/\lambda$ can be expressed in terms of the basis vectors $\mathbf{B}_1, \mathbf{B}_2, \mathbf{B}_3$ reciprocal to $\mathbf{A}_1, \mathbf{A}_2, \mathbf{A}_3$, using h_1, h_2, h_3 as continuous co-ordinates:

$$(\mathbf{S} - \mathbf{S}_0)/\lambda = h_1 \mathbf{B}_1 + h_2 \mathbf{B}_2 + h_3 \mathbf{B}_3.$$

Putting

$$\frac{2\pi}{\lambda} (\mathbf{S} - \mathbf{S}_0) \cdot \Delta_m = \theta_m$$

we obtain the following general formula for the diffracted intensity:

$$I = \Phi^2 \sum_{m=-N}^N N_m \langle f_j f_{j+m} \exp i\theta_m \rangle_{av.} \exp 2\pi i m h_3. \quad (6)$$

(b) Evaluation of $\langle f_j f_{j+m} \exp i\theta_m \rangle_{av.}$

It remains to evaluate $\langle f_j f_{j+m} \exp i\theta_m \rangle_{av.}$. This can be written in the form

$$\langle f_j f_{j+m} \exp i\theta_m \rangle_{av.} = P_{11} f_1^2 \langle \exp i\theta_m \rangle_{11} + 2P_{12} f_1 f_2 \langle \exp i\theta_m \rangle_{12} + P_{22} f_2^2 \langle \exp i\theta_m \rangle_{22}, \quad (7)$$

where P_{11}, P_{12}, P_{22} are the probabilities that layers $j, j+m$ have atoms of average scattering power f_1 and f_1, f_1 and f_2, f_2 and f_2 , and $\langle \exp i\theta_m \rangle_{11} \dots$ are the corresponding values of $\langle \exp i\theta_m \rangle_{av.}$ for all such pairs of layers.

(i) $m = 0$

For $m = 0, \theta_m = 0$ and $\langle \exp i\theta_m \rangle = 1$. Further, $P_{12} = 0$, and P_{11}, P_{12} are the probabilities that a given layer j has scattering power f_1, f_2 respectively;

these probabilities can be readily found from Fig. 1(b), showing four different sequences for the layers $j-1, j, j+1$. The stacking line is shown as a broken line, and the j th layer is f_1 -type in the first pair of sequences and f_2 -type in the last pair. Clearly, $P_{11} = \alpha^2 + (1-\alpha)^2$ and $P_{22} = 2\alpha(1-\alpha)$, where α is the faulting parameter, i.e. the probability that an arbitrarily chosen layer is faulted.

Substituting these P values into (7) gives:

$$\langle f_j f_{j+m} \exp i\theta_m \rangle = f_1^2 (1 - 2\alpha + 2\alpha^2) + f_2^2 (2\alpha - 2\alpha^2). \quad (8)$$

(ii) $m = 1$

P_{11} and P_{22} are the probabilities that neighbouring layers $j, j+1$ are both f_1 -type and both f_2 -type, and P_{12} is the probability that j is f_1 -type and $j+1$ is f_2 -type. We must now consider the six sequences in Fig. 1(c). P_{11} is the sum of the probabilities of the first pair of sequences, P_{22} the sum of the next pair, and P_{12} the sum of the last pair. Thus

$$P_{11} = 1 - 3\alpha + 3\alpha^2, \quad P_{22} = P_{12} = \alpha - \alpha^2.$$

Further, $\langle \exp i\theta_m \rangle$ can be written

$$\langle \exp i\theta_m \rangle = (1 - \alpha') \exp 2\pi i \left(\frac{-h_1 + h_2}{3} \right) + \alpha' \exp 2\pi i \left(\frac{h_1 - h_2}{3} \right), \quad (9)$$

where α' is the probability of a fault between the j th, $j+1$ th layers. From Fig. 1(c) we see that

$$\alpha' = \alpha^3 / (1 - 3\alpha + 3\alpha^2), \text{ if layer } j \text{ is } f_1\text{-type and layer } j+1 \text{ is } f_1\text{-type,} \\ = 1 - \alpha, \text{ if layer } j \text{ is } f_2\text{-type and layer } j+1 \text{ is } f_2\text{-type,} \\ = \alpha, \text{ if layer } j \text{ is } f_1\text{-type and layer } j+1 \text{ is } f_2\text{-type.}$$

$\langle \exp i\theta_m \rangle_{11}, \langle \exp i\theta_m \rangle_{22}, \langle \exp i\theta_m \rangle_{12}$ are then given by (9) using the appropriate value of α' .

There is appreciable intensity only for $h_1, h_2 =$ integers H_1, H_2 (see equation (5), taking $N_1, N_2 \gg 1$). For the reflexions having $H_1 - H_2 = 3M$ (M integral), (7) and (9) give

$$\langle f_j f_{j+m} \exp i\theta_m \rangle = f_1^2 [1 + 4\alpha(1-\alpha)\beta + \alpha(1-\alpha)\beta^2], \quad (10)$$

where $\beta = f_2/f_1 - 1$; and for the reflexions having $H_1 - H_2 = 3M \pm 1$

$$\langle f_j f_{j+m} \exp i\theta_m \rangle = -f_1^2 E \exp \pm i\varepsilon, \quad (11)$$

where

$$\left. \begin{aligned} E \cos \varepsilon &= \frac{1}{2} [1 + 4\alpha(1-\alpha)\beta + \alpha(1-\alpha)\beta^2] \\ \text{and} \\ E \sin \varepsilon &= \frac{1}{2} \sqrt{3} (1 - 2\alpha) [1 - \alpha(1-\alpha)\beta^2] \end{aligned} \right\}. \quad (11a)$$

(iii) $m \geq 2$

To evaluate the P 's we must consider the twelve sequences in Fig. 1(d); P_{11} is the sum of the prob-

abilities of the first four, P_{22} of the second four, and P_{12} of the last four. Thus $P_{11} = (1-2\alpha+2\alpha^2)^2$, $P_{22} = 4\alpha^2(1-\alpha)^2$ and $P_{12} = 2\alpha(1-\alpha)(1-2\alpha+2\alpha^2)$.

To determine $\langle \exp i\theta_m \rangle$ we write it as

$$\langle \exp i\theta_m \rangle = \langle \exp i\theta_{0-1} \rangle \langle \exp i\theta_{1-2} \rangle \langle \exp i\theta_{2-3} \rangle \dots, \quad (12)$$

where $\langle \exp i\theta_{0-1} \rangle, \langle \exp i\theta_{1-2} \rangle \dots$ are the average values of $\exp i\theta$ between layers j and $j+1, j+1$ and $j+2 \dots$. If α'' is the probability of a fault between any pair of neighbouring layers in the sequence j to $j+m$, then for the pairs $j, j+1$ and $j+m-1, j+m$ (see Fig. 1(d) or Fig. 1(b))

$$\begin{aligned} \alpha'' &= \alpha^2/(1-2\alpha+2\alpha^2), \quad j \text{ and } j+m \text{ } f_1\text{-type,} \\ &= \frac{1}{2}, \quad j \text{ and } j+m \text{ } f_2\text{-type.} \end{aligned}$$

For all other pairs $\alpha'' = \alpha$, independent of f_j, f_{j+m} . The individual averages on the r.h.s. of equation (12) can now be expressed by equation (9) with α' replaced by the appropriate value of α'' . Substituting the different values of $\langle \exp i\theta_m \rangle$ and P into (7) finally gives for the $3M$ reflexions:

$$\langle f_j f_{j+m} \exp i\theta_m \rangle = f_1^2 [1 + 4\alpha(1-\alpha)\beta + 4\alpha^2(1-\alpha)^2\beta^2]; \quad (13)$$

and for the $3M \pm 1$ reflexions

$$\langle f_j f_{j+m} \exp i\theta_m \rangle = f_1^2 (-Z \exp \pm i\gamma)^{m-2} D \exp \pm i\delta, \quad (14)$$

where

$$\left. \begin{aligned} Z^2 &= 1 - 3\alpha + 3\alpha^2, \\ \tan \gamma &= \sqrt{3}(1 - 2\alpha), \\ D \cos \delta &= -\frac{1}{2} + 3\alpha - 3\alpha^2, \\ D \sin \delta &= \frac{1}{2}\sqrt{3}(1 - 2\alpha)[1 + 2\alpha(1 - \alpha)\beta]. \end{aligned} \right\} \quad (14a)$$

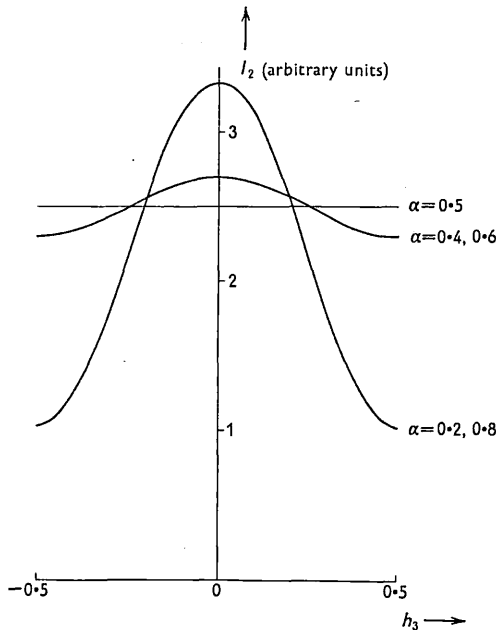


Fig. 2. Dependence of diffuse intensity on h_3 for different values of α .

For $m = -1$, equations (10), (11) apply with \pm in (11) replaced by \mp ; similarly (13), (14) apply for $m \leq -2$ with \pm in (14) replaced by \mp .

(c) Intensity of reflexions having $H_1 - H_2 = 3M$

Substituting (8), (10), (13) into (6) gives

$$I = I_1 + I_2$$

where

$$I_1 = f_1^2 [1 + 4\alpha(1-\alpha)\beta + 4\alpha^2(1-\alpha)^2\beta^2] \sum_{m=-N}^N (N - |m|) \exp 2\pi i m h_3$$

and

$$I_2 = 2\alpha(1-\alpha)f_1^2\beta^2 \times [1 - 2\alpha(1-\alpha) + (1 - 4\alpha + 4\alpha^2) \cos 2\pi h_3].$$

I_1 is a term equivalent to diffraction from a perfect crystal and gives sharp peaks at integral h_3 . I_2 is a term giving rise to diffuse intensity; its dependence on h_3 for different values of α is shown in Fig. 2. The maximum integrated diffuse intensity occurs for $\alpha = 0.5$; I_2 is then independent of h_3 , apart from the form-factor dependence of the quantity $f_1^2\beta^2$.

(d) Intensity of reflexions having $H_1 - H_2 = 3M \pm 1$

Substituting (8), (11), (14) into (6), and carrying out the summation, gives

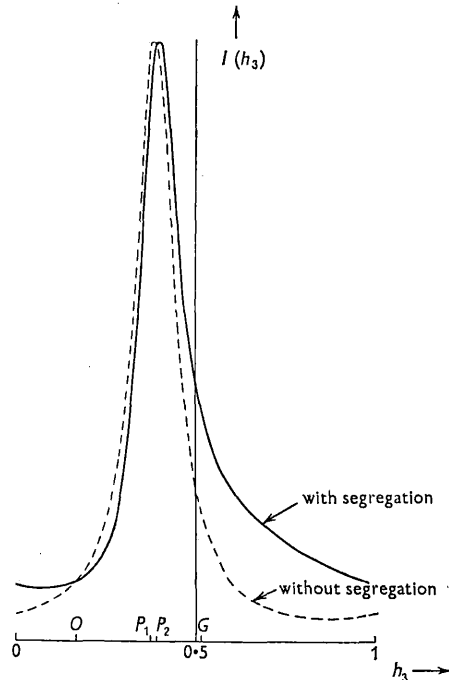


Fig. 3. Curves showing shapes of $3M+1$ diffraction peaks. --- $\alpha = 0.25, \beta = 0$ (faulting without segregation). — $\alpha = 0.25, \beta = 1.0$ (faulting with segregation). Faulting without segregation displaces the peak and the centre of gravity from 0 to P_1 ; segregation displaces the peak further to P_2 and the centre of gravity to G .

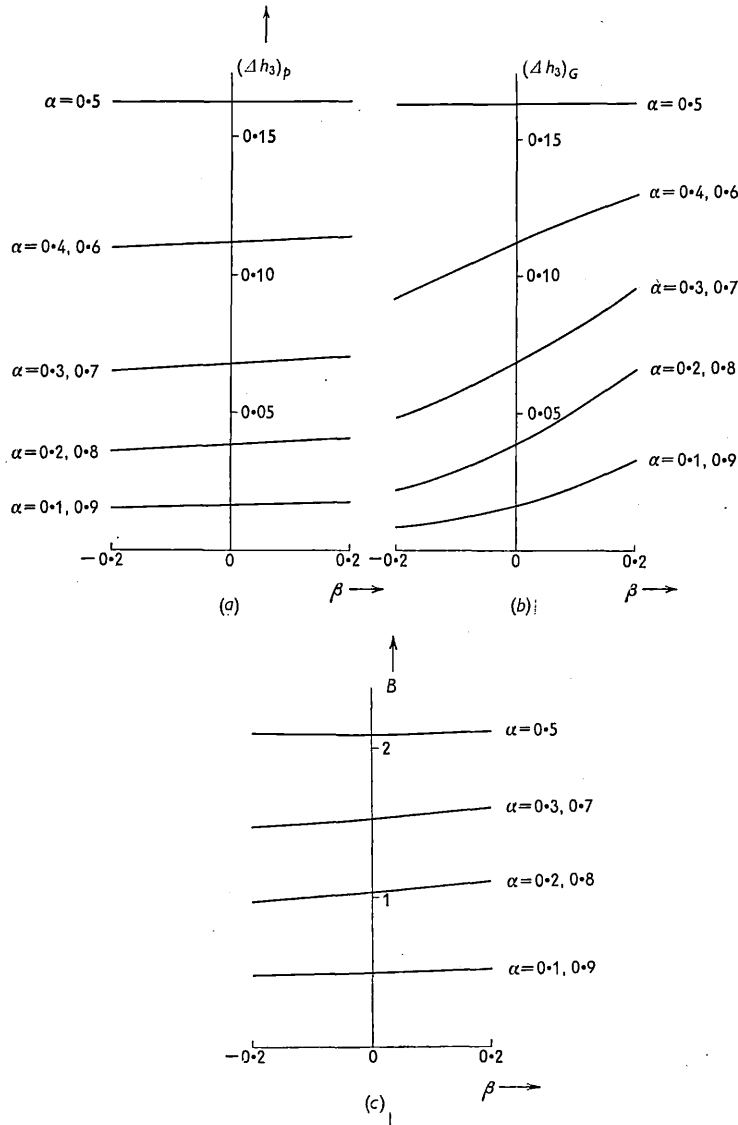


Fig. 4. (a) Peak displacement as a function of β for different values of α . The displacement is expressed as a fraction of an order separation. (b) Centroid displacement as a function of β for different values of α . The displacement is expressed as a fraction of an order separation. (c) Integral breadth B as a function of β for different values of α . B is defined as $\int_0^1 I(h_3) dh_3 \div I_{max.}$

$$I(h_3) = 1 + 2\alpha(1-\alpha)\beta(\beta+2) - 2E \cos(2\pi h_3 \pm \epsilon) + 2D \cdot \frac{\cos(4\pi h_3 \pm \delta) + Z \cos(2\pi h_3 \pm \delta \mp \gamma)}{1 + Z^2 + 2Z \cos(2\pi h_3 \pm \gamma)}, \quad (15)$$

where $I(h_3) \equiv I/(f_1^2 N \Phi^2)$. In obtaining (15) the assumption has been made that N_m in (6) can be replaced by N : this is a very close approximation provided $\alpha N \gg 1$. In this expression (15) for the dependence of the intensity on the co-ordinate h_3 there are two independent parameters, α and β , which are related to the degrees of faulting and of segregation respectively. The remaining symbols in (15) are defined in terms of α and β by equations (11a) and

(14a). $\beta = 0$ corresponds to the Paterson case of no segregation, and according to Suzuki (1952) β for most alloys will lie well within the range

$$-0.2 \leq \beta \leq +0.2.$$

For $\alpha = 0.5$, (15) simplifies to

$$I(h_3) = \frac{1}{4}\beta^2 + 3(1 + \beta + \frac{1}{4}\beta^2)/(5 + 4 \cos 2\pi h_3).$$

This represents a symmetrical distribution with maximum intensity at half-integral values of h_3 , just as for the case of no segregation.

If $\alpha \neq 0.5$, segregation gives rise to a change in the positions of the diffraction peaks, an asymmetry

about these positions, and a change in the integral breadths of the diffraction streaks. These effects are illustrated in Fig. 3, which shows the shape of the reflexions for $\alpha = 0.25$, $\beta = 0$ (faulting without segregation) and for $\alpha = 0.25$, $\beta = 1.0$ (faulting with segregation). (The value $\beta = 1.0$ is well outside the likely range of β : it is chosen here to make the asymmetry of the diffraction peak in Fig. 3 immediately obvious). In the former case faulting displaces the peak from 0 to P_1 and broadens the reflexion symmetrically, whereas segregation displaces the peak further (to P_2) and makes the reflexion asymmetrical, so that the centroid is at G , where $OG > OP_2$.

With the aid of the Harwell Mercury computer the values of OP_2 and OG (expressed as fractions of the order separation) and of the integral breadth B were evaluated from (15) for different combinations of α , β . The results are given in Figs. 4(a), (b), (c) for the ranges $0 \leq \alpha \leq 1$, $-0.2 \leq \beta \leq 0.2$; the curves are the same for α , $1-\alpha$ and for $3M+1$, $3M-1$ reflexions, as indicated by (15) which is unchanged (except for the sign of h_3) when α is replaced by $1-\alpha$ or \pm by \mp . These curves show that the position of the centroid of a reflexion is much more sensitive to a change in β than the peak position or the integral breadth. Thus for $\alpha = 0.1$, $\beta = 0$ the centroid and peak position are equally displaced by a given amount; if now β increases to 0.1 the peak displacement and integral breadth change by an additional 2%, whereas the centroid is displaced by a further 50%.

We conclude that as far as single crystal diffraction patterns are concerned the principal changes induced by segregation are the introduction of weak diffuse streaks between reflexions in the columns having $H_1-H_2=3M$, and of asymmetry in the remaining reflexions. These effects are shown schematically in Fig. 5 for the case $\beta > 0$; for $\beta < 0$ the asymmetry is reversed, the centroid displacement being less than the peak displacement.

3. Powder pattern

(a) General

The effect of combined faulting and segregation on the powder diffraction pattern can be determined in the way indicated by Paterson (1952). The value of H_1-H_2 for each component of an $\{hkl\}$ line is found from equation (1a); if $H_1-H_2=3M$ this component is sharp and undisplaced, whereas if $H_1-H_2=3M\pm 1$ the component is broadened asymmetrically and displaced to higher or lower Bragg angles, according to the sign \pm . Fig. 6 shows diagrammatically the appearance of the powder pattern up to $\{400\}$.

$\{311\}$ is broadened symmetrically, as it contains an equal number of components of the types $3M+1$ and $3M-1$; and for the same reason its change of integral breadth, as induced by segregation, is much greater than for the other lines.

The peak displacement $(\Delta 2\theta)_p$ of the component of

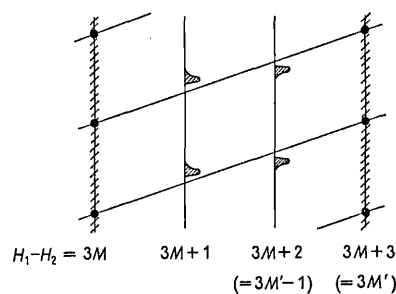


Fig. 5. Schematic diagram showing principal changes in reciprocal lattice induced by segregation. In the $3M$ columns of reflexions a diffuse intensity band appears, while the reflexions in the $3M\pm 1$ columns are broadened asymmetrically.



Fig. 6. Effect of combined faulting and segregation on the profiles of powder diffraction lines up to $\{400\}$.

a powder line is related to $(\Delta h_3)_p$ by the equation (Warren & Warekois, 1955):

$$(\Delta 2\theta)_p = 2 \tan \theta \cos^2 \varphi (\Delta h_3)_p / h_3, \quad (16)$$

where θ is the Bragg angle and φ the angle between the vectors B_3 and $H_1 B_1 + H_2 B_2 + H_3 B_3$. For $\alpha \ll 1$, the same form of equation applies to the centroid displacement:

$$(\Delta 2\theta)_G = 2 \tan \theta \cos^2 \varphi (\Delta h_3)_G / h_3. \quad (16a)$$

As $(\Delta h_3)_p$ is relatively insensitive to changes of β (§ 2(d)), the faulting parameter, α , can be deduced from the observed $(\Delta 2\theta)_p$, using (16) and Fig. 4(a) and assuming $\beta = 0$. β can then be found from the observed $(\Delta 2\theta)_G$, using (16a) and Fig. 4(b).

(b) Particular applications

It is clear that in looking for segregation effects we must choose alloys with values of β as high as possible. β increases with the difference in stacking fault energies and with the difference in atomic scattering factors of the alloy components, and it is preferable to choose an intermediate composition of an alloy with a wide solid solution range (Suzuki, 1952). Stacking fault measurements by diffraction methods have been reported on 50/50 Ag-Au (Smallman & Westmacott, 1957) and on 50/50 Co-Ni (Christian & Spreadborough, 1957); from Suzuki's theory and estimates of stacking fault energies by Thornton & Hirsch (1958) β would be about 0.03 for X-ray scattering from Ag-Au and about 0.1 for neutron scattering from Co-Ni. It is possible that segregation could be detected in these cases by comparing the shapes of the three types of line (Fig. 6) represented by $\{111\}$, $\{200\}$ and $\{311\}$.

APPENDIX

The treatment in § 2 can be extended to allow for the change of layer spacing accompanying segregation. Let $A_3, A_3(1+\varepsilon/2\pi), A_3(1+\varepsilon/\pi)$ be the spacings between layers with average scattering factors of f_1 and f_1, f_1 and f_2, f_2 and f_2 . It is easily shown that formula (15) for the intensity of the $3M\pm 1$ reflexions is then modified, assuming $\varepsilon \ll 1$, to

$$I(h_3) = 1 + 2\alpha(1-\alpha)\beta(\beta+2) - 2S \cos(2\pi h_3 + s) + \frac{1}{2}T \cdot \frac{\cos(4\pi h_3 + t) + P \cos(2\pi h_3 + t - p)}{1 + P^2 + 2P \cos(2\pi h_3 + p)}, \quad (17)$$

where

$$\begin{aligned} S \cos s &= \frac{1}{2} + \frac{1}{2}\alpha(1-\alpha)\beta(4+\beta) \\ &\quad \pm \sqrt{3}\alpha(1-\alpha)(1-2\alpha)\beta(1+\beta)\varepsilon h_3, \\ S \sin s &= \pm \frac{1}{2}\sqrt{3}(1-2\alpha)(1-\alpha\beta^2 + \alpha^2\beta^2) \\ &\quad + \alpha(1-\alpha)(1+\beta)(2+\beta)\varepsilon h_3; \\ Q \cos q &= 1 - 2\alpha + 2\alpha^2 \mp \sqrt{3}\alpha(1-\alpha)(1-2\alpha)\varepsilon h_3, \\ Q \sin q &= \pm \sqrt{3}(1-2\alpha) + \alpha(1-\alpha)\varepsilon h_3; \\ R \cos r &= -1 \mp \frac{1}{2}\sqrt{3}(1-2\alpha)\varepsilon h_3, \\ R \sin r &= -\frac{3}{2}\varepsilon h_3; \\ P \cos p &= \frac{1}{2}, \\ P \sin p &= \pm \frac{1}{2}\sqrt{3}(1-2\alpha) + 2\alpha(1-\alpha)\varepsilon h_3; \\ T \cos t &= Q^2 \cos 2q - 4\alpha(1-\alpha)(1+\beta)QR \cos(q+r) \\ &\quad + 4\alpha^2(1-\alpha)^2(1+\beta)^2R^2 \cos 2r, \\ T \sin t &= Q^2 \sin 2q - 4\alpha(1-\alpha)(1+\beta)QR \sin(q+r) \\ &\quad + 4\alpha^2(1-\alpha)^2(1+\beta)^2R^2 \sin 2r. \end{aligned}$$

For a given alloy, with finite values of α, β and ε , the profiles of the $3M+1$ and $3M-1$ reflexions are no longer equivalent; moreover, these profiles are different for the successive peaks occurring with increasing h_3 . Evaluation of (17) with the aid of the Mercury computer for the case $\varepsilon = 0.02$ showed that the values of the points on the curves in Figs. 4(a) and 4(b) (corresponding to $\varepsilon = 0$) were changed by about 7% for the first order peak and 22% for the second order peak. For many alloys, in particular those such as Ag-Au and Co-Ni with a wide range of solid solution, ε is practically zero and the simpler theory of S_2 is then adequate.

Thanks are due to Mr T. M. Valentine and Mr T. Vann for handling the bulk of the calculations.

References

- CHRISTIAN, J. W. & SPREADBOROUGH, J. (1957). *Proc. Phys. Soc. B*, **70**, 1151.
 COTTRELL, A. H. (1954). 'Relation of Properties to Microstructure'. A.S.M. Symposium Report, 131.
 PATERSON, M. S. (1952). *J. Appl. Phys.* **23**, 805.
 SMALLMAN, R. E. & WESTMACOTT, K. H. (1957). *Phil. Mag.* (8), **2**, 669.
 SUZUKI, H. (1952). *Sci. Reports Res. Inst. Tohoku Univ.* **A**, **4**, 455.
 THORNTON, P. R. & HIRSCH, P. B. (1958). *Phil. Mag.* (8), **3**, 738.
 WARREN, B. E. & WAREKOIS, E. P. (1955). *Acta Metallurg.* **3**, 473.
 WILLIS, B. T. M. (1958). *Proc. Roy. Soc. A*, **248**, 183.

(Reprinted from *Nature*, Vol. 197, No. 4869, pp. 755-756,
February 23, 1963)

POSITIONS OF THE OXYGEN ATOMS IN $\text{UO}_{2.13}$

By B. T. M. WILLIS

Metallurgy Division, Atomic Energy Research Establishment,
Harwell

URANIUM dioxide, UO_2 , can dissolve oxygen at high temperatures to form the single phase UO_{2+x} , where x assumes any value in the range $0 \leq x \leq 0.25$. For $\text{UO}_{2.10}$ the temperature must exceed 600°C and for $\text{UO}_{2.20}$ the minimum temperature is about $1,050^\circ \text{C}$ (ref. 1).

Neutron diffraction investigations have been made on a single-crystal of composition $\text{UO}_{2.13}$ with the aim of determining the positions of the oxygen atoms. The ratio of the slow neutron coherent scattering amplitudes of uranium and oxygen is 1.47, so that, unlike for X-rays, an appreciable proportion of the scattered intensity comes from oxygen. However, we must distinguish between oxygen atoms present in the UO_2 crystal before oxidation and 'extra' oxygen atoms; as the former predominate, the location of the extra atoms is analogous to a light-atom determination with X-rays. In these circumstances very accurate neutron structure-factors are required, and it is necessary to correct the observed intensities for extinction (affecting the strong reflexions) and double-Bragg scattering (mainly affecting the weak reflexions).

All non-equivalent hkk planes with an interplanar spacing greater than 0.53 \AA were measured at 800°C , inside the single-phase region of the phase diagram. No reflexions were observed other than those with h, k both odd or both even, and so it was assumed in the analysis by least-squares and Fourier methods that the space-group is $Fm\bar{3}m$, as for UO_2 .

Table 1 summarizes the results of the least-squares analysis, which was carried out using a *Mercury* computer programme specially written for this work by Dr. J. S. Rollett. The oxygen atoms in $\text{UO}_{2.13}$ occupy three different kinds of crystallographic site, and, as there are more equivalent positions for each site than oxygens to fill them, the oxygens are distributed at random among these positions. The programme allowed as adjustable parameters the probability of occupation of each atomic site, as well as the atomic co-ordinates and temperature factors. Altogether 11 parameters were obtained from 33 independent data, and the final 'discrepancy factor'

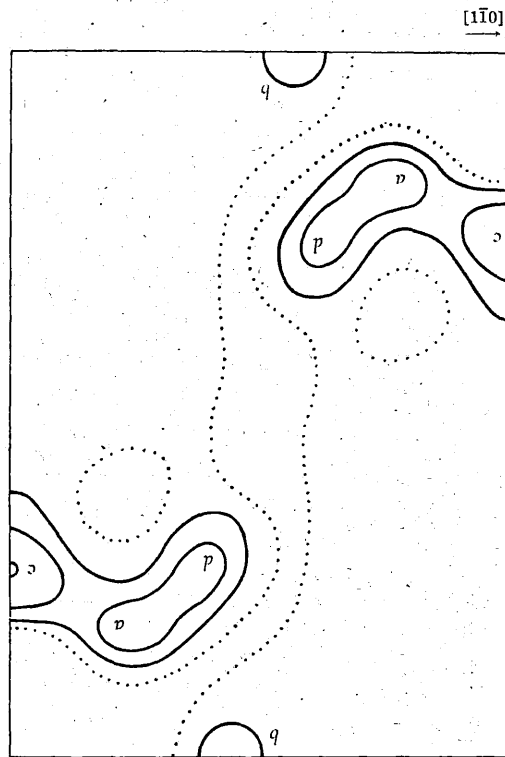


Fig. 2. Fourier projection along [110] with contributions from uranium and oxygen atoms O removed. Interval between contours is one-sixth of that in Fig. 1. Peaks at *a, b* represent oxygen atoms O' at 0.5 0.4 0.4 . . . and peaks at *c, d* oxygen atoms O'' at 0.4 0.4 0.4 . . .

where O, O', O'' refer to oxygen atoms in the three kinds of site.

(2) The uranium atoms occupy the face-centred positions 000 , $\frac{1}{2}\frac{1}{2}0$, $\frac{1}{2}0\frac{1}{2}$, $0\frac{1}{2}\frac{1}{2}$, and all these sites are filled, as in UO_2 .

(3) The O atoms at uuu . . . are close to the fluorite positions $\frac{1}{4}\frac{1}{4}\frac{1}{4}$. . . , but are shifted slightly along $\langle 111 \rangle$ towards the interstitial holes at $\frac{1}{2}\frac{1}{2}\frac{1}{2}$. . . (the $\frac{1}{2}\frac{1}{2}\frac{1}{2}$, $\frac{1}{2}00$, $0\frac{1}{2}0$, $00\frac{1}{2}$ positions are the largest holes in the UO_2 lattice). The O atoms represent approximately nine out of ten of the original oxygens in UO_2 before oxidation to $\text{UO}_{2.13}$; the remaining one-tenth are transferred during oxidation to O' or O'' positions.

(4) The interstitial atoms O' and O'' do not occupy the large interstitial holes at $\frac{1}{2}\frac{1}{2}\frac{1}{2}$. . . , but positions about 1 Å away.

Fourier analysis confirms the least-squares results.

Table 1. CRYSTAL STRUCTURE OF $\text{UO}_{2.13}$

Atom	Unit cell co-ordinates	Contribution to formula unit $\bar{U}_m\bar{O}_n$	Temperature factor B (\AA^2)
Uranium	0 0 0...	$m \doteq 1.00$ (0.01)	1.18 (0.06)
Oxygen O	$u u u...$	$n = \begin{cases} 1.82 & (0.02) \\ 0.08 & (0.05) \\ 0.23 & (0.11) \end{cases}$	1.45 (0.08)
Oxygen O'	0.5 $v v...$		1.8 (1.6)
Oxygen O''	$w w w...$		7.5 (2.7)

($u=0.267$ (0.001), $v=0.39$ (0.01), $w=0.38$ (0.01)). Space group $Fm\bar{3}m$. Standard deviations of parameters in brackets.)

($\frac{\sum ||F_{\text{obs}}| - |F_{\text{calc}}||}{\sum |F_{\text{obs}}|}$) was 2.2 per cent, which is close to the estimated accuracy of the individual data.

The principal conclusions from Table 1 are as follows:
 (1) The composition determined from the scattering results is $\text{UO}_{2.13}$ in agreement with that found chemically. A more complete expression for the formula unit is:

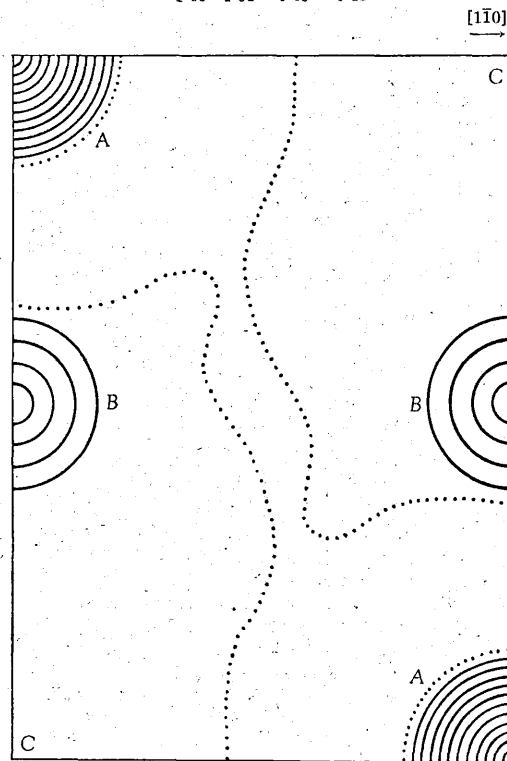
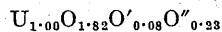


Fig. 1. Fourier projection along $[110]$ of nuclear density of $\text{UO}_{2.13}$ at 800°C . Peaks at A represent the uranium atoms at $000\dots$ and peaks at B the oxygen atoms O at $0.27\ 0.27\ 0.27\dots$. The interstitial holes are at C . Zero contours dotted.

Fig. 1 is a Fourier projection, based on a Fourier series with the F_{obs} data as coefficients, showing the uranium and oxygen O atoms. Fig. 2 is a difference Fourier projection, using $F_{\text{obs}} - F_{\text{UO}}$ as coefficients, where F_{UO} is calculated for the uranium and O atoms only. The contours in Fig. 2, which are on a much finer scale than in Fig. 1, show peaks representing the O' atoms at $0.5\ 0.5\ 0.5$ and O'' atoms at $0.5\ 0.5\ 0.5$.

The least-squares and Fourier results, based on an analysis of the coherent Bragg reflexions only, give the contents and atomic co-ordinates of the average unit cell of the disordered compound: they do not define the local atomic arrangement. However, a plausible interpretation in terms of the local relaxation around an isolated interstitial atom is as follows. This interstitial atom enters the lattice at the O' position $0.5\ 0.4\ 0.4$; to maintain charge balance the two nearest U^{4+} ions at $\frac{1}{2}\frac{1}{2}0$ and $\frac{1}{2}0\frac{1}{2}$ are converted to U^{5+} , and the polarizing influence of these U^{5+} ions prevents the interstitial atom occupying the hole at $\frac{1}{2}\frac{1}{2}\frac{1}{2}$. The two nearest oxygens at $\frac{1}{4}\frac{1}{4}\frac{1}{4}$ and $\frac{3}{4}\frac{1}{4}\frac{1}{4}$ are then displaced along $\langle 111 \rangle$ to O' positions and oxygens further out relax a much shorter distance along $\langle 111 \rangle$ to O sites at $uvw \dots$. The large 'temperature factor' of 7.5 \AA^2 for the O'' atoms is to be ascribed to the disorder accompanying the relaxation of the nearest-neighbour oxygens.

¹ Roberts, L. E. J., *Quart. Rev., Lond. Chem. Soc.*, 15, 442 (1961).

Reprinted from
 "PROCEEDINGS OF THE BRITISH CERAMIC SOCIETY
 No. 1, July 1964

2.—Point Defects in Uranium Oxides

By B. T. M. WILLIS

Metallurgy Division, Atomic Energy Research Establishment, Harwell

ABSTRACT

Neutron diffraction measurements on single crystals of uranium oxides, with compositions in the range $UO_{2.00}$ to $UO_{2.25}$, have led to an identification of the types of point defects arising from the departure from stoichiometry. Interstitial oxygen atoms enter the UO_2 lattice at two kinds of site, which are displaced by about 1\AA along $\langle 110 \rangle$ and along $\langle 111 \rangle$ from the holes at the $\frac{1}{2}\frac{1}{2}\frac{1}{2}$, $\frac{1}{2}00$, $0\frac{1}{2}0$, $00\frac{1}{2}$ positions. The solution of oxygen is accompanied by the formation of vacancies in the normal oxygen sites, but the uranium sublattice remains undisturbed. It is probable that the oxygen interstitials and vacancies are associated together as defect complexes; at the limiting composition of $UO_{2.25}$ these complexes are ordered to form a cubic phase based on the fluorite arrangement but with an enlarged unit cell.

1. INTRODUCTION

Uranium dioxide exists as the single-phase, stoichiometric oxide at all temperatures up to 1800°C . Above 1800°C it transforms to the sub-stoichiometric phase UO_{2-x} ,¹ whereas at lower temperatures it dissolves oxygen and changes into the super-stoichiometric phase UO_{2+x} . This paper is concerned with UO_{2+x} and, in particular, with the identification of the type, and the determination of the concentration, of the point defects arising from the departure from the stoichiometric composition $UO_{2.00}$. The neutron diffraction method has been used, and a brief preliminary account of work on $UO_{2.13}$ has already been published.²

To study point defects by examining their influence on the magnitude of the coherent Bragg reflexions requires unusually high accuracy in measuring the integrated intensities and, in general, this accuracy is achieved more readily with neutrons than with X-rays. For uranium oxide, however, the X-ray method is ruled out on two other grounds: the dominating scattering power of uranium, which masks the scattering from the oxygen atoms, and the very high X-ray absorption cross-section of the oxide, which is four or five orders of magnitude higher than for neutrons.

The intensities of the coherent neutron reflections of $\text{UO}_{2.12}$ and $\text{UO}_{2.13}$ have been measured at 800°C , within the single-phase region of the equilibrium diagram (Figure 1). Single crystals quenched

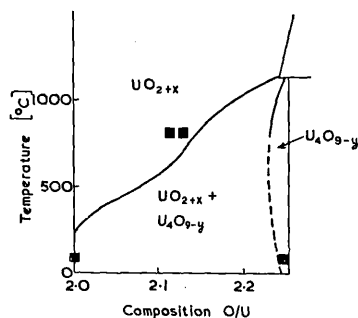


FIGURE 1.—Portion of the equilibrium diagram of uranium–oxygen system⁵. The squares (■) indicate the compositions examined by neutron diffraction.

from high temperature decomposed into a mixture of UO_2 and U_4O_9 , showing the characteristic superlattice reflexions of U_4O_9 ,³ and so it was necessary to carry out all measurements at high temperature.

2. EXPERIMENTAL

2.1 Preparation of Samples

Single crystals of UO_2 were available, grown from the melt, from solution or from the vapour. Solution-grown crystals were too small and too perfect for the present work: highly perfect crystals, containing relatively few dislocations, gave data which were subject to extinction and multiple scattering errors.⁴ More satisfactory results were obtained with melt-grown and vapour-grown crystals, and the bulk of the measurements reported here were taken on melt-grown samples.

Non-stoichiometric oxides were prepared by heating UO_2 crystals in association with powdered U_3O_8 in an evacuated silica tube, the oxygen being transferred *via* the vapour phase. After heating for several weeks at 1100°C , followed by annealing at the same temperature in the absence of U_3O_8 , the oxide content of the crystal was determined electrolytically.⁵ The crystal was then ground into a cylindrical pillar, 1 to 2 mm. in diameter and 5 mm. long, with the long axis along $[1\bar{1}0]$. Two-dimensional structure factor measurements were taken on a crystal of composition $\text{UO}_{2.13}$,² and three-dimensional measurements on a crystal of $\text{UO}_{2.12}$.

2.2 Measurement of Bragg Intensities

Figure 2 is a schematic diagram of the apparatus for measuring three-dimensional neutron scattering data at 800°C. The crystal was mounted in an evacuated silica tube surrounded by a cylindrical

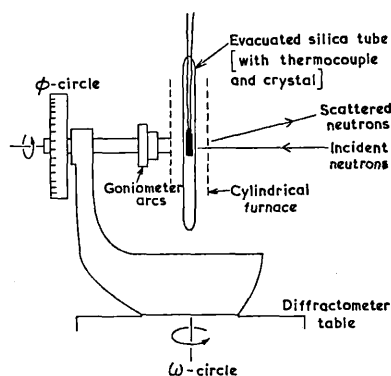


FIGURE 2.—Apparatus for measuring hkl reflections at 800°C.

heating element, consisting of a thin coating of platinum on an alumina tube. The whole furnace was mounted on a pair of goniometer arcs, which were adjusted initially to bring the $[1\bar{1}0]$ axis coincident with the vertical axis (ω) of the diffractometer table. hkl data were measured by rotating the furnace assembly about the ω -axis, and full three-dimensional hkl data by rotation about both the vertical ω -axis and the horizontal ϕ -axis.

Careful checks were made for the presence of extinction and double Bragg scattering by repeating the measurements at different azimuthal settings of the reflecting planes.⁴ All data showing any indication of these errors were rejected. The rocking curves, giving the reflected intensity as the crystal was scanned across the Bragg reflecting position, were wider for the non-stoichiometric crystals than for the initial starting material of UO_2 . This shows that the incorporation of oxygen increases the mosaic spread of the crystal and, therefore, tends to reduce the extinction and double scattering errors.

3. ANALYSIS OF DIFFRACTION DATA

3.1 Least-squares Method

The observed structure-factors for $\text{UO}_{2.12}$ at 800°C are shown in Figure 3 plotted against $h^2+k^2+l^2$. The broken curves represent

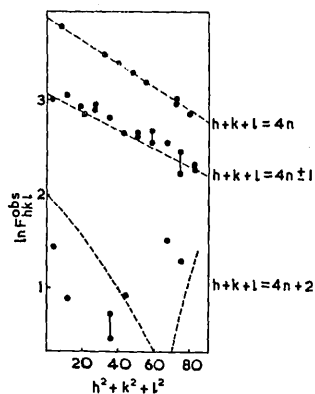


FIGURE 3.— $\text{UO}_{2.12}$: observed structure factors as a function of $h^2+k^2+l^2$. Broken curves given by fluorite model. Short vertical lines connect points such as 600 and 442 with the same $h^2+k^2+l^2$.

the best least-squares fit to the experimental points for the stoichiometric fluorite model with isotropic temperature factors B ($=1.1\text{\AA}^2$ for uranium and 1.5\AA^2 for oxygen). The data are divided into three groups with $h+k+l=4n$, $4n\pm 1$, $4n+2$, where n is an integer. The departure of the points from the smooth fluorite curves is due to the influence of the interstitial oxygen atoms and forms the basis on which the whole of the following analysis is derived.

The measurements were analysed by the crystallographic least-squares procedure. This requires minimization of the function

$$\sum_{hkl} w_{hkl} (|F_{hkl}^{obs}| - |F_{hkl}^{calc}|)^2,$$

where w_{hkl} is the weight of each individual F_{hkl} , F_{hkl}^{obs} is the observed F_{hkl} and F_{hkl}^{calc} the calculated F_{hkl} . The calculated structure factor is given by the expression:

$$F_{hkl}^{calc} = s \sum_r m_r b_r \exp 2\pi i (hx_r + ky_r + lz_r) \exp (-B_r \sin^2\theta/\lambda^2) \dots (1)$$

in which

$$\left. \begin{array}{l} s = \text{overall scale factor} \\ m_r = \text{occupation number} \\ b_r = \text{coherent scattering amplitude} \\ x_r, y_r, z_r = \text{positional co-ordinates} \\ B_r = \text{isotropic temperature factor} \\ 2\theta = \text{scattering angle} \end{array} \right\} \text{of the } r^{\text{th}} \text{ atom}$$

and λ = wavelength.

In the case of UO_{2+x} the number of atoms (r) is four: uranium, normal (fluorite-type) oxygen and two types of interstitial oxygens²,

O' and O".* The b_r 's are accurately known from previous work,⁴ leaving as unknowns to be determined by the refinement procedure the single scale factor and the occupation number, position and temperature factor of each atom. The occupation number m_r refers to the proportion of equivalent sites occupied by the r^{th} atom; for perfect structures it is unity for each atom, but for a disordered structure some of the available atomic sites are only partially (statistically) occupied and m_r is then less than unity. It must be emphasized that for a defect structure such as UO_{2+x} the 'structure factor expression (1) refers to the statistical unit cell, obtained by averaging over all the UO_2 -type cells in the crystal. The contents of the individual cells of $\text{UO}_{2.0}$ are no longer identical when oxygen is taken up to form the non-stoichiometric oxide.

Table 1 summarizes the results obtained by analysing thirty eight independent F^{obs} data of $\text{UO}_{2.12}$. The least-squares calculations

Table 1
Structure of $\text{UO}_{2.12}$: Least-squares Results

Atom	Co-ordinates in statistical cell			Contribution to formula unit U_mO_n	Temperature factor B (\AA^2)
	x	y	z		
Uranium	0	0	0	$m=1.00(0.01)$	1.18(0.02)
Oxygen O	u	u	u	$n=$ $\left\{ \begin{array}{l} 1.87(0.03) \\ 0.08(0.04) \\ 0.16(0.06) \end{array} \right.$	1.45(0.04)
Oxygen O'	0.5	v	v		1.8 (1.4)
Oxygen O"	w	w	w		2.0 (1.6)

$$u=0.267(0.001), \quad v=0.38(0.01), \quad w=0.41(0.01)$$

Space group Fm3m. Standard deviations of parameters in brackets.

were carried out on the IBM 7090 computer using the BUSING-LEVY⁶ programme. The space group, defining the symmetry properties of the statistical unit cell, was taken as Fm3m, as for UO_2 . Table 2 compares the observed structure factors with the structure factors calculated from the parameters listed in Table 1. The F^{obs} values are on a relative scale only, so that the F^{calc} figures include an arbitrary scale factor (s), derived from the refinement procedure. The agreement between F^{obs} and F^{calc} is good, as indicated by the low value of 3.5% for the conventional discrepancy factor,

$$R = \frac{\sum_{hkl} \left| |F_{hkl}^{\text{obs}}| - |F_{hkl}^{\text{calc}}| \right|}{\sum_{hkl} |F_{hkl}^{\text{obs}}|}$$

* The single and double primes are used to label the two different kinds of sites, and do not refer to the state of ionization of these atoms.

Table 2
Structure Factors of $\text{UO}_{2.12}$

<i>hkl</i>	<i>F_{obs}</i>	<i>F_{calc}</i>	<i>hkl</i>	<i>F_{obs}</i>	<i>F_{calc}</i>
002	57	49	246	335	329
004	538	543	331	257	254
006	21	1	333	257	256
008	291	296	335	193	200
0010	65	71	337	178	176
026	410	397	339	110	108
048	238	232	357	135	124
111	284	296	442	28	20
113	293	285	444	364	369
115	251	251	446	61	45
117	195	203	448	189	189
119	130	139	551	185	171
135	229	222	553	204	201
137	175	170	555	122	143
157	158	151	557	132	145
222	32	40	660	272	270
224	499	504	662	49	54
226	33	23	664	209	209
228	257	260	771	115	113

This *R* factor is higher than that given by the two-dimensional *hkl* data of $\text{UO}_{2.13}$ reported earlier.² However, the standard deviations of the atomic parameters for $\text{UO}_{2.12}$ (Table 1) are less than for $\text{UO}_{2.13}$ (Table 1 in reference 2), and this is due to the inclusion of three-dimensional measurements. For this reason, and because of the similarity of the two sets of results, the results for $\text{UO}_{2.12}$ only will be discussed below.

3.2 Atomic Positions: Identification of Defects

The fluorite structure of UO_2 contains holes at the $\frac{111}{222}$, $\frac{1}{2}00$, $0\frac{1}{2}0$, $00\frac{1}{2}$ sites of the unit cell. These holes are large enough to accommodate atoms up to 2.7Å diam., and it has been widely assumed⁷ by previous workers that the disordered UO_{2+x} structure consists of the fluorite arrangement with random occupation of the holes by interstitial oxygens (Figure 4).

The neutron results show that this is not correct for $\text{UO}_{2.12}$ and, in fact, no least-squares refinement of the data was possible using this model. The interstitial oxygens occupy two kinds of site which are located about 1Å along the $\langle 110 \rangle$ and the $\langle 111 \rangle$ directions from the centres of the large holes. The O' atoms, displaced along $\langle 110 \rangle$, are approximately half way from the hole to the centre of the line

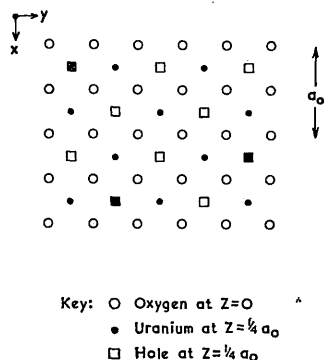


FIGURE 4.—Structure of UO_{2+x} : old model. The squares (■) indicate holes occupied at random by interstitial oxygen atoms.

joining two adjacent normal oxygen (fluorite-type) sites; the O'' atoms, displaced along $\langle 111 \rangle$, are half way from the hole to the nearest normal oxygen site. These displacements do not affect the uranium sub-lattice but cause the ejection of some of the normal oxygens from their fluorite positions.

The atomic positions for UO_{2+x} are shown schematically in Figure 5. In this figure the three types of oxygen defect—normal

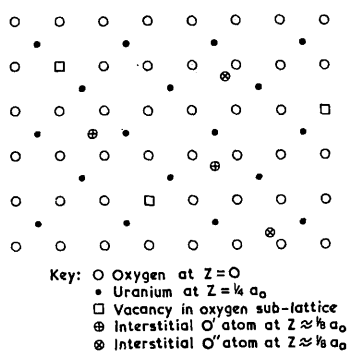
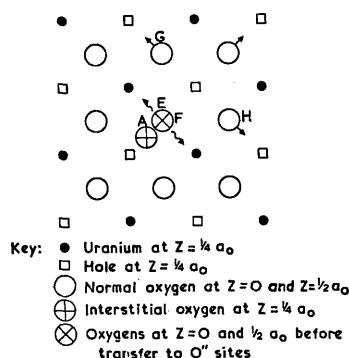


FIGURE 5.—Schematic diagram of UO_{2+x} : new model. The three kinds of oxygen defect are distributed at random in this diagram, but it is more likely that they associate to form defect complexes.

oxygen vacancy, interstitial oxygens O' and O'' —are distributed at random throughout the structure, but such an arrangement brings several oxygens too close together and it is more reasonable to

suppose that the different kinds of oxygen defect are associated together. Figure 6 illustrates a possible mechanism for the formation of a defect complex involving one O' atom, two O'' atoms and two normal oxygen vacancies.

FIGURE 6.—Local lattice distortion around interstitial atom O' at A. The nearest oxygens E, F are displaced along $\langle 111 \rangle$ (see arrows) to interstitial sites, O'', and the surrounding oxygens G, H . . . also relax along $\langle 111 \rangle$. The uranium sub-lattice is unchanged.



Neutron diffraction work on U_4O_9 has shown that the oxygen sites in U_4O_9 are closely related to those listed in Table 1, although the space group symmetry ($I\bar{4}3d$) is different.³ This shows that the transition from UO_{2+x} to U_4O_9 involves long-range ordering of the defect complexes, leading to a change in the symmetry relating the relative positions of the complexes, without producing any atomic re-arrangement within these complexes. In one sense, therefore, micro-domains of U_4O_9 already exist in UO_{2+x} at high temperature.

3.3 Occupation Parameters: Concentration of Defects

The composition of the $UO_{2.12}$ sample is given directly (Table 1) as

$$U_{1.00 \pm 0.01} O_{1.87 \pm 0.03} O'_{0.08 \pm 0.04} O''_{0.16 \pm 0.06}$$

The \pm figures represent standard deviations, as derived from the inversion of the least-squares matrix. The concentrations of the interstitial atoms O', O'' are not known precisely, and better diffraction data are required to fix the composition to closer limits. The occupation parameter of the normal oxygen atom O corresponds to a concentration of six or seven per cent of vacancies in the normal oxygen sub-lattice.

It appears that the defects are confined to the oxygen sub-lattice. The evidence for this is derived from both density and neutron diffraction measurements. The density of the $\text{UO}_{2.12}$ sample at room temperature was higher than that of UO_2 ; this increase can only occur if the uranium sub-lattice remains substantially intact on oxidation. A similar conclusion arose from the comparison of $\text{UO}_{2.12}$ and UO_2 diffraction data at 800°C , giving a direct measurement of the scaling factor s . This estimate was close to that given by the least-squares analysis, assuming complete occupation of the uranium sub-lattice.

The O/U ratio determines the relative proportion of the two phases, UO_2 and U_4O_9 , into which UO_{2+x} disproportionates on cooling, and can be determined from diffraction measurements at room temperature. U_4O_9 is a structure based on UO_2 but with long-range ordering of the interstitial oxygen atoms; this ordering gives rise to superlattice reflexions, which index on a cell four times the size of the UO_2 cell.⁷ From the ratio of the intensity of a superlattice reflexion to that of a fundamental reflexion it is possible to measure the oxygen content x . The superlattice reflexion is contributed by the U_4O_9 structure alone and the fundamental reflexion, occurring at the same Bragg angle for both phases, by both UO_2 and U_4O_9 . Figure 7 shows the ratio of the $10, 1, 1$ superlattice and

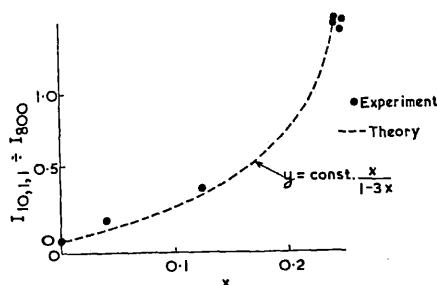


FIGURE 7.—Ratio of $10, 1, 1$ superlattice to 800 fundamental intensities plotted against the oxygen concentration x . Broken line is theoretical curve, calculated assuming complete conversion of UO_{2+x} to UO_2 and U_4O_9 [$(\text{UO}_{2+x} = (1-4x)\text{UO}_2 + x\text{U}_4\text{O}_9)$]. All measurements at room temperature.

the 800 fundamental intensities (both indices related to the $4a_c$ cell of U_4O_9) as a function of the concentration x . The broken curve is the theoretical curve, suitably scaled to pass through the experimental points obtained for different samples of U_4O_9 . The measurements for three quenched samples, $\text{UO}_{2.04}$, $\text{UO}_{2.12}$, $\text{UO}_{2.13}$, lie reasonably near the theoretical curve, and this shows that quenching

failed to prevent the complete disproportionation into UO_2 and U_4O_9 .

3.4 Thermal Vibration Parameters

The temperature parameter, B_U , of uranium is related to the mean square displacement $\overline{u_s^2}$ in any direction by $B_U = 8\pi^2\overline{u_s^2}$; this displacement arises from both the thermal motion of the uranium atom and its random displacement, due to disorder, from the 000. . . sites. The similarity of the B_U value (1.1\AA^2) with that for UO_2 at 800°C ⁸ indicates that the dominant contribution is from thermal motion, and that little, if any, disturbance occurs in the positions of the uranium atoms as interstitial oxygens are added.

On the other hand, the high B_O value for the interstitial O' and O'' atoms reflects the influence of disorder. The O' atoms are located at the $0.5\nu\nu$. . . sites and the O'' atoms at the $w\nu\nu$. . . sites of the Fm3m space-group. The values of ν and w probably change slightly from one interstitial oxygen to the next, and these changes are partially allowed for in the least-squares analysis by keeping ν and w constant and increasing B_O .

A similar interaction occurs between the positional and thermal parameters of the normal oxygen atoms. In this case, however, the B_O value can be lowered by allowing the atoms to relax along the four $\langle 111 \rangle$ directions, which join the fluorite-type site with the adjacent holes surrounding the site tetrahedrally. The oxygen positions refine as $1/4 + \delta$, $1/4 + \delta$, $1/4 + \delta$. . . etc. where $\delta = 0.020 \pm 0.002$. Exactly the same behaviour occurs in UO_2 at 800°C , and its interpretation has been discussed in terms of either disorder between the normal oxygen positions or as a breakdown in the harmonic approximation for the thermal vibrations of the oxygen atoms.⁸

4. CONCLUSIONS

The neutron diffraction measurements on non-stoichiometric UO_{2+x} give the contents of the statistical unit cell, obtained by averaging over all the fluorite-type cells of the crystal as a whole. The positions of the atoms in the statistical cell of $\text{UO}_{2.12}$, and also their concentrations and thermal vibration parameters, are summarized in Table 1.

The figures in brackets in this Table represent standard deviations, σ . The 95% confidence range, such that there is a 95% probability that the corresponding parameter lies in this range, is $\pm 2\sigma$. Thus, assuming that no systematic errors are present in the intensity data, the positions of the interstitial atoms are known reasonably well, whereas their concentrations are only very roughly defined.

To specify the atomic parameters more precisely it will be necessary to improve the accuracy of the intensity measurements (e.g. by using spherical crystals and by counting for longer periods) and to extend the work to other compositions and temperatures.

ACKNOWLEDGMENTS

The author is grateful to Mr. K. A. D. Lambe and Mr. T. M. Valentine for experimental assistance, to Mr. K. D. Rouse for computer processing of the data, and to Mr. R. W. M. Hawes for the density measurements.

REFERENCES

1. ROTHWELL, E., *J. Nucl. Mat.*, **6**, 229, 1962.
2. WILLIS, B. T. M., *Nature*, **167**, 755, 1963.
3. WILLIS, B. T. M., *J. de Physique et le Rad.* In the press.
4. WILLIS, B. T. M., *Proc. Roy. Soc. A.*, **274**, 122, 1963.
5. MARKIN, T. L., and ROBERTS, L. E. J., "Thermodynamics of Nuclear Materials", (I.A.E.A., Vienna), p. 693, 1962.
6. BUSING, W., MARTIN, K. O., and LEVY, H. A., *Oak Ridge Report, ORNL-TM-305*, 1962.
7. BELBEOCH, B., PIEKARSKI, C., and PERIO, P., *Acta Cryst.*, **14**, 837, 1961.
8. WILLIS, B. T. M., *Proc. Roy. Soc. A.*, **274**, 134, 1963.

NEUTRON DIFFRACTION STUDIES OF NON-STOICHIOMETRIC COMPOUNDS

B. T. M. Willis

Atomic Energy Research Establishment,
Harwell, Berks., England.

1. INTRODUCTION

The technique of neutron diffraction provides a direct approach to the study of the crystal structures of non-stoichiometric compounds. From measurements of the intensities of the Bragg reflexions it is possible not only to deduce whether the defects are vacancies or interstitials, but also to determine the kinds of crystallographic site they occupy. Because of the relatively small influence of the defects on the Bragg intensities, contributed mainly by atoms in undisturbed positions, it is only practicable to examine crystals showing gross departures from the stoichiometric composition, e.g., Fe_{0.9}O, UO_{2.1}, Ti_{0.95}O_{0.95}. Where the stoichiometric deviation is very small, as in PbS_{1+x} or alkali halides containing F-centres, the diffraction method is not sufficiently sensitive.

The principles involved in interpreting the neutron data are exactly the same as in X-ray diffraction, but neutron studies have a number of important advantages over X-rays. The dominance of scattering over true absorption allows the neutron intensities to be placed readily on an absolute scale, so that the fractional occupancy of each crystallographic site can be estimated. Highly accurate data are essential and, because of the small absorption, accuracy is achieved more readily with neutrons. Finally, the departure from stoichiometry in the oxides, carbides and hydrides of the transition metals (the most intensively studied non-stoichiometric compounds) is often due to defects in the anion sub-lattice, and neutrons are required to distinguish the anions from the relatively heavy metal atoms.

Earlier neutron work has been carried out on non-stoichiometric metal hydrides⁽¹⁾ and on ferrous oxide⁽²⁾, using polycrystalline samples. The work on Fe_{1-x}O was especially interesting in that it demonstrated the existence of both vacancies and interstitials in the metal sub-lattice. These positional defects, together with electronic defects, associate in a defect complex, and the co-ordination of the atoms within the complex is the same as in the next higher oxide, Fe₃O₄. It is not correct to describe the defect structure of non-stoichiometric ferrous oxide as the sodium-chloride arrangement with isolated cation vacancies, but powder data alone are insufficient to allow a determination of all the unknown structural parameters.

Clearly, it is desirable to examine non-stoichiometric compounds in the form of single crystals. Single-crystal neutron data are available for uranium dioxide UO_{2+x}: we shall describe briefly the procedure for analysing these data before discussing the results.

2. ANALYSIS OF SINGLE-CRYSTAL DATA

The theoretical intensity of the hkl reflexion is proportional to $|F_{hkl}|^2$, where the structure factor F_{hkl} is given by

$$F_{hkl} = s \sum_j m_j b_j \exp 2\pi i (hx_j + ky_j + lz_j) T_j \dots (1)$$

In this equation x_j, y_j, z_j are the co-ordinates of the j^{th} atom in the pseudo-cell, expressed as fractions of the cell edges, b_j is the neutron scattering amplitude of the atom, and m_j its fractional occupancy of the x_j, y_j, z_j site. For a disordered, non-stoichiometric compound we must refer to a pseudo-cell, which is equivalent to a true unit cell at the stoichiometric composition. s is a scale

factor, found by comparing the observed intensities with those of a standard crystal, and T_j is the temperature correction factor.

In the general case of anisotropic vibration of the j^{th} atom, it is customary in X-ray and neutron work to write T_j as

$$T_j = \exp [-(b_{11} h^2 + b_{12} hk + b_{13} hl + b_{22} k^2 + b_{23} kl + b_{33} l^2)]. \quad \dots (2)$$

The anisotropic thermal motion is represented by an ellipsoid of vibration in reciprocal space, and six temperature factors b_{11}, b_{12}, \dots for each atom define the lengths and direction cosines of the three principal axes of the ellipsoid. These temperature factors are treated as adjustable parameters in the least-squares comparison of the observed and calculated intensities. It is important to realize, however, that equation (2) is valid only within the limits of the "harmonic approximation". This approximation implies that, in expanding the potential energy of the crystal in powers of the amplitudes of the thermal vibrations, all terms beyond those which are quadratic in the amplitudes are neglected. Anharmonic contributions to the Debye-Waller factor, giving further terms in equation (2), may be especially important in the study of non-stoichiometric compounds, because anharmonic effects are more prominent at the higher temperatures where these compounds are stable. If the effects are neglected, errors will occur in the estimated site occupancy of each atom m_j , which correlates strongly with T_j in the least-squares refinement. The anharmonic contribution to T_j has been discussed elsewhere for UO_2 ⁽³⁾ and for CaF_2 ⁽⁴⁾; for the high-angle reflexions of CaF_2 , intensity changes of up to twenty per cent arise from the anharmonic contribution alone at 20°C, and at 500°C the changes can be three times higher. For atoms lying at centres of symmetry, the cubic term in the potential energy expansion is identically zero and there is no measurable anharmonic contribution to the Debye-Waller factor.

There is no serious "phase problem" in the study of non-stoichiometric compounds. An adequate first approximation to the phase of each reflexion is the phase given by the undisturbed atomic arrangement with no defects.

The presence of defects gives rise to weak non-Bragg diffuse scattering, which could be interpreted in terms of a model of the structure with randomly distributed, isolated defects. However, this is not a realistic model for the uranium-oxygen system, and also because of the experimental difficulty of separating the defect diffuse scattering from other sources of diffuse scattering, we have not attempted to interpret measurements other than those relating to the coherent Bragg reflexions.

3. URANIUM-OXYGEN SYSTEM

Non-stoichiometric uranium dioxide, UO_{2+x} , has a wide region of solid solution extending to $x = 0.15$ at 800°C and to $x = 0.25$ at 1120°C. At low temperatures disproportionation occurs into UO_2 and U_4O_9 , and it is difficult to retain the UO_{2+x} phase by quenching. X-ray and thermodynamic studies indicate that all three phases, UO_2 , UO_{2+x} and U_4O_9 , are based on the fluorite arrangement, and that non-stoichiometry in UO_{2+x} arises by the incorporation of extra oxygen atoms in the fluorite structure of UO_2 , with these extra atoms undergoing long-range order in U_4O_9 to form a very large cubic superlattice.

Neutron intensities have been measured up to $h^2 + k^2 + l^2 = 100$ for $\text{UO}_{2.12}$ and $\text{UO}_{2.13}$ at 800°C. Least-squares refinement using equation (1) for the calculated intensities, including anharmonic contributions to T_j for the tetrahedrally co-ordinated oxygen atoms, gave the parameters for $\text{UO}_{2.12}$ listed in Table 1. The results from the analysis of the $\text{UO}_{2.13}$ single crystal were essentially the same as for $\text{UO}_{2.12}$ and are not quoted. The figures in brackets are standard deviations, derived from the inversion of the least-squares matrix. There is a large uncertainty in the fractional site occupancies (which are directly proportional to

the composition figures given in the second column of the Table), even though the final R-index was as low as 3.5 per cent. This again emphasises the need to obtain accurate data and to analyze them with an adequate model. The overall composition determined from the m_j 's is approximately correct, but this agreement could be fortuitous.

The most natural place to accommodate the extra oxygens in UO_{2+x} is at the large holes with co-ordinates $\frac{1}{2} \frac{1}{2} \frac{1}{2} \dots$ in the UO_2 cell. Oxygen atoms at these sites are labelled O''' in Table 1. However, the occupancy number for O''' refines at a negative value close to zero, and this, together with the difficulty of refining the temperature factor, discounts the possibility of these sites being occupied.

Table 1. Crystal structure of $UO_{2.12}$ at $800^\circ C$

Atom	Contribution to m in formula unit UO_m	Co-ordinates in pseudo-cell		
		x	y	z
uranium	—	0	0	0
oxygen O	1.87(0.03)	$\frac{1}{4}$	$\frac{1}{4}$	$\frac{1}{4}$
oxygen O'	0.08(0.04)	$\frac{1}{2}$	0.38(0.01)	0.38(0.01)
oxygen O''	0.16(0.06)	0.41(0.01)	0.41(0.01)	0.41(0.01)

oxygen O'''	-0.02(0.02)	$\frac{1}{2}$	$\frac{1}{2}$	$\frac{1}{2}$

Table 1 shows that there are three different types of defect in the anion sublattice: interstitial oxygens at sites labelled O' and O'' and vacancies in the normal oxygen sites O. These defects must associate together into complexes, but, because of the uncertainty in the estimated m_j 's, the exact proportion of the various defects is unknown. If we assume the proportion of two vacancies to one O' interstitial to two O'' interstitials, the complex contains at least twenty uranium and oxygen atoms with co-ordinations different from the atoms in UO_2 .

Table 2. Crystal structure of U_4O_9 at $20^\circ C$

Atom	Contribution to m in formula unit UO_m	Co-ordinates in pseudo-cell		
		x	y	z
uranium	—	0	0	0
oxygen O	1.77(0.02)	$\frac{1}{4}$	$\frac{1}{4}$	$\frac{1}{4}$
oxygen O'	0.29(0.05)	$\frac{1}{2}$	0.37(0.01)	0.37(0.01)
oxygen O''	0.19(0.04)	0.39(0.01)	0.39(0.01)	0.39(0.01)

Turning to Table 2 for U_4O_9 we see that the oxygen sites are the same type as in $UO_{2.12}$. The results in this Table were derived by analyzing the neutron intensities of the fundamental reflexions only, and so relate to a pseudo-cell for U_4O_9 of the same size as the UO_{2+x} cell. (A very large number of weak superlattice reflexions occur, but these were not included in the analysis). Again, we conclude that the extra oxygen atoms segregate into complexes, separated by UO_2 -type regions. The complexes are now ordered to give a superstructure, which is based on the cubic

space-group $I\bar{4}3d$ and has a repeat distance four times that in $UO_2^{(f)}$.

4. CONCLUSIONS

Defect complexes, containing oxygen atoms in several different types of crystallographic site, occur in non-stoichiometric UO_{2+x} . The complexes are randomly distributed and separated by regions with the undisturbed UO_2 structure, but they already contain the atomic arrangement which, regularly repeated, constitutes the stable structure of the next higher ordered phase, U_4O_{14} . Further neutron work at other compositions and temperatures in the solid-solution region is desirable to establish the general validity of this structural model for UO_{2+x} .

REFERENCES

1. Sidhu, S. S., Satya Murthy, N. S., Campos, F. P. and Zauberis, D. D.: in "Non-Stoichiometric Compounds", American Chemical Society (1963).
2. Roth, W. L.: Acta Cryst. 13, 140 (1960).
3. Willis, B. T. M.: Proc. Roy. Soc., London, A 274, 134 (1963).
4. Willis, B. T. M.: Acta Cryst. 18, 75 (1965).
5. Willis, B. T. M.: Jour. de Physique 25, 431 (1964).

TECHNICAL REPORTS SERIES No. 39

THERMODYNAMIC
AND TRANSPORT PROPERTIES
OF URANIUM DIOXIDE
AND
RELATED PHASES

REPORT OF THE PANEL ON
THERMODYNAMIC AND TRANSPORT PROPERTIES
OF URANIUM DIOXIDE AND RELATED PHASES
HELD IN VIENNA
16 - 20 March 1964

The candidate was a member of the Panel whose findings were presented in this book. He contributed to all the chapters but was solely responsible for Chapter II, given here.

INTERNATIONAL ATOMIC ENERGY AGENCY
VIENNA, 1965

FOREWORD

Because of the growing importance of thermodynamics to nuclear technology, the International Atomic Energy Agency has initiated a project to assist in assessing and disseminating data on important nuclear materials. As a beginning, it organized a Symposium on the Thermodynamics of Nuclear Materials which was held in Vienna in May 1962. This was followed by a Panel on the Thermodynamic Properties of the Uranium-Carbon and Plutonium-Carbon Systems, held in Vienna in October 1962. The present Report is the result of a further Panel in this series, convened from 16 - 20 March 1964 to assess the thermodynamic and transport properties of the uranium dioxide phase and related uranium oxide phases. This Panel made a critical evaluation of the available data, bearing in mind the practical aspects of the use of uranium dioxide as a nuclear fuel. The findings of the Panel are presented by the Agency in this issue of the Technical Reports Series in the belief that they will prove to be of value for nuclear technology.

The Report was compiled and edited by Dr. Charles Holley of the Division of Research and Laboratories.

CONTENTS

I. INTRODUCTION	1
II. STRUCTURAL WORK	3
1. Stable phases in the U-O system	3
2. UO ₂ (room temperature)	3
2.1. Lattice parameter. Density	3
2.2. Atomic positions. Temperature factors	3
3. UO ₂ (high temperature)	5
3.1. Variation of lattice parameter with temperature	5
3.2. Temperature factors. Characteristic temperatures. Breakdown of harmonic approximation	6
4. UO _{2+x} region	7
4.1. Variation of lattice parameter and density with composition	7
4.2. Crystal structure	9
4.2.1. Atomic positions in statistical cell. Occupation numbers. Temperature factors	9
4.2.2. Interpretation of results for statistical cell	12
5. U ₄ O ₉	
5.1. Variation of lattice parameter with composition and temperature	15
5.2. Structure	15
5.2.1. X-ray studies	15
5.2.2. Neutron studies	17
6. Tetragonal phases	19
7. Conclusions	20
III. THERMODYNAMICS	23
1. Heat capacity measurements	23
1.1. Low temperature heat capacity data	23
1.2. High temperature heat capacity data	24
2. Lattice Dynamics of UO ₂	25
3. Free energy, enthalpy, and entropy measurements	29
3.1. Chemical thermodynamics of the UO _{2,00} - 2.25 region ...	29
3.2. The phase diagram, UO ₂ to U ₄ O ₉	38
3.3. Hypostoichiometric UO ₂	39
4. Vaporization processes	40

5.	Theoretical treatment of UO_{2+x} phase	42
5.1.	Statistical thermodynamics of interstitials and vacancies	42
5.2.	Application of defect theory to UO_{2+x}	44
IV.	SURFACE AND OXIDATION PROPERTIES	51
1.	Adsorption properties	51
2.	Oxidation processes	52
2.1.	Low temperatures	52
2.2.	High temperatures	53
V.	PHYSICAL PROPERTIES	55
1.	Thermal conductivity	55
1.1.	Low temperature thermal conductivity	55
1.2.	High temperature thermal conductivity	55
1.2.1.	Lattice conductivity	57
1.2.2.	Radiant transfer	58
1.2.3.	Electronic transfer	59
2.	Electrical properties	60
2.1.	Normal electrical properties	60
2.2.	Effect of irradiation on electrical properties	67
3.	Optical measurements	69
3.1.	Intrinsic absorption edge	69
3.2.	Defect absorption	70
3.3.	Infra-red absorption	72
4.	Magnetic measurements	73
5.	Diffusion processes in UO_2	75
5.1.	Oxygen diffusion	75
5.2.	Uranium self-diffusion	76
5.3.	Argon diffusion in calcium fluoride as a model process for fission gas transport in uranium dioxide ..	76
5.4.	Fission gas release	78
6.	Correlative theory of physical properties	81
6.1.	Transport of energy	81
6.2.	Transport of matter	83
VI.	PRACTICAL IMPLICATIONS OF THERMODYNAMIC AND TRANSPORT PROPERTIES	85
1.	Interaction of fuel and can	85
1.1.	Thermal cracking	85
1.2.	Dimensional changes in UO_2 under irradiation	86
2.	Thermal conductivity	88

(v)

3. Phase equilibria	88
4. Material transport processes	89
VII. CONCLUSIONS	93
Appendix: Mathematical treatment of defect absorption	95
References	99
List of participants	103
Reports submitted to the Panel	105

I. INTRODUCTION

The high melting point of uranium dioxide and its stability under irradiation have led to its use as a fuel in a variety of types of nuclear reactors. A wide range of chemical and physical studies has been stimulated by this circumstance and by the complex nature of the uranium dioxide phase itself. The boundaries of this phase widen as the temperature is increased; at 2000°K a single, homogeneous phase exists from $U_{2.27}$ to a hypostoichiometric (UO_{2-x}) composition, depending on the oxygen potential of the surroundings. Since there is often an incentive to operate a reactor at the maximum practicable heat rating and, therefore, maximum thermal gradient in the fuel, the determination of the physical properties of the UO_{2+x} phase becomes a matter of great technological importance. In addition a complex sequence of U-O phases may be formed during the preparation of powder feed material or during the sintering process; these affect the microstructure and properties of the final product and have also received much attention.

Uranium dioxide, therefore, provides an important example of a compound that exists as a single non-stoichiometric phase at high temperatures and becomes unstable as the temperature is reduced, disproportionating into phases of nearly ideal stoichiometry involving more or less complex ordered structures. Ideally, the thermodynamic stability and physical properties of UO_{2+x} should be related to the same atomic and electronic model, and its study should provide an opportunity for the correlation of a number of different properties.

The International Atomic Energy Agency (IAEA) therefore called a panel meeting to discuss the thermodynamic and transport properties of the non-stoichiometric uranium dioxide phase, and this Report presents a summary of the data placed before the Panel and of the conclusions reached. A considerable amount of data on the main features of the phase diagram and on the composition limits of the various phases exists and X-ray and neutron diffraction evidence indicate some possible structural models. Chemical thermodynamic values are known with some precision for most of the region concerned. Specific discussions were held on (i) the interrelation of vibrational constants deduced from structural work and heat capacity data; (ii) the correlation of thermal conductivity with electrical conductivity and optical data; and (iii) the calculation of entropy values by the statistical treatment of simple models that are consistent with the structural, optical, and electrical properties. The outline of a generalized theory that should allow better correlation of transport and thermodynamic properties in the future was presented. The importance of making all measurements of physical properties on samples of accurately known composition, which are structurally well-characterized, was emphasized.

II. STRUCTURAL WORK

1. STABLE PHASES IN THE U-O SYSTEM

There are as many as 16 well-characterized uranium oxide phases, and the existence of a dozen more has been claimed. A survey of work on the uranium-oxygen phase diagram up to 1961 has been made by ROBERTS [1]. Figure 1 is a reproduction of his phase diagram. The work described in

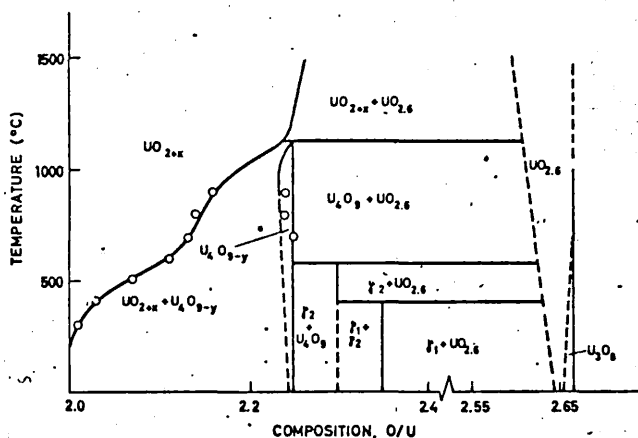


Fig. 1

Portion of U-O phase diagram. Circles denote X-Ray results.
(Reproduced by courtesy of L.E.J. Roberts [1])

this chapter is restricted to UO_2 , UO_{2+x} , U_4O_9 and the tetragonal phases with compositions in the range $UO_{2.3}$ to $UO_{2.4}$. The structures of these phases are based on the fluorite arrangement, with the additional oxygen atoms distributed either at random on the fluorite lattice or in an ordered fashion, forming a cubic or tetragonal superlattice.

2. UO_2 (ROOM TEMPERATURE)

2.1. Lattice parameter density

The stoichiometric oxide UO_2 has a cubic structure. The generally accepted value for the lattice parameter is $a_0 = 5.470 \text{ \AA}$ (see Table I), which corresponds to a theoretical density, assuming four UO_2 units in the unit cell of 10.952 g/cm^3 . This theoretical value is close to the density of 10.950 ± 0.005 recently measured on a single crystal of vapour-grown UO_2 [2].

2.2. Atomic positions. Temperature factors

The crystal structure of UO_2 was first determined by GOLDSCHMIDT and THOMASSEN [8]. The atomic positions are those for the fluorite arrangement (Fig. 2). Interatomic distances are [9],

$$\begin{aligned} \text{U} - 12\text{U} &= 3.868\text{\AA} \\ \text{O} - 6\text{O} &= 2.735\text{\AA} \\ \text{U} - 8\text{O} &= 2.369\text{\AA} \end{aligned}$$

The radius ratio (cation/anion) is 0.73; according to PAULING [10] 0.73 is the critical ratio, below which the fluorite structure is less stable than the tetragonal rutile structure.

TABLE I

LATTICE PARAMETER OF UO_2

Parameter (\AA)	Reference
5.4690 ± 0.0001	[3]
5.4704 ± 0.0008	[4]
5.4703 ± 0.0002	[5]
5.4698 ± 0.0008	[6]
5.4720 ± 0.0005	[7]
5.4698 ± 0.0002	[75]

This structure has been confirmed by neutron diffraction [11]. The coherent nuclear scattering cross-section of oxygen is about one half of that for uranium; consequently the oxygen atoms can contribute appreciably to the observed neutron intensities and can be located directly with neutrons. Moreover, the absorption cross-section of UO_2 for slow neutrons is at least four orders of magnitude less than for X-rays, so that more accurate measurements of the integrated intensities are possible by neutron diffraction.

The neutron measurements give the following values for the isotropic atomic temperature factors, B_U and B_O [11]:

$$B_U = 0.25 \pm 0.04 \text{\AA}^2, \quad B_O = 0.43 \pm 0.05 \text{\AA}^2.$$

The B's are the quantities appearing in the Debye-Waller factor $\exp(-2W) = \exp\{-2B(\sin\theta/\lambda)^2\}$ where θ is the Bragg angle and λ the wave length. The "R factor", giving the discrepancy between calculated and observed structure factors, is less than 2%. From Willis's study [11] it is seen that, to a very close approximation, the structure of UO_2 at room temperature is described by the fluorite arrangement with isotropic thermal motion of the uranium and oxygen atoms.

The temperature factor B is related to the mean-square displacement $\overline{U_i^2}$ of the atom in any direction from its mean position by the equation

$$B = 8\pi^2 \overline{U_i^2}.$$

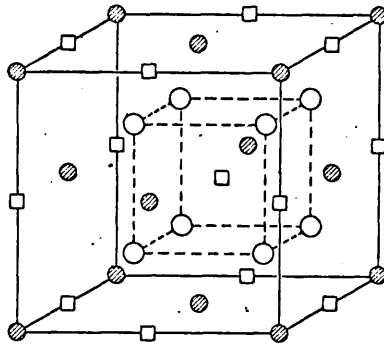


Fig. 2

Unit cell of uranium dioxide. Open circles are oxygen, shaded circles are uranium, and open squares are holes in the fluorite structure. Broken lines connect oxygen atoms which form a cubic array around the central hole.

(The total mean-square displacement is $3 \overline{U}_i^2$). Inserting the values quoted above gives rms displacements

$$\begin{aligned} \sqrt{\overline{U}_i^2} &= 0.056 \text{ \AA} \text{ for uranium} \\ &= 0.074 \text{ \AA} \text{ for oxygen.} \end{aligned}$$

3. UO₂ (HIGH TEMPERATURE)

3.1. Variation of lattice parameter with temperature

BAKER and BALDOCK [12] have observed a smooth variation of lattice parameter with temperature up to 2300°C, the highest temperature of measurement. Table II gives the linear expansion coefficient deduced by several

TABLE II

LINEAR EXPANSION COEFFICIENT (X-RAYS) OF UO₂

Temperature range (°C)	Expansion coefficient	Reference
20 - 2000	$9.4 \times 10^{-6} / ^\circ\text{C}$	[12]
20 - 950	$10.8 \times 10^{-6} / ^\circ\text{C}$	[4]
20 - 800	$9.9 \times 10^{-6} / ^\circ\text{C}$	[7]
20 - 1000	$10.5 \times 10^{-6} / ^\circ\text{C}$	[13]

authors from measurements of the lattice parameter in the temperature range indicated. The X-ray expansion coefficient is in reasonable agreement with the expansion coefficient obtained by dilatometry [9].

3.2. Temperature factors. Characteristic temperatures. Breakdown of harmonic approximation

It is possible to relate the temperature factors B at different temperatures with the characteristic temperatures of vibration of the solid. The Debye model can be used for representing the vibrations of the uranium atoms and the Einstein model for the lighter oxygen atoms. The results, discussed in Section III.2. (Lattice dynamics) are

$$\theta_{\text{Debye}} = 182^{\circ}\text{K}$$

$$\theta_{\text{Einstein}} = 542^{\circ}\text{K}.$$

As the temperature of UO_2 increases, the intensities of the neutron reflections depart progressively from those calculated for the fluorite model assuming isotropic thermal motion of the individual atoms. The effect is shown in the differences in intensities of reflections occurring at the same Bragg angle [14]. These differences can be accounted for in a phenomenological manner by displacing the oxygen atoms along the four $\langle 111 \rangle$ directions towards the adjacent holes in the structure (Fig. 3).

This displacement can be interpreted in one of two ways: either the oxygen atoms are displaced at random along the $\langle 111 \rangle$ directions to give a disordered structure, or the oxygen atoms undergo anisotropic vibrations across the ideal fluorite position (Fig. 4). The general occurrence of the effect in UO_2 and ThO_2 [14] and in CaF_2 [15], and its moderate dependence on temperature, favour the second interpretation. MARADUDIN and FLINN [16] have shown that the anisotropic vibration of atoms in positions with cubic point symmetry arises from anharmonic contributions to the Debye-Waller factor; it is clear that the harmonic approximation cannot be used to interpret the temperature factors of UO_2 at high temperature.

The neutron diffraction results for UO_2 can be summarized as follows:

(i) The uranium atoms occupy fluorite-type positions and execute isotropic thermal motion with a mean-square amplitude increasing with temperature. At low temperatures zero-point motion leads to a departure from linearity, but above 400°C $\overline{U^2}$ is proportional to the absolute temperature T and is given by

$$\overline{U^2} (\text{uranium}) = 1.33 \cdot 10^{-5} T (\text{\AA}^2).$$

At the highest temperature of observation, 1100°C , there is no evidence of anisotropic vibration.

(ii) The oxygen atoms occupy fluorite-type positions but vibrate isotropically at low temperatures only. The shape of the "vibrating surface" can be described roughly in terms of four spheres (Fig. 3). At room temperature these spheres are superimposed, but at 100°C they begin to separate along the four $\langle 111 \rangle$ directions joining the oxygen atom with its

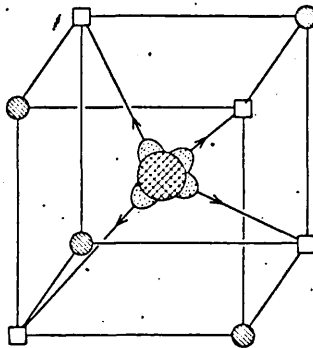


Fig. 3

Vibrational surface of oxygen atom.

Above 100°C the oxygen atom is displaced along the four [111] directions as shown. The large cross-hatched circle is the oxygen atom with the displacement along [111] shown stippled. The small shaded circles are uraniums and the open squares are holes.

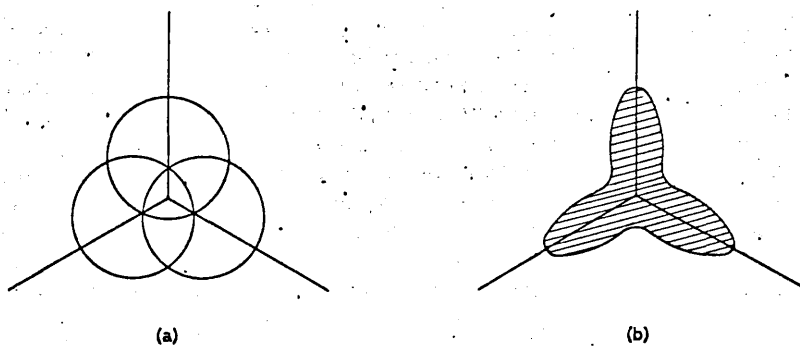


Fig. 4

Two models for vibration of oxygen atoms in UO_2 . Looking down [111]:

- (a) Oxygen atoms located statistically at displaced positions with each atom vibrating isotropically; and
 (b) Anharmonic vibration causing asymmetrical displacement of each atom across the normal position.

surrounding tetrahedron of holes. At 1000°C each sphere is displaced by as much as 0.15 Å from the ideal position [14].

4. UO_{2+x} REGION

4.1. Variation of lattice parameter and density with composition

GRØNVOLD [4] using high temperature X-ray techniques has shown that oxygen dissolves in a homogeneous UO_{2+x} phase above 400°C, the UO_{2+x} domain extending to $UO_{2.17}$ at 950°C (Fig. 1).

This section deals with the structure of this UO_{2+x} homogeneous phase.

X-ray measurements on quenched samples show that the unit cell contracts with increasing oxygen concentration [3, 6, 17, 18, 19, 20]. There is

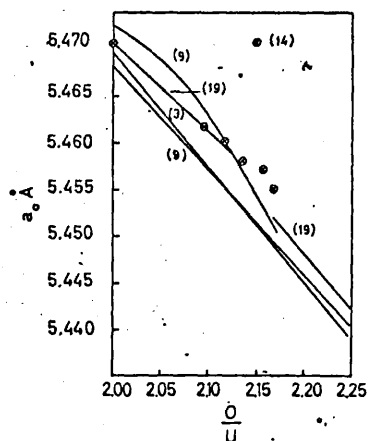


Fig. 5

Variation of lattice parameter with U/O ratio.

relatively good agreement between different X-ray studies of compositions up to $\text{UO}_{2.12}$, but not for higher O/U ratios (Fig. 5). LYND *et al.* [20] failed to observe the UO_{2+x} structure between $\text{UO}_{2.13}$ and $\text{UO}_{2.17}$ when quenching from 1100°C , whereas BELBEOCH *et al.* [6] succeeded in quenching the UO_{2+x} phase from a lower temperature. This discrepancy may be due to a more complex phase diagram than is generally recognized; Belbeoch suggested that for compositions higher than $\text{UO}_{2.13}$ the system may become diphasic again above 1000°C [6], or that there is a shift of the phase boundary between monophasic and diphasic regions towards lower O/U ratios (cf. Fig. 1) [6,20].

The quenching experiments may be vitiated by the extremely rapid self-diffusion of oxygen, and it is necessary to re-investigate the $\text{UO}_{2.10}$ - $\text{UO}_{2.25}$ region above 950°C with high-temperature X-ray techniques. Even then the X-ray method, using silica capillaries, is complicated by the reactivity of SiO_2 with uranium oxide at high temperature.

It is generally agreed that excess oxygen enters interstitial positions in the UO_2 lattice, causing a contraction of the lattice spacing, and that the U_4O_9 structure is an ordered structure. In principle, this model could be verified exactly by comparing the increase in density actually measured with the increase calculated from the interstitial model and the cell dimensions. In practice, the exact comparison is difficult for two reasons, namely, (a) the UO_{2+x} structure is not easily quenched-in, so that samples at room temperature tend to be mixtures of UO_2 and a poorly-crystalline U_4O_9 , and (b) many UO_2 preparations have densities much lower than the calculated value of 10.96 g/cm^3 , due to microstructure faults, and these tend to alter during oxidation. Furthermore, the densities of powders which have been exposed to air are lower than theoretical due to the chemisorption of oxygen on the surface.

Some of the most complete sets of density measurements reported to date are the following:

(i) The densities of samples of composition $\text{UO}_{2.026}$ to $\text{UO}_{2.234}$ which had been prepared by oxidation at temperatures below 165°C were determined

at the Atomic Energy Research Establishment (AERE), Harwell. The density increased regularly with composition from 10.89 to 11.21 g/cm³; the density of an annealed specimen of U₄O₉ (UO_{2.240}) was 11.18 g/cm³, giving a density increase of 0.29 g/cm³ from UO_{2.026} to UO_{2.240}, as compared with a calculated value of 0.28 g/cm³ [181].

(ii) GRØNVOLD [4] measured a regular density increase on samples that had been heated to high temperatures and cooled, but these were certainly mixtures of UO₂ and U₄O₉. The measured density difference between UO₂ and U₄O₉ was 0.376 g/cm³.

(iii) The densities of samples of UO_{2+x} which had been quenched from 1000°C were measured by LYNDSEY *et al.* [20]. According to their X-ray measurements, the quench was successful. The density increased with oxidation, but quantitative comparison with theory was impossible because of the low density of the starting material, indicative of closed porosity.

(iv) Density measurements on oxidized samples of (U_yTh_{1-y})O₂ solid solutions, which are stable at room temperature, always indicated an increase on oxidation, but quantitative comparison is again vitiated by microstructure faults [72].

The evidence favours a model in which an O₂ molecule dissolves in UO₂ to give a net gain of exactly two interstitial O atoms, but the quantitative evidence is not very good except in the case of U₄O₉ where $d = 11.2$ g/cm³ [2, 4, 20, 23].

4.2. Crystal structure

When UO₂ is oxidized to UO_{2+x} no extra lines appear on the X-ray photographs. Examination of single crystals by neutron diffraction confirms that no additional reflections appear, thus the space group of UO_{2+x} is the same (Fm3m) as for UO₂. The term "space group" now refers to the symmetry properties of the "statistical cell" obtained by superimposing all the original fluorite-type cells. Provided the extra atoms are distributed randomly, the space groups of the UO₂ unit cell and the UO_{2+x} statistical cell must be equivalent. Short range ordering between small groups of interstitial oxygens can occur, but any long range ordering, giving a different space group, is precluded.

4.2.1. Atomic positions in statistical cell. Occupation numbers.

Temperature factors

Willis has studied single crystals of compositions UO_{2.12} and UO_{2.13} at 800°C by neutron diffraction [21]. Two-dimensional F_{hkk} data were collected on UO_{2.13} and three dimensional F_{hkl} data on UO_{2.12}. The analysis of both sets of data gave similar results, but because the UO_{2.12} data were more complete only these will be discussed below.

The general expression for the structure factor of the hkl neutron reflection can be written

$$F_{hkl} = \sum_{r=1}^{r=n} m_r b_r \exp(2\pi i) (hx_r + ky_r + lz_r) \exp(-B_r \sin^2 \theta / \lambda^2) \quad (1)$$

where

- n is the number of atoms in the statistical cell,
 m_r is the occupation number of the r^{th} atom,
 b_r is the coherent scattering amplitude of the r^{th} atom,
 x_r, y_r, z_r are the positional co-ordinates of the r^{th} atom,
 B_r is the isotopic temperature factor of the r^{th} atom,
 θ is the Bragg angle, and
 λ is the wave-length.

The unknowns in this expression are the number of atoms n in the (statistical) cell, the positional co-ordinates xyz of each atom, their temperature factor B , and the relative proportions m of each atom in the cell. All these parameters can be derived by a least-squares treatment in which the calculated and observed F 's (38 independent hkl 's in all) are matched together.

The least-squares results are summarized in Table III. These results will be discussed in turn for each kind of atom.

TABLE III

UO_{2.12}: LEAST-SQUARES RESULTS FOR STATISTICAL CELL

Atom	Co-ordinates in statistical cell			Contribution m to formula UO _{m}	Temperature factor (\AA^2)
	x	y	z		
Uranium	0	0	0	-	1.18 ± 0.02
Oxygen O	u	u	u	$m = 1.87 \pm 0.03$	1.45 ± 0.04
Oxygen O'	0.5	v	v	0.08 ± 0.04	1.8 ± 1.4
Oxygen O''	w	w	w	0.16 ± 0.06	2.0 ± 1.6
Oxygen O'''	0.5	0.5	0.5	-0.02 ± 0.02	2.0 (fixed)

$u = 0.267 \pm 0.001$, $v = 0.38 \pm 0.01$, $w = 0.41 \pm 0.01$, and the "discrepancy factor" $R = 3.5\%$.

(a) Uranium. The uranium atoms remain fixed at the equivalent positions: 000, $\frac{1}{2}\frac{1}{2}0$, $\frac{1}{2}0\frac{1}{2}$, $0\frac{1}{2}\frac{1}{2}$. All attempts at refinement with the uraniums displaced from these positions were unsuccessful. The occupation number for uranium was fixed at 1.00, in accordance with the lattice parameter and density results; if this assumption is wrong the figures in the third column of Table III must be adjusted appropriately. The temperature factor $B = 1.18 \text{\AA}^2$ is slightly higher than that (0.90\AA^2) for UO₂ at the same temperature. The difference can be ascribed to a random rms displacement of the uranium atoms from their normal positions of about $1/10 \text{\AA}$.

(b) Normal oxygen. The oxygen atoms occupying fluorite-type sites are labelled O in Table III. As in the case of UO_2 at 800°C , there is an apparent displacement from $\frac{1}{4}\frac{1}{4}\frac{1}{4}\dots$ to $\frac{1}{4}+\delta \frac{1}{4}+\delta \frac{1}{4}+\delta \dots$ where $\delta = 0.017$, and this displacement can be ascribed to anharmonic vibration, which causes the oxygens to vibrate asymmetrically across the normal position. The magnitude of this effect is slightly greater than in UO_2 .

The most important change in O concerns its occupation number. Whereas all the $\frac{1}{4}\frac{1}{4}\frac{1}{4}\dots$ positions are filled in $\text{UO}_{2.00}$ an appreciable proportion are empty in $\text{UO}_{2.12}$. Unfortunately, the standard deviations of the occupation numbers in Table III are high, but the proportion of empty sites probably lies between five and eight per cent.

(c) Interstitial oxygen. The most natural place to accommodate the extra oxygens is at the holes $\frac{1}{2}\frac{1}{2}\frac{1}{2}\dots$. Oxygen at these sites are labelled O''' in Table III. However, the occupation number for O''' refines at a negative value close to zero, and this, together with the difficulty of refining the temperature factor (kept fixed in Table III), discounts the possibility of these positions being occupied.

In actual fact the extra oxygens occupy two kinds of site, labelled O' and O'' in Table III. These are shown in the statistical cell in Fig. 6; the O' sites are approximately half way from the hole to the centre of the line joining two normal oxygen atoms, and the O'' sites half way from the hole to the nearest normal oxygen. The displacement of the interstitial atoms from the nearest hole is roughly 1 \AA .

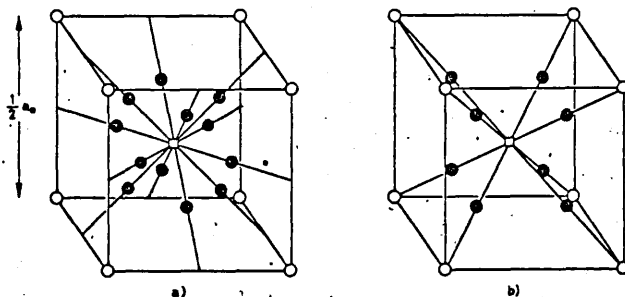


Fig. 6

Statistical cell of UO_{2+x} showing interstitial oxygen atoms in:

- (a) O' sites;
- (b) O'' sites.

Open circles are oxygens in fluorite-type sites, solid circles are interstitial oxygens, and open squares are holes at $\frac{1}{2}\frac{1}{2}\frac{1}{2}\dots$

In UO_{2+x} , therefore, there are three types of defect in the oxygen sublattice associated with the departure from stoichiometry, namely, interstitial oxygens at O' sites and O'' sites, and normal oxygen vacancies. These three defects cannot be distributed at random, as this inevitably brings several oxygen atoms too close together, and it is more reasonable to suppose that the defects associate together into complexes or zones.

4.2.2. Interpretation of results for statistical cell

It is tempting to interpret the results in Table III in terms of the local atomic configuration in UO_{2+x} . The number of structures compatible with this Table is unlimited, but can be reduced to a manageable number if we assume (a) the formation of defect zones rather than isolated defects, and (b) that each zone contains relatively few defects.

The ratios of the concentrations

normal O vacancies : O' atoms : O'' atoms

are given in Table III as 13 : 8 : 16. The model to be discussed first is one in which these ratios are idealized as 2 : 1 : 2. Ideal ratios suggest that an interstitial atom enters the lattice at an O' site, and thereby causes two normal oxygens to be ejected to two O'' sites. This situation seems reasonable, as an O' atom can be comfortably placed inside a $\text{UO}_{2.00}$ lattice, provided the two nearest oxygens at 1.7 Å are removed (Fig. 7).

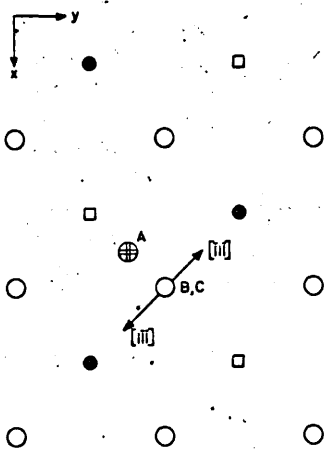


Fig. 7

O' atom at A ejects the two nearest oxygens at B, C.

B, C in turn are displaced along [111] towards the adjacent O'' sites.

● - uranium at $Z = \frac{1}{2} a_0$; □ - hole at $Z = \frac{1}{4} a_0$; ○ - normal oxygen at $Z = 0, \frac{1}{2} a_0$; ⊕ - O' oxygen at $Z = \frac{1}{4} a_0$.

A possible 2 : 1 : 2 structure based on this concept is shown in Fig. 8. The dotted lines in this diagram outline four cubes of side $\frac{1}{2}a_0$, and these are labelled from the top left-hand corner as I, II, III and IV. In the $\text{UO}_{2.00}$ arrangement, oxygen atoms are located at the corners of each of the $\frac{1}{2}a_0$ cubes. In UO_{2+x} an extra oxygen atom enters the lattice at the position marked E, where E is approximately 1 Å along the [110] direction from the centre of cube II. The two oxygens at A and B are displaced along the direction [111] to positions C, D on the body diagonals of cubes I, IV respectively.

Using the parameters quoted in Table III the positions of the atoms in Fig. 8 are as follows. The co-ordinates are given in units of a_0 , and the uranium atom G is chosen as the origin of co-ordinates.

U at	0.50	0	0.50
	0	-0.50	0.50
	0.50	-0.50	1.00
	0	0	1.00
	0.50	-0.50	0
	0	0	0
O at	-0.25	-0.25	0.25
	0.25	0.25	0.25
	0.25	0.25	0.75
 etc.		
O' at	0.12	-0.12	0.50
O'' at	0.09	-0.41	0.91
	0.41	-0.09	0.09

The bond distances are:

	(Å)
O' - 2U	= 2.18
O' - 2O''	= 2.75
O' - 4O	= 2.54
O'' - 3U	= 2.35
O'' - O'	= 2.75
O'' - 3O	= 2.24
O'' - 3O	= 2.78

A difficulty with the 2:1:2 model is that, although the relative concentrations of defects are in approximate agreement with observation, the absolute concentrations are predicted incorrectly. For $UO_{2.12}$ the predicted formula is $UO_{1.76} O'_{0.12} O''_{0.24}$, whereas the observed formula (Table III) is $UO_{1.87} O'_{0.08} O''_{0.16}$. The standard deviations of the occupation numbers are high (these standard deviations are calculated from the inverse least-square matrix and reflect the disagreement between observed and calculated intensities), but this still fails to account for the discrepancy between 1.76 and 1.87 for the number of normal oxygens in the formula unit. The difficulty may be resolved as indicated in Fig. 8. An extra O' atom can be inserted in cube III at the position F, where E and F are equivalent

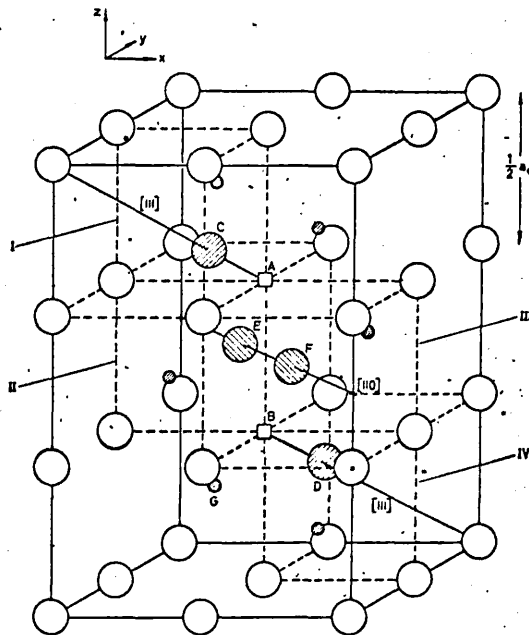


Fig. 8

Model for UO_{2+x} structure. The normal oxygens, at A and B in $UO_{2.00}$, are replaced by interstitial atoms O'' at C, D and O' atoms at E (2 : 1 : 2 structure), or at E and F (2 : 2 : 2 structure).

- Uranium atoms.
- Normal oxygen atoms.
- ⊙ Interstitial oxygen atoms O' .
- ⊙ Interstitial oxygen atoms O'' .

sites related by 180° rotation about the line AB. This leads to an alternative model for UO_{2+x} , in which the numbers of O' and O'' atoms and normal oxygen vacancies in the central defect complex are 2, 2, 2. For this 2 : 2 : 2 structure the predicted formula, $UO_{1.88} O'_{0.12} O''_{0.12}$ is in good agreement with the observed formula, $UO_{1.87 \pm 0.03} O'_{0.08 \pm 0.04} O''_{0.16 \pm 0.06}$. The bond lengths in the 2 : 2 : 2 structure are:

	(Å)
$O' - 2U$	= 2.18
$O' - O'$	= 2.01
$O' - 2O''$	= 2.75
$O' - 4O$	= 2.54
$O'' - 3U$	= 2.35
$O'' - 2O'$	= 2.75
$O'' - 3O$	= 2.24
$O'' - 3O$	= 2.78

The O' - O' distance (E-F Fig. 8) is short (2.01 Å), but a change of only one standard deviation in the v parameter (Table III) of O' changes this distance to 2.16 Å.

5. U_4O_9

5.1. Variation of lattice parameter with composition and temperature

The homogeneity range of U_4O_9 is not well known. PERIC [3] and GRØNVOLD [4] considered that the composition is close to $UO_{2.25}$ from 20 to 600°C and that there is a small spread on the oxygen deficient side for higher temperatures. On the other hand, SCHANER [18] found a wide range of hypostoichiometry; $UO_{2.22}$ at 20°C and $UO_{2.20}$ at 900°C.

In the vicinity of $UO_{2.25}$ two types of diffraction pattern, with or without superlattice lines, have been observed [6]. It appears that there are two structures; namely, " U_4O_{9+y} ", with superlattice lines and extra oxygens ordered on a $4a_0$ cubic cell, and " $UO_{2.25-y}$ ", with a unit cell of about 5.445 Å. A homogeneity range of 0.03 in O/U was observed in the U_4O_{9+y} structure by BELBEOCH et al. [6]. The $UO_{2.25-y}$ structure is disordered, or is ordered in a different way than in U_4O_9 , without significant displacements of the uranium atoms. It is difficult to deduce the composition from the a_0 value in the $UO_{2.25-y}$ region, because of the dependence of this parameter on both composition and quenching temperature.

The thermal expansion of U_4O_9 has been studied by GRØNVOLD [4] and by FERGUSON and STREET [22]. The agreement between these results is excellent. There is a small contraction of the lattice parameter between 20 and 100°C, and thereafter the lattice parameter expands uniformly with temperature.

5.2. Structure

5.2.1. X-ray studies

For U_4O_{9+y} superlattice lines have been observed on X-ray [4, 23], electron [24, 183] and neutron diffraction patterns [25, 11]. Since the superlattice lines are prominent at high angles on X-ray photographs, the uranium atoms must be displaced from the positions they normally occupy in the fluorite structure.

X-ray studies of single crystals, obtained by oxidizing UO_2 with U_3O_8 under the equilibrium pressure of the mixture $U_4O_9 + UO_{2.6}$ [23], showed that the unit cell is cubic with $a = 4a_0 = 21.77$ Å. The observed extinctions for the hkl reflections indicate the $I\bar{4}3d$ space group. A model has been proposed by BELBEOCH, PIEKARSKI and PERIO [23]. The 64 interstitial oxygen atoms are ordered within the large $4a_0$ cell which contains 832 atoms. The ideal positions are given in Table IV.

The extra oxygens in this ideal arrangement are distributed very heterogeneously (Fig. 9). There are twelve tetrahedra, each with four extra oxygens as nearest neighbours, and the remaining sixteen extra oxygens are equidistant from three of the twelve tetrahedra. The complete determination of the structure would require the knowledge of 49 positional para-

TABLE IV

IDEAL POSITIONS OF THE 832 ATOMS

Nature of the 832 atoms	48 (c) positions			16(c)	12 (a) and 12 (b) positions (special positions)			24 (d) positions			
	(x)	y	z)		x			x	0	1	
256 U atoms	0.1875	0.0625	0.0625	0.1875							
	0.4375	0.0625	0.0625								
	0.3125	0.1875	0.0625								
	0.4375	0.1875	0.1875								
	0.3125	0.0625	0.1875								
512 O atoms	0.125	0.25	0	0.125				0	0	1	
	0.125	0.125	0					0.125	0	1	
	0.125	0	0			1/2	0		0.25	0	1
	0.125	0.125	0.25								
	0.125	0.25	0.25			1/2	0				
	0.375	0	0.125								
	0.5	0.125	0.125								
0.357	0.125	0.125									
64 extra-oxygens	0.1875	-0.0625	0.0625	0.0625							

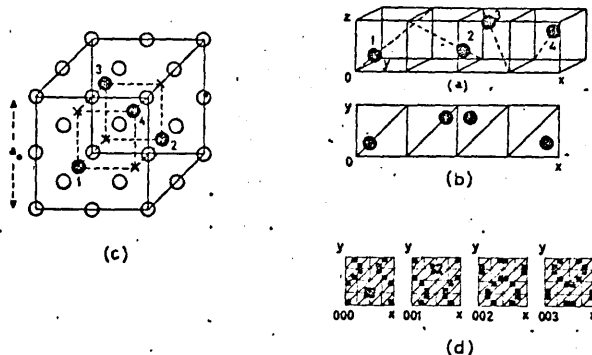


Fig. 9

- (a) UO_2 unit cell (the origin is at a normal oxygen atom).
 (b) The 4 interstitial sites are described with the $\bar{4}_x$ repetition-law.
 (c) Equivalent drawing to (b). Atoms on the same Z level lie on the same diagonal.
- Interstitial site
 - Normal oxygen atom
 - x Uranium atom
- (d) Distribution of the 64 extra oxygen atoms at the ideal positions 48 (e) and 16 (c).

meters which determine the displacements of 808 atoms from their ideal positions.

For $\text{UO}_{2.25-y}$ no superlattice lines have been detected. When the composition $\text{UO}_{2.25}$ is reached short range order may take place among the interstitial oxygen atoms [31]. These ordered zones would permit one to distinguish between the $\text{UO}_{2.25-y}$ phase and the UO_{2+x} phase.

From symmetry considerations based on $4a_0$ cells with successive occupancy of the four equivalent interstitial sites seven types of zones are possible [31]. They belong to the following space groups (one of them is $I\bar{4}3d$, described for U_4O_9):

Cubic	Tetragonal	Orthorhombic
$I\bar{4}3d$	$I\bar{4}$	Cmc
$I2_13$	$I\bar{4}2d$	C222
		C222 ₁

5.2.2. Neutron studies

Neutron diffraction intensity measurements have been made on two U_4O_9 crystals [26]. For both crystals only fundamental (i. e. non-superlattice) reflections were measured. The restriction to fundamental reflections means that the results apply to the "composite cell" obtained by superimposing the 64 UO_2 -type sub-cells in the 21.8\AA unit cell. Similar results were obtained by analysing both sets of data.

TABLE V
 U_4O_9 : LEAST-SQUARES RESULTS FOR COMPOSITE CELL

Atom	Co-ordinates in composite cell			Contribution m to formula UO_m	Temperature factor (\AA^2)
	x	y	z		
Uranium	0	0	0	-	0.56 ± 0.04
Oxygen O	0.25	0.25	0.25	1.77 ± 0.02	1.57 ± 0.08
Oxygen O'	0.5	v	v	0.29 ± 0.05	1.25 ± 0.70
Oxygen O''	w	w	w	0.19 ± 0.04	1.60 ± 0.90

$v = 0.372 \pm 0.005$, $w = 0.378 \pm 0.005$, $R = 3.7\%$.

The details of the analysis are described by ROUSE, VALENTINE and WILLIS [26] and the results are summarized below in Table V. The oxygen atoms in the composite cell occupy exactly the same kinds of position as the oxygens in the statistical cell of UO_{2+x} (Table III).

The following two points can be made concerning Table V:

(a) The 2:2:2 structure assumed for the composite cell gives a formula $UO_{1.75} O'_{0.25} O''_{0.25}$, in approximate agreement with $UO_{1.77} O'_{0.29} O''_{0.19}$ given by the third column. Thus the transition from UO_{2+x} to U_4O_9 probably involves long-range ordering of the oxygen zones or complexes, with the configuration within each zone remaining unchanged. It appears that zones of the U_4O_9 structures are already present in the disordered UO_{2+x} phase.

(b) The data were recorded at room temperature and there is no evidence of anharmonic contributions to the Debye-Waller factors. This is similar to the behaviour of UO_2 at room temperature, but the temperature factors of both uranium and oxygen are higher than in UO_2 . Each site in the composite cell is occupied by 64 atoms, each of which must be slightly displaced in different directions from the ideal position. Since the temperature factors are related to the mean-square displacement of the atoms from their average positions, it is not surprising that they are higher in U_4O_9 .

As a first approximation WILLIS [26] assumed that the uranium atoms are not displaced from the fluorite-type positions, although the existence of superlattice lines in X-ray photographs indicates that there must be small uranium displacements. It is likely that displacements of both uranium and oxygen atoms occur and that the magnitude of these displacements can only be found by the interpretation of neutron superlattice data.

Both X-ray and neutron studies agree that the unit cell is $4a_0$ and the space group is $I43d$.

6. TETRAGONAL PHASES

A number of tetragonal phases have been described in the range $\text{UO}_{2.3}$ to $\text{UO}_{2.4}$ [1].

The α - U_3O_7 phase occurs in the early stages of oxidation of UO_2 at temperatures below 135°C . There is disagreement whether c/a is less than or greater than unity; published values are 0.99 [3, 27, 28] and 1.01 [29]. It is possible that the intensities are reversed, indicating $c/a < 1$, by a small quantity of UO_2 superimposed on the tetragonal phase with $c/a > 1$. The O/U ratio of α - U_3O_7 is certainly less than 2.33 and probably less than 2.30.

At 180°C , for $\text{O}/\text{U} > 2.3$, there is a transition to the γ_1 (or β - U_3O_7) phase. The conversion is complete for $\text{O}/\text{U} = 2.33$. The γ_1 phase ($c/a = 1.033$, $c = 5.556 \text{ \AA}$) can be preserved indefinitely below 350°C , but above this temperature it transforms to $\gamma_2 + \text{UO}_{2.6}$:



The γ_2 phase probably exists over a range of compositions, with c/a varying from 1.017 at 350°C to 1.010 at 650°C . According to Eq. (2), γ_1 has a higher oxygen content than γ_2 .

The probable compositions are:

$\text{UO}_{2.33}$ for γ_1

$\text{UO}_{2.30}$ for γ_2 at 350°C .

$\text{UO}_{2.30}$ for γ_2 at 650°C .

Above 600°C reaction (3) occurs:



The reversibility of reactions (2) and (3) has not been confirmed, and the thermodynamic stability of the tetragonal phases has not yet been determined; it is not even known whether these phases are stable or metastable. There is good agreement concerning the γ_1 and γ_2 phases in recent studies [22, 27] on the basis of X-ray diffraction studies.

WESTRUM and GRØNVOLD [28] have reported the existence of an oxide $\text{UO}_{2.37}$ having a structure of lower than tetragonal symmetry, whereas BELBEOCH *et al.* [29] have interpreted the characteristic features of the diffraction lines as due to a strained tetragonal structure.

A brief summary of the various observations on the tetragonal oxides is given in Table VI, using the pseudo-fluorite cell as the basis for description.

The tetragonal phases are ordered structures based on the fluorite arrangement. ANDRESEN [25] has pointed out the similarity in the neutron diffraction patterns of U_4O_9 and α - U_3O_7 . The neutron diffraction pattern of γ_1 shows superlattice peaks [30] and the X-ray diffraction pattern of γ_2 shows numerous superlattice lines, but they are too close to be resolved into their components [31]. The true unit cells of the tetragonal phases are

TABLE VI
TETRAGONAL OXIDES

	Cell edge	c/a	Composition O/U	Stability range
(UO ₂)	5.470	1	2.00	-
α-U ₃ O ₇	5.46	0.99 or 1.01	2.26	<250°C
γ ₁	a = 5.371 - 5.384	1.030 - 1.033	2.33	<460°C
γ ₂	a = 5.394 - 5.408	1.010 - 1.017	≤2.30	<600°C

at least as large as that of U₄O₉. No structure determination has yet been published of any of the tetragonal phases.

7. CONCLUSIONS

In UO_{2+x} and the ordered phases based on the fluorite structure the excess oxygen occupies interstitial positions in the lattice.

In the UO_{2+x} domain the lattice contraction with increasing O/U ratio has been determined by different workers and the agreement is fairly reasonable.

At least up to 900°C there is general agreement on the positions of the phase boundaries. It is only at higher temperatures that the recent X-ray work [6] is at variance with the thermodynamic data.

There is agreement between X-rays and neutron results concerning the space group and the 4a₀ cubic cell of U₄O₉. A model of the U₄O₉ supercell has been proposed which gives the "ideal positions" of uranium and oxygen atoms.

Neutron diffraction work has been confined to the phases UO₂, UO_{2+x} and U₄O₉. Two main conclusions have emerged from these studies, namely:

(a) At room temperature the "vibration surface" of both uranium and oxygen atoms is spherical, but at higher temperatures this statement is true only for uranium. For oxygen the sphere becomes distorted at relatively low temperatures (100°C) to a more complex surface of the type shown in Figs. 3 and 4. This distortion arises from anharmonic contributions to the Debye-Waller factor.

(b) UO₂ is oxidized to UO_{2+x} by the formation of defect zones rather than isolated point defects. Each zone contains oxygen atoms at two different kinds of interstitial site, labelled O' and O''. The uranium sub-lattice is unaffected by the presence of these zones, but vacancies appear in the sub-lattice of normal (fluorite-type) oxygens. The most likely configuration of atoms in the zone is described by the 2:2:2 structure (Fig. 8) with two each of normal oxygen vacancies, interstitial O' and interstitial O'' atoms. This zone persists in the ordered U₄O₉ structure, and the transition to U₄O₉

involves simply an ordered linking together of these zones. Further speculation about the U_4O_9 structure must await the interpretation of neutron superlattice data.

Major problems, requiring further investigation by diffraction methods, are:

(i) Determination of the homogeneity range of U_4O_9 , particularly at low temperatures, and the investigation of $UO_{2.25-y}$ structures;

(ii) Examination of UO_{2+x} above 900°C to resolve the doubts raised by BELBEOCH *et al.* [6] about the validity of the phase diagram shown in Fig. 1.

(iii) Determination of the crystal structures of all the ordered phases with large unit cells.

REFERENCES

- [1] ROBERTS, L. E. J., *Quarterly Revs* **15** (1961).
- [2] HAWES, R., AERE, Harwell, private communication.
- [3] PERIO, P., Thesis, Paris (1955).
- [4] GRØNVOLD, F., *J. inorg. nucl. Chem.* **1** (1955) 357.
- [5] LYNDY, L., *J. inorg. nucl. Chem.* **24** (1962) 1007.
- [6] BELBEOCH, B., LAREDO, E. and PERIO, P., *J. nucl. Mat.* (in press).
- [7] VAUGHAN, D. A., BRIDGE, J. R. and SCHWARTZ, C. M., USAEC Rpt BMI-1241 (1957).
- [8] GOLDSCHMIDT, V. M. and THOMASSEN, L., *Videnskap. Skrift, I. Mat. - Nat. Klasse* (1923) I.
- [9] BELLE, J., *Uranium Dioxide: Properties and Nuclear Applications* USAEC (1961) 176, 190.
- [10] PAULING, L., *Nature of the Chemical Bond and the Structure of Molecules and Crystals*, Cornell Univ. Press (1960) 540; Ithaca, N. Y.
- [11] WILLIS, B. T. M., *Proc. roy. Soc.* **274** (1963) 122.
- [12] BAKER, T. W. and BALDOCK, P. J., AERE, Harwell, private communication.
- [13] KEMPTER, C. P. and ELLIOT, R. O., *J. chem. Phys.* **30** (1959) 1524.
- [14] WILLIS, B. T. M., *Proc. roy. Soc.* **274** (1963) 134.
- [15] LAMBE, K. A. D. and WILLIS, B. T. M., U.K.A.E.A. Rpt AERE - R 4401 (1963).
- [16] MARADUDIN, A. A. and FLINN, P. A., *Phys. Rev.* **129** (1963) 2529.
- [17] BURDESE, A., *Gazz. Chim. Ital.* **89** (1959) 718.
- [18] SCHANER, B. E., *J. nucl. Mater.* **2** (1960) 110.
- [19] SUDO, K. and KOGOSHI, A., *Sci. Rpts Res. Inst., Tohoku Univ.* **13A** (1961) 31.
- [20] LYNDY, L., YOUNG, W. A., MOHL, J. S. and LIBOWITZ, G. G., *Non-Stoichiometric compounds*, Amer. chem. Soc. (1963) 58.
- [21] WILLIS, B. T. M., U.K.A.E.A. Rpt AERE - R 4487; *Nature*, London **197** (1963) 755.
- [22] FERGUSON, J. F. and STREET, R. S., U.K.A.E.A. Rpt AERE - M 1192 (1963).
- [23] BELBEOCH, B., PIEKARSKI, C. and PERIO, P., *Acta Cryst.* **14** (1961) 837.
- [24] STEEB, S., *Naturwissenschaften* **47** (1960) 465.
- [25] ANDRESEN, A. J., *Symp. Reactor Materials*, Stockholm (1959).
- [26] ROUSE, K. D., VALENTINE, T. M. and WILLIS, B. T. M., U.K.A.E.A. Rpt. AERE - 4414 (1963).
- [27] HOEKSTRA, H. R., SANTORO, A. and SIEGEL, S., *J. inorg. nucl. Chem.* **18** (1961) 154.
- [28] WESTRUM, E. F., Jr. and GRØNVOLD, F., *Phys. and Chem. Solids* **23** (1962) 39.
- [29] BELBEOCH, B., PIEKARSKI, C. and PERIO, P., *J. nucl. Mater.* **3** (1961) 60.
- [30] MERIEL, P., private communication.
- [31] BELBEOCH, B. and PERIO, P., private communication.
- [32] JONES, W. M., GORDON, J. and LONG, E. A., *J. chem. Phys.* **20** (1952) 695.
- [33] DAWSON, J. K. and LISTER, M. W., *J. chem. Soc.* (1950) 2181.
- [34] HENRY, W. E., *Phys. Rev.* **109** (1958) 1976.
- [35] ARROTT, A. and GOLDMAN, J. E., *Phys. Rev.* **108** (1957) 948.
- [36] LEASK, J. F., ROBERTS, L. E. J., WALTER, A. J. and WOLF, W. P., *J. chem. Soc.* (1963) 4788.
- [37] HENSHAW, D. G. and BROCKHOUSE, B. N., *Bull. Amer. phys. Soc.* **2** (1952) 9.
- [38] WESTRUM, E. F., Jr. and GRØNVOLD, F., *J. Amer. chem. Soc.* **81** (1959) 1777.
- [39] OSBORNE, D. W., WESTRUM, E. F., Jr. and LOHR, H. R., *J. Amer. chem. Soc.* **79** (1957) 529.
- [40] WESTRUM, E. F., Jr. and GRØNVOLD, F., "Chemical thermodynamics of the actinide element chalcogenides", *Thermodynamics of Nuclear Materials*, IAEA, Vienna (1962) 3.
- [41] WESTRUM, E. F., Jr. and HUNTZICKER, J. J., private communication.
- [42] CONWAY, J. B., FINCEL, R. M., Jr. and HEIN, R. A., USAEC Rpt TM 63-6-6 (1963).
- [43] MOORE, G. E. and KELLEY, K. K., *J. Amer. chem. Soc.* **69** (1947) 2105.
- [44] RAND, M. H. and KUBASCHEWSKI, O., *The Thermochemical Properties of Uranium Compounds*, Oliver and Boyd, Edinburgh (1963).
- [45] WILLIS, B. T. M., Lambe, K. A. D. and VALENTINE, T. M., U.K.A.E.A. Rpt AERE - R 4001 (1962).
- [46] WEINSTOCK, R., *Phys. Rev.* **65** (1944) I.
- [47] SANDENAW, T. A., *J. nucl. Mater.* **10** (1963) 165.
- [48] ARONSON, S. and BELLE, J., *J. chem. Phys.* **29** (1958) 151.
- [49] BLACKBURN, P. E., *J. phys. Chem.* **62** (1958) 897.

- [50] ROBERTS, L.E.J. and WALTER, A., *J. inorg. nucl. Chem.* **22** (1961) 213.
- [51] HAGEMARK, K., Kjeller Rpt KR-67 (1964).
- [52] AUKRUST, E., FØRLAND, T. and HAGEMARK, K., "Equilibrium measurements and interpretation of non-stoichiometry in UO_{2+x} ", *Thermodynamics of Nuclear Materials*, IAEA, Vienna (1962) 713.
- [53] MARKIN, T.L. and BONES, R.J., U.K.A.E.A. Rpt AERE - R 4042 (1962).
- [54] KIUKKOLA, K., *Acta. chem. scand.* **16** (1962) 327.
- [55] GERDANIAN, P. and DODÉ, M., *C.R. Acad. Sci., Paris* **255** (1962) 665.
- [56] ANTHONY, A.M., KIYOURA, R. and SATA, T., *J. nucl. Mater.* **10** (1963) 8.
- [57] HUBER, E.J., HOLLEY, C.E. and MEIERKORD, E.H., *J. Amer. chem. Soc.*, **74** (1952) 3406; FARR, J.D., HUBER, E.J., HEAD, E.L. and HOLLEY, C.E., *J. phys. Chem.* **63** (1959) 1455.
- [58] GERDANIAN, P., MARUCCO, F. and DODÉ, M., *C.R. Acad. Sci., Paris* **256** (1963) 2591.
- [59] BURDESE, A. and ABBATISTA, F., *Ricerca Sci.* **28** (1958) 1634.
- [60] MARKIN, T.L., ROBERTS, L.E.J. and WALTER, A., "Thermodynamic data for uranium oxides between UO_2 and U_3O_8 ", *Thermodynamics of Nuclear Materials*, IAEA, Vienna (1962) 693.
- [61] ARONSON, S., RULLI, J.E. and SCHANER, B.E., *J. chem. Phys.* **35** (1961) 1382.
- [62] ROTHWELL, E.J., *J. nucl. Mater.* **6** (1962) 229.
- [63] AITKEN, E.A., BRASSFIELD, H.C. and MCGURTY, J.A., *ANS Trans.* **6** (1963) 153.
- [64] ANDERSON, J.S., SAWYER, J.O., WARNER, H.W., WILLIS, E.M. and BANNISTER, M.J., *Nature*, London **185** (1960) 915.
- [65] DUNCAN, R.N. and FERRARI, H.M., *ANS. Trans.* **6** (1963) 154.
- [66] MAY, J.E., NOTLEY, M.J.F., STOUTE, R.J. and ROBERTSON, J.A.L., *AECL - 1641* (1962).
- [67] ANDERSON, J.S., *Proc. roy. Soc. A* **185** (1946) 69.
- [68] ROBERTS, L.E.J. and WALTER, A.J., U.K.A.E.A. Rpt AERE - R 3345 (1960).
- [69] MARKIN, T.L. and BONES, R.J., U.K.A.E.A. Rpt AERE - R 4178 (1962).
- [70] ÖLANDER, A., *Z. Metallk.* **11** (1937) 361.
- [71] ARONSON, S. and CLAYTON, J.C., *J. chem. Phys.* **32** (1960) 749.
- [72] ANDERSON, J.S., EDGINGTON, D.N., ROBERTS, L.E.J. and WAIT, E., *J. chem. Soc.* (1954) 3324.
- [73] HUTCHINSON, C.A., private communication.
- [74] HAGEMARK, K., Kjeller Rpt. KR-48 (1963).
- [75] ACKERMANN, R.J., GILLES, P.W. and THORN, R.J., *J. chem. Phys.* **25** (1956) 1089.
- [76] ACKERMANN, R.J., THORN, R.J., TETENBAUM, M. and ALEXANDER, C., *J. phys. Chem.* **64** (1960) 350.
- [77] DeMARIA, G., BURNS, R.P., DROWART, D. and INGRAM, M.G., *J. chem. Phys.* **32** (1960) 1373.
- [78] CHUPKA, W.A., *ANL-5786* (1957).
- [79] ACKERMANN, R.J., RAUH, E.G. and THORN, R.J., *J. chem. Phys.* **37** (1962) 2693.
- [80] RAUH, E.G. and THORN, R.J., *J. chem. Phys.* **22** (1954) 1414.
- [81] McCONNELL, J.D.M. and ROBERTS, L.E.J., *Chemisorption*, (W.E. GARNER, Ed.), Butterworths, London (1957) 218.
- [82] ROBERTS, L.E.J., WALTER, A.J. and WHEELER, V.J., *J. chem. Soc.* (1958) 2472.
- [83] FERGUSON, J.F. and McCONNELL, J.D.M., *Proc. roy. Soc. A* **241** (1957) 67.
- [84] McCONNELL, J.D.M., *J. chem. Soc.* **1958**, 947.
- [85] ANDERSON, J.S., ROBERTS, L.E.J. and HARPER, E.A., *J. chem. Soc.* (1955) 3946.
- [86] HOEKSTRA, H.R., SANTORO, A. and SIEGEL, S., *J. inorg. nucl. Chem.* **18** (1961) 166.
- [87] JAKŠ, D. and SEDLAKOVA, L., *Proc. Prague Conf.* **1** (1963) 155.
- [88] KOLAR, D., *Croatia. Chem. Acta* **35** (1963) 123, 280; *NUS - R - 426* (1964).
- [89] ROBERTSON, J.A.L., ROSS, A.M., NOTLEY, M.J.F. and MacEWAN, J.R., *J. nucl. Mater.* **7** (1962) 225.
- [90] BETHOUX, D., THOMAS, P. and WEILL, L., *C.R. Acad. Sci., Paris* **253** (1961) 2043.
- [91] PENNINGCKX, R. and NAGELS, P., private communication.
- [92] BALARIN, M. and ZETZSCHE, A., *Phys. Stat. sql.* **2** (1962) 1670.
- [93] BATES, J.L., *Nucleonics* **19** (1961) 83.
- [94] DANIEL, J.L., MATOLICH, J., Jr. and DEEM, H.W., *HW-69945* (1962).
- [95] DeHALAS, D.R., *Nucleonics* **21** (1963) 92.
- [96] RUSSEL, L.E., U.K.A.E.A. Rpt AERE, Harwell, private communication.
- [97] CHRISTENSEN, J.A., *WCAP - 2531* (1963).
- [98] KLEMENS, P.G., *Solid State Physics*, **7**, Academic Press, London (1957) 1.

- [99] GENZEL, L., *Glastech. Berich.* 26 (1953).
- [100] WOLFE, R. A., WAPD-270 (1963).
- [101] BATES, J. L., HW-79033 (1963).
- [102] RALPH, J. E., Kings College, London, private communication.
- [103] SMITH, R. A., *Semi-Conductors*, Cambridge University Press (1959) 169.
- [104] BRIGGS, A., U.K.A.E.A. Rpt AERE, Harwell, private communication.
- [105] MEYER, W., *Z. Elektrochem.* 50 (1944) 274.
- [106] WILLARDSON, R. K. and MOODY, J. W., in *Uranium Dioxide* (J. BELLE, Ed.), USAEC, Washington, D.C. (1961) 243.
- [107] WILLARDSON, R. K., MOODY, J. W. and GOERING, H. L., *J. inorg. nucl. Chem.* 6 (1958) 19.
- [108] HEIKES, R. R. and JOHNSTON, W. D., *J. chem. Phys.* 26 (1957) 582.
- [109] VanHOUTEN, S., *Phys. Chem. Solids* 17 (1960) 7.
- [110] NAGELS, P., DEVRESE, J. and DENAYER, M., *J. appl. Phys.* 35 (1964) 1175.
- [111] HASIGUTI, R. R. and KIYOURA, R., "Fundamental researches on the physical metallurgy of nuclear fuels in Japan," *Proc. 2nd UN Int. Conf. PUAE* 6 (1958) 34.
- [112] NAGAIEV, E. L., *Fiz. Tverdogo Tela* 4 (1962) 2201; *Eng. Trans. Soviet Phys. Solid State* 4 (1963) 1611.
- [113] NAGELS, P., private communication.
- [114] AMELINCKX, S., *Physical Properties of UO₂ Single Crystals*, Euratom Quarterly Rpt No. 2 (1962) 21.
- [115] ACKERMANN, R. J., THORN, R. J. and WINSLOW, G. H., *J. opt. Soc. Amer.* 49 (1959) 1107.
- [116] WILLIAMS, J., private communication.
- [117] MOTT, N. F. and GURNEY, R. W., *Electronic Processes in Ionic Crystals*, Oxford Univ. Press, Oxford (1950) 160.
- [118] COMPANION, A. and WINSLOW, G. H., *J. opt. Soc. Amer.* 50 (1960) 1043.
- [119] DEXTER, D. L., *Phys. Rev.* 111 (1958) 119.
- [120] BODINE, J. H. and THIESS, F. B., *Phys. Rev.* 98 (1955) 1532.
- [121] GRUEN, D. M., *J. Amer. chem. Soc.* 76 (1954) 2117.
- [122] KIKUCHI, T. and NASU, S., private communication to BATES, J. L. [101].
- [123] TRZEBIATOWSKI, W. and SELWOOD, P. W., *J. Amer. chem. Soc.* 72 (1950) 4504.
- [124] SLOWINSKI, E. and ELLIOT, N., *Acta Cryst.* 5 (1952) 768.
- [125] FISHER, W. E., *Phil. Mag.* 7 (1962) 1731.
- [126] WESTRUM, E. F., Jr., HACKER, H. and LIN, M., private communication.
- [127] HUTCHINSON, C. A. and CANDELA, G. A., *J. chem. Phys.* 27 (1957) 707.
- [127a] DAWSON, J. K. and ROBERTS, L. E. J., *J. chem. Soc.* (1956) 78.
- [128] AUSKERN, A. B. and BELLE, J., *J. nucl. Mater.* 3 (1961) 267.
- [129] ROBERTS, L. E. J., *Far. Soc. Disc. No. 23* (1957) 156.
- [130] COMPAN, K. and HAVEN, Y., *Far. Soc. Disc. No. 23* (1957) 105.
- [131] AUSKERN, A. B. and BELLE, J., *J. nucl. Mater.* 3 (1961) 311.
- [132] LINDNER, R. and SCHMITZ, F., *Z. Naturf.* 16a (1961) 1373.
- [133] McNAMARA, P., Thesis, London (1963).
- [134] LAGERWALL, T., *Nukleonik* 4 (1962) 158.
- [135] LAGERWALL, T. and SCHMELING, P., HMI-B27 (1963).
- [136] LAGERWALL, T., *Nukleonik* 6 (1964) 179.
- [137] MacEWAN, J. R. and STEVENS, W. H., *J. nucl. Mater.* 11 (1964) 77.
- [138] CHILDS, B. G., *J. nucl. Mater.* 9 (1960) 217.
- [139] LINDNER, R. and MATZKE, H., *Atomkernenergie* 9 (1964) 2.
- [140] LONG, G., U.K.A.E.A. Rpt AERE-R-4090, 106.
- [141] BRENNER, A., FELIX, F., LAGERWALL, T., SCHMELING, P. and ZIMEN, K. E., EUR 1729d (1964).
- [142] BARNES, R. H., KANGILASKI, M., MELEHAN, J. B. and BOUGH, A., USAEC Rpt SMI-1533 (1961).
- [143] STEVENS, W. H. et al., TID-7160 (1961) 7.
- [144] LINDNER, R. and MATZKE, W., *Z. Naturf.* 14a (1959) 582.
- [145] HAWES, R., U.K.A.E.A. Rpt AERE-R3865 (1961).
- [146] ROTHWELL, E., *J. nucl. Mater.* 5 (1962) 241.
- [147] ROTHWELL, E., private communication.
- [148] MÖLLER, P., WAGNER, K. and ZIMEN, K. E., to be published.
- [149] DAVIES, D. and LONG, G., U.K.A.E.A. Rpt AERE-R4374 (1963).
- [150] DeHALAS, D. R. and HORN, G. R., *J. nucl. Mater.* 8 (1963) 207.

- [151] MacEWAN, J.R. and LAWSON, V.B., *J. Amer. ceram. Soc.* **45** (1962) 1.
- [152] MURRAY, P., PUGH, S.F. and WILLIAM, J. TD-7546 (1957).
- [153] ARMSTRONG, W.M., IRVINE, W.R. and MARTINSON, R.H., *J. nucl. Mater.* **7** (1962) 133.
- [154] ZIMAN, J.M., *Electrons and Phonons*, Oxford Univ. Press, London (1960) 175.
- [155] RICE, S.A., *Phys. Rev.* **112** (1958) 804; RICE, S.A. and FRISCH, H.L., *Annu. Rev. phys. Chem.* **11** (1960) 187.
- [156] SCOTT, R., HALL, A.R. and WILLIAMS, J., *J. nucl. Mater.* **1** (1959) 39.
- [157] ARMSTRONG, W.M. and IRVINE, W.R., *J. nucl. Mater.* **9** (1963) 121.
- [158] BERMAN, R.M., BLEIBERG, M. L. and YENISCAVICH, W., *J. nucl. Mater.* **2** (1960) 129.
- [159] BRADBURY, B. T., private communication.
- [160] WAIT, E., *et al.*, U.K.A.E.A. Rpt AERE-R-4268 (1963).
- [161] BELLAMY, R.G., *Inst. Met., Symposium on Uranium and Graphite*, Paper 8 (March 1962).
- [162] BARNES, R.S., U.K.A.E. A. Rpt AERE-R-4429 (1963).
- [163] ROAKE, W., HW-73072 (1962).
- [164] BURKE, J.E. and COBLE, R.L., *Progress in Ceramic Science*, **3** Pergamon Press (1963) 199.
- [165] COBLE, R.L., *J. appl. Phys.* **32** (1961) 787, 793.
- [166] WILLIAMS, J., *Science of Ceramics* **2** (1964).
- [167] PODÉŠŤ, M., JAKĚS, D., Rpt UJV.726/63 (1963).
- [168] PODÉŠŤ, M. and JADESOVA, L., "Theory of the fabrication of compacted uranium dioxide pellets by powder metallurgical methods," (in Russian) *New Nuclear Materials including Non-metallic Fuels* **1** IAEA, Vienna (1963) 117.
- [169] BEL, A., DELMAS, R. and FRANCOIS, B., *J. nucl. Mater.* **1** (1959) 259.
- [170] WILLIAMS, J., BARNES, E., SCOTT, R. and HALL, A., *J. nucl. Mater.* **1** (1959) 28.
- [171] JAKEŠOVÁ, L., *Silicates* (in press).
- [172] FOLWEILER, R., *J. appl. Physics* **32** (1961) 773.
- [173] WARSHAW, S. L. and NORTON, F. H., *J. Amer. ceram. Soc.* **45** (1962) 479.
- [174] CHANG, R., *J. nucl. Mater.* **2** (1959) 174.
- [175] PALADINO, A.E. and KINGERY, W.D., *J. chem. Phys.* **37** (1962) 957.
- [176] AUSTERMAN, S.B., NAA-SR-3170 (1958).
- [177] AUSKERN, A.B. and BELLE, J., *J. chem. Phys.* **28** (1958) 171.
- [178] ALCOCK, C. B. and McNAMARA, P., *Doctoral Thesis* (McNamara). London (1963).
- [179] DANIEL, R.C., BLEIBERG, M. L., MEIERAN, H.B. and YENISCAVICH, W., WAPD-263 (1963).
- [180] DAWSON, J.K. and LISTER, B.A.J., *J. chem. Soc.* (1952) 5041.
- [181] ANDERSON, J.S., "The oxidation of particles of uranium dioxide," *Proc. Symp. PUAE, Sydney, Australia* (1958), Australia AEC (1958) 588.
- [182] MOTT, N.F. and JONES, H., *Properties of Metals and Alloys*, chapter I, Clarendon Press, Oxford (1936).
- [183] NAGELS, P., private communication.
- [184] WINSLOW, G. H., private communication.

Papers 19-27

3. Single-Crystal Diffractometry (19-27)

This group of papers is concerned with the technique of making structure factor measurements, for either X-rays or neutrons, using a single-crystal diffractometer.

Some Theoretical Properties of the Double-Crystal Spectrometer Used in Neutron Diffraction

BY B. T. M. WILLIS

Atomic Energy Research Establishment, Harwell, Didcot, England

(Received 7 October 1959 and in revised form 4 February 1960)

A treatment is given of the angular dependence of certain intensity functions which are important in spectrometer design. It provides a basis for the choice of various parameters, including, in particular, the Bragg angle of the crystal monochromator.

1. Introduction

The structures of many single crystals have been examined by neutron diffraction: the instrument normally used is the double-crystal spectrometer, whose main features are sketched in Fig. 1. Slits S_1 and S_2 , representing the collimator, transmit a neutron beam with a divergence in the horizontal plane of about $\pm \frac{1}{2}^\circ$. The beam is reflected by the crystal monochromator A to the crystal B under investigation, and thence is reflected again into the counter C . The 'parallel' arrangement, with the incident and twice-reflected beams on opposite sides of the once-reflected beam, is used because of its well-known focusing property (Compton & Allison, 1935).

In §§ 2-4 the following features of the spectrometer are examined theoretically:

- The intensity of the beam reflected in a given direction by the monochromator A as a function of the angular setting of A . ('Rocking curve' of monochromator).
- The intensity of the beam reflected by the crystal B as a function of the angular setting of B . ('Double-reflexion curve').
- The divergence of the beam reflected by B .

The solution of (b) leads to the best choice of the parameters governing the properties of the collimator and monochromator. The treatment of (a) suggests a convenient method of measuring the mosaic spread of the monochromator, and (c) determines the minimum aperture which the counter must have to receive the whole of the beam reflected by the crystal.

Related problems have been examined theoretically by Sailor *et al.* (1956) and by Caglioti *et al.* (1958).

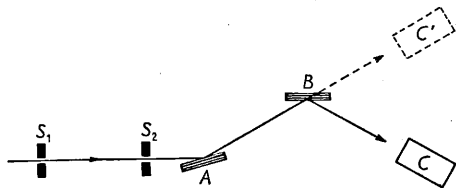


Fig. 1. Sketch of projection of spectrometer in horizontal plane.

Sailor studied the angular dependence of the intensity of the neutron beam reflected by the monochromator, with Soller slits restricting the horizontal divergence of incident and reflected beams to a few minutes of arc. Caglioti calculated the intensity of the beam, reflected by the monochromator and then by a powder sample, as a function of the angular position of the counter; again the incident, once- and twice-reflected beams were limited by Soller slits.

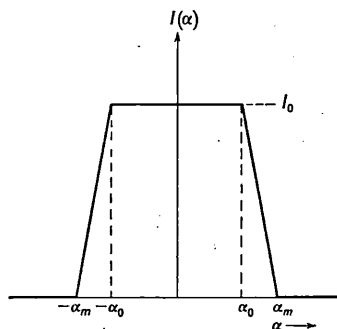


Fig. 2. Angular dependence of intensity of neutron beam striking monochromator.

In the absence of Soller slits the angular distribution of intensity of the incident neutron beam is approximately of the form shown in Fig. 2. The number of neutrons, $I(\alpha)d\alpha$, with a horizontal divergence between α and $\alpha + d\alpha$ is constant for $|\alpha|$ less than α_0 , and decreases uniformly to zero as $|\alpha|$ increases from α_0 to α_m . The formulae derived below refer to the special case $\alpha_0 = \alpha_m$, corresponding to a rectangular angular distribution of intensity. The general formulae for $\alpha_0 \neq \alpha_m$ are quoted elsewhere (Willis, 1959): they are cumbersome and introduce no modifications to the general conclusions given in § 5.

If crystal B is set at the Bragg angle θ_{hkl} , the change in glancing angle arising from a vertical divergence φ is $\frac{1}{2}\varphi^2 \tan \theta_{hkl}$. Observations in neutron diffraction rarely extend beyond $\theta_{hkl} = 60^\circ$, and so this change can be neglected compared with that arising from the horizontal divergence. For this reason it is only necessary to consider the projection of the neutron beam in the horizontal plane.

It is assumed that each crystal consists of mosaic blocks with a Gaussian distribution of orientation. Thus the fraction of mosaic blocks in A having their normals in the angular range Δ , $\Delta + d\Delta$ (as measured from the mean orientation) is $W(\Delta)d\Delta$, where

$$W(\Delta) = \frac{1}{\eta\sqrt{\pi}} \exp(-\Delta^2/\eta^2). \quad (1)$$

$\eta/\sqrt{2}$ is the standard deviation of the distribution and is a measure of the mosaic spread of A . A similar equation can be written for crystal B :

$$W'(\Delta') = \frac{1}{\eta'\sqrt{\pi}} \exp(-\Delta'^2/\eta'^2), \quad (1a)$$

where the primed quantities have the same meanings as the unprimed quantities but now refer to B . (Corresponding quantities for A and B will always be denoted by the same symbol with a prime to distinguish the symbol for B .) As $\eta, \eta' \ll 1$, (1) and (1a) also give the angular distributions of the projections of the normals in the horizontal plane.

2. Rocking curve of monochromator

The rocking curve of the monochromator is defined as the curve giving the intensity, $I(\beta)$, reflected by A in a fixed direction as a function of the angular setting, β , of A . A fixed direction is stipulated, as the incident beam has a white spectrum and the monochromator can reflect any wavelength in this spectrum, depending on the glancing angle of the neutrons incident on it. To measure the rocking curve experimentally crystal B must be removed and the counter moved round to the 'straight-through' position C' (Fig. 1); it is also necessary to define the fixed direction for reflexion by slits, restricting the horizontal divergence of the reflected beam to a value which is small compared with the mosaic spread, η .

Let $2\theta_B$ be the angle between the axis of the collimator and the fixed direction for reflexion. Neutrons with an initial divergence of α are reflected in

this direction by the mosaic blocks whose orientation is Δ , where

$$\Delta = -(\beta + \frac{1}{2}\alpha). \quad (2)$$

The signs of α, β, Δ are such that the glancing angle on A increases with these angles. $\beta=0$ is defined as the angular position of the monochromator, when neutrons passing along the axis of the collimator are reflected at the angle θ_B by the mosaic blocks of mean orientation.

Ignoring the crystal reflectivity, which varies relatively slowly with angle, the number of neutrons, of initial divergence α , reflected in the fixed direction is $I(\alpha)d\alpha W(\Delta)$, where

$$I(\alpha) = \begin{cases} I_0, & |\alpha| < \alpha_0 \\ 0, & |\alpha| > \alpha_0. \end{cases} \quad (3)$$

The total number reflected for all values of α is

$$I(\beta) = \int_{-\alpha_m}^{\alpha_m} I(\alpha)W(\Delta)d\alpha,$$

which from (1), (2) and (3) becomes

$$\begin{aligned} I(\beta) &= \frac{I_0}{\eta\sqrt{\pi}} \int_{-\alpha_m}^{\alpha_m} \exp[-(\beta + \frac{1}{2}\alpha)^2/\eta^2] d\alpha \\ &= I_0 \left[\operatorname{erf}\left(\frac{\beta + \frac{1}{2}\alpha_m}{\eta}\right) - \operatorname{erf}\left(\frac{\beta - \frac{1}{2}\alpha_m}{\eta}\right) \right]. \end{aligned} \quad (4)$$

Here $\operatorname{erf} x$ is the tabulated error function, defined by

$$\operatorname{erf} x = \frac{2}{\sqrt{\pi}} \int_0^x \exp(-\xi^2) d\xi.$$

$I(\beta)$ has been calculated as a function of β from (4), and the results for $\alpha_m=0, \eta, 2\eta$ are presented in Fig. 3. Provided $\alpha_m \gg 2\eta$, the half-width at half-height, H_1 , of the rocking curve is within 10% of 0.95η . Extinction will tend to make H_1/η larger, but not unduly so. Thus an approximate value of η can be found by measuring H_1 and using $H_1/\eta \approx 1$, unless the value obtained is less than $\frac{1}{2}\alpha_m$; in the latter case η is found by fitting the rocking curve to the equation (4).

3. Double-reflexion curve

This curve gives the intensity, $I(\beta')$, of the hkl Bragg reflexion of crystal B as a function of the angular position, β' , of B . The area under this curve is proportional to $F_{hkl}^2 \operatorname{cosec} 2\theta_{hkl}$. The dependence of the shape of this curve on the mosaic spreads and Bragg angles of the two crystals and on the collimation angle is investigated below.

A beam of neutrons of initial divergence α is reflected at a fixed wavelength by the mosaic blocks in A with a given orientation Δ ; this wavelength can then be reflected again only by the mosaic blocks in B , whose orientation, Δ' , satisfies Bragg's law. This value of Δ' is readily shown to be

$$\Delta' = (k-1)\alpha + (k-2)\Delta - \beta', \quad (5)$$

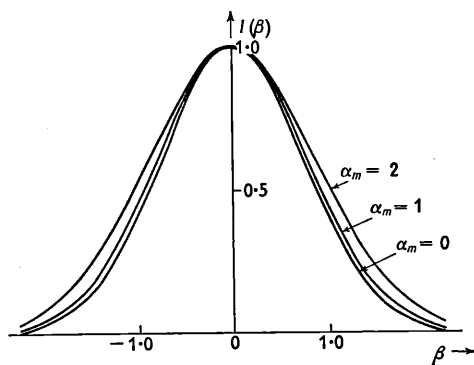


Fig. 3. Rocking curves of monochromator for different values of collimation angle, α_m , β and α_m are expressed in units of η , the mosaic spread of the monochromator.

where $k = \tan \theta_{hkl} / \tan \theta_B$. The sign of β' is chosen so that the glancing angle on B increases with β' , and the angular position $\beta' = 0$ is defined as that for which a neutron of no initial divergence is reflected by the mosaic blocks in A and B of mean orientation.

The number of neutrons reflected into the counter for fixed α, Δ is proportional to $I(\alpha)W(\Delta)W'(\Delta')$. $I(\beta')$ is obtained by integrating over α and Δ :

$$I(\beta') = \int_{-\alpha_m}^{\alpha_m} \int_{-\infty}^{\infty} I(\alpha)W(\Delta)W'(\Delta')d\alpha d\Delta,$$

which from (1), (1a) and (3) becomes

$$I(\beta') = \frac{I_0}{\pi\eta\eta'} \int_{-\alpha_m}^{\alpha_m} \int_{-\infty}^{\infty} \exp(-\Delta^2/\eta^2) \times \exp(-\Delta'^2/\eta'^2)d\alpha d\Delta. \quad (6)$$

Substituting for Δ' from (5) and using the identity

$$\int_{-\infty}^{\infty} \exp(-A\Delta^2 - 2B\Delta - C)d\Delta = \left(\frac{\pi}{A}\right)^{\frac{1}{2}} \exp\left(\frac{B^2}{A} - C\right),$$

the second integral in (6) can be written

$$\frac{\eta\eta'}{\varepsilon} \sqrt{\pi} \exp[-(k\alpha - \alpha - \beta')^2/\varepsilon^2],$$

where

$$\varepsilon^2 = \eta'^2 + (k-2)\eta^2.$$

Thus

$$\begin{aligned} I(\beta') &= \frac{I_0}{\sqrt{(\pi)\varepsilon}} \int_{-\alpha_m}^{\alpha_m} \exp[-(k\alpha - \alpha - \beta')^2/\varepsilon^2]d\alpha \\ &= \frac{I_0}{k-1} \left[\operatorname{erf}\left(\frac{\beta' + k\alpha_m - \alpha_m}{\varepsilon}\right) - \operatorname{erf}\left(\frac{\beta' - k\alpha_m + \alpha_m}{\varepsilon}\right) \right]. \end{aligned} \quad (7)$$

For the special case $k=1$, when the incident and twice-reflected beams are parallel, (7) simplifies to

$$I(\beta') = \frac{2}{\sqrt{\pi}} \frac{I_0\alpha_m}{\sqrt{(\eta^2 + \eta'^2)}} \exp\left(-\frac{\beta'^2}{\eta^2 + \eta'^2}\right).$$

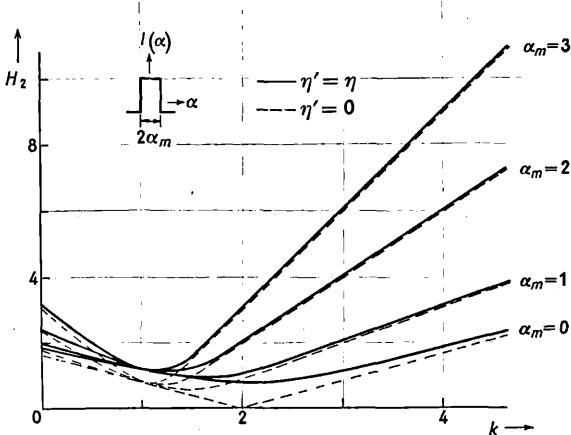


Fig. 4. Half-width of double-reflexion curve as a function of $k (= \tan \theta_{hkl} / \tan \theta_B)$. H_2 and α_m are expressed in units of η , the mosaic spread of the monochromator.

The half-width at half-height, H_2 , of the double-reflexion curve is then

$$H_2 = \sqrt{\ln 2 (\eta^2 + \eta'^2)},$$

and is independent of the collimation angle, α_m .

For all other values of k , H_2 depends on α_m and on η and η' . The nature of this dependence is illustrated by Fig. 4, where H_2 , calculated from equation (7), is plotted as a function of k . The different pairs of curves refer to $\alpha_m = 0, \eta, 2\eta, 3\eta$, the unbroken curve in each pair corresponding to $\eta' = \eta$ and the broken curve to $\eta' = 0$. H_2 passes through a minimum between $k=1$ and $k=2$ and is approximately proportional to α_m for $k > 3$.

It is clearly desirable that the Bragg angle, θ_B , of the monochromator should be chosen to make H_2 approximately the same at either end of the range of θ_{hkl} under investigation. This implies that, for a range of $0-60^\circ$ in θ_{hkl} , θ_B will be about 40° .

4. Angular divergence of twice-reflected beam

We shall consider only the case when crystal B is set exactly at the Bragg angle θ_{hkl} . The condition that neutrons are reflected by the mosaic blocks in A of orientation Δ and then by the blocks in B of orientation Δ' is given by equation (5) with $\beta' = 0$:

$$\Delta' = (k-1)\alpha + (k-2)\Delta. \quad (8)$$

Let φ' denote the angular position of these twice-reflected neutrons, where the sign of φ' is chosen to make the glancing angle on B increase with φ' , and the position $\varphi' = 0$ is defined as that corresponding to neutrons of no initial divergence reflected by the mosaic blocks in A and B of mean orientation. Then φ' is given by

$$\varphi' = \alpha + 2\Delta + 2\Delta', \quad (9)$$

and (8) and (9) together define the orientations Δ, Δ' of the mosaic blocks in A, B , which change the angular position of the neutrons from the incident value of α to the doubly-reflected value of φ' . Solving (8) and (9), these orientations are

$$\left. \begin{aligned} \Delta &= \frac{1}{2(k-1)} (\varphi' - 2k\alpha + \alpha) \\ \Delta' &= \frac{1}{2(k-1)} (k\varphi' - 2\varphi' + k\alpha). \end{aligned} \right\} \quad (10)$$

The total intensity of neutrons reflected for all values of α into the direction φ' is $I(\varphi')$, where

$$I(\varphi') = \int_{-\alpha_m}^{\alpha_m} I(\alpha)W(\Delta)W'(\Delta')d\alpha$$

and Δ, Δ' are given by (10). Using equations (1), (1a) and (3), $I(\varphi')$ can be finally manipulated into the form

$$I(\varphi') = c \exp \left[-\frac{(k-1)^2 \varphi'^2}{k^2 \eta^2 + (2k-1)^2 \eta'^2} \right] \times \left(\operatorname{erf} \left[\frac{\sqrt{a}(\alpha_m + b/a)}{2(k-1)} \right] + \operatorname{erf} \left[\frac{\sqrt{a}(\alpha_m - b/a)}{2(k-1)} \right] \right),$$

where

$$a = \frac{(2k-1)^2}{\eta^2} + \frac{k^2}{\eta'^2}$$

$$b = \varphi' \left(\frac{1-2k}{\eta^2} + \frac{k^2-2k}{\eta'^2} \right)$$

and c is a constant.

The curves in Fig. 5 have been plotted from this expression for the special case $\eta' = \eta$: they give the variation with k of H_3 , the half-width at half-height of the $I(\varphi')$ versus φ' distribution. H_3 is a measure of the divergence of the twice-reflected beam; it varies appreciably with k and attains a maximum value between $k=1$ and $k=3$, according to the value of α_m . For $\eta' < \eta$, H_3 is reduced approximately in the ratio $\eta' : \eta$.

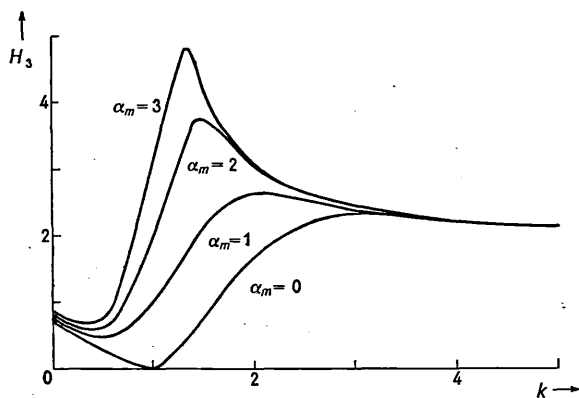


Fig. 5. Curves showing the dependence of the divergence of the twice-reflected beam on $k (= \tan \theta_{hkl} / \tan \theta_B)$. H_3 and α_m are expressed in units of η , the mosaic spread of the monochromator.

As a typical case, $\alpha_m = 30'$, $\eta = 20'$ and $\eta' = 10'$, giving a maximum value of H_3 of $30'$. More than 99% of the beam lies within the angular range $|\varphi'| < 2.5H_3$, and so the aperture of the counter must be large enough to receive a beam diverging from the crystal at an angle of $\pm 1.25^\circ$.

5. Conclusions

The analysis above provides a basis for the choice of various parameters appearing in spectrometer design. Using § 2 the mosaic spread of the monochromator can be determined from the experimental rocking curve; the best choice of collimation angle and Bragg angle, θ_B , of the monochromator then follows from § 3. Finally, the minimum counter aperture can be determined from § 4.

The choice of θ_B is particularly important, because of its influence on the widths of the Bragg reflexions of the second crystal. The curves in Fig. 4 show that, as θ_B increases, the reflexions become narrower over the whole range of θ_{hkl} of the crystal. This effect is to be ascribed primarily to the reduction in width of the wavelength band reflected by the monochromator. At the focusing position the whole of this band is reflected simultaneously by the mosaic blocks set at the Bragg angle θ_{hkl} , and the width of the reflexion is determined only by the mosaic spread. However, away from the focusing position simultaneous reflexion does not occur. As the crystal turns, each mosaic block reflects a sharp wavelength, which gradually sweeps across the wavelength band, and under these conditions the width of the reflexion is determined mainly by the width of the incident wavelength band.

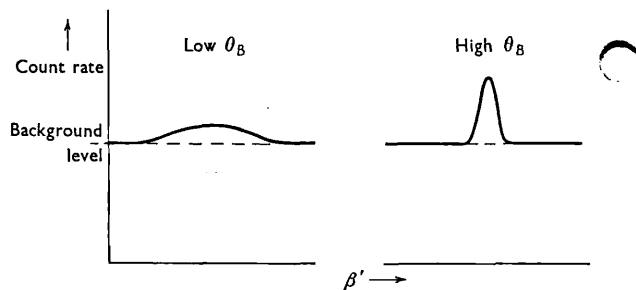


Fig. 6. Diagram illustrating advantage of using a relatively high value of θ_B to observe weak high-order reflexions.

By using relatively high values of $\theta_B (\sim 45^\circ)$ the hkl reflexions are made particularly narrow at high angles, where the integrated reflexions are reduced by the Lorentz ($\operatorname{cosec} 2\theta$) and Debye-Waller

$$(\exp [-2B \sin^2 \theta / \lambda^2])$$

factors. Frequently the peak intensities of the high-angle reflexions are only fractionally higher than the background intensity (produced, for example, by incoherent scattering from hydrogen atoms in the sample), and there is clearly much advantage in increasing θ_B (see Fig. 6). The fall-off with θ_B of the reflectivity of the monochromator can be partly off-set by relaxing the degree of collimation, but, in any case, measurements with several copper crystal monochromators have indicated that the reflectivity falls by a factor of only 2 or 3, as θ_B is increased from 10° to 45° .

References

CAGLIOTI, G., PAOLETTI, A. & RICCI, F. P. (1958). *Nucl. Instrum.* **3**, 223.
 COMPTON, A. H. & ALLISON, S. K. (1935). *X-rays in Theory and Experiment*. New York: Van Nostrand.
 SAILOR, V. L., FOOTE, H. L., LANDON, H. H. & WOOD, R. E. (1956). *Rev. Sci. Instrum.* **27**, 26.
 WILLIS, B. T. M. (1959). A. E. R. E. Report—R. 3104.

Acta Cryst. (1961). 14, 90

Use of a two-circle device to obtain three-dimensional neutron diffraction data. By B. T. M. WILLIS, Atomic Energy Research Establishment, Harwell, Didcot, Berks., England

(Received 23 February 1960)

It has been customary in neutron diffraction work to use a pillar-shaped crystal to obtain two-dimensional F^2 data, the long axis of the crystal corresponding to the zone axis of the reflexions to be examined (Bacon & Pease, 1953; Atoji & Rundlo, 1958). As this long axis is normal to the plane containing the incident and reflected beams, a maximum counting rate is achieved while the possibility of extinction errors is minimized. The purpose of this note is to point out that, by mounting the crystal on a two-circle device placed on the central table of the spectrometer, three-dimensional data (or two-dimensional data about an arbitrary zone axis) can be obtained from a pillar-shaped crystal with approximately the same accuracy as for the conventional two-dimensional arrangement. The method has been used successfully in this laboratory for several months.

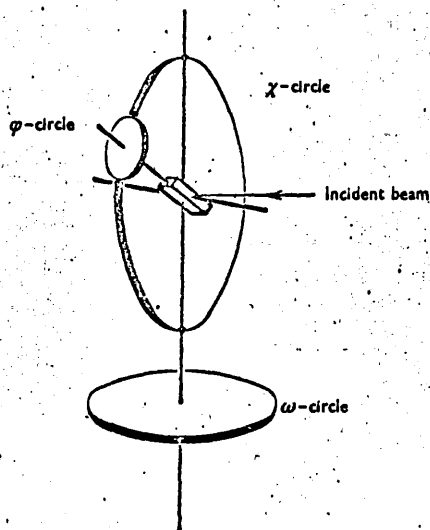


Fig. 1. Diagram of the φ -, χ - and ω -circles.

The device constitutes the φ - and χ -circles of a three-circle diffractometer (Furnas & Harker, 1955). χ is a vertical circle and φ a circle which rotates as a whole about the horizontal χ -axis (Fig. 1). The χ -circle and counter move independently round the third circle, ω , which is the large horizontal circle of the diffractometer. The crystal, mounted on a goniometer head attached to the φ -circle, is located at the common point of intersection of the φ -, χ - and ω -axes.

By appropriate adjustments of the three circles, the normal to any (hkl) plane is brought into the Bragg reflecting position in the equatorial plane, and the integrated intensity is then measured in the normal way by moving the counter round to the $2\theta_{hkl}$ position. The stereogram in Fig. 2 illustrates the adjustments required. OP represents the (hkl) normal initially, RO the incident neutron beam and $\chi O\chi'$ the χ -axis, set at an arbitrary angle to RO : it is required to move the pole P to P' , where OP' is in the equatorial plane and at an angle $\pi/2 - \theta_{hkl}$ to RO . Initially, the φ -circle is moved round the χ -circle to make the φ -axis vertical. The φ -axis is then rotated through the angle PQ , moving P to Q , where Q is the point of intersection of the two small circles of centre O , radius OP and centre χ' , radius $\chi'P'$. Finally, the χ -axis is rotated through the angle QP' ,

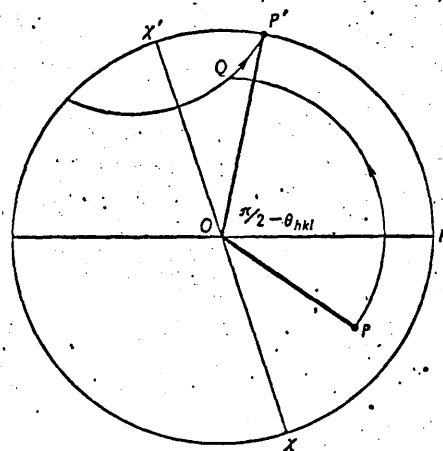


Fig. 2. Stereogram illustrating the rotations about the φ - and χ -axes necessary to bring the (hkl) normal, OP , to the reflecting position, OP' , in the equatorial plane. RO is the incident beam direction, $\chi O\chi'$ is the χ -axis and the φ -axis is initially vertical.

moving Q to P' . Clearly, the circle settings are not unique but depend on the arbitrary ω setting of the χ -circle. By mounting the crystal with its long direction along the φ -axis and by choosing the χ -axis perpendicular to the (hkl) normal in its reflecting position, OP' , the path length of the beam inside the crystal is a minimum (Fig. 3). The ω setting is then θ_{hkl} , and the φ and χ settings are given by

$$\tan \varphi = \frac{V}{abc} \left[\frac{k/b - l \cos \alpha / c}{h \sin^2 \alpha / a + k (\cos \alpha \cos \beta - \cos \gamma) / b + l (\cos \gamma \cos \alpha - \cos \beta) / c} \right]$$

and

$$\sin \chi = l d_{hkl} / c.$$

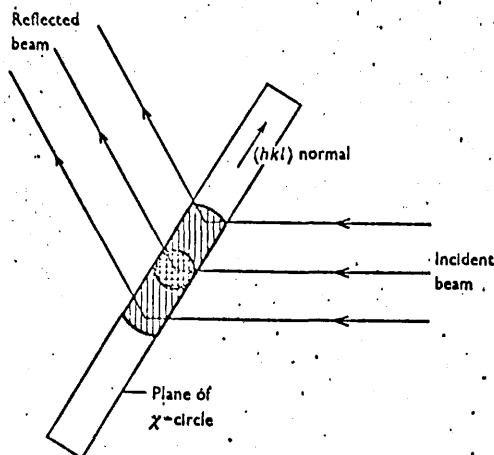


Fig. 3. Diagram showing the path of the beam inside the crystal. The cross-hatched region represents the crystal at $\chi = 0$ with its long axis vertical; the vertically shaded region represents the crystal after it has been moved round the χ -circle to bring the (hkl) normal into the horizontal plane.

V is the volume of the unit cell and it is assumed that the c -axis of the crystal is along the φ -axis, that $\varphi = 0$ corresponds to the a^* -axis in the plane of the χ -circle and that $\chi = 0$ corresponds to the φ -axis vertical.

Thus by attaching a two-circle device, representing the χ - and φ -circles, to the existing ω -circle of a neutron diffraction spectrometer, it is possible to extend collection of I^2 data to three dimensions. In essence, the method depends on the principle that a three-circle instrument not only allows any (hkl) plane to be brought into the reflecting position, but also allows rotation of the crystal about the normal to this plane to make the path length a minimum.

References

- ATOJI, M. & RUNDLE, R. E. (1958). *J. Chem. Phys.* **29**, 1306.
 BACON, G. E. & PEASE, R. S. (1953). *Proc. Roy. Soc. A*, **220**, 397.
 FURNAS, T. C. & HARKER, D. (1955). *Rev. Sci. Instrum.* **26**, 449.

Acta Cryst. (1961). **14**, 91

Crystallographic data for certain amidinium carboxylates. By OLGA KENNARD and JAMES WALKER, National Institute for Medical Research, Mill Hill, London, England

(Received 9 May 1960)

During an investigation of the mechanism of salt formation between carboxylic acids and substances containing an unsubstituted amidinium group the crystallographic constants of a number of these salts were determined (Kennard & Walker, 1954). Unit-cell dimensions were obtained from oscillation and Weissenberg photographs ($\lambda = 1.5418 \text{ \AA}$), except for the last two compounds listed below, where the θ method (Weisz, Cochran & Cole, 1948) was used. Densities were determined with an accuracy of $\pm 0.5\%$ by centrifuging the crystals in a continuous-gradient density column (Low & Richards, 1952). The three-dimensional structure analysis of *S*-methylthiuronium *p*-chlorobenzoate is being reported elsewhere (Kennard & Walker, 1961).

Benzamidinium benzoate $\text{C}_6\text{H}_5 \cdot \text{C}(\text{NH}) \cdot \text{NH}_2, \text{C}_6\text{H}_5 \cdot \text{CO}_2\text{H}$

Benzamidinium benzoate was prepared from benzamidinium hydrochloride and sodium benzoate in aqueous solution (cf. Pinner, 1892). It crystallized from water as flat plates elongated along [001], with marked striations in this direction. The striations were traces of an excellent cleavage plane.

The refractive index for white light was 1.680 ± 5 with the electric vector vibrating in the direction of elongation of the plates, and 1.630 ± 5 at right angles to this direction.

Orthorhombic

$a = 28.9(4)$, $b = 35.8(6)$, $c = 9.9(5) \text{ \AA}$, $U = 10326 \text{ \AA}^3$,
 $D_m = 1.25 \text{ g.cm.}^{-3}$, $Z = 32$, $D_x = 1.25 \text{ g.cm.}^{-3}$.

Space group *Ccc2*, with additional non-space-group absences. Absent spectra: hkl when $h+k$ odd, but very few weak reflexions of the type $h+l$ odd or $k+l$ odd were observed. The $hk0$ reflexions were with a few exceptions absent unless $h+k=4n$. The $0kl$ reflexions were absent unless $k=4n$, $l=2n$, and the $h0l$ reflexions if $h=4n+1$ or $l=2n+1$.

3,5-Dibromobenzamidinium benzoate $\text{C}_6\text{H}_3\text{Br}_2 \cdot \text{C}(\text{NH}) \cdot \text{NH}_2, \text{C}_6\text{H}_5 \cdot \text{CO}_2\text{H}$

3,5-Dibromobenzamidinium benzoate was prepared from 3,5-dibromobenzamidinium hydrochloride and sodium benzoate; it was recrystallized from water and had m.p. $228-229^\circ$ (decomp.). (Found: C, 42.0; H, 2.9; N, 6.8. $\text{C}_7\text{H}_6\text{Br}_2\text{N}_2$, $\text{C}_7\text{H}_6\text{O}_2$ requires C, 42.0; H, 3.0; N, 7.0%). The crystals were needle-shaped with diagonal extinction; they had faint striations and imperfect cleavage parallel to the needle axis.

Triclinic

$a = 15.21$, $b = 9.64$, $c = 12.34 \text{ \AA}$,
 $\alpha = 110$, $\beta = 110$, $\gamma = 100.7^\circ$,

$U = 1501 \text{ \AA}^3$, $D_m = 1.755$, $Z = 4$, $D_x = 1.77 \text{ g.cm.}^{-3}$.

Space group *P1* or $\bar{1}$. No absences.

3,5-Dibromobenzamidinium 3,5-dibromobenzoate $\text{C}_6\text{H}_3\text{Br}_2 \cdot \text{C}(\text{NH}) \cdot \text{NH}_2, \text{C}_6\text{H}_3\text{Br}_2 \cdot \text{CO}_2\text{H}$

3,5-Dibromobenzamidinium 3,5-dibromobenzoate was obtained from 3,5-dibromobenzamidinium hydrochloride and

Single-crystal neutron diffraction equipment at the DIDO reactor

B. T. M. WILLIS

Metallurgy Division, Atomic Energy Research Establishment, Harwell, Berks.

MS. received 20th July 1962

A description is given of the single-crystal equipment which has been in continuous operation at the DIDO reactor for the past two years. Two diffractometers are used on the same reactor hole and each employs a copper monochromator reflecting neutrons of wavelength 1.04 \AA through 90° . The advantages of this high reflecting angle are discussed.

1. Introduction

Since 1958 neutron diffraction work on both powder and single-crystal samples has been carried out at the DIDO reactor. A description of the powder and single-crystal diffractometers, together with their associated collimators, monochromators and shielding, has already been given by Bacon and Dyer (1959). In 1960 a new single-crystal assembly was installed, allowing two diffractometers to be operated in place of the original one.

A diagram showing a plan view of the new assembly is given in figure 1. The neutron beam issuing from the reactor

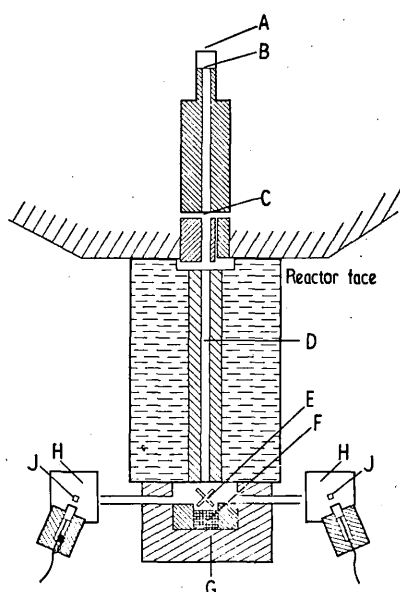


Figure 1. Plan view of the new single-crystal assembly. A, neutron source; BC, collimating channel; D, flight-tube with water shielding; E, monochromators; F and G, lead and compressed wood shielding; H, diffractometers; J, single-crystal samples.

source at A is collimated by the stainless-steel channel BC before striking two single-crystals of copper E, which act as neutron monochromators. Most of the radiation passes through the monochromators to be absorbed in the shielding of lead and tungsten alloy F and compressed wood G, but a small proportion of the slow neutron beam is reflected at a wavelength of 1.04 \AA to the two single-crystal diffractometers H. D is a flight-tube between the reactor face and the

monochromator housing enabling the diffractometers to be withdrawn to a position clear of the powder instrument on the beam hole above. Figure 2 is a schematic diagram of the assembly showing, in particular, the paths of the neutron

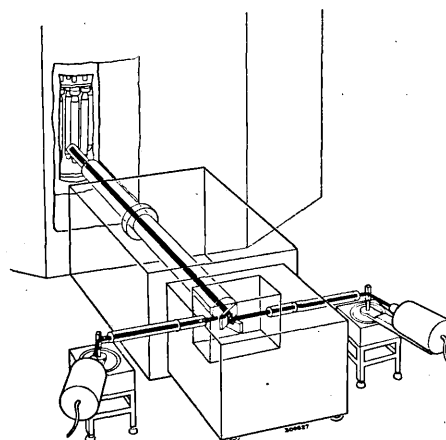


Figure 2. A schematic diagram of the new assembly, showing, in particular, the relative positions of the monochromators and diffractometers. The heavy lines show the paths of the neutron beams.

beams and the relative positions of the monochromators and diffractometers in the horizontal plane.

This paper outlines the features of the new assembly which are different from those described earlier for the original assembly, and compares the performance of a diffractometer, both as regards the resolution and the intensity of the Bragg reflections, with the two assemblies.

2. Neutron collimator

The original collimator consisted of a channel, 5 ft long, lined with stainless steel; its aperture was $1\frac{1}{4}$ in. across and 1 in. deep at the inner end, tapering to $\frac{1}{2}$ in. \times $\frac{1}{4}$ in. near the reactor face. An eccentrically mounted lead plug, 15 in. long, served as a stopper for the γ -beam: with this rotated to the closed position and the collimating channel flooded with water the radiation was switched off. The new collimator is of similar design, but different dimensions have been adopted for the collimating channel. The length of the channel is 5 ft and its cross section, $1\frac{1}{4}$ in. across \times $2\frac{1}{2}$ in. deep, is uniform along this length.

The wider aperture of the channel increases the divergence

SINGLE-CRYSTAL NEUTRON DIFFRACTION EQUIPMENT AT THE DIDO REACTOR

of the beam striking the monochromator and enhances the intensity at the sample. The vertical divergence only has been increased and this has little effect on the resolution of the different Bragg reflections from the sample. If the vertical divergence is ϕ the variation in Bragg angle θ_M at the monochromator for neutrons in the vertical plane is $\frac{1}{2}\phi^2 \tan \theta_M$ (Compton and Allison 1935). θ_M is 45° , so that the angular variation is $\frac{1}{2}\phi^2$, which is much less than the change of Bragg angle ($\sim 1^\circ$), and consequently of reflected wavelength, arising from divergence in the horizontal plane. Because of possible overlapping of reflections in adjacent layer lines, the angle ϕ fixes the maximum unit-cell size of the sample at about 30 \AA .

3. Flight-tube

The flight-tube is 6 ft long and consists of a steel-lined channel, terminated at both ends by aluminium windows, each 0.020 in. thick. It is surrounded by a large tank of water acting as a biological shield. Provision is available for evacuating the flight-tube, but experience has shown that this is only of marginal advantage. Evacuation removes air-scattering of the slow neutron beam in the 6 ft path length, leading to an increase of about 12% in the beam intensity, but this increase must be off-set against the extra absorption of the aluminium windows.

4. Monochromators

The two monochromating crystals are placed in the upper and lower halves of the direct beam emerging from the open collimating channel, and reflect mono-energetic slow neutrons to two single-crystal diffractometers on opposite sides of the monochromator housing (see figure 2). A scattering angle $2\theta_M$ of 90° , as compared with the previous value of 22° (Bacon and Dyer 1959), was chosen to give improved resolution of reflections at high Bragg angles θ_{hkl} of the sample. There are two reasons for this gain in resolution at high angles (Willis 1960): the 'focusing position', where the direct and doubly-scattered beams are parallel, occurs at $\theta_{hkl} = \theta_M$, and the width $\Delta\lambda$ of the band of wavelengths reflected by each mosaic block of the monochromator is proportional to $\cot \theta_M$ and is therefore reduced five-fold as θ_M is increased from 11° to 45° .

A number of single-crystals were tested as neutron monochromators, including lead, copper and magnesium oxide. The intensity and uniformity of the beam reflected by each crystal were determined both photographically, using the technique recently developed by Smith (1962), and with a BF_3 counter; in the latter case the counter on the arm of the diffractometer was moved to the 'straight-through' position, corresponding to $\theta_{hkl} = 0$, and the uniformity measured by scanning the beam with a $\frac{1}{16}$ in. hole pierced in a cadmium sheet. The wavelength distribution, determined in part by the mosaic-block distribution of the monochromator, was examined by plotting the 'rocking curve', giving the counter reading in the straight-through position as a function of the angular setting of the monochromator. The most satisfactory overall results were obtained with copper. In one case the (422) plane of a copper crystal, measuring $2 \text{ in.} \times 1 \text{ in.} \times \frac{3}{8} \text{ in.}$, gave a smooth rocking curve with a full width at half-height of 20 minutes of arc; the peak count rate was $2 \times 10^5 \text{ sec}^{-1} \text{ cm}^{-2}$ at $\lambda = 1.04 \text{ \AA}$ and the intensity was uniform to $\pm 5\%$ over an area of $\frac{1}{4} \text{ in.} \times \frac{1}{4} \text{ in.}$ at the position of the sample. With the original equipment,

using the (111) plane of a lead crystal, the intensity of the monochromatic beam was only $4 \times 10^4 \text{ sec}^{-1} \text{ cm}^{-2}$, although a wider wavelength band was selected by working at $\theta_M = 11^\circ$. This poor intensity was probably due to excessive tapering of the collimating channel.

Apart from the improved resolution of high-order diffraction peaks there are other important advantages in using a monochromator angle θ_M of 45° . For elastic scattering measurements, of the type involved in crystal structure investigations, the useful working range of wavelengths is approximately 0.8 to 1.5 \AA . Below this range the neutron intensity is too weak, unless the peak of the Maxwellian spectrum is displaced to lower wavelengths by using a hot source block at the inner end of the collimating channel, and above 1.5 \AA severe difficulties arise from extinction and from second-order contamination of the neutron beam. Now for $\theta_M = 45^\circ$ the reflecting planes of the monochromator are of relatively high order and more planes are available for reflection in the range 0.8 to 1.5 \AA than for $\theta_M = 11^\circ$. This point is illustrated by the table, which lists the different wavelengths obtained by reflecting

Plane	Copper at $\theta_M = 45^\circ$					Copper at $\theta_M = 11^\circ$			Lead at $\theta_M = 11^\circ$
	(244)	(044)	(511)	(422)	(400)	(111)	(002)	(111)	
Wavelength (\AA)	0.85	0.91	0.99	1.04	1.28	0.80	0.94	1.08	

from the (*hkk*) planes of copper and lead at $\theta_M = 45^\circ$ and 11° . For copper at 45° any one of five wavelengths can be selected by rotating the crystal about $[110]$, whereas only one wavelength is available at 11° . A continuously variable neutron wavelength can be obtained by continuous variation of θ_M but this also changes the conditions for resolution; the construction of the monochromator housing is much simplified if a fixed θ_M is used, as in the present case, and a set of several discrete wavelengths is adequate for crystal structure work.

Second-order contamination of the monochromatic beam is also reduced by using high-order reflecting planes of the monochromator. For the (422) plane of copper reflecting at 1.04 \AA , contamination with the 0.52 \AA wavelength arises from simultaneous reflection at the (844) plane. In the new single-crystal assembly the 0.52 \AA neutrons represented less than 0.2% of the total number of neutrons reflected by the monochromator, and this small proportion was partly due to the influence of the temperature factor e^{-2M} in reducing the reflectivity of the (844) plane.

5. Resolution of Bragg reflections

The profiles of the diffraction peaks from a single-crystal of ThO_2 are shown in figure 3: (a) refers to reflections recorded with the original assembly and (b) with the new. The area under each peak is a measure of the integrated reflection ρ_{hkl} , which is related to the structure factor F_{hkl} by the equation

$$\rho_{hkl} = F_{hkl}^2 \text{cosec } 2\theta_{hkl}.$$

Apart from a constant scale factor the area under each peak is therefore unchanged between figure 3(a) and 3(b). The widths of the reflections in (a) increase rapidly with scattering angle and the peak heights fall in proportion, so that at high values of θ_{hkl} it is difficult to measure the integrated reflections

SINGLE-CRYSTAL NEUTRON DIFFRACTION EQUIPMENT AT THE DIDO REACTOR

accurately. By contrast, there is only a small variation of width with scattering angle in (b). In both cases the minimum width occurs, as expected, near $\theta_{hkl} = \theta_M$ (see figure 4).

increasing the beam intensity at the sample and by operating two diffractometers in place of the original one. Increasing the Bragg angle at the monochromator to 45° has improved

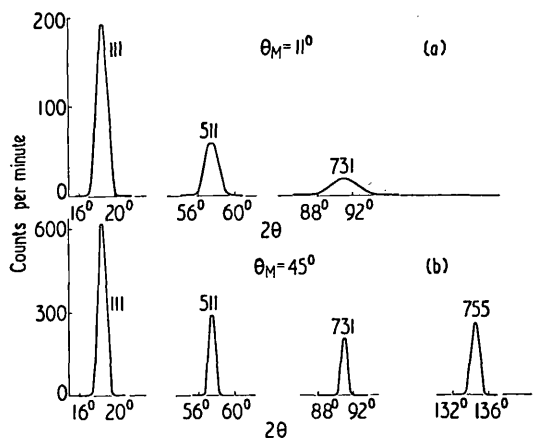


Figure 3. Profiles of a group of Bragg reflections from a single-crystal of ThO_2 . (a) Reflections recorded with the original assembly using a lead monochromator at $\theta_M = 11^\circ$; (b) reflections obtained with the new assembly using a copper monochromator at $\theta_M = 45^\circ$.

6. Conclusions

With the new single-crystal assembly greater efficiency in collecting neutron diffraction data has been achieved by

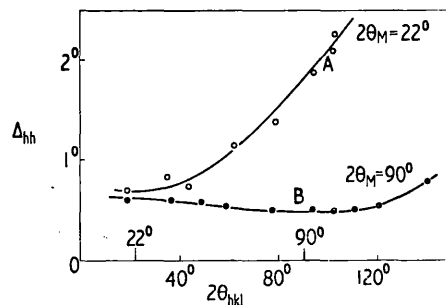


Figure 4. Half-width at half-height of Bragg reflections from ThO_2 plotted against scattering angle; A, with original assembly; B, with new: in each case the minimum width occurs near $\theta_{hkl} = \theta_M$.

the resolution of the diffraction peaks, particularly those occurring at high scattering angles, and has given a greater choice of wavelengths from the monochromator.

References

BACON, G. E., and DYER, R. F., 1959, *J. Sci. Instrum.*, **36**, 420.
 COMPTON, A. H., and ALLISON, S. K., 1935, *X-rays in Theory and Experiment* (Princeton: Van Nostrand), p. 714.
 SMITH, H. G., 1962, *Rev. Sci. Instrum.*, **33**, 128.
 WILLIS, B. T. M., 1960, *Acta Cryst.*, **13**, 763.

Use of a three-circle goniometer for diffraction measurements

B. T. M. WILLIS

Metallurgy Division, Atomic Energy Research Establishment, Harwell, Berks.

MS. received 20th July 1962

The principles governing the use of a three-circle goniometer for diffraction measurements are discussed. The vertical circle of the goniometer can be set at any arbitrary angle to the incident beam and this angle determines both the number of accessible hkl reflections and the azimuth of the (hkl) plane in the reflecting position.

1. Introduction

An increasing number of workers are using the three-circle goniometer to collect three-dimensional x-ray and neutron diffraction data. The present paper is concerned with the principles governing the use of the goniometer, bearing in mind (i) the range of reciprocal space to be explored, (ii) the necessity of measuring a reflection at different azimuthal settings of the reflecting plane. The importance of (ii) is that, in principle, diffraction measurements can be corrected for secondary extinction (Willis 1962) and for double Bragg scattering by determining the azimuthal dependence of the integrated intensity. Both these errors are particularly troublesome in neutron diffraction, but must also be considered in x-ray diffraction where accurate integrated intensities are required.

The three circles of the goniometer are usually labelled ϕ , χ , ω , but it is more convenient to use capital letters Φ , X , Ω for the circles and ϕ , χ , ω for the angles through which they turn. The detector moves around a fourth circle 2Θ concentric with Ω . A diagram of the four circles is given in figure 1. Normally X is a complete circle lying in the vertical

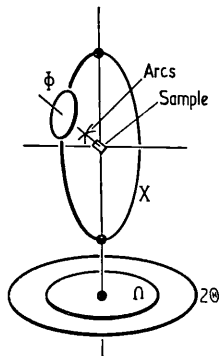


Figure 1. Diagram of the three goniometer circles Φ , X , Ω and the counter circle 2Θ .

plane and the goniometer head supporting the sample is off-set from the X -plane to allow ancillary equipment (e.g. a cryostat or furnace) to be placed around the sample. To measure a reflection with Bragg angle θ_{hkl} the three circles of the goniometer are turned to bring the (hkl) normal to the Bragg reflecting position in the horizontal plane and the detector moved to an angle $2\theta_{hkl}$ from the incident beam. The correct orientation of the crystal can be achieved with only two angular movements; by using three circles the X -plane can be set at an arbitrary angle to the incident beam,

and this arbitrariness can be exploited in considering points (i) and (ii) above.

2. Symmetrical orientation of vertical circle

2.1. Scattering vector in X -plane (A setting)

When the scattering vector* is in the X -plane ('A setting') or at right angles to the X -plane ('B setting'), the vertical circle is symmetrically related to the incident and scattered beams. The A setting is used in the 'cone diffractometer' scheme of data collection described by Furnas and Harker (1955) and is illustrated by the diagram in figure 2(a). At

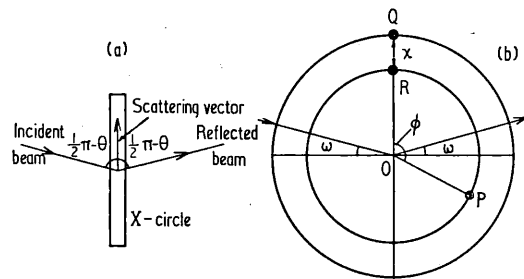


Figure 2. (a) symmetrical A setting, showing the X -circle in projection in the horizontal (equatorial) plane; (b) stereogram showing angular rotations ϕ , χ , ω required to bring hkl normal at P to reflecting position at Q .

the reflecting position the scattering vector is parallel to the line of intersection of the vertical X -plane and the horizontal equatorial plane. The stereographic projection in figure 2(b) shows the angular rotations ϕ , χ , ω required to bring the (hkl) normal at an arbitrary point P to the reflecting position Q ; these angles are measured from a standard position at which the Φ -axis is vertical and the X -axis is parallel to the incident beam. If P coincides with the centre of the stereogram at O , the (hkl) plane is normal to the Φ -axis and rotation about the Φ -axis provides continuous variation of the azimuth ψ about the scattering vector.

As $\omega (= \theta_{hkl})$ approaches 90° the X -plane obstructs the incident and reflected beams and this sets an upper limit to θ_{hkl} . For the B setting there is no such obstruction to the high-angle reflections.

* The scattering vector \mathbf{K} is defined by $\mathbf{K} = \mathbf{k} - \mathbf{k}_0$, where \mathbf{k} , \mathbf{k}_0 are the wave vectors of the scattered and incident beams respectively.

2.2. Scattering vector normal to X-plane (B setting)

Figure 3(a) shows the orientation of the X-plane with respect to the incident and scattered beams and figure 3(b)

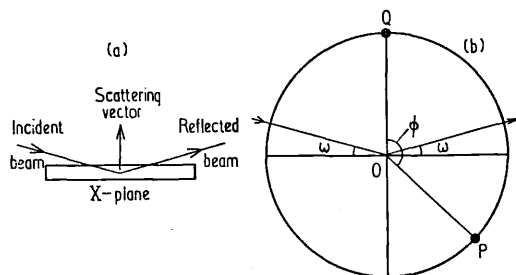


Figure 3. (a) symmetrical B setting; (b) stereogram showing angular rotations ϕ , ω required to bring hkl normal at P to reflecting position at Q.

is a stereogram illustrating the angular rotations required to bring P to the reflecting position Q. P must lie in the equatorial plane, so that two-dimensional data only can be collected. However, for each reflection rotation about the X axis, which in the reflecting position is parallel to the scattering vector, provides a 360° variation of azimuth.

3. Arbitrary orientation of vertical circle

In the general case the X-plane is at an arbitrary angle ξ to the scattering vector (figure 4(a)). To bring P to the

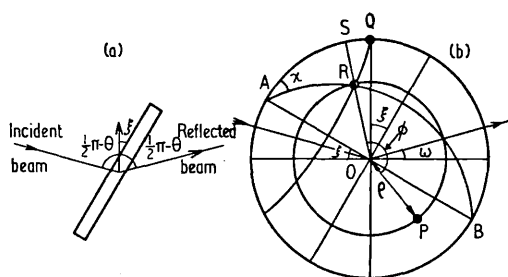


Figure 4. (a) unsymmetrical setting of X-circle; (b) stereogram showing angular rotations ϕ , χ , ω required to bring P to reflecting position Q; AB is the X-axis.

reflecting position Q (figure 4(b)) the Φ -circle is turned through $\phi = \widehat{P\hat{O}R}$, where R lies at the intersection of two small circles, one through P and normal to the vertical axis and the other through Q and normal to the X axis, AB. Rotation through χ then moves R to Q.

Let ρ be the angle OP between the (hkl) normal and the Φ -axis. In the spherical triangle ARS, $\widehat{SAR} = \chi$, $AR = 90^\circ - \xi$, $RS = 90^\circ - \rho$, so that

$$\sin \chi = \frac{\cos \rho}{\cos \xi} \quad (1)$$

This equation shows that P can be brought to the reflecting position provided $0 \leq \xi \leq \rho$. For $\xi = 0$ there is no restriction on ρ and the number of accessible planes is only limited by the wavelength and, at high scattering angles, by the size of the vertical circle (A setting). If $\xi = 90^\circ$, ρ is also 90° and the only accessible planes are those in the zone normal to the Φ -axis (B setting).

The azimuth ψ for each reflection hkl varies continuously as ξ moves in the permitted range from 0 to ρ_{hkl} . The relation between ψ and ξ is readily worked out from the

stereogram in figure 5. Here CED is a great circle representing the (hkl) plane after rotation by ϕ and R is the corresponding (hkl) normal. The χ rotation displaces R to

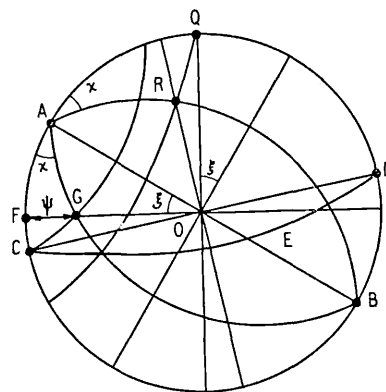


Figure 5. Stereogram showing the relation between the azimuth ψ and the angle ξ between the scattering vector and the X-circle; AB is the X axis.

Q and C to G along small circles normal to the X axis. The inclination of the vector OC to the horizontal plane is unaffected by the rotation around the Φ -circle and similarly the vector OG is unaffected by the Ω -rotation, so that the change of inclination OC to OG can be equated to ψ . Thus in the spherical triangle AFG, $FG = \psi$, $AF = \xi$, $\widehat{FAG} = \chi$ and $\tan \psi = \sin \xi \tan \chi$. Substituting for χ from (1) gives

$$\tan \psi = \frac{\sin \xi \cos \rho}{(\cos^2 \xi - \cos^2 \rho)^{1/2}} \quad (2)$$

Equation (2) shows that for a given reflection (characterized by a fixed angle ρ_{hkl}) the azimuth is 0 or 180° for $\xi = 0$ and is 90° for $\xi = \rho$. For intermediate values of ξ in the permitted range $0 \leq \xi \leq \rho$ the dependence of ψ on ξ is shown by the curves in figure 6, each curve corresponding to a fixed

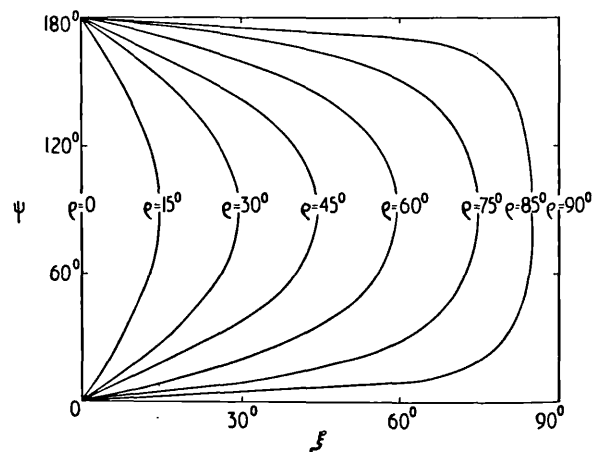


Figure 6. Dependence of azimuth of reflecting plane on the angles ξ and ρ_{hkl} .

value of ρ . For $\rho = 0$ or 180° the azimuth can take any value; for all other values of ρ the azimuth varies continuously with ξ , but as ξ changes so do the angles ϕ , χ , ω specifying the angular rotations necessary to maintain the reflecting condition. The formulae giving ϕ , χ , ω in terms of ξ and the indices hkl are derived elsewhere (B. T. M. Willis 1961, *A.E.R.E. Report R3773*).

Use of a three-circle goniometer for diffraction measurements

B. T. M. WILLIS

Metallurgy Division, Atomic Energy Research Establishment, Harwell, Berks.

MS. received 20th July 1962

The principles governing the use of a three-circle goniometer for diffraction measurements are discussed. The vertical circle of the goniometer can be set at any arbitrary angle to the incident beam and this angle determines both the number of accessible hkl reflections and the azimuth of the (hkl) plane in the reflecting position.

1. Introduction

An increasing number of workers are using the three-circle goniometer to collect three-dimensional x-ray and neutron diffraction data. The present paper is concerned with the principles governing the use of the goniometer, bearing in mind (i) the range of reciprocal space to be explored, (ii) the necessity of measuring a reflection at different azimuthal settings of the reflecting plane. The importance of (ii) is that, in principle, diffraction measurements can be corrected for secondary extinction (Willis 1962) and for double Bragg scattering by determining the azimuthal dependence of the integrated intensity. Both these errors are particularly troublesome in neutron diffraction, but must also be considered in x-ray diffraction where accurate integrated intensities are required.

The three circles of the goniometer are usually labelled ϕ , χ , ω , but it is more convenient to use capital letters Φ , X , Ω for the circles and ϕ , χ , ω for the angles through which they turn. The detector moves around a fourth circle 2Θ concentric with Ω . A diagram of the four circles is given in figure 1. Normally X is a complete circle lying in the vertical

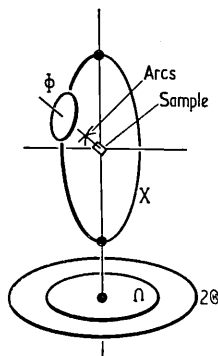


Figure 1. Diagram of the three goniometer circles Φ , X , Ω and the counter circle 2Θ .

plane and the goniometer head supporting the sample is off-set from the X -plane to allow ancillary equipment (e.g. a cryostat or furnace) to be placed around the sample. To measure a reflection with Bragg angle θ_{hkl} the three circles of the goniometer are turned to bring the (hkl) normal to the Bragg reflecting position in the horizontal plane and the detector moved to an angle $2\theta_{hkl}$ from the incident beam. The correct orientation of the crystal can be achieved with only two angular movements; by using three circles the X -plane can be set at an arbitrary angle to the incident beam,

and this arbitrariness can be exploited in considering points (i) and (ii) above.

2. Symmetrical orientation of vertical circle

2.1. Scattering vector in X -plane (A setting)

When the scattering vector* is in the X -plane ('A setting') or at right angles to the X -plane ('B setting'), the vertical circle is symmetrically related to the incident and scattered beams. The A setting is used in the 'cone diffractometer' scheme of data collection described by Furnas and Harker (1955) and is illustrated by the diagram in figure 2(a). At

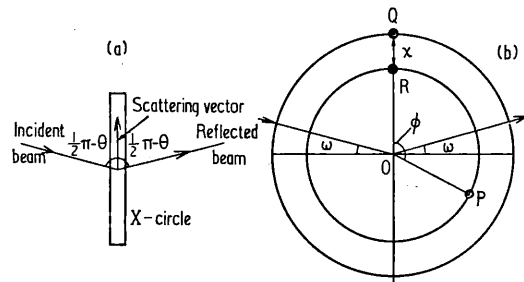


Figure 2. (a) symmetrical A setting, showing the X -circle in projection in the horizontal (equatorial) plane; (b) stereogram showing angular rotations ϕ , χ , ω required to bring hkl normal at P to reflecting position at Q.

the reflecting position the scattering vector is parallel to the line of intersection of the vertical X -plane and the horizontal equatorial plane. The stereographic projection in figure 2(b) shows the angular rotations ϕ , χ , ω required to bring the (hkl) normal at an arbitrary point P to the reflecting position Q; these angles are measured from a standard position at which the Φ -axis is vertical and the X -axis is parallel to the incident beam. If P coincides with the centre of the stereogram at O, the (hkl) plane is normal to the Φ -axis and rotation about the Φ -axis provides continuous variation of the azimuth ψ about the scattering vector.

As $\omega (= \theta_{hkl})$ approaches 90° the X -plane obstructs the incident and reflected beams and this sets an upper limit to θ_{hkl} . For the B setting there is no such obstruction to the high-angle reflections.

* The scattering vector \mathbf{K} is defined by $\mathbf{K} = \mathbf{k} - \mathbf{k}_0$, where \mathbf{k} , \mathbf{k}_0 are the wave vectors of the scattered and incident beams respectively.

USE OF A THREE-CIRCLE GONIOMETER FOR DIFFRACTION MEASUREMENTS

2.2. Scattering vector normal to X-plane (B setting)

Figure 3(a) shows the orientation of the X-plane with respect to the incident and scattered beams and figure 3(b)

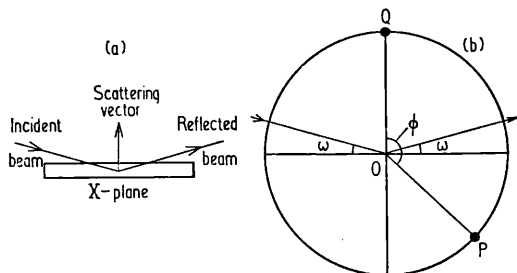


Figure 3. (a) symmetrical B setting; (b) stereogram showing angular rotations ϕ , ω required to bring hkl normal at P to reflecting position at Q.

is a stereogram illustrating the angular rotations required to bring P to the reflecting position Q. P must lie in the equatorial plane, so that two-dimensional data only can be collected. However, for each reflection rotation about the X axis, which in the reflecting position is parallel to the scattering vector, provides a 360° variation of azimuth.

3. Arbitrary orientation of vertical circle

In the general case the X-plane is at an arbitrary angle ξ to the scattering vector (figure 4(a)). To bring P to the

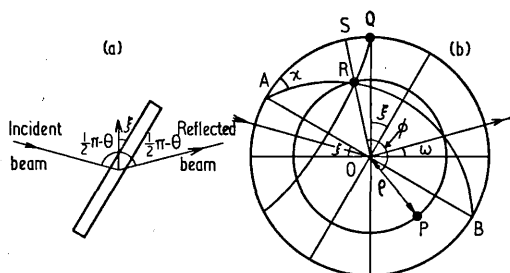


Figure 4. (a) unsymmetrical setting of X-circle; (b) stereogram showing angular rotations ϕ , χ , ω required to bring P to reflecting position Q; AB is the X-axis.

reflecting position Q (figure 4(b)) the Φ -circle is turned through $\phi = \hat{P}OR$, where R lies at the intersection of two small circles, one through P and normal to the vertical axis and the other through Q and normal to the X axis, AB. Rotation through χ then moves R to Q.

Let ρ be the angle OP between the (hkl) normal and the Φ -axis. In the spherical triangle ARS, $\hat{S}AR = \chi$, $AR = 90^\circ - \xi$, $RS = 90^\circ - \rho$, so that

$$\sin \chi = \frac{\cos \rho}{\cos \xi} \quad (1)$$

This equation shows that P can be brought to the reflecting position provided $0 \leq \xi \leq \rho$. For $\xi = 0$ there is no restriction on ρ and the number of accessible planes is only limited by the wavelength and, at high scattering angles, by the size of the vertical circle (A setting). If $\xi = 90^\circ$, ρ is also 90° and the only accessible planes are those in the zone normal to the Φ -axis (B setting).

The azimuth ψ for each reflection hkl varies continuously as ξ moves in the permitted range from 0 to ρ_{hkl} . The relation between ψ and ξ is readily worked out from the

stereogram in figure 5. Here CED is a great circle representing the (hkl) plane after rotation by ϕ and R is the corresponding (hkl) normal. The χ rotation displaces R to

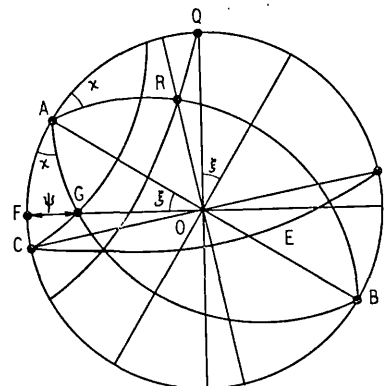


Figure 5. Stereogram showing the relation between the azimuth ψ and the angle ξ between the scattering vector and the X-circle; AB is the X axis.

Q and C to G along small circles normal to the X axis. The inclination of the vector OC to the horizontal plane is unaffected by the rotation around the Φ -circle and similarly the vector OG is unaffected by the Ω -rotation, so that the change of inclination OC to OG can be equated to ψ . Thus in the spherical triangle AFG, $FG = \psi$, $AF = \xi$, $\hat{F}AG = \chi$ and $\tan \psi = \sin \xi \tan \chi$. Substituting for χ from (1) gives

$$\tan \psi = \frac{\sin \xi \cos \rho}{(\cos^2 \xi - \cos^2 \rho)^{1/2}} \quad (2)$$

Equation (2) shows that for a given reflection (characterized by a fixed angle ρ_{hkl}) the azimuth is 0 or 180° for $\xi = 0$ and is 90° for $\xi = \rho$. For intermediate values of ξ in the permitted range $0 \leq \xi \leq \rho$ the dependence of ψ on ξ is shown by the curves in figure 6, each curve corresponding to a fixed

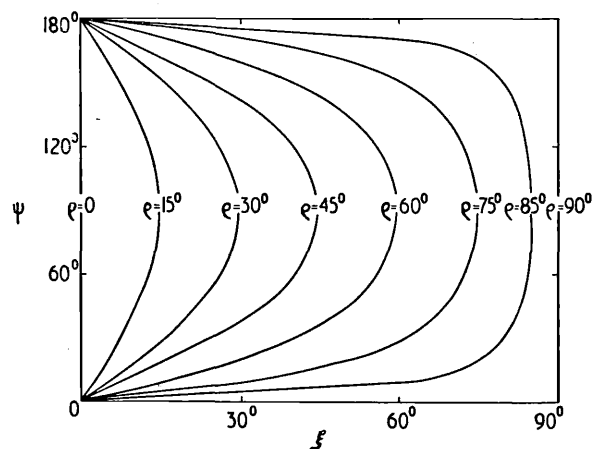


Figure 6. Dependence of azimuth of reflecting plane on the angles ξ and ρ_{hkl} .

value of ρ . For $\rho = 0$ or 180° the azimuth can take any value; for all other values of ρ the azimuth varies continuously with ξ , but as ξ changes so do the angles ϕ , χ , ω specifying the angular rotations necessary to maintain the reflecting condition. The formulae giving ϕ , χ , ω in terms of ξ and the indices hkl are derived elsewhere (B. T. M. Willis 1961, *A.E.R.E. Report R3773*).

USE OF A THREE-CIRCLE GONIOMETER FOR DIFFRACTION MEASUREMENTS

The two methods of setting a crystal on a three-circle goniometer described recently by Wooster and Wooster (1962) are special cases of the general case discussed here. The first case, with $\chi = 90^\circ - \rho$, corresponds to $\xi = 0$ (equation 1) and the second, with $\chi = 90^\circ$, to $\xi = \rho$. They therefore correspond to the two settings of ξ at the extreme ends of its permitted range.

4. Conclusions

The symmetrical A setting allows maximum exploration of reciprocal space, whereas only one plane in reciprocal space can be investigated with the symmetrical B setting. On the other hand, the B setting is useful for studying the dependence of the integrated reflection on the azimuth of the reflecting plane. If the vertical circle is set at an arbitrary angle ξ to the incident beam, the number of accessible planes lies between these two extremes.

A convenient way of estimating the reliability of intensity data is to repeat the measurements at two different values of ξ . The azimuth of the reflecting plane is altered by changing ξ , so that systematic errors arising from double Bragg scattering or secondary extinction can be detected and then eliminated by carrying out further measurements with the B setting.

References

- FURNAS, T. C., and HARKER, D., 1955, *Rev. Sci. Instrum.*, **26**, 449.
WILLIS, B. T. M., 1962, *Pile Neutron Research in Physics* (Vienna: International Atomic Energy Agency), p. 455.
WOOSTER, W. A., and WOOSTER, A. M., 1962, *J. Sci. Instrum.*, **39**, 103.

Reprinted from THE REVIEW OF SCIENTIFIC INSTRUMENTS, Vol. 34, No. 3, 224-230, March, 1963
Printed in U. S. A.

Automatic Neutron Diffractometer for Three-Dimensional Structure-Factor Determination*

U. W. ARNDT

Medical Research Council, The Royal Institution, 21 Albemarle Street, London, W.1., England

AND

B. T. M. WILLIS

Metallurgy Division, Atomic Energy Research Establishment, Harwell, Didcot, Berks, England

(Received 15 October 1962; and in final form, 26 November 1962)

This fully automatic single-crystal diffractometer employs the Eulerian hoop geometry. It is under punched-tape control and the three independent shafts are set simultaneously for each reflection to an accuracy of 0.03° using a moiré fringe positioning system. The reflection is then measured by moving the crystal in steps across the reflecting position. The time on each step is variable, being determined by a monitoring counter, and the number of steps is under program control. Results are both printed in plain language and punched on a paper tape, ready for direct processing in a computer.

I. INTRODUCTION

THE collection of neutron diffraction data from a single crystal is a costly and lengthy process, and it is highly desirable to use the neutron beam continuously during the running time of the reactor. This means that the process of data collection must be made automatic.

The techniques of single-crystal neutron diffractometry are derived from the older methods of x-ray counter diffractometry.¹⁻⁵ A wide variety of geometrical arrangements have been employed in single-crystal diffractome-

¹ W. Cochran, *Acta Cryst.* 3, 268 (1950).

² H. T. Evans, *Rev. Sci. Instr.* 24, 156 (1953).

³ U. W. Arndt and D. C. Phillips, *Acta Cryst.* 14, 807 (1961).

⁴ J. Clastre, *Acta Cryst.* 13, 986 (1960).

⁵ T. C. Furnas and D. Harker, *Rev. Sci. Instr.* 26, 449 (1955).

* Work performed under the auspices of the U.K.A.E.A. Research Group, Harwell.

TABLE I. Some geometrical arrangements for single-crystal diffractometers.

Method	Crystal axes	Detector axes	References
1. Normal beam	ω (goniometer head axis, normal to incident beam) ^a	T (coincident with ω axis) ν (normal to T axis)	b
2. Equi-inclination	ω (goniometer head axis at angle $\mu = -\nu$ to incident beam) μ (inclination axis)	As for method 1	c,d,e
3. Three-circle cone method: symmetrical A setting	Φ (goniometer head axis normal to X) X (normal to Ω axis and to scattering vector) Ω (normal to incident beam)	2Θ (coincident with Ω ; turns through twice the angle of the Φ -X assembly)	f,g,h
4. Three-circle method: unsymmetrical C setting	As for 3, except X axis at arbitrary angle to scattering vector.	As for method 3	i

^a The symbols for methods 1 and 2 correspond to those used by M. J. Bueger, *Crystal Structure Analysis* (John Wiley & Sons, Inc., New York, 1960), p. 118, and for methods 3 and 4 to those recommended by U. W. Arndt and D. C. Phillips, *Acta Cryst.* 11, 509 (1958) and by B. T. M. Willis, see footnote i.

^b See reference 1.

^c See reference 2.

^d See reference 3.

^e See reference 4.

^f See reference 5.

^g W. A. Wooster and A. M. Wooster, *J. Sci. Instr.* 39, 103 (1962).

^h H. A. Levy and W. R. Busing, 1962 (private communication).

ⁱ B. T. M. Willis, U.K.A.E.A. Report R.3773 (1961).

ters, but in nearly all such instruments two separate functions must be provided for the setting of the crystal and detector for a particular Bragg reflection, and the measurement of the integrated intensity of that reflection. In the course of a single structure determination some thousands of reflections may have to be measured.

The crystal and detector require at least three degrees of rotational freedom, which may be shared between them in a variety of ways (Table I). In methods 2, 3, and 4 of Table I four axes are used but only three necessarily are independent.

The measurement of a reflection consists of moving the crystal through the reflecting range while a detector records the integrated intensity. Separate measurements must be made of the background intensity in the neighborhood of each reflection. The shielded BF₃ counters used as detectors in neutron work are heavy and bulky and it is, therefore, preferable to employ the three-circle arrangement in which the detector travels in one plane. An additional advantage of methods 3 and 4 is that both the Lorentz factor and the width of a Bragg reflection vary with the Bragg angle only.

II. THE DIFFRACTOMETER

The three-circle geometry is illustrated schematically in Fig. 1. The three circles are designated Φ , X, Ω and the single crystal is mounted on a goniometer head attached

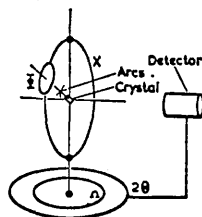


FIG. 1. Schematic diagram of crystal circles Φ , X, Ω and detector circle 2Θ .

to the small circle Φ . The Φ circle rotates about the horizontal X axis, which is normal to the Φ axis, and the Φ -X assembly rotates about the vertical Ω axis coincident with the detector axis 2Θ . Figure 2 is a general view of the diffractometer and Fig. 3 shows the Φ -X assembly.

The diffractometer was designed to be used in either method 3 or method 4 of Table I. In method 3, the normal to the reflecting plane is brought into the X plane by using the Φ circle and into the horizontal plane by rotation about the X axis. The whole Φ -X assembly is rotated an amount $\omega = \theta_{hkl}$, where θ is the Bragg angle, from the position where the X plane is perpendicular to the incident beam while the detector arm is rotated through $2\theta_{hkl}$ from the "straight-through" position. The X plane always bisects the angle between the incident and reflected beams; this "cone method" is also known as the symmetrical A setting.⁶

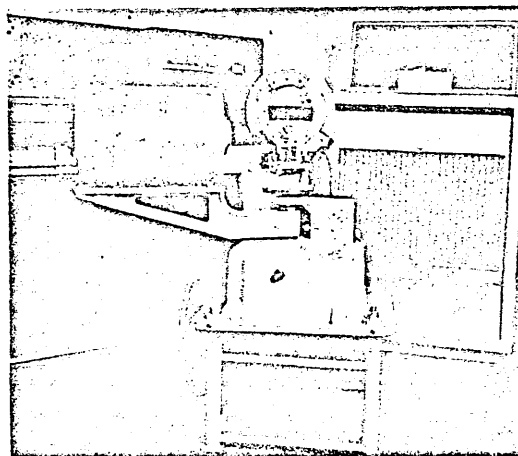


FIG. 2. General view of diffractometer. The console behind contains the input tape-reader and shaft setting circuits.

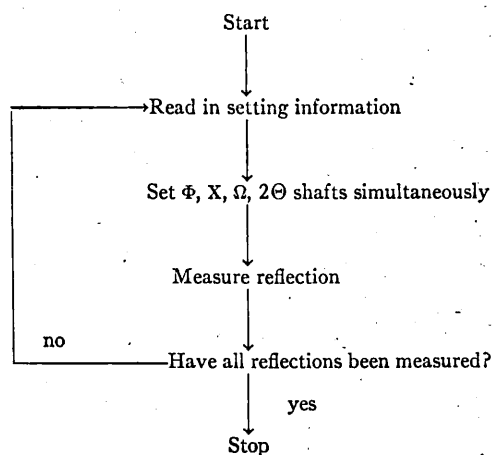
⁶ See Table I, footnote i.



FIG. 3. View of Φ -X assembly showing the circular gratings and motors. The pickup head of the Φ circle only is visible.

In the unsymmetrical C setting⁶ (method 4) the X plane is at an arbitrary angle ξ to the normal of the reflecting plane. This angle ξ enters into the expressions used for computing the setting angles ϕ , χ , ω and determines the azimuthal orientation ψ of the reflecting plane about its normal. A full 360° variation in ψ can be achieved by changing ξ ; this azimuthal variation is important in correcting for systematic errors due to absorption, secondary extinction, and double Bragg scattering. The Ω and 2Θ axes of the Mark I diffractometer are normally geared together so that the detector moves through twice the angle turned through by the Ω shaft; but for initial adjustments during the aligning procedure and for setting ξ the Ω shaft can be rotated independently of the detector arm.

TABLE II. Sequence for automatic operation.



The positions of all four shafts can be read visually; Φ and X are equipped with angle scales and verniers and Ω and 2Θ with optical scales. In addition, circular moiré fringe gratings and photoelectric pickup heads are provided for Φ , X, and Ω for automatic setting. The gratings for Φ and X and the pickup head for Φ can be seen in Fig. 3; the Ω grating and its pickup head are mounted inside the main base of the instrument.

The circles are motor-driven *via* worms and worm wheels at speeds of about $2^\circ/\text{sec}$. Backlash in the gear trains is reduced to less than one unit increment by spring-loading the final gears. All circles are protected against over-travel by suitable limit switches.

For correct functioning of the machine it is essential, with the detector assembly (weighing up to 100 lb) in position, that the axes intersect at a point and remain perpendicular to one another. The manufacturing tolerances are such as to ensure that the axes intersect to within 0.1 mm and are perpendicular to within $\pm 1'$ of arc. Plain bearings are used to produce the necessary rigidity.

In the A setting the maximum Bragg angle attainable is the semiangle subtended at the crystal by the inside of the X circle. This is 55° in the present design. A higher limit could have been achieved by mounting the Φ shaft in the center plane of the X circle, but this would have made it more difficult to mount a furnace or cryostat around the sample. The maximum Bragg angle available in the symmetrical B setting⁶ (for which the circles cannot obstruct the neutron beams) is 75° . Full 360° rotation is possible on both Φ and X shafts.

During the initial setting up of the sample its crystallographic axes must be aligned with respect to the X and Ω circles. This can be done by using the arcs of the goniometer head on which it is mounted. The crystal (Φ) shaft, which has an axial adjustment of $\frac{1}{2}$, has a fitting suitable for a goniometer head as laid down by the Apparatus Commission of the International Union of Crystallography.⁷ The angular position of the goniometer head axis with respect to the zero mark of the Φ circle must be adjustable; for this reason the worm for the Φ circle can be disengaged and the circle rotated by hand. The final adjustment can be made by setting the datum of the positioning circuits (see below).

III. AUTOMATIC OPERATION

The flow sheet in Table II illustrates the sequence followed in the automatic collection of intensity data. In the following subsections the various steps in this sequence are described in detail. We shall have occasion to refer to the various components of the apparatus, and these, together with their interconnections, are shown in block schematic form in Fig. 4.

⁷ Specification in *Acta Cryst.* 9, 376 (1956).

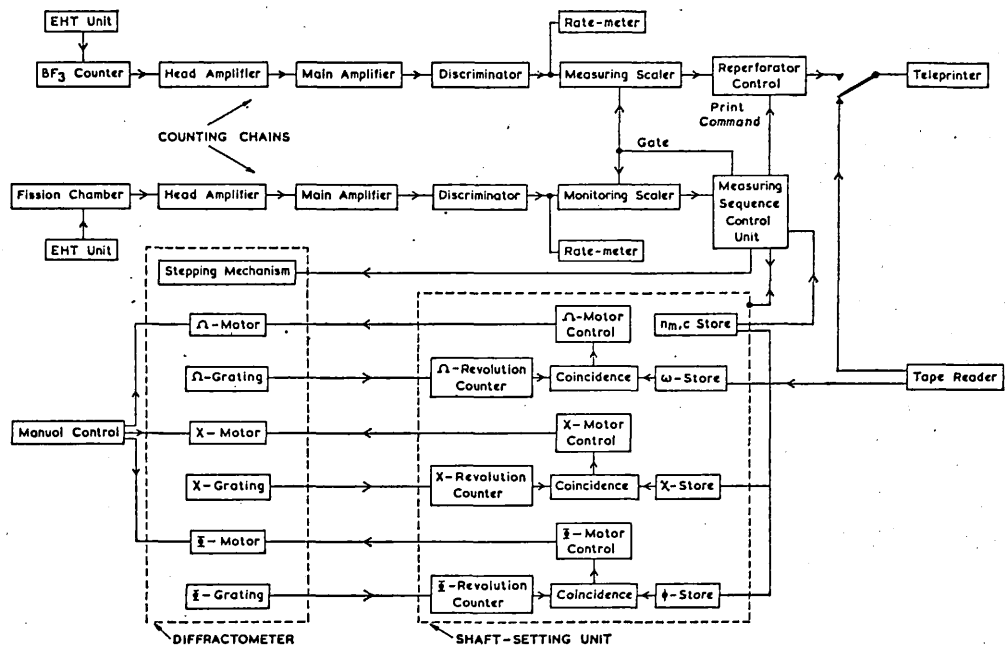


FIG. 4. Block schematic diagram of complete assembly.

The three crystal shafts Φ , X , Ω must be set individually to an accuracy of about $2'$. The most convenient automatic shaft setting system which allows this precision to be achieved directly (i.e., without having to rely on the accuracy of a gear train) is based on the use of circular moiré fringe gratings. It is particularly advantageous that the moving part of the grating can be a ring with a hollow center. The setting circuits, which were constructed by Ferranti Ltd., are a modification of their standard machine-tool setting system.⁸

A. Read-In Sequence

The settings of the three shafts are worked out on a Ferranti Mercury computer, which is programmed to punch out the angles in the form shown in Table III. The tape also includes, for each reflection, a single-decimal digit number N which determines the number of times the reflection is to be measured, and a two-decimal digit number R which defines the scanning range.

This 5-hole punched tape in Ferranti Pegasus/Mercury code is read into the setting circuit on a Creed model 92 tape reader and copied on a Creed model 75 teleprinter, which has a parallel input and is fitted with a reperforating attachment. The characters are read in and action is taken on recognition of the following code combinations:

"n" is the initiating symbol of the block of 24 characters containing the setting information for one reflection. Any code characters preceding "n" are simply copied from the input tape onto the output teleprinter; the input tape can

thus contain the indices of the reflection and any other information needed in the subsequent processing of the output tape. During read-in a format check is applied.

λ (letter-shift). Any information following this symbol is disregarded until the next figure-shift symbol has been read in.

\rightarrow (arrow). If this character appears after the character "n" the read-in sequence is halted and can only be re-started manually.

The next five characters, numbers 3-7 in Table III, are the five-decimal digit number, starting with the most significant digit, representing the absolute setting of the Ω shaft in multiples of $2'$. These digits are decoded and stored on miniature uniselectors. Similarly the X and Φ settings are read in and stored, checks being applied that "space" appears in the correct positions. The auxiliary digits N , R_1 , R_2 are also stored and used during the measuring sequence.

TABLE III. Setting information for one reflection.

Character number	Character	Meaning
1	n	Initiating symbol
2	space	
3-7	$\omega_1 \omega_2 \omega_3 \omega_4 \omega_5$	Absolute position of Ω shaft
8	space	
9-13	$\chi_1 \chi_2 \chi_3 \chi_4 \chi_5$	Absolute position of X shaft
14	space	
15-19	$\phi_1 \phi_2 \phi_3 \phi_4 \phi_5$	Absolute position of Φ shaft
20	space	
21	N	Number of measuring cycles
22-23	$R_1 R_2$	Scanning range
24	CR (carriage return)	

⁸ D. T. N. Williamson, Progr. in Automation 1, 127 (1960).

B. Shaft Setting

When all the setting information for one reflection is read in, the input tape is arrested and the output teleprinter is switched to the output of the measuring scaler. Analog circuitry, associated with the absolute position registers for the three shafts, now senses the direction of rotation required for each shaft to turn it from its existing to the desired position and the motors commence to drive simultaneously. Stationary photoelectric pickup heads associated with each shaft generate pulses as the moiré fringes pass them, one pulse being added to or subtracted from the five-decade reversible ring counter (absolute position register) for every $2'$. For each shaft, when coincidence is detected between the number set up on the appropriate uniselector store and the current contents of the ring counter, the corresponding motor is arrested: a single-overshoot slow return system then brings the circle to the correct position within one unit increment of $2'$. A ternary check system in the reversible ring counters ensures their correct functioning; in the case of a fault the sequence is interrupted, a fault light is lit, and the operator's intervention is required to restart the equipment. All four shafts are thus set simultaneously, 2:1

TABLE IV. Flow sheet when stationary on background (mode A).

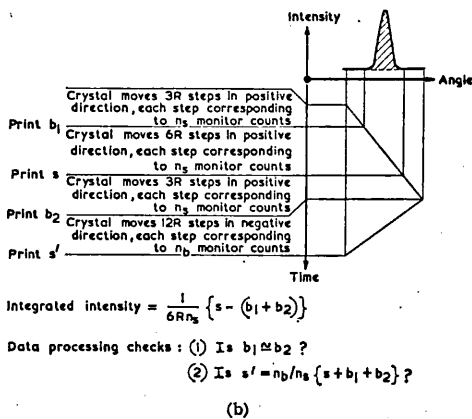
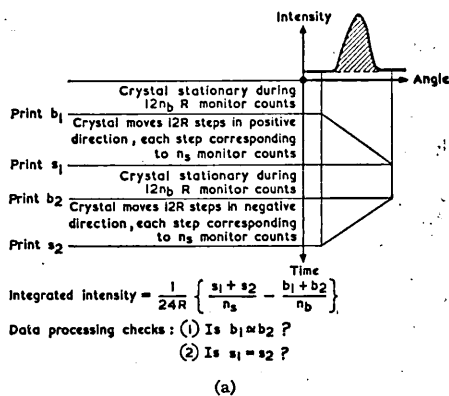
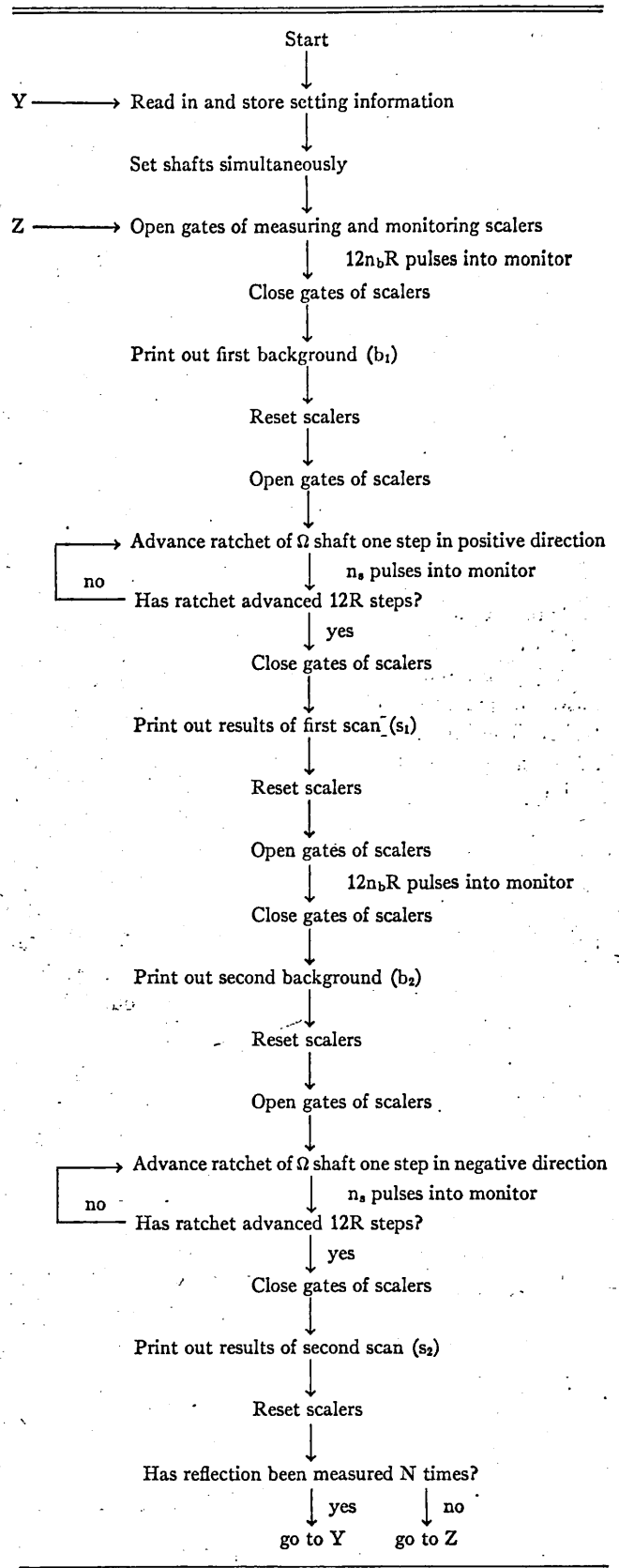


FIG. 5. (a) Measurement of one reflection in mode A. (b) Measurement of one reflection in mode B.

gearing between the Ω shaft and the detector arm having positioned the 2Θ shaft correctly.

During the alignment procedure the zero point of each circle is determined by locating the peaks of one or more suitable reference reflections and then returning the circles to their zero points by rotating them through calculated angles. At this stage the ring counters are used simply as difference indicators. When the datum points have been reached the ring counters are reset by pressing the appropriate "Set Datum" push buttons. From then on the counters register the absolute positions of their circles relative to these datum points. If the equipment is switched off, the zero points are lost and have to be redetermined before proceeding with automatic operation.

C. Measuring Sequence

The reflection is now measured under the control of the measuring sequence controller. Figures 5(a) and 5(b) illustrate the two modes in which this can be done. In mode A the background is measured with the crystal stationary, as illustrated by Fig. 5(a) and the flow sheet of Table IV, and in mode B the background is measured with the crystal moving, as shown in Fig. 5(b). The appropriate mode for the problem in hand is selected by means of a key switch on the measuring sequence controller. The integrated intensity of the reflection, defined as the area under the curve relating diffracted intensity and crystal angle ω , is shown shaded in Fig. 5, duly corrected for background.

In practice, since the incident neutron intensity may vary, the direct beam is monitored by a low-efficiency fission chamber and the crystal is moved through the reflecting position in a number of $\frac{1}{2}'$ steps. The crystal remains stationary between steps for a period determined by the accumulation of a preset number of counts in the

monitoring scaler. The stepping is effected by means of a solenoid-operated bidirectional ratchet mechanism.

The total number of steps across the reflection is under program control and is determined by the number R ; its value is computed from an analytical expression giving the approximate width of the reflection as a function of its Bragg angle.⁹

The scaling ratios of the monitoring scaler can be altered between the measurement of the background and of the peak. They are determined by the values of n_m and c (see Table V), which are set by means of decade hand-switches on the measuring sequence controller. In general, the value of n_m will be chosen from considerations of the total time which it is desired to spend on each reflection and the value of c from the expected peak-to-background ratio. The various parameters under program or manual control are summarized in Table VI.

The operation of the measuring sequence control circuit is normally initiated by a contact closure in the shaft setting circuit which signals that all three shafts have been set. In this case the quantities N , R for each reflection are specified on the input tape. Alternatively, the sequence can be started manually when measuring a single reflection; N and R are then selected by means of decade hand-switches. The circuit of the measuring sequence controller provides the necessary gating, print-out, resetting, and synchronizing signals to the scalers; in addition, by means of uniselector counters and relays, it times the different steps in the measuring sequence. During the measuring cycles the teleprinter is switched to the output of the measuring scaler so as to record the intensities of the peak and background. At the end of the specified number of cycles N , the teleprinter is switched back to the input channel and a contact closure restarts the input tape reader.

TABLE V. Setting and measuring parameters.

Parameter	Form	Meaning	Units	On punched tape?	Under manual control
ω	5 decimal digits	Absolute position of Ω circle	2'	yes	Decade switches on shaft-setting console
χ	5 decimal digits	Absolute position of X circle	2'	yes	Decade switches on shaft-setting console
ϕ	5 decimal digits	Absolute position of Φ circle	2'	yes	Decade switches on shaft-setting console
N	1 decimal digit	Number of measuring cycles		yes	Hand switch on measuring sequence controller
R	2 decimal digits	Stepping range	6'	yes	Hand switch on measuring sequence controller
n_m	2 decimal digits	n_m and c determine scaling rate of monitoring scaler: on background $n_b = 10n_m$ and on peak $n_p = c10n_m$.	6'	no	Decade switch on monitoring scaler
c	1 decimal digit			no	Decade switch on monitoring scaler

⁹ B. T. M. Willis, Acta Cryst. 13, 763 (1960).

TABLE VI. Format of printout of measured intensities.

CR LF six digits SP (background on left of peak)	SP six digits SP (scan from left to right)	SP six digits SP (background on right of peak)	SP six digits (scan from right to left)
---	---	---	--

D. Monitoring Scaler

A block diagram of the monitoring scaler is shown in Fig. 6. The input stage consists of four hard-valve flip-flops with feedback to produce a scale of ten; subsequent stages are 4-kc Dekatron selector tubes driven by double-triode pulse-shaping circuits.

E. Measuring Scaler

The solid-state measuring scaler is a standard digital microsecond chronometer/counter (Venner type TSA 3336), together with a modified reperforator unit (Venner type TSA 101). The latter translates the binary-coded decimal input from the counter decades into 5-bit Ferranti Pegasus/Mercury code and presents this in serial form, together with lay-out symbols, to the 5-wire input teleprinter, to produce the format shown in Table VI. The solid-state sampling ring circuit is synchronized at $11\frac{1}{2}$ characters/sec by timing contacts on the teleprinter.

The measuring scaler is reset automatically after each print out, but for test purposes the displayed count can be held until manually canceled. Appropriate synchronizing signals are supplied by the reperforator control unit to the measuring sequence controller, so that the latter can initiate a new count only after the previous one has been printed out.

F. Counting Chains

The remaining circuits in both measuring and monitoring counting chains are conventional A.E.R.E. 1000 series units.

The detector in the measuring chain is a BF_3 counter and in the monitoring chain a fission chamber.

The diffractometer described in this paper is the forerunner of a more versatile instrument at present under development by Ferranti Ltd. in collaboration with U.K.A.E.A. The principal changes introduced in the new design are:

(1) Provision of an "order code," covering the complete range of operations used in any scattering experiment. These operations are programmed as instructions or orders on the input data tape. Any conceivable elastic or inelastic scattering measurements can thus be programmed for automatic control.

(2) Ω and 2θ shafts are set independently.

(3) The shaft-setting is carried out sequentially by means of a common control unit. This same unit can be used to control several diffractometers.

ACKNOWLEDGMENTS

It would be difficult to list all the people who have been associated with the development of this instrument. However, our particular thanks are due to R. Causer, who has worked with R. S. Green on the mechanical design of the diffractometer and with A. Wingrove, J. Bence, and B. Kelly on the control circuitry. At all times we have enjoyed the closest cooperation from H. G. Hinckley and his staff of the Numerical Control Division, Ferranti Ltd., Edinburgh. We are deeply grateful for the encouragement and support of the Director of A.E.R.E. (Dr. F. A. Vick) and of Dr. P. Murray and J. Williams of the Metallurgy Division, A.E.R.E. One of us (U. W. A.) wishes to thank Sir Lawrence Bragg for permission to devote time to this project.

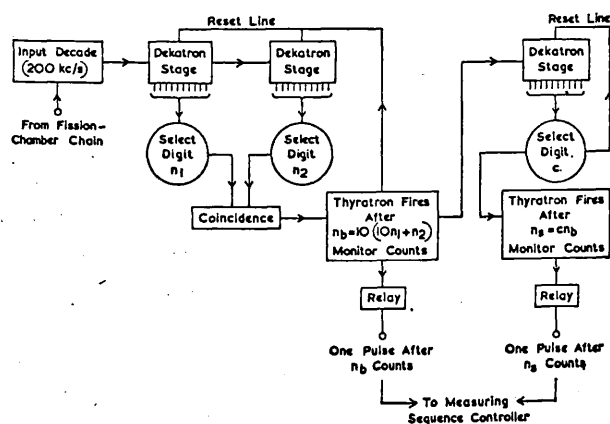


FIG. 6. Block schematic diagram of monitoring scaler.

A PROGRAMMED MULTI-CHANNEL NEUTRON DIFFRACTOMETER INSTALLATION*

U. W. ARNDT

Medical Research Council External Staff, The Royal Institution, 21 Albemarle St., London, W1

and

B. T. M. WILLIS

Metallurgy Division, Atomic Energy Research Establishment, Harwell, Didcot, Berks., England

Received 21 February 1963

The principal feature in the design of this installation is the provision of an order code allowing a large range of scattering experiments to be carried out under automatic control. It is possible to set up to sixteen shafts, which are shared between

a number of independent instruments. The standard instrument is a four-circle diffractometer, whose main features are briefly described.

1. Introduction

The techniques used for the collection of three-dimensional structure-factor data have been discussed earlier¹). It was shown that a convenient way of collecting data automatically is by means of a three-circle diffractometer, which permits rotation of the crystal about the three Eulerian axes ϕ , X and Ω ; the detector rotates about the 2θ axis, geared to move through twice the angle of the Ω -axis. Such an instrument has to carry out two distinct functions: the setting of the three crystal axes and of the coupled detector axis to pre-computed positions for each reflexion, and the actual measurement of that reflexion. The measurement involves the determination of the background on each side of the Bragg peak and the total intensity across the peak, recorded by stepping the crystal through the reflecting range.

This automatic instrument (described in ref.¹) and known as the Mark I diffractometer) allows the collection of three-dimensional data with much greater speed and convenience than a manually operated diffractometer, but there is a need for a more flexible system, designed to permit a variety of scattering experiments, including routine structure-factor measurements, to be carried out under automatic control. Such a system (Mark II) is

described in this paper. The installation will not be fully operational until late 1963 but a description of its principal design features at this stage may be of interest.

2. Special Design Considerations

2.1. MEASUREMENT OF HIGH-ANGLE REFLEXIONS

In the cone-method²) of setting, the maximum Bragg angle at which a reflexion can be measured is the semi-angle subtended by the inside of the X -circle at the crystal. To measure reflexions at higher angles the unsymmetrical C-setting^{3,4}) must be used in which the plane of the X -circle no longer bisects the angle between the incident and diffracted beams. In this method the Ω and 2θ -axes must not be geared together, as in the earlier instrument, but must be capable of being set independently under programme control.

2.2. CORRECTION FOR ABSORPTION, EXTINCTION AND DOUBLE BRAGG SCATTERING

Bragg's law allows the crystal at the reflecting position to have one degree of freedom, that of rotation about the scattering vector. The intensity

¹) U. W. Arndt and B. T. M. Willis, *Rev. Sci. Instr.* **34** (1963) 224.

²) T. C. Furnas and D. Harker, *Rev. Sci. Instr.* **26** (1955) 449.

³) B. T. M. Willis, *Brit. J. Appl. Phys.* **13** (1962) 548.

⁴) W. A. Wooster and A. M. Wooster, *J. Sci. Instr.* **39** (1962) 103.

* Work performed under the auspices of the UKAEA Research Group, Harwell.

diffracted by a non-absorbing, ideally imperfect crystal is independent of this azimuthal angle. However, in the presence of absorption or extinction or both, rotation of a non-spherical crystal varies the path-length of radiation through the crystal and causes a variation in intensity. A study of this variation with azimuthal angle permits an experimental correction for absorption and extinction⁵).

Double Bragg scattering can occur whenever a second reciprocal lattice point lies on the sphere of reflexion⁶); rotation of the crystal about the scattering vector allows the first reciprocal lattice point to remain on the surface of the sphere while all other points may pass through this surface. The presence of double Bragg scattering may often introduce unknown errors into intensity measurements, especially in neutron diffraction where the wavelength spread and depth of penetration of the incident beam are larger than for X-rays⁷). This phenomenon also can be studied by varying the azimuthal angle, and can be readily distinguished from absorption or extinction effects which give only a slow variation of intensity with azimuth.

The rotation about the scattering vector can be resolved into component rotations about the Φ , X and Ω -axes. The search for systematic errors is thus greatly facilitated by automatic registration of the diffracted intensity after programmed rotations about the three crystal axes. Again this requires that the Ω - and 2θ -axes are set independently.

2.3. MOUNTING OF CRYSTAL WITHOUT GONIOMETER HEAD

The normal method of mounting a crystal on a goniometer head, consisting of two arcs at right-angles and a pair of cross-slides, is convenient in that it allows an aligned crystal to be transferred from one instrument to another, e.g. from an optical goniometer to a diffractometer. On the other hand, the goniometer head necessarily offers some obstruction to the incident and diffracted beams and complicates the mounting of a furnace or cryostat around the specimen. (The three crystal shafts of the diffractometer already offer complete rotational freedom of the crystal and the goniometer arcs are strictly unnecessary.) It was therefore de-

vised to design the new diffractometer for operation both with and without goniometer arcs by incorporating an axial adjustment of one inch on the Φ -shaft. In principle, the initial setting of a crystal can be made completely automatic if the rotation of the crystal shafts is controlled by a computer capable of receiving current information of the scattered intensity.

2.4. USE OF ANALYSING CRYSTAL

In neutron diffraction it is often advantageous to place an analysing crystal between the sample and detector. It is then possible to separate the elastic and inelastic components of scattering; thus the Bragg reflexions can be measured in the absence of phonon scattering, which can cause errors of 20% or more in the measured intensities⁸), or alternatively the frequency/wavelength relationship of the normal modes of vibration can be investigated⁹) by

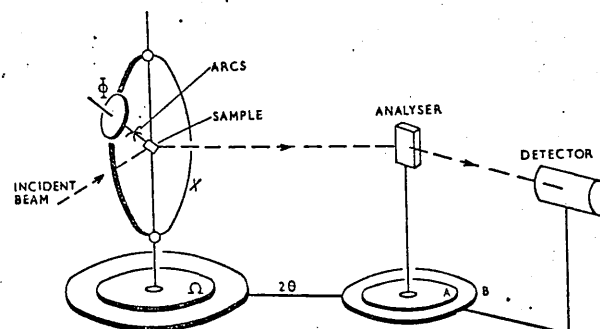


Fig. 1. Sketch of six circles: three for the sample, two for the analyser and one for the detector.

examining the neutrons scattered inelastically. For experiments of this type it is necessary under automatic operation to have the rotation of the analysing crystal and detector brought under programme control. Fig. 1 is a diagram of six possible axes to be controlled; three for the sample (Φ , X , Ω), two for the analyser and analyser arm (A, B) and one for the detector arm (2θ).

⁵) B. T. M. Willis, Proceedings of Conference on "Fibre Neutron Research in Physics" (International Atomic Energy Agency, Vienna 1962), p. 455.

⁶) M. Renninger, Z. phys. 106 (1937) 141.

⁷) B. T. M. Willis, UKAEA Report R3959 (1962).

⁸) N. Nilsson, Arkiv. för Fysik 12 (1957) 247.

⁹) B. N. Brockhouse, Proceedings of Conference on "Inelastic scattering in solids and liquids" (International Atomic Energy Agency, Vienna, 1962).

2.5. PROVISION OF SPECIAL FACILITIES

In some scattering experiments it may be necessary to carry out measurements, over a range of temperatures, in others in the presence or absence of magnetic fields. For completely automatic operation the temperature of the sample, the strength and orientation of a magnetic field etc., will be under programme control.

2.6. ON-LINE CONTROL BY A COMPUTER

The operation of the earlier instrument¹⁾ is necessarily of the open-loop type. A punched paper tape is prepared on an external digital computer, which computes, for instance, the crystal settings from the cell dimensions of the crystal. The diffractometer then carries out its programme of measurements under the control of this setting tape and records its output both in printed form and on a second output punched tape. When all the measurements have been made they are analysed by an external computer. From the results of this analysis a new setting tape can be prepared which, for example, may instruct the diffractometer to repeat the measurement of weak reflexions using longer counting times.

Clearly the complete process of measuring reflexions to a given statistical accuracy can be carried out more rapidly if the output of the diffractometer is coupled directly into the input of a digital computer. The computer can make any necessary decisions as to remeasurement under different conditions or correcting the crystal setting before moving to the next reflexion. With modern computers the time to make such decisions is very small compared with the time necessary to accumulate statistically significant neutron counts on which to base such decisions. It thus seems desirable that the computer control of a diffractometer should be carried out by a time-sharing computer, only one of whose tasks is the control of one particular instrument. While the actual computing time spent on problems of control would be very short, a considerable amount of storage capacity would be used in storing the sub-routines for dealing with the various operational contingencies. For on-line control a small or medium-size computer would therefore be uneconomical. Only a large time-

sharing computer possesses the organisation in its differing access-time stores to make this approach attractive, and a pilot investigation into the on-line control of an automatic X-ray diffractometer is at present in progress at Manchester University using the MUSE computer, the prototype of the Ferranti ATLAS computer¹⁰⁾.

During the design of the present installation it was felt that experience was insufficient to warrant exclusive on-line operation *ab initio* using the Harwell ATLAS computer. It must be remembered that neutron scattering experiments normally require much longer times than do corresponding X-ray investigations, so that longer periods of continuous trouble-free operation of the computer would be needed. However, the possibility of on-line control of the installation at a later date was borne in mind.

2.7. MULTI-CHANNEL OPERATION

The collimator system for the installation provides either two or four monochromatic neutron beams originating from a single horizontal hole of the PLUTO reactor. [The arrangement is the same, in principle, as that already described¹¹⁾ for the DIDO reactor.] Experimental space near the reactor is very restricted and so the measuring and control circuits must be as compact as possible. Saving in both space and cost can be effected by time-sharing some of the control circuits between the various diffractometer channels. This sharing is all the more feasible in that for any one diffractometer the time taken to read in and decode the setting tape and to set the crystal and detector is small compared with the measuring time.

2.8. FLEXIBILITY

Neutron crystallography is an expanding field and it is difficult to foresee all the types of measurement which will be needed. There is only the certainty that they will entail the setting of a crystal and detector and the actual process of counting, possibly accompanied by slow movement of one or more shafts. The ideal installation must be flexible, to allow for future developments and demands.

¹⁰⁾ K. Bowden, D. Edwards and O. S. Mills, private communication (1962).

¹¹⁾ B. T. M. Willis, J. Sci. Instr. 39 (1962) 590.

2.9. PRINCIPAL DESIGN FEATURES

The principal requirements of the installation can now be given:

(i) Provision for setting, under programme tape control a number of independent axes, up to six per instrument.

(ii) Provision for energising, under programme control, a number of solenoids for the performance of special functions.

(iii) Possibility of either off-line or on-line operation in conjunction with a digital computer.

(iv) Provision for controlling simultaneously several diffractometers.

(v) Maximum flexibility in the choice of sub-routines and the subsequent possibility of controlling instruments of different mechanical design from the four-circle diffractometer described in the next section.

3. The Four-Circle Diffractometer

This has been designed to allow rotation of the crystal about the three Eulerian axes Φ , X and Ω and of the detector about the vertical 2θ axis, concentric with Ω . All four axes are independent and the crystal is normally, but not necessarily, mounted on a standard goniometer head. The detector arm is in two parts so that the detector bracket alone can be readily interchanged with a second bracket supporting both an analysing crystal and detector. The appearance and dimensions of this instrument are very similar to those in the earlier instrument¹). The main differences are as follows:

(i) There is no 2:1 gearing between 2θ and Ω .

(ii) All four shafts are fitted with dc motors, each with its own tachogenerator. The circles are provided with moiré fringe gratings and photo-electric pick-up heads for positioning. Each circular grating contains 3600 lines so that, with a unit of increment of one-tenth of a fringe, the accuracy of setting is $\frac{1}{100}^\circ$ on each circle. A datum reference mark must be fitted on each circle, as the positioning system is incremental rather than absolute (§4). The datum mark of the Φ -circle can be adjusted to coincide with a chosen crystal axis. The positions of the datum marks are sensed by means of a second pick-up head on each circle.

(iii) The setting motors themselves can be used to provide stepwise rotation of the shafts; thus, in particular, there is no special stepping mechanism on the Ω -shaft.

(iv) A very strong main bearing incorporating tapered roller races is provided on the 2θ shaft to permit the attachment of a detector arm carrying an analysing crystal.

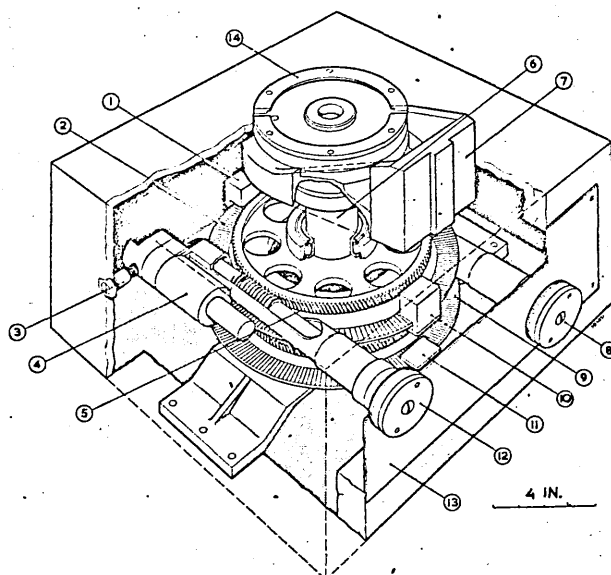


Fig. 2. Perspective view of base of diffractometer.

- | | |
|--|--|
| 1. Main pickup head on 2θ -circle. | 8. Ω -hand wheel. |
| 2. 2θ -grating. | 9. Ω -grating. |
| 3. Spring to eliminate backlash in 2θ -drive. | 10. Reference pick-up head on 2θ -circle. |
| 4. Motor and tachogenerator on 2θ -circle. | 11. Main pick-up head on Ω -circle. |
| 5. 2θ -worm wheel. | 12. 2θ -hand wheel. |
| 6. Hollow 2θ -shaft for detector arm. | 13. Removable front panel carrying control switches and sockets. |
| 7. Bracket for detector arm. | 14. Clamping ring for Φ/X assembly. |

Perspective views of the base of the instrument and of the $\Phi - X$ assembly are shown in figs. 2 and 3. The most important parts are labelled.

4. Circuits

The overall arrangement of the circuits is shown in fig. 4. The main components of this block schematic diagram are briefly described in this section.

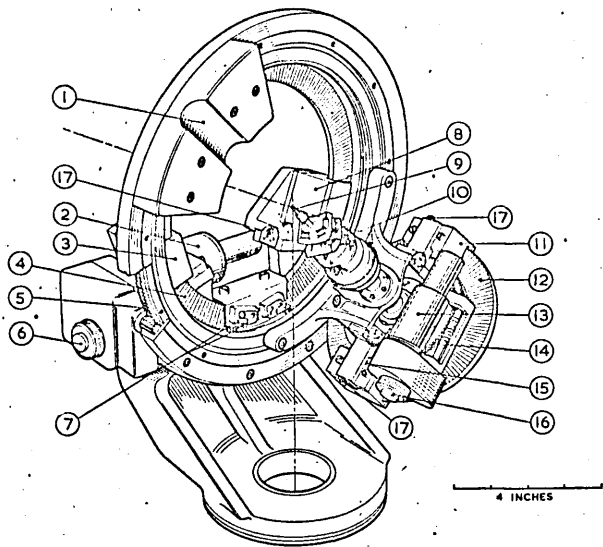


Fig. 3. The Φ/X assembly.

- | | |
|--|---|
| 1. Counterbalance of Φ -assembly. | 10. Goniometer head. |
| 2. Motor and tachogenerator on X-circle. | 11. Main pick-up head on Φ -circle. |
| 3. Main pick-up head on X-circle. | 12. Φ -grating. |
| 4. X-grating. | 13. Motor and tachogenerator on Φ -circle. |
| 5. X spur gear wheel. | 14. Φ worm wheel. |
| 6. X-micrometer head. | 15. Reference pick-up head on Φ -circle. |
| 7. Limit switches on X-circle. | 16. Φ hand wheel. |
| 8. Reference pick-up head on X-circle. | 17. Radial adjustment of pick-up head. |
| 9. Specimen. | |

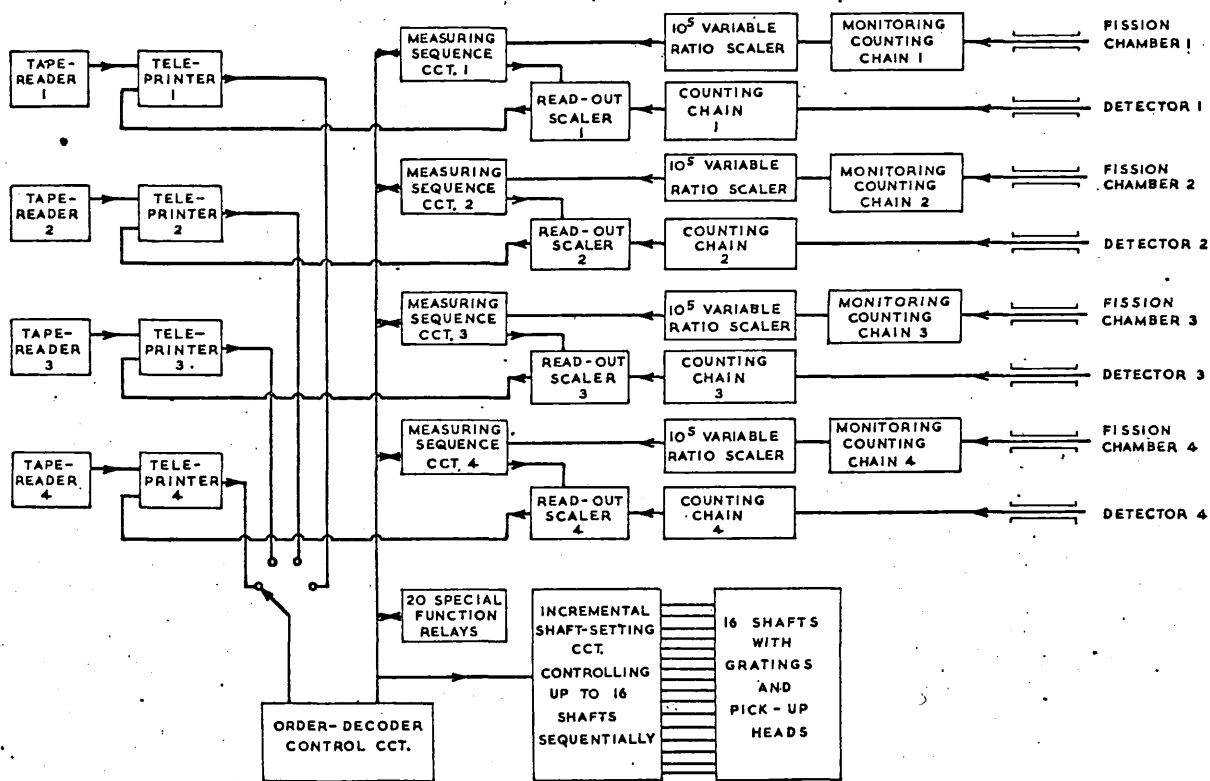


Fig. 4. Block schematic diagram of complete installation. Each counting chain consists of a pre-amplifier mounted adjacent to the detector, a main amplifier, a discriminator, a high-tension supply and a rate-meter.

4.1. INPUT CIRCUIT

The standard input circuit for each channel consists of a tape-reader reading 5-hole tape in the Ferranti PEGASUS/MERCURY code. Its output is read into a teleprinter arranged for five-wire parallel input and fitted with a reperforating attachment, keyboard and transmitting contacts. The output from the transmitting contacts is fed into a solid-state decoding circuit. All input information, therefore, is monitored by the teleprinter; during the initial setting-up procedure, and for testing purposes, the keyboard of the teleprinter can be used as an alternative input device.

The clock pulses for the solid-state routing circuits, which distribute the decoded signals to appropriate staticizers, are taken from the synchronising contacts of the teleprinter. These circuits, however, will function at a much higher clock frequency than the synchronous speed of $11\frac{1}{3}$ characters per second of the teleprinter, so that faster tape-readers can be substituted at will.

4.2. MEASURING SCALER

The scattered neutrons in each channel are detected by a neutron detector, whose output pulses are counted by a solid-state six-decade ring scaler. The output from the scaler is recorded sequentially, most significant digit first, by the teleprinter appropriate to that channel, and here, too, a faster output device may be substituted. The scaler is gated by signals from the main control circuit; closing of the counting gate initiates a print-out followed by re-setting of the scaler.

4.3. MONITORING SCALER

Clock pulses for the timing of individual counts and of steps during the scan across a reflexion are derived from a monitoring fission chamber via a scaler with a scaling ratio of up to 10^5 . The scaling ratio is under programme control and is specified in the measuring orders (§5).

In certain problems it is desirable to time a pre-set number of counts instead of counting for a pre-set time. For such cases the variable-ratio scaler is connected in the measuring chain and the read-out scaler in the monitoring chain.

4.4. OTHER COUNTING CIRCUITS

The remaining circuits in the measuring and monitoring chains are conventional AERE 2000 series circuits. It is hoped to replace these at a later date by compact fully transistorised units.

4.5. POSITIONING CIRCUITS

In the earlier instrument¹⁾ these consist of three absolute positioning circuits, one for each independent axis, capable of setting the diffractometer shafts simultaneously. The absolute position of each shaft is continuously stored on its own reversible decimal counter, and the setting information, read-in from punched tape, is the absolute position to which the shaft must move. Each new setting is stored on uniselectors and analogue circuitry derives an "error signal", as regards both sign and magnitude, from a comparison of the existing and the new absolute positions; the motor then turns the shaft in the appropriate direction until the error signal is zero.

This method ceases to be economical when a larger number of shafts has to be set, especially when the shafts are not all necessarily used in different experiments. It is then preferable to use an incremental system of setting, where the signed increment for the new setting is specified for each shaft in turn and the arrival at the correct position is determined by a count-down to zero. The incremental system has been adopted in the present installation. Advantage is taken of the high speeds obtainable with moiré fringe method by having a setting speed of 10° per second on Φ , X and Ω and 20° per second on 2Θ . These are reduced to creep speed when the circles are within 1° of the desired position.

Sequential setting requires the clamping of each circle after setting. This is achieved by providing registers with a capacity of five digits (corresponding to 0.05 degrees of arc), which remain coupled to their setting motor servo-circuits during the disengagement of these circuits from the main incremental register. A small departure of a shaft from its desired position through vibration or gravity is thus corrected by its own live servo-circuit.

Another consequence of the adoption of an in-

cremental system of setting is the need for an absolute datum point for each shaft. After a number of settings for one shaft have been carried out the shaft is returned to this datum point for checking purposes and to prevent the cumulative effects of small errors which individually can amount to 0.01° . Such a return to datum is readily accomplished by means of the x05 order (see below).

5. The Order Code

With the incremental setting method it is logical to supply the setting instruction for a particular shaft in the form of an order having the following four parts:

(i) Initiating symbol, indicating that the code groups immediately following represent a setting instruction.

(ii) Address of the shaft to be set.

TABLE 1
The order code

Order	Function	Address	Contents
x 01	set shaft position	any one of 16 shafts	± 5 decimal digit number of $\frac{1}{100}^\circ$ units
x 02	set Ω -shaft and 2θ shaft simultaneously at twice the speed of Ω	any one of four Ω -shafts	± 5 decimal digit number of $\frac{1}{100}$ units
x 03	set special function relay	any one of 20 relays	
x 04	reset special function relay	any one of 20 relays	
x 05	set shaft by specified amount to bring it back to datum; print error (\pm); set fault register if error exceeds $\pm \frac{4}{100}^\circ$; disengage channel after two faults unless fault count override key is on	any one of 16 shafts	5 decimal digit number of $\frac{1}{100}^\circ$ units
x 06	disengage	any one of 4 channels	
x 07	return to starting point of scan specified in preceding x 11, x 12, x 21 or x 22 order	any one of 16 shafts	
x 11	carry out measuring scan with one shaft moving in steps, each step timed by output of monitoring scaler; at end of scan print out and reset measuring scaler	any one of 16 shafts	\pm or *; 2 digits (plus necessary number of significant zeros) specifying monitor counter ratio; 3 digits specifying number of steps; 1 digit p specifying the step size $2^p/100^\circ$, where $p = 0$ to 6. The direction of the scan is specified by the sign \pm ; if the sign digit is * (in 5-hole code) measurement is made without movement
x 12	As for x 11 but with 2θ moving through steps of twice size as for Ω	any one of four Ω -shafts	as for x 11
x 21	as for x 11 but with print-out and scaler reset after each step	as for x 11	as for x 11
x 22	as for x 21 but with 2θ moving through steps of twice the size as for Ω	any one of four Ω -shafts	as for x 11

Letter shift: After this character is read all succeeding characters are ignored until the next "figure-shift" is received. If "letter-shift" occurs in the middle of an order the preceding codes are erased. (This is used in correcting orders set up on the keyboard.)

> character: If a limit-switch on any circle is operated during the programme, the tape is searched until the next > character is found. This character normally precedes x 05, the order for returning to datum, and appears with x 05 at regular intervals in the programme tape.

-> character: This provides a conditional disengage signal when the stop/run key is set at stop. It is used in programme testing.

(iii) Signed increment representing the new setting.

(iv) Terminating symbol.

The form of this instruction was extended into an order code to cover all the possible operations carried out during an experiment, including measurement instructions in addition to those for shaft-setting. This order code is listed in table 1.

It will be noticed that the initiating symbol has been expanded into three code groups; the first code is always the symbol *x* which is the initiating symbol proper and the next two symbols indicate the type of instruction following.

The fourth and fifth symbols indicate the address. This can be any of the shafts or special function switching relays referred to in §2.5.

The installation has provision for setting up to sixteen shafts, any of which can be allocated to one of four diffractometers by suitable plugging of an internal patchboard. The twenty special function relays can be similarly allocated. Each instrument has its own input channel and interlocking prevents the faulty addressing of a particular shaft not allocated to a given channel. The form of the patchboard is such that a relative method of addressing is possible. Thus in a given experiment an *x* 01 order addressed to shaft number 01 *via* input channel number one may result in the setting of the Ω -shaft of the first diffractometer. The same order read-in on the second input channel will set the Ω -shaft of the second diffractometer. For another experiment six shafts, together with their motor servo-circuits and pulse inputs from the pick-up heads, may be allocated to the first channel by suitable plugging; an *x* 01 order addressed *via* channel 1 to shaft number 05 will now utilise the same circuits as were energised by the *x* 01 01 order on channel 2 in the first experiment. The patchboards thus make possible the running of a given programme tape on any channel without having to prepare a new tape which has a different set of addresses.

The contents of the orders are sufficiently explained in the Table. Each order is terminated by a character which may be either "comma" or "full-stop". These two characters permit a certain degree

of priority to be assigned in the time-sharing during multi-channel operation.

After an order terminating in "comma" the next order is taken from the same input channel, but after an order terminating in "full-stop" the other input channels are scanned in turn to find the next channel waiting for a new order. Orders for shaft-setting, which are obeyed quickly, are normally terminated by "comma" whereas measuring-sequence orders are terminated by "full-stop".

In addition to the main orders a few special characters are employed which are also explained in table 1.

6. Execution of Orders

The orders in the order code fall into two classes. In the first class orders are executed instantaneously (energising of the special-function solenoids) or in only a few seconds (setting of a shaft). The second class includes the measuring instructions which may take 10 min or more to execute. The two types of order are dealt with in different ways so as to permit maximum speed of operation in a multi-channel installation. After the first kind of order is read-in on a particular input channel, no further order can be read-in on any of the other input channels until the signal, signifying execution of the instruction has been received. On the other hand, a measuring order does not make use of the input decoder or of the main increment store, so that after the order has been initiated the corresponding channel is disengaged and the main control unit is free to read-in another order on one of the other input channels.

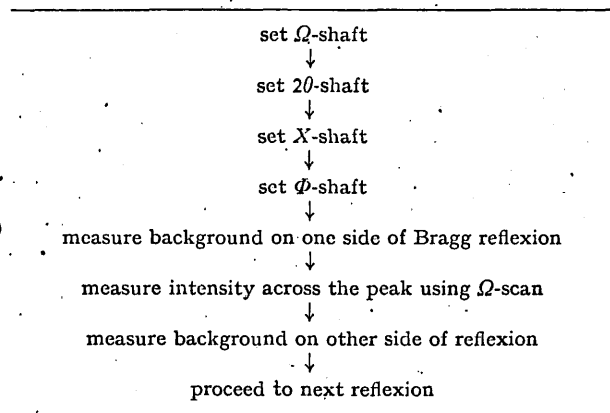
When an order referring to a particular channel has been executed an interrupt relay is set for that channel. A further order is then read-in as soon as that channel is reached in the scanning of the inputs which follows disengagement of the input circuitry.

Any channel can be disengaged either by a special *x* 06 order, or by a fault occurring in that channel, or by reaching the end of the input tape. After disengagement of an input channel it is omitted from the scan of the input channels determining the provenance of the next order; re-engagement is then only possible by the manual intervention of the operator.

7. A Programme Example

As an illustration we will assume that all four channels of the installation are occupied by identical four-circle diffractometers and that these are all making measurements according to the flow-sheet of table 2.

TABLE 2
Flow-sheet for one diffractometer



The part of the programme dealing with this sequence will be identical for all four channels,

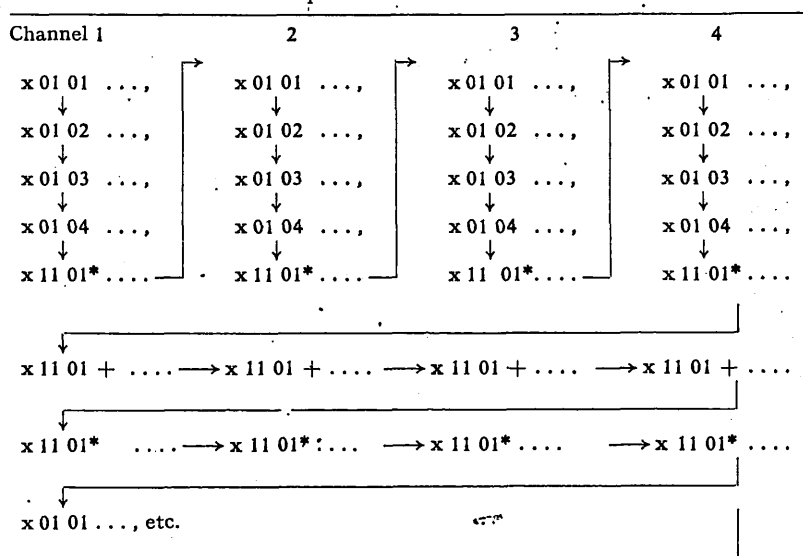
8. Manual Setting

For alignment purposes variable speed manual controls are provided for all diffractometer shafts. These can be operated only when a particular instrument is disengaged. Counting-rate meters are provided for observing the diffracted intensity during manual setting. The ϕ-shaft alone can be unclamped and rapidly spun by hand during alignment, and the absolute positions of each shaft can be read visually on scalers or dials engraved in both senses of rotation.

9. On-Line Control

The execution of an order is signalled to the input circuit which, if not otherwise engaged, accepts the next order before further action is possible. This is in contrast with the earlier instrument¹⁾ where completion of the setting operation automatically leads to the initiation of a measuring routine. The present method of operation greatly facilitates closed-loop operation in which the diffractometer communicates with the digital computer through the following connexions only:

TABLE 3
Sequence of order execution



assuming that the patchboard has been plugged appropriately for allocating the shaft addresses. The sequence in which the orders will probably be obeyed is indicated in table 3.

(i) Five-wire line from the computer output to the diffractometer input, used for conveying orders to the diffractometer.

(ii) Five-wire line from the diffractometer output

to the computer input, used for transmitting numerical results to the computer.

(iii) Single-wire line from the diffractometer to the computer, used for signalling to the computer the execution of an order and readiness to accept further instructions. This signal can be used to set an interrupt in a controlling computer which operates in a time-sharing fashion.

The design described here make provision for a wide range of scattering experiments. The same control and measuring circuitry can be used with different instruments, although only one kind of instrument, a four circle diffractometer, has been designed so far. For other instruments it is only necessary that they "look like" combinations of rotating shafts, solenoids with back contacts, and digital counters. The control of temperature or magnetic field measurements is not excluded if suitable transducers and analogue-to-digital converters are employed.

Acknowledgements

A large number of people have contributed to

the design of the Mark II installation. Our special thanks are due to Mr. L. W. G. Alexander of Ferranti Ltd., for his assistance with the detailed systems design and for his contribution to the overall concept. The mechanical design of the four-circle diffractometer is due principally to Mr. R. Causer of the Engineering Division, AERE, who was assisted in the preparation of drawings by Seton-Creaghe Ltd. We have benefited considerably from discussions with Mr. O. S. Mills and Mr. K. Bowden of Manchester University, who are engaged on an independent design of a computer-controlled X-ray diffractometer, mechanically identical to our neutron instrument. We are grateful to Mr. D. J. Merrett and Mr. J. Mackie of the Research Reactors Division, AERE for administrative assistance, and above all we wish to thank Dr. F. A. Vick, Dr. P. Murray and Mr. J. Williams of AERE for their support and encouragement of this scheme. One of us (U.W.A.) wishes to thank Sir Lawrence Bragg for his encouragement and for his permission to take part in the project.

UNIVERSITA' DEGLI STUDI DI PARMA

CENTRO NAZIONALE DI STRUTTURISTICA ROENTGENOGRAFICA DEL CNR

SEZIONE DI PARMA

ISTITUTO DI STRUTTURISTICA CHIMICA

DIFFRATTOMETRIA CON CRISTALLO SINGOLO

Dr. B.T.M. Willis

Atomic Energy Research Establishment, Harwell, Inghilterra.

CONFERENZA INTRODUTTIVA

Maggio 1965

UNIVERSITA' DI PARMA

CENTRO NAZIONALE DI STRUTTURISTICA ROENTGENOGRAFICA DEL CNR
Sezione di Parma

ISTITUTO DI STRUTTURISTICA CHIMICA

Seminario su:

DIFFRATTOMETRIA CON CRISTALLO SINGOLO

tenuto da

Dr. B.T.M. WILLIS

Atomic Energy Research Establishment, Harwell, Inghilterra.

Conferenza introduttiva

Maggio 1965

Fino a poco tempo fa quasi tutte le determinazioni di strutture cristalline con i raggi X furono compiute usando metodi fotografici. Sebbene la maggior parte delle strutture cristalline sia ancora risolta usando dati fotografici, questi ultimi anni sono stati testimoni di profondi cambiamenti nelle tecniche sperimentali in seguito all'introduzione di diffrattometri a cristallo singolo e all'automazione del loro controllo. Questi cambiamenti, insieme con i progressi nelle tecniche di calcolo cristallografico, preannunciano un netto aumento sia quantitativo che qualitativo del futuro lavoro cristallografico.

In questa conferenza verrà tratteggiato lo sviluppo delle tecniche usate per misurare le intensità diffratte e verrà dato un breve sguardo generale al campo della diffrattometria con cristallo singolo. Molti punti, introdotti ora, verranno spiegati più completamente in conferenze successive.

1. Breve storia delle tecniche usate nella diffrazione dei raggi X per la misura delle intensità delle riflessioni di Bragg.

La prima figura di diffrazione ottenuta da un cristallo, il solfato di rame, fu registrata su lastra fotografica (Friedrich, Knipping e Laue, 1912). Poco dopo lo spettrometro a ionizzazione (Bragg e Bragg, 1913) fu usato sia per misurare le lunghezze d'onda negli spettri dei raggi X che per determinare le strutture cristalline. Per esaminare il fascio di raggi X riflesso, il cristallo veniva opportunamente orientato e l'intensità del fascio riflesso era misurata con una camera a ionizzazione. A causa della difficoltà di misurare correnti di ionizzazione molto piccole lo spettrometro a ionizzazione non era in realtà adatto per l'esame delle strutture

di cristalli piccoli o per raccogliere una gran quantità di dati di intensità, perciò nel successivo decennio questo strumento cadde gradualmente in disuso nella ricerca strutturale. Il 1920 vide l'accettazione generale dei metodi fotografici, promossi specialmente dall'applicazione della teoria del reticolo reciproco e della sfera di riflessione di Ewald (1921) all'interpretazione dei fotogrammi di rotazione di cristallo singolo (Bernal, 1926), e dall'invenzione della camera a pellicola mobile (Weissenberg, 1924).

Il vantaggio principale della pellicola fotografica sui rivelatori a contatore sta nella possibilità di registrare un gran numero di riflessioni sulla stessa pellicola; il principale inconveniente sta invece nella difficoltà di mettere in relazione l'annerimento sulla pellicola con l'intensità del fascio diffratto che lo produce. Per molto tempo la misura dell'intensità dei raggi X fu compiuta confrontando visualmente l'annerimento delle macchie sulla pellicola fotografica con una serie di macchie di riferimento di intensità graduata. L'introduzione della camera di precessione (Buerger, 1942, 1944), fornendo una rappresentazione indistorta del reticolo reciproco stimolò un più ampio uso della microdensitometria. Anche ora tuttavia sembra che non vi sia strumento capace di misurare automaticamente l'intensità di ciascuna macchia su un fotogramma di precessione per non dire delle macchie su un fotogramma di Weissenberg che giacciono lungo linee di curvatura non uniforme.

Fin dal 1945 la camera a pellicola mobile di Weissenberg e quella di precessione di Buerger sono stati gli strumenti di uso corrente per lavoro strutturale. Ma durante lo stesso periodo ha ripreso vita l'interesse per i metodi basati su l'uso di contatori; Il contatore di Geiger, e più tardi quello proporzionale e a scintillazione, sono

stati perfezionati come rivelatori attendibili ed hanno soppiantato la camera di ionizzazione usata nello spettrometro di Bragg. Essi sono dei rivelatori quantici capaci di contare i singoli quanti di raggi X e di misurare l'intensità diffratta più direttamente e più accuratamente della pellicola fotografica. E' stato fatto un ampio uso di questi rivelatori per la registrazione diretta dei diagrammi di diffrazione ai raggi X di polveri ed i diffrattometri per polveri sono in commercio già da molto tempo. Lonsdale (1948) e Cochran (1950) furono fra coloro che per primi utilizzarono i metodi a contatori quantici nell'esaminare i cristalli singoli e molti ricercatori successivamente hanno impiegato diffrattometri per cristallo singolo come supplemento o in sostituzione nella raccolta dei dati di diffrazione mediante camere a raggi X. In questi ultimi anni vi è stata, specialmente in Inghilterra e negli Stati Uniti, una intensa attività dedicata allo sviluppo dei diffrattometri automatici per cristallo singolo ed attualmente è in commercio un certo numero di questi strumenti di diverse specie.

Si noti che il termine "diffrattometro" fu adottato nel 1952 dalla "Apparatus Commission of International Union of Crystallography" coll'estendersi dell'uso dei contatori quantici: esso si riferisce a strumenti impiegati per la misura di raggi X o di neutroni diffratti, mediante rivelatori a contatore. Il termine "spettrometro" è riservato a quegli strumenti la cui funzione principale è lo studio delle lunghezze d'onda (o dell'energia) degli spettri dei raggi X (o dei neutroni). Così gli strumenti usati nell'analisi per fluorescenza in raggi X o lo strumento a tre assi (Brockhouse, 1961) progettato per misurare il trasferimento di energia di neutroni diffusi, sono spettrometri, mentre lo spettrometro a ionizzazione di Bragg, usato per lavoro strutturale, dovrebbe ora essere chiamato diffrattometro.

2. Breve storia delle tecniche usate nella diffrazione di neutroni per misurare le intensità delle riflessioni di Bragg.

La natura ondulatoria del neutrone fu dimostrata per la prima volta da Mitchell e Povers (1936), che provocarono la diffrazione di un fascio di neutroni mediante sedici grossi cristalli singoli di ossido di magnesio distribuiti lungo una circonferenza di un cilindro. In questo lavoro d'anteguerra radio-berillio fu usato come sorgente di neutroni termici, ma non fu che con l'avvento dei reattori nucleari, i quali danno neutroni di sufficiente intensità da permettere sia la collimazione in un fascio nettamente definito che la monocromatizzazione in una banda ristretta di lunghezze d'onda, che furono possibili studi di rilievo mediante la diffrazione di neutroni.

I neutroni non hanno un effetto diretto sulle emulsioni fotografiche perciò il diffrattometro è rimasto lo strumento base per la misura delle intensità delle riflessioni di Bragg nella cristallografia neutronica. Il primo diffrattometro a neutroni progettato per lavoro con polveri fu costruito all'"Argonne National Laboratory" negli Stati Uniti nel 1945 (Zinn, 1947) e durante il periodo successivo di approssimativamente dodici anni furono disponibili reattori nucleari di flusso elevato per studi di diffrazione soltanto in pochi altri centri: Oak Ridge (Wollan e Shull, 1948), Brookhaven (Corliss e Hastings, 1953), Chalk River (Hurst et al, 1950) e Harwell (Bacon et al, 1950). Molti altri reattori per ricerca sono stati costruiti fin dalla metà del 1950 e diffrattometri a neutroni sono ora operanti in numerosi centri di ricerche nucleari in tutto il mondo. I principali centri di ricerche sono riportati nella tabella 1 insieme con le citazioni bibliografiche in cui sono descritti i diffrattometri a neutroni per cristallo singolo funzionanti in tali laboratori.

Tabella 1. Centri di ricerche sulla diffrazione di neutroni

Località	Citazioni Bibliografiche
U.S.A: Argonne National Laboratory	Mueller et al. 1962 Atoji 1964
Brookhaven National Laboratory	Langdon and Frazer 1959 Prince and Abrahams 1959
MIT	Shull 1960
Oak Ridge	Wollan et al. 1960
Westinghouse	Takei et al. 1960
Livermore	Mead and Sparks 1960
Los Alamos	-
Washington State University	-
Canada: Chalk River	Hurst et al. 1950
M ^C Master University	Petch et al. 1960
Europe: Harwell, England	Arndt and Willis 1963 a,b Bacon and Dyer 1959 Bacon 1962 Lambe et al. 1961 Willis 1962
Aldermaston, England	Allenden and Winkworth 1963
Saclay, France	Breton et al. 1957
Munich	Dachs 1961

Località	Citazioni Bibliografiche
Munich	Lutz 1960
Rosendorf, Dresden	Betzl and Kleinstück 1961 Kleinstück 1961
Budapest	Szabo et al. 1963
Ispra, Italy	Caglioti et al. 1962
Petten, Netherlands	Loopstra 1962
Kjeller, Norway	Barstad and Andresen 1957 Goedkoop and Loopstra 1959
Warsaw	O'Connor and Bonkowski 1959 Buras 1964 Krasnicki et al. 1962
Prague	Zivadinovic et al. 1961
USSR	Bykov et al. 1957 Ozerov et al. 1960 Yamzin 1959 Yamzin et al. 1962, 1963
India: Trombay	Iyengar 1963
Japan	Hagihara et al. 1962 Kunitoni et al. 1962 Miyake et al. 1962
China	Ang et al. 1961
Australia	Sabine 1962

3. Confronto fra le tecniche a raggi X e a neutroni.

Citiamo ora alcune importanti differenze fra le due tecniche.

La prima differenza sorge dal fatto che è diversa la sorgente di radiazione primaria. Nella cristallografia in raggi X è impiegata la radiazione caratteristica di un anticatodo: questa ha la forma di righe di emissione nette che s'innalzano rapidamente da un fondo di radiazione "bianca" o "continua", (fig. 1(a)). La radiazione bianca che provoca errori nel valutare il contributo della radiazione caratteristica alla riflessione di Bragg, può essere eliminata con un monocromatore a cristallo singolo. Tuttavia questo porta ad ulteriori difficoltà comprendenti la diminuzione d'intensità del fascio primario e può essere meglio usare filtri bilanciati o piuttosto semplici filtri beta. D'altro lato a parte l'uso di sorgenti di neutroni ad impulsi con analisi di lunghezza d'onda compiute all'istante (Buras e Leciejewcz, 1964), non vi è in realtà altra alternativa all'uso di monocromatori nella diffrazione di neutroni. Lo spettro di neutroni lenti provenienti da un reattore nucleare, consiste di un'ampia distribuzione di lunghezze d'onda: non vi è una lunghezza d'onda nettamente definita (fig. 1(b)), e radiazioni di lunghezze d'onda singole vengono ottenute con un monocromatore.

La seconda differenza riguarda le dimensioni dell'apparecchiatura. Con i reattori di più elevato flusso disponibili attualmente, il flusso di neutroni sul campione, misurato in neutroni/cm²sec., è da 100 a 1000 volte minore del flusso, in quanti/cm²sec., di raggi X provenienti da un tubo del commercio. Questa differenza di flusso porta all'impiego di campioni più grandi nella diffrazione di neutroni. Inoltre una pesante schermatura contro neutroni veloci deve

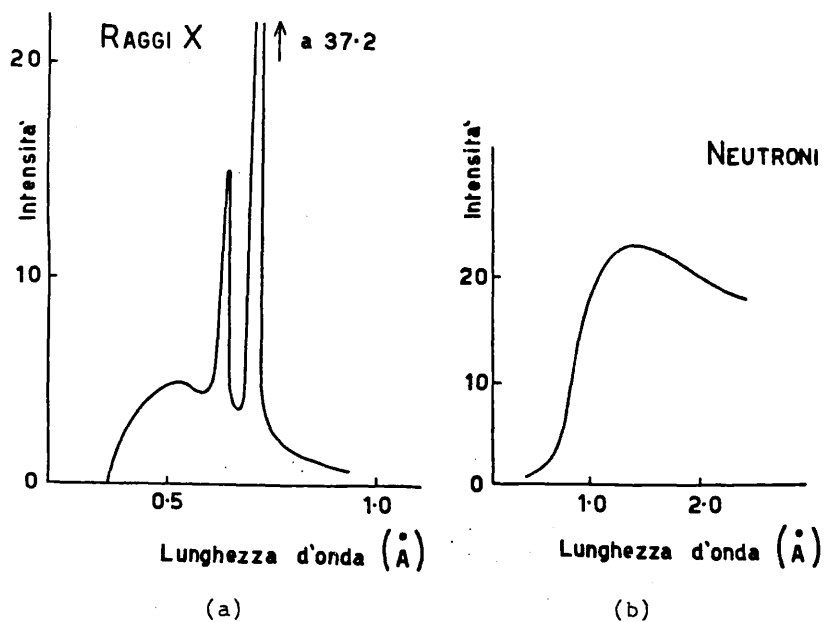


Figura 1. Curve d'intensità: (a) per i raggi X da un anticatodo di molibdeno che dà righe intense di radiazione K "caratteristica"; (b) per un fascio di neutroni emergenti da un reattore (da Bacon 1962).

essere disposta attorno al monocromatore e al rivelatore cosicchè i diffrattometri a neutroni vengono ad essere molto più ingombranti delle apparecchiature a raggi X.

Vi è sempre stato un forte incentivo a costruire diffrattometri a neutroni il più automatici possibile. La sorgente di neutroni è molto più dispendiosa di un generatore a raggi X e la spesa di un diffrattometro che permetta l'utilizzazione di una sorgente di neu-

troni per 24 h al giorno è giustificata più facilmente su basi economiche. Lo sviluppo dei diffrattometri automatici a raggi X ha beneficiato molto del precedente impiego dell'automazione nel campo dei neutroni.

4. Diffrattometri automatici

La figura 2 illustra lo schema della successione di operazioni in un sistema a diffrattometro automatico. Le informazioni in entrata consistono nelle istruzioni per disporre il cristallo rivelatore in modo da ricevere ciascuna riflessione di Bragg e per misurare l'intensità della riflessione quando i comandi siano messi a posto. Tutte le riflessioni sono misurate sequenzialmente ed i dati in uscita, che consistono del numero di quanti di raggi X o del numero di neutroni raccolti esplorando la riflessione sono di solito presentati in forma adatta per la diretta elaborazione da parte di un calcolatore elettronico (per es. su banda perforata). Nel sistema "fuori linea" questa elaborazione porta direttamente ad una serie di "ampiezze di struttura". Nel metodo "in linea" il calcolatore è legato sia dall'uscita del diffrattometro che al suo controllo; mediante opportuna programmazione è possibile controllare continuamente i dati sperimentali e, se una misura non soddisfa certi criteri programmati, vengono date le opportune correzioni compresa la regolazione automatica dei controlli fino a che questi criteri non sono soddisfatti. Il sistema "in linea" è indicato dalla linea tratteggiata nella fig. 2.

Come vi sono due differenti tipi di calcolatori, gli analogici e i numerici, così vi è una simile scelta di strumenti analogici o numerici in diffrattometria. Negli strumenti analogici le relazioni

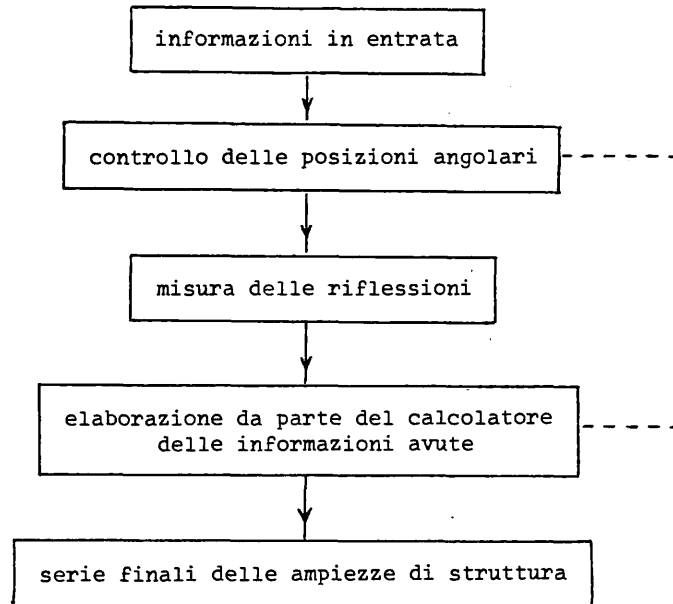


Figura 2. Successione di operazioni in un sistema a diffrattometro automatico. Per l'operazione "in linea" l'informazione d'entrata viene direttamente dal calcolatore come è indicato dalla linea tratteggiata.

fra angoli di posizione sono ottenute per mezzo di collegamenti meccanici e gli angoli di posizione corretti sono generati mediante semplici movimenti dei collegamenti: non vi è bisogno di calcolare il valore degli angoli di posizione e le informazioni in entrata consistono nei parametri reticolari precedentemente misurati e varie co-

stanti strumentali. Il tipo di collegamento determina la specie di operazioni che sono possibili sotto controllo automatico e una differente serie di operazioni richiede maggiori modificazioni nella progettazione meccanica. Per questa ragione il metodo analogico di controllo è meno flessibile di quello numerico.

Nel metodo di controllo numerico, dei codificatori convertono le posizioni angolari dei comandi del diffrattometro in forma numerica. E' possibile programmare sia le posizioni dei comandi che la misura delle riflessioni preparando delle istruzioni in entrata che consistono in numeri rappresentanti in successione i desiderati movimenti angolari dei comandi ed il tipo di esplorazione per la misura della intensità. Queste istruzioni in entrata sono di solito fornite da un calcolatore perchè le formule per il calcolo degli angoli di posizione sono troppo complicate per essere calcolate direttamente per ogni riflessione. Così senza un pronto accesso ad un calcolatore può essere preferibile usare un metodo analogico.

Nei diffrattometri automatici (ed in ogni diffrattometro) vi è un'ulteriore scelta riguardante il tipo di geometria di diffrazione adottata per il funzionamento meccanico dello strumento. Nella geometria a "raggio normale equatoriale" il raggio incidente è perpendicolare all'asse di oscillazione del cristallo ed il rivelatore si muove su una circonferenza nel piano equatoriale (cioè il piano che contiene il raggio incidente e normalmente a questo l'asse di oscillazione). L'orientazione del cristallo è determinata dai tre angoli di Eulero - ϕ, χ, ω - e questi angoli devono essere continuamente regolati fra una misura e l'altra delle singole riflessioni. Questa geometria è particolarmente utile nella diffrazione di neutroni dove il moto del rivelatore, con il suo ingombrante schermo per neutroni

veloci, è ristretto ad un singolo piano orizzontale. Nel tipo di geometria a "inclinazione generale" sia il fascio incidente che quello diffratto sono inclinati con un angolo variabile rispetto all'asse di oscillazione ed il rivelatore deve ruotare attorno a due assi indipendenti per ricevere il raggio diffratto. Per gli strumenti ad equi-inclinazione è necessario soltanto variare uno di questi assi ed un asse del cristallo per misurare tutte le riflessioni in un dato livello del reticolo reciproco; di solito si controllano automaticamente solo questi due assi e si regolano a mano i rimanenti assi fra una misura e l'altra dei differenti livelli.

Con il cristallo e il rivelatore regolati opportunamente per registrare una data riflessione, è impiegato per determinare l'intensità integrata uno dei tre seguenti tipi di cicli di misura. Il primo tipo di ciclo misura l'intensità del picco e del fondo su entrambi i lati della riflessione con il cristallo e il rivelatore entrambi stazionari (metodo del cristallo e del rivelatore stazionari). La differenza tra l'intensità del picco e l'intensità media del fondo è proporzionale all'intensità integrata, posto che il fascio incidente converga fortemente sulla posizione del campione ed abbia un'uniforme dipendenza angolare dell'intensità. Queste condizioni sono difficili da soddisfare in pratica e così, nonostante la sua semplicità, il metodo "cristallo e rivelatore stazionari" è raramente usato. Per gli altri due tipi di cicli il cristallo si muove lentamente attraverso la posizione in cui si ha riflessione quando è registrato il raggio riflesso: il cristallo solo si muove nel metodo a cristallo mobile e rivelatore stazionario (scansione ω) e il rivelatore si muove ad una velocità angolare doppia di quella del cristallo nel metodo a cristallo e rivelatore entrambi mobili (scansione $\omega/2\theta$). In questi due ci-

cli è misurato un profilo completo della riflessione e la sola restrizione sul raggio incidente è che esso sia uniforme in intensità lungo la porzione della sua sezione normale intercettata dal campione.

5. Accuratezza dei metodi a contatore

Anche misure relativamente poco accurate d'intensità possono portare alla soluzione di una struttura cristallina ed alla determinazione di distanze di legame con deviazioni standard minori di 0.1 Å. Tuttavia le attuali esigenze sono per deviazioni standard molto migliori di queste e per misurare lunghezze di legame accurate a 0.01 Å sono richiesti dati d'intensità accurati a l'uno o il due per cento. Per lo studio dell'ampiezza delle vibrazioni termiche o la distribuzione particolareggiata della densità elettronica sono essenziali dati accurati. E' questa ricerca di maggior accuratezza che ha fatto tornare ai metodi a contatore per rivelare i raggi X in cristallografia. I moderni contatori a scintillazione e proporzionali sono di gran lunga superiori alle vecchie camere di ionizzazione: è ora possibile contare ciascun quanto di raggi X ricevuto dal rivelatore e registrare direttamente l'intensità di ciascun raggio diffratto come numero di quanti ricevuti per secondo.

La produzione di raggi X da un tubo a raggi X o di neutroni termici da un reattore nucleare sono processi statistici e quindi soggetti a fluttuazioni statistiche casuali. Se il rivelatore registra un numero totale N di colpi in un dato tempo, la deviazione standard di misure ripetute di questo numero è $N^{\frac{1}{2}}$, e la deviazione standard frazionaria è $N^{-\frac{1}{2}}$. Questo significa che devono essere registrati almeno diecimila colpi per ottenere una deviazione standard frazionaria che

non superi l'uno per cento.

Si deduce che l'accuratezza finale dei dati sperimentali è più spesso limitata da errori sistematici che da errori casuali. Errori sistematici che sorgono da fattori fisici come l'assorbimento, l'estinzione e la diffusione di fononi (che colpiscono nella stessa posizione della riflessione di Bragg e causano errori nella valutazione del livello di fondo della riflessione) sono estremamente difficili da calcolare o correggere sperimentalmente. Può essere possibile correggere alcuni errori sistematici ripetendo o stendendo le misure a differenti condizioni (per esempio usando una lunghezza d'onda differente o differenti orientazioni azimutali del piano riflettente), ma è necessario un lavoro molto accurato e faticoso per raggiungere una accuratezza finale dell'un per cento per le ampiezze di struttura relative.

6. Rapidità dei metodi a contatore

Quasi tutti i diffrattometri a raggi X misurano i picchi di diffrazione in successione, mentre i metodi fotografici possono registrare un livello completo del reticolo reciproco sulla stessa pellicola. In compenso i diffrattometri possono essere adattati facilmente a metodi automatici di controllo: i diffrattometri automatici sono capaci di operare con velocità ed accuratezza elevate (sebbene queste due caratteristiche tendano ad escludersi mutualmente) ed eliminano molta parte del lavoro noioso richiesto dal metodo fotografico.

Possiamo confrontare le velocità relative dei metodi fotografici e a contatore considerando la misura di una serie tipica di 1000 riflessioni indipendenti da un cristallo singolo. Se le intensità sono determinate fotograficamente mediante la tecnica del film multiplo, sono necessarie circa 100 registrazioni fotografiche. Per fare 100 fo-

togrammi esposti correttamente occorre un mese di lavoro di un operatore esperto. La densità delle macchie su queste pellicole deve essere valutata mediante un microdensitometro e messa in relazione con l'intensità del raggio diffratto corrispondente, assumendo una conoscenza della curva densità-esposizione per quella pellicola. Con i migliori procedimenti fotografici è difficile superare l'accuratezza del 10% per l'intensità delle macchie. Correlando l'intensità delle stesse riflessioni su differenti fotogrammi tutti i valori sono posti su di una scala relativa comune e mediati per dare un unico elenco di 1000 dati d'intensità. L'operazione di fotometria, di riscaldamento e di media richiedono un altro mese di lavoro continuo dando un totale di circa due mesi di tempo per ottenere i dati d'intensità con una accuratezza del 10%.

Con un diffrattometro automatico la presenza di un osservatore è richiesta solo occasionalmente per controllare il comportamento dello strumento. 1000 intensità possono essere misurate facilmente con l'accuratezza del 10% in 24 h; la velocità di raccolta di 3000 intensità per giorno è stata raggiunta recentemente da Phillips (1964) usando una apparecchiatura a più contatori. L'uscita dei dati da un diffrattometro automatico è in forma adatta per la diretta elaborazione da parte di un calcolatore elettronico; il calcolatore ricava le intensità integrate da questi dati e quindi applica i fattori di correzione sistematici per fornire una serie finale di ampiezze di struttura. Conseguentemente, una volta che il cristallo è stato sistemato sul diffrattometro e il programma del calcolatore è stato scritto sia per produrre le istruzioni in entrata che per elaborare i dati in uscita, l'intero processo di raccolta di una serie di fattori di struttura può essere compiuto più convenientemente ed in una frazione del tempo richiesto con il metodo fotografico.

Citazioni Bibliografiche

- Allenden D. and Winkworth, R. (1963). Nucl. Instr. Methods, 23, 181.
- Ang, W., Chang, H., Yang, T., Chu, T. and Li, K. (1961).
Wu Li Hsueh Pao, 17, 222.
- Arndt, U. W. and Willis, B. T. M. (1963a). Rev. Sci. Instrum.
34, 224.
- Arndt, U. W. and Willis, B. T. M. (1963b). Nucl. Instr. Methods,
24, 155.
- Atoji, M. (1964). Argonne Report ANL-6920.
- Bacon, G. E. (1962). "Neutron diffraction". Oxford University
Press, Second Edition.
- Bacon, G. E. and Dyer, R. F. (1959). J. Sci. Instrum. 36, 419.
- Bacon, G. E., Smith, J. A. G. and Whitehead, C. D. (1950).
J. Sci. Instrum. 27, 330.
- Barstad, G. E. B. and Andresen, A. F. (1957). Rev. Sci. Instrum.
28, 916.
- Bernal, J. D. (1926). Proc. Roy. Soc. A 113, 117.
- Betzl, M. and Kleinstück, K. (1961). Fortschr. Mineral. 39, 327.
- Bragg, W. H. and Bragg, W. L. (1913). Proc. Roy. Soc. A 88, 428.
- Breton, C., Hubert, P. and Meriel, P. (1957). J. Phys. Radium
18, 25-35.
- Brockhouse, B. N. (1961). "Inelastic scattering of neutrons in
solids and liquids". I.A.E.A. Conference, Vienna, p.113.
- Buerger, M. J. (1942). "X-ray crystallography". John Wiley,
New York.
- Buerger, M. J. (1944). "The photography of the reciprocal
lattice". American Society for X-ray and electron diffraction.
Monograph No. 1.

- Buras, B. and Leciejewicz, J. (1964). Phys. Stat. Sol. 4, 349.
- Bykov, V. N., Vinogradov, S.I., Levдик, V. A. and Golovkin, V. S. (1957). Soviet Phys. - Cryst. 2, 626.
- Caglioti, G., Paoletti, A. and Ricci, F.P. (1960). Nucl. Instr. Methods 9, 195.
- Chadwick, J. (1932). Na ure 129, 312.
- Cochran, W. (1950). Acta Cryst. 3, 268.
- Corliss, L. M., Hastings, J. M. and Brockman, F. G. (1953). Phys. Rev. 90, 1013.
- Dachs, H. (1961). Z. Krist. 115, 80.
- Ewald, P. P. (1921). Z. P. (1921). Z. Krist. 56, 129.
- Friedrich, W., Knipping, P. and Von Laue, M. (1912). Proceedings Bavarian Academy of Sciences p.303; reprinted in Naturwiss, (1952) 368.
- Goedkoop, J. A. and Loopstra, B. O. (1959). Ned. Tijdschr. Natuurk. 25, 29.
- Hagihera, S., Miyashita, K., Yoshie, T., Ohno, E., and Mogi, M. (1962). Mitsubishi Denki Lab. Rep. 3, 111.
- Hurst, D. G., Pressessky, A. J. and Tunnicliffe, P. R. (1950). Rev. Sci. Instr. 21, 705.
- Iyengar, P. K. (1963). "Crystallography and Crystal Perfection" Academic Press, New York, 279.
- Kleinstück, K. (1961). Kernenergie 4, 913.
- Krasmicki, S., Pawelczyk, J. and Rapacki, H. (1962). Nukleonika Polska 7, 223.
- Kunitomi, N., Hamaguchi, Y., Sakamoto, M. and Komura, S. (1962). J. Phys. Soc. Japan 17, Suppl. B-II, 354.
- Lambe, K. A. D., Rouse, K. D., Valentine, T. M. and Willis B. T. M. (1961). AERE-R3709.

- Langdon, F. and Frazer, B.C. (1959). Rev. Sci. Instrum. 30, 997.
- Lonsdale, K. (1948). Acta Cryst. 1, 12.
- Loopstra, B. O. (1962). Atoomenergie Haar Toepassingen 4, 253.
- Lutz, G. (1960). Kerntechnik 2, 391.
- Mead, W. and Sparks, J. T. (1960). Bull. Amer. Phys. Soc. 5, 464.
- Mitchell, D. P. and Powers, P. N. (1936). Phys. Rev. 50, 486.
- Miyake, S., Hoshino, S., Suzuki, K., Katsuragi, H., Hāgihara, S., Yoshie, T. and Miyashita, K. (1962). J. Phys. Soc. Japan 17, Suppl. B-II, 358.
- Mueller, M. H., Heaton, L. and Sidhu, S. S. (1963). Rev. Sci. Instrum. 34, 74.
- O'Connor, D. and Bonkowski, L. (1959). Acta Phys. Polon. 18, 265.
- Ozerov, R. P., Kiselev, S. V., Karpovich, I. R., Goman'kov, V.I. and Loshmanov, A. A. (1960). Soviet Phys. - Cryst. 5, 294.
- Petch, H. F., Brouwer, W., Torrie, B. H., and Brown, I. D. (1960). Research Reactor J. 1, No. 1,8.
- Phillips, D. C. (1964). Reported at Institute of Physics meeting in London, November 1964.
- Prince, E. and Abrahams, S. C. (1959). Rev. Sci. Instrum. 30, 581.
- Sabine, T. M. (1962). J. Phys. Soc. Japan, Suppl. B-II 352.
- Shull, C. G. (1960). AFOSR TR 60-111.
- Szabo, P., Kren, E., and Gordon, J. (1963). Acta Phys. Acad. Sci. Hungary 15, 203.
- Takei, W. J., Frazer, B. C. and Shirane, G. (1960). Bull. Amer. Phys. Soc. 5, 464.
- Weissenberg, K. (1924). Z. physik. 23, 229.
- Willis, B. T. M. (1962). J. Sci. Instrum. 39, 590.

- Wollan, E. O. and Shull, C. G. (1948). Phys. Rev. 73, 830.
- Wollan, E. O., Wilkinson, M. K., Koehler, W. C., Cable, J. W. and Child, H. R. (1960). Bull. Amer. Phys. Soc. 5, 464.
- Yamzin, I. I. (1959). Soviet Phys. - Cryst. 4, 397.
- Yamzin, I. I., Stasitsyn, V. E. and Nozik, Y. Z. (1962). Soviet Phys. - Cryst. 7, 58.
- Yamzin, I. I., Kuz'minov, Y.S. and Staritsyn, V. E. (1963). Soviet Phys. - Cryst. 8, 234.
- Zinn, W. H. (1947). Phys. Rev. 71, 752.
- Zivadinovic, M. D., Jovic, D. M. and Konstantinovic, J. M. (1961). Bull. Instr. Nucl. Sci. 11, 59.

SINGLE CRYSTAL DIFFRACTOMETRY

BY

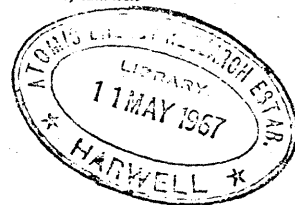
U. W. ARNDT

*Medical Research Council
Laboratory of Molecular Biology, Cambridge*

AND

B. T. M. WILLIS

Atomic Energy Research Establishment, Harwell



The chapters of this book
given here are the ones
written solely by the candidate.



CAMBRIDGE
AT THE UNIVERSITY PRESS

1966

Ha62432

CONTENTS

<i>Preface</i>	<i>page</i> xiii
<i>Acknowledgements</i>	xv
CHAPTER I	
Introduction	
1.1 X-ray techniques for measuring Bragg reflexions	1
1.2 Neutron techniques for measuring Bragg reflexions: comparison with X-ray techniques	3
1.3 Automatic diffractometers	5
1.4 Accuracy of counter methods	9
1.5 Speed of counter methods	11
1.6 Cost of counter methods	12
CHAPTER 2	
Diffraction Geometry	
2.1 General considerations	14
2.2 Cylindrical polar co-ordinates in reciprocal space	22
2.3 Inclination method	26
2.4 Normal-beam equatorial method	37
2.5 Comparison of inclination and equatorial methods	52
2.6 The simultaneous measurement of reflexions	56
CHAPTER 3	
The Design of Diffractometers	
3.1 Introduction	65
3.2 Digital shaft setting	67
3.3 Analogue shaft setting	73
3.4 Radiation shielding	76

viii	CONTENTS	
3.5	Collimator alinement	<i>page</i> 77
3.6	Crystal mounting	78
3.7	The provision of special environments	81
3.8	The Hilger-Ferranti four-circle diffractometer	82
3.9	The Royal Institution linear diffractometer	88
3.10.	A comparison of the four-circle and linear diffractometers	93
3.11	Some other designs	96
	CHAPTER 4	
	Detectors	
4.1	Introduction	99
4.2	X-ray gas ionization counters	101
4.3	Scintillation counters for X-rays	123
4.4	Semi-conductor detectors for X-rays	132
4.5	Principles of neutron detection	136
4.6	Gas-filled detectors for neutrons	140
4.7	Semi-conductor neutron detectors	142
4.8	Scintillation counters for neutrons	143
4.9	Counting losses	144
4.10	Co-ordinate detectors	147
	CHAPTER 5	
	Electronic Circuits	
5.1	Introduction	154
5.2	Valve and transistor circuits	155
5.3	The counting chain	156
5.4	Noise and interference	163
5.5	Testing of counting chain	166

	CONTENTS	ix
	CHAPTER 6	
	The Production of the Primary Beam (X-rays)	
6.1	Introduction	<i>page</i> 169
6.2	X-ray sources	169
6.3	Collimators	171
6.4	The elimination of unwanted radiation	180
6.5	Crystal monochromators	188
6.6	Total external reflexion	195
6.7	Primary beam monitoring	195
	CHAPTER 7	
	The Production of the Primary Beam (Neutrons)	
7.1	Neutron collimators	198
7.2	Neutron spectrum emerging from collimator	201
7.3	Crystal monochromators	203
7.4	Mechanical monochromators	214
7.5	Neutron diffractometry using 'white' primary beam	216
	CHAPTER 8	
	The Background	
8.1	Introduction	220
8.2	Thermal diffuse scattering	221
8.3	White radiation background	227
8.4	Incoherent scattering of X-rays	230
8.5	Incoherent scattering of neutrons	231
8.6	Parasitic scattering	232
8.7	Background and rocking range	232

CHAPTER 9

Systematic Errors in Measuring Relative Integrated Intensities

9.1 Absorption	page 234
9.2 Extinction	243
9.3 Simultaneous reflexions	251

CHAPTER 10

Procedure for Measuring Integrated Intensities

10.1 Choice of crystal size and shape	257
10.2 Alinement of crystal	258
10.3 Correct assignment of signs of crystallographic axes	260
10.4 Measurement of lattice parameters	262
10.5 Choice of scan	265
10.6 Strategy for exploring reciprocal space	267
10.7 Counting statistics and period of counting	268

CHAPTER 11

Derivation and Accuracy of Structure Factors

11.1 Lorentz factor	278
11.2 Polarization factor	284
11.3 Observed structure factors: absolute measurements	288
11.4 Calculated structure factors	291
11.5 Comparison of observed and calculated structure factors	296

CHAPTER 12

Computer Programs and On-line Control

12.1 Diffractometer input and output	page 303
12.2 Types of computer programs	305
12.3 Direct connexion to a computer	308

APPENDIX

Summary of differences between X-ray and neutron diffractometry	312
<i>References</i>	315
<i>Index</i>	327

PREFACE

The determination of a crystal structure normally proceeds in three distinct stages. The first is the measurement of the intensities of the Bragg reflexions and the calculation from them of amplitudes, reduced to a common scale and corrected for various geometrical and physical factors. These amplitudes are known as 'observed structure amplitudes' or 'observed structure factors'. The second stage is the solution of the phase problem: the phases of the reflexions cannot be measured directly, and yet they must be derived in some way before the structure can be solved by Fourier methods. Because of uncertainties in the amplitudes and phases, this first structure is only approximately correct. The third stage in the structure determination consists of refining the approximate atomic positions so as to obtain the best possible agreement between the observed structure factors and the 'calculated structure factors', that is, those calculated from the approximate atomic positions of the successive stages of refinement.

This book describes counter methods of obtaining the set of observed structure factors of a single crystal, and so is concerned with the first stage only. The rapidly developing interest in automatic methods of collecting structure-factor data, and in measuring intensities to a high level of accuracy, have stimulated the development of counter methods. Photographic methods are still widely used in X-ray crystallography, but in neutron diffraction the single crystal diffractometer has remained the basic instrument for measuring neutron structure amplitudes since systematic studies began in the early 1950's. We shall cover, therefore, the fields of both X-ray and neutron diffractometry: there are remarkably few points where the two fields diverge and we discuss only one subject—the production of the primary beam—in separate chapters for X-rays and for neutrons. Comparisons between X-ray and neutron diffractometry are both interesting and illuminating, and many examples of such comparisons are given in the text.

We assume that the reader has a general acquaintance with the properties of the radiations with which we are concerned: these

properties are described adequately in *X-rays in Theory and Experiment* by A. H. Compton and S. K. Allison, and in *Pile Neutron Research* by D. J. Hughes or *Neutron Diffraction* by G. E. Bacon. A familiarity with M. J. Buerger's *X-ray Crystallography*, a book which charted our own first steps in reciprocal space, and with F. C. Phillips's *An Introduction to Crystallography* would be very helpful.

Advances in single crystal diffractometry have been very rapid during the past few years, and some subjects which we discuss in this monograph are certain of further development. We anticipate, for instance, a better understanding of the various systematic errors occurring in the measurement of structure-factor data: the recent publication of the proceedings of a symposium of the American Crystallographic Association on 'Accuracy in X-ray Intensity Measurements' [Transactions of American Crystallographic Association, volume 1, 1965] testifies to the lively interest in this subject. We do not expect radically different geometrical or mechanical designs in diffractometers of the near future, but the on-line control of these instruments will become more common as cheaper small computers become available. In X-ray crystallography, diffractometers will have to compete in cost and simplicity of operation with computer-linked microdensitometers, and so there may be renewed interest in photographic methods. The eventual development of co-ordinate detectors, in both X-ray and neutron crystallography, could lead to a much more efficient data-collection procedure than any at present in use. For many years to come, however, it seems reasonably certain that automatic X-ray and neutron diffractometers will become standard instruments in an increasing number of laboratories.

We acknowledge the assistance generously given by many colleagues. Professor J. M. Ziman has made many editorial suggestions for improving the text. Individual chapters have been read by Drs D. M. Blow, E. Sandor and H. C. Watson, by Professor S. Ramaseshan, and by Mr J. F. Mallet, and many of their comments have been incorporated. We are especially indebted to Professor R. A. Young of Georgia State University, who has given us access to his extensive and unpublished writings on single crystal diffractometry. We are grateful to Valerie Arndt who prepared the

index. We wish to thank the authors, publishers, and learned societies who have allowed us to reproduce published diagrams and photographs; the sources of these are given in the text. Finally, we should like to express our thanks to the publishers for their co-operation and patience.

U. W. A.
B. T. M. W.

April 1966

CHAPTER I

INTRODUCTION

Until recently, nearly all crystal-structure determinations with X-rays were carried out using photographic methods. Although the majority of crystal structures are still solved using photographic data, the past few years have witnessed profound changes in experimental techniques with the introduction of single crystal diffractometers and with the application of automation procedures to their control. These changes, together with advances in crystallographic computing techniques, portend a sharp increase in both the quantity and quality of future crystallographic work.

In this chapter we shall sketch first the development of photographic and counter methods of measuring the set of X-ray intensities diffracted by a single crystal. This is followed by a survey of single crystal techniques in neutron diffraction and by a comparison of these techniques with X-ray methods. The chapter finishes with a discussion of automatic diffractometers and of the accuracy, speed and cost of counter methods. Our main aim in this chapter is to introduce briefly many points which are explained more fully later in the book.

1.1. X-ray techniques for measuring Bragg reflexions

The first diffraction pattern from a crystal, copper sulphate, was recorded on a photographic plate (Friedrich, Knipping & von Laue, 1912). Shortly afterwards, the ionization spectrometer (Bragg & Bragg, 1913) was developed and used both for the measurement of the wavelengths of X-ray spectra and for the determination of crystal structures. In order to examine the reflected X-ray beam with the spectrometer the crystal was suitably oriented and the intensity measured with an ionization chamber; however, because of the difficulty of measuring the very small ionization currents from an ionization chamber, the Bragg spectrometer was not really suited to the examination of the structures of small crystals or the collection of a large amount of intensity data,

and during the 1920's the instrument was gradually superseded in structural work by the X-ray camera. The general acceptance of photographic methods was promoted especially by the application of the theory of the reciprocal lattice and the Ewald sphere of reflexion (Ewald, 1921) to the interpretation of single crystal rotation photographs (Bernal, 1926), and by the invention of the moving-film camera (Weissenberg, 1924); the Weissenberg camera permitted the measurement of the X-ray reflexions in a systematic way, covering one layer of reciprocal space at a time.

The principal advantage of photographic film over a counter detector is the possibility of recording a large number of reflexions on the same film; the principal drawback is the difficulty of relating the blackness of the film to the intensity of the diffracted beam producing it. For a long time the measurement of X-ray intensities was carried out by comparing visually the blackening of spots on the photographic film with a series of reference spots of graded intensity. The introduction of the precession camera (Buerger, 1942, 1944, 1964), giving an undistorted representation of the reciprocal lattice, encouraged the wider use of microdensitometry. Even now, however, there are very few microdensitometers in use which are capable of measuring automatically the integrated intensity of every spot on a precession photograph, let alone the intensities of spots on a Weissenberg photograph which lie along lines of non-uniform curvature.

Since 1945 the Weissenberg moving-film and the Buerger precession cameras have been the standard instruments for structural work, but during the same period interest has revived in counter methods. The Geiger counter and, later, the proportional and scintillation counters have been developed as reliable detectors, which supersede the ionization chamber used in the Bragg ionization spectrometer. These counters are quantum detectors, capable of counting individual X-ray quanta and of giving a more direct and accurate estimate of the diffracted intensity than photographic film. Extensive use has been made of these detectors for the direct recording of X-ray powder diffraction diagrams. Lonsdale (1948) and Cochran (1950) were amongst the first to exploit quantum counter methods in the examination of single crystals, and many later workers have acquired single crystal diffractometers to

supplement or supplant the collection of diffraction data by X-ray cameras. In recent years there has been intense activity, especially in Europe and the U.S.A., devoted to developing automatic single crystal diffractometers, and a number of different kinds of these instruments is now available commercially.

We note here that, with the widespread use of quantum counters in diffraction work, the word 'diffractometer' was adopted in 1952 by the Apparatus Commission of the International Union of Crystallography to describe instruments for measuring diffracted X-rays (neutrons, electrons) by means of counter detectors. The word 'spectrometer' is reserved for instruments whose principal function is the investigation of X-ray wavelength (or neutron energy) spectra. Thus instruments used for X-ray fluorescence analysis, or the triple-axis instrument (Brockhouse, 1961) used to measure the energy transfer of neutrons scattered inelastically by crystals, are spectrometers. The Bragg ionization instrument would now be termed a diffractometer if used for structural work and a spectrometer for examining X-ray wavelength spectra.

1.2. Neutron techniques for measuring Bragg reflexions: comparison with X-ray techniques

Neutrons do not have a *direct* effect on photographic emulsions, and the diffractometer (using a proportional BF_3 counter as detector) has remained the basic instrument for measuring neutron structure factors. The first manual diffractometer designed for neutron work was built at the Argonne National Laboratory in the U.S.A. in 1945 (Zinn, 1947). During the following period of approximately twelve years nuclear research reactors were available for diffraction studies at only a few major centres: Oak Ridge (Wollan & Shull, 1948), Brookhaven (Corliss, Hastings & Brockman, 1953), Chalk River (Hurst, Pressessky & Tunnicliffe, 1950) and Harwell (Bacon, Smith & Whitehead, 1950). Many more research reactors have been constructed since the mid-1950's, and neutron diffractometers are now in operation at numerous nuclear research centres throughout the world.

In this book we are concerned mainly with those neutron techniques which have a counterpart in X-ray diffraction. For this

reason, inelastic scattering methods, using either the triple-axis spectrometer or time-of-flight techniques, are largely ignored.

In the Appendix at the end of the book we list a number of differences between neutron and X-ray diffractometry: here we shall mention only two of the more obvious differences. The first arises from the nature of the source of the primary radiation. In X-ray crystallography, characteristic radiation of the target element is employed: this is in the form of sharp emission lines, rising

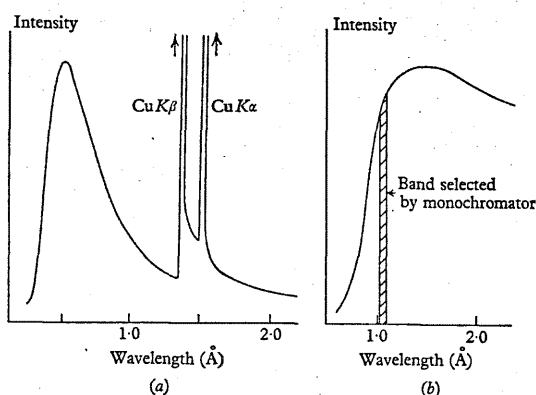


Fig. 1. Intensity curves: (a) for X-rays from a copper target which gives intense lines of characteristic K radiation; (b) for the slow neutron beam emerging from a reactor (after Bacon, 1962).

steeply from a background of 'white' or continuous radiation (Fig. 1a). The presence of white radiation can cause errors in estimating the contribution of the characteristic radiation to the Bragg reflexion. The white radiation can be removed with a single crystal monochromator, but this may lead to further difficulties, and frequently balanced filters or simple beta filters are used instead of crystal monochromators. In neutron diffraction, on the other hand, apart from a radically new technique which uses a pulsed neutron source and time-of-flight wavelength analysis (see p. 217), there is no real alternative to using a monochromator. The slow neutron spectrum from a nuclear reactor consists of a broad

distribution of wavelengths: there is no sharply defined wavelength (Fig. 1b), and radiation from a narrow band of wavelengths is selected with a monochromator.

The second difference concerns the scale of the apparatus. With the highest flux reactors available at present the neutron flux at the sample, measured in neutrons/cm²/s, is always very much less than the flux, in X-ray quanta/cm²/s, from an X-ray tube. This flux difference requires the employment of larger samples in neutron diffraction. Moreover, materials for shielding against fast neutrons must be placed around the monochromator assembly and around the detector; fast neutron shielding is necessarily bulky and so neutron diffractometer assemblies tend to be larger than corresponding X-ray equipment.

1.3. Automatic diffractometers

There has always been a strong incentive to making neutron diffractometers as fully automatic as possible. The neutron source is much more expensive than an X-ray generator, and expenditure on a neutron diffractometer allowing utilization of the neutron source for 24 h/day is justified more readily on economic grounds. The development of automatic X-ray diffractometers has benefited much from the early application of automatic methods in the neutron field.

The setting of the crystal and detector shafts of a diffractometer, and the measurement of each Bragg reflexion, involve repetitive procedures which are extremely tedious to carry out by hand. Fig. 2 illustrates a simplified flow of operations in a system designed to undertake these procedures automatically. The input information consists of instructions for setting the crystal and the detector for each Bragg reflexion, and of instructions for measuring the intensity of the reflexion once the shafts are correctly set. Normally all reflexions are measured sequentially. The output data, consisting of the number of X-ray quanta or slow neutrons which are recorded in scanning across the reflexions, are presented in a form (for instance, punched paper tape) suitable for direct processing by a computer. In the 'off-line' system this processing leads directly to a set of structure amplitudes. In the 'on-line' method the computer is linked both to the diffractometer output and to its

controls: by suitable programming, it is possible to scrutinize the experimental data as they are recorded and, if a measurement fails to satisfy certain programmed criteria, remedial action can be taken, consisting of automatic adjustment of the measuring

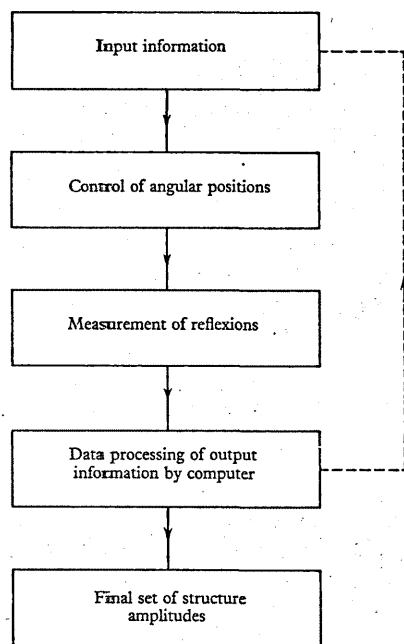


Fig. 2. Flow of operations in an automatic diffractometer system. For 'on-line' operation there is feedback from the processed data to the input via the computer, as indicated by the broken line.

conditions until these criteria are satisfied. The data are then reduced to a set of structure amplitudes as in the off-line system. The on-line system is indicated by the broken line in Fig. 2.

Just as there are two different classes of computers, analogue and digital, so is there a similar choice of analogue or digital instruments in diffractometry. In analogue instruments the relationships be-

tween the setting angles are reconstructed by means of mechanical linkages, and the correct setting angles are generated by simple movements of the linkages: there is no need to compute the magnitudes of the setting angles, and the input information consists of the lattice parameters only, apart from various instrumental constants. The type of linkage governs the mode of operation, such as the sequence in which the reflexions are measured. A different mode requires changes in the mechanical design, and for this reason the analogue method of control is less flexible than digital control.

In the digital method of control, angle encoders convert angular positions of the diffractometer shafts into digital form. The setting of the shafts and the measuring of the reflexions are programmed according to previously prepared input instructions. These input instructions are usually supplied by a computer, as the formulae for the setting angles are too cumbersome for manual computation of any but a very small number of reflexions. Thus, without ready access to a computer, it may be preferable to use the analogue method of setting.

As regards the design of diffractometers, automatic or otherwise, there is a further choice concerning the type of diffraction geometry used. In the 'normal-beam equatorial' geometry (Fig. 3) the incident beam lies in the same plane (the equatorial plane) as that in which the detector moves, and one of the axes about which the crystal rotates (the ω -axis) is normal to the equatorial plane. This ω -axis is used as the oscillation axis in scanning across the reflexion. The crystal orientation is determined by the three Eulerian angles— ϕ , χ , ω —and these angles must be reset between measurements of separate reflexions. This geometry is particularly useful in neutron diffraction, where the motion of the detector, with its bulky fast-neutron shielding, is best restricted to a single, horizontal plane. In the 'inclination' (Fig. 4) type of geometry both the incident and diffracted beams are inclined at variable angles, $90^\circ - \mu$ and $90^\circ - \nu$ respectively, to the crystal oscillation axis, which, in contrast with the equatorial geometry, coincides with the goniometer-head axis ϕ . The crystal is rotated about the single axis ϕ to bring each reflecting plane to the measuring position and the detector is rotated about two independent axes, ν and Υ , to receive the

diffracted beam. With inclination instruments used in one of the special settings (equi-inclination, normal-beam, flat-cone) discussed in Chapter 2, it is only necessary to alter one detector axis and one crystal axis in order to measure all the reflexions in a given reciprocal lattice level; for automatic operation it is usual to control these two axes automatically and to adjust the remaining axis by hand between the measurement of different levels.

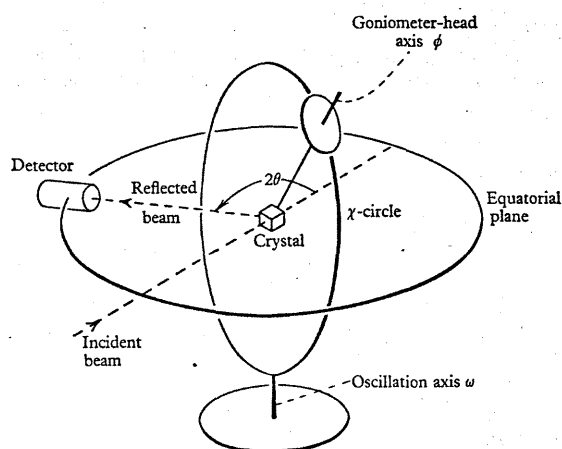


Fig. 3. Normal-beam equatorial geometry. The crystal is mounted on a goniometer-head attached to the ϕ -axis; the ϕ -circle moves round the vertical χ -circle, and the ϕ - χ assembly rotates as a whole about the vertical ω -axis. The detector moves in the horizontal, equatorial plane and the incident beam is normal to the crystal oscillation axis ω .

Once the crystal and detector are set correctly to record a given reflexion, one of three measuring procedures may be initiated to determine the magnitude of the integrated intensity. In the first (*stationary-crystal-stationary-detector* method) the peak intensity and the background in the vicinity of the reflexion are measured with the crystal and detector both stationary. The difference between the peak intensity and the background intensity is proportional to the integrated intensity, provided the incident beam has a wide and uniform angular distribution of intensity at the

specimen. These two conditions are difficult to satisfy simultaneously, and so, in spite of its speed and simplicity, the stationary-crystal-stationary-detector method is rarely used. In the other two measuring procedures, the crystal moves slowly through the reflecting position as the reflected beam is recorded: the crystal alone moves in the *moving-crystal-stationary-detector* method; the

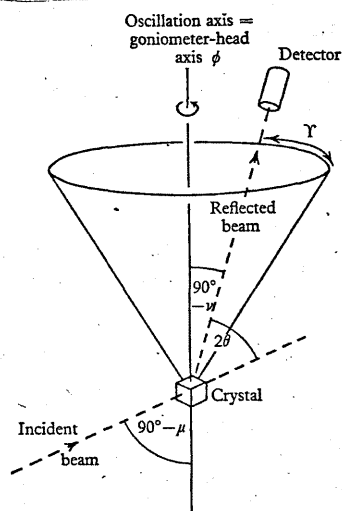


Fig. 4. Inclination geometry. The crystal is mounted on a goniometer-head attached to a single shaft ϕ . The detector moves around a cone with variable semi-angle, $90^\circ - \nu$, and the incident beam likewise makes a variable angle, $90^\circ - \mu$, with the crystal oscillation axis ϕ .

detector moves at twice the angular velocity of the crystal in the *moving-crystal-moving-detector* method. In these two scans a complete profile of the reflexion is measured and the area of this profile above the background is the required integrated intensity.

1.4. Accuracy of counter methods

One of the objects of crystal-structure determinations is often the derivation of bond lengths between neighbouring atoms. To measure bond lengths to an accuracy of 0.01 \AA requires extremely

good experimental data, and for the study of thermal vibration amplitudes or electron density distributions even higher quality may be necessary. This search for accuracy has contributed to the swing back to counter methods of detection in X-ray crystallography. Modern scintillation and proportional counters are far superior to the earlier ionization chambers: it is now possible to count the individual X-ray quanta received by the detector and to record directly the intensity of each diffracted beam in terms of the number of quanta received per second. In the photographic method a direct determination of intensity is not possible. The blackness of a spot on a photographic film must be related to the intensity of the beam producing it, and, even in the most careful work, this introduces errors of perhaps 10 per cent in the estimated intensities. The photographic determination of X-ray intensities is fully described in the book *Crystal-Structure Analysis* by M. J. Buerger (1960).

The production of X-rays in an X-ray tube, or of thermal neutrons in a nuclear reactor, is a statistical process and is subject to random statistical fluctuations. If the detector records a total of N counts in a given time, the standard deviation of repeated measurements of this number is $N^{1/2}$, and the fractional standard deviation is $N^{-1/2}$. This means that at least 10,000 counts must be recorded to achieve a percentage standard deviation not exceeding 1 per cent.

The final accuracy of the experimental data obtained with a diffractometer is very often limited by systematic errors rather than by the random statistical error. Systematic errors arising from such factors as absorption, extinction, simultaneous reflexions or thermal diffuse scattering (which peaks at the same position as the Bragg reflexion and causes errors in estimating the background level under the reflexion) are difficult to calculate or to correct for experimentally. It may be possible to correct some of the systematic errors by repeating or extending the measurements under different experimental conditions (for instance, by using a different wavelength or by changing the azimuthal orientation of the reflecting planes), but very careful and painstaking work is necessary to reduce the relative errors of the structure factors to the region of 1 per cent. In later chapters we shall discuss the questions of random and systematic errors, and analyse the results of intensity

measurements carried out on standard crystals with known structures.

1.5. Speed of counter methods

Nearly all X-ray diffractometers measure the diffraction peaks in succession, whereas photographic methods are capable of recording a complete reciprocal lattice level on the same film. On the other hand, diffractometers can be adapted readily to automatic methods of control: automatic diffractometers are capable of high speed and accuracy (although these two features tend to be mutually exclusive), and they eliminate much of the tedium and labour demanded by photographic work.

It is probably in the study of large biological molecules that the high speed of diffractometer methods is of greatest importance. The determination of the structure of even a relatively small protein requires the measurement of perhaps 250,000 reflexions: a data collection task of this magnitude could not readily be undertaken without an automatic diffractometer. An example from this field (H. C. Watson, private communication, 1965) illustrates the advantages of diffractometry in a particularly striking way.

The protein, glyceraldehyde 3-phosphate dehydrogenase, has a molecular weight of 140,000 and four molecules are contained in the unit cell of approximate dimensions $a = 150 \text{ \AA}$, $b = 140 \text{ \AA}$ and $c = 80 \text{ \AA}$. There are approximately 3,500 independent reflexions from planes with spacings greater than 6.5 \AA . These reflexions were measured first using two Buerger precession cameras operating simultaneously on two crystals. The resulting films were measured on a recording microdensitometer, the chart records analysed by experienced assistants, and the intensities punched on cards. The scaling of the measurements on different films and on different crystals, and the correction for Lorentz and polarization factors, were carried out by computer. (The data were not corrected for absorption.) Three months of full-time work by one scientist and one assistant were required to produce a list of 3,500 structure factors: this corresponds to an average output of about 50 reflexions/day. A total of 36 different crystals were used in this investigation since each crystal could withstand only 72 h in the X-ray beam.

The same reflexions were then measured on one crystal using a paper-tape-controlled three-circle diffractometer. The time taken—by one scientist—was 3 days, and the data were then already on paper tape, ready for further processing. Because a distant computer was used, an additional day was needed for this processing. This data collection rate of 1,000 reflexions/day can be enhanced by factors of three or five when employing multiple counter techniques (Phillips, 1964; Arndt, North & Phillips, 1964), without any increase in X-ray exposure to the specimen.

1.6. Cost of counter methods

In spite of the high capital costs of automatic-diffractometer installations, their use for data collection may give rise to real economic advantages. This is shown by analysing the data-collection problem discussed above.

(a) Photographic data collection (X-rays)

Capital cost of X-ray tube, two precession cameras, densitometer, darkroom equipment	£3,500
Annual costs	
Interest on capital at 5% p.a.	£175
Depreciation (assuming writing-off the equipment in 10 years)	£350
Materials, spares, servicing	£200
Scientist's salary	£2,000
Full-time technician	£800
	£3,525 p.a.

Number of reflexions measured in one year at 3,500 reflexions in 3 months = 14,000
Hence cost per 1,000 reflexions = £250

(b) Diffractometer data collection (X-rays)

Capital cost of diffractometer, X-ray tube, electronic test equipment	£20,000
Annual costs	
Interest on capital at 5% p.a.	£1,000
Depreciation (assuming writing-off the equipment in 7½ years)	£2,667
Materials, spares, servicing	£800
Scientist's salary	£2,000
Part-time electronics technician	£700
Part-time assistant	£500
	£7,667 p.a.

Number of reflexions measured per year at 5,000 per week for 48 weeks = 240,000
Hence cost per 1,000 reflexions = £32

It must be emphasized that economies of this magnitude are realized only if the diffractometer is fully employed: this in turn implies that the laboratory in which it is installed has data-collection problems of an adequate magnitude, and that the instrument is sufficiently reliable to function for a high fraction of the working year. These two conditions as yet apply simultaneously in very few laboratories.

Diffractometer data collection (neutrons)

The cost of providing a monochromatic neutron beam varies from reactor to reactor and is very difficult to determine: however, for a 20 MW reactor a figure of £10,000–£15,000 p.a. per diffractometer is perhaps appropriate. The costs of the remaining items in the diffractometer installation are essentially the same as for X-rays, and so we can estimate a total annual cost of about £20,000 per diffractometer. Assuming that 500 reflexions are measured in one week, the net cost per 1,000 reflexions is £1,000. This is a very crude overall figure but it does serve to emphasize that neutrons must only be used for those crystallographic problems—for instance, the determination of magnetic structures, and the location of light atoms in compounds containing heavy elements—which could not be tackled with X-rays.

CHAPTER 2

DIFFRACTION GEOMETRY

We have referred already (see p. 7) to the two principal methods of measuring a set of Bragg reflexions. The first is the *inclination* method, which is related to the photographic Weissenberg technique. The second, the *normal-beam equatorial* method, has no counterpart in photographic work. In this chapter we shall describe the diffraction geometry associated with these two methods and derive formulae for the setting angles of the crystal and detector, both in a general form and in various simplified forms for special settings and particular crystal symmetries. We shall then compare the two geometries and show how the special settings which are used in either method are related to one another. Finally, we shall discuss the problem of measuring several reflexions at the same time with a diffractometer.

It is necessary to describe first the geometrical requirements for setting the crystal and detector and for measuring the reflexion. Bragg's law imposes certain geometrical conditions on the positions of the crystal and the detector, and these conditions must be satisfied before the measurement begins. Once the crystal and detector are correctly set, the reflexion is measured by counting the number of diffracted X-ray quanta or slow neutrons received by the detector as the crystal rotates uniformly through the Bragg reflecting region. These geometrical considerations are best described in terms of the reciprocal lattice and the Ewald sphere of reflexion.

2.1. General considerations

The reciprocal lattice

The unit cell of the direct lattice is the parallelepiped with edges \mathbf{a} , \mathbf{b} , \mathbf{c} . The magnitudes of these vectors are a , b , c and their interaxial angles are α , β , γ , where α is the angle between \mathbf{b} and \mathbf{c} , β that between \mathbf{c} and \mathbf{a} and γ that between \mathbf{a} and \mathbf{b} .

DIFFRACTION GEOMETRY

The vectors \mathbf{a}^* , \mathbf{b}^* , \mathbf{c}^* defining the unit cell of the reciprocal lattice are derived from \mathbf{a} , \mathbf{b} , \mathbf{c} in the following way. The vector \mathbf{a}^* is normal to the plane containing \mathbf{b} and \mathbf{c} , and its magnitude a^* is proportional to the reciprocal of the spacing of the (100) family of planes in the direct lattice. Thus

$$\mathbf{a}^* \cdot \mathbf{b} = \mathbf{a}^* \cdot \mathbf{c} = 0,$$

where the dot indicates a scalar product, and

$$|\mathbf{a}^*| = a^* = K/d_{100},$$

where K is a constant. Unit cells in the direct and reciprocal lattices are shown in Fig. 5.

In considering the reciprocal lattice in relation to the diffraction process, it is convenient to choose $K = \lambda$, the wavelength of the incident radiation. This choice will be used throughout this book. We have then

$$a^* = \lambda/d_{100}.$$

Similarly, \mathbf{b}^* is defined as a vector normal to the \mathbf{ca} -plane and of magnitude

$$b^* = \lambda/d_{010},$$

and \mathbf{c}^* as normal to the \mathbf{ab} -plane and of magnitude

$$c^* = \lambda/d_{001}.$$

The relations between the cell edges in the direct lattice and those in the reciprocal lattice are:

$$\mathbf{a}^* \cdot \mathbf{a} = \lambda, \quad \mathbf{a}^* \cdot \mathbf{b} = 0, \quad \mathbf{a}^* \cdot \mathbf{c} = 0,$$

$$\mathbf{b}^* \cdot \mathbf{a} = 0, \quad \mathbf{b}^* \cdot \mathbf{b} = \lambda, \quad \mathbf{b}^* \cdot \mathbf{c} = 0,$$

$$\mathbf{c}^* \cdot \mathbf{a} = 0, \quad \mathbf{c}^* \cdot \mathbf{b} = 0, \quad \mathbf{c}^* \cdot \mathbf{c} = \lambda,$$

and the explicit expressions for \mathbf{a}^* , \mathbf{b}^* , \mathbf{c}^* in terms of \mathbf{a} , \mathbf{b} , \mathbf{c} are

$$\left. \begin{aligned} \mathbf{a}^* &= \lambda(\mathbf{b} \wedge \mathbf{c}/V), \\ \mathbf{b}^* &= \lambda(\mathbf{c} \wedge \mathbf{a}/V), \\ \mathbf{c}^* &= \lambda(\mathbf{a} \wedge \mathbf{b}/V). \end{aligned} \right\} \quad (2.1)$$

Here $\mathbf{b} \wedge \mathbf{c}$ denotes the vector product of \mathbf{b} and \mathbf{c} and V is the volume of the unit cell in the direct lattice, that is, $V = \mathbf{a} \cdot \mathbf{b} \wedge \mathbf{c}$.

The reciprocal lattice has two properties which are particularly useful in considering diffraction problems. These properties,

The same equations hold when the starred and unstarred quantities are interchanged.

Geometrical conditions for observing Bragg reflexion. The Ewald sphere

Bragg's law $\lambda = 2d\sin\theta$, (2.6)

expresses the condition that radiation of wavelength λ is diffracted at glancing angle θ by the planes of the direct lattice of spacing d . The law can be interpreted geometrically in terms of the reciprocal lattice and the Ewald sphere of reflexion. This interpretation is particularly convenient in calculating the setting angles of the crystal and detector for observing the Bragg reflexion, and it will be used extensively throughout this book.

The Ewald sphere is defined with reference to the unit vector s_0 , which lies in the direction of the incident beam. If s_0 terminates at the origin O of the reciprocal lattice and has its starting point at C , then the Ewald sphere is the sphere with centre C and radius 1 r.l.u.

Suppose that the reciprocal lattice point P with co-ordinates hkl lies on the surface of the Ewald sphere (Fig. 6). OP is normal to the family of planes (hkl) in the direct lattice and so the angle between the incident beam and OP is $90^\circ - \theta'$, where θ' is the glancing angle of incidence. The length of the diameter OA is 2 r.l.u. and of OP is λ/d , so that in the right-angled triangle APO

$$\cos(90^\circ - \theta') = \lambda/2d. \quad (2.7)$$

Comparison of (2.6) and (2.7) shows that the glancing angle θ' is equivalent to the Bragg angle θ . This is only true if P lies on the surface of the sphere.

Thus the condition for the family of planes (hkl) to diffract radiation of wavelength λ is equivalent to the requirement that the hkl point of the reciprocal lattice lies on the surface of the Ewald sphere of reflexion. We can represent the crystal by a collection of reciprocal lattice points, each point corresponding to a different family of planes in the direct lattice. As the reciprocal lattice rotates it sweeps through the Ewald sphere, and a reflexion occurs each time a reciprocal lattice point cuts the sphere.

In the idealized situation described above the reciprocal lattice points are geometrical points. In practice, the incident beam contains a range of directions and wavelengths and the crystal is of finite extent with reflecting planes that are not exactly parallel; these facts can be accommodated in our geometrical picture by regarding the reciprocal lattice 'points' as small regions of finite size in reciprocal space. Radiation is then diffracted when any part of the small regions lie on the surface of the sphere.

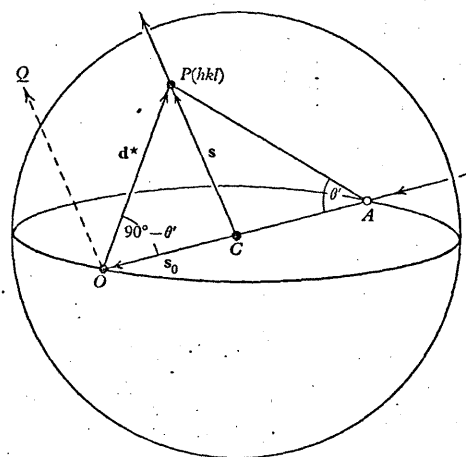


Fig. 6. Ewald sphere of reflexion. O is the origin of reciprocal space, s_0 and s are unit vectors along the incident and reflected beams, and P is a point with co-ordinates hkl with respect to the axes of the reciprocal lattice.

The diffracted beam lies along a direction which is at an angle 2θ to the incident beam and lies in a plane containing the incident beam and the reflecting normal. Fig. 6 shows that this direction is along the line CP , joining the centre of the Ewald sphere to the hkl reciprocal lattice point. To receive the diffracted radiation the detector must be placed along CP , where C is taken as the position of the crystal. In discussing angular relationships with the aid of the Ewald construction, we are at liberty to draw the diffracted beam as originating either at C , the crystal position, or at O , the

origin of the reciprocal lattice. The former practice is generally more convenient, but there are cases where it is preferable to draw the diffracted beam along OQ , parallel to CP (see Fig. 6).

If \mathbf{s} is a unit vector in the direction of the diffracted beam, the relation

$$\mathbf{d}^* = \mathbf{s} - \mathbf{s}_0 \quad (2.8)$$

holds at the reflecting position for the (hkl) plane, where

$$\mathbf{d}^* = h\mathbf{a}^* + k\mathbf{b}^* + l\mathbf{c}^*.$$

The 'scattering vector' \mathbf{S} is defined as $\mathbf{s} - \mathbf{s}_0$, so that the Bragg condition (2.6) is equivalent to bringing the vectors \mathbf{S} and \mathbf{d}^* into coincidence.

Geometrical conditions for measuring Bragg reflexion

The integrated intensity of a reflexion, also known as the integrated reflexion, is proportional to the total energy reflected by the crystal as it passes with uniform angular velocity through the Bragg reflecting position. (A more complete definition is given on p. 234.) The integrated intensity is measured by recording the number of quanta entering the detector as the crystal rotates through a small angular range 2Δ about the Bragg position. During this movement of the crystal the detector can be either kept stationary or given a small movement related to that of the crystal. Accordingly, there are two principal moving-crystal measuring procedures. In the *moving-crystal-stationary-detector* procedure (the ω -scan in the normal-beam equatorial geometry) the detector remains fixed at an angle 2θ to the incident beam during the rotation of the crystal. In the alternative *moving-crystal-moving-detector* procedure (the $\omega/2\theta$ -scan or 2θ -scan in the normal-beam equatorial geometry) the detector shaft is coupled to the crystal shaft by a 2:1 linkage or gear train, so that the crystal rotates from $\theta - \Delta$ to $\theta + \Delta$ while the detector moves from $2\theta - 2\Delta$ to $2\theta + 2\Delta$. The detector window widths, while different in these two scans, must be sufficient in both cases to accept the full angular spread of the diffracted beam.

The crystal rotation through 2Δ can take place about any axis not coincident with the normal to the reflecting plane. In the normal-beam equatorial method the crystal rotates about an axis

lying in the reflecting plane, and the velocity with which the reciprocal lattice point passes through the Ewald sphere is a function of θ only. A valuable feature of this method is that the view of the source is the same for all reflexions (Lang, 1954). In the general inclination method, on the other hand, the crystal rotates about the goniometer-head axis, which is inclined at a variable angle to the reflecting plane, and the magnitude of this angle depends on the particular reflexion and on the special inclination setting adopted for measuring it. The Lorentz factor, expressing the time spent by the reciprocal lattice point in passing through the Ewald sphere, has a more complicated form than in the normal-beam equatorial method (see p. 278). Moreover, reciprocal lattice points lying on or very close to the goniometer-head axis cannot cut across the Ewald sphere, and so these points are not accessible to measurement without re-orientating the crystal.

A third procedure for measuring the integrated intensity is to keep the crystal stationary at the Bragg position and to use a strongly convergent incident beam: the recorded intensity in this *stationary-crystal-stationary-detector* technique is then equivalent to that for a parallel beam and oscillating crystal (see Fig. 7). In X-ray work the effective source is a foreshortened view of a line focus, and the convergent beam can be produced merely by viewing the focus with a wide take-off angle.

The stationary-crystal, stationary-detector technique requires a uniform emission of X-rays from a substantial length of the line focus. This condition is difficult to meet in practice, and X-ray measurements made with an oscillating crystal technique tend to be better than those obtained with the stationary-crystal procedure. In neutron diffraction, where the incident beam is reflected by a plane-crystal monochromator, the divergence of the beam is considerably less than that required to give flat-topped diffraction peaks; the divergence can be increased by bending the monochromator but this is likely to give a non-uniform angular distribution of neutron flux. For these reasons the stationary-crystal technique is rarely used in either X-ray or neutron diffraction, in spite of the greater speed and simplicity it offers in data collection.

In all three measuring procedures, in addition to obtaining the diffracted intensity, we must measure the background intensity

(see Chapter 8) in the immediate neighbourhood of the Bragg position. The difference between the intensities of the peak and of the background then gives the true integrated intensity.

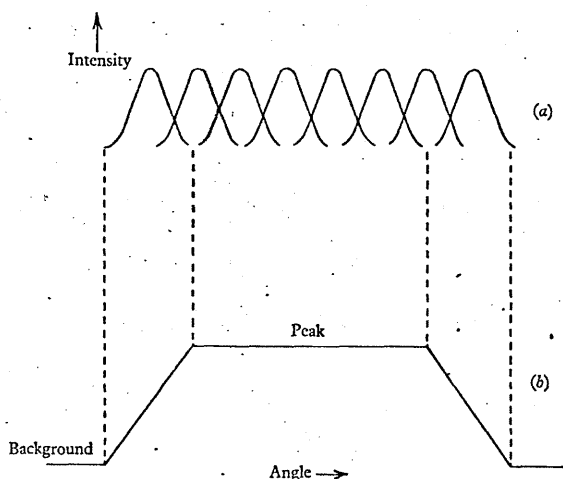


Fig. 7. Principle of stationary-crystal, stationary-detector procedure. The individual profiles of the reflexion in (a), each contributed by a different portion of the convergent incident beam, are summed in (b) to give a flat-topped peak. The integrated intensity is proportional to the peak level minus the background level in (b) (after Buerger, 1960).

2.2. Cylindrical polar co-ordinates in reciprocal space

We can now consider the problem of applying the Ewald construction to the determination of the setting angles for the crystal and detector. General formulae for these setting angles are derived in §§2.3 and 2.4, but to apply these formulae we need first to convert the co-ordinates hkl in reciprocal space to cylindrical polar co-ordinates, taking the 'goniometer-head axis' as the polar axis of cylindrical co-ordinates. This is the axis of the diffractometer on which the goniometer-head carrying the crystal is directly mounted, and we shall always denote the axis by the symbol ϕ .

The cylindrical co-ordinates are ξ, ζ, τ , where ξ is the radial co-ordinate, ζ the axial co-ordinate and τ the angular co-ordinate

(see Fig. 8). These symbols are used by Waser (1951) and others; in chapter 4 of the *International Tables*, volume II, the symbol ϕ is used instead of τ . For our purpose, it is more convenient to adopt Waser's notation and to reserve ϕ for rotation about the

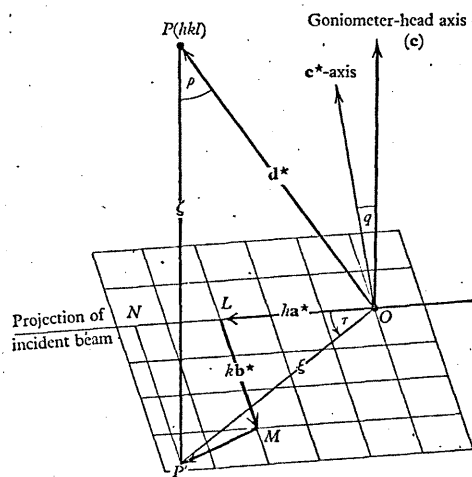


Fig. 8. View of reciprocal-lattice point hkl above a^*b^* plane.

goniometer-head axis in both the inclination and the normal-beam equatorial methods. The angle τ is measured in a clockwise direction, looking along the positive direction of the polar axis, with zero τ coinciding with the projection of the incident beam on the plane normal to the polar axis.

We shall assume that the goniometer-head axis ϕ is parallel to the c -axis of the crystal and that for $\tau = 0$ the a^* -axis is along the trace of the incident beam. Thus the ϕ -axis is normal to the plane a^*b^* of the reciprocal lattice. In using the inclination geometry to measure a set of Bragg reflexions it is customary to align the crystal with the ϕ -axis normal to a reciprocal-lattice plane: this type of alignment is not necessary with the normal-beam equatorial geometry and, in fact, it may be preferable to avoid it and to place the crystal at an arbitrary orientation on the goniometer head.

However, in comparing the two kinds of geometry it is convenient to consider an identical orientation of the crystal in the two geometries. In a later section (p. 51) we discuss the general case in which the crystal assumes an arbitrary orientation in the equatorial geometry.

The expression for $\xi\zeta\tau$ in terms of hkl and the lattice parameters of a triclinic crystal can be derived from Figs. 8 and 9. Fig. 8 is a perspective view looking onto the a^*b^* -plane. Fig. 9a is a projection on the a^*b^* -plane and Fig. 9b is a stereogram giving the angular relationships between p and q , where p is the angle between a^* and the projection of c^* on the a^*b^* -plane and q is the angle between c and c^* . From the Napierian triangle ABC in Fig. 9b, bounded by $90^\circ - q$, p and β^* :

$$\sin q \cos p = \cos \beta^*, \quad (2.9)$$

$$\sin q \sin p = -\cos \alpha \sin \beta^*, \quad (2.10)$$

and $\cos q = \sin \alpha \sin \beta^*. \quad (2.11)$

The ζ co-ordinate is the magnitude of the vector lc^* , projected on the goniometer-head axis. Thus

$$\begin{aligned} \zeta &= lc^* \cos q, \\ &= lc^* \sin \alpha \sin \beta^*, \end{aligned} \quad (2.12)$$

from equation (2.11). ζ can be positive or negative, depending on the sign of l .

The ξ co-ordinate can now be derived from the relation

$$|\mathbf{d}^*|^2 = \xi^2 + \zeta^2.$$

Substituting for $|\mathbf{d}^*|^2$ from equation (2.3) and for ζ^2 from (2.12) gives

$$\begin{aligned} \xi = [h^2 a^{*2} + k^2 b^{*2} + l^2 c^{*2} (1 - \sin^2 \alpha \sin^2 \beta^*) + 2hka^*b^* \cos \gamma^* \\ + 2klb^*c^* \cos \alpha^* + 2lhc^*a^* \cos \beta^*]^{\frac{1}{2}}. \end{aligned} \quad (2.13)$$

ξ must be positive, and so the positive root is taken in (2.13).

The third co-ordinate τ follows from Fig. 9a using the relation

$$\tan \tau = \frac{P'N}{ON} = \frac{kb^* \sin \gamma^* + lc^* \sin q \sin p}{ha^* + kb^* \cos \gamma^* + lc^* \sin q \cos p}.$$

Substituting for $\sin q \cos p$ from (2.9) and for $\sin q \sin p$ from (2.10) gives:

$$\tan \tau = \frac{\sin \tau}{\cos \tau} = \frac{kb^* \sin \gamma^* - lc^* \cos \alpha \sin \beta^*}{ha^* + kb^* \cos \gamma^* + lc^* \cos \beta^*}. \quad (2.14)$$

τ lies in the range $0-360^\circ$. The correct quadrant follows by giving $\sin \tau$ the sign of the numerator in (2.14) and $\cos \tau$ the sign of the denominator.

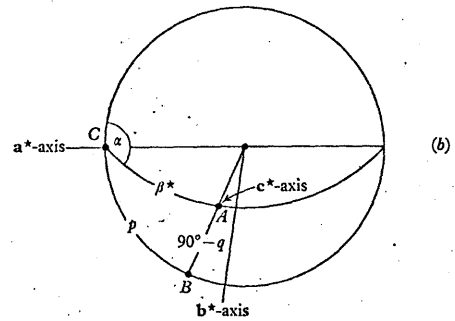
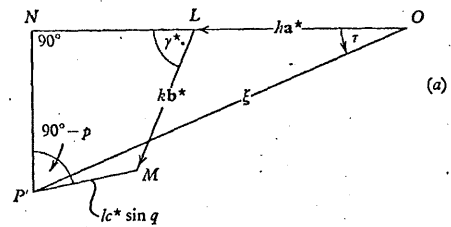


Fig. 9. (a) Vectors in a^*b^* -plane; (b) stereogram projected on to a^*b^* -plane.

Equations (2.13), (2.12) and (2.14) are the required expressions for the cylindrical co-ordinates ξ , ζ , τ in terms of hkl and the lattice parameters. To obtain formulae related to the parameters of the reciprocal cell only, the angle α is replaced by

$$\cos^{-1} \left(\frac{\cos \beta^* \cos \gamma^* - \cos \alpha^*}{\sin \beta^* \sin \gamma^*} \right).$$

The resultant expressions are cumbersome, but considerable simplification occurs for crystal systems of higher symmetry than triclinic.

Table I gives expressions for ξ , ζ , τ for the different crystal systems. The table includes expressions for both the first and second settings of the monoclinic system. In both settings the unique diad axis is along the goniometer-head axis, but is labelled **c** in the first setting (with τ measured from the **a*** axis as zero) and **b** in the second setting (with zero τ along **c***). A similar table has been constructed by Prewitt (1960).

2.3. Inclination method

This is the counter diffractometer version of the photographic Weissenberg method, which is very fully described by Buerger (1942). The Bragg reflexions are measured by rotating the crystal with uniform angular velocity about the goniometer-head axis, ϕ . The incident beam is inclined at an angle $90^\circ - \mu$ to the ϕ -axis and the Bragg reflexion occurs in a direction at $90^\circ - \nu$ to this axis.

If the crystal is mounted with a zone axis, say $[001]$ or the **c**-axis, along the goniometer-head axis, the reciprocal lattice layers or levels at $l = 0, 1, 2, \dots$ are normal to the ϕ -axis. As the crystal rotates, these levels intersect the Ewald sphere in circles ('reflecting circles') and give reflexions lying in cones of semi-angles $90^\circ - \nu$, where each level is associated with a particular value of ν . To pick up a reflexion in a given level the detector is set at the correct angle $90^\circ - \nu$ to the ϕ -axis and is then moved through an angle Υ about an axis concentric with the ϕ -axis. By measuring the reflexions level-by-level, μ and ν can be kept fixed and only two angles, ϕ for the crystal and Υ for the detector, need be varied within each level (see Fig. 4 on p. 9).

If the crystal is mounted in an arbitrary orientation on the goniometer head, so that the ϕ -axis does not coincide with a zone-axis, it is still possible to measure the reflexions, varying three angles ϕ , ν and Υ between measurements. μ can have a fixed value. However, this procedure would be inconvenient as it requires a variation of all three angles, even within a given level. We shall discuss only that orientation of the crystal in which a zone axis is along the ϕ -axis.

TABLE I. Cylindrical co-ordinates of reciprocal lattice point (hkl) for various crystal systems

Crystal system	ξ	ζ	τ
Triclinic; polar axis, c	$\left[\begin{aligned} &h^2a^{*2} + k^2b^{*2} + l^2c^{*2} \\ &+ \cos^2\beta^* - 2\cos\alpha^*\cos\beta^*\cos\gamma^* \\ &+ 2hka^*b^*\cos\gamma^* + 2kbl^*c^*\cos\alpha^* \\ &+ 2llc^*a^*\cos\beta^* \end{aligned} \right]^{1/2}$	$\frac{lc^*}{\sin\gamma^*} \left[\frac{1 - \cos^2\alpha^*}{- \cos^2\beta^* - \cos^2\gamma^*} + 2\cos\alpha^*\cos\beta^*\cos\gamma^* \right]^{1/2}$	$\tan^{-1} \left[\frac{hb^*\sin\gamma^* + lc^*\cos\beta^*\cos\gamma^*}{ha^*\sin\gamma^* + lc^*\cos\gamma^*} \right]$
Monoclinic, first setting ($\alpha^* = \beta^* = 90^\circ$); polar axis, c	$[h^2a^{*2} + k^2b^{*2} + 2hka^*b^*\cos\gamma^*]^2$	lc^*	$\tan^{-1} \left[\frac{hb^*\sin\gamma^*}{ha^* + kb^*\cos\gamma^*} \right]$
Monoclinic, second setting ($\alpha^* = \gamma^* = 90^\circ$); polar axis, b	$[h^2a^{*2} + l^2c^{*2} + 2lhc^*a^*\cos\beta^*]^2$	hb^*	$\tan^{-1} \left[\frac{ha^*\sin\beta^*}{lc^* + ha^*\cos\beta^*} \right]$
Hexagonal ($a^* = b^*$; $\alpha^* = \beta^* = 90^\circ$; $\gamma^* = 120^\circ$); polar axis, c	$[h^2 + k^2 + hk]a^{*2}$	$-lc^*$	$\tan^{-1} \left[\frac{\sqrt{3}k}{2h + k} \right]$
Orthorhombic ($\alpha^* = \beta^* = \gamma^* = 90^\circ$); polar axis, c	$[h^2a^{*2} + k^2b^{*2}]^2$	lc^*	$\tan^{-1} \left[\frac{kb^*}{ha^*} \right]$
Tetragonal ($a^* = b^*$; $\alpha^* = \beta^* = \gamma^* = 90^\circ$); polar axis, c	$[h^2 + k^2]a^{*2}$	lc^*	$\tan^{-1} \left[\frac{k}{h} \right]$
Cubic ($a^* = b^* = c^*$; $\alpha^* = \beta^* = \gamma^* = 90^\circ$); polar axis, c	$[h^2 + k^2]a^{*2}$	lc^*	$\tan^{-1} \left[\frac{k}{h} \right]$

For monoclinic system, second setting, polar axis is along **b** and zero τ is along **c***. For all other cases polar axis is along **c** and zero τ is along **a***. ξ is always positive. ζ takes the same sign as the index l . τ lies between 0 and 360° ; to obtain the correct quadrant the numerator in the expression for $\tan\tau$ gives the sign of $\sin\tau$ and the denominator the sign of $\cos\tau$.

General setting angles of crystal and detector

We wish to derive formulae giving the setting angles ϕ , ν , Υ in terms of the inclination angle μ and the cylindrical co-ordinates $\xi\zeta\tau$ of the hkl point. In the general inclination geometry μ can take an arbitrary value.

The reference orientation of the crystal is chosen with the c -axis along the goniometer-head axis, $+c$ upwards in Fig. 4, and the a^* -axis along the projection of the incident beam in the plane normal to the goniometer-head axis. ϕ is the angle of rotation from this standard orientation, measured in a clockwise manner looking along the positive c direction. Υ is the angle which the detector moves round from the 'straight through' position: positive Υ corresponds to clockwise rotation of the detector arm looking along c , or counter-clockwise rotation as seen looking down from above in Fig. 4. Thus Υ lies between 0 and 180° for instruments with counter-clockwise 2θ motion and between 0 and -180° for instruments with clockwise 2θ motion. By defining Υ in this way we can derive formulae which apply to both left-handed and right-handed instruments.

Fig. 10a is a perspective drawing of the Ewald sphere, showing the reciprocal lattice point $P (= hkl)$ at the standard orientation of the crystal and the same point S after rotation through ϕ to bring it to the surface of the sphere. S lies in the l -level of the reciprocal lattice, normal to the rotation axis. The figure also shows the zero level, passing through the origin O of the reciprocal lattice, and the equatorial level which is normal to the rotation axis and passes through the centre C of the Ewald sphere. The setting angles ν , Υ of the detector are given by

$$\sin \nu = \zeta + \sin \mu, \tag{2.15}$$

and
$$\cos \Upsilon = \frac{CQ^2 + CM^2 - QM^2}{2CQ \cdot CM}$$

$$= \frac{[1 - (\zeta + \sin \mu)^2] + \cos^2 \mu - \zeta^2}{2[1 - (\zeta + \sin \mu)^2]^{\frac{1}{2}} \cos \mu},$$

or
$$\cos \Upsilon = \frac{2 \cos^2 \mu - 2\zeta \sin \mu - \zeta^2 - \zeta^2}{2 \cos \mu (\cos^2 \mu - 2\zeta \sin \mu - \zeta^2)^{\frac{1}{2}}}. \tag{2.16}$$

The inclination angles μ , ν are restricted to the first quadrant, $0-90^\circ$, and the positive root is taken in the denominator of (2.16).

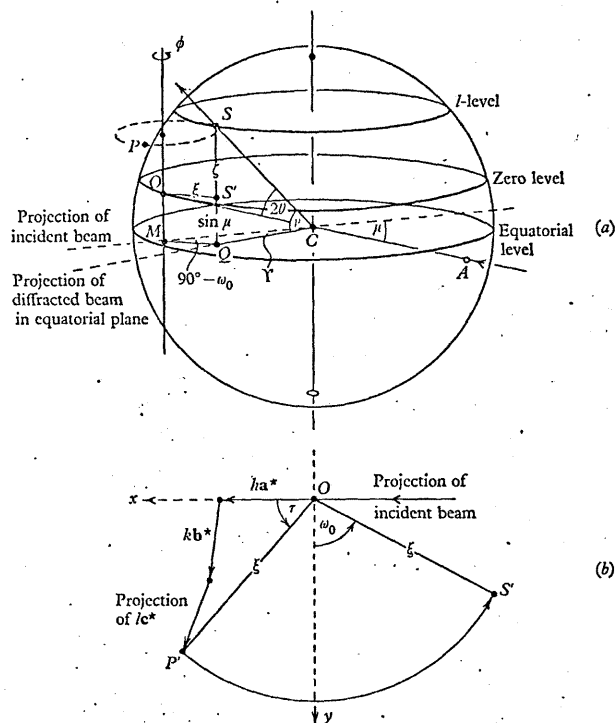


Fig. 10. (a) Ewald sphere with crystal in general inclination setting. The crystal is mounted with its c -axis along the goniometer-head axis ϕ . S is the reciprocal-lattice point hkl in the reflecting position, and P in the reference position. (b) Zero level in general inclination setting. P' is the projection of the hkl point in the reference position of the crystal and S' the projection of hkl in the reflecting position. ϕ is the angle between OP' and OS' .

The correct quadrant of Υ is determined by the sense of the 2θ motion, clockwise or anti-clockwise (see above).

The crystal setting angle ϕ is derived from Fig. 10b, which is a projection of Fig. 10a on the zero level. The points P and S project as P' and S' . The Cartesian axes xyz are laboratory axes with the z -axis parallel to c and the x -axis initially along a^* . ϕ is related to

the angle ω_0 between the y -axis and OS' in Fig. 10*b* by the equation

$$\phi = 180^\circ - \tau - (90^\circ - \omega_0). \quad (2.17)$$

From Fig. 10*a*

$$\begin{aligned} \cos(90^\circ - \omega_0) &= \frac{QM^2 + CM^2 - CQ^2}{2QM \cdot CM} \\ &= \frac{\xi^2 + \cos^2 \mu - (1 - \xi^2 - \sin^2 \mu - 2\xi \sin \mu)}{2\xi \cos \mu} \\ &= \frac{\xi^2 + \xi^2 + 2\xi \sin \mu}{2\xi \cos \mu}. \end{aligned} \quad (2.18)$$

Combining (2.17) and (2.18):

$$\phi = 180^\circ - \tau - \cos^{-1} \left(\frac{\xi^2 + \xi^2 + 2\xi \sin \mu}{2\xi \cos \mu} \right). \quad (2.19)$$

The last term of (2.19) lies in the first quadrant for counter-clockwise 2θ motion and in the fourth quadrant for clockwise motion.

The setting angles for a crystal of any symmetry, examined in the general inclination setting, are readily derived by combining (2.15), (2.16) and (2.19) with the formulae for $\xi\zeta\tau$ in Table I.

We have derived the formulae for the setting angles without placing any restriction on the inclination angle μ . Thus μ can be assigned an arbitrary value before each hkl reflexion is measured. However, if we alter μ , the whole diffractometer assembly tilts with respect to the incident beam, and so it is mechanically desirable to carry out the intensity measurements at a minimum number of μ settings. Moreover, with μ fixed, the inclination angle ν of the detector is also fixed, in accordance with equation (2.15), for a given reciprocal lattice level which is normal to the goniometer-head axis ($\zeta = \text{constant}$). For these reasons it is customary to assign μ a particular value for each level, measuring the hkl reflexions level by level and varying only the angles ϕ (for the crystal) and Υ (for the detector) within each level. The particular value chosen for μ gives rise to the normal-beam, equi-inclination, anti-equi-inclination and flat-cone settings.

Normal-beam setting ($\mu = 0$). The normal-beam setting is so-called, because the incident beam strikes the crystal at 90° to the

axis of rotation. Putting $\mu = 0$ in (2.15), (2.16) and (2.19) gives the following expressions for the three setting angles:

$$\left. \begin{aligned} \nu &= \sin^{-1} \zeta, \\ \Upsilon &= \cos^{-1} \left(\frac{2 - \xi^2 - \zeta^2}{2(1 - \zeta^2)^{\frac{1}{2}}} \right), \\ \phi &= 180^\circ - \tau - \cos^{-1} \left(\frac{\xi^2 + \zeta^2}{2\xi} \right). \end{aligned} \right\} \quad (2.20)$$

For the zero level, $\zeta = 0$, the detector angle Υ is equal to 2θ . An instrument used in the normal-beam setting can be considered equally well as the diffractometer version of the photographic Weissenberg normal-beam method or the photographic rotating-crystal method.

A fundamental weakness of the normal-beam method is that the zero level only can be fully explored. A high proportion of the reflexions on upper levels lie in blind regions: they can be measured only by remounting the crystal in a new orientation. These blind regions are shown in Fig. 11. The small sphere in this figure represents the Ewald sphere of reflexion and the large sphere is the limiting sphere, of radius 2 r.l.u. and centre at the origin of the reciprocal lattice. The limiting sphere includes all hkl points up to the maximum Bragg angle of 90° . For $\zeta \neq 0$ there is an annular blind region around the rim of the reflecting circle at high Bragg angles, and an inner blind region at the centre of this circle of radius $1 - (1 - \zeta^2)^{\frac{1}{2}}$.

Equi-inclination setting ($\mu = -\nu$). The incident and diffracted beams are equally inclined to the positive direction of the rotation axis. The setting angles in (2.15), (2.16) and (2.19) reduce to

$$\left. \begin{aligned} \sin \nu &= \frac{1}{2} \zeta, \\ \Upsilon &= 2 \sin^{-1} \left(\frac{\xi}{2 \cos \mu} \right), \\ \phi &= 180^\circ - \tau - \cos^{-1} \left(\frac{\xi}{2 \cos \mu} \right). \end{aligned} \right\} \quad (2.21)$$

The angles Υ and ϕ are independent of ζ , so that there is a resemblance between the different levels, which in photographic work leads to simplifications in interpreting photographs of the various levels (Buerger, 1942).

There are no blind regions within the limiting sphere, because the axis of rotation ϕ passes through the reflecting circle of the l -level (Fig. 12). However, reciprocal lattice points close to the rotation axis have a large Lorentz factor and cannot be measured accurately. The equi-inclination setting is also liable to give intensity errors arising from simultaneous reflexions (see p. 251).

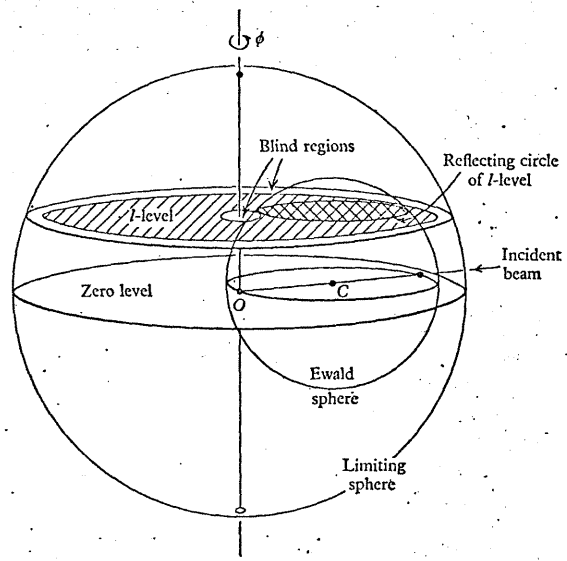


Fig. 11. Normal-beam setting, showing zero level and l -level. The l -level intersects the Ewald sphere in the cross-hatched region; as this region rotates the shaded area is scanned, leaving blind regions inside limiting sphere.

Such errors occur if at least two reciprocal lattice points lie simultaneously on the sphere of reflexion. This condition is automatically satisfied if the crystal is mounted in the equi-inclination setting with c^* (which coincides with c for orthogonal crystals) along the axis of rotation (Yakel & Fankuchen, 1962). In measuring the reflexions in the l -level the ool point will then always lie on the surface of the Ewald sphere, and when hkl is in the reflecting

position the hko point is on the Ewald sphere too, as shown in Fig. 12. The simultaneous presence of hkl , hko and ool on the Ewald sphere can lead to serious errors in measuring hkl alone. A similar difficulty also occurs in the normal-beam setting: if c^* is along the axis of rotation, hkl and hkl lie on the Ewald sphere simultaneously.

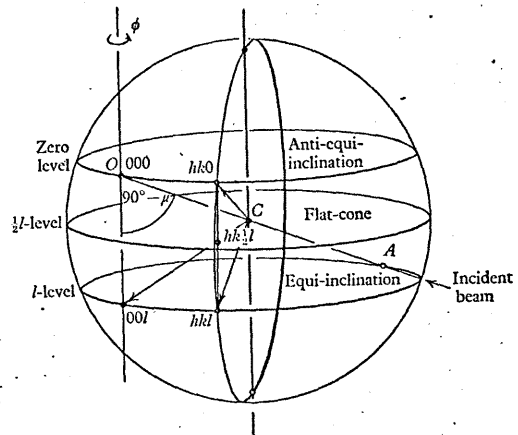


Fig. 12. Ewald sphere showing equi-inclination, flat-cone and anti-equi-inclination levels.

Anti-equi-inclination setting ($\mu = \nu$). From equation (2.15), $\zeta = 0$ if $\mu = \nu$. Consequently, this setting can only be used for reflexions in the zero level and is limited to the collection of two-dimensional data. The incident and diffracted beams are on opposite sides of the equatorial level, and are equally inclined to the rotation axis. The setting angles (equations 2.16 and 2.19) reduce to

$$\left. \begin{aligned} \gamma &= 2 \sin^{-1} \left(\frac{\xi}{2 \cos \mu} \right), \\ \phi &= 180^\circ - \tau - \cos^{-1} \left(\frac{\xi}{2 \cos \mu} \right), \end{aligned} \right\} \quad (2.22)$$

which are the same expressions as for the equi-inclination setting.

Flat-cone setting ($\nu = 0$). If the incident beam makes an angle of $90^\circ - \mu$ with the rotation axis, where μ is given by

$$\sin \mu = -\zeta, \quad (2.23)$$

then from equation (2.15) the inclination angle ν of the diffracted beam is zero. Thus for each level the diffracted beam is normal to the rotation axis and lies in a 'flat cone'. The l -level defined by (2.23) coincides with the plane passing through the centre of the Ewald sphere, normal to the goniometer-head axis, and the detector moves in this plane. The angular position of the detector is

$$\Upsilon = \cos^{-1} \left(\frac{2 - \xi^2 - \zeta^2}{2(1 - \zeta^2)^{\frac{1}{2}}} \right), \quad (2.24)$$

and the setting angle of the crystal is given by

$$\phi = 180^\circ - \tau - \cos^{-1} \left(\frac{\xi^2 - \zeta^2}{2\xi \cos \mu} \right), \quad (2.25)$$

where $\sin \mu = -\zeta$.

Blind regions occur, as in the normal-beam setting, in measuring upper levels. The radius of the circular blind region at the centre of the l -level is $1 - (1 - \zeta^2)^{\frac{1}{2}}$, which is the same magnitude as for the normal-beam setting.

Fig. 12 is a perspective drawing of the sphere of reflexion, showing the equi-inclination, flat-cone and anti-equi-inclination settings. Whenever a general l -level is measured in the equi-inclination setting, the zero level will be in the anti-equi-inclination setting. This is a special case of the situation which arises whenever two levels are located symmetrically on either side of the flat-cone level, and gives rise to the possibility of measuring reflexions simultaneously in pairs (see §2.6).

The orientations of the incident and diffracted beams with respect to the rotation axis of the crystal in the normal-beam, equi-inclination and flat-cone settings are illustrated in Fig. 13; this figure is drawn for the measurement of the $l = 2$ level, and so does not include the anti-equi-inclination setting which can only be used for the zero level, $l = 0$.

Table II summarizes the formulae for the setting angles derived in this section. The first column gives the inclination angle μ of

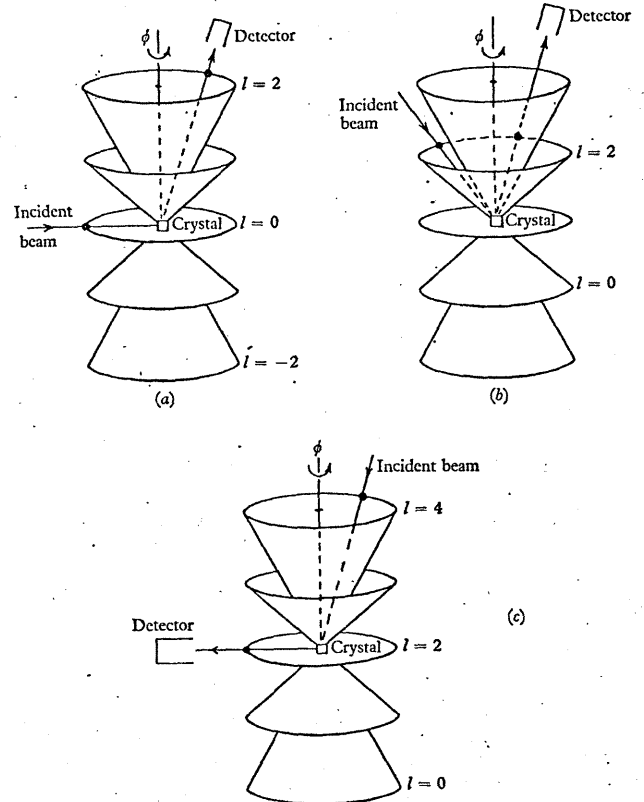


Fig. 13. Measurement of $l = 2$ level in (a) normal-beam, (b) equi-inclination, and (c) flat-cone settings. The diffraction cones for other levels are also shown.

the incident beam, which assumes a particular value for the normal-beam, equi-inclination and flat-cone settings. The remaining columns give the setting angles in terms of μ and the polar coordinates $\xi\zeta\tau$ of the hkl reciprocal lattice point. Combining Tables I and II leads to formulae for the setting angles in terms of hkl and the lattice parameters of the sample.

TABLE II. Setting angles of crystal and detector: inclination geometry

Setting	Inclination angle μ	Setting angle of crystal ϕ	Setting angles of detector	
			ν	γ
General	Arbitrary	$180^\circ - \tau - \cos^{-1} \left(\frac{\xi^2 + \zeta^2 + 2\xi\zeta \sin \mu}{2\xi \cos \mu} \right)$	$\sin^{-1}(\xi + \sin \mu)$	$\cos^{-1} \left(\frac{2 \cos^2 \mu - 2\xi \sin \mu - \xi^2 - \zeta^2}{2 \cos \mu (\cos^2 \mu - 2\xi \sin \mu - \xi^2 - \zeta^2)} \right)$
Normal-beam	0	$180^\circ - \tau - \cos^{-1} \left(\frac{\xi^2 + \zeta^2}{2\xi} \right)$	$\sin^{-1} \xi$	$\cos^{-1} \left(\frac{2 - \xi^2 - \zeta^2}{2(1 - \xi^2)} \right)$
Equi-inclination	$-\sin^{-1}(\frac{1}{2}\xi)$	$180^\circ - \tau - \cos^{-1} \left(\frac{\xi}{2 \cos \mu} \right)$	$\sin^{-1}(\frac{1}{2}\xi)$	$2 \sin^{-1} \left(\frac{\xi}{2 \cos \mu} \right)$
Anti-equi-inclination	Arbitrary	$180^\circ - \tau - \cos^{-1} \left(\frac{\xi}{2 \cos \mu} \right)$	Arbitrary ($= \mu$)	$2 \sin^{-1} \left(\frac{\xi}{2 \cos \mu} \right)$
Flat-cone	$\sin^{-1}(-\xi)$	$180^\circ - \tau - \cos^{-1} \left(\frac{\xi^2 - \zeta^2}{2\xi \cos \mu} \right)$	0	$\cos^{-1} \left(\frac{2 - \xi^2 - \zeta^2}{2(1 - \xi^2)} \right)$

The angles μ, ν lie in the first quadrant. Positive root is taken in expression for γ . γ lies in first and second quadrants for counter-clockwise 2θ motion and in third and fourth quadrants for clockwise 2θ motion. Last term in expression for ϕ lies in first quadrant for counter-clockwise 2θ motion and in fourth quadrant for clockwise 2θ motion. The c-axis of the crystal is along the goniometer-head axis, and at its reference position the crystal is orientated with the a^* -axis along the trace of the incident beam.

2.4. Normal-beam equatorial method

We now come to the second general class of diffraction geometry. Instruments using this kind of geometry are variously known as goniostats, single crystal orienters, three-circle or four-circle diffractometers. We shall use the term 'three-circle diffractometer' to denote an instrument in which the detector shaft is geared to one of the crystal shafts, and the term 'four-circle diffractometer' for an instrument with four independently driven shafts. During the measurement of each reflexion, carried out by oscillating the

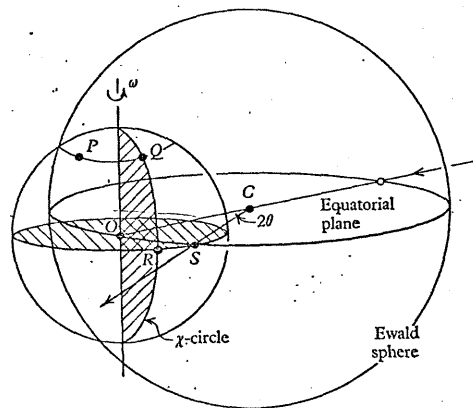


Fig. 14. The Ewald sphere, and the sphere through the reciprocal lattice point P with centre at the origin of the reciprocal lattice. In the symmetrical- A setting the ϕ rotation moves P to Q , the χ -rotation moves Q to R and the ω -rotation moves R to the reflecting position S .

crystal through the Bragg reflecting position, both the incident and diffracted beams are normal to the oscillation axis. Thus the incident and diffracted beams lie in the equatorial plane, which is the plane normal to the crystal oscillation axis and passing through the centre of the sphere of reflexion. We shall call this type of diffraction geometry Normal-Beam Equatorial Geometry (Fig. 3).

Fig. 14 shows the Ewald sphere of reflexion. The oscillation axis is denoted by ω : in contrast with the situation in the inclination method, this axis must be distinguished from the goniometer-head

axis, which we denote again by ϕ . The detector rotates about the 2θ -axis, coincident with the ω -axis; its movement is restricted to the equatorial plane and a rotation through an angle 2θ from the incident beam brings the detector to the correct position for receiving the diffracted beam. To bring the crystal to the reflecting position for the hkl plane, the corresponding reciprocal lattice point P must move to S , where OS is in the equatorial plane and at $90^\circ - \theta$ to the incident beam.

Conventions for setting angles

In a four-circle diffractometer the crystal has three rotational degrees of freedom. Three rotations are sufficient to give any vector, referred to axes in the crystal, any arbitrary orientation in laboratory space. The three circles (see Fig. 15) are the ω -circle, the χ -circle which is carried on the ω -circle and whose axis is normal to the ω -axis, and the ϕ -circle which is mounted on the χ -circle and carries the goniometer head supporting the crystal.

Before deriving expressions for the setting angles of the crystal we must adopt certain conventions for defining the setting angles and the standard orientation of the diffractometer with respect to the laboratory axes x, y, z . The x -axis is defined as the direction of the incident beam, outwards from the source, and is assumed to be horizontal. The z -axis is vertically upwards and the y -axis completes a right-handed system. ω is the angle of rotation of the χ -circle about a vertical diameter and χ is the angle made by the ϕ -axis with this diameter. We define the zero positions of ω and χ when the ϕ -axis is along z and below the crystal and the plane of the χ -circle is normal to x (Fig. 15). The zero value of ϕ , the angle of rotation about the goniometer-head axis, is arbitrary in the sense that it depends on the orientation of the crystal on the goniometer head. As in §2.3, we shall assume that the crystal is mounted with its c -axis along the goniometer-head axis and that $\phi = 0$ when the a^* -axis is along the positive x direction. The positive direction of the goniometer-head axis is defined as along $+z$ in Fig. 15.

We must also give conventions for the positive senses of rotation of the setting angles. When $\chi = 0$, ω and ϕ increasing represent clockwise rotation looking along the positive z -axis. When $\omega = 0$, χ increasing represents a clockwise rotation looking along the

positive x -axis. These conventions are in accordance with the right-handed screw rule, previously used in defining the cylindrical co-ordinate τ and the inclination setting angles ϕ and Υ . The detector angle is measured as a clockwise rotation through 2θ about the positive z -axis; thus 2θ is positive for counter-clockwise movement of the detector as viewed from above the instrument, and negative for clockwise rotation. By allowing for both positive and negative values of θ we can use the formulae derived below for both left-handed and right-handed diffractometers.

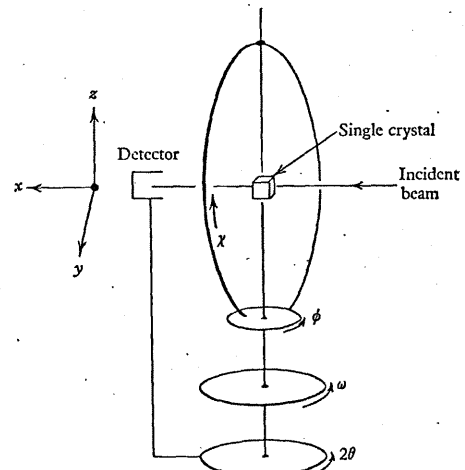


Fig. 15. Positive senses of rotation of $\phi, \chi, \omega, 2\theta$ in equatorial method. The positive direction of the goniometer-head axis is along $+z$.

We note here that the orientation of the crystal, corresponding to the angles ω, χ, ϕ as defined above, is identical to that corresponding to $\omega + 180^\circ, -\chi, \phi + 180^\circ$.

Azimuthal orientation of reflecting plane

In the most commonly used setting, which we shall call the symmetrical- A setting or cone setting (Furnas & Harker, 1955), the χ -plane bisects the incident and diffracted beams at the measuring position. To bring the reciprocal lattice point P ,

Fig. 14, to this position, the crystal is rotated through an angle ϕ so that P coincides with Q in the plane of the χ -circle, through an angle χ to move Q to R along the vertical χ -circle, and through an angle ω to move R to the surface of the sphere of reflexion at S . In general, however, it is not necessary that the hkl normal lies in the χ -plane at the measuring position. Within certain limits, to be determined below, the hkl normal can make any arbitrary angle ϵ with the χ -plane. This degree of freedom arises because the reflecting condition still holds if the crystal rotates about an axis normal to the reflecting plane; the choice of ϵ determines the azimuthal orientation ψ of the plane, measured as the angle of rotation about its normal. We shall take ϵ as positive when the χ -plane lies between the scattering vector and the incident beam (see Fig. 16a), so that the sense of increasing ϵ is the same as that for θ and ω .

To determine the permissible range of ϵ we refer to the stereogram in Fig. 16b, showing the crystal rotations ω, χ, ϕ which are necessary to bring the reciprocal lattice vector OP to the reflecting position OS lying along the scattering vector $S = s - s_0$ in Fig. 16a. The ϕ -rotation moves the reciprocal lattice point P to Q , where Q lies at the point of intersection of two small circles, one through P and normal to the vertical z -axis and the other through R and normal to the x -axis. The χ -rotation moves Q to R , and the ω -rotation moves R to the reflecting position S at $90^\circ - \theta$ to the incident beam. (Fig. 24 on p. 54 is a perspective drawing showing the χ -plane and the ϕ, ω -axes at the reflecting position.)

Let ρ be the fixed angle between the reciprocal lattice vector OP and the positive direction of the goniometer-head axis. ρ is related to the cylindrical co-ordinates ξ, ζ by the equation

$$\tan \rho = \xi / \zeta, \quad (2.26)$$

and we will assume for the present that it lies in the range

$$0 \leq \rho \leq 90^\circ.$$

In the Napierian triangle BQT of Fig. 16b

$$QT = 90^\circ - \rho, \quad \widehat{BQT} = -\chi, \quad BQ = 90^\circ - \epsilon,$$

so that

$$\sin \chi = -\frac{\cos \rho}{\cos \epsilon}. \quad (2.27)$$

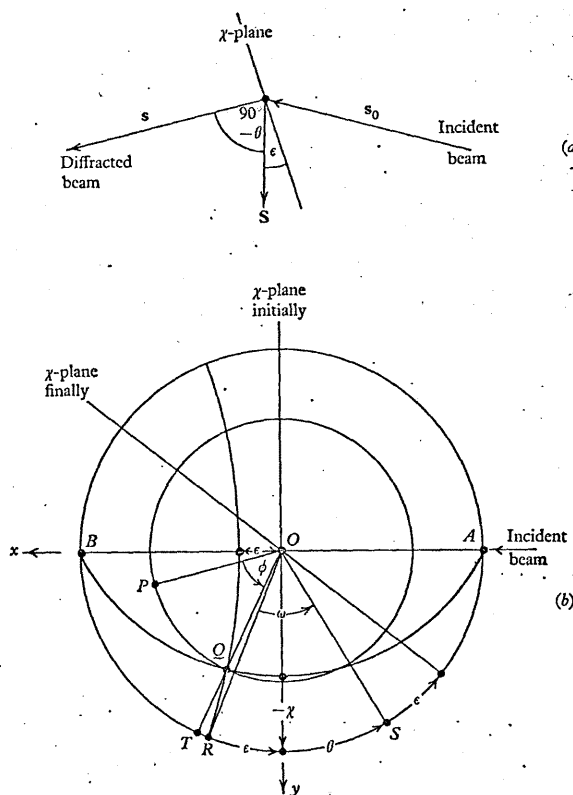


Fig. 16. Normal-beam equatorial method in general setting: (a) definition of off-set angle ϵ , which is positive when the χ -plane lies between the scattering vector S and the incident beam; (b) stereographic projection onto equatorial plane, showing relations between ϵ and the angles ω, χ, ϕ (after Willis, 1962 a).

Thus the reciprocal lattice vector, which is characterized by the angle ρ , can be brought into the reflecting position provided that ϵ lies in the range $\rho \geq \epsilon \geq -\rho$. Any value of ϵ can be chosen in this range, and the particular value selected determines the azimuthal orientation ψ of the reflecting plane.

The stereogram in Fig. 17 gives the relation between ϵ and ψ . CED represents the (hkl) plane after rotation by ϕ , and Q is the pole of the corresponding normal. The χ -rotation displaces Q to R and C to G along small circles normal to the x -axis AB . The inclination of the vector \vec{OC} to the equatorial plane is not affected by the ϕ -rotation and the vector \vec{OG} likewise is unaffected by the

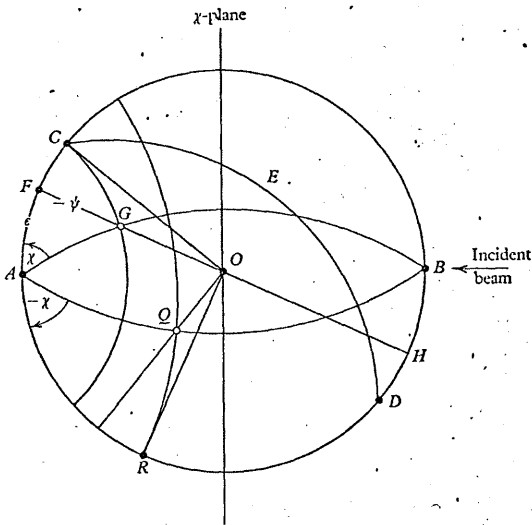


Fig. 17. Stereogram showing relation between azimuth ψ and the offset angle ϵ . CED is the reflecting plane before the χ -rotation and FOH its position after the χ -rotation (after Willis, 1962a).

ω -rotation. Consequently, the azimuth ψ of the plane CED changes only during the rotation about the χ -axis. ψ is the angle of rotation of the crystal about the scattering vector S ; we define it as positive for clockwise rotation looking along the positive direction of S and as zero when $\epsilon = 0$. In Fig. 17, ψ is equivalent to the change in inclination to the equatorial plane of the vector \vec{OC} as it moves to the position \vec{OG} during the rotation about the

χ -axis. Thus $FG = -\psi$, and from the Napierian triangle AFG , with $AF = \epsilon$ and $FAG = \chi$, we have

$$-\tan \psi = \sin \epsilon \tan \chi. \quad (2.28)$$

Combining (2.27) and (2.28) gives

$$\tan \psi = \frac{\sin \epsilon \cos \rho}{(\cos^2 \epsilon - \cos^2 \rho)^{1/2}}. \quad (2.29)$$

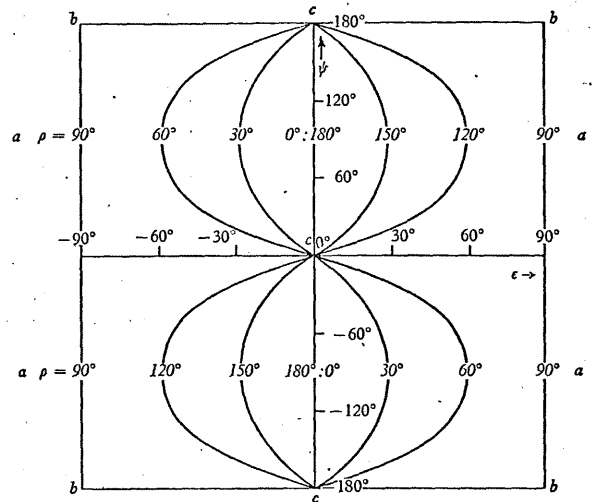


Fig. 18. Dependence of azimuth ψ on the offset angle ϵ for different values of ρ . ρ is the angle between the reciprocal lattice vector and the positive ϕ -axis. For a particular reflexion, characterized by a fixed value of ρ , the azimuth can be varied through 360° by varying ϵ in the range $-\rho \leq \epsilon \leq \rho$ for $\rho < 90^\circ$, or in the range $-(180^\circ - \rho) \leq \epsilon \leq 180^\circ - \rho$ for $\rho > 90^\circ$. The fixed- χ setting is represented by the horizontal lines aa and the symmetrical- B setting by the vertical lines bb . The symmetrical- A setting corresponds to the points c where all the curves converge.

Equation (2.29) is the required relation between the azimuth ψ and the offset angle ϵ of the χ -circle, for those reflecting planes inclined at an angle ρ to the ϕ -axis.

Fig. 18 shows graphically the relation between ψ and ϵ for the full range $0-360^\circ$ in ψ . For reflexions with $\rho = 0 (180^\circ)$ or 90° the

azimuth can be changed without altering the offset angle. If $\rho = 0$ (180°) the scattering vector lies along the goniometer-head axis and ψ can be made to vary continuously by changing ϕ , whereas if $\rho = 90^\circ$ the scattering vector lies along the χ -axis and ψ can be varied continuously by changing χ . For intermediate values of ρ , ψ depends on the value chosen for the angle ϵ , and there are corresponding changes in the setting angles ω , χ , ϕ , which also depend on ϵ . We must now derive expressions for ω , χ , ϕ in terms of the offset angle and the co-ordinates ξ , ζ , τ .

General setting angles of crystal

ω , χ , ϕ are the setting angles required to bring the crystal from the standard orientation (defined on p. 38) to the reflecting position for the (hkl) plane.

ω is given from Fig. 16b as

$$\omega = \theta + \epsilon, \quad (2.30)$$

and χ is given by equation (2.27). To derive an expression for ϕ , we have from Fig. 16b:

$$\phi = \hat{B}OT - \hat{B}OP. \quad (2.31)$$

But $\hat{B}OP = \tau$, the angular polar co-ordinate of P , and $\hat{B}OT$ is related to the angles $-\chi$ and $90^\circ - \epsilon$ in the Napierian triangle BQT by

$$\tan \hat{B}OT = \sin(90^\circ + \chi) \cot \epsilon. \quad (2.32)$$

Combining (2.27), (2.31) and (2.32) gives:

$$\phi = \tan^{-1} \left(\frac{(\cos^2 \epsilon - \cos^2 \rho)^{\frac{1}{2}}}{\sin \epsilon} \right) - \tau. \quad (2.33)$$

The required equations for the setting angles are (2.27), (2.30) and (2.33).

Let us suppose that the offset angle is ϵ_0 , where ϵ_0 is negative. Thus ϵ_0 lies in the range $0 \leq \epsilon_0 \leq -\rho$, and the hkl point is in the upper hemisphere of reciprocal space (that is, ρ lies between 0 and 90°). From equation (2.29) the azimuthal orientation ψ_0 of the reflecting plane lies between 0 and 90° and is given by

$$\tan \psi_0 = \frac{\sin \epsilon_0 \cos \rho}{(\cos^2 \epsilon_0 - \cos^2 \rho)^{\frac{1}{2}}}.$$

The setting angles are

$$\left. \begin{aligned} \omega &= \theta + \epsilon_0, \\ \chi &= -90^\circ + \chi_0 \quad (0 \leq \chi_0 \leq \rho), \\ \phi &= \phi_0 - \tau \quad (0 \leq \phi_0 \leq 90^\circ), \end{aligned} \right\} \quad (2.34)$$

and

$$\cos \chi_0 = \frac{\cos \rho}{\cos \epsilon_0},$$

where

$$\tan \phi_0 = \frac{(\cos^2 \epsilon_0 - \cos^2 \rho)^{\frac{1}{2}}}{\sin \epsilon_0}.$$

and

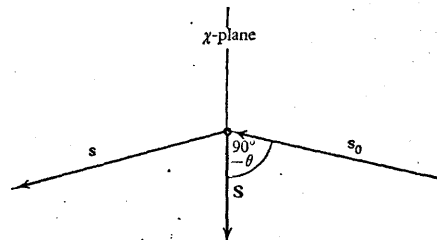


Fig. 19. Relation of χ -plane and scattering vector in symmetrical-A setting.

The expressions (2.34) for the setting angles can be extended to include the full range of azimuth from 0 to 360° . The results are presented in Table III.

Special settings in the equatorial method arise, when ϵ is assigned a particular value for each reflexion. Some of these special settings are discussed below.

Symmetrical-A setting ($\epsilon = 0$). At the reflecting position the χ -circle is symmetrically related to the incident and reflected beams (Fig. 19) and contains the scattering vector S . The expressions for the setting angles in (2.30), (2.27) and (2.33) simplify to:

$$\left. \begin{aligned} \omega &= \theta, \\ \sin \chi &= -\frac{\zeta}{(\xi^2 + \zeta^2)^{\frac{1}{2}}}, \\ \phi &= 90^\circ - \tau. \end{aligned} \right\} \quad (2.35)$$

and

The detector is at an angle 2θ to the straight-through direction of the incident beam, so that the ω and 2θ shafts of the diffractometer can be geared together in a 1:2 ratio, reducing the number of setting angles for the crystal and detector to three. Each reflexion is observed at only one azimuthal orientation of the reflecting plane, apart from the single plane normal to the ϕ -axis, for which any value of the azimuth ψ can be chosen by varying ϕ .

TABLE III. Setting angles for different values of the azimuth ψ : equatorial geometry

	$\psi = 0$	$\psi = \psi_0$	$\psi = 90^\circ$	$\psi = 180^\circ - \psi_0$	$\psi = 180^\circ$
ϵ	0	ϵ_0	$-\rho$	ϵ_0	0
ω	θ	$\theta - \epsilon_0 $	$\theta - \rho$	$\theta - \epsilon_0 $	θ
χ	$-90^\circ + \rho$	$-90^\circ + \chi_0$	-90°	$-90^\circ - \chi_0$	$-90^\circ - \rho$
ϕ	$90^\circ - \tau$	$\phi_0 - \tau$	$-\tau$	$-\phi_0 - \tau$	$-90^\circ - \tau$
Type of setting:	Symmetrical-A	General	Fixed- χ	General	Symmetrical-A
	$\psi = 180^\circ + \psi_0$	$\psi = 270^\circ$	$\psi = 360^\circ - \psi_0$	$\psi = 360^\circ$	
ϵ	$-\epsilon_0$	ρ	$-\epsilon_0$	0	
ω	$\theta + \epsilon_0 $	$\theta + \rho$	$\theta + \epsilon_0 $	θ	
χ	$-90^\circ - \chi_0$	-90°	$-90^\circ + \chi_0$	$-90^\circ + \rho$	
ϕ	$180^\circ + \phi_0 - \tau$	$180^\circ - \tau$	$180^\circ - \phi_0 - \tau$	$90^\circ - \tau$	
Type of setting:	General	Fixed- χ	General	Symmetrical-A	

In this table:

$$\sin \epsilon_0 = -\frac{\tan \psi_0 \sin \rho}{(\tan^2 \psi_0 + \cos^2 \rho)^{1/2}}$$

$$\cos \chi_0 = \cos \rho / \cos \epsilon_0,$$

and $\tan \phi_0 = (\cos^2 \epsilon_0 - \cos^2 \rho)^{1/2} / \sin \epsilon_0$ ($0 \leq \phi_0 \leq 90^\circ$).

ξ, ζ, τ are the cylindrical polar co-ordinates of the hkl point and $\tan \rho = \xi / \zeta$.

In the upper hemisphere of reciprocal space ($0 \leq \rho \leq 90^\circ$) $0 \leq \epsilon_0 \leq -\rho$ and $0 \leq \chi_0 \leq \rho$.

In the lower hemisphere of reciprocal space ($90^\circ \leq \rho \leq 180^\circ$) $0 \leq \epsilon_0 \leq -180^\circ + \rho$ and $0 \leq \chi_0 \leq 180^\circ - \rho$.

In this setting all reflexions lying within the limiting sphere are, in theory, accessible. In practice, the χ -circle, if it is a complete circle, may obstruct the passage of the incident and reflected beams at high Bragg angles θ . For the symmetrical-B setting with $\epsilon = 90^\circ$ (or -90°) there is no such difficulty in observing high-angle reflexions.

We show in §2.5 that the symmetrical-A setting corresponds to the equi-inclination setting of the inclination method, and so has

similar limitations (for instance, with respect to the occurrence of simultaneous reflexions). The symmetrical-A setting is widely used for making intensity measurements, even though the general setting can be employed just as easily in a four-circle instrument. With the general setting the azimuthal orientation of the reflecting plane can be varied: we shall refer to the importance of this variation in Chapter 9.

Symmetrical-B setting ($\epsilon = 90^\circ$). Here the χ -circle is symmetrically oriented with respect to the incident and diffracted beams, and is normal to the scattering vector S (Fig. 20). The hkl plane can be brought into the reflecting position provided it lies in a zone with the ϕ -axis as the zone axis. All other reflexions are

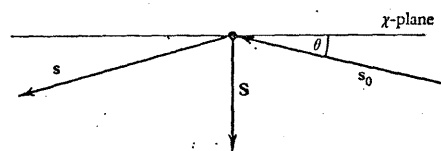


Fig. 20. Relation of χ -plane and scattering vector in symmetrical-B setting.

inaccessible. Thus, as for the anti-equi-inclination Weissenberg setting, the symmetrical-B setting is restricted to the collection of two-dimensional intensity data in the zero level.

Each accessible reflexion can be measured at any arbitrary value of the azimuth ψ . The reflecting normal lies along the χ -axis, and a 360° variation in ψ is achieved by rotating the crystal in the reflecting position about the χ -axis.

The setting angles ω, ϕ are

$$\left. \begin{aligned} \omega &= \theta + 90^\circ, \\ \phi &= -\tau. \end{aligned} \right\} \quad (2.36)$$

Fixed- χ setting ($\epsilon = |\rho|$). If the offset angle ϵ is equal to the value of ρ for each reflexion to be measured, we have the so-called 'fixed- χ ' setting. This setting has been discussed by Wooster & Wooster (1962).

Fig. 21 is the stereogram showing the setting angles required to

bring the reciprocal lattice point P to the reflecting position at S . The setting angles are given by:

$$\left. \begin{aligned} \omega &= \theta + \rho, \\ \chi &= -90^\circ, \\ \phi &= -\tau. \end{aligned} \right\} \quad (2.37)$$

Thus χ is fixed at -90° and there are three variable setting angles in all, including 2θ for the detector. The fixed- χ setting is particularly useful where physical access to the crystal is required, as in

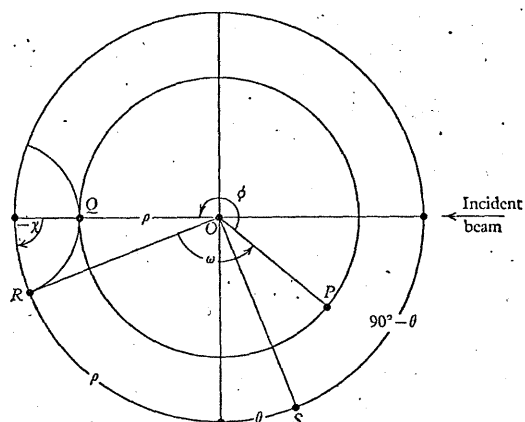


Fig. 21. Stereogram for fixed- χ setting.

the provision, for instance, of ancillary apparatus such as a furnace (see p. 81): the χ -circle is replaced by a simple bracket and so there is no obstruction to access to the crystal from above.

Table III summarizes the formulae given above for the setting angles in the general, symmetrical- A and fixed- χ settings: the table includes the full range of 360° in the azimuthal angle. By combining this table with Table I containing the formulae for the cylindrical polar co-ordinates ξ, ζ, τ , we obtain expressions for the setting angles ω, χ, ϕ in terms of the indices hkl and the lattice parameters.

Regions of physical interference

In the normal-beam equatorial geometry there are angular regions of the diffractometer in which no measurements can be made because of physical interference between parts of the instrument. These obstructions are particularly serious in X-ray diffractometers if long collimators are used which extend right up to the crystal position: such collimators are used to reduce air scattering (see p. 172). These obstructed regions are different in type from the 'blind regions' discussed in §2.3 for inclination geometry. The blind regions are a property of inclination geometry and they have no counterpart in equatorial geometry.

There are at least three kinds of obstructed regions. The first of these is a small cone-shaped region in which the incident or diffracted beam is shadowed by the goniometer head. The second kind arises from interference between the sides of the χ -circle and the detector collimator (Fig. 22). The result of this form of obstruction is that there is a range of inaccessible values of $|2\theta - \omega|$. The third kind of interference is between the source collimator and the χ -circle (Fig. 23): it can be reduced by making this circle an incomplete one (Eulerian cradle) at the expense of reducing the range of χ to less than a complete 360° rotation.

The plane of the χ -circle is frequently offset from the ω -axis: this procedure reduces obscuration of the incident beam and increases that of the diffracted beam, or vice versa, depending on whether the χ -circle is on the detector or the source side of the crystal (Fig. 22). It is frequently impossible to pass from one non-obscured region to another via an intervening obscured region without removing a collimator: this fact complicates the writing of setting programs.

In spite of the limitations described above there are, in practice, no blind regions in reciprocal space for a crystal examined with a four-circle diffractometer, even if the χ -circle is a complete circle. This is because of the extra rotational degree of freedom (see p. 40) given by this instrument. All reflexions can be observed up to a maximum scattering angle $2\theta_{\max}$, and the physical limitations can be considered as restrictions on the accessible range of the azimuth ψ for each reflexion. A practical procedure is to calculate

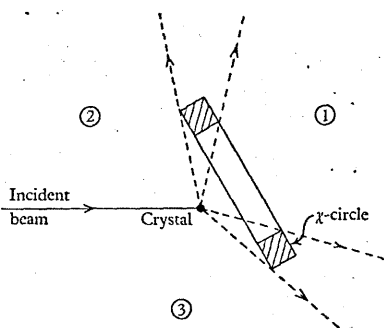


Fig. 22. Regions obstructed by the vertical circle, which is offset and viewed in projection on the equatorial plane. If the detector collimator is close to the crystal it is not possible to pass between regions ①, ② or ③ without removing the collimator. The broken lines represent limiting positions of the reflected beam. In this case the χ -circle is on the detector side of the crystal.

the setting angles for a particular value of ψ using the formulae given in Table III: if this combination of setting angles is unacceptable because of physical interference, a new ψ is chosen and the calculation repeated until a satisfactory combination is found.

If χ is restricted to the range $0-90^\circ$, as in the instruments described by Furnas & Harker (1955) and by Mayer (1964), we can only observe a hemisphere in reciprocal space on one side of the 'straight-through' position of the incident beam. To observe the other hemisphere we must either measure the reflexions on both sides of the incident beam (that is, θ both positive and negative), or rotate the χ -circle through 180° about the ω -axis: if neither of these alternatives is possible, the crystal must be re-orientated on the goniometer head between measuring each hemisphere.

Setting angles for general crystal orientation

The setting angles in Table III and the formulae for the cylindrical polar co-ordinates ξ, ζ, τ in Table I have been derived assuming that the c -axis of the crystal is along the goniometer-head axis ϕ and that the a^* -axis, at the standard orientation of the crystal, is along the incident beam direction. This implies that the crystal is mounted on goniometer arcs, which are adjusted to bring c into coincidence with the ϕ -axis.

However, goniometer arcs are not really necessary, in that the three circles ϕ, χ, ω allow the crystal to be rotated to any orientation in the laboratory space. The problem then remains of calculating the magnitudes of the setting angles when the crystal is mounted in any arbitrary orientation on the goniometer head. The appropriate formulae are given in a paper by Wooster (1965).

Powell (1966) has written a computer program in 'Fortran' which calculates the setting angles of a four-circle diffractometer for an arbitrary crystal orientation. The program has the following general features:

(i) A least-squares fitting procedure is used such that the precise orientation of the crystal with respect to the xyz laboratory co-ordinates is determined from the observed setting angles for a few hkl reflexions.

(ii) The azimuthal angle ψ is chosen so that unwanted reciprocal lattice points (giving simultaneous reflexions) are at least a

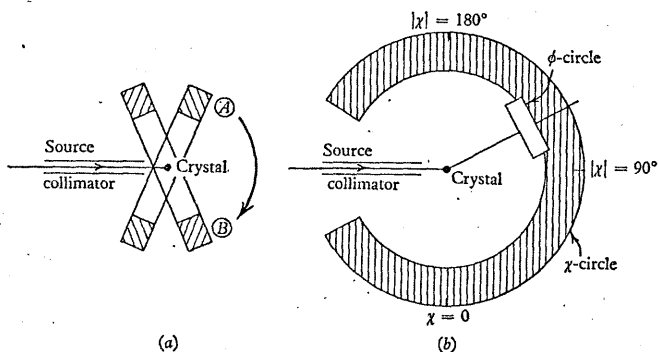


Fig. 23. An incomplete vertical circle viewed (a) in projection on the equatorial plane and (b) in elevation. It is possible to move from position ① to position ③ without removing the source collimator. The $|\chi| = 90^\circ$ position must be available, so that at least one arm of the vertical circle must extend above the equatorial plane.

certain distance from the Ewald sphere. This criterion defines a number of intervals in which ψ may lie, and the optimum angle is chosen to be at the mid-point of the longest interval.

(iii) Obstructed regions in reciprocal space, caused by the shape of the instrument obstructing the incident or diffracted beams, are avoided by expressing them as a number of inequality constraints; each constraint restricts one of the angles ω , ϕ , χ , 2θ and $\omega - 2\theta$, or involves logical 'and' combinations of pairs of these setting angles.

2.5. Comparison of inclination and equatorial methods

Table IV summarizes the properties of the inclination and equatorial methods, grouped under the special settings appropriate to each method. In X-ray work both methods are used, although the general inclination setting, requiring alteration of the inclination of both the X-ray tube and the detector to the goniometer-head axis, is not convenient for mechanical reasons. For neutron work the equatorial method is more suitable, as the detector requires heavy shielding and it is preferable to restrict its motion to a single rotational axis 2θ . Moreover, intensity errors arising from simultaneous reflexions are more troublesome in neutron diffraction, and by working in the general equatorial setting the azimuth ψ of the reflecting plane can be chosen to minimize these errors.

Because of differences in their mechanical construction we have described the geometries of inclination and four-circle diffractometers separately. However, the two geometries must be related, as they both achieve the same requirements, discussed in §2.1, for setting the crystal and detector and for measuring the reflexion. This correspondence was first pointed out by Phillips (1964), who discussed the correspondence between special settings used in the two geometries.

Fig. 24 shows the χ -plane and the equatorial plane in the general equatorial setting, and the two inclination angles μ , ν in the general inclination setting. The χ -plane is denoted by the great circle WUV , where WCV is a vertical diameter and CU is in the horizontal, equatorial plane. ACO is along the incident beam direction; CS is the bisector of the angle ACT , so that the angle

TABLE IV. Summary of properties of inclination and equatorial methods

Method	Setting angles		Special features and limitations
	Crystal	Detector	
Inclination: General	ϕ, μ	Υ, ν	Azimuth ψ varies with μ , but mechanically inconvenient to vary μ, ν together between reflexions
Normal-beam	ϕ ($\mu = 0$)	Υ, ν	Only two angles, ϕ and Υ , to be set within each reciprocal lattice level. Blind regions in upper levels. No choice of ψ
Equi-inclination	ϕ ($\mu = -\nu$)	Υ, ν	Only two angles to be set within each level. No blind regions. No choice of ψ
Anti-equi-inclination	ϕ ($\mu = \nu$)	Υ	One level only, $\xi = 0$, accessible. This level can be measured at any $\mu (= \nu)$ and ψ is varied by changing μ
Flat-cone	ϕ, μ ($\nu = 0$)	Υ	Detector moves in one plane only. Blind regions for upper levels. No choice of ψ . Used for simultaneous measurement of several reflexions (see p. 56)
Equatorial: General	ω, χ, ϕ	2θ	Detector moves in equatorial plane. Each reflexion can be measured at any azimuth ψ
Symmetrical-A	ϕ, χ ($\nu = 0$)	2θ	No choice of ψ
Symmetrical-B	ϕ, χ	2θ	One level only, $\xi = 0$, is accessible. Each reflexion in this level can be measured at any ψ
Fixed- χ	ϕ, ω ($ \chi = 90^\circ$)	2θ	No choice of ψ . Crystal accessible for high- or low-temperature attachments
Flat-cone	ϕ, χ ($\omega = 2\theta$)	2θ	As for flat-cone setting in inclination method

$UCS = \epsilon$. The ϕ -axis, which lies in the χ -plane, is tilted forwards at an angle $WCB (= -\chi)$ to the vertical axis.

In the inclination method the angle between the incident beam and the positive goniometer-head axis is $90^\circ + \mu$, and the angle

between the positive goniometer-head axis and the reflected beam is $90^\circ - \nu$. Thus

$$\widehat{ACB} = 90^\circ + \mu, \quad \widehat{BCT} = 90^\circ - \nu$$

and these angles are related to other angles in the Napierian triangles BUT , BUA , as shown in Fig. 25. Application of Napier's rules gives

$$\cot \omega = \frac{\cos 2\theta - (\sin \nu / \sin \mu)}{\sin 2\theta} \quad (2.38)$$

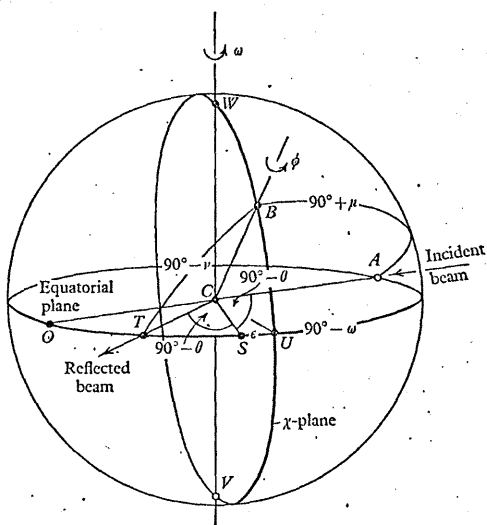


Fig. 24. Perspective view of χ -plane and Ewald sphere in general setting of normal-beam equatorial method.

We can apply this equation directly to the special settings of the inclination method:

(1) *Equi-inclination setting*, $\mu = -\nu$. From equation (2.38) $\omega = \theta$ and from (2.30) $\epsilon = 0$, so that this setting corresponds to the symmetrical- A setting of the equatorial method, in which the χ -circle bisects the angle between the incident and reflected beams.

(2) *Anti-equi-inclination setting*, $\mu = \nu$. From the same equations

$\omega = 90^\circ + \theta$ and $\epsilon = 90^\circ$, which corresponds to the symmetrical- B setting of the equatorial method.

(3) *Flat-cone setting*, $\nu = 0$. Here $\omega = 2\theta$ and $\epsilon = \theta$, that is, the axis of the χ -circle is parallel to the reflected beam.

(4) *Normal-beam setting*, $\mu = 0$. Here $\omega = 0$ and $\epsilon = -\theta$, that is, the axis of the χ -circle is parallel to the incident beam.

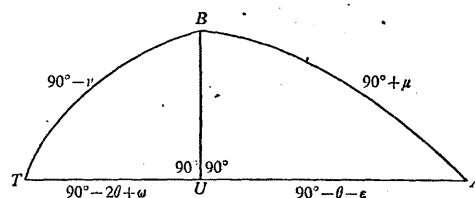


Fig. 25. Spherical triangles in Fig. 24 bounded by χ -plane and equatorial plane.

It is instructive to consider the correspondence between the special settings of the two methods in studying problems associated with the occurrence of simultaneous reflexions. Thus in the symmetrical- A setting of an equatorial instrument the conditions for simultaneous reflexions must be automatically satisfied if the goniometer-head axis is perpendicular to a set of planes in the reciprocal lattice, just as they are in an equi-inclination instrument.

An example where it is easier to prove a property of a special setting in one type of geometry, by considering its counterpart in the other type, is the following in the anti-equi-inclination setting a reflexion in the $\zeta = 0$ level can be observed at any inclination angle μ ; because of the formal equivalence of this setting with the symmetrical- B setting, in which χ assumes any arbitrary value and provides a continuous variation of the azimuth ψ , this change in μ must also correspond to an alteration of ψ . However, because of mechanical limitations on μ , a complete variation of ψ is not possible in the anti-equi-inclination setting.

Of course, the correspondence between inclination and four-circle instruments is not complete. The ω - and χ -axes in the equatorial method have no mechanical counterpart in the inclination method, and the single rotation about the 2θ -axis in the equatorial method is resolved into component rotations about ν

and Υ in the inclination case. The main feature of the inclination method is that the inclination angles μ , ν remain constant for all reflexions within any one level of the reciprocal lattice, and the level can be surveyed by varying Υ and ϕ only. Measuring the reflexions level-by-level ceases to be the logical procedure in an equatorial instrument.

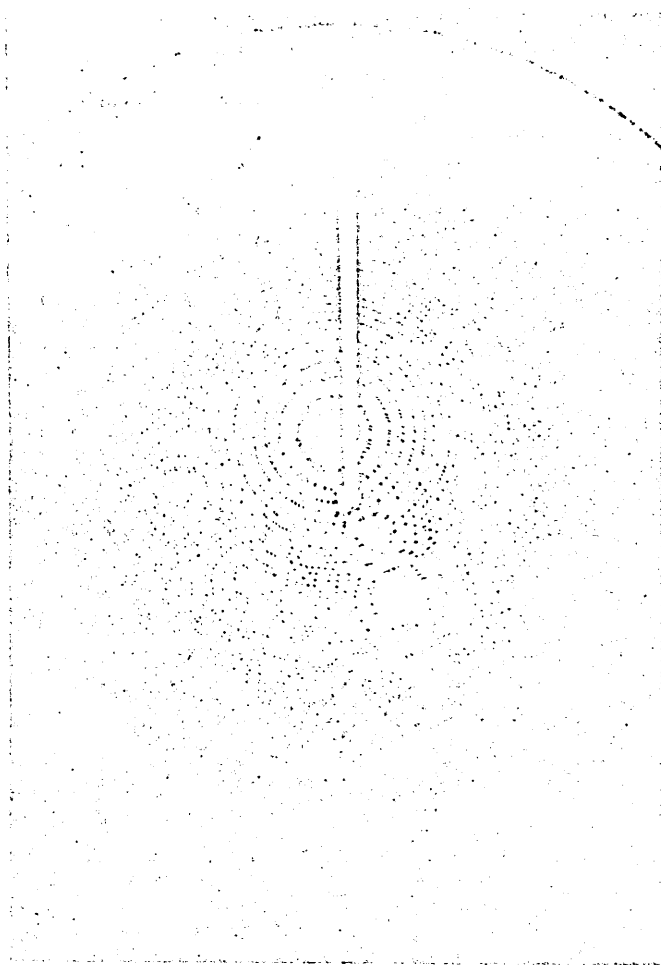
2.6. The simultaneous measurement of reflexions

The diffractometer methods which have been described so far have an obvious limitation when compared with photographic techniques: only one reflexion is recorded at a time even though the conditions may be satisfied for two or more reflexions to occur simultaneously. In crystals with very large unit cells, for instance protein or virus single crystals, several thousand reflexions may occur at once. This situation is illustrated by Plate I. Area detectors of the type discussed in Chapter 4 offer the possibility of recording these reflexions simultaneously; the development of such detectors is still in its infancy, but they may eventually give rise to a radically new concept of diffractometer design. Phillips (1964) has shown how a limited increase in the efficiency of existing single crystal diffractometers, based on either the inclination or equatorial geometry, is possible by measuring a few reflexions at a time.

The measurement of simultaneous reflexions in pairs

We have referred on p. 32 to the occurrence of double or triple reflexions, which arise from the simultaneous presence of two or three reciprocal lattice points on the surface of the Ewald sphere. The conditions for a reflexion to occur are satisfied when the corresponding reciprocal lattice point lies on the Ewald sphere. These conditions are still satisfied when the crystal is rotated about the normal to the (hkl) plane: during this rotation many other reciprocal lattice points pass through the sphere of reflexion, and repeatedly give rise to the conditions for the occurrence of simultaneous reflexions. The intensity of the hkl reflexion is affected by the simultaneous occurrence of a second reflexion, producing errors in the measurement of hkl . Fortunately, these errors are often small and there are many investigations where, far from having to

PLATE I



X-ray photograph (CuK α radiation) of stationary crystal of poliomyelitis virus (Finch & Klug, 1959).

eliminate simultaneous reflexions, we can exploit their occurrence to speed up the collection of intensity data.

Fig. 26 shows the Ewald sphere in the general inclination setting, with a negative value of the inclination angle μ . Let us suppose that the crystal is mounted with a reciprocal-lattice axis, say \mathbf{c}^* , along the goniometer-head axis ϕ . (Note that this mounting of the crystal is different from that which we have discussed in earlier

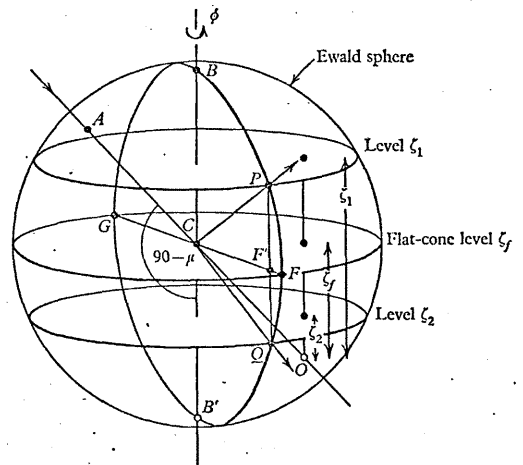


Fig. 26. Measurement of two reflexions P, Q simultaneously using the inclination geometry.

sections of this chapter, where we assumed that a crystal axis, \mathbf{c} , coincides with the goniometer-head axis.) Any pair of reciprocal lattice points with co-ordinates hkl_1 and hkl_2 will lie simultaneously on the surface of the Ewald sphere, if they are symmetrically related to the flat-cone level at $\zeta = \zeta_f$ passing through the centre of the sphere. Thus the points P and Q lying on levels ζ_1 and ζ_2 will give simultaneous reflexions if

$$\zeta_f = \frac{1}{2}(\zeta_1 + \zeta_2). \quad (2.39)$$

The reflected beams CP, CQ lie in a plane $BPFQB'$ containing the

rotation axis BB' , to which they are inclined at angles $90^\circ \pm \nu$, where

$$\sin \nu = \frac{1}{2}(\zeta_1 - \zeta_2). \quad (2.40)$$

The flat-cone level can either coincide with a possible reciprocal lattice level or lie half way between two such levels.

An inclination diffractometer can be adapted, therefore, for the simultaneous measurement of reflexions in pairs by providing it with two detector arms inclined at $\pm \nu$, where ν is given by (2.40). The instrument is set at the inclination angle μ for the flat-cone level—that is, $\sin \mu = -\zeta_f = -\frac{1}{2}(\zeta_1 + \zeta_2)$ from (2.39)—and any pair of reflexions hkl_1, hkl_2 with $\zeta = \zeta_1$ and $\zeta = \zeta_2$ can be measured simultaneously, provided they do not fall into the blind region which always exists for levels other than the equi-inclination (and anti-equi-inclination) levels.

Because of the correspondence between the general inclination and equatorial methods, discussed in §2.5, we expect that a similar procedure is possible for measuring two reflexions simultaneously using a four-circle diffractometer. Fig. 27 illustrates the situation for measuring the two reflexions CP and CQ in symmetrical positions above and below the equatorial plane $AUFOTG$, here viewed from below; the goniometer-head axis CB is drawn vertically to facilitate comparison with Fig. 26. The crystal is mounted with c^* along the goniometer-head axis, which moves round the χ -circle $BWTVU$. The great circle FGH represents the flat-cone level at ζ_f with the point $P (= hkl_1)$ at $\Delta\zeta$ above the flat-cone level and the point $Q (= hkl_2)$ at $\Delta\zeta$ below; both P and Q lie simultaneously on the Ewald sphere and the line PQ is parallel to c^* . To measure P and Q together two detectors are mounted on the detector arm CF . These detectors are inclined at $\pm \nu$ to CF , where

$$\sin \nu = \Delta\zeta = \frac{1}{2}(\zeta_1 - \zeta_2).$$

The detectors lie in a plane which contains the c^* -axis and is at right-angles to the χ -plane, in accordance with the condition $\omega = 2\theta$ for the flat-cone setting (§2.5). All reflexions of the type P, Q are measured in pairs which have a fixed difference of $2\Delta\zeta$ in their ζ co-ordinates. It is only necessary to set three independent angles ω, χ, ϕ for each pair, as the detector arm at the setting angle 2θ is permanently locked to the ω -shaft in order to keep the arm normal to the χ -plane.

Quasi-simultaneous reflexions

It is customary to measure integrated intensities by recording the number of diffracted quanta as the crystal is rocked through the reflecting position. The rocking range must be sufficient to allow all parts of the crystal to reflect radiation from all parts of the X-ray tube focus, and the range depends on a number of factors, such as mosaic spread of the crystal, divergence of the

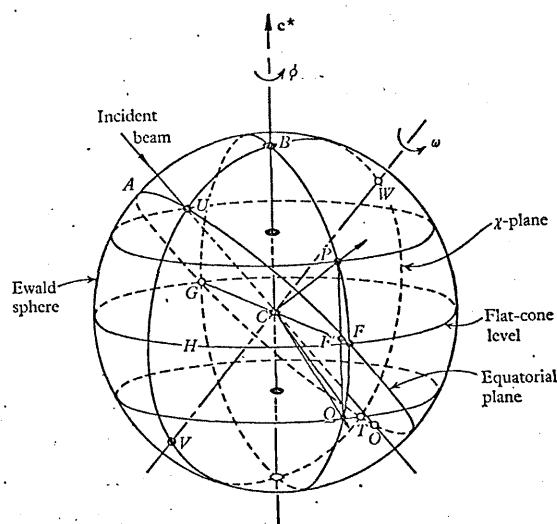


Fig. 27. Measurement of two reflexions P, Q simultaneously using the equatorial geometry.

incident beam and the range of incident wavelengths. For many investigations a rocking range of $1-2^\circ$ is adequate. Phillips (1964) has shown that when the spacing between reciprocal-lattice levels is small enough, reflexions from a number of levels can appear quasi-simultaneously, that is, during the $1-2^\circ$ rocking range of the crystal, even though the corresponding reciprocal-lattice points do not touch the Ewald sphere together.

Referring to Figs. 26 and 27 we shall assume that the points P, F', Q represent three reciprocal-lattice points in adjacent levels. Thus their ξ co-ordinates are all equal and their ζ co-ordinates are $\zeta_f + \Delta\zeta, \zeta_f, \zeta_f - \Delta\zeta$, respectively. P and Q touch the Ewald sphere together; but at a different time from F' , and we shall calculate the

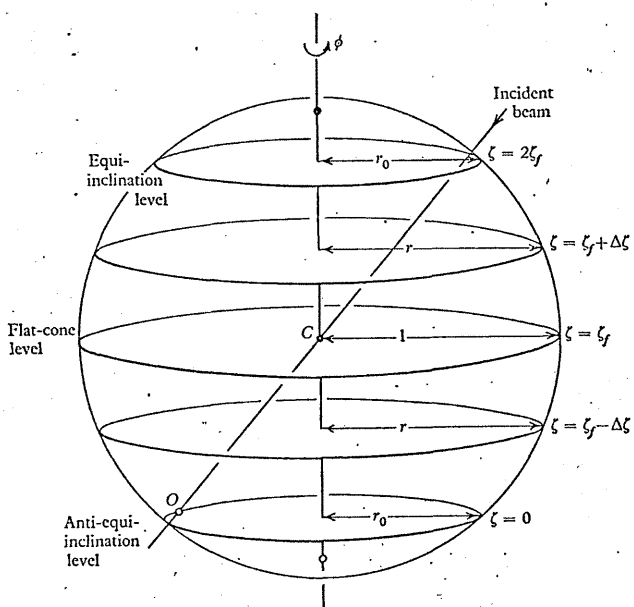


Fig. 28. Ewald sphere showing general levels at $\zeta = \zeta_f + \Delta\zeta$ symmetrically related to the flat-cone level at $\zeta = \zeta_f$. O is the origin of reciprocal space and C the centre of the Ewald sphere.

difference $\Delta\phi$ in the setting angle of the crystal between the measurement of F' and of P and Q .

Fig. 28 is a view of the Ewald sphere with the crystal set for the non-zero level ζ_f to be recorded in the flat-cone setting. The levels $\zeta_f + \Delta\zeta, \zeta_f - \Delta\zeta$ are also shown. The corresponding circles of reflexion are illustrated in Fig. 29, together with the angle $\Delta\phi$ and

the points F' and P at the reflecting position. The radii of the various circles of reflexion are given by

$$r_0^2 = 1 - \zeta_f^2 \text{ for the equi-inclination level } (\zeta = 2\zeta_f),$$

$$\text{and } r^2 = 1 - \Delta\zeta^2 \text{ for the } \zeta_f \pm \Delta\zeta \text{ levels,}$$

while the flat-cone level has unit radius.

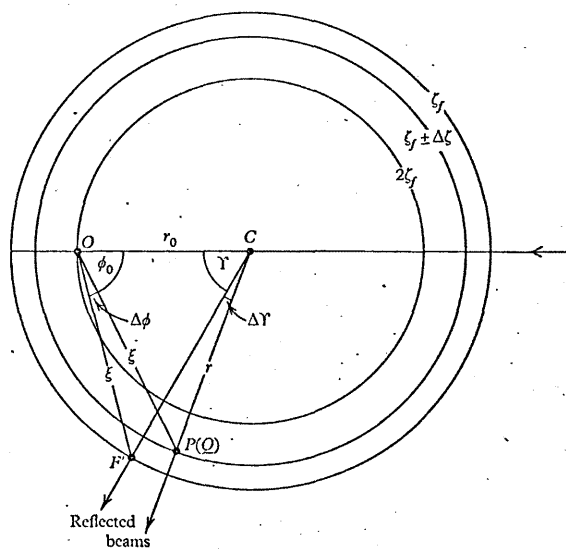


Fig. 29. Projection of Fig. 28 down ζ -axis, showing reflected beams for reciprocal lattice points $F', P(Q)$ in levels $\zeta = \zeta_f, \zeta_f \pm \Delta\zeta$ and at distance ξ from crystal rotation axis (after Phillips, 1964).

We have from Fig. 29:

$$\cos\phi_0 = \frac{\xi^2 + r_0^2 - 1}{2\xi r_0},$$

$$\text{and } \cos(\phi_0 - |\Delta\phi|) = \frac{\xi^2 + r_0^2 - r^2}{2\xi r_0},$$

$$\text{so that } \cos\phi_0 - \cos(\phi_0 - |\Delta\phi|) = \frac{r^2 - 1}{2\xi r_0}. \tag{2.41}$$

For small values of $\Delta\phi$ equations (2.41) can be rewritten

$$\Delta\phi = \frac{r^2 - 1}{2\xi r_0 \sin\phi_0},$$

or

$$\Delta\phi = -\frac{\Delta\xi^2}{2\xi(1-\xi_f^2)^{1/2} \sin\phi_0},$$

where

$$\cos\phi_0 = \frac{\xi^2 - \xi_f^2}{2\xi(1-\xi_f^2)^{1/2}}. \quad (2.42)$$

Fig. 30 has been calculated from equation (2.42) and shows how $\Delta\phi$ varies with ξ and $\Delta\xi$ for either an inclination or a four-circle diffractometer in the flat-cone setting. Each line on this figure refers to a different value of ξ_f for the flat-cone level and is a contour within which $\Delta\phi \leq 0.2^\circ$. As noted in an earlier section, there is a blind region whose area increases with ξ_f , the minimum observable value of ξ being $1 - (1 - \xi_f^2)^{1/2}$.

The separation of levels, $2\Delta\xi$, in which reflexions can be measured at the same time as those in the flat-cone setting may be rather larger than Fig. 30 suggests. Equation (2.42) shows that $\Delta\phi$ is always negative with respect to the flat-cone level. If ϕ is set at $+0.2^\circ$ from its correct value for the flat-cone level, a value of $\Delta\phi = -0.4^\circ$ can be tolerated, since the reflexions in the flat-cone and the neighbouring levels would each be displaced by only 0.2° from the centre of the rocking range. Assuming that $\Delta\phi \leq 0.4^\circ$ is the maximum allowable deviation in the setting angle, the limiting observable values of ξ can be calculated. These are plotted as full lines in Fig. 31 for the complete range of ξ_f from $\xi_f = 0$ to $\xi_f = 1.0$ r.l.u., and for $\Delta\xi$ up to 0.08 r.l.u. For moderate values of $\Delta\xi$ the condition $\Delta\phi \leq 0.4^\circ$ imposes only a small addition to the blind region at the centre of the flat-cone level. Thus the additional blind region within which $\Delta\phi > 0.4^\circ$ comprises only 0.7 per cent of the accessible reflexions near $\xi_f = 0$ when $\Delta\xi = 0.04$ r.l.u.; the corresponding figure for $\xi_f = 0.5$ r.l.u. is 0.9 per cent.

An additional restriction on the accessible range of reflexions is also caused by the change $\Delta\Upsilon$, shown in Fig. 29, of the setting angle of the detector. The maximum allowable value of $\Delta\Upsilon$ is determined by the maximum possible width of the detector aperture. The restriction imposed by $\Delta\Upsilon$ is only important at high values of ξ ;

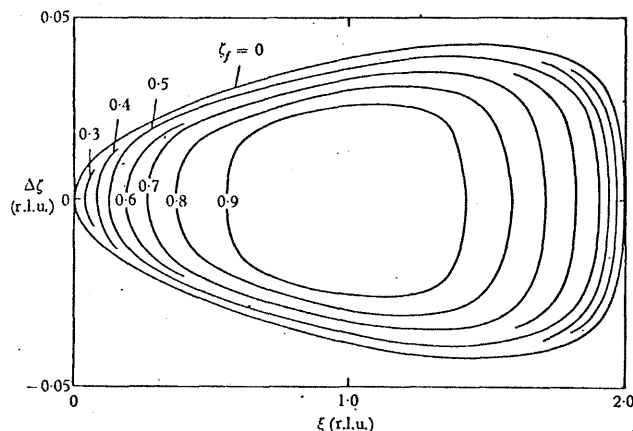


Fig. 30. Regions of reciprocal space within which $\Delta\phi \leq 0.2^\circ$. The numbers 0, 0.3, 0.4, ..., 0.9 on the lines indicate the values of ξ_f for the flat-cone setting (after Phillips, 1964).

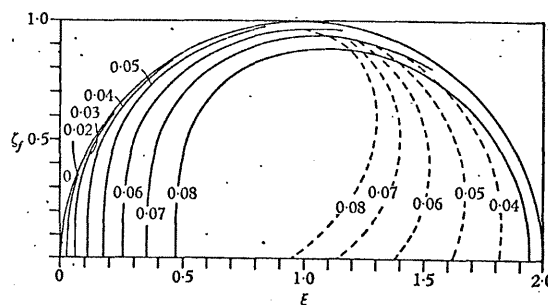


Fig. 31. Maximum and minimum values of ξ near the flat-cone setting when $\Delta\xi = 0$ to 0.08 r.l.u. Full lines show limitations due to $\Delta\phi \leq 0.4^\circ$, broken lines those due to $|\Delta\Upsilon| < 0.1^\circ$ (after Phillips, 1964).

this is illustrated by Fig. 31 in which the broken lines, corresponding to different values of $\Delta\xi$, are the boundaries of regions within which $|\Delta\Upsilon|$ is less than 0.1° .

Arndt, North & Phillips (1964) have described the adaptation of a linear diffractometer to permit the quasi-simultaneous measure-

ment of three reciprocal lattice levels near the flat-cone setting. The single detector of the original instrument was replaced by a group of three detectors with their windows vertically above each other and in a line parallel to the goniometer-head axis. The detectors were equally spaced and ν was changed by mounting the detectors on a draw-tube, which allowed variation in the angles subtended at the crystal by the detectors. Separate counting circuits were provided for each detector, and the results recorded sequentially by means of a printing-out programmed scaler. Data collection rates of 3,000 reflexions/day have been achieved with this arrangement.

CHAPTER 7

THE PRODUCTION OF THE PRIMARY BEAM (NEUTRONS)

Quantitative neutron diffraction studies were not possible until 1945 with the advent of the nuclear reactor as a powerful source of neutrons. A high-flux reactor, such as the Harwell *Dido* or *Pluto* research reactors, has a central flux of about 10^{14} slow neutrons/cm²/sec. These neutrons move in all directions and only a proportion of about 1 in 10^5 travel in the right direction down the collimator; of these collimated neutrons, in turn, a fraction of between 10^{-3} and 10^{-2} has the right wavelength to be reflected by the monochromator. The collimated flux of monochromatic neutrons striking the sample is, therefore, 10^6 to 10^7 /cm²/sec. This compares with a flux exceeding 10^{10} quanta/cm²/sec at the sample in the X-ray case. To compensate for this disparity in the incident flux and for the smaller cross-section for scattering of neutrons as compared with X-rays (Bacon, 1962), larger samples are used in neutron diffraction and the time required to count the diffracted neutrons is usually made longer.

In this chapter we shall describe briefly the collimators and monochromators used for the production of the primary neutron beam striking the sample. Only those points are discussed which relate to single crystal diffractometry; other neutron techniques are covered in Chapter 4 of G. E. Bacon's *Neutron Diffraction* (1962) and in Chapter 3 of *Thermal Neutron Scattering* (1965), edited by P. A. Egelstaff. In §7.3 on monochromators we include a discussion of the resolution of neutron reflexions, as this is closely connected with the properties of monochromators.

7.1. Neutron collimators

The size and complexity of neutron collimators are in marked contrast with the X-ray collimators described in the previous chapter. Neutron collimators are large because they must extend from the inner part of the reactor to the outside of its biological

PRODUCTION OF THE PRIMARY BEAM (NEUTRONS) 199

shield. Their complexity arises from a number of causes. In high-flux reactors the inner section of the collimator must be cooled: in the absence of cooling this section would be raised to a high temperature by the intense γ -radiation near the reactor core. There is a need to shut off the direct beam (for instance, by means of a floodable water switch), and to seal the collimator inside the reactor to prevent the ingress of atmospheric argon, which would be made radioactive by the high flux of neutrons.

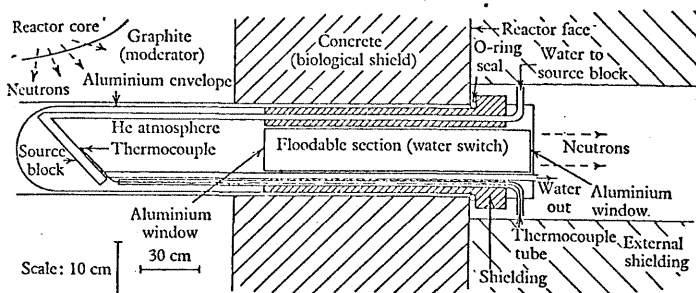


Fig. 83. Sketch of neutron collimator used with *Pluto* reactor. Access to the reactor face is possible only when the reactor is shut down and the water switch is flooded.

Fig. 83 is a diagram of a collimator designed for single crystal diffraction work at the Harwell *Pluto* reactor. The collimator does not point directly at the reactor core, and so a 'source block', consisting of a water-filled aluminium box, is installed at the inner end of the collimator; the water scatters slow neutrons in all directions and is the effective neutron source. In many reactors the collimators point at the core itself which is then the effective source.

Let us assume that the distance from the source to the outside of the biological shield is 4 m and that the cross-section of the beam as it passes down the collimator is 5×5 cm. The angular divergence of the beam, in both the horizontal and vertical planes, is 1.25×10^{-2} rad, and so the neutrons emerge from the collimator at angles of up to 0.7° from the axis of the collimator. The fraction of neutrons passing down the collimator is

$$\text{or about } 10^{-5}. \quad \frac{1}{4\pi} (1.25 \times 10^{-2})^2,$$

The most appropriate value for the collimation angle depends on the nature of the crystal under investigation. The figure of $\pm \frac{1}{2}^\circ$ represents a reasonable compromise between the opposing requirements of high intensity and good resolution of the reflexions from crystals with unit cell dimensions less than 10 Å, examined with a neutron wavelength of about 1 Å. For crystals with larger unit

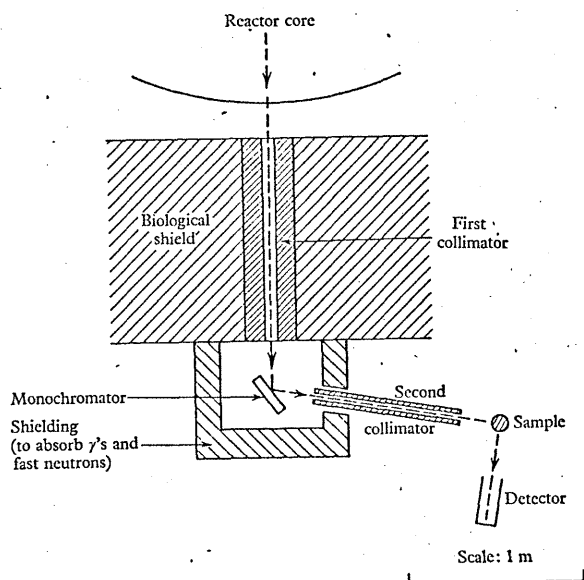


Fig. 84. Schematic diagram of neutron diffraction assembly. A second collimator is used after the monochromator, in case the degree of primary collimation is insufficient.

cells, tighter collimation or a longer wavelength are necessary to avoid overlapping of reflexions from adjacent levels of the reciprocal lattice. It is an advantage, therefore, to provide variable collimation of the beam striking the sample. One method, adopted in the Brookhaven High Flux Beam Reactor (Kevy, 1964), is to have a rotary collimator arrangement, whereby any one of three collimators of different cross-sections can be selected by remote

control, without having to remove the collimator assembly as a whole from the reactor. An alternative procedure is to use an in-pile collimator for primary collimation of the beam, and to insert a second collimator *after* the monochromator (Fig. 84) to reduce the beam divergence further. The second collimator consists simply of an open channel, which is shielded from the main gamma and fast-neutron radiation, and so can be interchanged readily with conical channels of different dimensions, in order to alter the divergence of the incident beam.

7.2. Neutron spectrum emerging from collimator

In the centre of the reactor the slow neutrons are in thermal equilibrium with atoms of the moderating material, and the velocity distribution of the neutrons follows the Maxwellian law

$$n(v) = \frac{4N}{\sqrt{\pi}} \frac{v^2}{v_0^3} e^{-v^2/v_0^2} \quad (7.1)$$

Here $n(v)dv$ is the number of neutrons per unit volume with a speed lying within the range v to $v + dv$, and N is the total number of neutrons per unit volume. v_0 is the most probable velocity, corresponding to the maximum value of $n(v)$ in (7.1), and is given by

$$v_0 = \left(\frac{2kT}{m} \right)^{\frac{1}{2}},$$

where k is Boltzmann's constant, T the moderator temperature and m the neutron mass.

The neutron flux $\phi(v)$ emerging from unit area of the collimator is v times the neutron density, that is,

$$\phi(v) = vn(v) = \frac{4N}{\sqrt{\pi}} \frac{v^3}{v_0^3} e^{-v^2/v_0^2} \quad (7.2)$$

To express the neutron flux in terms of the wavelength λ , we use the de Broglie relationship

$$\lambda = h/mv, \quad (7.3)$$

where h is Planck's constant, together with the expression

$$\phi(v)dv = -\phi(\lambda)d\lambda, \quad (7.4)$$

where $\phi(\lambda)d\lambda$ is the neutron flux crossing unit area with a

wavelength lying within the range λ to $\lambda - d\lambda$. Substituting (7.3) and (7.4) in equation (7.2) gives

$$\phi(\lambda) = \frac{4N}{\sqrt{\pi}} \frac{h}{m} \frac{\lambda_0^3}{\lambda^5} e^{-\lambda_0^2/\lambda^2} \quad (7.5)$$

where

$$\lambda_0 = \frac{h}{mv_0} = \frac{h}{(2mkT)^{1/2}}$$

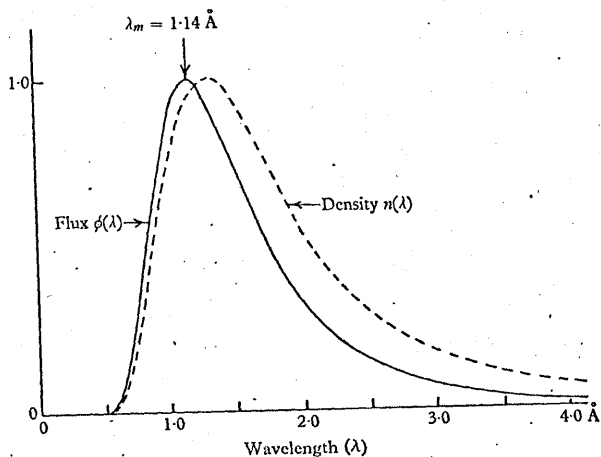


Fig. 85. Wavelength distribution of neutrons in equilibrium with a moderator at temperature $T = 20^\circ\text{C}$. Full curve is neutron flux emerging from collimator and broken curve is neutron density in reactor core; both curves are normalized to a peak value of unity. The curves are shifted towards shorter wavelengths for higher values of the moderator temperature.

The maximum value of $\phi(\lambda)$, found by differentiating (7.5), occurs at a wavelength λ_m , given by

$$\lambda_m = \frac{h}{(5mkT)^{1/2}}$$

Fig. 85 shows the calculated neutron flux $\phi(\lambda)$ for a moderator temperature of 20°C . In neutron diffractometry we are concerned mainly with the distribution $\phi(\lambda)$ and with the wavelength λ_m . A typical moderator temperature is in the range 20 – 100°C : at 20°C , λ_m is 1.14 \AA and at 100°C , λ_m is close to 1.00 \AA .

7.3. Crystal monochromators

The selection of a narrow wavelength band from the continuous distribution shown in Fig. 85 is readily accomplished with a crystal monochromator. Crystals are chosen for their high intrinsic reflectivity Q (p. 277) and large mosaic spread. If the monochromator is a perfect crystal (for example, germanium), it selects neutrons of a fixed wavelength from a very narrow angular range of the incident beam. On the other hand, for a mosaic crystal, neutrons are selected over an angular range corresponding to its mosaic spread: the total reflected intensity is several orders of magnitude higher than for a perfect crystal (Fig. 86). Ideally, the

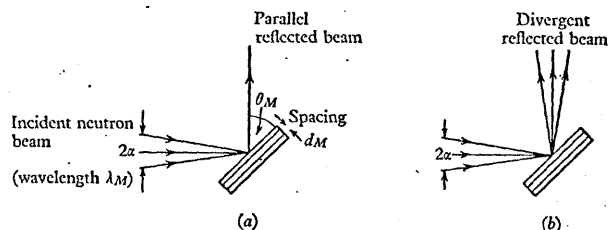


Fig. 86. Increase of reflectivity by using a mosaic crystal (b) instead of a perfect crystal (a) as monochromator. In (b) the full angular range $\pm\alpha$ of the incident beam is reflected at the wavelength $2d_M \sin \theta_M$, provided the mosaic spread η_M exceeds α . A parallel beam is reflected by a perfect crystal, (a). (The diagram applies only to the single wavelength $\lambda_M = 2d_M \sin \theta_M$; other wavelengths are reflected as shown in Fig. 88.)

mosaic spread of the monochromator should match the angular divergence of the incident beam, so as to give maximum intensity at a resolution which is still governed primarily by the collimator divergence.

Attempts have been made to produce crystals with a controlled mosaic spread, but only limited success has been attained. Thus Shull (1960) has described experiments on Si and Ge, in which nearly perfect single crystals were distorted to improve their reflectivities. The reflecting range was increased by curving the crystals at high temperature in the plastic state, followed by a straightening treatment. Appreciable increases in reflectivity were

achieved, but the distortion was not uniform and so the beam intensity was not constant across the reflecting area of the crystal. Other experiments were reported by Barrett, Mueller & Heaton (1963), who introduced imperfections in several ways into neutron transmission monochromators of germanium. The recommended technique was uniaxial compression along the [110] direction at 650 °C to reduce the thickness by 2.5 per cent; this treatment improved the efficiency of the monochromator by a factor of 25–40 over that of an undeformed slab. Table XVII, taken from the paper of Barrett, Mueller & Heaton, compares the performance of a hot-pressed Ge monochromator used in transmission with a Cu monochromator used in reflexion, both set for a wavelength of 0.98 Å. The monitor rate in the table is the neutron flux recorded by a low-efficiency monitoring counter in the beam reflected by the monochromator, and the peak intensity and integrated intensity are those recorded for the 002 reflexion of a specimen crystal of alpha-uranium. The monitor rate and peak intensity are somewhat higher for the Cu monochromator, even though the integrated intensity is less; it is the peak intensity which is important, so that the comparison favours the copper monochromator rather than the germanium.

TABLE XVII. Comparison of a Ge monochromator used in transmission and Cu monochromator used in reflexion (wavelength = 0.98 Å)

Mono-chromator	Crystal condition	Relative monitor rates	Relative peak intensities	Relative integrated intensities
Ge	Hot pressed	63	56	174
Cu	As grown	100	100	100

Table XVIII lists a number of single crystals used as neutron monochromators, with comments indicating any special features.

In correcting for the effects of extinction or simultaneous reflexions (see Chapter 9), it is often useful to repeat measurements at different values of the wavelength of the beam diffracted by the sample. If only a number of discrete wavelengths is required, this can be done by changing the orientation of the monochromator so that reflexion takes place at a different family of planes. If a continuous variation of wavelength is needed, the glancing angle

θ_M of the neutrons striking the reflecting planes must be capable of continuous alteration. In this second case, the bulky shielding around the monochromator must be designed to allow extraction of the beam at a variable scattering angle $2\theta_M$. It must be noted, however, that as θ_M changes there is not only a continuous change in the wavelength λ_M but also a variation in the wavelength spread $\delta\lambda$ (p. 207) and in the focusing position of the beam diffracted by the sample (p. 208).

TABLE XVIII. Single crystal neutron monochromators

Crystal	Special features	References
Lead	Tends to have 'lineage' structure, causing non-uniformity of reflected beam; low Debye-Waller factor e^{-2W} , and so unsuitable for high scattering angles $2\theta_M$	Shull & Wollan, 1951; Alikhanov, 1959
Copper	Beam more uniform in cross-section than for lead; good reflectivity, even at high $2\theta_M$	Shull & Wollan, 1951
Germanium	No $\frac{1}{2}\lambda$ contamination, if (111) is reflecting plane; large unit cell and so suitable for long wavelengths; poor reflectivity in as-grown condition	McReynolds, 1952; Shull, 1960; Barrett, Mueller & Heaton, 1963
Beryllium	Low mosaic spread, but high intrinsic reflectivity; small absorption so that thick crystals can be used in transmission; Debye-Waller factor near to unity and so suitable for high $2\theta_M$	—
LiF, NaCl, CaF ₂	Tend to be more perfect than metal crystals, and to have lower intrinsic reflectivities ρ	Sturm, 1947; Wollan & Shull, 1948
Magnetite	Suitable for long wavelengths	McReynolds, 1952

Harmonic contamination of primary beam striking sample

A crystal monochromator, set to reflect the wavelength λ_M from the (hkl) family of planes, will also simultaneously reflect neutrons of wavelengths λ_M/n (where $n = 2, 3, \dots$) from the $n(hkl)$ planes at the same crystal orientation. Harmonics of wavelengths $m\lambda_M$ and $(m/n)\lambda_M$ would also be reflected if h, k, l have a common factor m such that the corresponding plane gives an allowed reflexion.

For $\lambda_M \approx 1 \text{ \AA}$ the flux is still appreciable at $2\lambda_M, 3\lambda_M, \dots$ (Fig. 85), and so the reflecting plane must be chosen with this second possibility in mind. Thus the (422) plane of copper can be used, as the 211 reflexion is absent, but not the (222) plane. For the λ_M/n harmonics, we calculate from equation (7.5) that the flux at $\lambda = \frac{1}{2}\lambda_m$ is only 2 per cent of that at $\lambda = \lambda_m$ (peak of wavelength distribution curve), and the flux at $\frac{1}{3}\lambda_m, \frac{1}{4}\lambda_m, \dots$ is smaller still. The weak 'second-order contamination', $\frac{1}{2}\lambda_M$, may constitute a serious handicap to the examination of weak Bragg reflexions: in studies of magnetic structures, for instance, it is often necessary to distinguish between a weak magnetic reflexion, obtained by reflecting the wavelength λ_M , and a nuclear reflexion occurring at the same angular position and corresponding to the diffraction of the wavelength $\frac{1}{2}\lambda_M$ by a strongly reflecting plane with half the spacing.

Several methods are available for reducing or eliminating this second-order contamination. By orienting the monochromator to scatter neutrons at wavelengths lower than the peak wavelength λ_m , some intensity is sacrificed but the second-order contamination is reduced appreciably (see Fig. 87). A more effective method is to use a filter. For example, ^{239}Pu has a sharp resonance absorption for slow neutrons of energy 0.295 eV, corresponding to a wavelength of 0.53 Å: by selecting a monochromatic beam of 1.06 Å and passing the beam through a thin layer of plutonium, the $\frac{1}{2}\lambda_M$ component is attenuated. Suitable thicknesses of plutonium filter for reducing the second-order contamination by a given amount have been calculated by Atoji (1964); Atoji also tabulates the characteristics of other resonance filters which can be used in the wavelength range 0.7–1.8 Å. In germanium single-crystal monochromators, the second-order component is suppressed automatically by choosing a reflecting plane such as (111) with a forbidden second-order reflexion. Finally, the second-order and higher-order components can be removed by placing a mechanical velocity selector in the incident beam (see p. 214).

Width of reflected wavelength band

The neutron monochromator isolates a narrow band of wavelengths from the wavelength spectrum emerging from the colli-

mator. The ratio of the wavelength spread $\delta\lambda$ to the mean wavelength λ_M is

$$\frac{\delta\lambda}{\lambda_M} = \cot\theta_M \delta\theta_M, \quad (7.6)$$

where θ_M is the Bragg angle of the monochromator and $\delta\theta_M$ is the angular spread of the reflected beam. If the monochromator is a

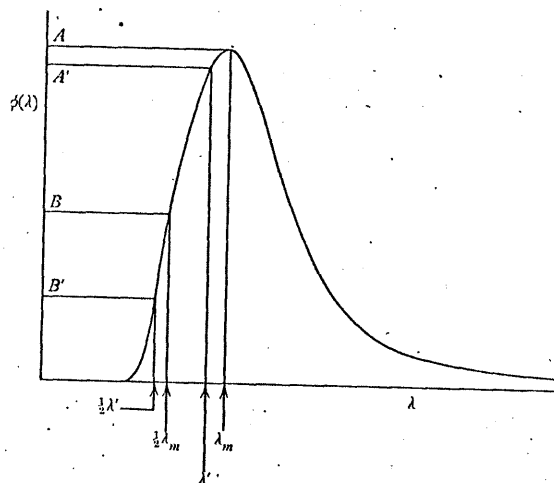


Fig. 87. The second-order contamination $\phi_B/\phi_{A'}$ is less at a wavelength λ' (where $\lambda' < \lambda_m$) than the contamination ϕ_B/ϕ_A at the peak wavelength λ_m .

perfect crystal, the angular spread $\delta\theta_M$ arises solely from the divergence of the beam emerging from the collimator. For a collimation angle of $\pm\frac{1}{2}^\circ$, $\delta\theta_M$ is $1.0^\circ = 0.017$; from (7.6)

$$\frac{\delta\lambda}{\lambda_M} = 1.7 \text{ per cent for } \theta_M = 45^\circ,$$

and

$$\frac{\delta\lambda}{\lambda_M} = 10 \text{ per cent for } \theta_M = 10^\circ.$$

An additional contribution to $\delta\theta_M$ arises from the divergence produced by the mosaic spread of the monochromator. However,

we can estimate roughly that for $\lambda_M \sim 1 \text{ \AA}$ the wavelength band has a width of 0.02 \AA for $\theta_M = 45^\circ$ and a width greater than 0.10 \AA for $\theta_M = 10^\circ$.

At high values of θ_M the bandwidth is less, and so the resolution of the Bragg reflexions is improved. However, the overall intensity of the primary beam falls, first, because of the narrower wavelength band selected by the monochromator, and second, because of the effect of the Debye-Waller factor in reducing the reflectivity of the monochromator. Another effect, however, tends to outweigh the loss of intensity in measuring reflexions at high values of θ_M : this is the focusing effect, which is well-known in the theory of the double-crystal X-ray spectrometer (Compton & Allison, 1935).

Focusing effect

Let us suppose that the collimator is of such a length and width that it permits passage of neutrons making angles $\pm \alpha$ to the central path, and that the neutrons in this central path are scattered at a glancing angle θ_M by the monochromator. The glancing angles for the extreme paths of the neutrons in the horizontal plane are then $\theta_M + \alpha$ and $\theta_M - \alpha$ (Fig. 88). In the vertical plane the range of Bragg angles is much less, $\theta_M \pm \frac{1}{2} \tan \theta_M \alpha^2$, and so we need discuss only neutrons in the horizontal plane. We shall ignore the effect of the mosaic spread of the monochromator in increasing the divergence of the primary monochromatized beam, although the mosaic spread is incorporated readily in the more general treatment (Willis, 1960).

If scattering at a glancing angle θ_M corresponds to a wavelength λ_M , then scattering at $\theta_M + \alpha$ corresponds to a wavelength

$$\lambda_M(1 + \alpha \cot \theta_M),$$

and scattering at $\theta_M - \alpha$ to

$$\lambda_M(1 - \alpha \cot \theta_M).$$

(These formulae follow from equation (7.6).) Thus the monochromator not only reflects a narrow band of wavelengths, but it sorts out in angle the wavelengths within this band: the shorter wavelengths emerge at the side of low scattering angles and the longer wavelengths at high angles.

The integrated intensities for the various hkl reflexions of a single crystal sample are now measured by placing the sample in this monochromatic beam and oscillating the crystal through the reflecting range. If the scattered intensity is plotted against ω , where ω is the angle of rotation about the goniometer-head axis, the area under this curve gives the integrated intensity. This intensity curve can be obtained with the sample scattering the

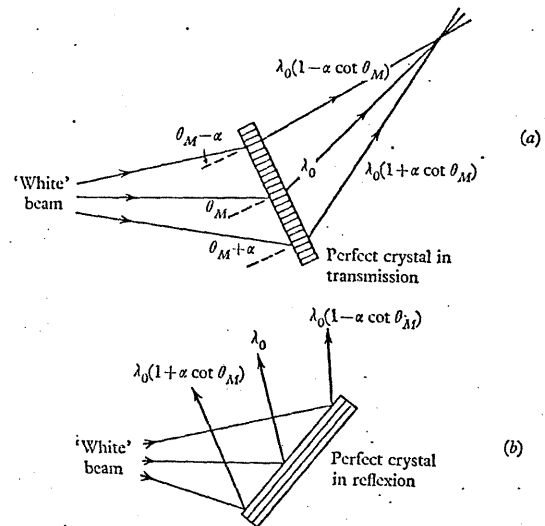


Fig. 88. Reflexion introduces a correlation between wavelength and direction of scattered beam. The correlation occurs whether the monochromator operates in transmission (a) or in reflexion (b).

monochromatic beam either to the right (Fig. 89a) or to the left (Fig. 89b): for a given reflecting plane the intensity integrated over the full reflecting curve is the same in the two cases, but the widths of the reflecting curves are quite different. The reason for this difference is that the various wavelengths in the 'monochromatic' beam from the crystal monochromator have been sorted out in angle: for scattering to the right the longer wavelengths strike the second crystal at larger glancing angles to the reflecting plane,

while the longer wavelengths are incident at smaller glancing angles in scattering to the left. Thus in Fig. 89a the full range of glancing angles for the band of wavelengths $\delta\lambda$ is covered in a smaller rotation of ω than in Fig. 89b, that is, the reflecting curves are narrower in (a). In the special case for which the reflecting

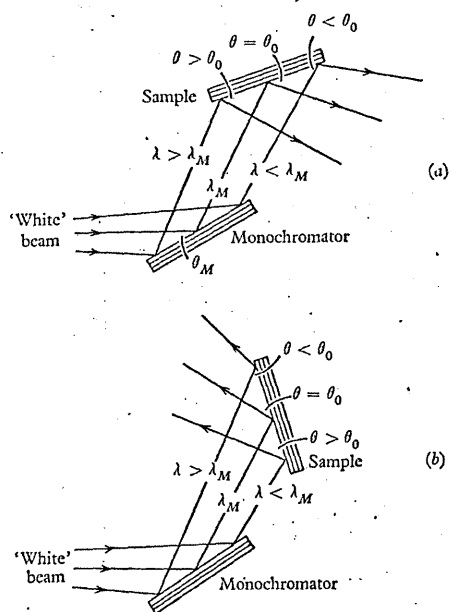


Fig. 89. Two arrangements for measuring the Bragg reflexions of a single crystal sample. The 'parallel' arrangement (a) is used in preference to (b), because the longer wavelengths in (a) have larger glancing angles whereas the reverse is true in (b): this difference gives rise to sharper reflexions from the sample in (a).

planes of the specimen and monochromator are parallel, all wavelengths are reflected to the right at the same angular position of the specimen: the width of the reflecting curve is then independent of the collimation angle of the primary beam and is determined solely by the mosaic spreads of the monochromator and the specimen.

To obtain narrow reflecting curves and hence good signal-to-

background ratios from the sample the 'parallel' arrangement of Fig. 89a is used. The theory of the dependence of rocking-curve width on Bragg angle θ of the sample has been derived for the parallel arrangement by a number of authors (Willis, 1960; Dachs, 1961; Caglioti & Ricci, 1962). The full-width at half height H of the reflexion occurring at a Bragg angle equal to the glancing angle of the monochromator ($\theta = \theta_M$) is

$$H = 2\sqrt{[\ln 2(\eta^2 + \eta_M^2)]},$$

where η is the mosaic spread of the sample and η_M the mosaic spread of the monochromator. ('Mosaic spread' is defined on p. 174.) For other values of θ , H depends on the collimator angle α as well as on η and η_M . The nature of this dependence is shown in Fig. 90, where H is plotted against the quantity $\tan\theta/\tan\theta_M$, the 'resolution parameter'. The divergence of the beam passing down the primary collimator is $\pm\alpha$, and each pair of broken and unbroken curves in Fig. 90 refers to a different value of α : the unbroken curve in each pair corresponds to $\eta = \eta_M$ and the broken curve to $\eta = 0$.

The width of the reflecting curve is a minimum in the region of $\theta = \theta_M$, and θ_M should be chosen to make the width about the same at either end of the θ range under investigation. This implies that, for a range of $0-60^\circ$ in θ , θ_M is about 40° . Moreover, by using relatively high values of θ_M , the hkl reflexions from the sample are made sharp at high Bragg angles, where the intensities are reduced more by thermal vibration.

The advantages in using a high glancing angle θ_M are demonstrated by the experimental data shown in Fig. 91. The reflecting curves were recorded using a single crystal of ThO_2 as the specimen, and the fall-off of peak intensity with scattering angle 2θ is very marked for measurements taken with a small monochromator angle, $\theta_M = 11^\circ$. The 755 reflexion, occurring at $2\theta = 134^\circ$, is easily observed using $\theta_M = 45^\circ$, but for $\theta_M = 11^\circ$ it is so broad that it has almost disappeared into the general background. We see then that, although there is a fall in the intensity of the incident beam arising from a reduction in its wavelength range, increasing the glancing angle θ_M gives a striking improvement in the signal-to-background ratio. For the measurement of weak reflexions

an improvement in the signal-to-background ratio is more important than increasing the signal alone (see p. 274).

In the study of magnetic structures the maximum value of 2θ for the sample is generally less than 50° for an incident wavelength in the neighbourhood of 1 \AA . This is so because magnetic reflexions arise from the scattering of neutrons by the outer unpaired electrons

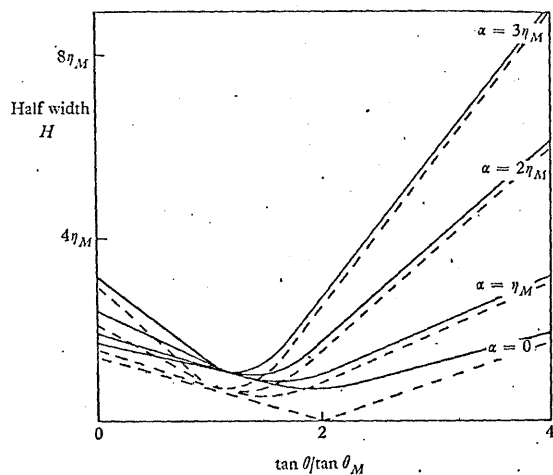


Fig. 90. Dependence of half-width of reflecting curve on resolution parameter $\tan \theta / \tan \theta_M$. Full curves for sample with same mosaic spread as monochromator ($\eta = \eta_M$); broken curves for sample consisting of perfect crystal ($\eta = 0$). $\pm \alpha$ is the divergence of the beam striking the monochromator (Willis, 1960).

of the atom, so that there is a steep fall-off in magnetic scattering amplitude with θ . The form-factor dependence of magnetic scattering contrasts with nuclear scattering, which is independent of θ because the scattering centres are nuclei whose dimensions are smaller by a factor of 10^{-4} than the wavelength of thermal neutrons. Thus for magnetic work the most suitable value of θ_M , or the value which gives focusing conditions near the middle of the accessible 2θ range, will be considerably lower than for general studies involving the nuclear reflexions alone.

Uniformity of monochromatized beam

In measuring a set of reflexions from a single crystal it is usual to bathe the crystal completely in the incident beam and to assume that each reflecting plane intercepts the same proportion of the beam while the crystal is turned from one reflexion to the next. This is not true, however, if the crystal is not spherical and if the incident monochromatized beam is not uniform in cross-section.

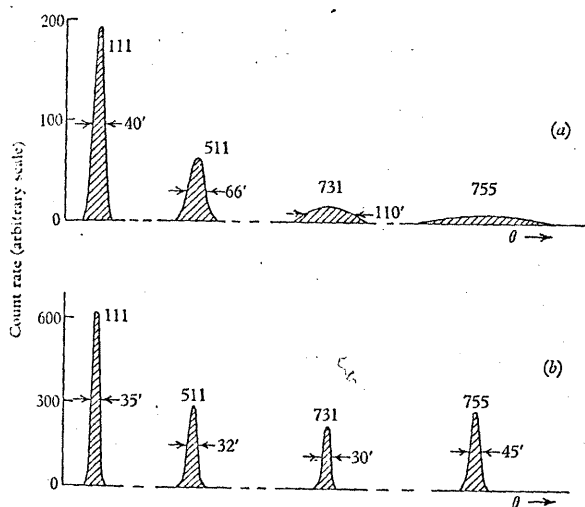


Fig. 91. Experimental reflecting curves for ThO_2 single crystal: (a) $\theta_M = 11^\circ$, (b) $\theta_M = 45^\circ$. The focusing position is near the 111 reflexion in (a) and near 731 in (b). A different collimator was used for recording the two sets of measurements (a) and (b) (Willis, 1962b).

The uniformity of the beam used in neutron diffractometry is typically ± 5 per cent over an area of $3 \times 3 \text{ mm}$ at the specimen. Fig. 92 shows the contours of constant neutron flux in the beam reflected by a single-crystal copper monochromator: the measurements were made by scanning the beam with a $\frac{1}{2} \text{ mm}$ pinhole of cadmium placed at the position of the specimen and recording the transmitted beam with a BF_3 detector.

For the highest accuracy in measuring the relative values of the integrated intensities, spherical specimens are used. Errors will still arise from a lack of uniformity of the incident beam, if the absorption of the specimen is large. Fortunately, in most neutron studies the absorption is very small.

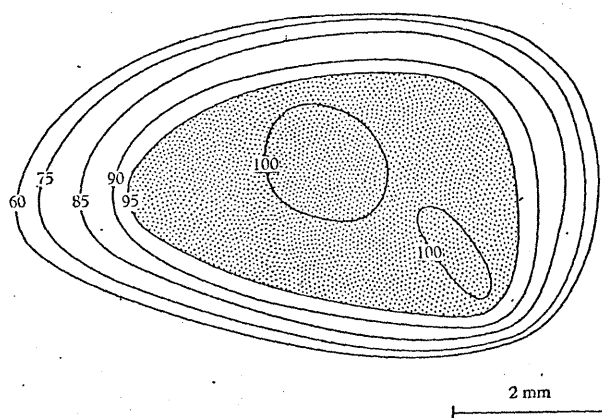


Fig. 92. Experimental contours of equal neutron flux in a beam reflected by a copper-crystal monochromator. The beam is uniform in intensity to ± 5 per cent in dotted region. Contours marked on an arbitrary scale.

7.4. Mechanical monochromators

Neutron diffractometers are normally operated in association with crystal monochromators, but there seems to be no fundamental reason why mechanical neutron-velocity selectors, or mechanical monochromators, should not be used instead. Moreover, a mechanical selector is more versatile in that it allows a choice in the values of both λ and $\delta\lambda/\lambda$ within fairly wide limits. Mechanical selectors are particularly attractive for wavelengths greater than 2 \AA , as the second-order and higher-order harmonics, appearing well up the wavelength distribution curve (Fig. 85), would be very troublesome with a crystal monochromator.

The flight time between the specimen and the detector for the neutrons used in neutron-beam experiments is between 10^{-5} and 10^{-3} sec, and it is possible, therefore, to use mechanical choppers

suitably spaced apart to produce monochromatic neutrons of selected λ and $\delta\lambda$. The principle of the mechanical selector for slow neutrons is illustrated in Fig. 93. Several discs, containing cadmium to make them opaque to neutrons, are mounted on the same axis, which is parallel to the neutron beam. Each disc contains a radial slit which transmits neutrons as the disc rotates. The continuous flux of reactor neutrons is chopped by the first disc into a neutron pulse having a broad wavelength spectrum. This burst then travels a known distance to the second disc, whose slit has a fixed phase

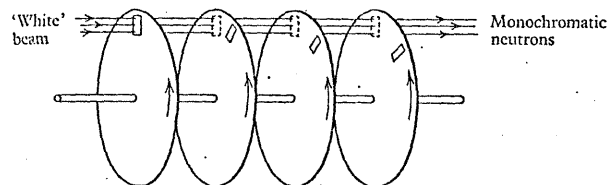


Fig. 93. Principle of mechanical velocity selector for slow neutrons (after Hughes, 1953).

relation with respect to the first. When it opens, the second disc passes only a band of wavelengths, and both the mean wavelength and the width of the band are related to the time-of-flight of the neutrons between the two discs, the relative phase of the discs and the open-time of the slits. Greater flexibility in varying both λ and $\delta\lambda$ is achieved by using a multi-rotor system of three or four rotating discs.

Curved slot rotors are used in the apparatus for cold neutron measurements described by Otnes & Palevsky (1963). Here the path of the neutrons is normal to the axis of rotation and the neutrons pass down a curved slot in the rotor (Fig. 94) to emerge in a broad wavelength band. The slot follows a circular arc, which is a sufficiently good approximation to the ideal curve (an Archimedean spiral). The values of λ and $\delta\lambda/\lambda$ can be varied independently between 3.5 and 10 \AA and between 1.5 and 6 per cent respectively; this variation is achieved by using several rotors, which are operated at various speeds and separations.

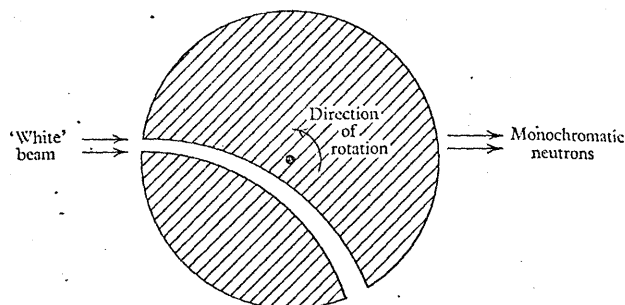


Fig. 94. Curved slot rotor.

7.5. Neutron diffractometry using 'white' primary beam

Slow neutrons have a speed of about 4,000 m/s at a wavelength of 1 Å, and this speed can be readily measured by time-of-flight techniques. Moreover, the speed varies inversely as the wavelength of the neutrons, in accordance with equation (7.3), and this gives rise to the possibility of carrying out experiments in neutron diffractometry using a radically different technique from any discussed so far.

If the direct beam from the nuclear reactor is pulsed with a mechanical chopper, then all those neutrons recorded at a given instant of time after the pulse have the same wavelength. The chopper with a single electronic time-gate constitutes a device for producing and recording monochromatic neutrons: if there are many adjacent time channels, diffraction of a range of wavelengths can be investigated simultaneously.

A single-channel arrangement for elastic scattering studies with long wavelength neutrons (~ 5 Å) has been developed by Low & Collins (1963). A diagram of their apparatus is shown in Fig. 95. The direct neutron beam passes through a filter of polycrystalline beryllium, which removes by Bragg scattering all those neutrons with a wavelength less than 3.95 Å, representing twice the maximum lattice spacing in beryllium. The beam then passes through a filter of single-crystal bismuth, which serves to attenuate the gamma radiation. Thus the final emergent beam consists pre-

dominantly of slow neutrons with wavelengths greater than 4 Å. A simple chopper pulses the beam and the neutrons scattered by the specimen are recorded in BF_3 counters after traversing a 1 m flight path. The counter assembly is gated in synchronism with the chopper, with a gating delay corresponding to the time-of-flight of neutrons with a wavelength of about 5 Å. The mean wavelength and the wavelength spread are changed by altering the gating delay and gate width, respectively.

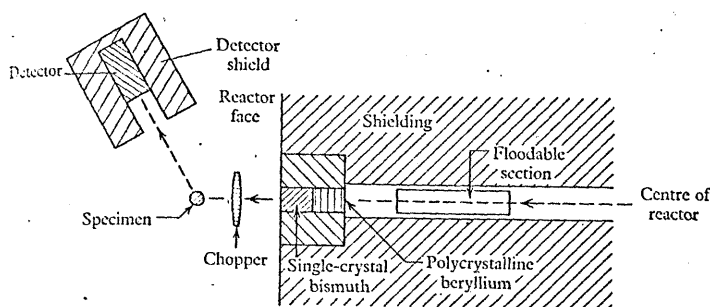


Fig. 95. Apparatus for elastic scattering studies with 5 Å neutrons (after Low & Collins, 1963).

The second type of experimental arrangement, using many adjacent time channels, has been developed recently by Buras & Leciejewicz (1964) as a modified form of the Laue method. (A similar technique was proposed by Lowde (1956), who emphasized that higher counting rates are achieved by integrating the diffracted intensity over wavelength rather than crystal angle.)

In the conventional method of crystal structure analysis, neutrons of a fixed wavelength are scattered by the sample and the intensity $I(\theta)$ of the diffracted beam is measured as a function of the variable angle θ (Fig. 96a). The curve of $I(\theta)$ versus θ shows a maximum when the Bragg equation, $\lambda = 2d \sin \theta$, is satisfied by the particular set of planes with spacing d . However, it is possible to reverse the roles of λ and θ , and to measure the intensity $I(\lambda)$ as a function of the wavelength λ at a fixed value of the scattering angle 2θ (Fig. 96b). A single disc of the type used in Fig. 95 chops the

slow neutron beam from the reactor, giving a pulse of neutrons with widely varying wavelengths at the specimen; the sample then scatters those neutrons with wavelengths satisfying the Bragg equation, and the scattered neutrons are counted by means of a neutron detector connected to a multichannel time-analyser. The wavelength is determined from the distance between the specimen and detector and the time taken to traverse this distance.

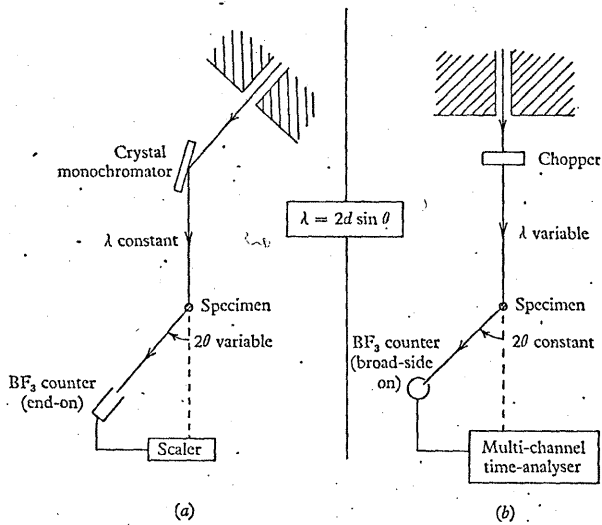


Fig. 96. (a) Conventional method, and (b) time-of-flight method of measuring Bragg reflections. To define the flight-path precisely the BF_3 counter is used in the 'broadside-on' position in (b). (After Buras & Lęciejewicz, 1964.)

Fig. 97 shows a neutron diffraction pattern of nickel powder taken by the time-of-flight method (Schwartz, 1965, private communication). Distinct peaks appear, which are readily indexed from a knowledge of the wavelength at which they occur. So far the method has been used for powder specimens only, but it could be applied equally well to the examination of single crystals. It is particularly promising for neutron diffraction work at long wavelengths as the counting rate is proportional to λ^4 .

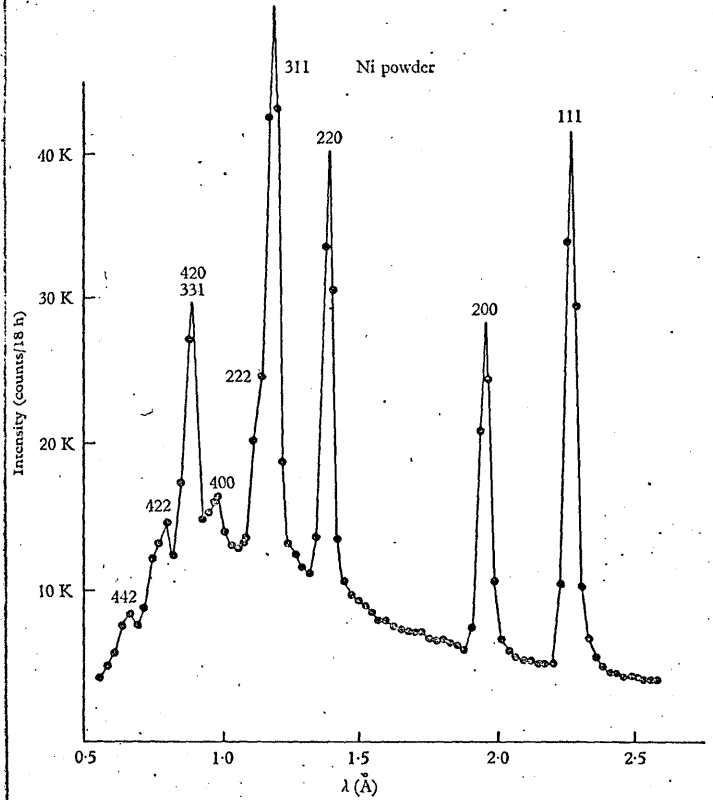


Fig. 97. Neutron diffraction pattern of nickel powder obtained by time-of-flight method (Schwartz, 1965).

THE BACKGROUND

8.1. Introduction

Before describing the measurement of the coherent Bragg reflexions, we shall discuss the various sources of background scattering occurring with the reflexions. The background scattering introduces both systematic and random errors in the determination of the diffracted intensity. Systematic errors arise from those components of the background scattering which have a non-linear dependence on scattering angle in the neighbourhood of the Bragg peak: the contribution of the background to the peak cannot then be estimated by simply extrapolating background measurements taken on either side of the peak. The random or statistical error associated with the presence of the background is discussed later in Chapter 10: we shall note there the importance of reducing the background as much as possible in order to improve the statistics of counting, especially in measuring weak reflexions.

Thus the conditions under which the reflexions are measured must be chosen with two points in mind: first, we must obtain a good estimate of the background under the Bragg peak, in order to make a valid background subtraction; secondly, the background must be as small as possible, so as to enhance the signal-to-background ratio.

The principal contributions to the background are the following:

- (1) Contributions which peak at the Bragg reflexions.
 - (a) Bragg scattering of harmonics or subharmonics of the fundamental wavelength (p. 205). These must be removed by one of the techniques discussed in Chapters 6 and 7, since corrections are not normally possible.
 - (b) Thermal diffuse scattering (§8.2).
- (2) White radiation background: X-rays only (§8.3).
- (3) Contributions which vary slowly with scattering angle.

- (a) Incoherent-scattering (§§8.4 and 8.5) in the form of
 - Fluorescence scattering (X-rays)
 - Compton scattering (X-rays)
 - Isotope incoherent scattering (neutrons)
 - Spin incoherent scattering (neutrons)
- (b) Parasitic scattering from amorphous regions in the specimen, from the specimen support, and from the air surrounding the specimen (mainly with X-rays) (§8.6).
- (4) Detector background: in X-ray counters due to cosmic radiation and radioactive contamination; in neutron counters due to γ -rays and fast neutrons (see Chapter 4).

We shall now examine some of these contributions.

8.2. Thermal diffuse scattering

Shortly after the first experiments in X-ray diffraction, Debye (1914) gave a mathematical treatment of the effect of thermal motion on the scattering of X-rays by a crystal. His calculations showed that thermal motion causes a decrease in the intensity, but not in the sharpness, of the Bragg reflexions by a factor e^{-2W} , where

$$W = 8\pi^2 \bar{u}_z^2 \frac{\sin^2 \theta}{\lambda^2}. \quad (8.1)$$

In this expression \bar{u}_z^2 is the mean-square displacement of the atoms along the normal to the reflecting planes. In addition, Debye demonstrated that an equivalent intensity should appear as a general diffuse background.

Faxén (1923) showed that this diffuse background ('thermal diffuse scattering', or TDS) was not uniform throughout reciprocal space, but possessed broad maxima which were centred at the reciprocal lattice points. The extra spots observed by Laval (1938) on Laue photographs were identified as those predicted by Faxén and by Waller (1928) as due to thermal motion. Laval's work stimulated a wide interest in the thermal diffuse scattering of X-rays by matter: the study of X-ray diffuse scattering is now a well-established technique in lattice dynamics, giving information about vibrational frequency spectra, the dispersion curves for elastic waves propagating along the principal crystallographic

directions, and the atomic force constants of solids. Neutron inelastic scattering has been used with even greater success in recent years to derive the same kind of information.

Nilsson (1957) first discussed the effect of thermal diffuse scattering on the measurement of the Bragg reflexions and showed that the diffuse scattering can make a considerable contribution to the measured intensity under the Bragg peak. The scattering rises to a maximum under the peak, and so a large part of the TDS is included if we assume, in the usual way, that the diffracted intensity is represented by the peak intensity minus the background intensity at the sides of the peak. In the case of the high-angle reflexions of rock salt observed with $\text{CuK}\alpha$ radiation, Nilsson showed that the integrated intensity derived in this way is over-estimated by as much as 30 per cent.

The amount of thermal diffuse scattering which is included in the measurement of a Bragg reflexion increases with the volume of reciprocal space illuminated during the intensity scan. Burbank (1964) has calculated this volume for the ω and $\omega/2\theta$ scans: his recommendations for minimizing the illuminated volume under different conditions are listed on p. 267.

The diffuse scattering under the Bragg peak has been observed directly by O'Connor & Butt (1963) who used 14.4 keV (0.86 Å) X-rays from a Mössbauer source. The diffuse scattering of X-rays in the region of the Bragg peaks involves the exchange of energy between the X-rays and the longest-wavelength phonons in the crystal; typically, the change of energy might be 10^{-9} eV. The Mössbauer effect permits the separation of the radiation scattered elastically (without energy change) from the inelastically scattered component. Fig. 98 shows some recent results obtained by O'Connor & Butt on the reflexion of 14.4 keV X-rays by the (111) plane of a single crystal of aluminium and by the (200) plane of a single crystal of KCl. It is seen that the inelastic intensity does indeed increase at the Bragg angle, as predicted theoretically. The extremely weak intensity of Mössbauer sources limits their general use for separating the elastic and inelastic components of the Bragg reflexions.

Chipman & Paskin (1958) have corrected for the TDS effect in X-ray powder work by measuring the wings of the Bragg peak

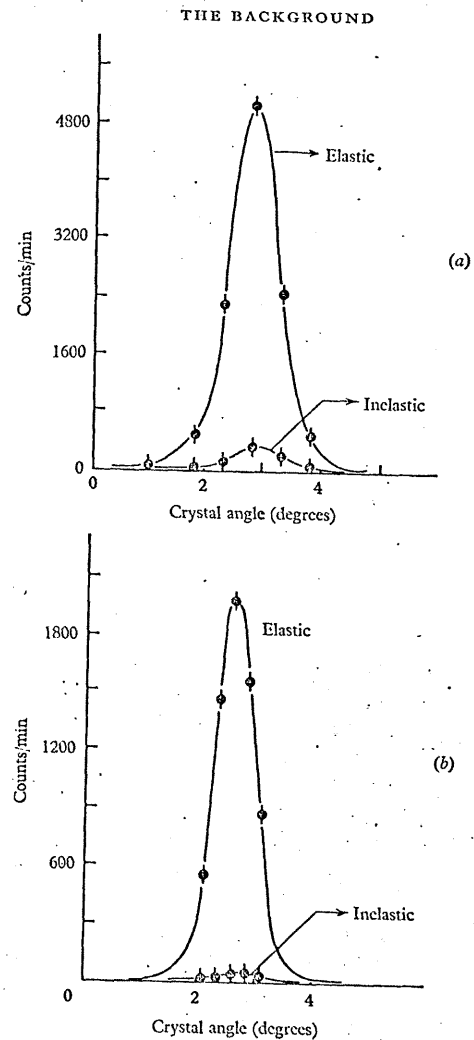


Fig. 98. Angular variation of elastic and inelastic scattering in the neighbourhood of: (a) 111 reflexion from aluminium; (b) 200 reflexion from potassium chloride (after O'Connor & Butt, 1965).

where the scattering is contributed by TDS alone, and calculating from these measurements the TDS contribution at the centre of the Bragg peak. This method has not been used in single crystal work: the calculation would require a knowledge of the spectrum

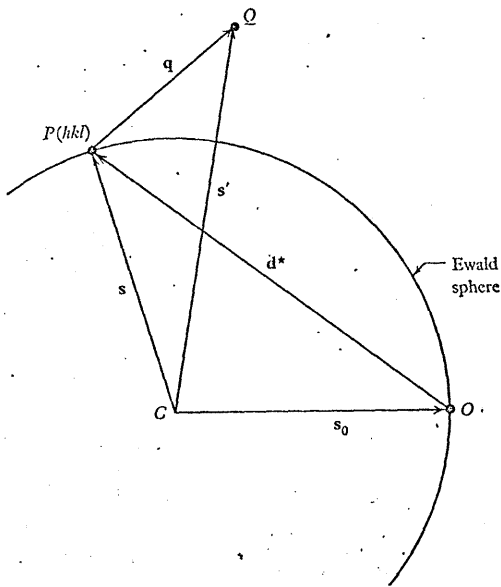


Fig. 99. Geometry of single-phonon annihilation process. \mathbf{q} is the wave-vector of the phonon absorbed by the crystal and \mathbf{d}^* is the reciprocal lattice vector of the hkl point. The elastically scattered neutrons \mathbf{s} can be separated from the inelastic neutrons \mathbf{s}' , provided $|\mathbf{s}'|$ is very different from $|\mathbf{s}|$ ($=|\mathbf{s}_0|$). In the single-phonon creation process, the end-point of \mathbf{q} lies inside the Ewald sphere and $|\mathbf{s}'|$ is less than $|\mathbf{s}_0|$.

of thermal vibrations of the atoms in the crystal and of the principal elastic constants of the crystal—information which is certainly not available for the majority of crystals.

Caglioti (1964) has examined the possibility of eliminating the inelastic component of the Bragg peak in neutron diffraction. The energy of a single phonon is comparable with that of a thermal neutron, and so the neutron suffers an appreciable change of

energy when it is scattered and emits, or absorbs, one phonon. The situation is depicted in Fig. 99, which shows the geometry of the single-phonon annihilation process. A neutron of wave vector \mathbf{s}_0 is

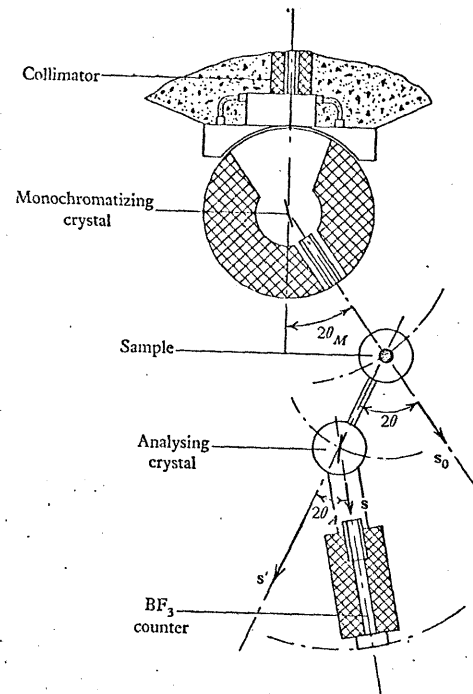


Fig. 100. A triple-axis spectrometer adapted for 'elastic' neutron diffraction. As in a conventional diffractometer, the monochromator provides a beam of neutrons of wavelength λ_0 impinging on the sample. The angle $2\theta_A$ of the analysing crystal is set to reflect neutrons of wavelength λ_0 . In principle, only those diffracted neutrons of energy corresponding to λ_0 are allowed to be Bragg-reflected by the analyser and to reach the BF_3 detector. In practice, the energy resolution of the spectrometer limits the degree of discrimination between elastically and inelastically scattered neutrons (after Caglioti, 1964).

scattered in the direction \mathbf{s}' by the single-phonon interaction, and, if the magnitude of \mathbf{s}' ($=|\mathbf{s}'|$) is very different from unity ($s_0 = 1$), the inelastically scattered neutron can be prevented from reaching

the BF_3 detector by using a 'triple-axis spectrometer' of the type illustrated in Fig. 100. The analysing crystal of the spectrometer is set for Bragg reflexion of the neutrons having the same energy as those impinging on the specimen, and neutrons of very different energy are not Bragg reflected.

The ability to discriminate in this way between inelastically and elastically scattered neutrons depends critically on the energy resolution of the analysing spectrometer. This resolution is governed by the angular divergences of the neutrons passing between the sample and analyser and between the analyser and detector; to maintain a reasonable neutron intensity these divergences must be about $30'$ of arc, and this angle gives an energy resolution of a few meV (10^{-3} eV). Neutrons interacting with phonons of lower energy than this cannot be separated from the elastically scattered neutrons, and so energy selection is poor near the reciprocal lattice points where the diffuse intensity is high and is contributed by low-energy single-phonon processes ($\sim 10^{-9}$ eV). For those substances which could be studied most efficiently by the 'elastic' diffraction method, namely 'hard' materials characterized by comparatively high values of the Debye temperature, the intensity of the thermal diffuse scattering is intrinsically low anyway. Thus, because the use of an analysing crystal causes a loss of intensity of the diffracted beam, there is probably little gain in employing such a crystal to reduce the effect of thermal diffuse scattering in the neighbourhood of the neutron reflexions.

There are, in fact, no generally satisfactory experimental techniques, either for X-rays or for neutrons, which lead to the elimination or correction of the TDS contribution to the Bragg reflexion. However, the ratio of the true integrated intensity arising from elastic scattering, to the intensity which is measured on the assumption of a linear background under the Bragg reflexion, is of the approximate form $e^{-2W'}$, where

$$W' = \text{constant} \frac{\sin^2 \theta}{\lambda^2} \quad (8.2)$$

(Nilsson, 1957). This means that W' is of the same form as the W factor in equation (8.1). Thus W' and W can be combined and the effect of thermal diffuse scattering treated as an artificial increase in

the Debye-Waller factor: in many crystallographic studies the temperature factors are considered as empirical quantities whose magnitudes do not seriously affect the final results of the investigation. It is only in certain investigations, such as the determination of the characteristic Debye temperature from the experimental Debye-Waller factors, that serious difficulties of interpretation are likely to arise.

8.3. White radiation background

An X-ray beam which is not monochromatic gives rise to a 'white radiation background'. As the crystal is rocked through the Bragg reflecting position, different wavelengths in the continuous spectrum which is superimposed on the characteristic radiation are Bragg-reflected into the counter. The white radiation background is not uniform across the reflexion, and its form depends on the type of intensity scan adopted in measuring the reflexion.

Let us consider the idealized case of the diffraction of a parallel beam of strictly monochromatic X-rays by a very small and perfect crystal. The reciprocal lattice point $P(hkl)$ is brought onto the surface of the sphere of reflexion by turning the crystal through an angle ω_0 : the corresponding diffracted beam emerges in the direction $\mathbf{s} = \overrightarrow{OP}$ (see Fig. 101*a*) at an angle $2\theta_0$ to the incident beam. If the detector is kept stationary at $2\theta_0$ and the crystal oscillated through an angular range from $\omega_0 - \delta\omega_0$ to $\omega_0 + \delta\omega_0$, the detector effectively moves along a circular path in reciprocal space with centre at the origin O . This path corresponds to the ' ω -scan', in which the crystal moves while the detector is stationary. On the other hand, in the $\omega/2\theta$ -scan the crystal and detector are co-ordinated in a 1:2 angular motion, and the detector moves through reciprocal space along a line passing radially through O .

If the X-ray beam contains a white radiation component, wavelengths other than the primary monochromatic wavelength

$$\lambda_0 \quad (= 2d_{hkl} \sin \theta_0)$$

are diffracted by the (hkl) plane along a radial line in reciprocal space, as shown in Fig. 101*b*. The magnitude of the reciprocal lattice vector is λ/d , so that the point P slides radially along this line for different wavelengths λ . The finite size and mosaic spread

of the crystal cause diffraction to occur along a narrow cone rather than a line in reciprocal space.

According to Fig. 101, the intensity contributed to the background of the Bragg reflexion by the white radiation differs in the

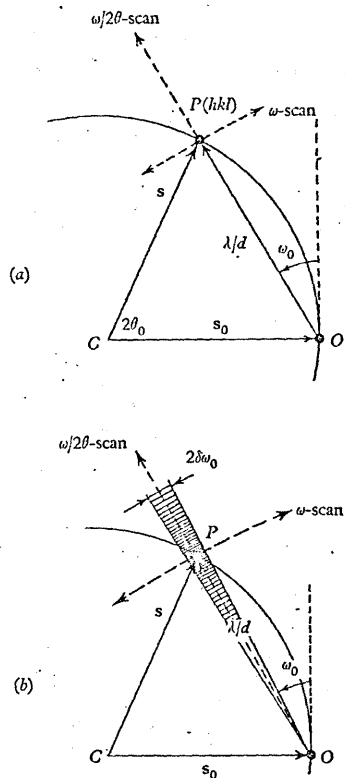


Fig. 101. (a) Idealized measurement of hkl reflexion by ω -scan and by $\omega/2\theta$ -scan; (b) real case showing effects of white radiation streak and of finite size and mosaic spread of crystal (after Alexander & Smith, 1962).

ω -scan and $\omega/2\theta$ -scan. In the ω -scan the path of the scan is tangential to the radial reciprocal lattice vector and proceeds across the white streak (Fig. 101 b) from points in reciprocal space lying

well outside the 'ridge' of white radiation. The resultant experimental profile (see Fig. 102) shows a Bragg peak superimposed on a low background, but the peak contains a large contribution from wavelengths other than λ_0 in the white radiation zone. In contrast to this, the path of the $\omega/2\theta$ -scan lies along the radial vector, that is, along the ridge of the white radiation zone: the background is

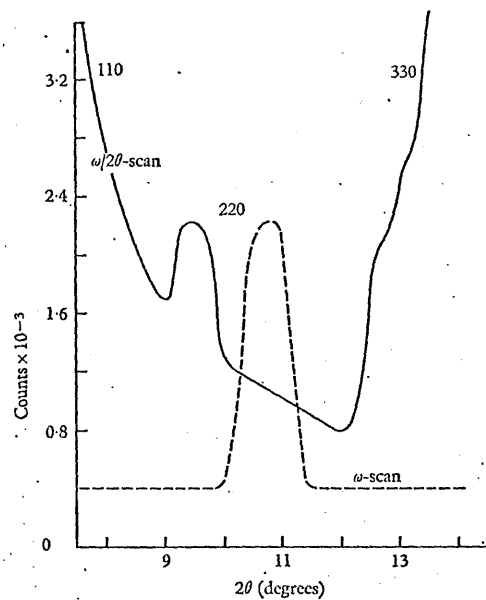


Fig. 102. Experimental profiles of 220 reflexion of $(C_6H_6)_4Sn$ obtained with $\omega/2\theta$ -scan (full curve) and ω -scan (broken curve): unmonochromatized $MoK\alpha$ radiation (after Alexander & Smith, 1962).

higher on either side of the reflexion than for the ω -scan, but the extrapolated background under the peak is closer to the true background.

The argument, given above, for interpreting the ω -scan and the $\omega/2\theta$ -scan as tangential and radial motions respectively of the detector through reciprocal space, assumes that the aperture or window of the detector is infinitesimally small. Burbank (1964) points

out that the correct interpretation of the two types of scan requires consideration of the finite size of the detector aperture and, in fact, by choosing the aperture appropriately for the two procedures the profile of the reflexion and the white radiation background can be made the same for either scan. The Laue streak will merely be shorter with the ω -scan and will appear as a pair of shoulders instead of a continuous background. Burbank shows that, if the aperture for the ω -scan is made wide enough, a line drawn through the shoulders will allow an adequate subtraction of the white radiation background.

Fig. 102 also illustrates another point. In the ω -scan the detector remains at a fixed position and will not catch radiation diffracted by neighbouring reciprocal lattice points. For this reason, resolution of adjacent reflexions is better with the ω -scan than with the $\omega/2\theta$ -scan.

With monochromatized radiation the white radiation background is absent, but other difficulties are introduced by using monochromators in X-ray work (p. 188).

In neutron diffraction there is no white radiation background, as the beam is monochromatized.

8.4. Incoherent scattering of X-rays

The scattering of X-rays due to the Compton effect and the photoelectric effect (fluorescence scattering) is incoherent, as the wavelength of the scattered radiation is modified and there is no fixed phase relationship between the wavelets of the scattered beam. The absence of interference effects means that incoherent scattering is distributed fairly evenly throughout reciprocal space: it does not peak at the Bragg reflexions and so does not cause difficulties in deriving the true integrated intensity of the type associated with the coherent thermal diffuse scattering and the coherent white radiation background. This type of background, therefore, affects the statistics of counting only.

The fluorescence yield for any element is strongly dependent on the wavelength of the incident radiation: it is greatest when this wavelength is a little shorter than a prominent absorption edge of one of the elements in the specimen. Thus it is almost impossible to use $\text{CuK}\alpha$ radiation ($\lambda = 1.54 \text{ \AA}$) with a specimen containing a

large proportion of cobalt (K absorption edge at 1.61 \AA) or iron (K absorption edge at 1.74 \AA), and a longer wavelength radiation must be used. However, fluorescence is also caused by the white radiation in the primary beam and this is present whatever the choice of X-ray tube target. The effects of specimen fluorescence can often be greatly reduced by inserting a suitable filter between the sample and the detector: this filter must have an absorption edge a little longer than the characteristic radiation excited in the specimen.

In Compton scattering the incident X-ray quantum loses energy by collision with one of the outer electrons of an atom in the sample (see, for example, Compton & Allison, 1935). According to classical theory, the increase in wavelength for a scattering angle 2θ is given by

$$\Delta\lambda = \frac{h}{mc}(1 - \cos 2\theta), \quad (8.3)$$

where $h/mc = 0.024 \text{ \AA}$, and so the maximum increase in wavelength is 0.05 \AA . This is too small to allow any significant reduction of the Compton component by filtration. Fortunately, the intensity of the Compton scattering is always small compared with that of the Bragg scattering.

8.5. Incoherent scattering of neutrons

In neutron diffraction there are two main sources of incoherent scattering. 'Isotope incoherence' is produced if the sample contains a random distribution of isotopes, each of which has a different scattering amplitude. Incoherent scattering also occurs when the neutrons are scattered by atoms of non-zero nuclear spin: this 'spin incoherence' is especially prominent with hydrogen-containing samples but it can be appreciably reduced by replacing hydrogen by deuterium. There is no incoherent scattering with samples which contain single isotopes with zero nuclear spin.

The two neutron incoherent scattering components are both unmodified in wavelength and are examples of disorder scattering. This is in contrast with the incoherent X-ray contributions of §8.4 which are of a different wavelength from the elastically scattered radiation.

Apart from hydrogen spin incoherence, neutron incoherent scattering is usually too small to be very troublesome.

8.6. Parasitic scattering

Radiation may be scattered by materials surrounding the specimen, especially if this is enclosed in a high- or low-temperature container; biological crystals frequently need to be in contact with the mother liquor of crystallization. Precautions consist of reducing the amount of such foreign matter to a minimum and selecting the material of the container or of the mounting cement with regard to its scattering and fluorescence properties.

X-rays are also scattered by the column of air which surrounds the specimen: this volume can be reduced by the use of a backstop and a detector collimator (p. 172).

8.7. Background and rocking range

Equation (6.1) is an expression for the minimum angle through which the crystal rotates to allow a valid measurement to be made of the integrated intensity. Generally, it is not safe to employ a rocking range which approaches this minimum value: lack of precision in the value of the unit cell dimensions, back-lash in the shafts of the diffractometer, and setting errors all combine to provide a small uncertainty in the peak position. The crystal must be oscillated through an angle rather bigger than the minimum indicated by equation (6.1) to make certain that the complete reflexion is measured. The 'peak-to-background' ratio deteriorates in proportion to the unnecessary background which is taken in on either side of the reflexion: it is very important that the observed and calculated peak positions coincide as closely as possible, if the peak-to-background ratio is poor and so requires the rocking range to assume the smallest permissible value. The safest procedure in such cases is to use some method of hunting for the peak. This can be done in a number of ways. A very large number of intensity ordinates are recorded across the reflexion: when the diffractometer output is processed, the computer program inspects the slope of the intensity curve and determines the points at which the reflexion profile rises above the background. This procedure is practicable only with a diffractometer which is connected on-line to a computer: the volume of output data becomes unmanageable on punched cards or punched tape. An on-line computer offers the

alternative possibility of keeping the actual scanning range small and of locating the peak precisely before the measurement is made. It is not necessary to hunt for the peak of every reflexion: instead a smaller number of reflexions strategically distributed in reciprocal space can be selected so that reflexions in their neighbourhood will then be located with sufficient accuracy. Special-purpose peak-hunting circuits have been incorporated in the off-line diffractometer 'Cascade' (Cowan, Macintyre & Werkema, 1963).

CHAPTER 9

SYSTEMATIC ERRORS IN MEASURING
RELATIVE INTEGRATED INTENSITIES

In a crystal structure determination the measured intensity of the reflexions must be converted to a set of relative 'integrated intensities'; from these a set of structure factors is derived by applying various geometrical and scale factors (see Chapter 11). The integrated intensity, also called 'integrated reflexion', is defined in the following way.

Let the crystal be placed in an incident beam, which has a uniform intensity I_0 and bathes the crystal completely. The crystal is rotated with uniform angular velocity ω through the reflecting position for the (hkl) family of planes: the angle of rotation is sufficient to allow all the mosaic blocks in the crystal to diffract the complete band of wavelengths $\delta\lambda$ comprising the 'monochromatic' beam. If E is the total amount of energy diffracted from the incident beam, then the integrated intensity ρ_{hkl} is:

$$\rho_{hkl} = E\omega/I_0. \quad (9.1)$$

Before the quantities ρ_{hkl} defined by (9.1) can be converted to structure factors, which express the amplitude of scattering in the hkl direction from a single unit cell, we must relate the integrated intensities for the macroscopic crystal to the integrated intensity for an infinitesimal volume element δV . This requires an examination of various physical factors, such as absorption, extinction and simultaneous reflexions (Renninger effect), which affect the magnitudes of the observed intensities from a macroscopic crystal. It is customary to consider these factors to be systematic errors in measuring the integrated intensities. Systematic errors associated with thermal diffuse scattering and with the white X-radiation background have been described in the previous chapter.

9.1. Absorption

X-rays and neutrons are absorbed as well as scattered in their passage through matter, although the relative importance of the

two processes is markedly different for the two radiations. Thus the absorption of X-rays due to the photo-electric effect is much larger than the attenuation due to scattering, whereas in neutron diffraction scattering is a principal cause of attenuation of the neutron beam. To relate the intensity scattered by a single atomic plane to that scattered by the whole crystal, we must know the amount by which both the incident and diffracted beams are reduced by absorption in the crystal. This calculation must be carried out separately for each reflexion and depends on the path of the incident and diffracted beams through the crystal.

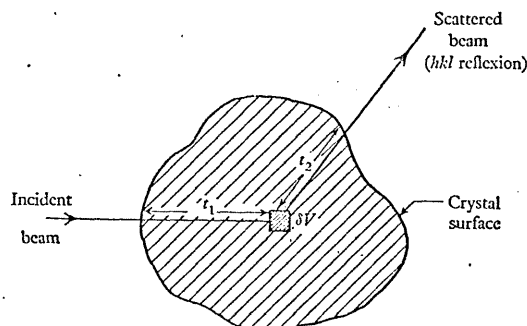


Fig. 103. Scattering from volume element δV of crystal.

The amount by which the intensity of the hkl reflexion is reduced by absorption is denoted A_{hkl} . The reciprocal of A_{hkl} is the absorption factor $A_{hkl}^* = 1/A_{hkl}$: A^* represents the factor by which the observed intensity is multiplied to obtain the corrected intensity.

Fig. 103 shows the volume element δV scattering the incident beam into the hkl reflexion. t_1 is the path length of the incident beam inside the crystal before being scattered by δV , and t_2 is the path length of the diffracted beam. The absorption factor is

$$A_{hkl}^* = \frac{V}{\int_V e^{-\mu x} dV}, \quad (9.2)$$

where μ is the linear absorption coefficient of the crystal for the particular type of incident radiation used, $x = t_1 + t_2$, and V is the volume of the crystal.

The linear absorption coefficient

If a narrow beam of monochromatic radiation passes through a thickness t of the crystal, the emergent intensity I is related to the incident intensity I_0 by $I = I_0 e^{-\mu t}$. (9.3)

(We assume the crystal is oriented to avoid a Bragg reflexion.)

In X-ray diffraction the dominant contribution to μ is the true absorption arising from the photoelectric effect (fluorescence). μ is computed from the relation

$$\mu = \rho_c \left\{ p_1 \left(\frac{\mu}{\rho} \right)_1 + p_2 \left(\frac{\mu}{\rho} \right)_2 + p_3 \left(\frac{\mu}{\rho} \right)_3 + \dots \right\}, \quad (9.4)$$

where ρ_c is the density of the crystal, p_1, p_2, \dots are the fractions by weight of elements 1, 2, ... in the crystal, and $(\mu/\rho)_1, (\mu/\rho)_2, \dots$ their mass absorption coefficients. *The International Tables for X-ray Crystallography*, volume III, contains tables of the mass absorption coefficients of the elements.

Values of μ for typical single crystals and MoK α and CuK α radiations are listed in Table XIX, taken from a paper of Jeffery & Rose (1964).

TABLE XIX. Values of μ for typical specimens examined with MoK α and CuK α radiations

μ (cm ⁻¹)		Specimen
MoK α	CuK α	
1.5	10	Molecular organic compounds with no atoms heavier than oxygen
4	30	Sodium salts of organic acids; inorganic crystals composed of atoms of low atomic number and containing large amounts of water of crystallization
12-80	100	Organic bromides; inorganic crystals composed of light elements, and heavier elements with water of crystallization
35-200	300	Organic crystals containing fairly heavy atoms; inorganic crystals composed of elements in the intermediate range of atomic numbers
200	500	Crystals containing very heavy elements

In neutron diffraction, a few elements (including lithium, boron and cadmium) have relatively high values of μ , but for the majority of elements μ is less than 1.0 cm⁻¹. Values of μ for typical specimens examined with 1 Å neutrons are given in Table XX. Incoherent scattering processes, particularly nuclear spin incoherence from nuclei with non-zero spin, may contribute more than true absorption to the effective absorption coefficient μ . Thus for the hydrogen nucleus there is a difference in sign, as well as in magnitude, of the scattering amplitudes for the two spin states of the compound nucleus formed between the neutron and proton: this difference gives rise to appreciable incoherent scattering, which is isotropic and accounts for the relatively large μ value of 2.5 cm⁻¹ in Table XX for hydrated compounds. μ can be computed for a particular crystal using tables of nuclear cross-sections, but it is preferable to determine the effective coefficient experimentally by measuring the attenuation of a narrow monochromatic beam in passing through a known thickness of the sample.

TABLE XX. Values of μ for typical specimens examined with neutrons of wavelength 1-1.5 Å

μ (cm ⁻¹)	Specimen
2.5	Organic or inorganic crystals containing large amounts of water of crystallization
10-100	Crystals containing lithium, boron or cadmium
0.01-0.5	Nearly all other crystals not containing H, Li, B, Cd

Absorption factor for spherical crystal

For $\theta = 0^\circ$ and $\theta = 90^\circ$, equation (9.2) can be integrated directly for a sphere of radius R . The result is

$$A^* = \frac{2}{3}(\mu R)^3 \left[\frac{1}{2} - e^{-2\mu R} \left(\frac{1}{2} + \mu R + \mu^2 R^2 \right) \right]^{-1}$$

for $\theta = 0^\circ$, and

$$A^* = \frac{4}{3}\mu R \left[\frac{1}{2} - \frac{1}{16\mu^2 R^2} (1 - e^{-4\mu R} - 4\mu R e^{-4\mu R}) \right]^{-1}$$

for $\theta = 90^\circ$. For other values of θ , A^* can be evaluated by numerical methods; A^* is tabulated at 5° intervals between 0 and 90° and for $\mu R = 0, 0.1, 0.2, \dots, 10.0$ in *The International Tables for X-ray Crystallography*, volume II. The same volume includes a

similar table for cylindrical crystals, examined in two dimensions, with the incident and scattered beams normal to the cylinder axis. The correction of the observed intensities for absorption in the sample is most conveniently applied, in both X-ray and neutron diffraction, when the crystal is ground into a spherical (or cylindrical) shape.

TABLE XXI. Absorption factor, A^* for a spherical crystal

μR	$\theta = 0^\circ$	15°	30°	45°	60°	75°	90°
0.0	1.00	1.00	1.00	1.00	1.00	1.00	1.00
0.1	1.16	1.16	1.16	1.16	1.16	1.16	1.16
0.2	1.35	1.34	1.34	1.34	1.33	1.33	1.33
0.3	1.56	1.55	1.55	1.53	1.52	1.51	1.51
0.4	1.80	1.79	1.78	1.75	1.73	1.70	1.70
0.5	2.08	2.06	2.03	1.99	1.94	1.91	1.90
0.8	3.15	3.11	2.99	2.83	2.69	2.58	2.55
1.0	4.12	4.03	3.79	3.50	3.25	3.07	3.01
1.5	7.80	7.38	6.44	5.52	4.83	4.39	4.23
2.0	14.0	12.6	10.0	7.96	6.59	5.78	5.50
2.5	23.8	20.0	14.5	10.7	8.46	7.23	6.80
3.0	38.4	29.9	19.5	13.6	10.4	8.70	8.11
4.0	86.5	56.0	31.0	19.8	14.4	11.7	10.8
5.0	167	89.1	43.5	26.4	18.5	14.7	13.4
6.0	288	127	56.8	33.0	22.7	17.8	16.1
8.0	683	213	84.4	46.6	31.1	23.9	21.4
10.0	1333	308	113	60.5	39.0	30.1	26.7

Table XXI, which is a section from the *International Tables* giving the absorption correction for a spherical crystal, brings out a number of important points. The figures in each vertical column show that A^* varies rapidly with μR , particularly at low Bragg angles, and so slight departures from the ideal spherical shape cause an appreciable uncertainty in the estimate of the absorption correction. Jeffery & Rose (1964) have calculated the magnitude of this uncertainty, expressed as the fractional standard deviation $\sigma(A^*)/A^*$, as a function of θ . They assumed an average variation in the radius, $\sigma(R)/R$, of 2.5 per cent, corresponding to the average variation of the spheres used in their investigation. Their results, plotted in Fig. 104, show that small departures from sphericity can introduce large errors in the determination of the integrated intensities, and for this reason alone the relative integrated intensities of many X-ray samples cannot be measured to an accuracy better than a few per cent.

Reading the figures across in Table XXI we note that there is no need to apply the absorption correction for a perfect sphere, provided that μR is very small (< 0.2) and provided that relative intensities are required only. If, however, the intensities are to be measured on an absolute scale, the absorption correction must be applied even at very low values of μR : for $\mu R = 0.1$, the correction

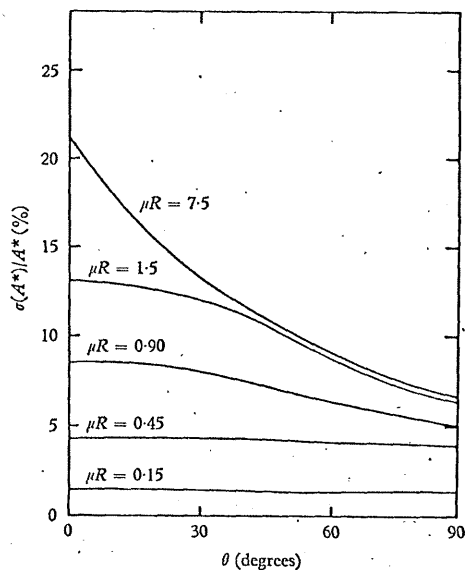


Fig. 104. Graphs showing uncertainty in absorption correction for a spherical crystal due to a 2.5 per cent uncertainty ($\sigma(R)/R$) in the radius (after Jeffery & Rose, 1964).

to the absolute intensities is already as high as 16 per cent. The greater significance of the absorption correction in absolute intensity measurements is one reason why these are more difficult to make than relative intensity measurements (p. 290).

For a cylindrical crystal or a flat plate examined in transmission, absorption causes a fall in the total diffracted energy above a certain crystal size, but for a spherical crystal there is no such critical size and the energy increases continuously from $R = 0$ to

$R = \infty$. This is illustrated by Fig. 105 in which the quantity R^3/A^* is plotted against μR : R^3 is proportional to the crystal volume and R^3/A^* to the total diffracted energy.

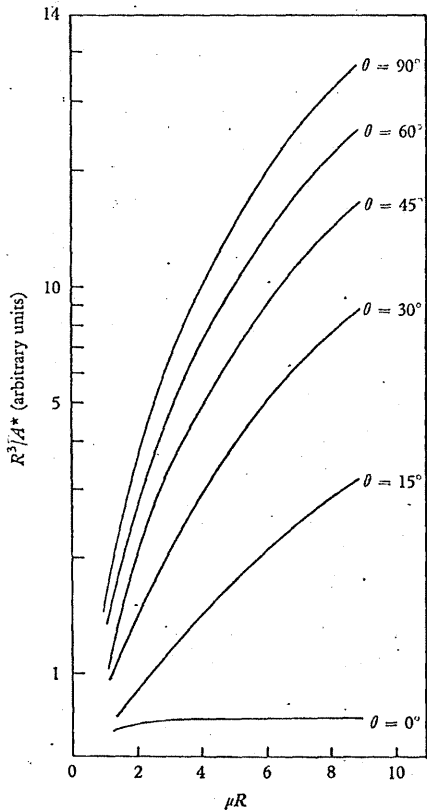


Fig. 105. Total diffracted intensity for spherical crystal plotted against μR . There is no 'critical size' at which the total intensity is a maximum.

If possible, the crystal should be sufficiently small for the absorption correction to vary only slowly with θ and large enough to give an adequate intensity. From these criteria the optimum size would correspond to a μR value of about 1.0.

Absorption factor for any crystal

The correction of single crystal intensity measurements for the effect of absorption is greatly simplified if the crystal is ground into a sphere or cylinder, but often this is not possible. Grinding the crystal may lead to fragmentation or twinning; shaping is also difficult if there are strong cleavage planes.

For an unground crystal, if the dimensions of the faces bounding the crystal are measured, A^* can be evaluated either graphically or with a computer. In Albrecht's graphical method (Albrecht, 1939), the specimen is divided into small volume elements and the integral $\int_V e^{-\mu x} dV$ in equation (9.2) evaluated by summing $e^{-\mu x}$ for each element. Other graphical methods are described in *The International Tables for X-ray Crystallography*, volume II: they are all very laborious and their accuracy decreases as the magnitude of the correction increases.

Computer programs for deriving the absorption corrections for single crystal specimens of arbitrary shape bounded by flat faces have been described by Busing & Levy (1957) and by Wells (1960). Wells also considers specimens mounted in a tube in which an absorbing liquid may be trapped between the crystal and the tube wall: biological crystals are often mounted in this way. The calculation of the absorption correction with these programs is relatively slow and may require as much as one second per reflexion even on a large computer such as the IBM 7090.

Another approach to the absorption problem has been suggested by Furnas (1957). The method makes use of the fact that the azimuthal orientation ψ of the reflecting plane of the crystal can be changed, thereby altering the total radiation path $x = t_1 + t_2$, without destroying the Bragg reflecting condition. Both extinction and simultaneous reflexions give rise to variations in the intensity with ψ (see §§9.2 and 9.3), and so both these effects must be small for the method to work satisfactorily.

An empirical method based on this idea has been developed by North, Phillips & Mathews (1966). A low-angle reflexion, whose scattering vector is parallel to the ϕ -axis, is observed with a four-circle diffractometer; the azimuth ψ is altered simply by changing

ϕ and so the intensity can be plotted as a function of azimuth (Fig. 106c). In Fig. 106a, AA and BB are the projections of the incident and reflected beams for two particular values of ϕ , and the

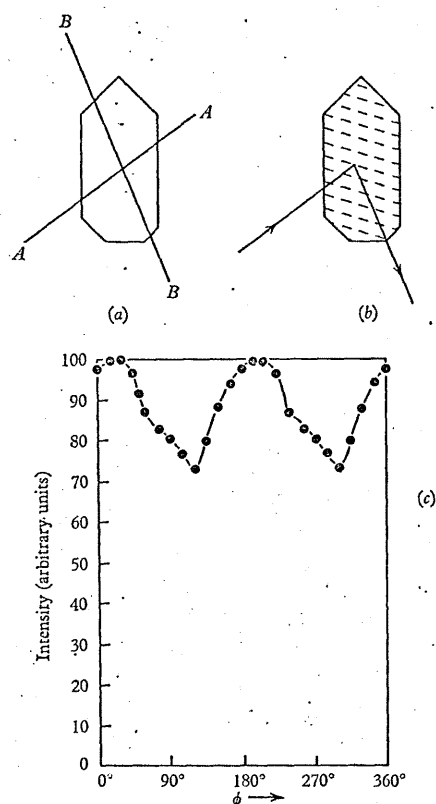


Fig. 106. Absorption correction using the method of North, Phillips & Mathews. (a) Reflecting plane in plane of paper and ϕ -axis normal to paper; (b) reflecting planes normal to plane of paper and incident (reflected) beams parallel to AA (BB); (c) azimuthal scan for reflexion in (a) showing effect of absorption.

absorption correction for a reflexion (Fig. 106b) incident along AA and reflected along BB is taken as the mean of the absorptions along the paths AA and BB in setting (a). The method is most

effective with low-angle reflexions where it is possible to derive the absorption for the projected paths to a close approximation; with protein crystals absorption corrections of up to 40 per cent, determined by this method, have been shown to agree closely with those determined analytically by the much slower method of Busing & Levy (1957).

The absorption factor A^* , given by the expression (9.2), is often the most serious source of error in X-ray work. This is so because A^* cannot be evaluated precisely, unless the crystal has a well-defined shape and size or has a low linear coefficient of absorption μ . In neutron diffraction the μ values are normally much lower: consequently, the absorption effect is small and an adequate correction can be applied relatively easily.

9.2. Extinction

Extinction is the attenuation of the incident beam which is caused by Bragg reflexion. If the crystal is perfect, the apparent absorption along directions in which Bragg reflexions occur may be many times as large as the ordinary value: the incident beam can only penetrate a short distance into the crystal before being reflected, and the inner parts of the crystal have no chance to diffract the radiation. This enhanced absorption in a crystal with a perfect arrangement of atoms is called 'primary extinction'.

Most crystals, however, possess irregularities in their atomic arrangement, in the form of dislocations, point defects, sub-grain boundaries, and the like. These irregularities tend to destroy the coherence, or fixed phase relationship, between the components of the incident beam scattered by different parts of the crystal. The crystal is divided effectively into small regions, perhaps 10,000 Å across, which are sufficiently perfect to reflect the beam coherently, but between which there is no coherence. These perfect regions are known as 'mosaic blocks', and if there is negligible primary extinction of the beam in passing through a single block the crystal is 'ideally mosaic'.

The passage of an X-ray or neutron beam through a mosaic crystal will be quite different from that through a perfect crystal. The angular range of reflexion for a perfect crystal is only a few seconds of arc, whereas the angular misorientation of adjacent

mosaic blocks is measured in *minutes* of arc. Consequently, the beam will penetrate deeply into a mosaic crystal before it reaches mosaic blocks which are identical in orientation to those near the surface and which will reflect the same part of the beam again. Attenuation of the beam by Bragg scattering from identically oriented mosaic blocks is known as 'secondary extinction' (see Fig. 107). In primary extinction the *amplitudes* of the scattered waves must be added to obtain the scattering from the whole crystal; for secondary extinction there is no coherence between the mosaic blocks and the *intensities* must be summed.

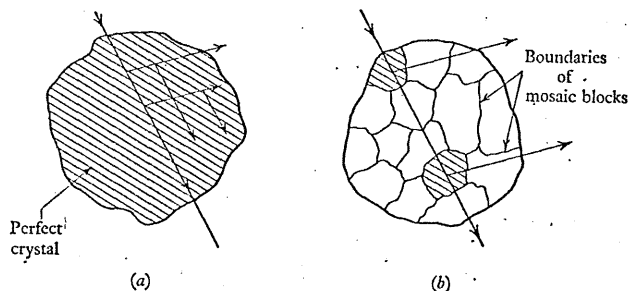


Fig. 107. (a) Primary extinction, causing attenuation of beam in a perfect crystal, or in a single mosaic block. (b) Secondary extinction, causing attenuation by reflexion at two mosaic blocks with same orientation.

In spite of the large volume of theoretical work on extinction, the correction factors to be applied to the measured integrated intensities for taking into account the affect of extinction can be calculated exactly in a few idealized cases only. Thus Zachariasen (1945), Bacon & Lowde (1948) and James (1962) have based their theoretical treatments of extinction on crystals in the form of infinite plane-parallel plates, whereas we are usually concerned with finite crystals which are completely bathed in the beam. An approximate treatment of secondary extinction for crystals of any shape has been given by Hamilton (1957, 1963), and this will be discussed later. Our main purpose here, however, is to describe the procedure of detecting and correcting for extinction, and we shall only sketch the relevant theoretical background. The reader

interested in the detailed theory of extinction is recommended to study the books by Zachariasen (1945) and James (1962).

Both primary and secondary extinction are dependent on the strength of the reflexion, on the wavelength of the incident beam and on the dimensions of the crystal. A number of methods for detecting and correcting for extinction exploit these various relationships.

Dependence on intensity

The effect of extinction is most pronounced for the strongest reflexions, because these scatter the maximum amount of energy

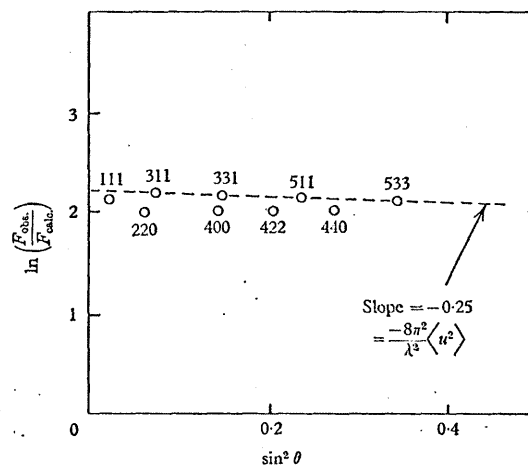


Fig. 108. Secondary extinction in UO_2 . The intensities of the strong reflexions, with even indices, are reduced by extinction (after Willis, 1963).

from the incident beam. One procedure in structure determinations is to ignore the strongest reflexions in the initial stages of the least-squares refinement of the data, in which the observed structure factors ($F_{\text{obs.}}$) are matched with those calculated from the trial structure; they may then be introduced in the later refinement stages, and any systematic tendency for $F_{\text{obs.}}$ to be lower than $F_{\text{calc.}}$ indicates the presence of extinction. An example of the detection of extinction in this way is illustrated by Fig. 108, showing results

obtained by neutron diffraction in the examination of a single crystal of UO_2 . The quantity $\ln(F_{\text{obs.}}/F_{\text{calc.}})$ is plotted against $\sin^2\theta$, and as $F_{\text{calc.}}$ was derived without taking into account the effect of thermal motion this curve should be a straight line with a slope of $-(8\pi^2/\lambda^2)\langle u^2 \rangle$, where $\langle u^2 \rangle$ is the mean square displacement of the atoms due to thermal agitation. The reflexions with odd indices have points lying on this straight line, but the stronger reflexions with indices obeying the relation $h+k+l=4n$ are contributed by atoms which are all scattering in-phase, and the corresponding points lie below the line because of extinction.

Chandrasekhar (1956, 1960*a, b*) has devised an elegant method of correcting for extinction in X-ray diffraction, which does not require any previous knowledge of the atomic positions in the unit cell and which applies to any kind of extinction, primary, or secondary, or both. In the absence of extinction, the intensity reflected by a mosaic crystal is proportional to the square of the structure factor

$$I_{\text{obs.}} = \alpha |F|^2,$$

and Chandrasekhar has shown that to a first approximation this formula is modified to

$$I_{\text{obs.}} = \alpha |F|^2 - \beta |F|^4 \quad (9.5)$$

by the effects of extinction. α is a known factor whose calculation is described in Chapter 11; β is unknown and depends on the nature and amount of extinction. If the intensity is measured with plane-polarized X-rays, the diffracted intensities will be different for the two states of polarization in which the plane of polarization is perpendicular or parallel to the plane of incidence. Equation (9.5) can be applied to the two states separately, giving

$$I_{\text{obs.}}^{\perp} = \alpha |F|^2 - \beta |F|^4 \quad (9.6)$$

$$\text{and } I_{\text{obs.}}^{\parallel} = \alpha |F|^2 \cos^2 2\theta - \beta |F|^4 \cos^4 2\theta. \quad (9.7)$$

$I_{\text{obs.}}^{\perp}$ and $I_{\text{obs.}}^{\parallel}$ denote the intensities which are measured with the X-rays polarized in the perpendicular and parallel directions. The structure factors for the two polarization states differ by the factor $\sin(90^\circ - 2\theta)$ (see p. 284), and this difference accounts for

the replacement of F in (9.6) by $F \cos 2\theta$ in (9.7). Eliminating the unknown β from these two equations leads to

$$|F|^2 = \frac{I_{\text{obs.}}^{\perp} - I_{\text{obs.}}^{\parallel} \cos^4 2\theta}{\alpha (\cos^2 2\theta - \cos^4 2\theta)}. \quad (9.8)$$

Thus by making two measurements for each reflexion, using X-rays polarized perpendicular and parallel to the plane of incidence, an extinction-free estimate of $|F|^2$ is derived by applying equation (9.8).

The principal limitation of Chandrasekhar's method is that equation (9.8) is ill-conditioned for values of θ approaching 0° , 45° and 90° : the extent of this limitation depends on the accuracy with which the intensities are measured. The incident beam can be polarized by one of the two methods discussed on p. 192. The loss of intensity associated with the polarization of the beam by either of these methods; and the experimental difficulties of repeating each measurement under identical conditions for each polarization state, have prevented the wide adoption of Chandrasekhar's method.

A modified form of the method has been used in neutron diffraction for the study of magnetic reflexions (Chandrasekhar & Weiss, 1957; Szabo, 1961). However, it cannot be used in general neutron work as there is no polarization effect for nuclear reflexions.

Dependence on wavelength

The amount of extinction decreases with decreasing wavelength, and we can write approximately (Chandrasekhar, 1960*b*):

$$I_{\text{obs.}} = I_{\text{corr.}} \left[1 - \left(P^2 + \frac{S^2}{\mu} \right) p \lambda^2 \right]. \quad (9.9)$$

Here $I_{\text{obs.}}$ is the observed intensity and $I_{\text{corr.}}$ the intensity corrected for the effect of extinction; p is the polarization factor, λ the wavelength and P, S are constants representing the amount of primary, secondary extinction respectively. A wavelength dependence of the relative values of $I_{\text{obs.}}$ for different reflexions indicates the presence of extinction. The linear absorption coefficient μ for X-rays varies

with λ^3 between absorption edges, so that I_{obs} is not a linear function of λ^2 unless there is no secondary extinction ($S = 0$ in equation 9.9).

Dependence on crystal size

To a first approximation, the effect of secondary extinction is to increase the absorption coefficient from μ to $\mu + gQ$, where g is the 'secondary extinction coefficient' (related to the mosaic spread of the crystal) and Q is the quantity:

$$Q = N_c^2 \lambda^3 (e^2/mc^2)^2 L_p F^2 \quad (9.10)$$

(Darwin, 1922). N_c is the number of unit cells per unit volume and L_p is the Lorentz-polarization factor (see Chapter 11): the term $(e^2/mc^2)^2$ is replaced by unity in neutron diffraction (Hamilton, 1957). Thus the attenuation of the beam inside the crystal is $e^{-(\mu+gQ)x}$, where x is the optical path length; if the secondary extinction is small ($gQx \ll 1$), the attenuation is

$$(1 - gQx)e^{-\mu x}.$$

The term $e^{-\mu x}$ represents the effect of true absorption and $1 - gQx$ is the factor by which the observed intensity decreases on account of secondary extinction.

Thus the effect of secondary extinction can be eliminated by measuring the intensity, corrected for true absorption, for different values of x , and extrapolating to zero path length. The procedure was first used in X-ray diffraction by Bragg, James & Bosanquet (1921), and more recently by Cochran (1953) and by Witte & Wölfel (1955). Cochran measured the relative intensities of the reflexions from spherical crystals of different radii, and corrected for extinction by plotting the changes in relative intensities against the radius of the spheres.

The method of varying path length has also been used in neutron diffraction (Willis, 1962c). A convenient method of altering the path length is to change the azimuthal angle ψ . Figure 109 shows the neutron intensities of the $h00$ reflexions of KBr, measured at different azimuthal orientations ψ of the $\{100\}$ plane. The crystal was in the form of a flat plate, cleaved parallel to the $\{100\}$ faces; for $\psi = 0^\circ$ or 180° the total path length x was a minimum, and the

path was longest for $\psi = 90^\circ$. The experimental measurements were corrected for the small effect of true absorption; they showed that the intensity of the weakest reflexion 800 was independent of the path length through the crystal, but for 600, 400, 200 the maximum intensity occurred at the minimum path length. The

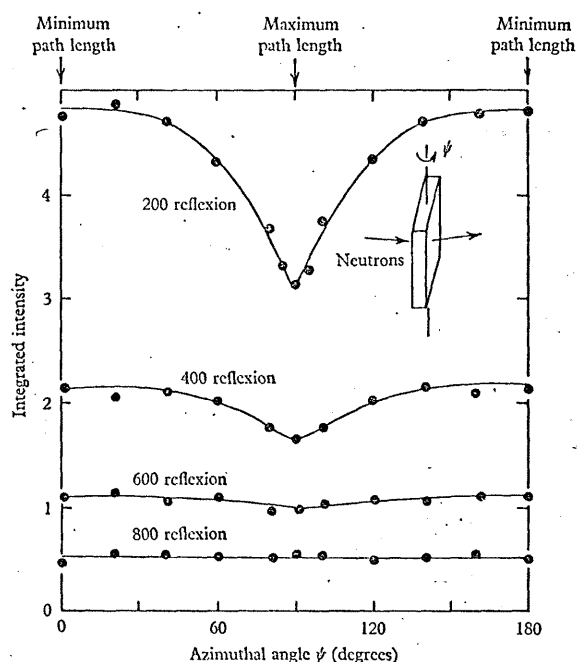


Fig. 109. Integrated intensities of $h00$ reflexions of KBr crystal as a function of ψ (after Willis, 1962c).

proportional reduction in intensity due to secondary extinction increased with the strength of the reflexion and was largest for the strongest reflexion, 200. The slight fluctuation of the experimental points from the smooth curves in Fig. 109 may be due to the influence of simultaneous reflexions (see §9.3). The derivation of the corrected intensities from these curves is described in the original paper.

Hamilton (1957, 1963) has discussed the calculation of secondary extinction corrections for crystals of any arbitrary polyhedral shape. If the extinction is large, so that the intensities are reduced by 30 per cent or more, Hamilton recommends that the crystal be ground to a cylindrical shape, and he has prepared tables for the correction of the equatorial reflexions of cylindrical crystals. A section of these tables is reproduced in Table XXII: the numbers represent the factors by which the observed intensities are multiplied to correct them for secondary extinction, and are given as a function of 2θ and the quantity aRQ . R is the radius of the cylinder, Q is given by (9.10) and is proportional to the intensity of the reflexion, and a is a numerical constant related to the mosaic spread of the specimen. The tables cannot be used directly as a is normally unknown, but Hamilton has written a computer program, based on these tables, which allows a least-squares comparison of the observed and calculated intensities: a is treated as an extra empirical constant to be determined in the least-squares procedure.

TABLE XXII. Secondary extinction corrections for cylindrical crystal (Hamilton 1963)

aRQ	$\theta = 0^\circ$	22.5°	45°	67.5°	90°
0.0	1.000	1.000	1.000	1.000	1.000
0.2	1.178	1.177	1.173	1.170	1.169
0.4	1.374	1.368	1.354	1.341	1.336
0.6	1.585	1.571	1.538	1.511	1.501
0.8	1.811	1.785	1.727	1.682	1.666
1.0	2.050	2.007	1.917	1.852	1.830
2.0	3.389	3.196	2.880	2.700	2.641
3.0	4.863	4.437	3.846	3.545	3.444
4.0	6.393	5.684	4.812	4.387	4.143
6.0	9.490	8.172	6.741	6.070	5.832
8.0	12.61	10.65	8.667	7.752	7.416
10.0	15.75	13.12	10.59	9.432	8.996

Hamilton assumes that the effective absorption coefficient in the presence of secondary extinction is $\mu + gQ$, in accordance with the original treatment of Darwin (1922). However, Zachariasen (1963) has shown that, for incident unpolarized X-radiation, Darwin's formula is in error, and that the effective coefficient is instead

$$\mu + 2gQ \frac{(1 + \cos^4 2\theta)}{(1 + \cos^2 2\theta)^2}$$

This expression reduces to $\mu + gQ$ at $\theta = 0^\circ$ and $\theta = 90^\circ$ but to $\mu + 2gQ$ at $\theta = 45^\circ$. The error arises from the incorrect treatment of the effect of polarization in Darwin's theory; the theory remains strictly valid for neutrons, because there is no polarization of nuclear scattering. Thus Table XXII applies to the scattering of neutrons from a cylindrical specimen, but the numbers in the columns for $\theta = 22.5^\circ, 45^\circ, 67.5^\circ$ require small corrections for the scattering of unpolarized X-rays.

None of the methods for correcting for the effect of extinction is entirely satisfactory; they are all based on theoretical approximations and several involve an elaborate experimental technique, which may not be justified by the final results. If the extinction correction is small, requiring, say, a 5 per cent correction to the measured intensities, a reasonable correction is possible, but for large extinction a rough correction only can be made.

The safest procedure for dealing with extinction is to ignore those reflexions for which extinction is suspected. This is legitimate in the refinement of intensity data, when atomic co-ordinates are to be determined by least-squares methods: it is not permissible in deriving electron density distributions, where all reflexions must be included up to the maximum observed Bragg angle. It may be possible to reduce extinction by grinding the crystal or by subjecting it to thermal shock, but this will rarely eliminate extinction altogether (Lonsdale, 1947).

9.3. Simultaneous reflexions

In interpreting the intensity reflected by a family of planes (hkl) it is normally assumed that no other Bragg reflexion is occurring at the same time as the hkl reflexion under observation. However, at certain crystal orientations the Bragg reflecting condition may be satisfied for more than one family of planes, and the presence of a second reflexion can modify the intensity of the first. The occurrence of simultaneous reflexions is by no means uncommon, and may even be unavoidable, particularly when working at short wavelengths or with crystals of large inter-planar spacings. Fortunately, the magnitudes of the intensity fluctuations caused by simultaneous reflexions tend to be relatively small in X-ray diffraction, and the effect has received little attention in the X-ray literature since

the work of Renninger (1937), who was the first to make a thorough study of simultaneous reflexions. More recently, with the advent of counter methods and the demand for higher accuracy, further X-ray studies have been reported (Cole, Chambers & Dunn, 1962; Cohen, Fraenkel & Kalman, 1963; Zachariasen, 1965). In neutron diffraction, simultaneous reflexions are more troublesome, because the specimens are larger and absorb neutrons less readily than X-rays: consequently, the neutron beam penetrates a long way into the crystal, and there is a greater chance of energy being exchanged between different families of reflecting planes. Several authors have examined experimentally the influence of simultaneous reflexions on the measurement of integrated intensities with neutrons (Borgonovi & Caglioti, 1962; Willis, 1963; Moon & Shull, 1964).

The geometrical problem of determining those crystal orientations for which two or more reflexions occur is conveniently treated in terms of the reciprocal lattice and the Ewald sphere of reflexion. The condition for a single reflexion to occur is that the Ewald sphere passes through the hkl reciprocal lattice point, and this condition is maintained if the sphere rotates about the axis OP passing through the hkl point P and the origin of the reciprocal lattice O (see Fig. 110a). During this rotation the sphere sweeps through the reciprocal lattice and each time it touches a second reciprocal lattice point, such as $h'k'l'$, the conditions are satisfied for hkl and $h'k'l'$ to occur simultaneously.

In Fig. 110a the directions of the incident beam and the first and second reflexions are denoted by the unit vectors s_0 , s and s' . The beam s_0 is scattered along the directions s , s' , but the beams s and s' can then each be rescattered along two directions, giving rise to six scattering processes in all. The rescattering processes for the first reflexion s are illustrated by Fig. 110b. The once-scattered beam in the direction s is treated as the 'incident beam' for the second scattering process and we can transfer the origin of the reciprocal lattice to the end-point of s . The process $s \rightarrow s_0$ takes place by rescattering of the first reflexion at the family of planes ($\bar{h}\bar{k}\bar{l}$), and $s \rightarrow s'$ by rescattering at the family with indices ($h'-h, k'-k, l'-l$). Both processes cause a diminution of intensity of the first reflexion s . An intensity reduction is also contributed by the

process $s_0 \rightarrow s'$, which removes power from the incident beam and thereby decreases the power available for the reflexion $s_0 \rightarrow s$, whereas a gain in intensity follows the transfer of energy to the first reflexion by the roundabout process ('Umweganregung'):

$$s_0 \rightarrow s' \rightarrow s.$$

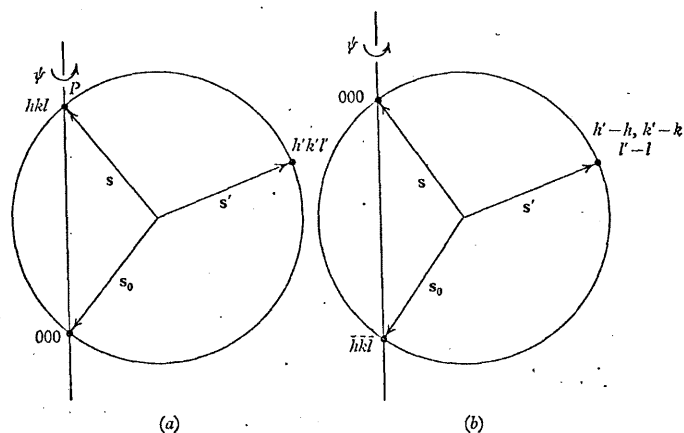


Fig. 110. (a) Simultaneous reflexion $h'k'l'$ recorded during rotation of crystal about hkl scattering vector OP . The circle represents a section of the Ewald sphere through OP . (b) Once reflected hkl beam in (a) can be rescattered by planes with indices $\bar{h}\bar{k}\bar{l}$ and $h'-h, k'-k, l'-l$.

Clearly, the net effect on the intensity of the hkl (or s) reflexion is very difficult to calculate and depends on the reflecting powers of the planes $\pm(hkl)$, $\pm(h'k'l')$ and $\pm(h-h', k-k', l-l')$. If more than two reciprocal lattice points lie simultaneously on the Ewald sphere, the number of different scattering processes is much larger.

Experimental curves showing the intensity in the direction of the primary reflexion are shown as a function of ψ in Figs. 111 and 112. Fig. 111 shows a large number of intensity peaks at different values of ψ when a germanium crystal is so oriented that the 222 reciprocal lattice point is on the Ewald sphere. These peaks occur even though the 222 reflexion is a forbidden one in the diamond

structure of germanium. The extra peaks are caused by the round-about excitation of 222 by the process $s_0 \rightarrow s' \rightarrow 222$: s_0 is the incident beam and s' is a reflexion which occurs simultaneously with 222. In all, there are over two hundred peaks in a 360° rotation of ψ , and these are associated with a corresponding number of simultaneous reflexions s' . Similarly, the true 200 reflexion in the neutron diffraction pattern of iron (Fig. 112) is the base line between the peaks (and dips) caused by simultaneous reflexions: at $\lambda = 1.57 \text{ \AA}$ there are seven calculated positions of ψ in a 45° range at which reflexions occur simultaneously with 200, while at $\lambda = 0.72 \text{ \AA}$ this number increases to seventy-eight.

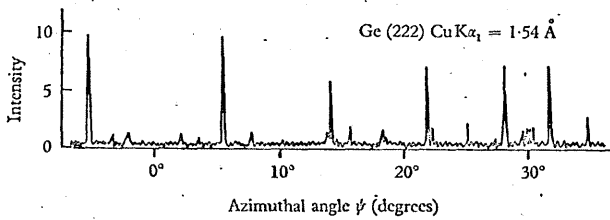


Fig. 111. Simultaneous reflexions observed with X-rays in the 'forbidden' 222 reflexion from germanium, as the crystal is rotated about the 222 scattering vector (after Cole, Chambers & Dunn, 1962).

An approximate theory of Moon & Shull (1964) accounts for the intensity changes caused by simultaneous reflexions. It applies to crystals in the shape of flat plates which are larger than the incident beam cross-section and is restricted to small secondary extinction and low absorption.

In the absence of a general theory allowing the calculation of the correction to the observed intensities, the most satisfactory practical procedure is to take steps either to avoid or to minimize the effect of simultaneous reflexions. An obvious precaution is to choose the azimuthal angle ψ of the reflecting plane hkl (the angle of rotation about the line OP in Fig. 110a), so that the Ewald sphere is as far as possible from all other reciprocal lattice points. The calculation of the 'forbidden' ψ values which give rise to simultaneous reflexions is straightforward: a graphical method for

cubic crystals is described by Cole, Chambers & Dunn (1962), and an analytical method, suitable for crystals of any symmetry, by Santoro & Zocchi (1964). Powell (1966) has written a computer program which derives suitable setting angles of a four-circle diffractometer for minimizing simultaneous reflexion effects; for a particular reflexion there is an infinite number of combinations of setting angles, each of which corresponds to a different value of ψ ,

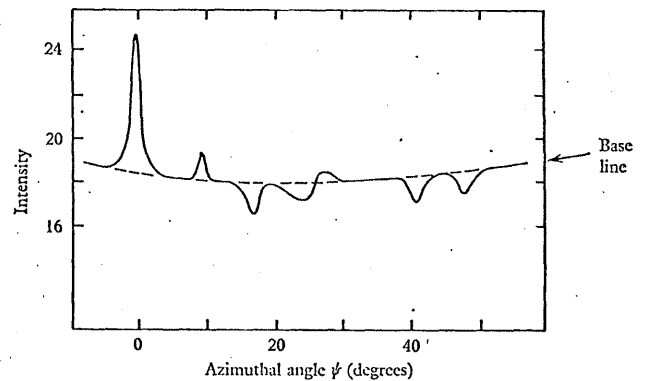


Fig. 112. Simultaneous reflexions observed with neutrons ($\lambda = 1.57 \text{ \AA}$) in the 200 reflexion from iron, as the crystal is rotated about the 200 scattering vector (after Moon & Shull, 1964).

and the particular combination selected is that for which other reciprocal lattice points are greater than a given distance from the Ewald sphere.

It is well known (see p. 32) that systematic double and triple diffraction occur for the normal-beam and equi-inclination cases respectively, if the crystal is oriented with a symmetry axis parallel to the goniometer-head axis (ϕ -axis). According to Burbank (1965), the situation is even worse for the single crystal orienter technique (four circle diffractometer), although the systematic diffraction he describes will occur only in the special symmetrical- A setting and is avoided in the general setting.

We conclude that the occurrence of simultaneous reflexions is

minimized by carefully selecting the azimuthal angle ψ of the primary reflexion, although it may not be possible to avoid simultaneous reflexions altogether. On the other hand, if the exchange of energy between the reflexions is small and measurements of the highest accuracy are not required, their occurrence may be deliberately exploited to speed up the collection of intensity data by using multiple-counter methods (see p. 56).

minimized by carefully selecting the azimuthal angle ψ of the primary reflexion, although it may not be possible to avoid simultaneous reflexions altogether. On the other hand, if the exchange of energy between the reflexions is small and measurements of the highest accuracy are not required, their occurrence may be deliberately exploited to speed up the collection of intensity data by using multiple-counter methods (see p. 56).

CHAPTER 10

PROCEDURE FOR MEASURING
INTEGRATED INTENSITIES

In this chapter we shall describe the main features in the procedure for measuring the set of relative integrated intensities ρ_{hkl} of the crystal. We shall assume that the diffractometer has been correctly positioned and aligned with respect to the incident beam. The methods of making these adjustments are fully described by Furnas (1957).

10.1. Choice of crystal size and shape

To minimize errors arising from the effects of absorption, extinction and simultaneous reflexions, the crystal must be as small as possible. The ultimate limit to the specimen size is determined by counting statistics (see §10.7), and, because of the greater intensity of primary X-ray beams compared with monochromatic neutron beams, the crystal size tends to be much larger in neutron diffraction. In the early period of neutron diffraction the linear dimensions of the crystal were measured in centimetres, but now, with the availability of high-flux reactors and with the use of automatic methods to speed up the collection of data, the size of crystal is down to 1 or 2 mm.

On p. 240 we gave the criterion $\mu R \sim 1$ as a rough indication of the optimum size of the crystal, where μ is the linear absorption coefficient and R the average crystal radius. From Table XIX, this corresponds to an average radius for X-ray work of about 0.1 mm. The diffracted intensity decreases with the size of the unit cell, so that larger specimens are used when the cell size is large and the absorption is relatively low.

The ideal shape of crystal is a sphere for three-dimensional diffraction measurements and a cylinder for two dimensions. With such a crystal it is not only possible to calculate the correction due to absorption, but also to minimize errors arising from non-uniformity of the incident beam. A widely used method for

cutting spherical crystals is that devised by Bond (1951) and later improved by Belson (1964). The crystal is placed in a circular tunnel, whose inside periphery is lined with fine abrasive material, and is tumbled randomly against the walls of the tunnel by a jet or jets of compressed air. A cylindrical crystal can be prepared by directing a fine jet of abrasive powder against the crystal as it turns about its axis.

10.2. Alinement of crystal

By 'crystal alinement' we mean the centring of the crystal and the setting of a principal crystallographic axis along the ϕ -axis of the diffractometer. (It is always necessary to centre the crystal, but with a four-circle diffractometer measurements can proceed without further adjustments to the crystal, p. 51.) The crystal is 'centred', if it remains in the same portion of the incident beam while being turned from one Bragg reflexion to the next. The alinement is carried out conveniently by mounting the crystal on a goniometer head which has two arcs, two translational movements and a height adjustment: suitable designs of goniometer head are described on p. 79.

Let us suppose that the crystal is monoclinic and that it is to be aligned with the unique axis (diad axis) parallel to the goniometer-head axis, or the ϕ -axis, of a four-circle diffractometer. If the diad axis is along $[010]$, then the normal to the $\{0k0\}$ planes lies along the ϕ -axis. At this orientation the intensity of the $0k0$ reflexions will be unchanged as the crystal turns through 360° about the ϕ -axis. This is not quite true if systematic errors are present of the type discussed in the previous chapter, but for correct alinement there is a minimum variation of the diffracted intensity with the angle ϕ , and the intensity will not fall to zero at any point in the complete rotation about ϕ .

The alinement proceeds, therefore, as follows. The crystal is viewed through a telescope and is centred using the translational movements of the goniometer head. The ϕ -axis of the four-circle diffractometer is then moved into the horizontal plane containing the incident beam by rotating it around the χ -circle (see Fig. 113a). The goniometer head is turned about the ϕ -axis to bring one of the arcs into the horizontal plane and that arc is adjusted for maximum

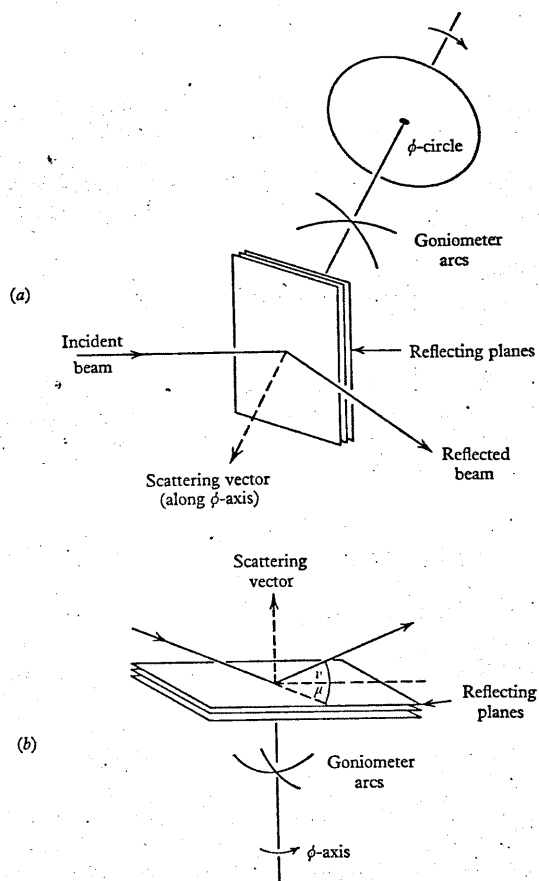


Fig. 113. (a) Alinement of crystal on four-circle diffractometer: incident and reflected beams are in horizontal plane. (b) Alinement of crystal on equi-inclination diffractometer: incident and reflected beams are in vertical plane.

intensity of the $0k0$ reflexion. The head is rotated through 180° and the same arc is adjusted again for maximum intensity. If the arc settings differ for the two orientations of the goniometer head, the correct setting is taken as the mean. The second arc is adjusted in the same way at the 90° and 270° positions of the goniometer head. For a eucentric goniometer head (see p. 79), with the crystal accurately positioned at the centre of the arcs, the centring will not be affected by any movement of the arcs, but for other mountings alternate movements of cross-slides and arcs are necessary during the alinement. With an equi-inclination instrument a similar alinement procedure is possible (see Fig. 113*b*).

A great convenience during the alinement process is the provision of two pairs of masks which can obscure the right or left halves or the top or bottom halves of the aperture of the detector. These masks allow one to judge easily in which direction the arcs need to be moved for correct alinement since they define where the reflexion is, relative to the centre of the detector aperture. The reflexion is correctly centred when the intensities in the four quadrants are approximately equal.

Alinement is much more difficult if the crystal cannot first be approximately oriented and if nothing is known about its unit-cell dimensions. The necessary steps in this situation have been described so fully and clearly by Furnas (1957) that no further comments are needed here.

Wooster (1965) describes a procedure for determining the setting angles of a crystal for a four-circle diffractometer assuming no prior knowledge of its orientation or lattice parameters.

10.3. Correct assignment of signs of crystallographic axes

For a crystal of any symmetry it is not possible to distinguish the configuration of the axes a , b and c from $-a$, $-b$ and $-c$ using the observed positions only of the Bragg reflexions. This distinction is important in determining the absolute configuration of a non-centrosymmetrical crystal, and can be made from the intensities of the hkl , $\bar{h}\bar{k}\bar{l}$ pairs of reflexions (Ramaseshan, 1964). Let us suppose, for instance, that the intensities of 200 and $\bar{2}00$ are related by the inequality $I_{200} > I_{\bar{2}00}$. If the crystal is replaced by a different crystal of the same material, the second crystal must

be indexed in such a way that the same inequality holds; should the initial assignment of axes lead to $I_{200} < I_{\bar{2}00}$, it will be necessary to invert the a -, b - and c -axes.

We referred on p. 80 to the problem of determining the correct sense, $+b$ or $-b$, of the diad axis in a monoclinic crystal relative to the vectors a , c , when the crystal is mounted with the b -axis

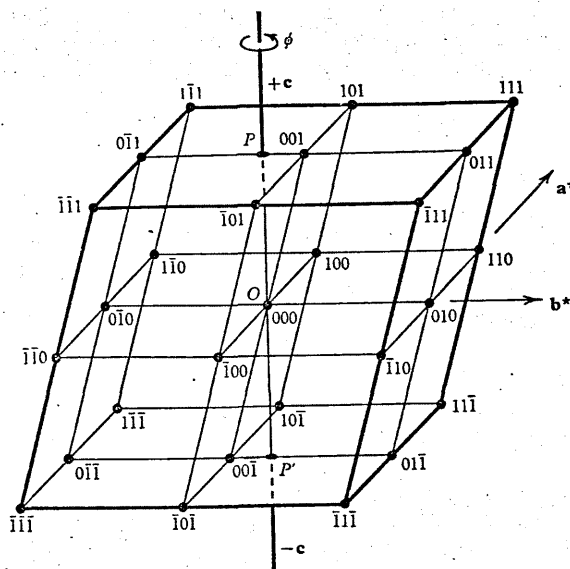


Fig. 114. Monoclinic reciprocal lattice with unique axis along b or b^* and rotation axis along c . If the sense of c is chosen incorrectly the point $00\bar{1}$ in the $l = 1$ level will lie on the other side of the ϕ axis, OP .

parallel to the goniometer-head axis ϕ . If the a - or c -axes of the crystal are along the ϕ -axis, the correct sense of b cannot be found from observations in the zero level alone (see Fig. 114). However, the observed positions of reflexions in the higher level will immediately reveal any wrong choice of sign, which can be corrected by inverting the crystal or reversing the sense of rotation of the ϕ -shaft: this may be more convenient than recomputing the setting angles with a revised assignment of signs.

10.4. Measurement of lattice parameters

It is necessary to determine the lattice parameters of the crystal before calculating the setting angles for each reflexion, using the formulae given in Chapter 2.

The lattice parameters can be measured with a diffractometer to a precision equal to that with the best X-ray camera, and the same instrument can then be used to measure the integrated intensities without further adjustment of the crystal. The crystal is aligned on the diffractometer (for instance, with the goniometer-head axis lying along the normal to a family of reflecting planes), and the lattice parameters are derived from the observed scattering angles $2\theta_{\text{obs}}$ for a number of different reflexions.

There are at least two ways of measuring 2θ with a four-circle diffractometer. In the first (Fig. 115a) the reflexion is observed with a wide detector aperture and the profile of the reflexion is plotted using an ω -scan. The crystal is then set at the peak position, the detector aperture is closed down to a narrow vertical slit, and a second intensity scan is performed with the crystal stationary and the detector moving. $2\theta_{\text{obs}}$ is taken as the difference between two readings of the angular position of the detector, one at the peak of the reflexion and the other at the point of maximum intensity of the direct beam, suitably attenuated.

In the second method of determining 2θ , there is no need to measure the 'straight-through' position of the direct beam. The hkl reflexion is observed with the ω shaft of the crystal and the θ shaft of the detector coupled together in a 1:2 angular ratio. The detector aperture remains wide open and so the reflexion need not enter the detector centrally. The value of ω is noted for the peak position of the reflexion. With ω and θ remaining coupled, the ω -axis is then turned so that the beam enters the detector by reflexion at the reverse side of the hkl reflecting plane (see Fig. 115). $2\theta_{\text{obs}}$ is the difference in the readings of the ω scale for the peak positions of hkl and $\bar{h}\bar{k}\bar{l}$. By measuring the angle between the two positions of the crystal, rather than the angle between the two detector positions as in the first method, not only the zero error but also errors due to absorption and incorrect centring of the crystal are eliminated: absorption and eccentricity

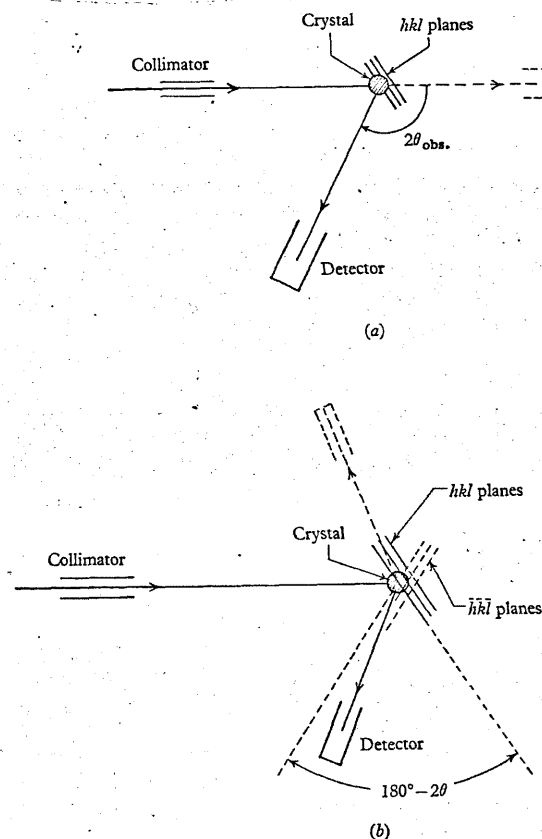


Fig. 115. Two ways of measuring scattering angle 2θ . The zero position of the detector arm ($2\theta = 0$) must be known in (a), but not in (b).

both alter the angle at which the beam enters the detector, but the crystal angles are still correct if the detector window is wide open. Bond (1960) gives further details of this second method and discusses the various sources of systematic error. He shows that the scattering angles of a perfect crystal, such as silicon, can be

measured with X-rays by this method to better than one part in 10^5 . Further development of this method by Baker (1966) gives results accurate to one part in 10^7 .

After the measurement of the scattering angles for a number of reflexions, the lattice parameters of the reciprocal unit cell can readily be determined by a least-squares analysis, using equation (2.3) in the form:

$$\frac{4 \sin^2 \theta}{\lambda^2} = h^2 a^{*2} + k^2 b^{*2} + l^2 c^{*2} + 2hka^*b^* \cos \gamma^* + 2k lb^*c^* \cos \alpha^* + 2lhc^*a^* \cos \beta^*. \quad (10.1)$$

The observed quantities are the set of 2θ values and the variables are the six lattice parameters. The final accuracy of these parameters is related to the precision with which the wavelength λ is known: this precision is lower in neutron diffraction than in X-ray work because of the larger bandwidth $\delta\lambda$ of the incident neutron beam.

Table XXIII illustrates some results obtained by Busing (1965), who analysed X-ray diffractometer data from a single crystal of monoclinic barium chloride dihydrate, $\text{BaCl}_2 \cdot 2\text{H}_2\text{O}$. Twelve independent values of 2θ were determined by the method illustrated in Fig. 115*a*, and these observed values were compared with the calculated values assuming a triclinic unit cell. The values of α and γ refined to within one standard deviation of the expected monoclinic values of 90° .

TABLE XXIII. Unit cell dimensions of $\text{BaCl}_2 \cdot 2\text{H}_2\text{O}$ from least-squares refinement of X-ray data (after Busing, 1965)

Initial values of lattice parameters before least-squares refinement	Final values of lattice parameters
$a = 6.7380 \text{ \AA}$	$6.7215 \pm 0.0002 \text{ \AA}$
$b = 10.8600 \text{ \AA}$	$10.9077 \pm 0.0003 \text{ \AA}$
$c = 7.1360 \text{ \AA}$	$7.1315 \pm 0.0003 \text{ \AA}$
$\cos \alpha = 0$	-0.00004 ± 0.00007
$\cos \beta = -0.0166$	-0.01924 ± 0.00006
$\cos \gamma = 0$	-0.00007 ± 0.00006

10.5. Choice of scan

On p. 20 we described the three measuring procedures which may be used to determine the intensity of a Bragg reflexion. These are the stationary-crystal-stationary-detector method, the moving-crystal-stationary-detector method (ω -scan), and the moving-crystal-moving-detector method ($\omega/2\theta$ -scan).

The simplest procedure is the stationary-crystal-stationary-detector method which requires a uniform convergent incident beam (see Fig. 7, p. 22). Unfortunately, this requirement is difficult to meet in both X-ray and neutron diffraction.

Alexander & Smith (1962) have examined the relation between peak height and peak area when the incident beam is not sufficiently convergent to give flat-topped peaks. They showed that the peak height is proportional to the peak area in a very limited range of θ only. The same relation has been examined for neutron diffraction by Chidambaram, Sequeira & Sikka (1964) who claimed that the data collection rate can be speeded up by a factor of about 10 using peak heights and an experimental calibration curve relating peak height and peak area.

For accurate intensity measurements stationary-crystal methods are not recommended and in most investigations the choice of measuring procedures will be between the ω -scan and the $\omega/2\theta$ -scan.

As Burbank (1964) has pointed out, the preferred scan is that which yields the true integrated intensity by illuminating the smallest volume in reciprocal space: the background is then as low as possible, especially that part which is contributed by thermal diffuse scattering and which tails off slowly at the sides of the Bragg reflexion (p. 221). Using this criterion of smallest volume in reciprocal space, the $\omega/2\theta$ -scan is generally preferred in neutron work, because of the large bandwidth $\delta\lambda$ of the incident radiation (see Fig. 116*a*). On the other hand, if the mosaic spread of the crystal is large, the ω -scan may be preferable at low Bragg angles (see Fig. 116*b*), where the spectral dispersion is least.

Both the horizontal and vertical dimensions of the detector aperture must be carefully chosen for both scans. These dimensions vary with the angle θ and, in the case of inclination diffractometers, with the level of the reciprocal lattice under investigation. They are

best found experimentally by examining the integrated intensities of a number of reflexions as a function of the aperture size, and selecting the minimum size at a particular θ which gives the full integrated intensity.

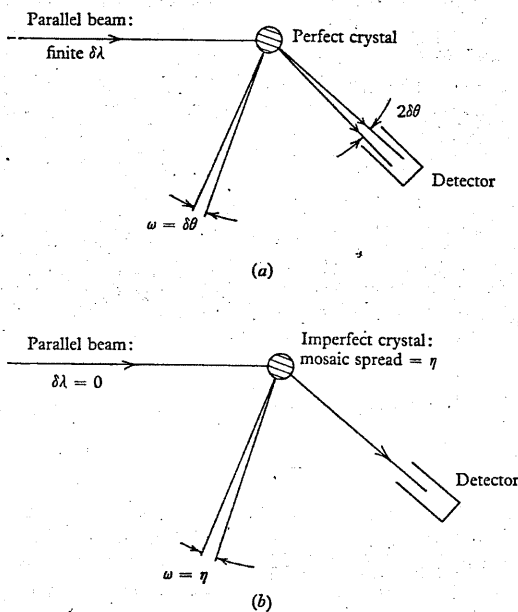


Fig. 116. Diagrams illustrating use of: (a) $\omega/2\theta$ -scan (2θ -scan) for perfect crystal illuminated by radiation with spectral range $\delta\theta = \tan\theta\delta\lambda/\lambda$; (b) ω -scan for crystal with large mosaic spread η .

Alexander & Smith (1962, 1964) and Burbank (1964) have derived theoretical expressions for the minimum aperture dimensions in terms of the mosaic spread of the crystal and the divergence and spectral dispersion of the incident beam. Burbank's results are summarized in Table XXIV using the notation adopted in Chapter 6. The table includes the minimum value of the rocking range of the crystal which was discussed on p. 174.

TABLE XXIV. Comparison of ω and $\omega/2\theta$ scans

	ω -Scan	$\omega/2\theta$ -Scan
Minimum horizontal detector aperture	$2\delta\theta + \delta_F^H + 2\delta_O^H \cos^2\theta$	$\delta_F^H + 2\delta_O^H \sin^2\theta + \eta$
Minimum vertical detector aperture	$\delta_F^V + \delta_O^V + \eta$	$\delta_F^V + \delta_O^V + \eta$
Minimum rocking range	$\delta_F^H + \delta_O^H + \eta + \delta\theta$	$\delta_F^H + \delta_O^H + \eta + \delta\theta$
Preferred scan using	—	Always preferred
(a) X-rays with balanced filters	At small Bragg angles when η is large	Always at large θ ; at small θ when η is small
(b) X-rays or neutrons with monochromator, X-rays with simple filtration	At small Bragg angles when η is large	Always at large θ ; at small θ when η is small

The quantities $\delta\theta$, δ_F , δ_O and η are defined on p. 174. The superscripts H and V refer to the horizontal and vertical planes, respectively.

10.6. Strategy for exploring reciprocal space

With an equi-inclination instrument it is convenient to measure the reflexions layer-by-layer in reciprocal space. It is then necessary to alter only one angular setting (ϕ) for the crystal and one (Υ) for the detector in moving from one reflexion to the next within the same layer. This procedure also involves minimum alteration of the size of the detector aperture, which must be changed in moving to the upper layers.

With a four-circle diffractometer the strategy adopted in exploring reciprocal space will depend on the setting speeds of the diffractometer shafts. When the time taken for shaft setting is an appreciable fraction of the total measuring time, the reflexions must be measured in a sequence which minimizes the angular increments between one reflexion and the next; in practice, a zigzag scan along neighbouring reciprocal lattice lines does this quite effectively. When the setting speed is high enough for the setting time to become small compared with the measuring time (as is nearly always the case in neutron diffraction), it becomes better to measure the reflexions in the order of increasing Bragg angle. This has the advantage that the angular range of scan for each reflexion and the correct size of the detector aperture, both of which are dependent on θ only, can be kept fixed for all reflexions within a limited range of θ . Furthermore, the maximum observed Bragg angle θ_{max} . (or, more accurately, the quantity $\sin\theta_{max}/\lambda$) deter-

mines the limit of resolution of the atoms in the Fourier map of the unit cell; by recording the reflexions in increasing θ the investigation can be terminated when the desired resolution is reached.

It is advisable to return at regular intervals during the intensity measurements to one or more standard reflexions. These standards are extremely useful in checking the correct functioning of the apparatus (for example, the stability of the detector and of the counting circuits) and in ensuring that the crystal retains its correct alignment during the experiment and that it does not deteriorate in the incident beam. The extra time spent in measuring the standard reflexions is a small price to pay for the satisfaction of knowing that the measurement of the remaining reflexions is proceeding satisfactorily.

10.7. Counting statistics and period of counting

The emission of photons by an X-ray tube, or of neutrons by a nuclear reactor, is a random process and gives rise to a statistical uncertainty in the measurement of the diffracted intensities. In theory, this statistical uncertainty can be reduced to any required level by prolonging the counting process for a sufficient period of time. In practice, however, the total time available for measuring a set of integrated intensities is limited, and it is important to know how best to divide the time so as to obtain the greatest overall precision in the measurements.

We note here the distinction that is drawn between the terms *uncertainty* and *error*. The term *uncertainty* is used to indicate the statistical fluctuation between different measurements of the same quantity made under identical experimental conditions, and is independent of any systematic error present. *Error* refers to the difference between the measured value and the 'real' value of the physical quantity, and includes the effects of both statistical uncertainty and systematic error. The same distinction is made between the terms *precision* and *accuracy*: *precision* indicates the closeness with which measurements agree with one another, whereas *accuracy* denotes the closeness of the measurements to the real value.

Let us assume that the number of counts N , measured in equal

times t , fluctuates according to a Gaussian distribution about the mean \bar{N} . The standard deviation of the distribution is

$$\sigma(N) = \bar{N}^{\frac{1}{2}},$$

so that each individual determination of N has a relative statistical uncertainty given by $\epsilon = Q\sigma/\bar{N} = Q\bar{N}^{-\frac{1}{2}}$, (10.2)

where Q is a constant determined by the 'confidence level'. For the 50 per cent confidence level, representing a 50 per cent probability that $N - \bar{N}$ is less than ϵ , Q is 0.67. Q is 1.64 for the 90 per cent level and 2.58 for the 99 per cent level. Fig. 117 shows the percentage uncertainty as a function of N for the 50, 90 and 99 per cent confidence levels. For a percentage uncertainty of 1 per cent the total number of counts to be accumulated is 4,500 for the 50 per cent level, 27,000 for the 90 per cent level, and 67,000 for the 99 per cent level. Thus, to raise the confidence level from 50 to 99 per cent the total number of accumulated counts must be multiplied fifteen times.

Effect of background and optimization of counting period

The magnitude of the integrated intensity is determined as the difference between two counts, N_1 and N_2 , where N_1 is the count for the Bragg peak and N_2 is the background count. Assuming equal times on peak and background the integrated intensity is ρ , where

$$\rho \propto N_1 - N_2.$$

The standard deviation of the difference is given by

$$\sigma = (\sigma_1^2 + \sigma_2^2)^{\frac{1}{2}}, \quad (10.3)$$

where σ_1 and σ_2 are the standard deviations of the two individual counts. Thus, if in a certain experiment the overall background count is 100 and that due to the peak-plus-background is 200, the standard deviation of the difference is

$$\sigma = (200 + 100)^{\frac{1}{2}} = 17.$$

For a zero background, the peak-plus-background would be recorded as 100, and the standard deviation would be only 10. The percentage standard deviation, $100\sigma/(N_1 - N_2)$, is given in Table XXV for different values of N_1 and N_2 .

TABLE XXV. Percentage standard deviation of $(N_1 - N_2)$ as a function of N_1 and N_2

N_2	Values of N_1																			
	1,000	2,000	3,000	4,000	5,000	6,000	7,000	8,000	9,000	10,000	12,000	15,000	20,000							
100	3.7	2.4	1.9	1.6	1.5	1.3	1.2	1.1	1.1	1.0	0.9	0.8	0.7							
200	4.3	2.6	2.0	1.7	1.5	1.4	1.2	1.1	1.1	1.0	0.9	0.8	0.7							
300	5.1	2.8	2.1	1.8	1.5	1.4	1.3	1.1	1.1	1.0	0.9	0.8	0.7							
400	6.2	3.1	2.2	1.8	1.6	1.4	1.3	1.2	1.1	1.0	0.9	0.9	0.7							
500	7.7	3.3	2.4	1.9	1.7	1.5	1.3	1.2	1.2	1.1	1.0	0.9	0.7							
600	10.0	3.7	2.5	2.0	1.7	1.5	1.3	1.3	1.2	1.1	1.0	0.9	0.7							
700	13.7	4.0	2.6	2.1	1.8	1.5	1.4	1.3	1.2	1.1	1.0	0.9	0.7							
800	21.2	4.4	2.8	2.2	1.8	1.6	1.4	1.3	1.2	1.1	1.0	0.9	0.8							
900	43.5	4.9	3.0	2.3	1.9	1.6	1.5	1.3	1.2	1.2	1.0	0.9	0.8							
1,000	—	5.5	3.2	2.1	2.0	1.7	1.5	1.4	1.3	1.2	1.0	0.9	0.8							
1,100	—	6.2	3.3	2.5	2.0	1.7	1.5	1.4	1.3	1.2	1.1	0.9	0.8							
1,200	—	7.1	3.6	2.6	2.1	1.8	1.6	1.4	1.3	1.2	1.1	0.9	0.8							
1,300	—	8.2	3.9	2.7	2.1	1.8	1.6	1.4	1.3	1.2	1.1	0.9	0.8							
1,400	—	9.7	4.1	2.8	2.2	1.9	1.6	1.5	1.3	1.2	1.1	0.9	0.8							
1,500	—	11.8	4.5	3.0	2.3	1.9	1.7	1.5	1.4	1.3	1.1	1.0	0.8							
1,600	—	15.0	4.9	3.1	2.4	2.0	1.7	1.5	1.4	1.3	1.1	1.0	0.8							
1,700	—	20.3	5.2	3.3	2.5	2.0	1.8	1.6	1.4	1.3	1.1	1.0	0.8							
1,800	—	30.8	5.8	3.5	2.6	2.1	1.8	1.6	1.4	1.3	1.2	1.0	0.8							
1,900	—	62.5	6.4	3.7	2.7	2.2	1.9	1.6	1.5	1.4	1.2	1.0	0.8							
2,000	—	—	7.1	3.9	2.8	2.2	1.9	1.7	1.5	1.4	1.2	1.0	0.8							
3,000	—	—	—	8.4	4.5	3.1	2.5	2.1	1.8	1.6	1.4	1.1	0.9							
4,000	—	—	—	—	9.5	5.0	3.5	2.7	2.3	2.0	1.6	1.3	1.0							
5,000	—	—	—	—	—	10.5	5.5	3.8	3.0	2.5	1.9	1.5	1.1							

We must now consider the problem: given counting rates n_1, n_2 which are determined by counting for periods T_1, T_2 respectively on a reflexion, how should the total time $T = T_1 + T_2$ be divided so that the

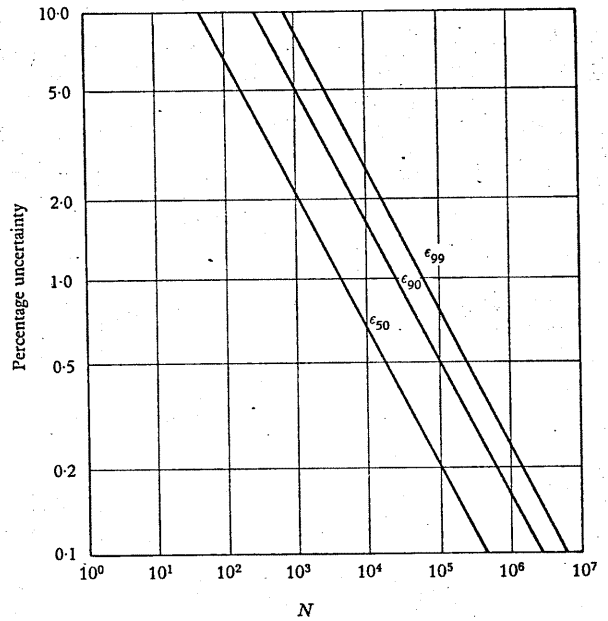


Fig. 117. Percentage statistical uncertainty as a function of the total number of counts N . The straight lines refer to the 50, 90, 99 per cent confidence levels.

percentage statistical uncertainty in $\rho (=n_1 - n_2)$ is a minimum? The following treatment of this problem is similar to that of Mack & Spielberg (1958).

Let ϵ_1 and ϵ_2 be the relative statistical uncertainties in n_1 and n_2 . The absolute magnitudes of these uncertainties are $n_1\epsilon_1$ and $n_2\epsilon_2$ and the uncertainty of the difference $n_1 - n_2$ is

$$[(n_1\epsilon_1)^2 + (n_2\epsilon_2)^2]^{\frac{1}{2}}$$

The relative uncertainty of ρ , therefore, is

$$\epsilon = \frac{[(n_1\epsilon_1)^2 + (n_2\epsilon_2)^2]^{\frac{1}{2}}}{n_1 - n_2} \quad (10.4)$$

The total number of counts accumulated in measuring the peak-plus-background is n_1T_1 and the number for the background alone is n_2T_2 . Thus, from equation (10.2),

$$\epsilon_1 = Q(n_1T_1)^{-\frac{1}{2}},$$

and

$$\epsilon_2 = Q(n_2T_2)^{-\frac{1}{2}}.$$

Substituting in equation (10.4) gives

$$\epsilon = \frac{Q}{n_1 - n_2} \left(\frac{n_1}{T_1} + \frac{n_2}{T_2} \right)^{\frac{1}{2}} \quad (10.5)$$

n_1, n_2 are fixed counting rates and ϵ is a function of the two variables T_1, T_2 :

$$\epsilon = \epsilon(T_1, T_2). \quad (10.6)$$

Our problem is now reduced to finding the minimum value of ϵ , subject to the restraining condition

$$T = T_1 + T_2. \quad (10.7)$$

From (10.6), the minimum condition is

$$\frac{\partial \epsilon}{\partial T_1} dT_1 + \frac{\partial \epsilon}{\partial T_2} dT_2 = 0, \quad (10.8)$$

and from (10.7) the condition $T = \text{constant}$ gives

$$dT_1 + dT_2 = 0. \quad (10.9)$$

Combining (10.8) and (10.9):

$$\frac{\partial \epsilon}{\partial T_1} = \frac{\partial \epsilon}{\partial T_2}, \quad (10.10)$$

and substituting equation (10.5) for ϵ into (10.10) yields

$$\left(\frac{T_1}{T_2} \right)^2 = \frac{n_1}{n_2} = K, \quad (10.11)$$

where K is the ratio of the counting rates. Finally, (10.7) and (10.11) give

$$\left. \begin{aligned} T_1 &= \frac{K^{\frac{1}{2}}}{1+K^{\frac{1}{2}}} T, \\ T_2 &= \frac{1}{1+K^{\frac{1}{2}}} T. \end{aligned} \right\} \quad (10.12)$$

Equations (10.12) describe the optimum division of time T between T_1 and T_2 . For a weak reflexion, with the peak counting rate only slightly higher than the background rate, $K \approx 1$ and equal times should be spent on the peak and on the background. On the other hand, if the peak-to-background ratio is very high, only a small proportion of the time should be spent in measuring the background.

We ask next: given an optimum division of the total time T between the peak and the background, what is the minimum value of T to achieve a stipulated level of precision in the integrated intensity ρ ? The answer to this second question determines the optimum division of time between all the reflexions which are to be recorded in a particular investigation.

By manipulating equations (10.5) and (10.11) we arrive at

$$\left. \begin{aligned} N_1 = n_1T_1 &= \frac{Q^2}{\epsilon^2} K^{\frac{1}{2}} \frac{K^{\frac{1}{2}} + 1}{(K-1)^2}, \\ N_2 = n_2T_2 &= \frac{Q^2}{\epsilon^2} \frac{K^{\frac{1}{2}} + 1}{(K-1)^2}. \end{aligned} \right\} \quad (10.13)$$

and

These equations give the total number of counts accumulated on the peak, N_1 , and on the background, N_2 , as a function of the relative uncertainty ϵ in measuring $n_1 - n_2$. Note that N_1 and N_2 are each independent of the total time T spent in measuring the reflexion: to attain a specific precision, corresponding to a fixed value of Q/ϵ , a predetermined number of counts must be accumulated, irrespective of the counting time.

Table XXVI gives values of N_1, N_2, T_1, T_2 , for a fixed background counting rate n_2 of 10 counts/s and for different values of the peak-to-background ratio n_1/n_2 . These quantities are calculated from equations (10.13) for a probable uncertainty of 1 per cent in the integrated intensity. (The probable uncertainty corresponds to a confidence level of 50 per cent, or $Q = 0.67$.)

TABLE XXVI. Total time for measuring $n_1 - n_2$ to a probable relative uncertainty of 1 per cent ($n_2 = 10$ counts/s)

n_1 (counts/s)	$\frac{n_1}{n_2} = K$	N_1 (counts)	N_2 (counts)	T_1 (s)	T_2 (s)	$T = T_1 + T_2$
12	1.2	310,000	240,000	26,000	24,000	14 h.
15	1.5	73,000	40,000	4,900	4,000	2½ h.
20	2	31,000	11,000	1,600	1,100	45 min.
40	4	12,000	1,500	300	150	7½ min.
100	10	6,000	190	60	19	79 s.
1,000	100	5,000	5	5	0.5	5.5 s.

The table shows that the total time for measuring a weak reflexion with a peak-to-background ratio of 2:1 is 34 times longer than the corresponding time for a strong reflexion with a ratio of 10:1. Obviously, a very considerable economy of time results, provided all reflexions are to be measured to about the same relative precision, by reducing the time spent in measuring the strong reflexions. It is also worth emphasizing again the crucial importance of reducing the background level as much as possible. The background level, and not the absolute magnitude of the Bragg peak above this level, sets the main limit to the magnitude of the reflexion which can be observed.

Statistics of monitoring

When a monitoring system is employed to register the strength of the incident radiation, statistical fluctuations in the monitored beam affect the measured intensity of the diffracted beam. If N is the number of diffracted pulses from the specimen, and these are recorded in the time taken to count N_0 pulses in the monitoring counter, the standard deviation of the measured counting rate from the specimen is

$$N^{\frac{1}{2}}(1 + N/N_0).$$

Thus, provided N_0 is at least ten times greater than N , the effect of the monitoring statistics can be ignored.

Time optimization by on-line computer control

We have discussed the optimization of measuring time between the different reflexions of the crystal, and between the peak and background of an individual reflexion, using the criterion that the

minimum total time should be spent in measuring all the integrated intensities to a given relative precision.

A different division of time occurs if we measure the structure factors F to a constant absolute precision: thus if we were able to neglect the background we should have to spend equal times on each reflexion. This is shown by writing the integrated intensity ρ as

$$\rho = n = cF^2, \quad (10.14)$$

where n is the peak counting rate and c is a constant incorporating the Lorentz-polarization conversion factor (see Chapter 11). If T is the time of counting for one reflexion, the total number of counts accumulated is nT and the uncertainty in this number is $(nT)^{\frac{1}{2}}$. Thus the uncertainty in the counting rate is $(nT)^{\frac{1}{2}} \div T$, that is

$$\sigma(\rho) = \sqrt{\frac{n}{T}}.$$

From equation (10.14)

$$\sigma(\rho) = 2cF\sigma(F),$$

or

$$\begin{aligned} \sigma(F) &= \frac{\sigma(\rho)}{2cF} = \frac{1}{2c} \cdot \sqrt{\frac{n}{T}} \cdot \sqrt{\frac{c}{n}} \\ &= \frac{1}{2} \left(\frac{1}{cT} \right)^{\frac{1}{2}}. \end{aligned}$$

$\sigma(F)$, therefore, is independent of n : its magnitude is determined by the period of counting T and is the same for all values of F . This contrasts with the corresponding condition for $\sigma(\rho)/\rho$ to be constant, which is that counting continues until a fixed number of counts nT is accumulated.

To determine the optimum division of time between the different reflexions we require to know the values of F , the very quantities we aim to measure. One way around this difficulty is to make a rapid preliminary set of measurements to a low statistical accuracy to determine the counting strategy for a final run. A more sophisticated approach is possible when the diffractometer is connected on-line to a computer.

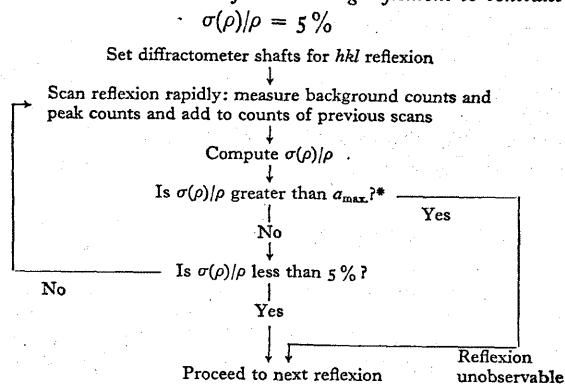
Let us suppose that the total time for measuring a reflexion is, on average, ten minutes and that the integrated intensity is to be measured to a relative uncertainty $\sigma(\rho)/\rho$ [$= \sigma(F)/F$] of 5 per cent. By scanning quickly across the reflexion in one minute and

registering N_1 counts on the peak and N_2 counts on the background, the quantity

$$\frac{\sigma(\rho)}{\rho} = \frac{(N_1 + N_2)^{\frac{1}{2}}}{(N_1 - N_2)}$$

can be computed at the end of the scan. The scan is then repeated, the total counts added to those found in the first scan, and $\sigma(\rho)/\rho$ recomputed. The repeated scanning continues until the value of $\sigma(\rho)/\rho$ falls to 5 per cent, and the control equipment then switches to the next reflexion. Table XXVII indicates the flow-sheet for measuring the reflexions in this way.

TABLE XXVII. Flow-sheet for measuring reflexions to constant



* The value of a_{\max} is, perhaps, 100%: its precise value is dependent on the maximum time spent on measuring the weakest reflexions.

CHAPTER II

DERIVATION AND ACCURACY OF STRUCTURE FACTORS

In the previous chapter we described the procedure for measuring the relative integrated intensities of a single crystal. If an infinitesimally small block of volume δV reflects the incident X-ray beam, it can be shown (see, for example, Buerger, 1960) that the absolute magnitude of the integrated intensity is proportional to δV :

$$\rho_{hkl} = Q \delta V,$$

where the constant of proportionality Q is

$$Q = \left(\frac{e^2}{mc^2}\right)^2 N_c^2 \lambda^3 L p |F_{hkl}|^2. \quad (11.1)$$

(X-rays)

In this expression N_c is the number of unit cells per unit volume, λ the wavelength, and F_{hkl} the structure factor: the Lorentz factor L and polarization factor p are angle factors, which depend on the experimental arrangement used in measuring the intensities, and whose forms are discussed in §§11.1 and 11.2. In general, the structure factor F_{hkl} , characterizing the wave scattered by the (hkl) plane, is a complex quantity: its magnitude $|F_{hkl}|$ only is related to the observed intensity. The determination of its phase, which can have any value between 0° and 360° relative to a wave scattered at the origin of the unit cell, constitutes the familiar 'phase problem'.

In neutron diffraction the nuclear scattering amplitude is analogous to the X-ray atomic scattering factor multiplied by e^2/mc^2 (Bacon, 1962). Consequently, equation (11.1) applies also to neutrons with $(e^2/mc^2)^2$ replaced by unity:

$$Q = N_c^2 \lambda^3 L p |F_{hkl}|^2. \quad (11.2)$$

(neutrons)

The experimental values of ρ_{hkl} are measured on a relative scale: to measure their absolute magnitudes the appropriate scale factor is determined in a separate experiment, as described in §11.3.

Thus we can express both (11.1) and (11.2) more conveniently in the form

$$\rho_{hkl} = cLp|F_{hkl}^{obs}|^2, \quad (11.3)$$

where c is a single scale factor for all the reflexions and the superscript 'obs.' indicates observed structure factors.

Later in this chapter we shall compare the observed and calculated structure factors for crystals of known simple structure, quoting results obtained with X-rays and with neutrons. This comparison gives some indication of the accuracy to be expected in measuring with a diffractometer the structure factors of any crystal. (It is worth emphasizing that in the examination of complex structures, such as protein crystals, speed of data collection is more important than extreme accuracy: many thousands of reflexions are measured, often while the crystal is deteriorating in the X-ray beam, and the final accuracy of the structure factors is determined primarily by counting statistics (see p. 268) and not by systematic errors.) First, however, we shall describe the evaluation of the three terms L , p , c , in equation (11.3), which allow the conversion of the integrated intensities to a set of observed structure factors.

11.1. Lorentz factor

The intensity of a reflexion is proportional to the time during which the corresponding reciprocal lattice point is close to the surface of the reflecting sphere: the Lorentz factor is a geometrical term which corrects for the different rates at which the reciprocal lattice points sweep through the sphere. If ω is the angular velocity of the crystal and v_n is the component of the velocity of the reciprocal lattice point along the radius of the sphere, the Lorentz factor is defined as the ratio of these velocities:

$$L = \omega/v_n. \quad (11.4)$$

The expression for L in terms of measurable crystal and instrumental angles depends on the particular diffraction geometry used.

Normal-beam equatorial geometry (see §2.4)

Both the incident and reflected beams are normal to the vertical axis of rotation through O (Fig. 118). The linear velocity of the reciprocal lattice point $P (= hkl)$ is $\omega\xi$ along a direction normal to

the radial co-ordinate ξ , and the velocity normal to the sphere of reflexion is

$$v_n = \omega\xi \cos\theta.$$

The radius of the circle of reflexion is unity, so that

$$\xi = 2 \sin\theta$$

and the inverse Lorentz factor is

$$L^{-1} = 2 \sin\theta \cos\theta = \sin 2\theta. \quad (11.5)$$

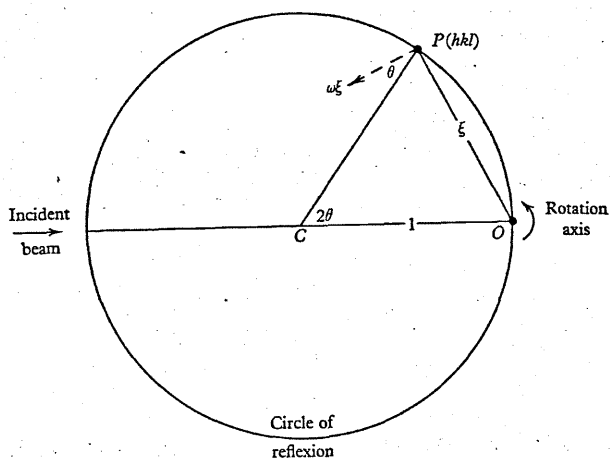


Fig. 118. Derivation of Lorentz factor for normal-beam equatorial geometry.

The variation of L with θ is shown in Fig. 119. At low Bragg angles, L is large because the reciprocal lattice point is close to the origin of the reciprocal lattice; and at high θ , L is large because the hkl point passes tangentially, or nearly so, through the surface of the reflecting sphere. The Lorentz factor reduces the intensities by the maximum amount at $\theta = 45^\circ$.

General inclination geometry (see §2.3)

The Lorentz factor assumes a very simple form for the equatorial method, but this is not so for inclination geometry, where the

incident beam is inclined at a variable angle $90^\circ - \mu$ to the axis of rotation and the reflected beam at a variable angle $90^\circ - \nu$.

To derive an expression for L we refer to Fig. 120a. If ω is the angular velocity of the crystal about the axis OO_1 , the reciprocal lattice point P in the l -level has a linear velocity $\omega\xi$ along the

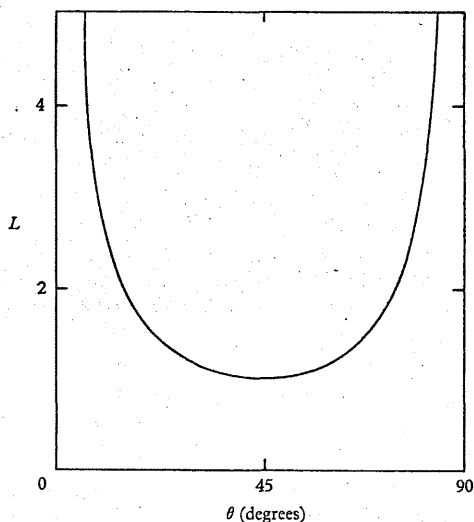


Fig. 119. Lorentz factor for normal-beam equatorial geometry, as a function of θ .

direction PU : PU is a vector in the l -level which is perpendicular to PO_1 . The component of this velocity normal to the sphere of reflexion is

$$v_n = \omega\xi \cos r,$$

where r is the angle between PU and the line PC joining the hkl point and the centre of the sphere of reflexion. The inverse Lorentz factor is, therefore,

$$L^{-1} = v_n/\omega = \xi \cos r. \tag{11.6}$$

We obtain an expression for $\cos r$ in equation (11.6) as follows. PU is normal to the radial co-ordinate ξ and lies in the l -level whose circle of reflexion has centre C_1 . Let us choose the position

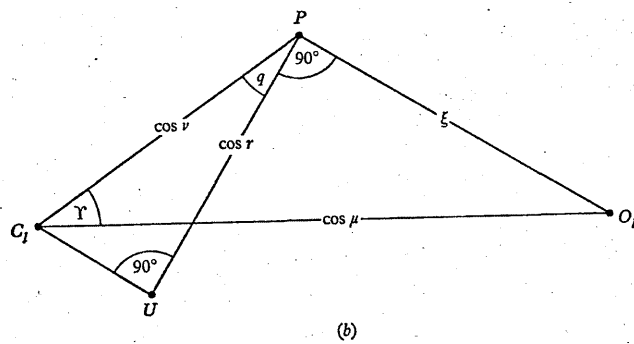
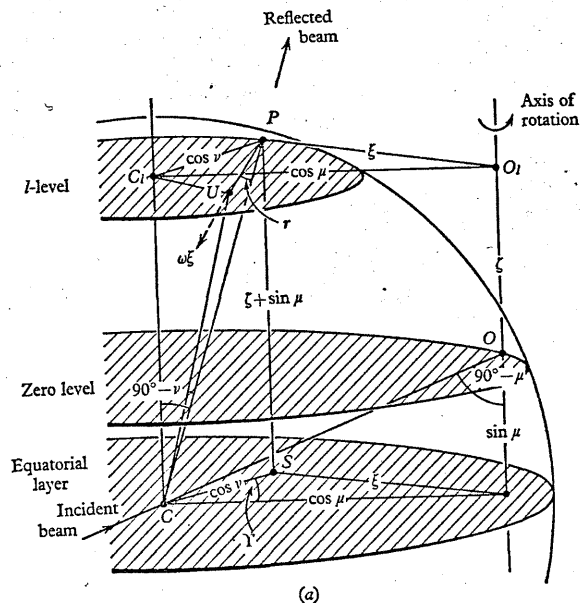


Fig. 120. Derivation of Lorentz factor for general inclination geometry: (a) portion of sphere of reflexion; (b) points in l -level.

of U so that it lies at the foot of the perpendicular from C_1 to PU ; then PU is horizontal and normal to the vertical plane C_1CU and to every line in that plane. In particular the angle between PU and UC is 90° and $\cos r = PU/PC = PU$. (11.7)

Now from Fig. 120b,

$$PU = PC_1 \cos q = \cos \nu \cos q, \quad (11.8)$$

where q , the angle between PC_1 and PU , is given by

$$\frac{\sin(q+90^\circ)}{\cos \mu} = \frac{\sin \Upsilon}{\xi},$$

or $\cos q = \frac{\cos \mu \sin \Upsilon}{\xi}$. (11.9)

Combining (11.7), (11.8), (11.9):

$$\cos r = \frac{\cos \mu \cos \nu \sin \Upsilon}{\xi},$$

and substituting into (11.6) we obtain finally

$$L^{-1} = \cos \mu \cos \nu \sin \Upsilon. \quad (11.10)$$

The angles μ , ν , Υ are the setting angles of the diffractometer. The expression (11.10) is readily evaluated for each reflexion as part of the computer program for reducing the intensity data to observed structure factors.

Equation (11.5) for the Lorentz factor in the equatorial method can be considered as a special case of the general formula (11.10), with $\mu = \nu = 90^\circ$ and $\Upsilon = 2\theta$. The general formula also reduces to simpler forms for the special settings of inclination geometry.

(a) *Normal-beam setting* ($\mu = 0$). The incident beam is normal to the rotation axis ($\mu = 0$) and (11.10) reduces to

$$L^{-1} = \cos \nu \sin \Upsilon. \quad (11.11)$$

From equation (2.20)

$$\left. \begin{aligned} \cos \Upsilon &= \frac{2 - \xi^2 - \zeta^2}{2(1 - \xi^2)^{\frac{1}{2}}}, \\ \sin \nu &= \zeta, \end{aligned} \right\} \quad (11.12)$$

and

where ξ , ζ are the cylindrical co-ordinates of the reciprocal lattice point hkl . Table I on p. 27 lists ξ , ζ in terms of h , k , l , and the lattice parameters of the crystal. L is computed for a crystal of any

symmetry using the equations (11.11), (11.12) in conjunction with Table I.

(b) *Equi-inclination setting* ($\mu = -\nu$). The incident and reflected beams are equally inclined to the rotation axis, with $\mu = -\nu$. Thus $\cos \mu = \cos \nu$ and the inverse Lorentz factor, equation (11.10), is

$$L^{-1} = \cos^2 \nu \sin \Upsilon. \quad (11.13)$$

From equation (2.21)

$$\left. \begin{aligned} \sin \nu &= \frac{1}{2} \zeta, \\ \sin \frac{1}{2} \Upsilon &= \frac{\xi}{2 \cos \mu}, \end{aligned} \right\} \quad (11.14)$$

and

and L is computed for the hkl reflexion of any crystal using (11.13), (11.14) and Table I.

The Lorentz factor is large for points close to the rotation axis, with $\xi \approx 0$. Such points are always near the sphere of reflexion: a relatively long time is taken in cutting through the sphere, and the rocking curves relating the diffracted intensity with the angular position of the crystal are correspondingly wide. Reflexions lying in a cylindrical region around the goniometer-head axis cannot be measured with any accuracy because of the large Lorentz factor; they are best examined in an alternative mounting of the crystal.

(c) *Anti-equi-inclination setting* ($\mu = \nu$). In this setting, which can only be used for the zero level ($\zeta = 0$), the incident and reflected beams are equally inclined to the rotation axis, with $\mu = \nu$. Thus $\cos \mu = \cos \nu$, and L^{-1} is given by the same equation, (11.13), as for the equi-inclination setting. In this equation (11.13) ν can have any value, provided it is equal to μ , and Υ is given by equation (2.22):

$$\sin \frac{1}{2} \Upsilon = \frac{\xi}{2 \cos \nu}.$$

(d) *Flat-cone setting* ($\nu = 0$). The reflected beam emerges at 90° to the rotation axis, $\nu = 0$, and (11.10) reduces to

$$L^{-1} = \cos \mu \sin \Upsilon. \quad (11.15)$$

The angles μ , Υ in this expression are related to the cylindrical co-ordinates ξ , ζ by equations (2.23) and (2.24):

$$\left. \begin{aligned} \sin \mu &= -\zeta, \\ \cos \Upsilon &= \frac{2 - \xi^2 - \zeta^2}{2(1 - \xi^2)^{\frac{1}{2}}}. \end{aligned} \right\} \quad (11.16)$$

11.2. Polarization factor

In X-ray diffraction, a polarization factor arises because of the dependence of the scattered amplitude on the orientation of the electric vector E of the X-ray beam. From the Thomson theory of X-ray scattering, the amplitude scattered by a single electron is proportional to $\sin\phi_0$, where ϕ_0 is the angle between E and the direction of the reflected beam. Accordingly, a factor p is introduced in the basic equation (11.3) to account for the $\sin\phi_0$ effect of polarization.

The magnitude of p depends on the degree of polarization of the X-ray beam. Characteristic radiation direct from the target is unpolarized, whereas radiation is partially polarized by reflexion at a crystal monochromator. We shall discuss, therefore, the evaluation of p separately for direct and for monochromatized incident radiation.

In neutron diffraction, there is no polarization effect associated with the nuclear reflexions, and so $p = 1$.

Incident unpolarized radiation

We resolve the incident beam into two equal components with their electric vectors parallel and perpendicular to the plane containing the incident and reflected beams (see Fig. 121). The amplitude of each reflected component is proportional to $\sin\phi_0$, where ϕ_0 is $90^\circ - 2\theta$ for the parallel component and 90° for the perpendicular component. Thus the amplitudes are in the ratio $\cos 2\theta:1$ and the intensities in the ratio $\cos^2 2\theta:1$. The mean intensity for the two states of polarization is defined as the polarization factor p :

$$p = \frac{1}{2}(1 + \cos^2 2\theta). \quad (11.17)$$

For $\theta = 0$ or 90° , p is unity and the intensities of the parallel and perpendicular components are equal, that is, the reflected beam is unpolarized. For $\theta = 45^\circ$, $p = \frac{1}{2}$ and the intensity of the parallel component is zero, so that the reflected beam is completely polarized. (Chandrasekhar (1960b) used this property to produce a polarized X-ray beam in his method of correcting intensities for the effect of extinction (p. 192.) At all other values of θ the reflected X-ray beam is partially polarized (Fig. 122).

The basic equation (11.3) applies to an ideally mosaic crystal with diffracted intensities proportional to F^2 . For a perfect crystal, the integrated intensities are proportional to $|F|$, not F^2 , and the polarization factor in (11.17) is modified to

$$p = \frac{1}{2}(1 + |\cos 2\theta|). \quad (11.18)$$

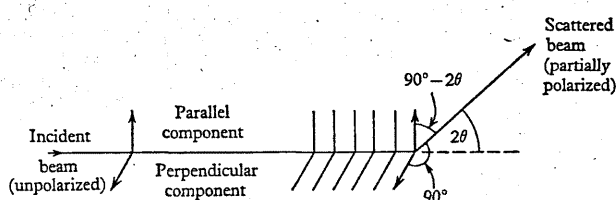


Fig. 121. Derivation of polarization factor for unpolarized incident beam.

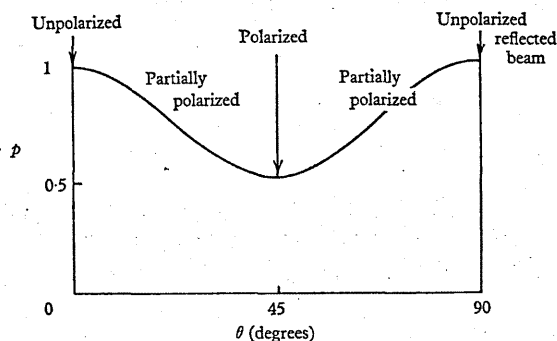


Fig. 122. Polarization factor for unpolarized incident beam, as a function of θ .

We usually assume that the specimen crystal behaves like a mosaic crystal, and express any departure from this behaviour by the term 'extinction'. Those reflexions which require an extinction correction have a polarization factor which is intermediate between (11.17) and (11.18) and is dependent on the strength of the reflexion and on the degree of perfection of the crystal. This emphasizes yet another difficulty in dealing with the problem of extinction. To derive accurate structure factors, the extinction must

be small, as this not only allows an adequate estimate to be made of the extinction correction but also ensures that there is no uncertainty in the polarization factor given by equation (11.17).

Incident monochromatized radiation: equatorial geometry

If θ_M is the Bragg angle of the monochromator, the beam striking the sample is partially polarized, with the intensities of the parallel and perpendicular components in the ratio $\cos^2 2\theta_M:1$. In the equatorial method, the plane of incidence for the sample coincides with the horizontal (equatorial) plane; if we assume that the same plane coincides with the plane of incidence for the monochromator, the polarization factor is given by

$$p = \frac{1 + \cos^2 2\theta_M \cos^2 2\theta}{1 + \cos^2 2\theta_M} \quad (11.19)$$

This formula is derived with the aid of Fig. 123: the intensity of the beam striking the sample is proportional to $\frac{1}{2}(1 + \cos^2 2\theta_M)$ and the intensity reflected by the sample is proportional to

$$\frac{1}{2}(1 + \cos^2 2\theta_M \cos^2 2\theta).$$

In equation (11.19) we assume that both the monochromator and the sample behave like ideally mosaic crystals. However, the monochromator is set to reflect radiation at a family of strongly reflecting planes, and it seems likely that it operates under conditions of strong extinction: if appreciable attenuation of the beam occurs within a single mosaic block, the monochromator approaches the behaviour of a perfect crystal. For such a crystal the polarization factor in (11.19) is replaced by

$$p = \frac{1 + |\cos 2\theta_M| \cos^2 2\theta}{1 + |\cos 2\theta_M|} \quad (11.20)$$

The uncertainty in the correct form of polarization factor is reduced by selecting θ_M close to 0 (or 90°), and so it is preferable to use a reflecting plane of low Bragg angle θ_M . Miyake, Togawa & Hosoya (1964) have shown that with $\text{CuK}\alpha$ radiation, reflected by the (200) plane of a lithium-fluoride monochromator for which

$$2\theta_M = 45^\circ,$$

the polarization factor given by equation (11.19) had a maximum error of 3.5 per cent when θ for the specimen was 45° . They concluded that the effect of extinction in the monochromator is important for accurate intensity measurements and requires a separate examination of the monochromator to determine the correct form of p , which is intermediate between (11.19) and (11.20).

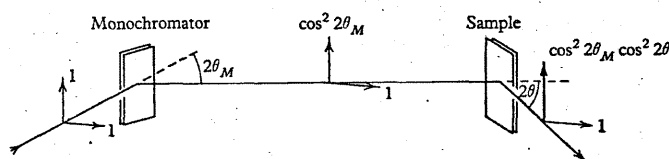


Fig. 123. Derivation of polarization factor for crystal-reflected incident beam. The primary, once-reflected and twice-reflected beams are co-planar.

Incident monochromatized radiation: inclination geometry

We shall quote without proof the expression for the polarization factor in the general inclination method using monochromatized radiation (Azaroff, 1955):

$$p = \frac{(\cos^2 2\theta_M \cos^2 \epsilon + \sin^2 \epsilon) \cos^2 2\theta + \cos^2 2\theta_M \sin^2 \epsilon + \cos^2 \epsilon}{1 + \cos^2 2\theta_M} \quad (11.21)$$

Here θ_M is the Bragg angle of the monochromator, θ that of the sample, and ϵ is the angle between the planes of incidence at the monochromator and at the sample. It is assumed that the monochromator (and sample) reflect as ideally mosaic crystals, although we have already noted the inherent danger in this assumption.

To apply equation (11.21) to a particular type of setting we must evaluate ϵ in terms of the setting angles. For the normal-beam setting, ϵ is given by (Levy & Ellison, 1960):

$$\left. \begin{aligned} \sin \epsilon &= \sin \nu \operatorname{cosec} 2\theta, & \sigma &= 90^\circ, \\ \cos \epsilon &= \sin \nu \operatorname{cosec} 2\theta, & \sigma &= 0, \end{aligned} \right\} \quad (11.22)$$

where σ is the angle between the plane of incidence at the monochromator and the plane generated by the Weissenberg rotation

axis and the primary monochromatized beam. For the equi-inclination setting, ϵ is given by:

$$\left. \begin{aligned} \sin \epsilon &= \tan \nu \cot \theta, & \sigma &= 90^\circ, \\ \cos \epsilon &= \tan \nu \cot \theta, & \sigma &= 0. \end{aligned} \right\} \quad (11.23)$$

The angle σ is constant for a particular experimental configuration of monochromator and diffractometer.

11.3. Observed structure factors: absolute measurements

Nowadays it is customary to base crystal-structure determinations on relative structure factors, although the importance of absolute intensities in structural work has been emphasized by Bragg & West (1928) and more recently by Lipson & Cochran (1957). If the scale factor c in (11.3) is known, it is easier to detect the presence of systematic errors in the intensity data: extinction, for example, reduces the observed intensities of the strongest reflexions below the values calculated for an ideally mosaic crystal, and the presence of extinction is revealed by comparing the experimental value of c with that determined by a least-squares comparison of the observed and calculated intensities. Accurate bond distances and angles require a proper correction for the effects of thermal motion (Cruickshank, 1956): errors in the thermal parameters are caused by scale factor errors, and it is preferable to measure c independently so as to avoid having to introduce it as an adjustable parameter in the analysis of the intensity data. In the study of defect structures the number of atoms in the 'average unit cell' is not integral, but can be determined from absolute intensity measurements. Absolute values are also important in the study of non-Bragg scattering, such as thermal diffuse scattering or defect diffuse scattering, and in the application of direct methods to the solution of the phase problem. Finally, from a knowledge of the absolute magnitudes of the structure factors, we can calculate the ratio of the observed strength of the reflexions to the hypothetical strength with all atoms scattering in-phase: this information may be of considerable significance in the subsequent determination of the structure.

An approximate value of c can be derived from a complete set of relative intensities ρ_{hkl} without further recourse to experiment: the

ρ_{hkl} 's contain their own inherent absolute standard. Wilson's method (Wilson, 1942) is based on the statistical result that the mean value of $|F_{hkl}|^2$ is equal to the sum of the squares of the scattering factors f_j for all the N atoms in the unit cell:

$$\langle |F_{hkl}|^2 \rangle = \sum_{j=1}^N f_j^2. \quad (11.24)$$

This equation follows directly from the expression for F_{hkl} in terms of the atomic positions (x_j, y_j, z_j) in the cell

$$F_{hkl} = \sum_j f_j e^{2\pi i(hx_j + ky_j + lz_j)}, \quad (11.25)$$

assuming that there is a large number of atoms in the unit cell, with none occupying positions of special symmetry. The value of f_j in (11.24) must be corrected for the effect of thermal motion by introducing an approximate correction of the form $e^{-B \sin^2 \theta / \lambda^2}$, where B is the 'overall temperature factor'. This exponential term is constant for reflexions in a sufficiently narrow range of $\sin \theta / \lambda$ and is unity for $\sin \theta / \lambda = 0$. Thus the mean relative values of $|F_{hkl}^{\text{obs}}|^2$ can be evaluated over small ranges of $\sin \theta / \lambda$, and the constants c' within each range found from the equation

$$c' \langle |F_{hkl}^{\text{obs}}|^2 \rangle = \sum_j (f_j)^2,$$

where f_j is the theoretical scattering factor, uncorrected for thermal motion. If $\ln c'$ is plotted against the mean value of $\sin^2 \theta / \lambda^2$ in each range, an approximately linear relationship is obtained and the intercept at $\sin \theta / \lambda = 0$ gives the required value of $\ln c$.

The statistical result (11.24) will not apply strictly if there are atoms in special symmetry positions or if the number of reflexions in a given range of $\sin \theta / \lambda$ is small, and an error of 30 per cent in c is typical of Wilson's method. Better values, correct to 10 per cent, are given by Kartha's method (Kartha, 1953), which uses an exact relationship between the sum of the squares of the observed structure factors and an integral involving the atomic scattering factors. Macintyre (1963) describes the application of this relationship in the routine reduction of the intensity data to absolute structure factors.

Experimental determination of scale factor

The scale factor can be more precisely determined by experimental methods. The simplest procedure involves comparing the intensities of the Bragg reflexions from the sample with those from a standard crystal, examined under identical conditions. On p. 239 we noted the importance of knowing exactly the quantity μR in calculating the *absolute* magnitude of the absorption factor of a spherical crystal, where R is the radius of the crystal and μ its coefficient of linear absorption. The absorption in both the sample and standard crystals should be very small, and so the method is less satisfactory for X-rays than for neutrons.

Other experimental methods used in X-ray work are based on the measurement of the intensity of the main beam striking the sample. From equations (9.1) and (11.1)

$$\frac{E\omega}{I_0} = N_c^2 \lambda^3 |F_{hkl}|^2 \left(\frac{e^2}{mc^2}\right)^2 L\rho \delta V, \quad (11.26)$$

where E is the reflected energy in the hkl reflexion, ω is the angular velocity of the crystal, I_0 is the intensity (energy per unit area per unit time) of the main beam, N_c is the number of unit cells per unit volume, and δV is the volume of the crystal. In making relative intensity measurements we equate the reflected energy, corrected for absorption, to $L\rho |F_{hkl}|^2$, so that the scale factor is

$$c = \frac{E}{L\rho |F_{hkl}|^2} = \frac{N_c^2 \lambda^3 \left(\frac{e^2}{mc^2}\right)^2 \delta V I_0}{\omega}. \quad (11.27)$$

c can be readily found from the quantities on the right-hand side of (11.27), provided I_0 is known.

The main X-ray beam is too strong to be measured directly with a proportional counter: it must be attenuated first so that the dead-time of the counter is appreciably less than the mean time interval between the arrival of the X-ray quanta. To evaluate the intensity I_0 , the attenuation factor must be accurately known. Multiple foils can be used for attenuation, but difficulties are caused by the progressive hardening of the beam, due to the preferential absorption of the softer components in the passage through successive

foils. The multiple-foil technique is, therefore, most suitable for measurements with monochromatized radiation or with balanced filters: according to Burbank (1965), it is then capable of establishing the intensity scale factor to within 3 per cent of its true value. Wagner, Witte & Wölfel (1955) compared the flux in the direct and diffracted beams with an ionization chamber. They attenuated the direct beam by means of a rotating sector: this method avoids changes in the spectral composition of the beam caused by filtering, but it can only be used with a current ionization chamber which has no counting losses. Another method of determining I_0 (Buyers, 1964) consists of measuring the intensity scattered by a small block of paraffin placed in the main beam, and using theoretical values for the absolute magnitude of this scattering. In an amorphous solid such as paraffin the scattering from each atom bears a random phase relation to that from the other atoms; thus the total scattering is contributed by independent unmodified scattering and by modified (Compton) scattering, and both of these can be calculated from the unmodified and modified scattering intensities of the separate atoms.

11.4. Calculated structure factors

In § 11.5 we shall examine the experimental measurements of the structure factors of a number of crystals and discuss these measurements in relation to the magnitude of the R -index, defined by

$$R = \frac{\sum_{hkl} \left| |F_{hkl}^{\text{obs}}| - |F_{hkl}^{\text{calc}}| \right|}{\sum_{hkl} |F_{hkl}^{\text{obs}}|}. \quad (11.28)$$

If the structure is known, that is, the positions of the atoms in the unit cell are known, this index gives some indication of the errors in the observed structure factors, *provided* the F_{hkl}^{calc} terms are known precisely: R is zero, only if there are no uncertainties in the observed *and* calculated structure factors. Thus, first we must discuss the limitations in evaluating the calculated structure factors.

The calculated structure factors are given by

$$F_{hkl}^{\text{calc}} = \sum_{j=1}^N f_j e^{2\pi i(hx_j + ky_j + lz_j)}. \quad (11.29)$$

The same formula applies in neutron diffraction with the X-ray atomic scattering factor f_j replaced by the nuclear scattering amplitude b_j . x_j, y_j, z_j are the co-ordinates of the j th atom in the unit cell, expressed as fractions of the cell edges, and the summation extends over all N atoms in the cell. f_j must be computed for the atom undergoing thermal motion: the effect of this motion is allowed for by writing f_j as the product of two quantities

$$f_j = f_{0,j} \times T_j \quad (11.30)$$

where $f_{0,j}$ is the value of f_j for the atom at rest and T_j is a temperature correction factor dependent on the particular atom j . The evaluation of these two quantities may lead to uncertainties in determining F^{calc} , even though the x_j, y_j, z_j 's are exactly known.

Atomic scattering factor for stationary atom

The X-ray scattering factor $f_{0,j}$ (or f_0) is defined as the ratio of the amplitude of the radiation scattered by the atom at rest to the amplitude scattered under the same conditions by an electron. The electrons in the atom occupy a volume whose linear dimensions are comparable with the wavelength of X-radiation, so that the phase differences between X-rays scattered by different parts of the atom must be taken into account in evaluating f_0 . At low angles of diffraction these phase differences are small and the value of f_0 is simply the total number of electrons in the atom or ion. As the scattering angle 2θ increases, the scattering amplitude is reduced by interference: a typical theoretical curve showing this form-factor dependence on $\sin \theta/\lambda$ is shown in Fig. 124.

The calculation of the X-ray scattering factors of different atoms and ions is described by James (1962) and in volume III of *The International Tables*. The results are presented in the form of tables giving f_0 at fixed intervals of $\sin \theta/\lambda$, and the scattering factor at any value of $\sin \theta/\lambda$ is readily found by interpolation. These calculated scattering factors are reliable only in so far as the total wave function used in the calculations is a reliable representation of the electron density: the exact form of wave function is not known for any atom, with the exception of hydrogen. Furthermore, the calculations usually assume that the electron density of the atom is spherically symmetrical, whereas many atoms are aspherical and

the scattering factor is a function not only of $\sin \theta/\lambda$ but also of the orientation of the atom with respect to the direction of the reflected beam.

The validity of scattering factors based on a spherically averaged electron density (the 'spherical approximation') has been examined by Dawson (1964*a, b*). Dawson considers the example of bonding

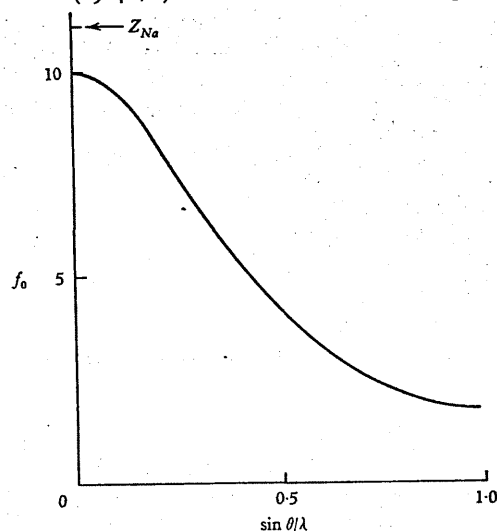


Fig. 124. Atomic scattering factor for Na^+ at rest, plotted against $\sin \theta/\lambda$. The charge distribution is spherical and there is no acentric component of f_0 (cf. Fig. 125).

electrons which impose an aspherical charge distribution on the scattering atom; he finds that for non-centro-symmetric valency states the scattering factor is complex and of the form

$$f_0 = f_c + if_a$$

where f_c corresponds to the centric component of the overall charge distribution and f_a to the antisymmetric component. f_a is zero at $\theta = 0$, and the general form of f_c and f_a as a function of $\sin \theta/\lambda$ is illustrated in Fig. 125. The antisymmetric component f_a , which is 90° out-of-phase with f_c , is ignored in the spherical approximation.

Dawson has calculated that for a simple hypothetical structure, consisting of two sp^3 nitrogen atoms which are centrosymmetrically disposed in a unit cell, the contribution to the R -index arising from the neglect of the intrinsic shape of the nitrogen atoms is as high as 8 per cent. This R -index would be obtained by comparing a perfect set of observed structure factors with a set of structure factors calculated on the basis of the spherical approximation. Careful experimental work on a number of simple structures is

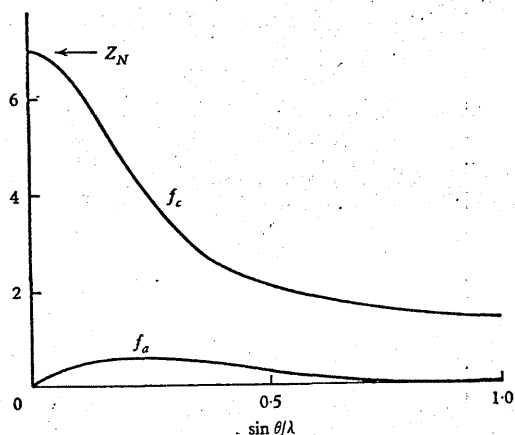


Fig. 125. Centric f_c and acentric f_a components of atomic scattering curve of nitrogen in sp^3 valence state (after Dawson, 1964b).

required before Dawson's work can be fully evaluated, but it is clear that the spherical approximation can be a serious limitation to the calculation of accurate X-ray scattering factors of stationary atoms.

In neutron diffraction, the scattering centre is the nucleus of the atom. The radius of the nucleus is approximately 10^{-12} cm, so that it behaves as a point scatterer for wavelengths of the order of 1 \AA . For this reason, there is neither a $\sin \theta/\lambda$ dependence nor an orientation dependence of the atomic scattering amplitude. The scattering amplitude b for the atom at rest of all but a few elements is independent of the wavelength λ : it has the dimensions of length

and is usually expressed in units of 10^{-12} cm. In the absence of an adequate theory of the nucleus, b is measured experimentally: it is tabulated for different elements and isotopes by Bacon (1962) and in many cases is known to an accuracy of better than 1 per cent.

Thermal motion

To take into account the effect of thermal motion, the correction factor T_j in equation (11.30) must be determined for each atom j . For isotropic thermal motion, T_j can be written as

$$T_j = e^{-B_j \sin^2 \theta / \lambda^2}, \quad (11.31)$$

where B_j is the 'isotropic temperature factor'. B_j is a constant for each atom at a given temperature; it is related to the mean-square displacement $\overline{u^2}$ of the atom in any direction from its mean position by the equation

$$B = 8\pi^2 \overline{u^2}. \quad (11.32)$$

B is usually treated as an empirical constant to be derived from a least-squares comparison of the observed and calculated intensities.

In the more general case of anisotropic vibration of the atom j , equation (11.31) for T_j is replaced by (Cruickshank, 1956):

$$T_j = \exp[-(b_{11}h^2 + b_{12}hk + b_{13}hl + b_{22}k^2 + b_{23}kl + b_{33}l^2)]. \quad (11.33)$$

The anisotropic thermal motion is represented by an ellipsoid of vibration in reciprocal space: six temperature factors b_{11}, b_{12}, \dots for each atom define the principal axes and direction cosines of the ellipsoid. (This number may be reduced by symmetry for atoms at special positions.) As in the isotropic case, the temperature factors are treated as adjustable constants in the least-squares refinement of the experimental data.

It is important to realize that both (11.31) and (11.33) are valid only within the limitations of the 'harmonic approximation'. Thermal motion causes the atoms in a crystal to execute small oscillations about their mean positions: the harmonic approximation means that, in expanding the potential energy of the crystal in powers of the amplitudes of these oscillations, all terms beyond those which are quadratic in the amplitudes are neglected. Harmonic interatomic forces imply that the crystal has no thermal expansion and has other properties not possessed by real crystals.

The harmonic approximation also requires that the so-called 'smearing functions' around atom centres are ellipsoids (transforming into ellipsoids in reciprocal space), which degenerate into spheres for atoms at sites of cubic point symmetry: anharmonicities cause the smearing functions to be more complicated, although they must still conform with the local site symmetry. Experimental diffraction measurements which demonstrate the breakdown of the harmonic approximation have been described by Willis (1965).

We can summarize this section by stating that the evaluation of $F^{\text{calc.}}$ in equation (11.29) cannot be made exactly. An estimate of the correction due to thermal motion, using up to six adjustable parameters to describe the vibration ellipsoid of each atom, ignores the effect of anharmonicities. There are serious limitations to current methods of calculating the X-ray scattering factor of a stationary atom, although there is no corresponding difficulty in describing the nuclear scattering amplitude in neutron diffraction.

11.5. Comparison of observed and calculated structure factors

The need for improving the accuracy of structure determinations has been stressed by Cruickshank (1960): if bond lengths are measured to within a limit of error of 0.01 Å, the final R -index must approach a value of about 1 per cent. We have noted that a low R -index requires not only accurate intensity measurements, corrected for absorption, extinction and other systematic errors, but also accurate theoretical scattering factors, corrected for anomalous dispersion, orientation effects and thermal motion. We shall describe now some results obtained with X-ray and neutron diffractometers on a few crystals of known structure.

Rock-salt (X-rays)

Some X-ray measurements by Abrahams (1964) are listed in Table XXVIII. These were carried out on a small sphere of sodium chloride, using an equi-inclination diffractometer with beta-filtered $\text{CuK}\alpha$ radiation. All equivalent reflexions accessible to the diffractometer were measured: the number of equivalent reflexions of the general type $\{hkl\}$ is 48, and this large redundancy allows the use of statistical methods in estimating the mean value of the hkl

structure factor $F^{\text{obs.}}$ and the variance s^2 of the mean. The last column in Table XXVIII represents the standard deviation σ derived from counting statistics alone (see p. 269). Finally, the $F^{\text{calc.}}$ values were derived from the equations:

$$\left. \begin{aligned} F^{\text{calc.}} &= 4f_{\text{Na}} \exp(-B_{\text{Na}} \sin^2 \theta / \lambda^2) + 4f_{\text{Cl}} \exp(-B_{\text{Cl}} \sin^2 \theta / \lambda^2) \\ &\quad \dots h, k, l \text{ even,} \\ F^{\text{calc.}} &= 4f_{\text{Na}} \exp(-B_{\text{Na}} \sin^2 \theta / \lambda^2) - 4f_{\text{Cl}} \exp(-B_{\text{Cl}} \sin^2 \theta / \lambda^2) \\ &\quad \dots h, k, l \text{ odd,} \end{aligned} \right\} \quad (11.34)$$

where f_{Na} and f_{Cl} are the atomic scattering factors for Na^+ and Cl^- , and B_{Na} and B_{Cl} the individual atomic temperature factors. (These equations follow from (11.29), with four sodium atoms at $000 +$ face-centred positions and four chlorine atoms at $00\frac{1}{2} +$ face-centred positions: isotropic temperature factors are used, as all the atoms occupy sites of cubic point symmetry, $m\bar{3}m$.) The intensity measurements were made on a relative scale, and the scale factor, together with the temperature factors B_{Na} , B_{Cl} , were treated as adjustable parameters in the least-squares refinement of the structure factor data.

The table shows that the fractional error in $F^{\text{obs.}}$, when expressed as $s/F^{\text{obs.}}$, varies from less than 1 per cent for the strong, even-index reflexions to about 6 per cent for the weaker, odd-index reflexions. Only a small part of this error is explained by counting statistics: σ is, on average, only one-seventh of s . Clearly, the random errors in $F^{\text{obs.}}$ have been reduced to such an extent that the principal errors are of systematic nature.

If we assume that different estimates of $F^{\text{obs.}}$ would be normally distributed about the 'true' value, the mean deviation of each estimate is

$$\sqrt{\frac{2}{\pi}} s = 0.7979s.$$

Thus the contribution to the R -index due to the uncertainty in $F^{\text{obs.}}$ is

$$\sum_{hkl} 0.7979 s_{hkl} \div \sum_{hkl} |F^{\text{obs.}}|,$$

which is 1.3 per cent for the figures in Table XXVIII. This is not sufficient to account for the actual value for the R -index of 2.1 per

cent. It is unlikely that the extra 0.8 per cent can be ascribed to uncertainties in estimating $F^{\text{calc.}}$: from the discussion in §11.4, appreciable errors in $F^{\text{calc.}}$ can arise if the atoms are aspherical or execute large amplitudes of thermal vibration, but neither of these conditions applies to NaCl. We conclude that the estimated standard deviation s , determined from the variance in the measurements of symmetry-equivalent reflexions, is probably an underestimate of the real standard deviation, but the origin of this difference is not known.

TABLE XXVIII. Sodium chloride structure factors at 295° K (X-rays) (Abrahams, 1964)

<i>hkl</i>	$\overline{F^{\text{obs.}}}$	$F^{\text{calc.}}$	$\overline{F^{\text{obs.}}} - F^{\text{calc.}}$	s	σ
111	19.84	19.79	+0.05	0.18	0.06
200	79.34	83.43	-4.09	0.55	0.05
220	66.96	67.03	-0.07	0.40	0.06
311	10.90	10.08	+0.82	0.44	0.13
222	57.39	56.73	+0.66	0.31	0.05
400	50.17	49.55	+0.62	0.25	0.04
331	9.86	9.56	+0.30	0.36	0.13
420	44.97	44.16	+0.81	0.27	0.08
422	39.99	40.03	-0.04	0.34	0.08
333	10.00	9.99	+0.01	0.38	0.13
511	10.11	9.99	+0.12	0.35	0.11
440	32.78	33.23	-0.45	0.17	0.08
531	9.76	10.10	-0.34	0.53	0.12
442	30.47	30.62	-0.15	1.61	0.08
600	30.42	30.62	-0.20	1.22	0.05
620	28.76	28.24	+0.52	0.63	0.07
533	9.15	9.87	-0.72	0.67	0.09
622	24.18	26.07	-1.89	0.35	0.05

In this table: s^2 is variance of $\overline{F^{\text{obs.}}}$, estimated from measurements on symmetry-equivalent reflexions; σ is standard deviation from counting statistics; $F^{\text{calc.}}$ is calculated from $B_{\text{Na}} = 1.60 \text{ \AA}^2$, $B_{\text{Cl}} = 1.17 \text{ \AA}^2$.

Some further measurements of Abrahams (1965) using an equi-inclination diffractometer with balanced filters indicate that the standard errors of the observations on NaCl are up to 4.0 per cent. Half of this is attributed to instrumental causes and half to systematic errors (absorption, extinction, etc.).

Tetrahedrite (X-rays)

The reliability of X-ray equi-inclination counter-diffractometer data has also been examined by Wuensch (1963), from the analysis

of data recorded on the mineral tetrahedrite, $\text{Cu}_{12}\text{Sb}_4\text{S}_{13}$. Diffracted intensities were obtained from a spherical sample using β -filtered $\text{CuK}\alpha$ radiation. Tetrahedrite is cubic, space-group $I\bar{4}3m$, and each general reflexion occurs as 48 symmetry-equivalent reflexions. Thus, as with NaCl, the comparison of reflexions required by symmetry to be equivalent provides a method of checking the data. Three kinds of check were carried out:

(1) Repeated measurement of certain reflexions, over periods of several weeks. The reproducibility of these measurements is affected by counting statistics and by drift in the electronic equipment.

(2) Comparison of equivalent reflexions, hkl and hkl , within a given level l . Systematic errors such as absorption affect the agreement.

(3) Comparison of equivalent reflexions, hkl and hkl , between different levels. Agreement is affected by further systematic errors, such as differences in the way in which the white-radiation streak is crossed.

Some of the results are summarized in Table XXIX. The deviation between equivalent structure factors both within each level and between levels exceeds the reproducibility of the data. This difference must be ascribed to systematic errors in measuring \overline{F} . The main source of error was absorption, and the uncertainty in the absorption correction (arising from a 1.7 per cent variation in radius of the nominally spherical sample) was sufficient to account for the increase in the r.m.s. deviation in tests (2) and (3).

TABLE XXIX. Reliability of structure factors for cubic tetrahedrite (X-rays) (Wuensch, 1963)

Test	Range of deviations	
	from mean \overline{F} (%)	r.m.s. deviation (%)
(1) Reproducibility	0.016-2.8	1.15
(2) Comparison of hkl and hkl	0.066-7.5	2.92
(3) Comparison of hkl and hkl	0.43-6.0	2.82

Uranium dioxide (neutrons)

A systematic study of the neutron reflexions of a spherical crystal of cubic UO_2 has been undertaken by Rouse & Willis

(1966). The reflexions were recorded at $\lambda = 1.04 \text{ \AA}$ using an automatic four-circle diffractometer.

Table XXX summarizes their results. $\overline{F^{\text{obs.}}}$ in the third column is the mean of the measurements on n symmetry-related reflexions, where n is the number in the second column. S^2 is the variance of the n measurements, given by the equation

$$S^2 = \sum_{i=1}^n \frac{(F_i - \overline{F})^2}{(n-1)},$$

and σ^2 is the variance expected from Poisson counting statistics. The reflexions occur in three groups, strong, medium and weak, corresponding to $h+k+l = 4m$, $4m \pm 1$ and $4m+2$, respectively ($m = \text{integer}$). The variance S^2 is related to the variance s^2 of $\overline{F^{\text{obs.}}}$ by

$$s^2 = \frac{S^2}{n}$$

(see, for example, *Statistics* section in *International Tables for X-ray Crystallography*, vol. II).

A measure of the consistency of the internal (S) and external (σ) errors of a single observation is provided by the last column of Table XXX. The quantity $\chi^2 = (n-1)S^2/\sigma^2$ is distributed in the χ^2 -distribution on $n-1$ degrees of freedom, and P_{χ^2} is the probability that χ^2 for the sample exceeds that actually found. If P_{χ^2} is close to 0.5 there is no inconsistency between the internal and external estimates of error, and if P_{χ^2} is near zero or unity the estimates are inconsistent and some kind of systematic error is present. Judged from this criterion, the weak reflexions are most consistent, the medium reflexions are less so, and the strong reflexions are the worst.

The $F^{\text{calc.}}$ values for the three groups of reflexions are given by the equations

$$\begin{aligned} F^{\text{calc.}} &= 4b_U e^{-B_U \sin^2 \theta / \lambda^2} + 8b_O e^{-B_O \sin^2 \theta / \lambda^2} & (h+k+l = 4m) \\ &= 4b_U e^{-B_U \sin^2 \theta / \lambda^2} & (h+k+l = 4m \pm 1) \\ &= 4b_U e^{-B_U \sin^2 \theta / \lambda^2} - 8b_O e^{-B_O \sin^2 \theta / \lambda^2} & (h+k+l = 4m+2). \end{aligned}$$

Here b_U , b_O are the nuclear scattering amplitudes of uranium and oxygen, and B_U , B_O are the two temperature factors. Preliminary analysis of the data in Table XXX using these equations showed that the strong reflexions were affected by extinction and so these reflexions were omitted from the final least-squares refinement of the remaining 14 reflexions. The final analysis gave $B_U = 0.19 \text{ \AA}^2$, $B_O = 0.43 \text{ \AA}^2$, $b_U/b_O = 1.47$ and an R -index of 0.9 per cent. This

TABLE XXX. Uranium dioxide structure factors (neutrons)

	{hkl}	No. of independent observations		$\overline{F^{\text{obs.}}}$	S	σ	$S/\overline{F^{\text{obs.}}}$ (%)	P_{χ^2}
		n						
Strong reflexions ($h+k+l = 4m$)	008	4		100.44	0.51	0.24	0.5	<0.01
	022	10		115.34	2.31	0.23	2.0	<0.01
	044	17		108.66	1.32	0.24	1.2	<0.01
	044	7		107.28	0.77	0.24	0.7	<0.01
	224	14		113.32	0.86	0.24	0.8	<0.01
	246	25		104.16	0.80	0.23	0.8	<0.01
	444	3		105.58	1.26	0.23	1.2	<0.01
Medium reflexions ($h+k+l = 4m \pm 1$)	113	14		52.65	0.40	0.24	0.8	<0.01
	115	15		51.24	0.37	0.24	0.7	<0.01
	117	14		49.31	0.29	0.24	0.6	0.13
	133	12		52.02	0.36	0.24	0.7	0.02
	135	27		50.62	0.35	0.25	0.7	<0.01
	137	27		48.60	0.39	0.25	0.8	<0.01
	155	12		49.15	0.30	0.24	0.6	0.10
	333	6		51.52	0.13	0.24	0.3	0.92
	335	12		49.86	0.32	0.25	0.6	0.07
	553	12		48.88	0.26	0.24	0.5	0.30
Weak reflexions ($h+k+l = 4m+2$)	006	5		14.94	0.37	0.34	2.5	0.32
	024	18		17.62	0.32	0.33	1.8	0.52
	046	16		12.86	0.34	0.34	2.6	0.49
	244	13		15.31	0.27	0.32	1.8	0.73

R -index was reduced even further, to 0.5 per cent, by introducing one extra parameter to represent the anharmonic contribution to B_O .

It is too early to draw any general conclusions about the accuracy of X-ray and neutron diffractometer data. From the very limited studies to date, it seems that a final R -index approaching 1 per cent is attainable in cubic crystals provided

measurements are averaged over symmetry-equivalent reflexions. Furthermore, there is some evidence that a lower R -index is obtained with neutrons than with X-rays: this may be due to the lower absorption correction with neutrons and to the difficulty of calculating X-ray atomic scattering factors.

CHAPTER 12

COMPUTER PROGRAMS AND
ON-LINE CONTROL

12.1. Diffractometer input and output

The automatic diffractometer, whatever its type, can be regarded as a black box which accepts numerical input information of one kind and produces numerical information of another kind. The input information consists of the settings of the various crystal and detector shafts and all the instructions necessary to make valid measurements of the intensities of Bragg reflexions. The output data consist of the results of those measurements. The generation of the input information and the processing of the diffractometer output must inevitably be carried out by means of a computer: the rate at which measurements are made by an automatic diffractometer is such as to make manual computation with a desk calculator quite impracticable.

It is important, therefore, that the input and output medium of an automatic diffractometer be one which is readily generated and read by a computer. (In the case of analogue diffractometers, discussed in §3.3, only the output medium needs to be considered.) The most common media are punched cards or punched paper tape: the choice between these two is generally dictated by the computer installation which is used in conjunction with the diffractometer. It may be noted in passing that punched cards offer a greater flexibility in that the sequence in which reflexions are to be measured and the sequence in which experimental results are listed can be varied by simply resorting a stack of cards. The total number of cards which can be read or punched without manual intervention is, however, limited by the capacity of the card-holding hoppers of commercially available punches and readers. These hoppers cannot hold more than 1,000 cards: card-controlled diffractometers usually require at least one input card per reflexion and produce at least one output card. The hoppers are loaded with alternate input and blank cards and so the

APPENDIX

SUMMARY OF DIFFERENCES BETWEEN
X-RAY AND NEUTRON DIFFRACTOMETRY

Property	X-rays	Neutrons	Effect of difference
Flux at specimen	At least 10^{10} quanta/cm ² /s, using unmonochromatized radiation	10^6 to 10^7 neutrons/cm ² /s, using radiation from high-flux reactor	Samples are larger with neutrons, and counting times longer
Wavelength λ , and width of wavelength band $\delta\lambda$	λ restricted to characteristic K-radiations of elements between Cr and Ag ($\sim 2 \text{ \AA} - 0.5 \text{ \AA}$). Characteristic line is very sharp ($\delta\lambda < 10^{-4} \text{ \AA}$), but superimposed on 'white' background	With a crystal monochromator, λ can take any value in the range 0.8 to 2.0 \AA ; $\delta\lambda$ is between 0.02 and 0.05 \AA . With hot and cold sources and mechanical velocity selectors the range of λ can be extended from 0.5 to 10 \AA .	Long wavelength measurements possible with neutrons. Bragg peaks are wider with neutrons. White background error with X-rays
Nature of general scattering	Electronic: scattering amplitude f falls off with scattering angle	Nuclear: scattering is isotropic	Bragg reflexions can be observed at higher θ values with neutrons. Scattering amplitude of atom for neutrons is represented by a single number; for X-rays it must be calculated from the electronic structure and is known only approximately
Absorption coefficient	$\mu \sim 10$ to 10^2	$\mu \sim 10^{-1}$, except for B, Cd, Li and rare-earths	Absorption correction much more important with X-rays

APPENDIX

Property	X-rays	Neutrons	Effect of difference
Anomalous dispersion	Always present, even far from an absorption edge. $f = f^0 + \Delta f' + i\Delta f''$ where $\Delta f'$, $\Delta f''$ depend on wavelength	Absent, except for a few elements (e.g. Cd), which have $\Delta f'$, $\Delta f''$ contributions much larger than for X-rays	For most samples $I_{hkl} = \overline{I_{\bar{h}\bar{k}\bar{l}}}$ with neutrons
Extinction	Primary (within each mosaic block) and secondary (between blocks)	Primary extinction less than for X-rays, as scattering amplitude per atomic plane is less; secondary extinction is larger, as beam penetrates further	Especially care required in neutron diffraction to correct for secondary extinction
Thermal diffuse scattering	Takes place with negligible change of wavelength (X-ray energy \gg phonon energy)	Takes place with appreciable change of wavelength (neutron energy \sim phonon energy)	A portion of the one-phonon T.D.S. background of the Bragg reflexions can be removed in neutron diffraction, using an analyser crystal to reflect the diffracted beam
Incoherent background	Compton scattering. Fluorescence scattering (inelastic)	Spin and isotopic incoherent scattering: spin incoherence very prominent with hydrogen (elastic disorder scattering)	Background between reflexions tends to be higher with neutrons, particularly for crystals containing hydrogen
Absolute intensity determination	Very difficult as direct beam cannot be measured easily in presence of white radiation: comparison with reference sample complicated by high absorption	Relatively straightforward	Experimental structure factors are more readily placed on absolute scale with neutrons

Property	X-rays	Neutrons	Effect of difference
Polarization factor p	Varies with θ and is uncertain for crystal-reflected radiation	$p = 1$ for nuclear reflexions	Extinction can be corrected in X-ray diffraction by examining change of intensity with state of polarization
Method of detection	Proportional or scintillation counter, with pulse-height discrimination	BF ₃ counter: neutron converted into α -particle	Pulse-height discrimination not possible with neutrons
Velocity of propagation	3×10^{10} cm/s	4×10^5 cm/s (1 Å neutrons); inversely proportional to wavelength	λ can be measured with neutrons by time-of-flight technique. Neutron structure factors can be determined by Laue method

REFERENCES AND AUTHOR INDEX

The numbers in square brackets are the pages where the references occur.

- ABRAHAMS, S. C. (1962). *Rev. scient. Instrum.* **33**, 973. [97]
 ABRAHAMS, S. C. (1964). *Acta crystallogr.* **17**, 1190. [296, 298]
 ABRAHAMS, S. C. (1965). Private communication. [298].
 ABRAHAMS, S. C. *see also* PRINCE & ABRAHAMS (1959).
 ABSON, W., SALMON, P. G. & PYRAH, S. (1958a). *Proc. Instn elect. Engrs*, **105B**, 357. [141].
 ABSON, W., SALMON, P. G. & PYRAH, S. (1958b). *Proc. Instn elect. Engrs*, **105B**, 349. [142].
 AGRON, P. A. *see* LEVY, AGRON & BUSING (1963).
 ALBRECHT, G. (1939). *Rev. scient. Instrum.* **10**, 221. [241]
 ALEXANDER, L. E., KUMMER, E. & KLUG, H. P. (1949). *J. appl. Phys.* **20**, 735. [145]
 ALEXANDER, L. E. & SMITH, G. S. (1962). *Acta crystallogr.* **15**, 983. [229, 265, 266]
 ALEXANDER, L. E. & SMITH, G. S. (1964). *Acta crystallogr.* **17**, 447. [266]
 ALIKHANOV, R. A. (1959). *J. exp. theor. Phys. U.S.S.R.* **36**, 1690. [205]
 ALLISON, S. K. *see* COMPTON & ALLISON (1935).
 ARNDT, U. W. (1949). *J. scient. Instrum.* **26**, 45. [146]
 ARNDT, U. W. (1955). *X-ray Diffraction by Polycrystalline Materials*, ch. 7. Eds. H. S. Peiser, H. P. Rooksby and A. J. C. Wilson (London: The Institute of Physics). [106, 107, 122]
 ARNDT, U. W. (1963). *Hilger J.* **8**, 4. [82, 98]
 ARNDT, U. W. (1964). *Acta crystallogr.* **17**, 1183. [74]
 ARNDT, U. W. (1966). *J. scient. Instrum.* To be published. [150]
 ARNDT, U. W., COATES, W. A. & RILEY, D. P. (1953). *Proc. phys. Soc. Lond. B*, **66**, 1009. [196]
 ARNDT, U. W., FAULKNER, T. H. & PHILLIPS, D. C. (1960). *J. scient. Instrum.* **37**, 68. [72, 89, 90]
 ARNDT, U. W., GOSSLING, T. H. & MALLET, J. F. W. (1966). To be published. [98]
 ARNDT, U. W., JONES, F. B. & LONG, A. R. (1965). Unpublished. [72]
 ARNDT, U. W. & MACGANDY, E. L. (1962). Unpublished. [82]
 ARNDT, U. W., NORTH, A. C. T. & PHILLIPS, D. C. (1964). *J. scient. Instrum.* **41**, 421. [12, 63, 88, 94]
 ARNDT, U. W. & PHILLIPS, D. C. (1957). *Acta crystallogr.* **10**, 508. [66]
 ARNDT, U. W. & PHILLIPS, D. C. (1959). *Br. J. appl. Phys.* **10**, 116. [75]
 ARNDT, U. W. & PHILLIPS, D. C. (1961). *Acta crystallogr.* **14**, 807. [75, 88, 91, 97]
 ARNDT, U. W. & PHILLIPS, D. C. (1966). To be published. [94]
 ARNDT, U. W. & RILEY, D. R. (1952). *Proc. phys. Soc. Lond. A*, **65**, 74. [180]

- ARNDT, U. W. & WILLIS, B. T. M. (1963a). *Nucl. Instrum. Meth.* **24**, 155. [69, 82, 98]
- ARNDT, U. W. & WILLIS, B. T. M. (1963b). *Rev. scient. Instrum.* **34**, 224. [72, 82, 98]
- ATKINSON, H. H. (1958). *Phil. Mag.* **3**, 476. [192]
- ATOJI, M. (1964). Argonne National Laboratory Report, ANL-6920. [97, 206]
- AZAROFF, L. V. (1955). *Acta crystallogr.* **8**, 701. [287]
- BACON, G. E. (1962). *Neutron Diffraction* (Oxford: Clarendon Press). [xii, 198, 277, 295]
- BACON, G. E. & LOWDE, R. D. (1948). *Acta crystallogr.* **1**, 303. [244]
- BACON, G. E., SMITH, J. A. G. & WHITEHEAD, C. D. (1950). *J. scient. Instrum.* **27**, 330. [3]
- BAKER, T. W. (1966). A.E.R.E. Harwell Report. [264]
- BARNES, D. C. & FRANKS, A. (1962). *J. scient. Instrum.* **39**, 648. [76]
- BARRETT, C. S., MUELLER, M. H. & HEATON, L. (1963). *Rev. scient. Instrum.* **34**, 847. [204, 205]
- BEAR, R. S. *see* BOLDUAN & BEAR (1949).
- BELSON, H. S. (1964). *Rev. scient. Instrum.* **35**, 234. [258]
- BENEDICT, T. S. (1955). *Acta crystallogr.* **8**, 747. [67, 97]
- BERNAL, J. D. (1926). *Proc. R. Soc. A*, **113**, 117. [2]
- BILANIUK, O. M. (1960). *see* BILANIUK, O. M., HAMANN, A. K. & MARSH, B. B. (1960). University of Rochester Report. AT(30-1) 875, May 1960. [150]
- BINNS, J. V. (1964). *J. scient. Instrum.* **41**, 715. [76, 93]
- BLALOCK, T. V. (1964). *I.E.E. Trans. Nucl. Sci.* NS-11, 365. [156]
- BLOCHIN, M. A. (1957). *Physik der Röntgenstrahlen* (Berlin: Verlag d. Technik). [170]
- BLOW, D. M. & GOSSLING, T. H. (1965). Unpublished. [306]
- BOLDUAN, O. E. A. & BEAR, R. S. (1949). *J. appl. Phys.* **20**, 983. [173]
- BOLLINGER, L. M., THOMAS, G. E. & GINTHER, R. J. (1962). *Nucl. Instrum. Meth.* **17**, 97. [144]
- BOND, W. L. (1951). *Rev. scient. Instrum.* **22**, 344. [258]
- BOND, W. L. (1955). *Acta crystallogr.* **8**, 741. [67, 97]
- BOND, W. L. (1960). *Acta crystallogr.* **13**, 814. [263]
- BORGONOV, G. & CAGLIOTI, G. (1962). *Nuovo Cim.* **24**, 1174. [252]
- BORRMANN, M. (1941). *Phys. Z.* **42**, 157. [193]
- BORRMANN, M. (1950). *Z. Phys.* **127**, 297. [193]
- BOSANQUET, C. H. *see* BRAGG, JAMES & BOSANQUET (1921).
- BOWDEN, K., EDWARDS, D. & MILLS, O. S. (1963). *Acta crystallogr.* **16**, A 177. [98, 311]
- BOWMAN, H. R., HYDE, E. K., THOMPSON, S. G. & JARED, R. C. (1966). *Science*, **151**, 562. [136]
- BOZORTH, R. M. & HAWORTH, F. E. (1938). *Phys. Rev.* **53**, 538. [190]
- BRAGG, W. H. & BRAGG, W. L. (1913). *Proc. R. Soc. A*, **88**, 428. [1, 97]
- BRAGG, W. L., JAMES, R. W. & BOSANQUET, C. H. (1921). *Phil. Mag.* **42**, 1. [248]
- BRAGG, W. L. & WEST, J. (1928). *Z. Kristallogr. Miner.* **69**, 118. [288]
- BROAD, D. A. G. (1956). *Acta crystallogr.* **9**, 834. [170]

- BROCKHOUSE, B. N. (1961). In *Inelastic Scattering of Neutrons in Solids and Liquids*, p. 113. (Vienna: I.A.E.A.) [3]
- BROCKMAN, F. G. *see* CORLISS, HASTINGS & BROCKMAN (1953).
- BROWN, I. D. (1958). *Acta crystallogr.* **11**, 510. [66]
- BROWN, P. J. & FORSYTH, J. B. (1960). *Acta crystallogr.* **13**, 985. [97]
- BUDAL, K. (1963). Arkiv f. d. Fysiske Seminar Trondheim (9); *Nucl. Instrum. Meth.* **23**, 132. [150]
- BUERGER, M. J. (1942). *X-ray Crystallography* (New York: John Wiley). [xii, 2, 26, 31]
- BUERGER, M. J. (1944). *The Photography of the Reciprocal Lattice*. A.S.X.R.E.D. [2]
- BUERGER, M. J. (1960). *Crystal Structure Analysis* (New York: John Wiley). [10, 97, 277]
- BUERGER, M. J. (1964). *The Precession Method* (New York: John Wiley). [2]
- BURAS, B. & LECIEJEWICZ, J. (1964). *Phys. Stat. Sol.* **4**, 349. [217, 218]
- BURBANK, R. D. (1964). *Acta crystallogr.* **17**, 434. [222, 229, 265, 266]
- BURBANK, R. D. (1965). *Acta crystallogr.* **18**, 88. [291]; **19**, 957. [255]
- BUSING, W. R. & LEVY, H. (1957). *Acta crystallogr.* **10**, 180. [241, 243]
- BUSING, W. R. *see also* LEVY, AGRON & BUSING (1963).
- BUTT, N. M. *see* O'CONNOR & BUTT (1963).
- BUTT, N. M. *see* O'CONNOR & BUTT (1965).
- BUYERS, T. (1964). Ph.D. Thesis. University of Aberdeen. [291]
- CAGLIOTI, G. (1964). *Acta crystallogr.* **17**, 1202. [224, 225]
- CAGLIOTI, G. & RICCI, F. P. (1962). *Nucl. Instrum. Meth.* **15**, 155. [211]
- CAGLIOTI, G. *see also* BORGONOV & CAGLIOTI (1962).
- CATH, P. G. *see* LADELL & CATH (1963).
- CHAMBERS, F. W. *see* COLE, CHAMBERS & DUNN (1962).
- CHAMBERS, F. W. *see* COLE, CHAMBERS & WOOD (1961).
- CHAMBERS, F. W. *see* COLE, CHAMBERS & WOOD (1962).
- CHAMBERS, F. W. *see* COLE, OKAYA & CHAMBERS (1963).
- CHANDRASEKHAR, S. (1956). *Acta crystallogr.* **9**, 954. [192, 246]
- CHANDRASEKHAR, S. (1960a). *Acta crystallogr.* **13**, 588. [192, 246]
- CHANDRASEKHAR, S. (1960b). *Adv. Phys.* **9**, 363. [192, 246, 247, 284]
- CHANDRASEKHAR, S. & PHILLIPS, D. C. (1961). *Nature, Lond.* **190**, 1164. [192]
- CHANDRASEKHAR, S. & WEISS, R. J. (1957). *Acta crystallogr.* **10**, 598. [247]
- CHANDRASEKHARAN, K. S. (1956). *Proc. Indian Acad. Sci. A* **44**, 387. [193]
- CHIDAMBARAM, A., SEQUEIRA, A. S. & SIKKA, S. K. (1964). *Nucl. Instrum. Meth.* **26**, 340. [265]
- CHIPMAN, D. R. & PASKIN, A. (1958). *J. appl. Phys.* **29**, 1608; **30**, 1992; **30**, 1998. [222]
- CLASTRE, J. (1960). *Acta crystallogr.* **13**, 986. [97]
- CLIFTON, D. F., FILLER, A. & MCLACHLAN, D. (1951). *Rev. scient. Instrum.* **22**, 1024. [97]
- COATES, W. A. *see* ARNDT, COATES & RILEY (1953).
- COCEVA, C. (1963). *Nucl. Instrum. Meth.* **21**, 93. [143, 144]
- COCHRAN, W. (1950). *Acta crystallogr.* **3**, 268. [2, 97, 146]
- COCHRAN, W. (1953). *Acta crystallogr.* **6**, 260. [248]

- COCHRAN, W. *see also* LIPSON & COCHRAN (1957).
 COHEN, L., FRAENKEL, B. S. & KALMAN, Z. H. (1963). *Acta crystallogr.* **16**, 1192. [252]
 COLE, D. G. *see* GILLAM & COLE (1953).
 COLE, H., CHAMBERS, F. W. & DUNN, H. M. (1962). *Acta crystallogr.* **15**, 138. [252, 254, 255]
 COLE, H., CHAMBERS, F. W. & WOOD, C. G. (1961). *J. appl. Phys.* **32**, 1942. [193, 194]
 COLE, H., CHAMBERS, F. W. & WOOD, C. G. (1962). *Rev. scient. Instrum.* **33**, 435. [171, 173]
 COLE, H. & OKAYA, Y. (1964). ACA Meeting, Paper A 5. [310]
 COLE, H., OKAYA, Y. & CHAMBERS, F. W. (1963). *Acta crystallogr.* **16**, A 154; *Rev. scient. Instrum.* **34**, 872. [98]
 COLLINS, M. F. *see* LOW & COLLINS (1963).
 COMPTON, A. H. & ALLISON, S. K. (1935). *X-rays in Theory and Experiment* (New York: Van Nostrand). [xii, 146, 170, 195, 208]
 COOKE-YARBOROUGH, E. H., FLORIDA, C. D. & DAVEY, C. N. (1949). *J. scient. Instrum.* **26**, 124. [123]
 CORLISS, L. M., HASTINGS, J. M. & BROCKMAN, F. G. (1953). *Phys. Rev.* **90**, 1013. [3]
 COSSLETT, V. E. & NIXON, W. C. (1960). *X-ray Microscopy* (Cambridge University Press). [170, 171]
 COWAN, J. P., MACINTYRE, W. M. & THOMAS, R. (1965). ACA Meeting, Paper A 4. [150]
 COWAN, J. P., MACINTYRE, W. M. & WERKEMA, G. J. (1963). *Acta crystallogr.* **16**, 221. [233]
 CRUICKSHANK, D. W. J. (1956). *Acta crystallogr.* **9**, 757. [288]
 CRUICKSHANK, D. W. J. (1956). *Acta crystallogr.* **9**, 747. [295]
 CRUICKSHANK, D. W. J. (1960). *Acta crystallogr.* **13**, 774. [296]
 DACHS, H. (1961). *Z. Kristallogr. Miner.* **115**, 80. [211]
 DARWIN, C. G. (1922). *Phil. Mag.* **43**, 800. [248, 250]
 DAVEY, C. N. *see* COOKE-YARBOROUGH, FLORIDA & DAVEY (1949).
 DAVIES, D. A., MATHIESON, A. McL. & STIFF, G. M. (1959). *Rev. scient. Instrum.* **30**, 488. [170]
 DAWSON, B. (1964a). *Acta crystallogr.* **17**, 990. [293]
 DAWSON, B. (1964b). *Acta crystallogr.* **17**, 997. [293, 294]
 DEBYE, P. (1914). *Annln Phys.* **43**, 49. [221]
 DEARNALEY, G. & NORTHROP, D. C. (1963). *Semiconductor Counters for Nuclear Radiations* (London: E. and F. N. Spon). [136]
 DIAMANT, H. *see* DRENCK, PEPINSKY & DIAMANT (1959).
 DRENCK, R., DIAMANT, H. & PEPINSKY, R. (1959). ACA Meeting, Cornell, Paper G 8. [73, 97]
 DUMOND, J. W. M. *see* HENKE & DUMOND (1953).
 DUMOND, J. W. M. *see* HENKE & DUMOND (1955).
 DUNN, H. M. *see* COLE, CHAMBERS & DUNN (1962).
 EASTABROOK, J. N. & HUGHES, J. W. (1953). *J. scient. Instrum.* **30**, 317. [146]
 EDWARDS, D. W. G. *see* BOWDEN, EDWARDS & MILLS (1963).
 EHRENBERG, W. (1949). *J. opt. Soc. Amer.* **39**, 741. [195]

- EHRENBERG, W. & FRANKS, A. (1952). *Nature, Lond.* **170**, 1076. [195]
 ELLIOTT, A. (1965). *J. scient. Instrum.* **42**, 312. [192, 195]
 ELLISON, R. D. *see* LEVY & ELLISON (1960).
 EVANS, H. T. (1953). *Rev. scient. Instrum.* **24**, 156. [66, 97]
 EVANS, D. F. (1961). *Digital Data* (London: Hilger and Watts). [70]
 EVANS, R. C., HIRSCH, P. B. & KELLAR, J. N. (1948). *Acta crystallogr.* **1**, 124. [190, 191]
 EWALD, P. P. (1921). *Z. Kristallogr. Miner.* **56**, 129. [2]
 FAIRSTEIN, E. (1961a). NAS-NRC Nucl. Sci. Series Rep. **32**, 210. [157]
 FAIRSTEIN, E. (1961b). *I.R.E. Trans. Nucl. Sci.* NS-8, 129. [157]
 FAIRSTEIN, E. (1962). In *Nuclear Instruments and their Uses*. Ed. A. H. Snell (New York: John Wiley). [164]
 FANKUCHEN, I. (1937). *Nature, Lond.* **139**, 193. [190]
 FANKUCHEN, I. (1938). *Phys. Rev.* **53**, 910. [190]
 FANKUCHEN, I. *see also* WILLIAMSON & FANKUCHEN (1959).
 FANKUCHEN, I. *see also* YAKEL & FANKUCHEN (1962).
 FARKAS, G. & VARGA, P. (1964). *J. scient. Instrum.* **41**, 704. [129]
 FAULKNER, T. H. *see* ARNDT, FAULKNER & PHILLIPS (1960).
 FAXÉN, H. (1923). *Z. Phys.* **17**, 266. [221]
 FILLER, A. *see* CLIFTON, FILLER & McLACHLAN (1951).
 FINCH, J. T. & KLUG, A. (1959). *Nature, Lond.* **183**, 1709. [Plate 1]
 FLORIDA, C. D. *see* COOKE-YARBOROUGH, FLORIDA & DAVEY (1949).
 FORSYTH, J. B. *see* BROWN & FORSYTH (1960).
 FOURNET, G. *see* GUINIER & FOURNET (1955).
 FRAENKEL, B. S. *see* COHEN, FRAENKEL & KALMAN (1963).
 FRANKS, A. (1955). *Proc. phys. Soc. B*, **68**, 1054. [195]
 FRANKS, A. *see also* BARNES & FRANKS (1962).
 FRANKS, A. *see also* EHRENBERG & FRANKS (1952).
 FRIEDRICH, W., KNIPPING, P. & VON LAUE, M. (1912). *Proc. Bavarian Acad. Sci.* p. 303. Reprinted in *Naturwissenschaften* (1952), p. 368. [1]
 FURNAS, T. C. (1957). *Single Crystal Orienter Instruction Manual* (Milwaukee: The General Electric X-ray Corp.). [97, 171, 241, 257, 260]
 FURNAS, T. C. & HARKER, D. (1955). *Rev. scient. Instrum.* **26**, 449. [39, 51, 79, 97]
 GELLER, S. & KATZ, H. (1962). *Bell Syst. tech. J.* **41**, 425. [67]
 GETTING, I. A. (1947). *Phys. Rev.* **53**, 103. [123]
 GILLAM, E. & COLE, D. G. (1953). *Phil. Mag.* **44**, 999. [196]
 GILLESPIE, A. B. (1953). *Signal, Noise and Resolution in Nuclear Counter Amplifiers* (London: Pergamon Press). [114, 164]
 GINTHER, R. J. *see* BOLLINGER, THOMAS & GINTHER (1962).
 GOODRICH, G. W. & WILEY, W. C. (1962). *Rev. scient. Instrum.* **33**, 761. [130, 131]
 GOSSLING, T. H. *see* ARNDT, GOSSLING & MALLETT (1966).
 GOSSLING, T. H. *see* BLOW & GOSSLING (1965).
 GOULDING, F. S. & HANSEN, W. L. (1961). *Nucl. Instrum. Meth.* **12**, 249. [136, 165]
 GOULDING, F. S. *see* LANDIS & GOULDING (1964).
 GUILD, J. (1956). *The Interference Systems of Cross Diffraction Gratings: Theory of Moiré Fringes* (Oxford: Clarendon Press). [71]

- GUINIER, A. & FOURNET, G. (1955). *Small-Angle Scattering of X-rays* (New York: John Wiley). [171]
- HAMILTON, W. C. (1957). *Acta crystallogr.* **10**, 629. [244, 248, 250]
- HAMILTON, W. C. (1963). *Acta crystallogr.* **16**, 609. [244, 250]
- HAMILTON, W. C. (1964). ACA Meeting, Bozeman, Paper A 6. [98, 310]
- HANSEN, W. L. *see* GOULDING & HANSEN (1961).
- HARGREAVES, C. M., PRINCE, E. & WOOSTER, W. A. (1952). *J. scient. Instrum.* **29**, 82. [196]
- HARKER, D. *see* FURNAS & HARKER (1955).
- HARRIS, D. H. C. (1961*a*). A.E.R.E. Harwell Report, R-3688. [144]
- HARRIS, D. H. C. (1961*b*). A.E.R.E. Harwell Report, M-827. [144]
- HASTINGS, J. M. *see* CORLISS, HASTINGS & BROCKMAN (1953).
- HAWORTH, F. E. *see* BOZORTH & HAWORTH (1938).
- HEATON, L. & MUELLER, M. H. (1960). Private communication; *see* *Rev. scient. Instrum.* (1961), **31**, 456; *ibid.* (1963), **34**, 74. [72]
- HEATON, L. *see* BARRETT, MUELLER & HEATON (1963).
- HENKE, B. & DUMOND, J. W. M. (1953). *Phys. Rev.* **89**, 1300. [195]
- HENKE, B. & DUMOND, J. W. M. (1955). *J. appl. Phys.* **26**, 903. [195]
- HIRSCH, P. B. (1955). *X-ray Diffraction by Polycrystalline Materials*, ch. 11. Eds. H. S. Peiser, H. P. Rooksby and A. J. C. Wilson (London: The Institute of Physics). [171, 173, 179]
- HIRSCH, P. B. *see also* EVANS, HIRSCH & KELLAR (1948).
- HODGSON, L. I. *see* BOWDEN, K. *et al.* (1963).
- HOFSTADTER, R., O'DELL, E. W. & SCHMIDT, C. T. (1964). *Rev. scient. Instrum.* **35**, 246. [125]
- HOFSTADTER, R. *see also* WEST, MAYERHOF & HOFSTADTER (1951).
- HOLMES, K. C. (1964). Private communication. [196]
- HOSOYA, S. *see* MIYAKE, TOGAWA & HOSOYA (1964).
- HUGHES, D. J. (1953). *Pile Neutron Research* (Cambridge, Mass.: Addison-Wesley). [xii, 215]
- HUGHES, J. W. *see* EASTBROOK & HUGHES (1953).
- HURST, D. G., PRESSESSKY, A. J. & TUNNICLIFFE, P. R. (1950). *Rev. scient. Instrum.* **21**, 705. [3]
- HUXLEY, H. E. (1953). *Acta crystallogr.* **6**, 457. [173]
- HYDE, E. K. *see* BOWMAN, HYDE, THOMPSON & JARED (1966).
- International Tables. (The International Tables for X-ray Crystallography.)* 3 vols. (Birmingham: Kynoch Press). [*passim*]
- INTERNATIONAL UNION CRYSTALLOGRAPHIC APPARATUS COMMISSION (1956). *Acta crystallogr.* **9**, 976. [79]
- JAMES, R. W. (1962). *The Optical Principles of the Diffraction of X-rays* (London: G. Bell). [16, 244, 245, 292]
- JAMES, R. W. *see also* BRAGG, JAMES & BOSANQUET (1921).
- JARED, R. C. *see* BOWMAN, HYDE, THOMPSON & JARED (1966).
- JEFFERY, J. W. & ROSE, K. M. (1964). *Acta crystallogr.* **17**, 343. [238, 239]
- JENTZSCH, F. & NÄHRING, E. (1931). *Z. tech. Phys.* **12**, 185. [179]
- JOHANN, H. H. (1931). *Z. Phys.* **69**, 185. [190]
- JOHANSSON, T. (1932). *Naturwissenschaften*, **20**, 758. [191]
- JONES, F. B. *see* ARNDT, JONES & LONG (1965).
- KALMAN, Z. H. *see* COHEN, FRAENKEL & KALMAN (1963).

- KARTHA, G. (1953). *Acta crystallogr.* **6**, 817. [289]
- KATZ, H. *see* GELLER & KATZ (1962).
- KELLAR, J. N. *see* EVANS, HIRSCH & KELLAR (1948).
- KEVEY, A. (1964). Brookhaven Report, BNL 851 (T-337). [200]
- KIRKPATRICK, P. (1939). *Rev. scient. Instrum.* **10**, 186. [184]
- KIRKPATRICK, P. (1944). *Rev. scient. Instrum.* **15**, 223. [184]
- KLUG, A. *see* FINCH & KLUG (1959).
- KLUG, H. P. *see* ALEXANDER, KUMMER & KLUG (1949).
- KNIPPING, P. *see* FRIEDRICH, KNIPPING & VON LAUE (1912).
- KOHLER, T. R. *see* PARRISH & KOHLER (1956).
- KUMMER, E. *see* ALEXANDER, KUMMER & KLUG (1949).
- LADELL, J. & CATH, P. G. (1963). Norelco Reporter Special Issue. [72, 97]
- LADELL, J. & LOWITSCH, K. (1960). *Acta crystallogr.* **13**, 205. [75]
- LADELL, J., PARRISH, W. & SPIELBERG, N. (1963). ACA Conference Report. *See* LADELL & CATH (1963). [75]
- LANDIS, D. & GOULDING, F. S. (1964). Publication 1184. Nat. Acad. Sci., N.R.C., Washington, D.C. [130, 159]
- LANG, A. R. (1954). *Rev. scient. Instrum.* **25**, 1039. [21]
- LAUE, M. VON *see* FRIEDRICH, KNIPPING & VON LAUE (1912).
- LAUE, M. VON (1960). *Röntgenstrahlinterferenzen* (Frankfurt a. M.: Akademische Verlagsgesellschaft). [193]
- LAVAL, J. (1938). *C.r. hebd. Séanc. Acad. Sci., Paris*, **207**, 169. [221]
- LECIEJEWICZ, J. *see* BURAS & LECIEJEWICZ (1964).
- LEVY, H. A., AGRON, P. A. & BUSING, W. R. (1963). ACA Meeting, Cambridge, Mass., Paper E 7, *see* BUSING, SMITH, PETERSON & LEVY (1964). [98]
- LEVY, H. A. & ELLISON, R. D. (1960). *Acta crystallogr.* **13**, 270. [287]
- LEVY, H. A. *see* BUSING & LEVY (1957).
- LIPSON, H. & COCHRAN, W. (1957). *The Determination of Crystal Structures* (London: Bell). [288]
- LIPSON, H., NELSON, J. B. & RILEY, D. P. (1945). *J. scient. Instrum.* **22**, 184. [189]
- LONG, A. R. *see* ARNDT, JONES & LONG (1965).
- LONGLEY, W. (1963). Ph.D. Thesis, University of London. [173]
- LONSDALE, K. (1947). *Min. Mag., Lond.* **28**, 14. [251]
- LONSDALE, K. (1948). *Acta crystallogr.* **1**, 12. [2]
- LOW, G. C. E. & COLLINS, M. F. (1963). *J. appl. Phys.* **34**, 1195. [216]
- LOWDE, R. D. (1950). *Rev. scient. Instrum.* **21**, 835. [142]
- LOWDE, R. D. (1956). *Acta crystallogr.* **9**, 151. [217]
- LOWDE, R. D. *see also* BACON & LOWDE (1948).
- LOWITZSCH, K. *see* LADELL & LOWITZSCH (1960).
- LUTZ, G. (1960). *Kerntechnik*, **2**, 391. [97]
- MACGANDY, E. L. *see* ARNDT & MACGANDY (1962).
- MACINTYRE, W. M. (1963). *Acta crystallogr.* **16**, 315. [289]
- MACINTYRE, W. M. *see also* COWAN, MACINTYRE & THOMAS (1965).
- MACINTYRE, W. M. *see also* COWAN, MACINTYRE & WERKEMA (1963).
- MACK, M. & SPIELBERG, N. (1958). *Spectrochim. Acta*, **12**, 169. [271]
- McLACHLAN, D. *see* CLIFTON, FILLER & McLACHLAN (1951).

- McREYNOLDS, A. W. (1952). *Phys. Rev.* **88**, 958. [205]
 MALLETT, J. F. W. (1963). A.E.R.E. Harwell Memorandum. [143]
 MALLETT, J. F. W. *see also* ARNDT, GOSSLING & MALLETT (1966).
 MALMBERG, P. R. *see* SUN, MALMBERG & PECJAK (1956).
 MARTIN, A. J. P. *see* WOOSTER & MARTIN (1936).
 MATHEWS, F. S. *see* NORTH, PHILLIPS & MATHEWS (1966).
 MATHIESON, A. McL. (1958). *Acta crystallogr.* **11**, 433. [75, 97]
 MATHIESON, A. McL. *see* DAVIES, MATHIESON & STIFF (1959).
 MAYER, E. A. (1964). *Z. analyt. Chem.* **205**, 153. [51, 98]
 MAYERHOF, W. E. *see* WEST, MAYERHOF & HOFSTADTER (1951).
 MILLS, O. S. *see* BOWDEN, EDWARDS & MILLS (1963).
 MIYAKE, S., TOGAWA, S. & HOSOYA, S. (1964). *Acta crystallogr.* **17**, 1083. [189, 286]
 MOON, R. M. & SHULL, C. G. (1964). *Acta crystallogr.* **17**, 805. [252, 254, 255]
 MUELLER, M. H. *see* BARRETT, MUELLER & HEATON (1963).
 MUELLER, M. H. *see also* HEATON & MUELLER (1960).
 NÄHRING, E. *see* JENTZSCH & NÄHRING (1931).
 NELSON, J. B. *see* LIPSON, NELSON & RILEY (1945).
 NICHOLSON, K. P. & SNELLING, G. F. (1955). *Br. J. appl. Phys.* **6**, 104. [144]
 NILSSON, N. (1957). *Ark. Fys.* **12**, 247. [222, 226]
 NIXON, W. C. *see* COSSLETT & NIXON (1960).
 NORTH, A. C. T. (1964). *J. scient. Instrum.* **41**, 41. [306]
 NORTH, A. C. T., PHILLIPS, D. C. & MATHEWS, F. S. (1966). To be published. [241, 242]
 NORTH, A. C. T. *see* ARNDT, NORTH & PHILLIPS (1964).
 NORTHROP, D. C. *see* DEARNALEY & NORTHROP (1963).
 O'CONNOR, D. A. & BUTT, N. M. (1963). *Physics Letters*, **7**, 233. [222]
 O'CONNOR, D. A. & BUTT, N. M. (1965). Private communication. [223]
 O'DELL, E. W. *see* HOFSTADTER, O'DELL & SCHMIDT (1964).
 OKAYA, Y. *see* COLE, OKAYA & CHAMBERS (1963).
 OKAYA, Y. *see* COLE & OKAYA (1964).
 OTNES, K. & PALEVSKY, H. (1963). In *Inelastic Scattering of Neutrons in Solids and Liquids*, vol. 1, p. 95. (Vienna: I.A.E.A.) [215]
 OWEN, R. B. (1958). *I.R.E. Trans. Nucl. Sci.* NS-5, p. 189. [159]
 OWEN, R. B. (1961). *5th Int. Instrum. Meas. Conf., Stockholm*, IMS 10. [159]
 PARRISH, W. (1962). *Advances in X-ray Diffractometry and X-ray Spectrography* (Eindhoven: Centrex). [171]
 PARRISH, W. & KOHLER, T. R. (1956). *Rev. scient. Instrum.* **27**, 795. [109, 118, 181]
 PARRISH, W. & SPIELBERG, N. (1964). ACA Meeting. Paper B 5. [171]
 PARRISH, W. *see also* LADELL, PARRISH & SPIELBERG (1963).
 PARRISH, W. *see also* ROBERTS & PARRISH (1962).
 PASKIN, A. *see* CHIPMAN & PASKIN (1958).
 PECJAK, F. A. *see* SUN, MALMBERG & PECJAK (1956).
 PALEVSKY, H. *see* OTNES & PALEVSKY (1962).
 PELL, E. M. (1960). *J. appl. Phys.* **31**, 291. [135]

- PEPINSKY, R. *see* DRENCK, PEPINSKY & DIAMANT (1959).
 PHILLIPS, D. C. (1964). *J. scient. Instrum.* **41**, 123. [12, 52, 56, 59]
 PHILLIPS, D. C. (1966). Unpublished. [120]
 PHILLIPS, D. C. *see also* ARNDT, FAULKNER & PHILLIPS (1960).
 PHILLIPS, D. C. *see also* ARNDT, NORTH & PHILLIPS (1964).
 PHILLIPS, D. C. *see also* ARNDT & PHILLIPS (1957).
 PHILLIPS, D. C. *see also* ARNDT & PHILLIPS (1959).
 PHILLIPS, D. C. *see also* ARNDT & PHILLIPS (1961).
 PHILLIPS, D. C. *see also* ARNDT & PHILLIPS (1966).
 PHILLIPS, D. C. *see also* NORTH, PHILLIPS & MATHEWS (1966).
 PHILLIPS, F. C. (1963). *An Introduction to Crystallography*, 3rd. ed. (London: Longmans). [xii]
 POTTER, R. (1962). *J. scient. Instrum.* **37**, 379. [76, 97]
 POWELL, M. J. D. (1966). A.E.R.E. Harwell Report. [51, 255]
 PRESSESKY, A. J. *see* HURST, PRESSESKY & TUNNICLIFFE (1950).
 PRESSMAN, A. I. (1959). *Design of Transistorized Circuits for Digital Computers* (New York: John F. Rider). [154]
 PREWITT, C. T. (1960). *Z. Kristallogr. Miner.* **114**, 355. [26]
 PRICE, W. J. (1964). *Nuclear Radiation Detection*, 2nd ed. (New York: Magraw Hill). [154]
 PRINCE, E. *see* HARGREAVES, PRINCE & WOOSTER (1952).
 PRINCE, E. & ABRAHAMS, S. C. (1959). *Rev. scient. Instrum.* **30**, 581. [98]
 PYRAH, S. *see* ABSON, SALMON & PYRAH (1958a).
 PYRAH, S. *see* ABSON, SALMON & PYRAH (1958b).
 RADEKA, V. (1963). *I.E.E. Trans. Nuclear Sci.* N.S.-11, 358. [155]
 RAMASESHAN, S. (1964). In *Advanced Methods of Crystallography* (London: Academic Press). [260]
 RENNINGER, M. (1937). *Z. Phys.* **106**, 141. [252]
 RICCI, F. P. *see* CAGLIOTI & RICCI (1962).
 RILEY, D. P. *see* ARNDT, COATES & RILEY (1953).
 RILEY, D. R. *see* ARNDT & RILEY (1952).
 RILEY, D. P. *see* LIPSON, NELSON & RILEY (1945).
 ROBERTS, B. W. & PARRISH, W. (1962). *Int. Tables*, vol. 3, §2.3. [182, 188, 189, 192]
 ROSE, K. M. *see* JEFFERY & ROSE (1964).
 ROSS, P. A. (1928). *J. opt. Soc. Am.* **16**, 375, 433. [182]
 ROUSE, K. & WILLIS, B. T. M. (1966). A.E.R.E. Harwell Report. [299]
 SALMON, P. G. *see* ABSON, SALMON & PYRAH (1958a).
 SALMON, P. G. *see* ABSON, SALMON & PYRAH (1958b).
 SANDOR, E. (1964). Private communication. [192]
 SANTORO, A. & ZOCCHI, M. (1964). *Acta crystallogr.* **17**, 597. [255]
 SCHMIDT, C. T. *see* HOFSTADTER, O'DELL & SCHMIDT (1964).
 SCHWARTZ, L. H. (1965). Private communication. [218, 219]
 SEQUEIRA, A. S. *see* CHIDAMBARAM, SEQUEIRA & SIKKA (1964).
 SHULL, C. G. (1960). MIT Report AFOSR TR 60-111. [203, 205]
 SHULL, C. G. & WOLLAN, E. O. (1951). *Phys. Rev.* **81**, 527. [205]
 SHULL, C. G. *see also* MOON & SHULL (1964).
 SHULL, C. G. *see* WOLLAN & SHULL (1948).
 SIKKA, S. K. *see* CHIDAMBARAM, SEQUEIRA & SIKKA (1964).

- SMALLMAN, R. E. *see* WILLIAMSON & SMALLMAN (1953).
 SMITH, G. S. *see* ALEXANDER & SMITH (1962).
 SMITH, G. S. *see* ALEXANDER & SMITH (1964).
 SMITH, J. A. G. *see* BACON, SMITH & WHITEHEAD (1950).
 SNELLING, G. F. *see* NICHOLSON & SNELLING (1955).
 SPIELBERG, N. *see* LADELL, PARRISH & SPIELBERG (1963).
 SPIELBERG, N. *see* MACK & SPIELBERG (1958).
 SPIELBERG, N. *see* PARRISH & SPIELBERG (1964).
 STIFF, G. M. *see* DAVIES, MATHIESON & STIFF (1959).
 STURM, W. J. (1947). *Phys. Rev.* **71**, 757. [205]
 SUN, K. H., MALMBERG, P. R. & PECJAK, F. A. (1956). *Nucleonics*, **14** (July), 46.
 SZABO, P. (1961). *Acta crystallogr.* **14**, 1206. [247]
 TAYLOR, A. (1949). *J. scient. Instrum.* **26**, 225. [170]
 TEARE, P. W. (1960). *J. scient. Instrum.* **37**, 132. [189]
 THOMAS, G. E. *see* BOLLINGER, THOMAS & GINTHER (1962).
 THOMAS, R. *see* COWAN, MACINTYRE & THOMAS (1965).
 THOMPSON, S. G. *see* BOWMAN, HYDE, THOMPSON & JARED (1966).
 TOGAWA, S. *see* MIYAKE, TOGAWA & HOSOYA (1964).
 TUNNICLIFFE, P. R. *see* HURST, PRESSESKY & TUNNICLIFFE (1950).
 VARGA, P. *see* FARKAS & VARGA (1964).
 WAGNER, B., WITTE, H. & WÖLFEL, E. (1955). *Z. phys. Chem. (N.F.)*, **3**, 273. [291]
 WALLER, I. (1928). *Z. Phys.* **51**, 213. [221]
 WASER, J. (1951). *Rev. scient. Instrum.* **22**, 563. [23]
 WATSON, H. C. (1965). Private communication. [11]
 WELLS, M. (1960). *Acta crystallogr.* **13**, 722. [241]
 WEISSENBERG, K. (1924). *Z. Phys.* **23**, 229. [2]
 WERKEMA, G. J. *see* COWAN, MACINTYRE & WERKEMA (1963).
 WEST, H. I., MAYERHOF, W. E. & HOFSTADTER, R. (1951). *Phys. Rev.* **81**, 141. [123]
 WEST, J. *see* BRAGG & WEST (1928).
 WESTCOTT, C. H. (1948). *Proc. R. Soc. A*, **194**, 508. [145]
 WHITEHEAD, C. D. *see* BACON, SMITH & WHITEHEAD (1950).
 WILEY, W. C. *see* GOODRICH & WILEY (1962).
 WILKINSON, D. H. (1950). *Ionization Chambers and Counters* (Cambridge University Press). [107, 110, 112, 113]
 WILLIAMSON, D. T. N. (1960). *Progress in Automation*, **1**, 127. [71]
 WILLIAMSON, G. K. & SMALLMAN, R. E. (1953). *J. scient. Instrum.* **30**, 341. [196]
 WILLIAMSON, R. S. & FANKUCHEN, I. (1959). *Rev. scient. Instrum.* **30**, 908. [190]
 WILLIS, B. T. M. (1960). *Acta crystallogr.* **13**, 763. [208, 211]
 WILLIS, B. T. M. (1962a). *Br. J. appl. Phys.* **13**, 548. [40]
 WILLIS, B. T. M. (1962b). *J. scient. Instrum.* **39**, 590. [213]
 WILLIS, B. T. M. (1962c). In *Pile Neutron Research in Physics*, p. 455. (Vienna: I.A.E.A.) [248, 249]
 WILLIS, B. T. M. (1963). *Proc. R. Soc. A*, **274**, 122. [245, 252]
 WILLIS, B. T. M. (1965). *Acta crystallogr.* **18**, 75. [296]

- WILLIS, B. T. M. *see also* ARNDT & WILLIS (1963a).
 WILLIS, B. T. M. *see also* ARNDT & WILLIS (1963b).
 WILLIS, B. T. M. *see also* ROUSE & WILLIS (1965).
 WILSON, A. J. C. (1942). *Nature, Lond.* **150**, 152. [289]
 WITTE, H. *see* WAGNER, WITTE & WÖLFEL (1955).
 WITTE, H. & WÖLFEL, E. (1955). *Z. phys. Chem.* **3**, 296. [248]
 WÖLFEL, E. *see* WAGNER, WITTE & WÖLFEL (1955).
 WÖLFEL, E. *see also* WITTE & WÖLFEL (1955).
 WOLLAN, E. O. & SHULL, C. G. (1948). *Phys. Rev.* **73**, 830. [3, 205]
 WOLLAN, E. O. *see also* SHULL & WOLLAN (1951).
 WOOD, C. G. *see* COLE, CHAMBERS & WOOD (1961).
 WOOD, C. G. *see* COLE, CHAMBERS & WOOD (1962).
 WOOSTER, W. A. (1965). *J. scient. Instrum.* **42**, 685. [51, 260]
 WOOSTER, W. A. & MARTIN, A. J. P. (1936). *Proc. R. Soc. A*, **155**, 150. [98]
 WOOSTER, W. A. & WOOSTER, A. M. (1962). *J. scient. Instrum.* **39**, 103. [47, 98]
 WOOSTER, W. A. *see also* HARGREAVES, PRINCE & WOOSTER (1952).
 WUENSCH, B. J. (1963). *Acta crystallogr.* **16**, 1259. [298, 299]
 YAKEL, H. L. & FANKUCHEN, I. (1962). *Acta crystallogr.* **15**, 1188. [32]
 YOUNG, R. A. (1963). *Z. Kristallogr. Miner.* **118**, 233. [184 ff.]
 ZACHARIASEN, W. H. (1945). *Theory of X-ray Diffraction in Crystals* (New York: John Wiley). [244, 245]
 ZACHARIASEN, W. H. (1963). *Acta crystallogr.* **16**, 1139. [250]
 ZACHARIASEN, W. H. *Acta crystallogr.* **18**, 705. [252]
 ZINN, W. H. (1947). *Phys. Rev.* **71**, 752. [3]
 ZOCCHI, M. *see* SANTORO & ZOCCHI (1964).

SUBJECT INDEX

- absorbing foils
 for direct beam measurement, 290-1
 hardening of radiation by, 147
- absorption
 and scale factor determination, 290
 neutrons, 137-8
 X-ray, in Ge and Si, 135
 X-ray, in NaI, 128
 X-ray, in noble gases, 106
- absorption coefficient
 neutron, 237, 312
 X-ray, 185, 236, 247-8, 312
- absorption correction, 94, 178, 234-43, 312
 computed, 241, 308
 empirical, 241-3
 for spherical crystal, 237, 257
 accuracy and precision, 268
- accuracy of diffractometer methods, 9, 93
- amplifier
 coupling of counter to, 115-17
 gain, 104, 156
 input impedance, 155
 time constants, 104, 111-14, 116
 upper frequency cut-off, 157
- analogue setting of diffractometer shafts, 7, 73-6
- anisotropic thermal motion, 295
- anomalous dispersion, 313
- anti-equi-inclination setting, 33
 Lorentz factor, 283
- apertures, minimum detector, 267
- Apparatus Commission of the International Union of Crystallography, 3
- arbitrary crystal orientation in normal-beam equatorial method, 51
- area detectors, 56, 147-52
- argon, as counter filling, 105, 106, 121
- arrays, detector, 120, 130, 131
- atomic scattering factor, 277, 292-5
- Auger electrons, 102
- azimuthal orientation, 39 ff., 94, 248, 255-6
- background, counting rate, 117, 119, 126-30, 168
 γ -ray, 139, 143
 effect on counting statistics, 269 ff.
 fast neutron, 139, 143
 general, 220-33
- backstop, X-rays, 172
 barn, 138
- blind regions, 21, 31, 32, 34, 49-51, 94, 306
- blocking condenser, 115-17
- bond length determination, 288, 296
- boron trifluoride, 138, 140-1
 foil absorber, 138
- Borrmann effect, 193-4
- Bremsstrahlung, 169, 180, 227-30
- capacity, counter, 104, 117
 cable, 117, 156
- 'Cascade I'—automatic X-ray diffractometer, 233
- 'Cascade II'—co-ordinate detector system, 150
- cathode follower, 117, 156
- characteristic radiation, 4, 169
- chopper, 214
- circuits, electronic, 154-68
- clamping of shaft, 82
- clipping network, 112-13
- closed-loop operation, *see* on-line control
- code, punched paper tape, 161, 304
- coded discs, 70-1
- cold neutron studies, 215-17
- collimator, neutron, 198 ff.
 X-ray, 171-9
 X-ray, alinement of, 77
- Compton scattering, 231, 313
- computer, data-processing, 5, 95-6, 306-8
- computer programs, 302-11
- cone setting, 39
- confidence level, 269
- continuous spectrum, 169, 180
- convergent beam procedure, 21, 265
- converter foil, 138
- cost of diffractometer methods, 12-13, 96
- counter, 99-153
 area, 147-53
 co-ordinate, 147-53
 gas ionization, for neutrons, 140-2

- counter (*cont.*)
 gas ionization, for X-rays, 101-23
 Geiger, 101-2, 110-11, 119-23, 139
 neutron, 136-44
 proportional, neutrons, 138-42
 proportional, X-rays, 101-20, 180-1
 scintillation, neutrons, 143-4
 scintillation X-rays, 123-32, 180-1
 semi-conductor, neutrons, 142-3
 semi-conductor, X-rays, 132-6
 X-ray, 101-36
- counting losses, 119, 122, 144-7
 counting rate, background, 117, 119,
 126-30, 139
 maximum, 115
 meter, 159-60
 counting statistics, 10, 268-76
 critical angle, X-rays, 195
 cross-section, 138
 crystal alinement, 258-60
 crystal axes, 14 ff.
 assignment of, 260
 sense of, 80, 261
 crystal gazing, xii, 147-53
 crystal mounting, arbitrary, 51, 260,
 306
 crystal size, 174 ff., 257, 312
 crystals for neutron monochromators,
 204-5
 crystals for X-ray monochromators, 189
 cylindrical polar co-ordinates in re-
 ciprocical space, 22-6
- data link, 304
 data processing, 307-8
 data verification, 306
 datum point of shaft, 69, 83
 dead time, Geiger counter, 121
 Debye-Waller factor, 221, 226-7
 decoupling, 163
 detection, neutron, 136-40
 detectors, 99-153
 area, 147-53
 co-ordinate, 147-53
 neutron, 136-44
 X-ray, 101-36
 differentiation, pulse, 112-13
 diffractometer, alinement of, 257
 definition of, 3
 manually set, 66
 on-line operation of, 6, 67
 diffractometers, list of, 97-8
 digitizer, 69-71
 direct beam, determination of, 291
 intensity, 312
- discrimination, X-ray wavelength,
 109-10, 117-18
 X-ray wavelength, at high counting
 rates, 115
 discriminator, 158
 dispersion, X-ray, 174
 dynode, 123
- earth loops, 166
 efficiency, counter, 118-19, 126-8, 139
 EHT, 161
 electronegative gases, 110
 electron multiplier, 132
 channel, 130
 electronic circuits, 154-68
 emitter follower, 117, 156
 encoders, shaft, 69-71
 equatorial and inclination methods,
 correspondence, 52-6
 equi-inclination setting, 31
 Lorentz factor, 283
 error-detection programs, 307
 escape peak, 108-9
 eucentric goniometer head, 79, 260
 Eulerian axes, 38
 Eulerian cradle, 49
 Ewald sphere, 2, 18-20, *et passim*
 extinction, 178, 243-51, 257, 313
 and polarization, 285-6
 primary, 243, 313
 revealed by absolute measurements,
 288
 secondary, 244, 313
- field-effect transistor, 155-6
 filters, balanced, 84, 92, 182-7
 beta, 182-3
 EHT, 161
 neutron, 206, 216
 fission chamber, 142
 fixed- χ setting, 47, 81
 flat-cone setting, 34, 58
 Lorentz factor, 283
 flat-topped peak procedure, 21
 fluorescence photons, 124
 fluorescence scattering, 230, 313
 focus, X-ray tube, 78, 170
 focusing effect, neutron diffracto-
 meters, 208
 foreshortening of X-ray tube focus,
 78, 170-1
 form factor of X-ray source, 145-6
 four-circle diffractometer, 37, 82
 comparison with linear diffracto-
 meter, 93-6

- gas
 amplification, 103, 140
 multiplication, 103
 gases, filling for counters, 101
 general inclination method, 28-30
 geometry, types of diffraction, 7, 14-
 64
 glass scintillators, 143-4
 goniometer-head axis, 22
 goniometer heads, 51, 79
 goniostat, 37
- harmonic approximation, 295
 harmonic content of neutron beam,
 205-6
 helium-3, 141
 high voltage supply, 161
 Hilger-Ferranti diffractometer, 82-8
 hole, semi-conductor, 132
 hunting for a reflexion, 66
- image intensifier, 150
 impulse motor, 72
 inaccessible reflexions, 21, 31, 32, 34,
 49-51, 94
 inclination and equatorial methods,
 correspondence, 52-6
 inclination method, 14
 Lorentz factor, 279
 incoherent scattering, neutrons, 231,
 313
 X-rays, 230-1, 313
 inelastic scattering, neutrons, 4, 224-6
 X-rays, 221-7
 integrated intensity, 20, 277
 definition, 234
 measurement of, 8
 mosaic and perfect crystals, 285
 integrated reflexion, 20, 277
 definition, 234
 integration, pulse, 112-14
 interrupt signal, 310-1
 ionization energy, 132
 ionization of gas by X-rays, 101 ff.
 ionization chamber, 1, 103-4, 107
 use in determining intensity of
 direct beam, 291
 isotope incoherence, 231
- kicksorter, 109
 krypton, as counter filling, 105-6,
 121
- labyrinth, ray-proof, 76
 lattice parameter, 260
- measurement of, 262
 refinement of, 264
 Laue method for neutrons, 152, 217-
 19
 limiting sphere, 31
 linear diffractometer, 63, 73-6, 88-92
 comparison with four-circle diffrac-
 tometer, 93-6
 logic circuits, 154-5
 Lorentz factor, 21, 76, 277
 computed for various geometries,
 278-83
 definition of, 278
- machine code, 305
 magnetic structures, 212
 Maxwellian distribution, 201
 microdensitometer, 2, 11
 Moiré-fringe measuring system, 71,
 82
 monitoring, 146
 and counting statistics, 274
 X-ray primary beam, 195-7
 monochromators, neutron, 203 ff.
 X-ray, polarization correction, 189
 X-ray, polarization factors, 286-7
 monochromators, X-ray, 188-94
 focusing, 190
 plane, 189
 point focusing, 192
 polarizing, 192-4
 mosaic crystal, ideally, 243
 integrated intensity, 285
 mosaic spread, 174, 243, 248
 of neutron monochromator crystals,
 203, 211
 Mössbauer effect, 222
 motor drive, diffractometer, 71
 moving-crystal-moving-detector pro-
 cedure, 20
 moving-crystal-stationary-detector
 procedure, 20
 multiple-counter technique, 12, 56-64,
 88, 120, 130-1, 256
- neutron diffractometry, compared with
 X-ray diffractometry, 3, 312-14
 neutron spectrum, 201
 noise, amplifier, 104, 136
 scintillation counter, 130, 159
 normal-beam equatorial method, 14,
 37-52
 comparison with inclination method,
 52 ff.
 Lorentz factor, 278

- normal-beam setting, 30, 148
 Lorentz factor, 282
 nuclear reaction energy, 137
 nuclear scattering amplitude, 277, 294-5
 off-set angle, 40 ff.
 off-set χ -circle, 49
 omega-scan, 20, 94
 compared with omega/two theta scan, 227-30, 265-7
 omega/two theta scan, 20, 94
 on-line operation of diffractometers, 6, 67, 88, 147, 232-3, 308-11
 optimization of counting statistics, 274-6
 order code, 87
 oscillation mechanism, 72, 76, 90
 oscilloscope, 166
 'Paired', 75
 paralysis time, 122, 145-6
 parasitic scattering, 232
 pass band, balanced filters, 184-7
 peak hunting, 233
 peak to background ratio, 310
 effect on counting statistics, 269 ff.
 phase problem, 277
 phonon interactions, 224-6
 phosphor, neutron, 144
 X-ray, 123 ff.
 photo cathode, 124
 photo-electron, 102-3, 124
 photographic methods, 2, 10, 173
 cost of, 12
 photomultiplier, 123 ff.
 pile-up, 114, 142
 plateau, Geiger counter, 121
 polarization factor, 277, 314
 definition, 284
 monochromatized radiation, 286-7
 pre-amplifier, 117, 156-7
 polarization of X-rays, 146-7, 192-4
 dependent on monochromator perfection, 189
 precession camera, 2, 11
 precision and accuracy, 268
 protein structures, 11, 56
 pulse, generator, 166
 shape discrimination, 130, 143, 159
 shape in ionization counter, 110-11
 shaping, 111-14
 size in ionization counter, 103 ff., 114, 119
 size in scintillation counter, 125
 size in semi-conductor counter, 135-6
 pulse height analysis, 105, 180, 314
 single channel, 109, 158-9, 167, 187
 pulse shapes, correct, 167
 punched cards, 67, 161, 232
 compared with punched paper tape, 303-4
 punched paper tape, 67, 86, 161, 232
 compared with punched cards, 303-4
 quantum, X-ray energies, 103
 quasi-simultaneous reflexions, 59 ff.
 quenching agent, 121
 circuit, 122-3
 R-index, 196, 198, 291, 301
 radiation damage, 11, 308
 of monochromator crystals, 189
 radiation hazard, 76-7
 radioactive sources, 168
 rate-meter, 159-60
 reciprocal lattice, 14, 15
 unit, 17
 recovery time, Geiger counter, 122, 145
 reference reflexions, 95, 268, 308
 reflecting circle, 26
 reliability of electronic circuits, 96
 Renninger effect, 234, 251-6
 resolution of neighbouring reflexions, X-rays, 174, 178, 230
 neutrons, 200
 resolving time of detector, 144 ff.
 rocking range, and background, 232
 minimum, 267
 neutron, 211 ff.
 quasi-simultaneous measurements, 59 ff.
 X-ray, 173-4
 rock-salt, structure of, 296
 scale factor, 278, 288
 determination of, 290
 scaler, 160
 scintillators, neutron, 144
 X-ray, 123 ff.
 setting angles, inclination method, 28-35, Table II
 normal-beam equatorial method, 44-52, Table III
 setting programs, 305
 shaft-setting methods, 66
 absolute, 68
 digital, 67-72
 incremental, 68

- shielding, of neutron detector, 143, 139
 radiation, 76-7
 signal-to-noise ratio, amplifier, 114, 164-5
 simultaneous reflexions, 32-3, 51, 56-64, 94, 234, 251-7
 single crystal orienter, 37
 slewing speed, shaft, 71-2, 83
 source block, 199
 spark chamber, 150
 spectra, X-ray and neutron, 4, 312
 spectrometer, ionization, 1, 3
 definition of, 3
 triple-axis, 3
 speed of diffractometer methods, 11, 64, 94
 sphere grinder, 258
 spherical approximation, 293
 spin incoherence, 231
 stabilized power supplies, 162-3
 for X-ray tubes, 171
 standard deviation, 269
 standard orientation of crystal, 28, 38
 standard reflexions, 95, 268, 308
 starting voltage, Geiger counter, 121
 staticizer, 68
 stationary-crystal-stationary-detector procedure, 21
 statistical method of determining absolute structure factors, 289
 statistics, counting, 10, 268-76
 of gas multiplication, 106-7
 of rate-meter, 160
 of scintillation counter pulse height, 125
 store, setting, 68-9
 structure factors, 234
 absolute measurements, 288-91
 calculated, 291-6
 definition of, 289
 derivation and accuracy of, 277-302
 suppression of inductive surges, 163-4
 symmetrical-A setting, 39, 45
 symmetrical-B setting, 43, 47
 take-off angle, 78, 83, 170-1
 teleprinter, 86, 96, 304
 television camera, 150
 temperature factor, 221, 226, 289, 292, 295-6
 tetrahedrite, structure of, 298-9
 thermal diffuse scattering, 221-7, 313
 thermal parameters, 288, 295
 three-circle diffractometer, 37
 time constant, amplifier, 104, 111-14, 116
 rate meter, 160
 time-of-flight experiments, 143, 152-3, 216-19, 314
 time sharing, computer, 310
 of setting device, 69, 88
 top/bottom masks, 172, 260
 total reflexion, 179
 Townsend avalanche, 103
 transistors, compared with valves, 155
 two-theta scan, 20
 Umweganregung, 253
 uncertainty, statistical, 268
 unit cell, 14
 uranium dioxide, structure of, 299-302
 valves, compared with transistors, 155
 velocity, neutron, 201, 216, 314
 velocity selector, neutron, 214
 Weissenberg camera, 2, 14, 26, 148
 white radiation, 169, 180, 227-30
 window, counter entrance, 101, 105, 121
 pulse height analyser, 109, 158
 xenon, as counter filling, 105-6
 X-ray diffractometry, compared with neutron diffractometry, 3, 312-14
 X-ray tubes, 170
 X-rays, wavelengths and energies, 130
 Zener diode, 164

Acta Cryst. (1966). **21**, 175

A note on Burbank's paper on 'Intrinsic and systematic multiple diffraction'. By B. T. M. WILLIS, *Metallurgy Division, A.E.R.E., Harwell, England*

(Received 20 January 1966)

Burbank (1965) has recently discussed under the title *Intrinsic and Systematic Multiple Diffraction* the conditions giving rise to multiple diffraction for the single-crystal orienter and for the precession camera. He concludes that there are important differences between the two techniques. For the single-crystal orienter, multiple diffraction will always occur if the crystal is mounted with a symmetry axis parallel to, or a symmetry plane normal to, the rotation axis (φ axis). For the precession camera, the conditions for multiple diffraction can be created or avoided at will by the choice of μ , regardless of crystal orientation. Burbank suggests that the zero-level precession technique is the only method in common use which offers the possibility of direct experimental observation of the magnitude of multiple diffraction effects.

The purpose of this note is to point out that there are no such differences between the two techniques if the orienter is used as a four-circle instrument with independent motion of the ω and 2θ axes. Although the original single-crystal orienter described by Furnas (1957) was a three-circle diffractometer, the majority of instruments commercially available today have four independent axes: the direct experimental observation of multiple diffraction with these four-circle instruments has been fully described by Willis (1962) and by Santoro & Zocchi (1964). The situation discussed by Burbank corresponds to the use of the orienter as a three-circle instrument, with the angle ε between the χ plane and the normal to the hkl plane under observation as zero. This $\varepsilon=0$ (or 'symmetrical A' ') setting is formally equivalent to the equi-inclination Weissenberg setting (Phillips, 1964) and gives rise, therefore, as Burbank shows in another way, to multiple diffraction under the same conditions as for the equi-inclination setting (Yakel & Fankuchen, 1962).

The limitation of Burbank's analysis to the $\varepsilon=0$ setting is apparent in his answer to the question: Is there a reciprocal lattice plane coincident with the vertical circle of reflexion? Burbank states that, if the crystal is oriented with a reciprocal lattice vector along the rotation axis (the φ axis of the single-crystal orienter), there will be a reciprocal lattice plane coincident with the vertical circle of reflexion. This is true only if the φ axis is in the plane of the vertical circle of reflexion. The φ axis is mechanically constrained to lie in the vertical χ plane, and the vertical circle of reflexion and the vertical χ plane are in coincidence for $\varepsilon=0$ but not in the general case, $\varepsilon \neq 0$.

The essential *similarity* of the precession and single-crystal orienter techniques as regards observing multiple diffraction effects is strikingly illustrated by reference to the last section of Burbank's paper. The procedure described there for creating or avoiding at will multiple diffraction with the precession technique is exactly paralleled for the orienter technique. If a symmetry axis of the crystal is parallel to the φ axis of the orienter, the hkl intensity is first recorded with a zero off-set angle ε , corresponding to the condition for intrinsic multiple diffraction. ε is then given a small increment, positive or negative, sufficient to destroy the multiple diffraction condition, and the intensity re-measured. Any difference in the two intensities is due to multiple diffraction.

References

BURBANK, R. D. (1965). *Acta Cryst.* **19**, 957.
PHILLIPS, D. C. (1964). *J. Sci. Instrum.* **41**, 123.
SANTORO, A. & ZOCCHI, M. (1964). **17**, 597.
WILLIS, B. T. M. (1962). *Brit. J. Appl. Phys.* **13**, 548.
YAKEL, H. L. & FANKUCHEN, I. (1962). *Acta Cryst.* **15**, 1188.

Papers 28-41

4. Neutron Crystallography (28-41)

These papers are concerned with various investigations in the neutron diffraction field. They include studies of anharmonic lattice vibrations in uranium dioxide and calcium fluoride, the determination of hydrogen atom positions in ferrocene and in vitamin B₁₂, the solution of the magnetic structure of UO₂, and miscellaneous papers on extinction, double-Bragg scattering and anomalous dispersion.

15.8. Three-dimensional neutron diffraction study of ferrocene. By B. T. M. WILLIS, *Atomic Energy Research Establishment, Harwell, Didcot, Berks., England.*

Ferrocene has been examined in order to determine the hydrogen atom positions and to investigate the suggestion of J. W. Edwards, G. L. Kington & R. Mason, *Trans. Faraday Soc.* (1960), to be published, based on thermodynamic grounds, that the cyclopentadienyl rings are rotationally disordered at room temperature. A number of attempts were made to solve the structure by a least-squares analysis of two-dimensional F_{h0l} and F_{hk0} data; these proved only partially successful, because the ratio of the number of measured F values to the number of unknown parameters was too small. The spectrometer was accordingly modified to allow collection of full three-dimensional F_{hkl} data.

The modification consists of the addition of a two-circle device to the spectrometer table, which acts as the third circle. By mounting the crystal on the innermost circle and rotating the three circles through appropriate angles, each (hkl) plane of the crystal can be brought into the Bragg reflecting position, with the reflected neutron beam entering the counter moving in the horizontal plane. The choice of these three angles is not unique, but for one set the normal to the (hkl) plane lies in the plane of the vertical circle. The advantage of this method of setting is that three-dimensional data can be obtained from a pillar-shaped crystal with approximately the same accuracy (with respect to absorption and extinction) as two-dimensional data, obtained with a conventional (one-circle) spectrometer by rotating the crystal about its long axis.

The analysis of the three-dimensional data indicated that the hydrogen atoms were in the planes of the rings and that the rings were rotationally disordered.

UNCLASSIFIED

AERE - R 3708

(Approved for Publication)

A THREE-DIMENSIONAL NEUTRON DIFFRACTION

STUDY OF FERROCENE

by

B.T.M. WILLIS.

ABSTRACT

The analysis of three-dimensional neutron diffraction data indicates that at room temperature the crystal structure is disordered, with the molecules assuming two different orientations in the proportion 2:1. The interpretation of the thermodynamic data of Edwards, Kington & Mason leads to a similar conclusion. The hydrogen atoms are coplanar with the carbon atoms of the cyclopentadienyl ring, and the C-H distance is 1.09 Å.

Metallurgy Division,
U.K.A.E.A. Research Group,
Atomic Energy Research Establishment,
HARWELL

April, 1961.

HL61/2300

(C.16)

CONTENTS

1. Introduction.
 2. Experimental.
 3. Analysis of data.
 4. Discussion.
- Acknowledgements.

ILLUSTRATIONS

- Figure 1. Diagram of molecular structure of ferrocene.
- Figure 2. (a) Projection of nuclear density on (001). The full lines are the positive contours for the iron and carbon atoms; the broken lines are the negative contours for the hydrogen atoms.
- (b) Projection on (001) of Dunitz structure used for calculating signs of $F(hk0)$ in (a). Comparison of (a) and (b) shows extra negative peaks in $\rho(xy)$ plot.
- Figure 3. Various hypothetical configurations of the ferrocene molecule within the lattice. I and II are staggered, III and IV eclipsed.
- Figure 4. R_1 and R_2 plotted against the proportion of configuration I.
- Figure 5. R_1 plotted against the normal displacement of the hydrogen atoms from the plane of the carbon ring.
- Figure 6. R_1 plotted against the average length of the C-H bond.

1. Introduction

X-ray diffraction studies of $\text{Fe}(\text{C}_5\text{H}_5)_2$ (bis-cyclopentadienyl iron, or ferrocene) have been reported by Eiland & Pepinsky⁽¹⁾, Pfab & Fischer⁽²⁾, Dunitz & Orgel⁽³⁾ and Dunitz, Orgel & Rich⁽⁴⁾. The most complete work is that of Dunitz, Orgel & Rich, who carried out a three-dimensional Fourier and least-squares analysis of the crystal and molecular structure. The X-ray results indicate that the space-group is $P2_1/a$ and that the molecule has a sandwich structure (figure 1) with the iron atom centrally placed between two staggered cyclopentadienyl rings.

The original aim of the neutron investigation was to locate the hydrogen atoms. Later it was realised that the crystal structure may be disordered and that three-dimensional data were therefore required. Thus additional aims were to establish a technique for collecting three-dimensional neutron data and to investigate the possibility of disorder.

2. Experimental

Crystals were grown from solution in benzene-ligroin (60-80°C) and mounted on the single-crystal equipment described by Bacon & Dyer⁽⁵⁾. Two-dimensional $hk0$ data were collected from a needle-shaped crystal (A) with a cross-section of 1.0mm x 0.8mm normal to the rotation axis. 58 reflexions were measured for $\sin \theta/\lambda < 0.5$; no reflexions were measured at higher Bragg angles as their peak intensities were less than twice the background intensity. 40 $h0l$ reflexions were also measured on a second crystal (B).

Systematic absences in the neutron reflexions confirmed that the space-group is $P2_1/a$. Values of $a \sin \beta/b$ and $a \sin \beta/c$ were determined by measuring the angles between equivalent reflexions, and these values were in much closer agreement with the lattice parameters of Pfab & Fischer than with those of Dunitz et al. The Pfab & Fischer parameters were accordingly adopted in the subsequent analysis:

$$a = 10.51\text{\AA}, b = 7.52\text{\AA}, c = 5.91\text{\AA}, \beta = 121.1^\circ.$$

Preliminary analysis of the two-dimensional data (see § 3) indicated that the cyclopentadienyl rings were rotationally disordered, and that the structure required at least twice as many independent parameters to specify it as for the ordered Dunitz structure. To obtain a more favourable ratio of the number of observed reflexions to the number of independent atomic parameters full

three-dimensional data were collected on a third crystal (C), a diamond-shaped plate bounded by {110} and {001}.

For three-dimensional work the spectrometer was converted to a three-circle instrument by attaching two circles, ϕ and χ ⁽⁶⁾, to the central specimen table. The crystal was placed on a goniometer head attached to the inner ϕ -circle, and the reflexions were measured by bringing the normal to each (hkl) plane in turn to the Bragg reflecting position in the equatorial plane. In this way three-dimensional data were collected without tilting the BF₃ counter, weighing with its shielding about 100 lb., out of the horizontal plane. A useful feature of a three-circle instrument for neutron work is that the single-crystal can be rapidly and accurately aligned by observing a single reflexion with the ϕ -axis in the horizontal position, parallel to the incident beam.

The integrated intensities of 215 hkl reflexions were measured and each was corrected for absorption ($\mu = .22\text{mm}^{-1}$) using the Mercury computer programme written by N.A. Curry. Secondary extinction was corrected for by measuring the strongest reflexions for different path lengths of the neutron beam in the crystal⁽⁷⁾. The intensity of 001 was reduced 20% by extinction, but the remaining reflexions were reduced in intensity by less than 8%. Relative F² values were obtained by multiplying the corrected integrated intensities by the Lorentz factor, $\sin 2\theta$.

The accuracy of the F(hkl) data was estimated by comparing the two-dimensional hk0 data for crystal A and h0l data for B with the corresponding data for C. Thus the "unreproducibility factors", defined as

$$\frac{\sum_{hk0} \left| |F|^A - |F|^C \right|}{\sum_{hk0} |F|^C} \quad \text{and} \quad \frac{\sum_{h0l} \left| |F|^B - |F|^C \right|}{\sum_{h0l} |F|^C}$$

were 5.5% and 9% respectively. The overall reproducibility of the complete hkl data was probably about 10%. This is a high figure, indicating relatively poor reliability, and is mainly due to the large number of weak reflexions.

3. Analysis of data

As a starting point the atomic co-ordinates of Dunitz were used for the iron and carbon atoms, and the hydrogen atoms were assumed to lie in the plane of the cyclopentadienyl ring at 1.0Å from the neighbouring carbon atoms

(figure 2(b)). The Dunitz temperature factors of $\exp(-5.5 \sin^2 \theta / \lambda^2)$ for the carbon atoms and $\exp(-3.2 \sin^2 \theta / \lambda^2)$ for the iron atom were adopted, together with an assumed temperature factor of $\exp(-7.0 \sin^2 \theta / \lambda^2)$ for the hydrogen atoms. The nuclear density function $\rho(xy)$ was computed using signs given by this model and the observed values of $|F(hk0)|$. The carbon atoms in this projection (figure 2(a)) are not well resolved, but the hydrogen atoms, being further apart, appear as distinct negative peaks. Between the main hydrogen peaks subsidiary negative peaks appear, and these cannot be ascribed to an extinction effect, as extinction is small and has already been accounted for. In the X-ray case (4) an accumulation of electron density was observed between carbon atoms of the cyclopentadienyl ring, but Dunitz considered it to be spurious and arising from extinction. Dunitz pointed out that the accuracy of his data was severely limited by absorption and extinction errors, but both of these are relatively small in the neutron case.

It was concluded that at room temperature the crystal structure of ferrocene is disordered, with each molecule assuming one of two or more different configurations. Two possible configurations of the molecule in the crystal are I and II in figure 3 : I is the staggered Dunitz configuration and II the staggered configuration related to I by a rotation of 36° ($2\pi/10$) about the five-fold molecular axis. Eclipsed configurations such as III and IV are ruled out if the space-group is $P2_1/a$.

The "unreliability factors"

$$R_1 = \frac{\sum_{hkl} \left| |F_o| - |F_c| \right|}{\sum_{hkl} |F_o|}$$

$$\text{and } R_2 = \left[\frac{\sum_{hkl} (|F_o| - |F_c|)^2}{\sum_{hkl} F_o^2} \right]^{1/2}$$

for the ordered structure (configuration I only) were 34% and 45% respectively.

These fell rapidly when the F_c 's were re-calculated, allowing an admixture of configurations I and II. Figure 4 shows R_1 and R_2 plotted against the proportion, p_1 , of configuration I. Both curves pass through a minimum near $p_1 = 67\%$, indicating that the best fit is given by a mixture of the two configurations in the proportion 2 : 1 of I : II.

Least-squares refinement of the data beyond this stage, varying the

atomic parameters of both I and II and using anisotropic temperature factors, was not possible. However, refinement proceeded if the atomic parameters of II were kept fixed, and after three cycles an R_1 value of 12.8% was attained. The final isotropic B factors were 3.1 \AA^2 (iron), 4.5 \AA^2 (carbon) and 8.9 \AA^2 (hydrogen). Re-calculation of the R_1 versus p_1 curve gave a minimum at the same position of p_1 as in figure 4.

Because of the inadequacy of the data it was decided to confine further analysis to the determination of two quantities: the displacement, if any, of the hydrogen atoms from the plane of the carbon ring, and the average length of the C-H bond. Using the disordered 2 : 1 model and assuming ideal five-fold D_{5d} molecular symmetry R_1 was recalculated as a function of the normal displacement, Δ , of the hydrogen atoms from the ring. The curve in figure 5 shows that R_1 is a minimum for $\Delta = 0$ and that the hydrogen atoms must be within an average distance of 0.01 \AA from the plane of the cyclopentadienyl ring. In a similar way figure 6 shows that the average length of the C-H bond is $1.09 \pm 0.01 \text{ \AA}$.

4. Discussion

The co-planarity of the carbon and hydrogen atoms indicates that there is little, if any, hybridisation of the hydrogen orbitals with the orbitals of the iron atom. The C-H bond length of 1.09 \AA fits in well with the scheme of Vainshtein (9) relating C-H distance with aromaticity.

No extra reflexions were observed, and so the two orientations, I and II, are presumably distributed randomly throughout the crystal. The disordered 2 : 1 model is strongly supported by the work of Edwards, Kington & Mason, who observed a λ -type anomaly at 164°K in the heat capacity versus temperature curve and attributed the extra entropy associated with the λ -change to a transition from a perfectly ordered to a partially disordered structure. The extra entropy per mole, S , is given by

$$S = -R [p_1 \ln p_1 + p_2 \ln p_2 + p_3 \ln p_3 \dots]$$

where R is the Gas Constant and $p_1, p_2, p_3 \dots$ are the mole fractions of the configurations in the disordered state. The neutron analysis indicates that $p_1 = 0.67, p_2 = 0.33, p_3 \dots = 0$, giving a calculated entropy of $R \ln 1.89$, in agreement with the observed value of $R \ln (1.89 \pm 0.02)$. For $p_1 = 1, p_2 = 0$ (no

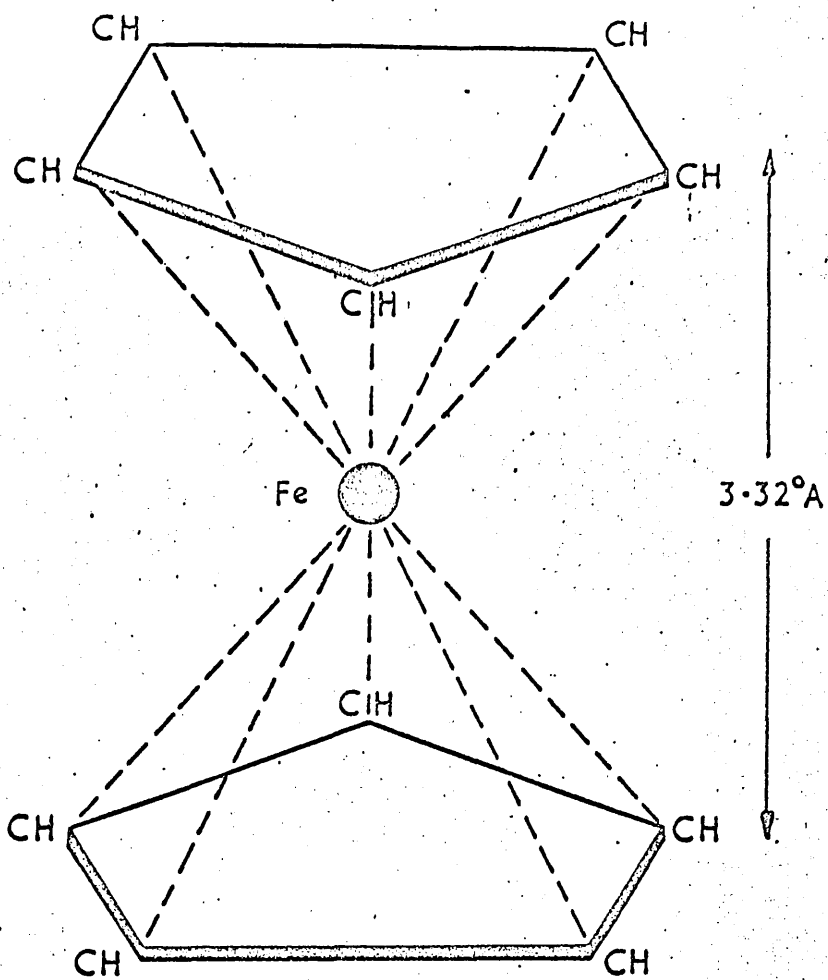
disorder: Dunitz model) the calculated entropy is $R \ln 1 (= 0)$, and for $p_1 = p_2 = 0.5$ (random mixture of I and II in equal proportions) the entropy is $R \ln 2$.

Acknowledgements

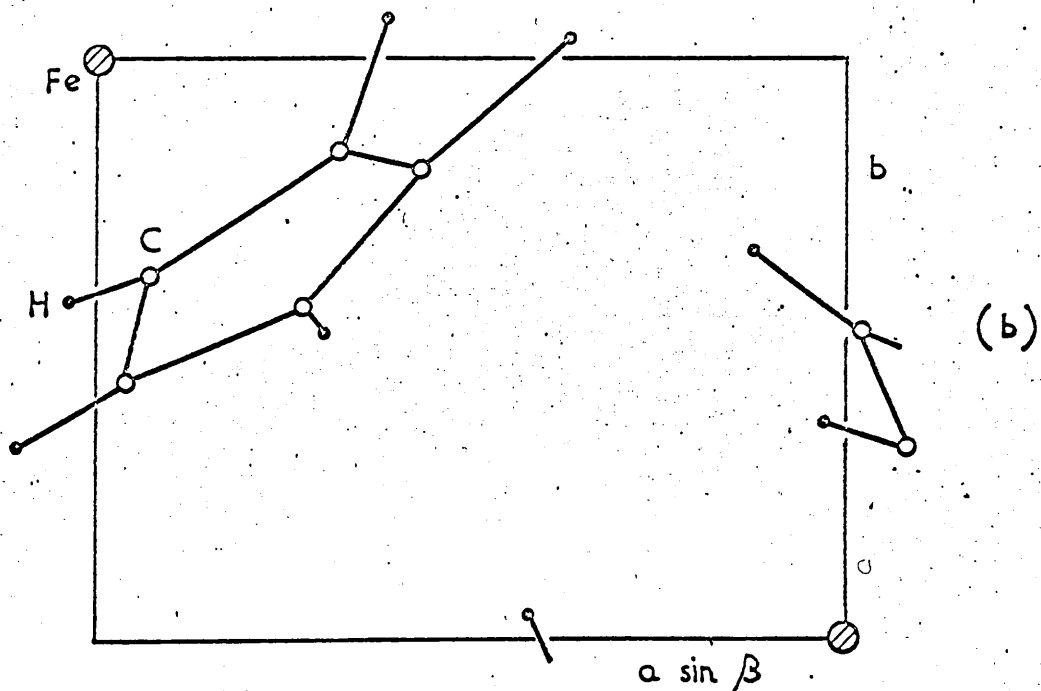
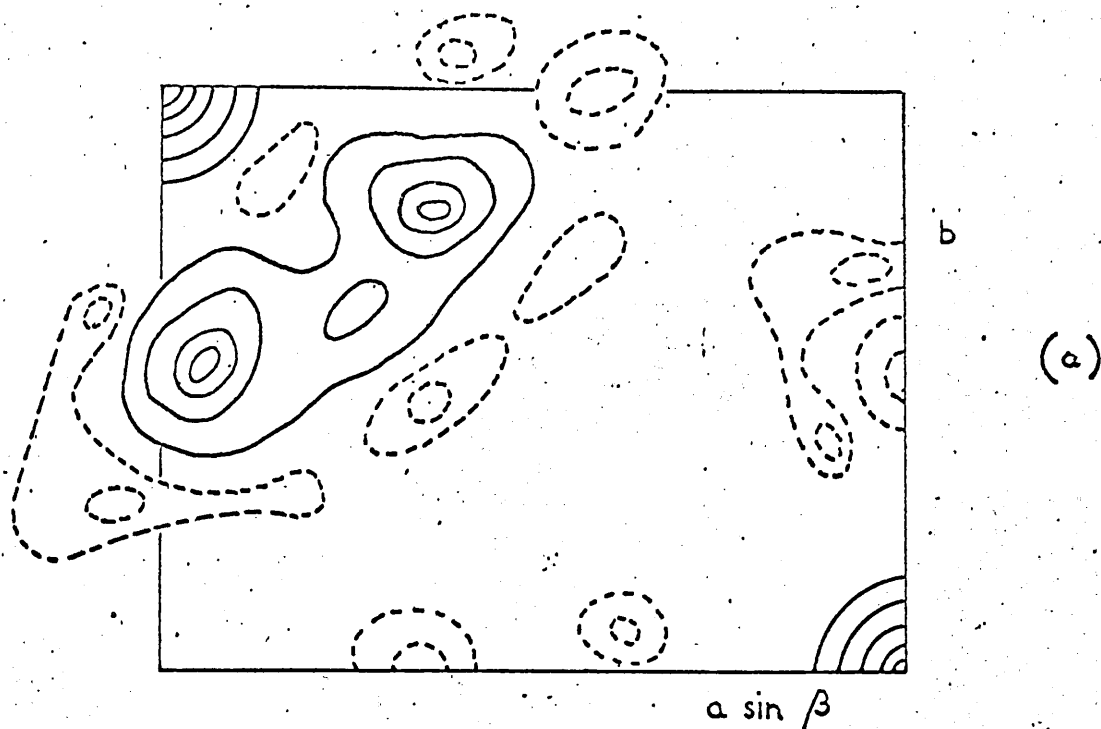
I wish to thank Mr. S.A. Wilson for growing the crystals; Dr. H.J. Milledge London University, for considerable help in analysing the data; Dr. J.S. Rollett, Oxford University, for providing three-dimensional computer programmes; and Dr. J.W. Edwards, London University, for communicating his results on the thermodynamic data before publication.

References

1. Eiland, P.F. & Pepinsky, R. (1952). J. Amer. Chem. Soc. 74, 4971.
2. Pfab, W.P. & Fischer, E.O. (1953). Z. anorg. and allg. Chem. 274, 317.
3. Dunitz, J.D. & Orgel, L.E. (1953). Nature, Lond. 171, 121.
4. Dunitz, J.D., Orgel, L.E. & Rich, A. (1956). Acta Cryst. 9, 373.
5. Bacon, G.E. & Dyer, R.F. (1959). A.E.R.E. Report. R.2984.
6. Willis, B.T.M. (1961). Acta Cryst. 14, 90.
7. Willis, B.T.M. (1961). To be published.
8. Edwards, J.W., Kington, G.L. & Mason, R. (1960). Trans. Far. Soc. 56, 660.
9. Vainshtein, B.K. (1960). Quart. Rev. 14, 105.



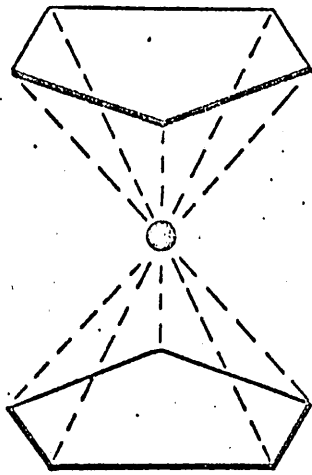
AERE. R. 3708.
FIG. I. DIAGRAM OF MOLECULAR STRUCTURE
OF FERROCENE.



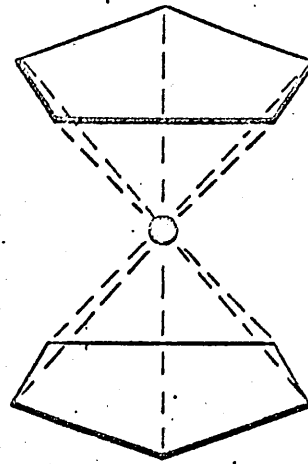
AERE. R. 3708.

FIG. 2. (a) PROJECTION OF NUCLEAR DENSITY ON (00). THE FULL LINES ARE THE POSITIVE CONTOURS FOR THE IRON AND CARBON ATOMS; THE BROKEN LINES ARE THE NEGATIVE CONTOURS FOR THE HYDROGEN ATOMS.

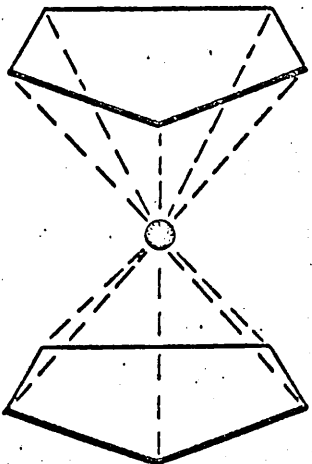
(b) PROJECTION ON (00) OF DUNITZ STRUCTURE USED FOR CALCULATING SIGNS OF $F(hk0)$ IN (a). COMPARISON OF (a) AND (b) SHOWS EXTRA NEGATIVE PEAKS. IN $\rho(x,y)$ PLOT.



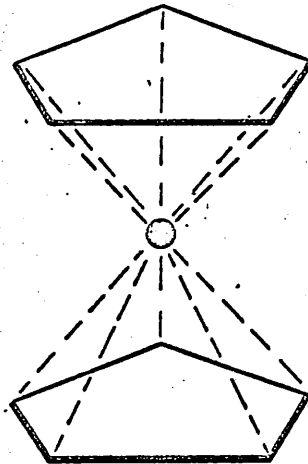
I



II



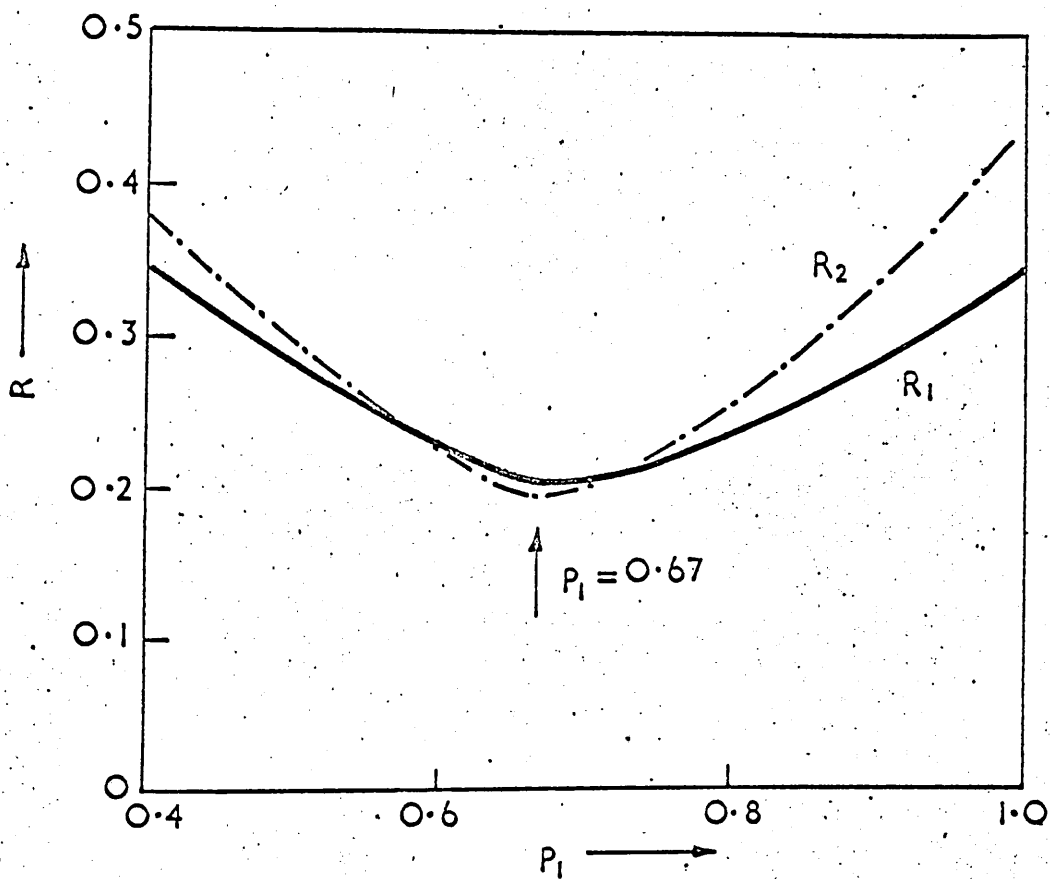
III



IV

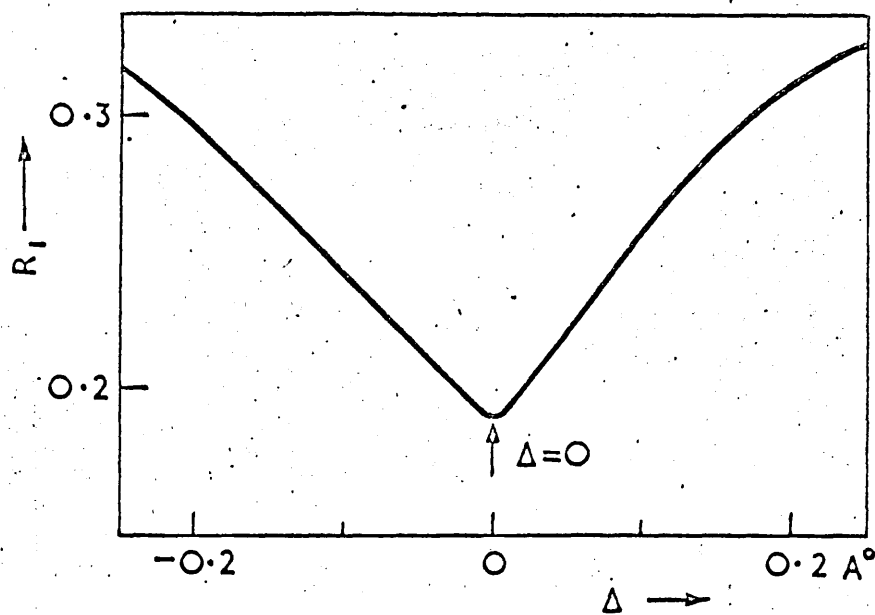
AERE. R. 3703.

FIG. 3. VARIOUS HYPOTHETICAL CONFIGURATIONS OF THE FERROCENE MOLECULE WITHIN THE LATTICE. I AND II ARE STAGGERED, III AND IV ECLIPSED.



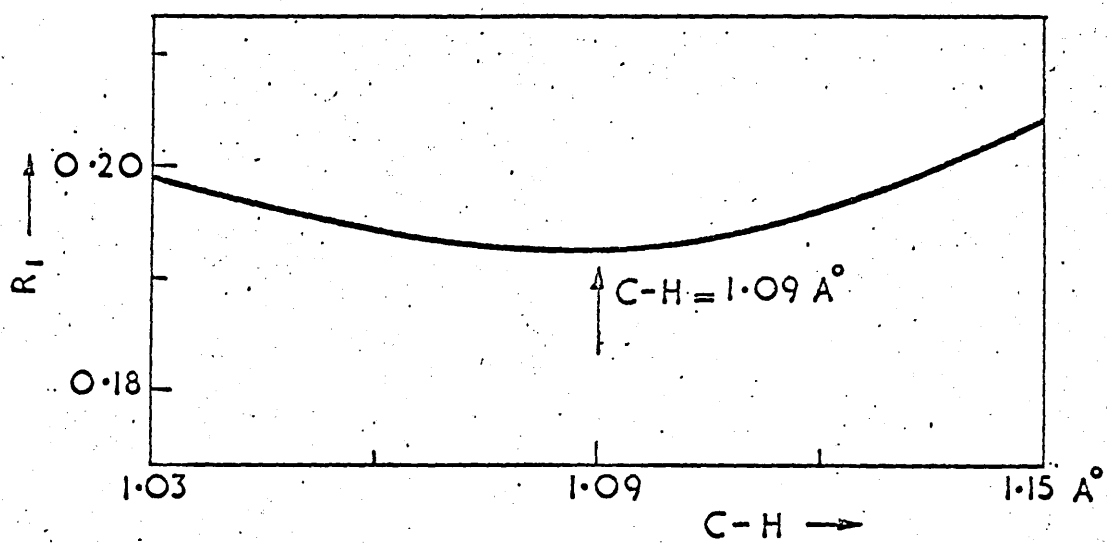
AERE. R. 3708.

FIG. 4. R_1 AND R_2 PLOTTED AGAINST P_1 , THE PROPORTION OF CONFIGURATION I.



AERE. R.3708.

FIG. 5. R_1 PLOTTED AGAINST THE NORMAL DISPLACEMENT OF THE HYDROGEN ATOMS FROM THE PLANE OF THE CARBON RING.



AERE. R. 3708.

FIG. 6. R_1 PLOTTED AGAINST THE AVERAGE LENGTH OF THE C-H BOND.

UNCLASSIFIED
(Approved for Sale)

AERE R.3818

THE MEASUREMENT AND INTERPRETATION
OF DIFFRACTION LINE PROFILES

*
Papers presented at the

Fifth Colloquium

of the

U.K.A.E.A. Diffraction Analysis Conference

held at Bournemouth

March 9th and 10th 1961

Edited by M.H. Rand

* The paper presented by the candidate is the only paper included here.

Chemistry Division,
U.K.A.E.A. Research Group,
Atomic Energy Research Establishment,
HARWELL

April, 1962

HL62/1665 (C.16)
RR

THE INTERPRETATION OF TOTAL INTENSITY MEASUREMENTS

IN X-RAY AND NEUTRON DIFFRACTION

by

B.T.M. Willis (Harwell)

INTRODUCTION

1. The total intensity, or "integrated reflexion", ρ_{hkl} is an experimental quantity connected with the structure factor F_{hkl} by the equation:

$$\rho_{hkl} = m_{hkl} L_{hkl} P_{hkl} A_{hkl} E_{hkl} |F_{hkl}|^2 \quad \dots\dots(1)$$

Here m is the multiplicity factor, L and p the Lorentz and polarisation factors, A the absorption factor and E the extinction factor; all these factors depend on the indices hkl of the reflecting plane. The multiplicity factor accounts for the overlapping of reflexions from equivalent planes; it is listed for all classes of symmetry in the International Tables for X-ray Crystallography. L and p are geometrical factors, determined by the experimental technique chosen and similarly listed. The remaining factors A , E and $|F|^2$ are physical quantities related to the properties of the sample under investigation.

2. This report is concerned with the factors A and E and with that part of the factor $|F|^2$, normally called the temperature factor, which is determined by the thermal vibration of the atoms. We shall see how measurements of the total intensity can give information about physical properties such as the amplitudes of atomic vibration and the 'mosaic spread'. Equation (1) applies equally to X-rays and neutrons but interesting differences occur in the scattering of X-rays and neutrons by the same sample, and so both kinds of data will be freely discussed below.

ABSORPTION FACTOR

3. When a beam of X-rays or neutrons irradiates a sample, it is absorbed as well as scattered, and, in relating the total intensity to the intensity scattered by an atomic plane, a correction must be made for the amount by which the incident and scattered beams are absorbed within the sample. In Fig. 1 the incident beam travels a distance t_1 in the sample before it is scattered by the volume element dV , and the scattered beam then traverses a distance t_2 before leaving the sample. The absorption factor for

radiation scattered by dV is therefore $e^{-\mu(t_1+t_2)}$, where μ is the linear coefficient of absorption. The total absorption factor A is given by

$$A = \frac{1}{V} \int e^{-\mu(t_1+t_2)} dV, \quad \dots\dots(2)$$

where the integration is over the volume of sample bathed in radiation. Tables of A are available for certain special cases such as cylindrical samples and powder camera geometry. Many graphical methods have been devised for other cases but the most satisfactory way of calculating A is by means of a computer. A programme for calculating the absorption factor for a crystal with plane faces but arbitrary shape has been written by N.A. Curry for the Mercury computer; the input data consist of μ , the xyz coordinates of the corners of the crystal and its orientation with reference to a fixed plane.

4. It is interesting to compare the absorption factors for X-rays and neutrons. For X-rays the absorption cross-section is normally much larger than the scattering cross-section, whereas the reverse is the case with neutrons. Table 1 compares the linear absorption coefficients of a number of elements for both X-rays and neutrons. Boron has a higher μ value for neutrons but this is exceptional, and is not even true for cadmium, which has a very large absorption cross-section for thermal neutrons.

TABLE 1

Element	Absorption coefficient $\mu(\text{cm}^{-1})$	
	X-rays (1.54Å)	Neutrons (1.0Å)
Boron	7.6	60
Iron	2,570	0.1
Cadmium	2,020	97
Natural Uranium	6,600	0.3

A neutron beam is hardly attenuated in passing through several mm of uranium, whereas X-rays are absorbed by a layer less than 10 microns thick. This means that unless the sample is only a few microns in size X-rays are scattered from the surface only, and to study, for instance, the preferred orientation in uranium bars by diffraction methods, neutrons can be used but not X-rays. The evaluation of the absorption factor for compounds of

the heavy elements is also much easier with neutrons, as A_{hkl} for X-rays is critically dependent on the exact shape of the sample.

TEMPERATURE FACTOR

5. The temperature factor enters into the formula (1) for ρ_{hkl} through the expression for F_{hkl} :

$$F_{hkl} = \sum_n f_n \exp 2\pi i \left(\frac{hx_n}{a} + \frac{ky_n}{b} + \frac{lz_n}{c} \right) \exp (- B_n \sin^2 \theta / \lambda^2) ,$$

.....(3)

where f_n is the scattering factor of the n^{th} atom in the unit cell, x_n, y_n, z_n are its coordinates with reference to the cell edges abc , λ is the wavelength and 2θ is the scattering angle. B_n is the temperature factor, given by

$$B_n = 8\pi^2 \overline{U_n'^2}$$

where $\overline{U_n'^2}$ is the mean square displacement of the n^{th} atom from the hkl plane. For cubic crystals $\overline{U_n'^2} = \frac{1}{3} \overline{U_n^2}$, where $\overline{U_n^2}$ is the mean square displacement of the n^{th} atom from its equilibrium position, and for crystals containing one kind of atom the temperature factor is related to the Debye temperature Θ by

$$B = \frac{6h^2 T}{mk\Theta^2} \left(\Phi(x) + \frac{x}{4} \right)$$

.....(4)

Here m is the atomic mass, T the absolute temperature, h Planck's constant, k Boltzmann's constant, x is the ratio Θ/T and $\Phi(x)$ is the tabulated function:

$$\Phi(x) = \frac{1}{x} \int_0^x \frac{\xi d\xi}{e^\xi - 1}$$

6. If the structure factor F_c is calculated from (3) with $B_n = 0$, and if F_o is the observed structure factor derived from (1), then

$$F_o = F_c \exp (- B \sin^2 \theta / \lambda^2)$$

and a plot of $\ln (F_o/F_c)$ versus $\sin^2 \theta / \lambda^2$ will be a straight line of slope $-B$. (For more than one kind of atom B represents a mean temperature factor for those atoms contributing to the reflexion). Such a plot is

shown in Fig. 2 for single crystal neutron data from UO_2 . UO_2 has the calcium fluoride structure, and the reflexions are divided into three groups: If $h + k + l = 4n$ (n integral) the U and O scatter in-phase and the reflexion is strong; the U and O scatter out-of-phase for $h + k + l = 4n+2$ and the reflexion is weak; and for odd $h + k + l$ the U atoms only contribute to the scattering and the reflexion is of medium intensity. The $4n \pm 1$ and $4n + 2$ reflexions only are shown in Fig. 2, as the $4n$ reflexions are affected by extinction (see §8 et seq.). The $4n \pm 1$ line has a slope corresponding to $B_U = 0.25 \text{ \AA}^2$, where B_U is the temperature factor of the uranium atom. The $4n + 2$ line has a steeper slope as the oxygen atoms vibrate more strongly than the uranium atoms and both kinds of atom contribute to these reflexions. The r.m.s. displacements of the atoms from their equilibrium positions at 20°C , as calculated from $B = \frac{8\pi^2}{3} u^2$, are 0.10\AA for uranium and 0.13 \AA for oxygen.

7. Figure 3 shows some X-ray results of Thewlis⁽¹⁾ on β -uranium. The slope of the $\ln(F_o/F_c)$ versus $\sin^2\theta/\lambda^2$ curve is positive, as F_c was calculated with the temperature factor included and an assumed Debye temperature of 162°K , equal to that of α -uranium. The positive slope shows that the assumed Debye temperature is too low, and to get a zero slope the Θ value of β -uranium must be taken as 270°K .

EXTINCTION FACTOR

8. The total intensity suffers from 'extinction' if the scattering process removes an appreciable amount of energy from the incident beam. The intensity scattered by the crystal as a whole is then no longer proportional to the intensity scattered by a single atomic plane, and an extinction factor E must be introduced in equation (1). E is a number between 0 and 1; for weak reflexions (no extinction) $E = 1$, but for strong reflexions E can be much less than unity.

9. Darwin discussed many years ago the two types of extinction, primary and secondary, which arise in a crystal consisting of a mosaic of perfect blocks. Primary extinction occurs if the incident beam is strongly attenuated by scattering during its passage through a single coherent block; for a perfect crystal, such as dislocation-free germanium, primary extinction only can take place. Secondary extinction involves the shielding of an underlying mosaic block by one closer to the surface; there is no coherence between the blocks, so that secondary extinction is concerned with scattered power rather than scattered amplitude and is akin to the normal absorption process. In Fig. 4 an attempt has been made to

illustrate schematically the two kinds of extinction.

10. Because it is analogous to absorption, secondary extinction will vary with the path length of the beam in traversing the crystal. Fig. 5 shows how this feature has been exploited to reveal the presence of secondary extinction in a single-crystal of KBr. The crystal was cut as a flat plate and the total intensity for neutrons was measured for the 200, 400, 600 and 800 reflexions. By rotating the crystal about the [100] direction the Bragg condition was maintained but the path length in the crystal was altered, between a maximum of 5mm at the azimuthal angle ψ of 90° and a minimum of 1mm at $\psi = 0^\circ$. The variation of ρ_{h00} with ψ shows that secondary extinction is very prominent at $\psi = 90^\circ$ for the 200 reflexion, but is progressively less important for 400, 600, 800. This is because the total intensities diminish as the order increases and a smaller proportion of the incident beam is scattered away.

11. In the presence of secondary extinction the effective absorption coefficient can be written⁽²⁾:

$$\mu_{\text{eff}} = \mu + \frac{\rho_{hkl} V}{2 \sqrt{\pi} \eta} .$$

where μ is the true absorption coefficient, V the volume of the irradiated sample and η the average spread in orientation of the mosaic blocks.

Putting $\mu = \mu_{\text{eff}}$ and $A = AE$ in equation (2) the absorption and secondary extinction factors can be combined, and η can be deduced by studying the variation of this combined factor with path length⁽³⁾. A typical value obtained in this way for fused Spencer UO_2 is 4 minutes of arc.

12. This method of studying secondary extinction is unlikely to be useful in X-ray work unless true absorption is very small. A better method, not applicable to neutrons, is that developed by Chandrasekhar⁽⁴⁾.

Chandrasekhar employs polarised X-rays and by studying the variation of total intensity with polarisation angle the extinction factor (both primary and secondary) can be measured.

13. Some X-ray data of Ferguson⁽⁵⁾ on powdered ThO_2 show the effect of extinction. The samples were prepared at different temperatures in the range $600\text{-}2500^\circ\text{C}$, and Ferguson found that the $\ln(F_c/F_o)$ versus $\sin^2\theta$ curves (Fig.6) varied according to the temperature of preparation. He ascribed this to a variation of absorption factor from sample to sample; the absorption factor is very large and the assumption of a homogeneous

cylindrical sample is certainly not true. The irregular kinks in the curves are therefore probably due to incorrect estimates of the absorption factors, but the differences in the general trends of the curves arise from extinction. The 600°C curve has a positive slope corresponding to $E = 1$ (no extinction) and $B \approx 0.5 \text{ \AA}^2$. As the preparation temperature rises the intensities of the low-order reflexions fall in comparison with the high order intensities; this is what we expect with extinction, as the Lorentz factor L_{hkl} in equation (1) weights the intensities in favour of the low-order reflexions. (Note that for X-rays $f_{Th} \gg f_O$ and $F_{hkl} = f_{Th} \exp(-B_{Th} \sin^2 \theta / \lambda^2)$ for all reflexions). Ferguson also showed from line-broadening measurements that, as the preparation temperature rises, the crystallite size increases and the lattice strain decreases. These observations provide the physical explanation of the extinction effect, as the extinction increases with temperature and if it is primary it will increase with increase with the size of a mosaic block, and if secondary it will increase as the angle between the mosaic blocks (i.e. the strain) falls.

TOTAL INTENSITY AND COLD-WORK

14. During the last decade, with the advent of accurate counter methods of measuring the total intensity, there has been much discussion of the relation between total intensity and cold-work. Averbach and Warren⁽⁶⁾ observed an increase in the intensity of the strong lines from α -brass after cold-work and this effect, attributed to extinction, has been noted later by other workers. The discussion has centred round two questions (see Fig. 7):

- (a) Is the extinction in annealing powders primary or secondary?
- (b) Does the background level between the Debye-Scherrer lines increase on cold-work?

15. Averbach and Warren interpreted their results in terms of primary extinction. Hall and Williamson⁽⁷⁾ claimed that their work on aluminium indicated a reduction of secondary extinction on cold-work, but their interpretation was criticised by Weiss⁽⁸⁾ and by Lang⁽⁹⁾, and in a later work Williamson⁽¹⁰⁾ re-interpreted his results in terms of primary extinction. From the observed extinction factor Williamson estimated the size of the mosaic blocks in aluminium to be 3.5μ , and as the penetration of the X-ray beam was only about ten such blocks, it is not surprising that secondary extinction was absent.

16. The second question has also been the subject of some controversy between the Birmingham school and American workers. Smallman and Williamson⁽¹⁰⁾

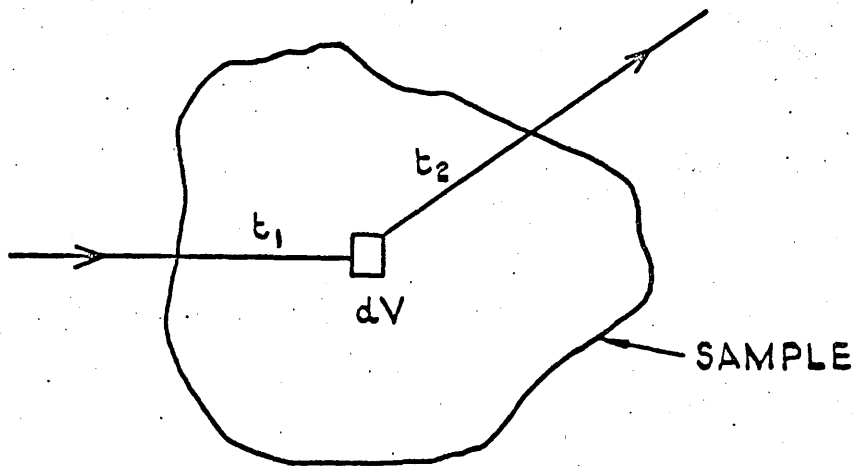
measured a slight increase of background level between the Debye-Scherrer lines of metals after cold-work, and attributed this to the scattering from dislocations, but this effect was not observed by Averback and Warren. Weiss *et al.*⁽¹¹⁾ have measured the total intensity of annealed and heavily cold-work α - brass by neutron diffraction; the advantage of neutrons is that the scattering cross-sections are considerably smaller than for X-rays and extinction is probably absent. The total intensity was the same to within 1% for the two samples, indicating that a rise in the background level between the lines must be very small or absent.

CONCLUSIONS

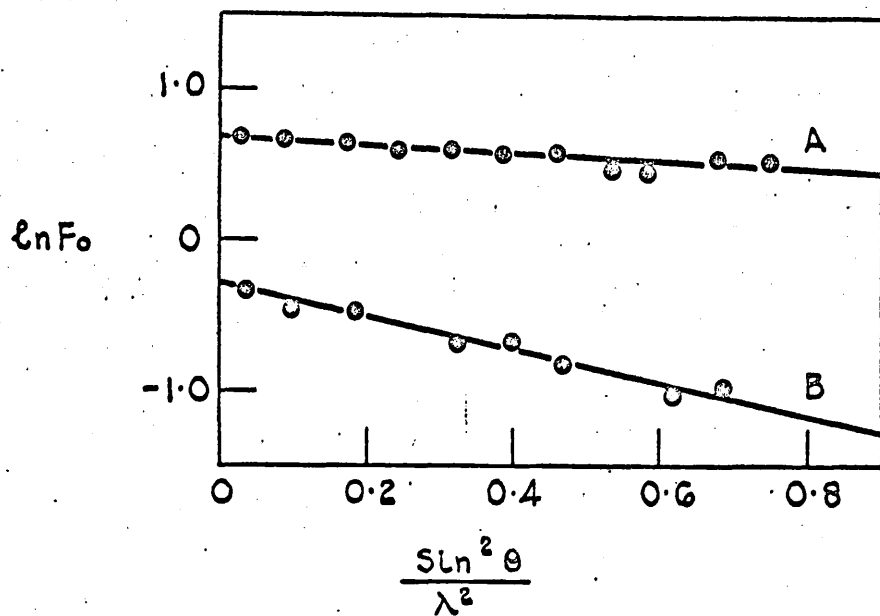
17. Some physical factors have been discussed which affect the magnitude of the observed total intensity. Information about these factors can be gained by accurately measuring the total intensity of the different hkl planes. This information includes the r.m.s. amplitudes of vibration of the different atoms in the crystal, the average size of the coherent mosaic blocks and the average mosaic spread.

REFERENCES

1. J. Thewlis, *Acta Cryst.* 1952 5 790.
2. W.H. Zachariasen, "Theory of X-ray diffraction in crystals", 1945 John Wiley, New York.
3. B.T.M. Willis, Vienna Symposium on Pile Neutron Research, 1960.
4. S. Chandrasekhar, *Acta Cryst.* 1956 2 954.
5. I.F. Ferguson, A.E.R.E.-R.3495 1960.
6. B.L. Averbach and B.E. Warren, *J. App. Phys.* 1949 20 1066.
7. W.H. Hall and G.K. Williamson, *Proc. Phys. Soc.* 1951 B64 937.
8. R.J. Weiss, *Proc. Phys. Soc.* 1952 B65 553.
9. A.R. Lang, *Proc. Phys. Soc.* 1953 B66 1003.
10. R.E. Smallman and G.K. Williamson, *Proc. Phys. Soc.* 1955 B68 577.
11. R.J. Weiss, J.R. Clark, L. Corliss and J.M. Hastings, *J. App. Phys.* 1952 23 1379.



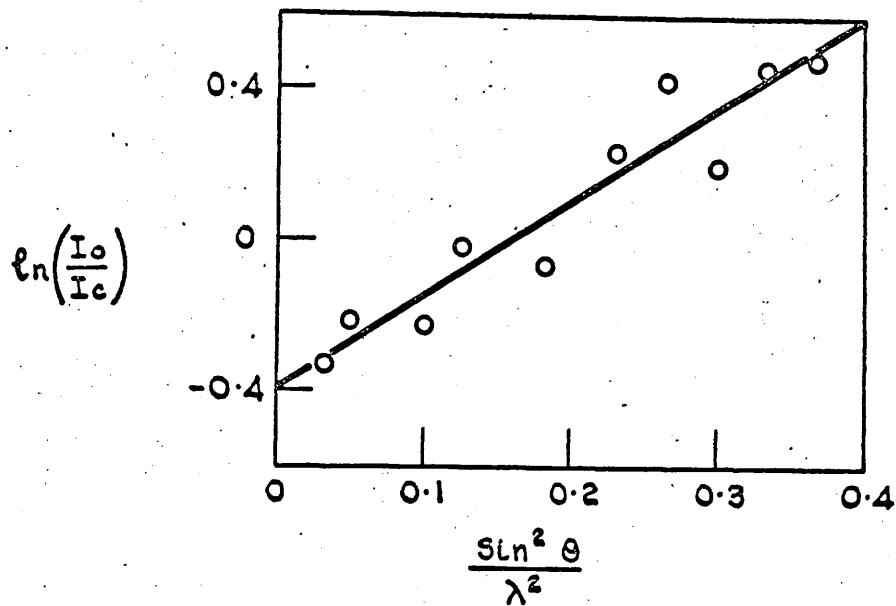
A.E.R.E.R3818. FIG.1. PATH OF BEAM SCATTERED
BY VOLUME ELEMENT dV .



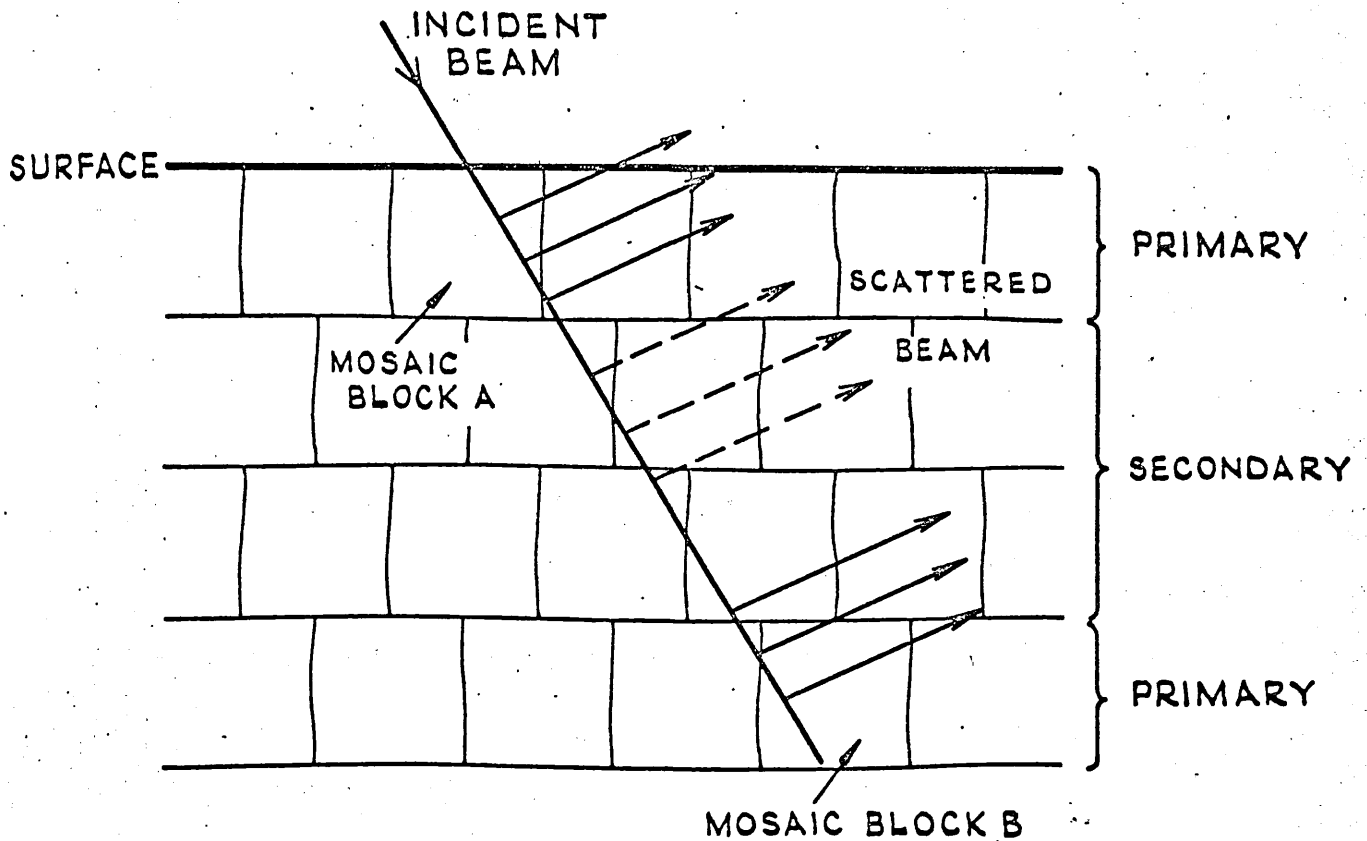
A.E.R.E. R3818. FIG. 2. NEUTRON SINGLE CRYSTAL FOR
UO₂ (FUSED) AT 290° K.

CURVE A - 4n ± 1 REFLEXIONS (U SCATTERING ONLY)

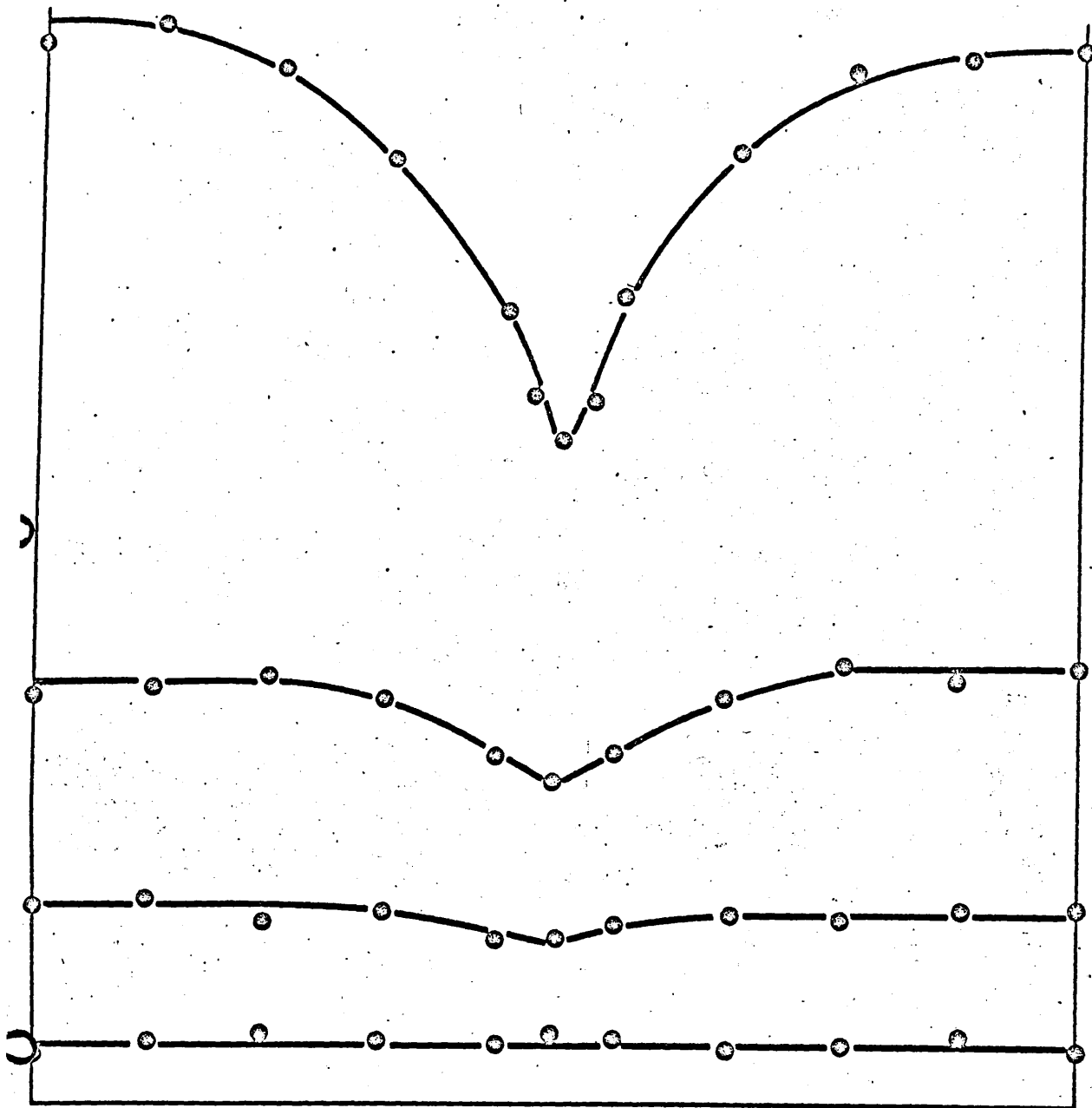
CURVE B - 4n + 2 REFLEXIONS (U AND O SCATTERING
OUT OF PHASE).



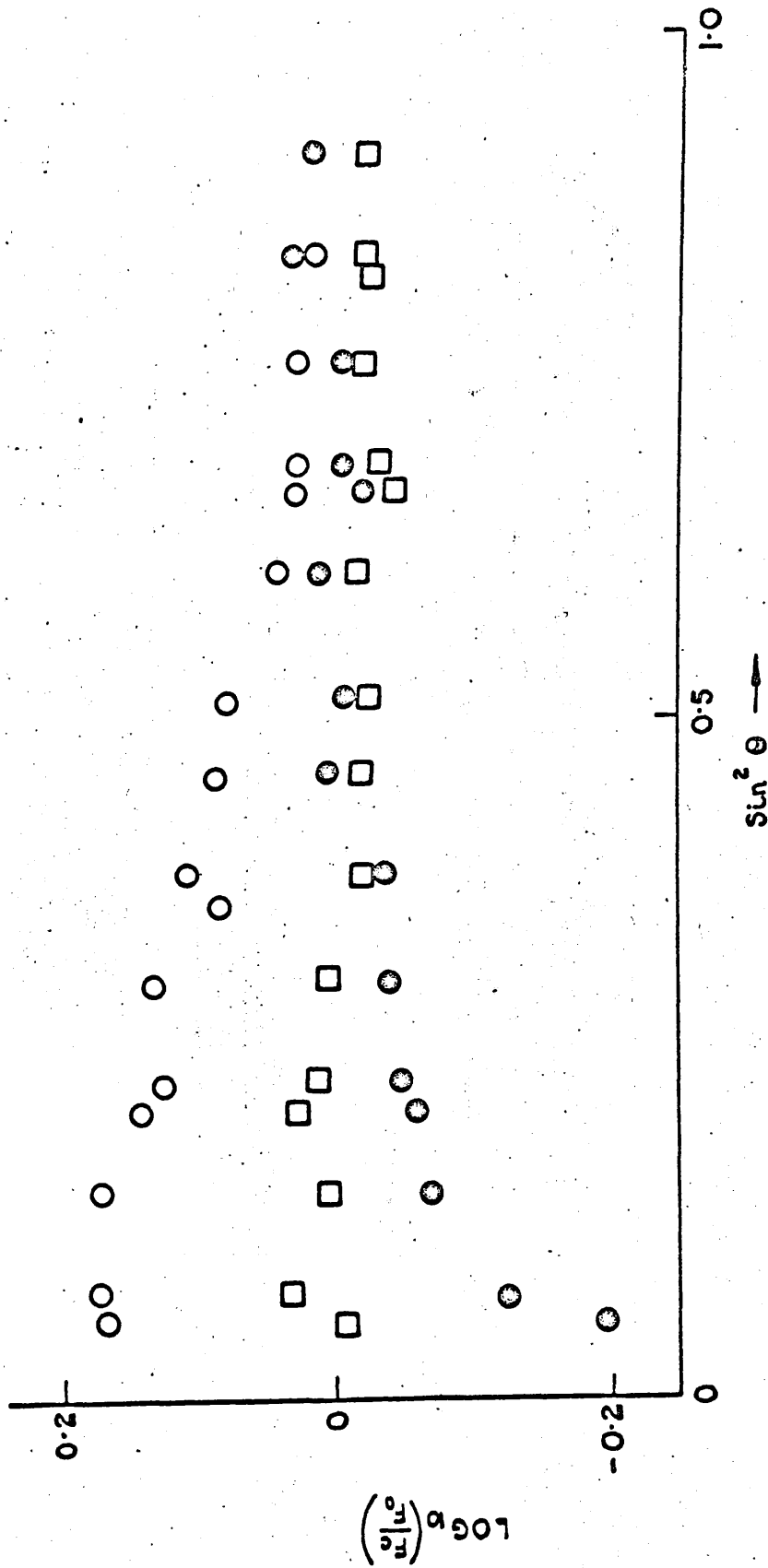
A.E.R.E.R 3818. FIG.3. X - RAY POWDER DATA
FOR β - URANIUM (THEWLIS⁽¹⁾).



A. E. R. E. R 3818. FIG. 4. DIAGRAM ILLUSTRATING THE DIFFERENCE BETWEEN PRIMARY AND SECONDARY EXTINCTION. THE EXTINCTION IS PRIMARY IF THE BEAM IS STRONGLY ATTENUATED BY SCATTERING WITHIN A BLOCK A ; IT IS SECONDARY IF THE BEAM IS ATTENUATED IN PASSING BETWEEN TWO BLOCKS A AND B OF THE SAME ORIENTATION.

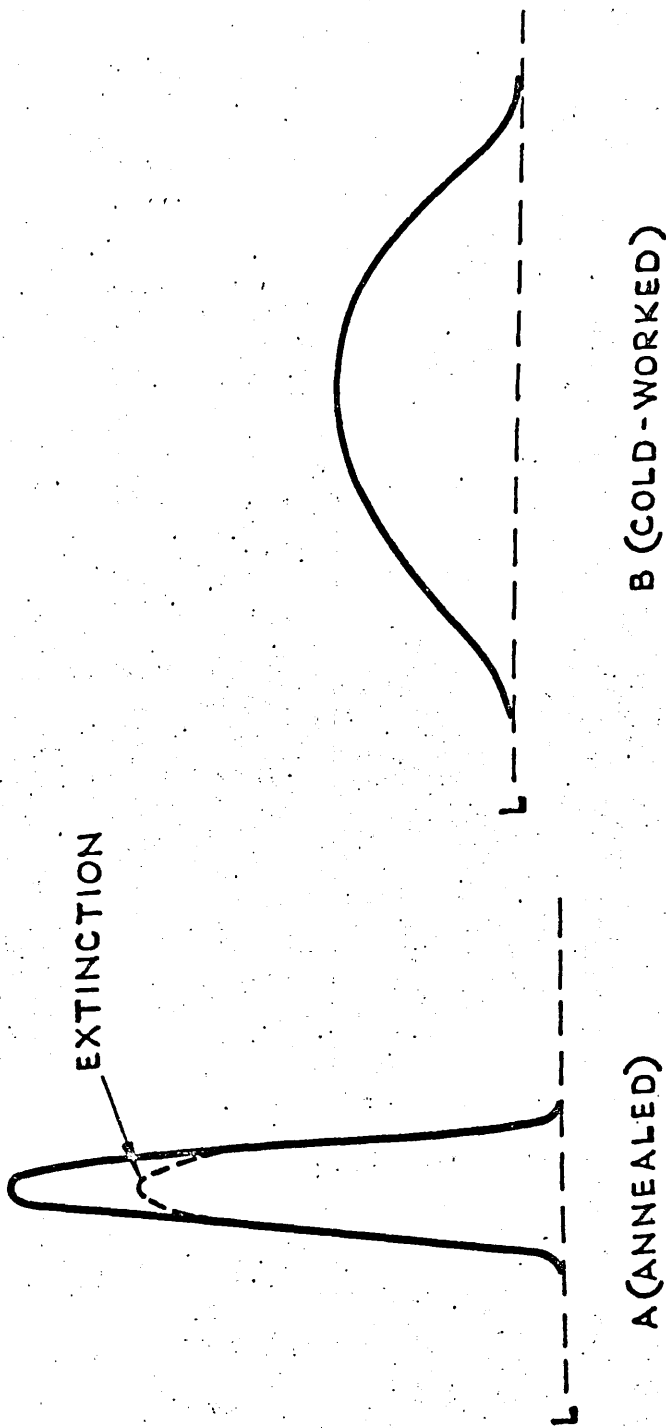


A.E.R.E. R3818. FIG.5. NEUTRON SINGLE CRYSTAL DATA FOR KBr.



A.E.R.E. R3818. FIG. 6. X-RAY POWDER DATA FOR ThO₂ (FERGUSON⁽⁵⁾).

- ThO₂ PREPARED AT 2500°C
- ThO₂ PREPARED AT 800°C
- ThO₂ PREPARED AT 600°C



A.E.R.E. R3818. FIG.7. POWDER LINE PROFILES FOR ANNEALED (A) AND COLD-WORKED (B) SAMPLES. THE TOTAL INTENSITIES FOR A AND B WILL BE DIFFERENT, IF COLD-WORKING EITHER REDUCES EXTINCTION OR RAISES THE BACKGROUND LEVEL L.

SECONDARY EXTINCTION AND NEUTRON
DIFFRACTION

B. T. M. WILLIS
ATOMIC ENERGY RESEARCH ESTABLISHMENT, HARWELL
UNITED KINGDOM OF GREAT BRITAIN AND NORTHERN IRELAND

Reprinted from
"PILE NEUTRON RESEARCH IN PHYSICS"

INTERNATIONAL ATOMIC ENERGY AGENCY
VIENNA 1962

SECONDARY EXTINCTION AND NEUTRON DIFFRACTION

B. T. M. WILLIS

ATOMIC ENERGY RESEARCH ESTABLISHMENT, HARWELL

UNITED KINGDOM OF GREAT BRITAIN AND NORTHERN IRELAND

Abstract — Résumé — Аннотация — Resumen

Secondary extinction and neutron diffraction. The term "secondary extinction" is used to denote the loss of power due to diffraction for a neutron beam passing through a mosaic crystal. To derive accurate estimates of the integrated intensities from single crystals (as is required, for instance, in crystal structure investigations) it is necessary to correct for the effect of secondary extinction, which is normally more serious than the effect of true absorption from nuclear capture processes. Several authors have examined the theoretical problem of secondary extinction in neutron crystallography, but no satisfactory methods have been developed for the correction of extinction.

In this paper a method of correcting for secondary extinction is proposed based on the measurement of the integrated intensity for different path-lengths of the beam in the crystal. The theory of the method is developed for the two cases of small and large extinction. The measurements are conveniently carried out by using a 3-circle arrangement, or Eulerian cradle; two of these circles are effectively used to bring the (hkl) normal into the reflecting position in the horizontal plane and the third circle to rotate the crystal about the normal to the reflecting plane, whilst maintaining the Bragg reflecting condition.

The application of the method to the correction of the intensities from several single crystals, including KBr and UO_2 , is described.

Extinction secondaire et diffraction neutronique. Le terme «extinction secondaire» est utilisé pour désigner la perte d'énergie par diffraction dans un faisceau de neutrons passant par un cristal genre «mosaïque». Pour parvenir à une estimation exacte des intensités intégrées de faisceaux issus de monocristaux (une telle estimation est indispensable pour étudier par exemple la structure des cristaux), il est nécessaire d'appliquer un facteur correctif pour tenir compte de l'effet produit par l'extinction secondaire, effet qui est, en général, plus important que celui de l'absorption véritable due aux processus de capture nucléaires. Plusieurs spécialistes ont étudié le problème théorique de l'extinction secondaire dans la cristallographie des neutrons, mais ils n'ont pu mettre au point aucune méthode satisfaisante de correction permettant de tenir compte de ce phénomène.

L'auteur propose, pour tenir compte de l'extinction secondaire, une méthode de correction fondée sur la mesure de l'intensité intégrée pour différentes longueurs de parcours du faisceau dans le cristal. Du point de vue théorique, cette méthode a été mise au point pour les deux cas: extinction faible et extinction forte. Un moyen pratique d'effectuer ces mesures consiste à utiliser un dispositif composé de trois cercles dit «berceau d'Euler»; deux de ces cercles sont effectivement utilisés pour amener la normale à la face réfléchissante (hkl) vers la position de réflexion dans le plan horizontal, et le troisième pour faire pivoter le cristal autour de la normale à la face réfléchissante tout en maintenant les conditions de réflexion dites de Bragg.

L'auteur décrit l'application de cette méthode à la correction des intensités des faisceaux issus de plusieurs monocristaux, dont KBr et UO_2 .

Вторичное затухание и дифракция нейтронов. Термин «вторичное затухание» применяется для обозначения потери энергии в результате дифракции пучка нейтронов, про-

ходящих через мозаичный кристалл. Для того, чтобы точно определить интегрированную интенсивность от единичных кристаллов (как это требуется, например, для исследований структуры кристалла), необходимо корректировать действие вторичного затухания, которое нормально является более серьезным, чем действие настоящего поглощения от процессов ядерного захвата. Несколько авторов изучили теоретическую проблему вторичного затухания в нейтронной кристаллографии, однако не было разработано никаких удовлетворительных методов для корректирования затухания. В этом документе предлагается метод корректирования для вторичного затухания, который основан на измерении интегрированной интенсивности для различных длин прохождения пучка в кристалле.

Теория этого метода разработана для двух случаев малого и большого затухания. Измерения проводятся удобным способом путем применения трехкругового приспособления или Eulerian cradle; два из этих кругов эффективно применяются, чтобы поставить нормаль (hkl) в отражающее положение на горизонтальной плоскости, а третий круг — чтобы вращать кристалл около нормали на отражающей поверхности, поддерживая в то же время отражающее условие Брэгга.

Описывается применение этого метода для корректирования затухания от нескольких единичных кристаллов, включая KBr и UO_2 .

Extinción secundaria y difracción neutrónica. La expresión «extinción secundaria» se emplea para designar la disminución de energía debida a la difracción que un haz neutrónico sufre al atravesar un cristal mosaico. Para poder evaluar con exactitud las intensidades integradas de los haces que emergen de monocristales (esta evaluación resulta indispensable para determinar estructuras cristalinas, por ejemplo), es preciso aplicar un factor de corrección a fin de tener en cuenta el efecto de la extinción secundaria que, generalmente, es más importante que el efecto de la absorción verdadera debida a procesos de captura nuclear. Varios autores han investigado el problema teórico de la extinción secundaria en la cristalografía neutrónica, pero ninguno ha logrado un método de corrección satisfactorio que permita tener en cuenta este fenómeno.

En la memoria, el autor propone un método basado en la medición de la intensidad integrada para distintas longitudes de recorrido del haz en el cristal. Desarrolla la teoría del método para los casos de extinción débil y de extinción fuerte. Un medio práctico de efectuar las mediciones consiste en emplear un dispositivo formado por tres aros, o «cuna» de Euler; dos de los aros se utilizan para llevar la normal a la cara reflectora (hkl) a la posición de reflexión en el plano horizontal y el tercero, para hacer girar el cristal alrededor de la normal a la cara reflectora, sin dejar de mantener la condición de reflexión de Bragg.

La memoria describe la aplicación del método a la corrección de las intensidades de los haces que emergen de distintos monocristales, entre otros, de KBr y de UO_2 .

1. Introduction

The problem of extinction is of great importance in neutron diffraction as the loss of power of the direct beam due to diffraction is often much greater than that due to pure absorption. The attenuation of the beam by diffraction within a coherent region, or mosaic block, is known as "primary extinction", whereas "secondary extinction" is the term used for the loss of power in passing between two mosaic blocks with the same orientation. Secondary extinction is the more usual form of extinction encountered in neutron diffraction and is the only one considered here.

Several authors have examined the problem of secondary extinction theoretically [1, 2], but no satisfactory methods have been developed by which it can be corrected for. In this paper a method of doing so is proposed, based

on the measurement of the intensity of a reflection for different path-lengths of the neutron beam in the crystal.

It is to be noted that the absence of extinction and pure absorption implies that the crystal is uniformly bathed in radiation as it moves through the Bragg reflecting position. Under these circumstances the "integrated reflection" ϱ as recorded by the rotating-crystal method is given by

$$\varrho = QV. \quad (1)$$

Here V is the volume of the crystal and Q is the crystallographic quantity defined by

$$Q = \frac{\lambda^3 N_c^2 F^2}{\sin 2\theta},$$

where λ is the wavelength, N_c the number of unit cells per unit volume, θ the Bragg angle and F the structure factor of the reflection. In the presence of secondary extinction, Eq. (1) must be rewritten

$$\varrho = E_s QV, \quad (2)$$

where E_s is the "secondary extinction coefficient" ($1 \geq E_s \geq 0$). Correction for secondary extinction means determination of the coefficient E_s .

2. Theoretical

(a) SMALL EXTINCTION

ZACHARIASEN [3] has shown that the effect of small secondary extinction can be taken into account by replacing the true absorption coefficient, μ , by an effective absorption coefficient, μ_{eff} , defined by

$$\mu_{\text{eff}} = \mu + gQ. \quad (3)$$

Here g is the quantity $\frac{1}{2\sqrt{\pi}\eta}$, where η is the parameter defining the "mosaic spread" (see Eq. (6) below). The absorption and extinction effects can therefore be corrected together by putting $\mu = \mu_{\text{eff}}$ in the usual expression for the absorption factor, A :

$$A = \frac{1}{V} \int e^{-\mu T} dV.$$

Here T is the total path-length in the crystal of the beam reflected by the volume element dV .

Thus

$$\varrho = Q \int e^{-(\mu + gQ)T} dV.$$

For small extinction $gQT \ll 1$ and e^{-gQT} in the above expression can be replaced by $1 - gQT$, giving

$$\varrho = Q \int e^{-\mu T} dV - gQ^2 \int T e^{-\mu T} dV.$$

The unknowns in this equation are g and Q . By setting up two equations for different values of the path-length T (or, more accurately, for different values of the two integrals) g can be eliminated and Q determined. The path-length can be altered by rotating the crystal about the normal to the reflecting plane.

It is customary in neutron diffraction to work with pillar-shaped crystals and so the variation in path-length will depend on the orientation of the reflecting plane with respect to the exterior faces of the crystal. If ρ_1, ρ_2 are the integrated intensities, measured for two azimuthal positions of the reflecting plane, and if the subscripts 1, 2 are used to label the integrals for the two positions, then eliminating g gives:

$$Q = \frac{1}{V} \cdot \frac{\rho_1 \int_2 T e^{-\mu T} dV - \rho_2 \int_1 T e^{-\mu T} dV}{\int_1 e^{-\mu T} dV \int_2 T e^{-\mu T} dV - \int_2 e^{-\mu T} dV \int_1 T e^{-\mu T} dV} \dots (4)$$

It is clear that for the accurate determination of Q from (4) the ratio of the two integrals in the numerator must be 1.5:1 or greater. These integrals can be considered as "effective path-lengths" for positions 1 and 2 and their values are determined by the exterior shape of the crystal. All the integrals can be evaluated numerically and a programme for this purpose has been written for the Harwell MERCURY computer. The programme is based on that of BUSING and LEVY [4], but is extended to three dimensions.

(b) LARGE EXTINCTION

The extinction is "large" if the secondary extinction coefficient E_s is less than about 0.8, i.e. if extinction reduces the intensities by more than 20%. It is then no longer permissible to increase the absorption coefficient by a constant factor gQ as in Eq. (3), since the effective absorption varies appreciably in passing through the Bragg reflection.

It can be shown [2] that for zero Bragg angle and zero coefficient of true absorption the ratio of the powers of the diffracted and incident beams is given by

$$\frac{P_H(T)}{P_0} = \frac{1}{2} (1 - e^{-2\sigma T}), \quad (5)$$

where T is the path-length through the crystal and σdT is the reflecting power of the layer of thickness dT ; σ is equal to $QW(\Delta)$, where $W(\Delta)$ is the distribution function for mosaic blocks in terms of Δ , the angular deviation of a block from the mean Bragg angle θ . $W(\Delta)$ is normally assumed to be of the form

$$W(\Delta) = \frac{1}{\sqrt{2\pi}\eta} e^{-\Delta^2/2\eta^2} \quad (6)$$

with η the standard deviation of the distribution. Putting $\sigma = QW$ into Eq. (6) and remembering that the integrated intensity is defined as

$$\rho = \int \frac{P_H(T)}{P_0} d\Delta$$

gives

$$\begin{aligned} \rho &= QT \int_{-\infty}^{\infty} W d\Delta - Q^2 T^2 \int_{-\infty}^{\infty} W^2 d\Delta + \frac{2}{3} Q^3 T^3 \int_{-\infty}^{\infty} W^3 d\Delta - \dots \\ &= QT \left[1 - \frac{QT}{2\sqrt{\pi}\eta} + \frac{2}{3} \frac{Q^2 T^2}{2\sqrt{3}\pi\eta^2} - \dots \right]. \end{aligned}$$

Substituting

$$\kappa = \frac{QT}{\sqrt{\pi} \eta}:$$

gives
$$\rho = 2\sqrt{\pi} \eta \kappa \left[1 - \frac{1}{2} \kappa + \frac{1}{3\sqrt{3}} \kappa^2 - \frac{1}{12\sqrt{2}} \kappa^3 + \dots \right],$$

and the extinction coefficient E_s , defined by the equation

$$E_s = \frac{\rho}{QT}$$

is

$$E_s = 1 - \frac{1}{2} \kappa + \frac{1}{3\sqrt{3}} \kappa^2 - \frac{1}{12\sqrt{2}} \kappa^3 + \dots \tag{7}$$

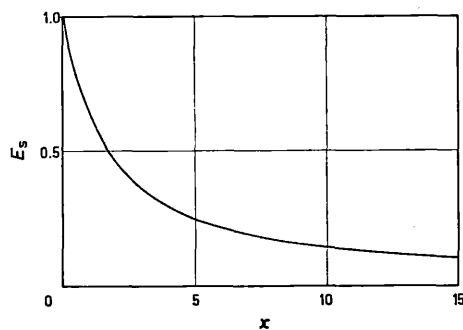


Fig. 1

Dependence of the secondary extinction coefficient on the parameter κ .

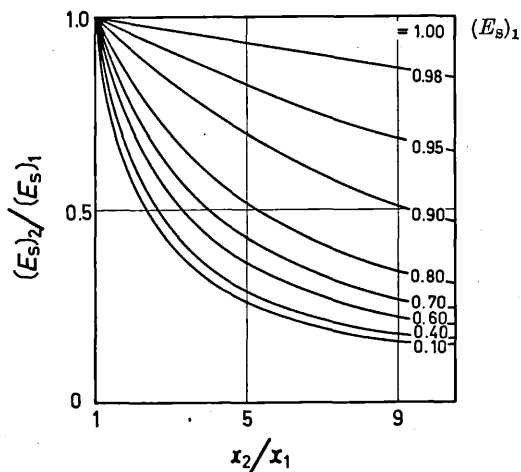


Fig. 2

Ratio of extinction coefficients, $(E_s)_2 / (E_s)_1$, as a function of ratio of path-lengths, for different values of $(E_s)_1$.

The treatment described in Section 2 (a) for small extinction corresponds to ignoring x^2 and higher powers of x in Eq. (7).

Fig. 1 shows the variation of E_s with x ; and Fig. 2 shows the variation of $(E_s)_2/(E_s)_1$ with x_2/x_1 for different values of $(E_s)_1$, where $(E_s)_1$ and $(E_s)_2$ are the extinction coefficients for two different values, x_1 and x_2 , of x . The ratio $(E_s)_2/(E_s)_1$ is equal to the ratio of the measured integrated intensities ρ_2/ρ_1 for two path-lengths T_2 , T_1 and x_2/x_1 is equal to T_2/T_1 . Fig. 2 can therefore be used to correct for extinction, if we assume that T_1 and T_2 can be replaced by the *average* path-lengths in the crystal. The curves show that for high accuracy T_2/T_1 should exceed 2, and that in any case the extinction correction becomes less accurate as the extinction increases. If the absorption coefficient, μ , is not zero the value of ρ_2/ρ_1 must first be corrected for absorption by dividing by $e^{-\mu(T_2 - T_1)}$.

3. Experimental procedure

A three-circle arrangement, or Eulerian cradle [5], can conveniently be so adapted as to allow rotation of the crystal about the normal to the reflecting plane. Fig. 3 is a diagram of the three circles, normally referred to as φ , χ and ω .

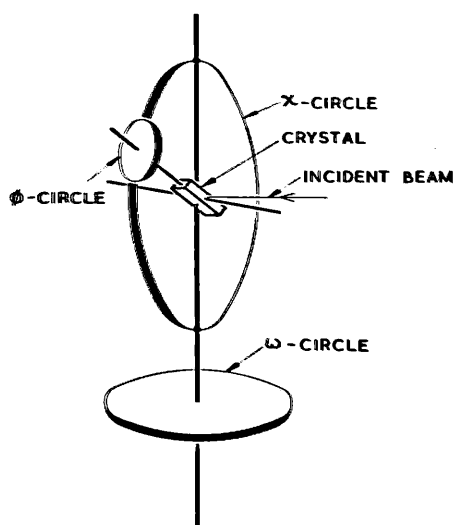


Fig. 3

Diagram of the three circles φ , χ and ω .

The crystal is mounted on the φ -circle, which can rotate as a whole about the vertical χ -circle, and the χ -circle in turn is mounted on the horizontal ω -circle. Two of the circles only are necessary to bring the normal into the Bragg reflecting position in the horizontal plane, and the third circle provides an extra degree of freedom for rotating the crystal about the (hkl) normal.

One way of achieving this is illustrated in Fig. 4. The crystal is mounted with its long axis, say c , along the φ -axis and the neutron beam is reflected

symmetrically at an angle of θ to the χ -plane. In the reflecting position the $(hk0)$ normal is along the χ -axis and the crystal rotates about this normal as

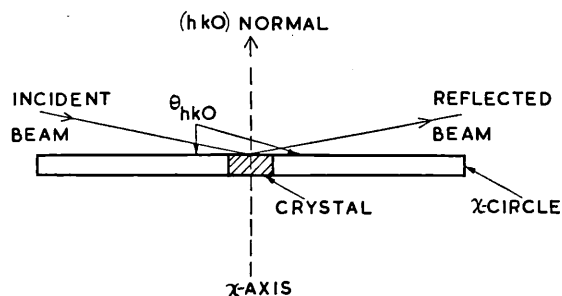


Fig. 4

Method of mounting crystal to allow rotation about $(hk0)$ normal whilst in Bragg reflecting position. The diagram shows the projection of the χ -circle in the horizontal plane. The φ -circle is not shown.

the φ -circle is rotated about the χ -axis. The integrated intensities ϱ_1 and ϱ_2 are measured at intervals of 90° for the positions of minimum and maximum path-lengths.

4. (a) Extinction correction in UO_2

A single crystal of uranium dioxide, UO_2 , was examined and from the variation of intensity of the strongest reflection, 220, with path-length, the extinction was observed to be small. The extinction was accordingly corrected for by the method indicated in Section 2 (a). Fig. 5 shows $\ln F$ as a function of $\sin^2 \theta/\lambda^2$ for the three classes of reflection with $h+k+l=4n$, $4n \pm 1$ and $4n \pm 2$, where

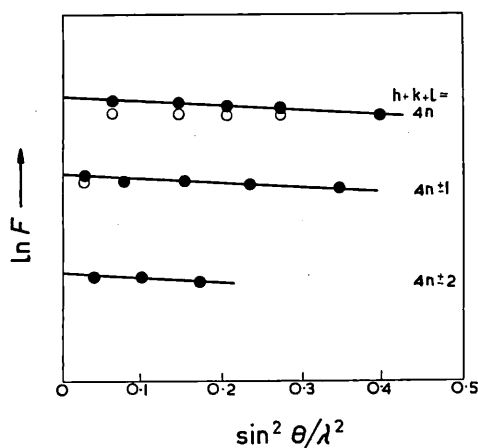


Fig. 5

$\ln F$ versus $\sin^2 \theta/\lambda^2$ for the three classes of reflection in UO_2 . The closed circles represent points corrected for secondary extinction and the open circles uncorrected points.

n is an integer. The open circles represent points uncorrected for extinction and the closed circles are for corrected points. The corrected data can be interpreted assuming the fluorite structure for UO_2 with an over-all isotropic Debye-Waller factor, B , of approximately 0.40 \AA^2 . The lengths of the intercepts made by the straight lines in Fig. 5 with the ordinate axis indicate that the ratio of the elastic scattering lengths of natural uranium and O^{16} is 1.484 ± 0.020 .

4. (b) Extinction correction in KBr

A crystal of potassium bromide was cleaved along the $[100]$ planes to produce a rectangular block of dimensions $5.42 \times 5.36 \times 1.24 \text{ mm}^3$. It was mounted on the φ -circle of an Eulerian cradle with the longest dimension along the φ -axis,

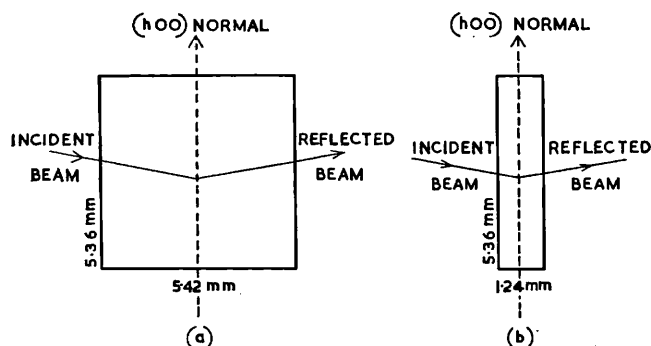


Fig. 6

Orientation of KBr crystal for (a) maximum path-length of neutron beam (b) minimum path-length of beam.

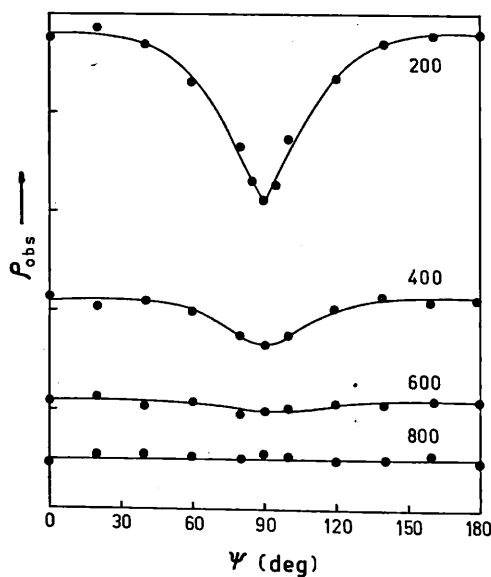


Fig. 7

Integrated intensities of the $h00$ reflections as a function of the azimuthal position of the $(h00)$ plane.

and the integrated intensities of the 200, 400, 600 and 800 reflections were measured for different azimuthal positions of the (h00) plane. Fig. 6 shows the orientation of the crystal for the maximum and minimum path-lengths of the neutron beam. The integrated intensities, corrected for pure absorption, are plotted in Fig. 7 as a function of the azimuth ψ .

The curves show clearly the effect of secondary extinction. As the path-length increases the measured intensity falls, the depth of the minimum at $\psi=90^\circ$ being greater for the stronger reflections. Table I gives the ratio of the integrated intensities, I_2/I_1 , of 200, 400... together with the corresponding values of the ratio of maximum and minimum path-lengths, T_2/T_1 . The final two columns are the values of the extinction coefficients, as determined from Fig. 2.

TABLE I
EXTINCTION COEFFICIENTS FOR KBr CRYSTAL

h00	e_2/e_1	T_2/T_1	Extinction Coefficients	
			$(E_s)_1$ Minimum path-length	$(E_s)_2$ Maximum path-length
200	0.65	4.1	0.85	0.55
400	0.795	3.8	0.92	0.73
600	0.92	3.6	0.97	0.89
800	1.00	3.2	1.00	1.00

The experimental points in Fig. 7 fluctuate in position about the smooth curves. This is to be ascribed, at least in part, to the lack of uniformity in the cross-sectional intensity of the direct beam. Many reciprocal-lattice points cross the sphere of reflection as the crystal rotates about the h00 scattering vector, so that intensity fluctuations can also arise from double Bragg scattering.

5. Conclusions

To a good approximation, secondary extinction can be treated as a straightforward absorption process and the most natural way to correct for it is to study the variation of the reflected intensity with the path-length in the crystal. After correcting for secondary extinction in this way, the presence of primary extinction can then be detected by studying the dependence of the corrected intensities on wavelength. Primary extinction is present if these corrected intensities increase with falling wavelength.

REFERENCES

- [1] BACON, G. E. and LOWDE, R. D., *Acta cryst.* **1** (1948) 303.
- [2] HAMILTON, W. C., *Acta cryst.* **10** (1957) 629.
- [3] ZACHARIASEN, W. H., *Theory of X-ray Diffraction in Crystals*. Wiley, New York (1945).
- [4] BUSING, W. R. and LEVY, H. A., *Acta cryst.* **10** (1957) 180.
- [5] FURNAS, T. C. and HARKER, D., *Rev. sci. Instrum.* **26** (1955) 449.

DISCUSSION

R. Brill (Federal Republic of Germany): Have you ever observed changes in secondary extinction caused by the irradiation of neutrons? Several years ago, in an investigation of ice carried out in conjunction with Mr. Corliss and Mr. Hastings, we found that there was less and less extinction as irradiation time increased.

B. T. M. Willis: No, I have not observed this phenomenon. However, in the uranium oxide crystals which I have begun to study, extinction is sometimes very strong. There is probably primary and secondary extinction in this case, and I hope to remove it by a light irradiation of the crystal.

N. Sirota (Byelorussian Soviet Socialist Republic) (Chairman): Does not secondary extinction apparently depend on the presence of dislocations, not only in the mosaic structure as caused by the presence of a block, but also dislocations of other types? Did you take that factor into account in your investigations?

B. T. M. Willis: No; what I have done is to treat extinction in the classical Darwinian manner, i.e., as being caused by a lack of coherence between different parts of the crystal. Now of course this lack of coherence is due to the presence of dislocations in the crystal; but when Darwin originally put forward his theory, dislocations had not been heard of. Nevertheless, it seemed to be a good first approximation to treat the crystal as mosaic blocks of the kind dealt with by Darwin, and at this stage I do not think that there is anything to be gained by making the treatment more complicated by going into the properties of dislocations and so forth in the crystal.

W. Marshall (United Kingdom): I would disagree with Mr. Willis about the relative theoretical position of primary and secondary extinction. I would say that primary extinction is almost a straightforward theoretical exercise for a student, but that secondary extinction is a very difficult subject, for exactly the reasons just mentioned by Mr. Sirota.

B. T. M. Willis: I agree; but I still want to insist that secondary extinction can be treated in the simple way that I have indicated, and that, even if one does it properly, i.e., by working out the appropriate formulae for particular dislocation distributions in the crystal, it is still a straightforward absorption process. When I said that primary extinction is a more difficult theoretical problem, I did so in the hope that some theoretician would—because the equations can be set up and are well known—be able to solve it for the general case of a crystal of arbitrary shape. It is not the kind of problem that would appeal to Mr. Marshall, but I think it might appeal to a Ph. D. student. It could probably be worked out with brute force on a computer, but it has not been done yet.

R. Brill: Mathematical treatment is possible where true primary extinction is present, i.e., where there is reflection by an ideal crystal. The difficulty occurs in the case of the nearly ideal crystal. It is still impossible to deal with the situation when there is a slight deviation from the ideal crystal.

B. N. Brockhouse (Canada): Is the division into secondary and primary extinction possible in a strictly mathematical sense, or is it not just an approximation that one uses?

B. T. M. Willis: I should certainly say that it is an approximation; but Mr. Marshall is more competent to answer this question than I am.

W. Marshall: It is an approximation.

J. A. Goedkoop (Netherlands): It might be well to point out that grain boundaries as found between mosaic blocks can often be interpreted in terms of dislocations, so that there is no sharp distinction between the effects of the mosaic structure and of the dislocations.

N. Sirota: Do you think it possible, in measurements, to use secondary extinction for evaluating the thickness and character of a dislocation or of defects in various crystallographical directions?

B. T. M. Willis: In my own experience I have observed secondary extinction in simple cubic crystals. It has been very strong on, say, the (200) planes; yet the extinction was the same in going from the (200) to the other equivalent (200) planes in the crystal. Therefore, I do not think there is any evidence for directional dependence of the effect of dislocations on secondary extinction.

UNCLASSIFIED
(Approved for Publication)

AERE-R 3959

DOUBLE BRAGG SCATTERING OF THERMAL
NEUTRONS BY ThO₂ AND UO₂

by

B. T. M. Willis
T. M. Valentine

ABSTRACT

The coherent scattering of neutrons by small single-crystals of ThO₂ and UO₂ has been measured as a function of the azimuthal orientation ψ of the reflecting plane. Intensity fluctuations occur which are attributed to double scattering ('Reminger reflexions'). These fluctuations have a proportionally greater effect on the weak reflexions, whose intensities can vary by a factor of two or more as ψ changes. The effect of double scattering on the accuracy of measuring neutron structure-factors is discussed.

Metallurgy Division,
U.K.A.E.A. Research Group,
Atomic Energy Research Establishment,
HARWELL

February, 1962

/DS.

HL.62/724 (C.14)

C/J

CONTENTS

	<u>Page</u>
1. Introduction	1
2. Condition for double scattering	2
3. Experiments with ThO_2 and UO_2	3
4. Conclusions	6
References	7

TABLE

Table

I Renninger reflexions associated with 200 reflexion of ThO_2	7
--	---

ILLUSTRATIONS

Fig.

1. Cones of reflexion for planes of spacing d_1 and d_2 .
 2. Ewald construction for double scattering.
 3. Diagrammatic representation of the possible single- and double-scattering processes, when two planes simultaneously satisfy the Bragg condition.
 4. Dependence of intensity of 200 reflexion of ThO_2 on azimuthal setting of reflecting plane.
 5. Reciprocal lattice and Ewald sphere of reflexion for experimental arrangement used in deriving Figure 4.
 6. Variation of intensity of 400 reflexion of ThO_2 with azimuthal setting of reflecting plane.
 7. Recorder trace of intensity of 200 reflexion of UO_2 , taken during continuous rotation of the crystal about the scattering vector.
 8. Recorder trace of intensity of 511 reflexion of UO_2 , taken during continuous rotation of the crystal about the scattering vector.
-

1. Introduction

The Bragg equation

$$\lambda = 2d \sin \theta \quad \dots\dots\dots(1)$$

expresses the condition that radiation of wavelength λ is reflected at the glancing angle θ by lattice planes with spacing d . The equation allows one degree of freedom to the reflecting crystal, which can rotate about the normal to the reflecting plane without violating the Bragg condition.

This freedom can be expressed alternatively by imagining the crystal to be fixed and allowing the incident beam to generate a cone with semi-angle $\frac{\pi}{2} - \theta$ and with axis normal to the reflecting plane. Figure 1 illustrates two such cones for planes of spacing d_1 and d_2 ; the semi-angles of the cones are $\frac{\pi}{2} - \theta_1$ and $\frac{\pi}{2} - \theta_2$, where

$$\lambda = 2d_1 \sin \theta_1 = 2d_2 \sin \theta_2.$$

OP and OQ are the lines of intersection of the cones, and when the radiation is parallel to either of these directions it can be reflected by each plane.

Moreover, whichever path is chosen by the once-reflected beam, it then obeys the Bragg condition for a third plane whose indices are simply related to those of the first two (§2). This phenomenon of double scattering ('Renninger effect') is well-known in X-ray crystallography⁽¹⁾, where it can introduce serious errors in measuring the normal Bragg reflexions and occasionally gives rise to extra reflexions, forbidden by the space-group. In neutron crystallography, where crystals are larger and the incident 'monochromatic' radiation covers a wider band of wavelengths, Renninger reflexions are likely to be even more troublesome. This report describes some observations of double scattering in single-crystals of ThO_2 and UO_2 and attempts to estimate the limit it sets, in general, on the accuracy of measuring structure-factors with thermal neutrons.

2. Condition for double scattering

The most convenient way of determining the condition for double scattering, i.e. the condition for the incident radiation to lie along the line of intersection of any two reflexion cones, is by means of the Ewald reciprocal-lattice construction. In figure 2, O is the origin of reciprocal space, \vec{CO} the direction of the incident beam, and OPQ the Ewald reflecting sphere with centre C and radius $CO = \frac{1}{\lambda}$. The distance of any reciprocal lattice point hkl from the origin is $\frac{1}{d_{hkl}}$. It can easily be shown that, if the Bragg condition (1) is fulfilled for any plane $h_1 k_1 l_1$, its reciprocal lattice point P lies on the surface of the reflecting sphere and the radiation scattered by this plane lies along the direction \vec{CP} joining the centre of the sphere with P. Clearly, for double reflexion to occur the two points $P = h_1 k_1 l_1$ and $Q = h_2 k_2 l_2$ must lie simultaneously on the Ewald sphere, and the incident beam \vec{CO} is then reflected in both directions \vec{CP} and \vec{CQ} .

Let us consider the scattered beam \vec{CQ} . By transferring the origin of reciprocal space to Q, \vec{CQ} can be taken as a primary beam: the position of the Ewald sphere is unaffected by this change of origin, so that P, which will now correspond to a different set of indices, still lies on the surface of the sphere and the beam \vec{CQ} can be reflected again in the direction \vec{CP} . In this double-scattering process the first scattering is from the $h_2 k_2 l_2$ plane and the second (for which the origin of reciprocal space is transferred from OOO to $h_2 k_2 l_2$) from the plane with indices $h_1 - h_2, k_1 - k_2, l_1 - l_2$. This roundabout excitation ('Umweganregung') of scattering in the direction \vec{CP} (process A) confuses the measurement of the beam singly-scattered in this direction by the $h_1 k_1 l_1$ plane and produces an error in the determination of the structure factor $F(h_1 k_1 l_1)$. Further confusion is caused by the converse process (B) involving the scattering of the once-reflected beam \vec{CP} by the plane with indices $h_2 - h_1, k_2 - k_1, l_2 - l_1$.

These two double-scattering processes are represented diagrammatically in figure 3. Excitation via $\vec{OQ} - \vec{QR}$ tends to enhance the scattering in the \vec{OP} direction while process B via $\vec{OP} - \vec{PR}$ tends to reduce it; the net scattering along \vec{OP} depends on the relative reflectivities of the various planes indicated in figure 3. However, we can see qualitatively that double-scattering tends to increase the apparent structure-factor of a weak reflexion and to decrease that of a strong reflexion. Ultimately, in the case of a very large crystal with no absorption, multiple scattering will reduce all Bragg reflexions to the same intensity.

3. Experiments with ThO_2 and UO_2

Small single-crystals of ThO_2 and UO_2 were mounted on a three-circle goniometer and the peak intensities of the Bragg reflexions were measured as a function of the azimuthal setting ψ of the reflecting plane, using the small ϕ -circle to provide the required variation of ψ . Figure 4 shows a portion of the intensity versus azimuth curve for the 200 reflexion of a crystal of ThO_2 , presenting a path length of 1-2 mm to the neutron beam. Pronounced fluctuations of intensity occur, which repeat at intervals of 90° and are symmetrical about the mid-point ($\psi = 45^\circ$) of each quadrant. Renninger reflexions are expected to have the same 45° and 90° symmetry, as ThO_2 is cubic, but to identify the fluctuations definitely as Renninger peaks it is necessary to determine the indices of the two planes associated with each fluctuation.

This can be accomplished by working out the relation between ψ and the indices $h_2k_2l_2$ of the plane, other than 200, satisfying the Bragg condition (1). The experiment required constraining the point $P = 200$ (figure 5) to lie on the reflecting sphere and measuring the intensity reflected in the direction \vec{CP} as a function of ψ , the angle of rotation of the crystal about the axis OP . During a complete rotation many reciprocal lattice points such as $Q = h_2k_2l_2$ intersect

the sphere, and at each intersection double-scattering can take place. Let Ox^* , Oy^* , Oz^* represent the orthogonal reciprocal axes and let $\psi = 0$ correspond to the position of the crystal with the incident beam normal to Oz^* . Then for an angle of rotation ψ the x^* y^* z^* co-ordinates of Q are:

$$\frac{\sin \theta_{200}}{\lambda} \quad \frac{\cos \theta_{200} \cos \psi}{\lambda} \quad \frac{\cos \theta_{200} \sin \psi}{\lambda}$$

The co-ordinates of Q are

$$\frac{h_2}{a} \quad \frac{k_2}{a} \quad \frac{l_2}{a},$$

so that the condition for Q to lie on the surface of the reflecting sphere is

$$\left(\frac{h_2}{a} - \frac{\sin \theta_{200}}{\lambda} \right)^2 + \left(\frac{k_2}{a} - \frac{\cos \theta_{200} \cos \psi}{\lambda} \right)^2 + \left(\frac{l_2}{a} - \frac{\cos \theta_{200} \sin \psi}{\lambda} \right)^2 = \frac{1}{\lambda^2},$$

which reduces to

$$k_2 \cos \psi + l_2 \sin \psi = \frac{1}{2} \tan \theta_{200} (h_2^2 + k_2^2 + l_2^2 - 2 h_2). \quad \dots\dots(2)$$

With the aid of equation (2) all the peaks in figure 4 have been identified as Renninger reflexions. They arise from A-type scattering at the planes

$$h_2 k_2 l_2 \text{ and } 2-h_2 -k_2 -l_2,$$

producing an increase of intensity above the level (shown by horizontal arrows in figure 4) calculated for no multiple scattering. There is little or no reduction of intensity below this level, so that the converse double-scattering process B, involving the planes

$$200 \text{ and } h_2 - 2 k_2 l_2,$$

is much less important. Table I lists the observed values of ψ for the most prominent peaks, labelled a,b,c ... in figure 4, together with the values of ψ calculated from equation (2), assuming pairs of reflecting planes with the indices in the last two columns of the table. The close agreement between ψ_{obs} and ψ_{calc} leaves no doubt about the identification of the peaks as Renninger reflexions.

It is to be noted that the indices of the pairs of reflecting planes, simulating the 200 reflexion are all odd. These are planes of medium reflectivity for which all the metal atoms scatter in-phase and the scattering from the oxygen atoms cancels. The remaining planes have even indices and are of two kinds: $h+k+l = 4n$ and $4n + 2$, where n is an integer. These planes do not give recognisable Renninger reflexions in figure 4, as the $4n + 2$ plane scatters very weakly (metal and oxygen atoms out-of-phase) and one such plane must take part in any double-scattering process simulating the 200 reflexion and involving planes of even indices.

Figure 6 shows the intensity versus azimuth curve for the 400 reflexion of the same ThO_2 crystal. 400 is a strong $4n$ -type of reflexion and double-scattering has proportionally less effect on its intensity than for the weak 200 reflexion. The small fluctuations of intensity are symmetrical about $\psi = 45^\circ$ and are presumably due to double-scattering. The most pronounced fluctuations, at $\psi = 37^\circ$ and 53° , represent a reduction in the average level of intensity and are caused by scattering of the once-scattered 400 beam by the $\bar{2}20$ and $\bar{2}02$ planes. We thus confirm that the weak 200 reflexion tends to be enhanced by the double-scattering process A and the strong 400 reflexion to be reduced by the process B, as discussed in § 2.

Figure 7 and 8 are recorder traces of the peak intensities of the 200 and 511 reflexions of a small single-crystal of UO_2 , taken as the crystal was continuously rotated about the normal to the reflecting plane. The intensity fluctuations, which are symmetrical about $\psi = 45^\circ$, are less prominent for 511 than for the weaker 200, and 200 in turn has smaller fluctuations than the weaker 200 reflexion of ThO_2 . We conclude that for medium or strong reflexions the intensity normally fluctuates by $\pm 2\%$ about the mean value but, for certain critical values of ψ and particularly for weak reflexions, the variation can be considerably larger.

4. Conclusions

The presence of double-scattering limits the accuracy attainable in measuring the structure-factors $F(hkl)$ of single-crystals. Renninger reflexions are extremely numerous in UO_2 and ThO_2 and figure 4 shows that there is hardly a single azimuthal position of the reflecting plane for which the measured intensity is unaffected by their presence. Under these circumstances it is difficult to see how the measured intensities can be corrected for analytically in an unknown crystal. For medium or strong reflexions the structure-factors (proportional to the square root of the intensity) are unlikely to be out by more than 1 or 2%, but for weak reflexions the structure-factors can be in error by 50% or more. Unlike the extinction error, which predominantly affects the strong reflexions, the error from double-scattering has little influence on the conventional R-factor

$$R = \frac{\sum \left| \left| F_{obs} \right| - \left| F_{calc} \right| \right|}{\sum \left| F_{obs} \right|}$$

expressing the discrepancy between the observed and calculated structure.

Double-scattering can be reduced, in principle, by reducing the size of the crystal, by increasing its mosaic spread or by increasing the wavelength of the incident radiation⁽¹⁾. Its effect can be altered by changing the azimuthal position of the reflecting plane, although this is not possible in rotating-crystal methods for which observations are only carried out at a single value of ψ . With a three-circle goniometer there is an extra degree of freedom, which can be used to vary ψ , and so $F(hkl)$ can be measured at two or more values of ψ : if these measurements indicate that double-scattering is excessive they should be repeated with a smaller crystal.

Reference

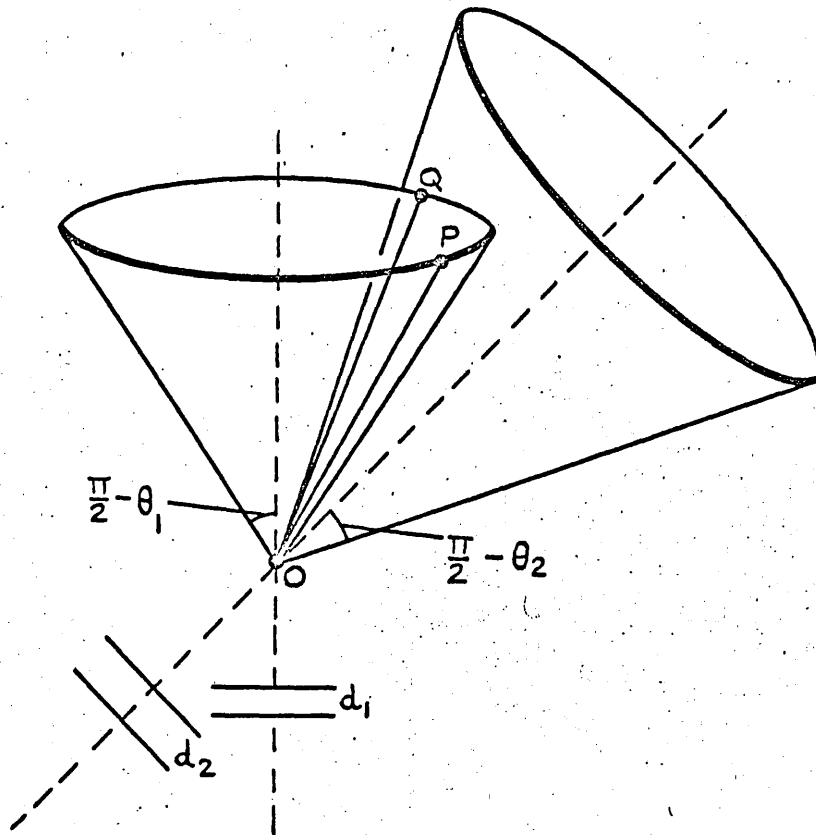
1. RENNINGER, M. "Umweganregung": a hitherto unobserved phenomenon in X-ray scattering. Z. phys., vol. 106, pp. 141-176, 1937.

TABLE I

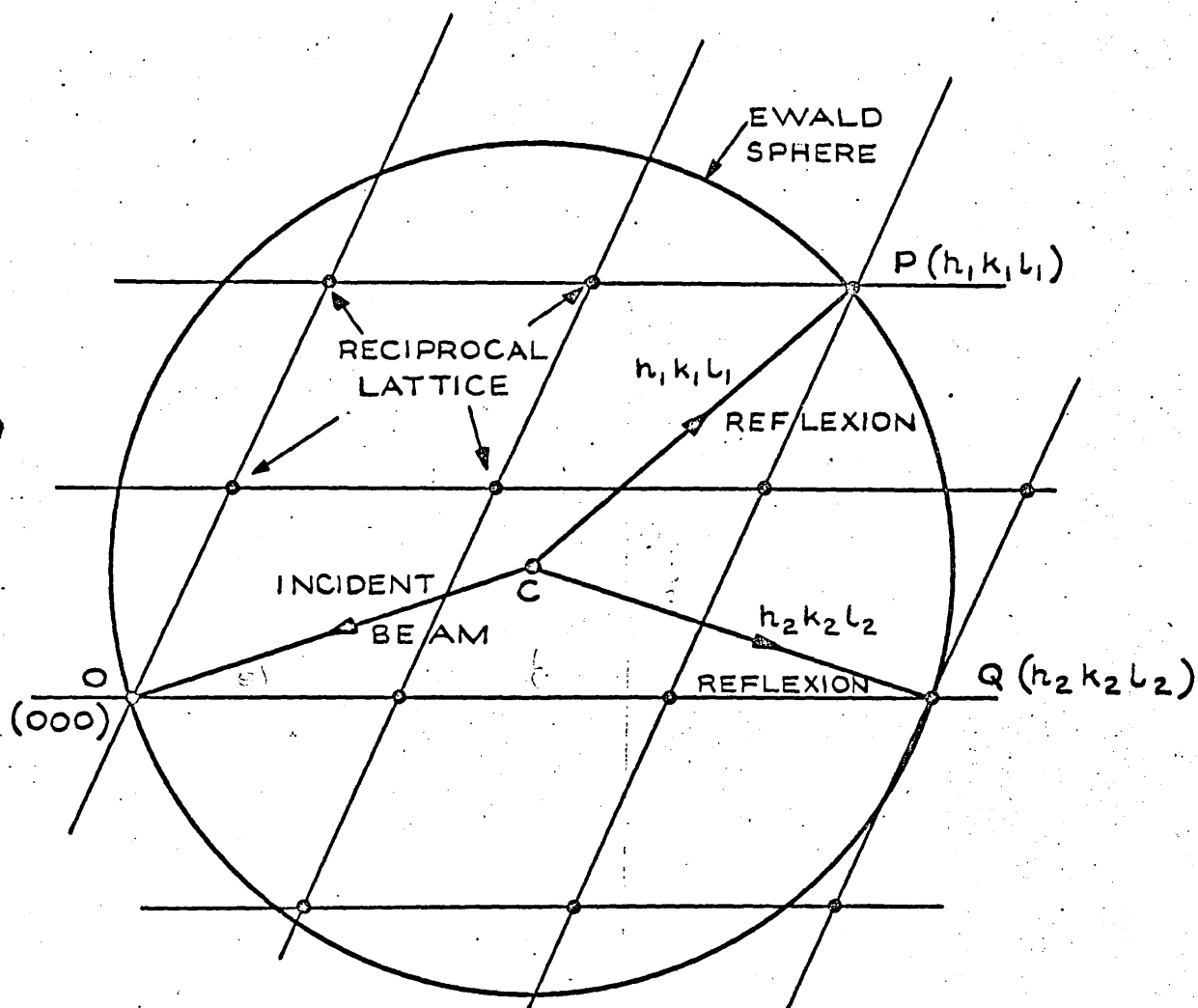
Renninger reflexions associated with 200 reflexion of ThO₂

Intensity Peak	ψ_{obs}	ψ_{calc}^*	$h_2 k_2 l_2$	$2-h_2 \quad -k_2 \quad -l_2$
c'	37° 50'	37° 59'	515	$\bar{3}\bar{1}\bar{5}$
b'	41 10	41 10	11 $\bar{1}$	1 $\bar{1}$ 1
a'	43 35	43 46	$\bar{1}\bar{1}\bar{5}$	31 $\bar{5}$
a	46 25	46 14	$\bar{1}\bar{5}\bar{1}$	3 $\bar{5}$ 1
b	48 50	48 50	1 $\bar{1}$ 1	11 $\bar{1}$
c	52 10	52 1	551	$\bar{3}\bar{5}\bar{1}$
d	56 0	55 59	13 $\bar{1}$	1 $\bar{3}$ 1
e	60 15	60 11	$\bar{3}\bar{3}\bar{1}$	5 $\bar{3}\bar{1}$
f	64 15	64 29	$\bar{1}\bar{1}\bar{1}$	31 $\bar{1}$
g	66 30	66 41	$\bar{3}\bar{1}\bar{3}$	51 $\bar{3}$

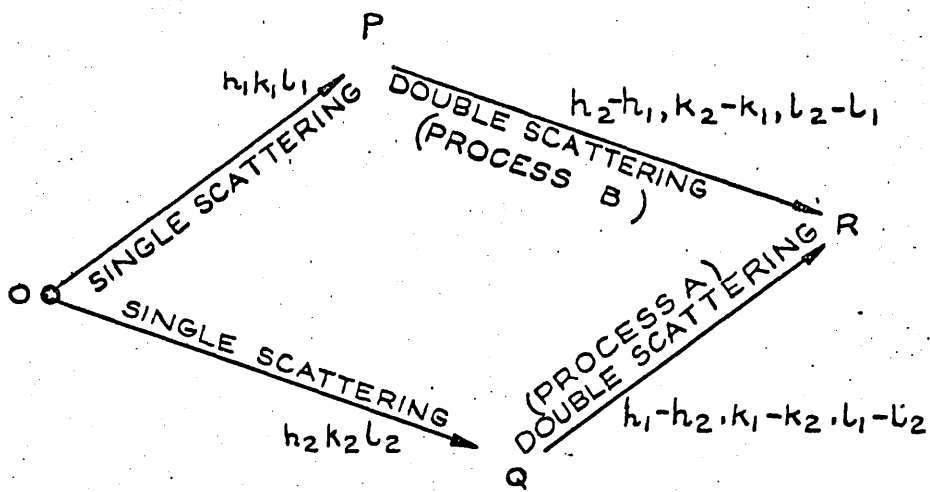
*calculated from equation (2) using $\tan \theta_{200} = 0.1887$
 (corresponding to $a_0 = 5.600 \text{ \AA}$, $\lambda = 1.038 \text{ \AA}$).



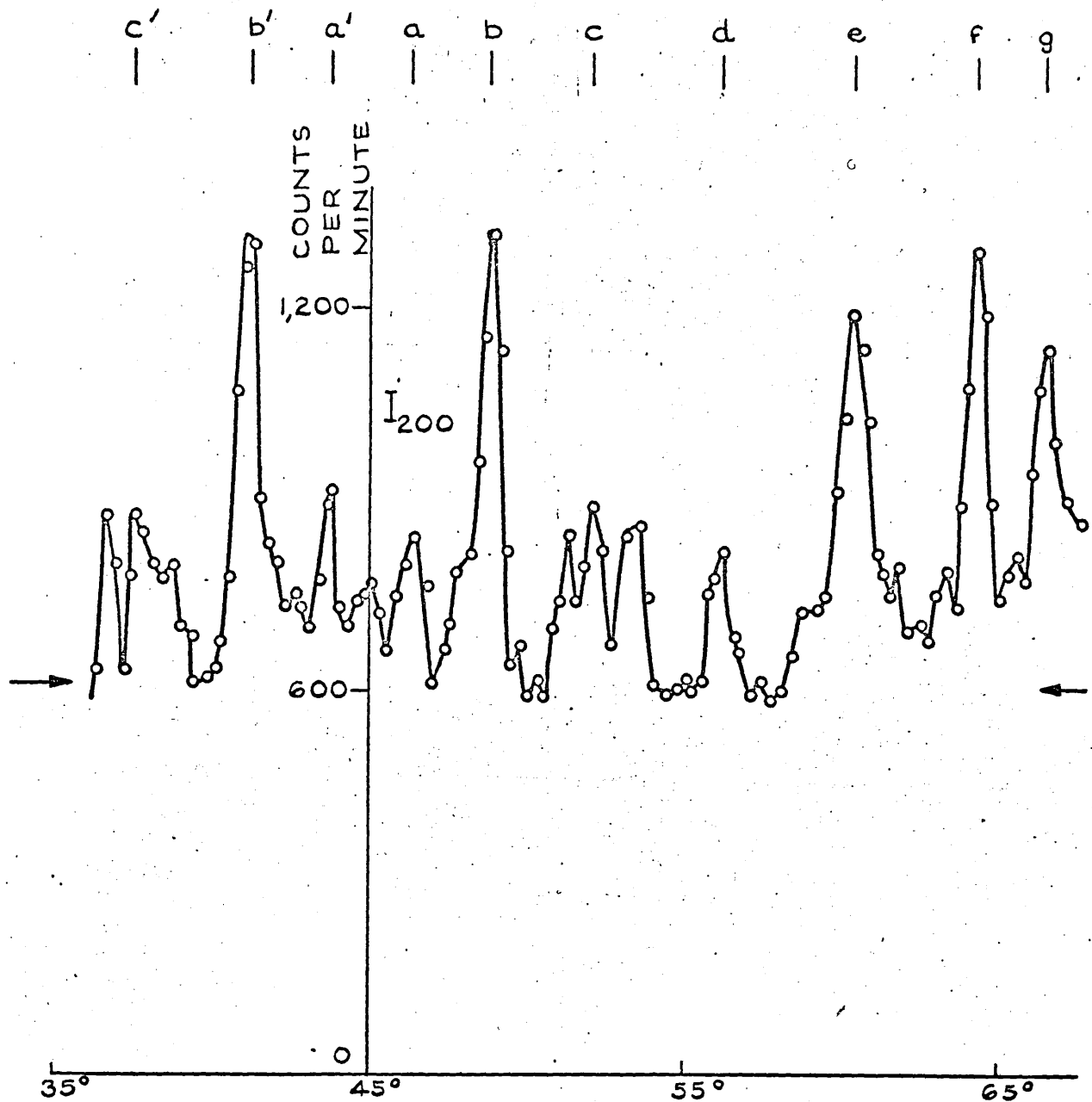
A.E.R.E. R.3959. FIG.1. CONES OF REFLEXION FOR PLANES OF SPACING d_1 AND d_2 . THE CONES INTERSECT ALONG THE LINES OP AND OQ .



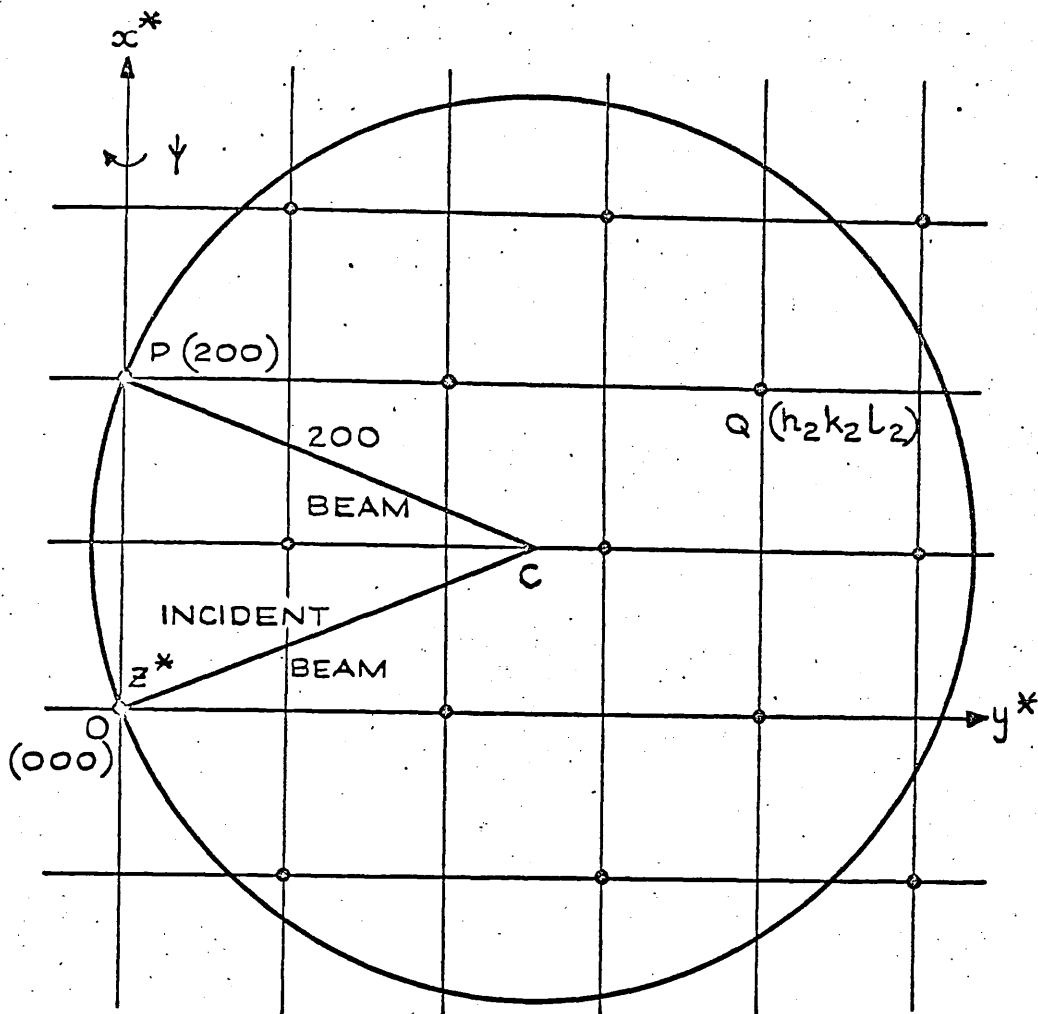
A.E.R.E. R.3959. FIG.2. EWALD CONSTRUCTION FOR DOUBLE SCATTERING. THE POINTS $P(h_1 k_1 l_1)$ AND $Q(h_2 k_2 l_2)$ SIMULTANEOUSLY LIE ON THE SPHERE OF REFLEXION. THE DIAGRAM ILLUSTRATES THE SPECIAL CASE WITH P AND Q IN THE EQUATORIAL PLANE; IN GENERAL, O, C, P, Q , ARE NOT CO-PLANAR.



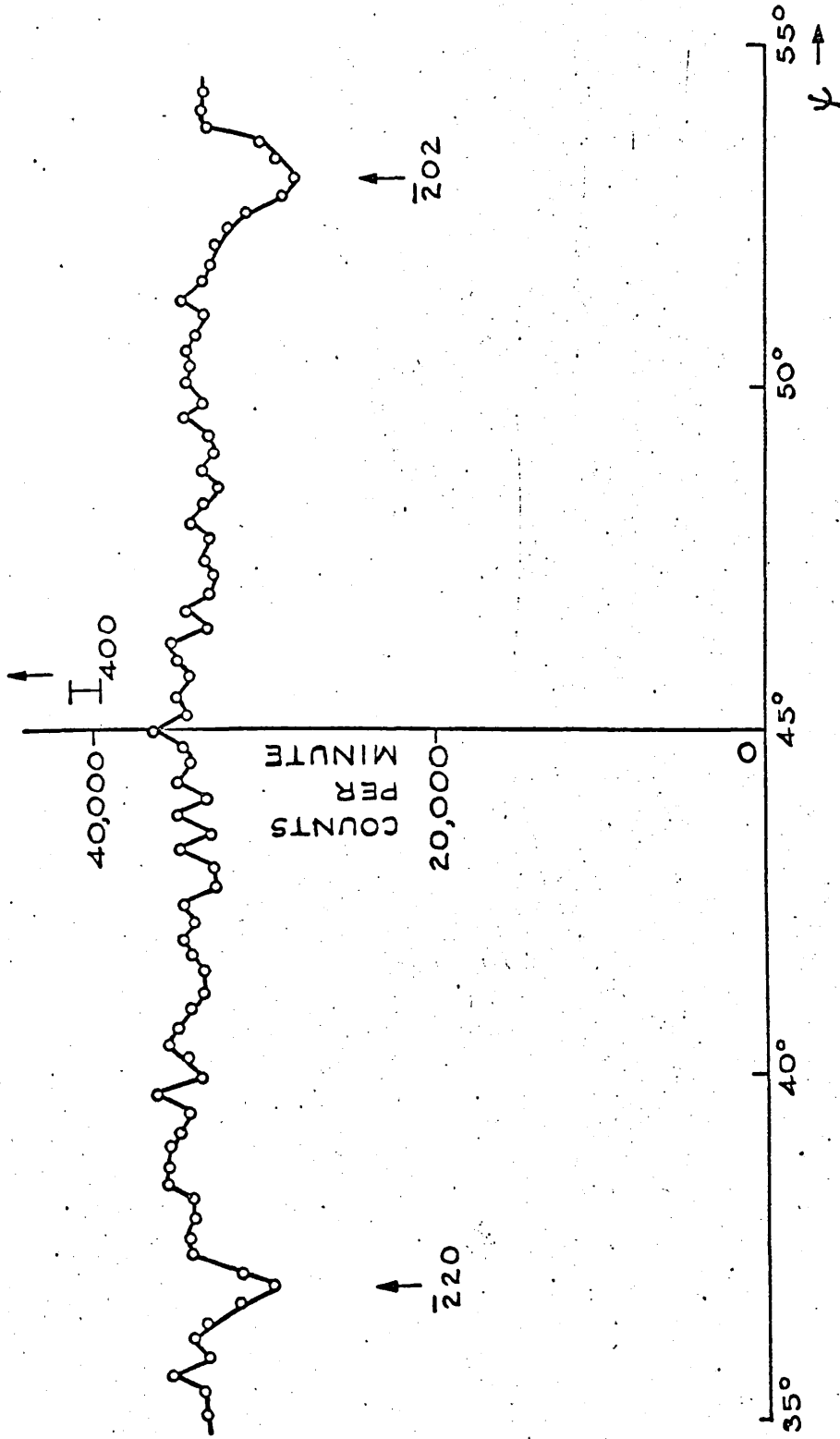
A.E.R.E. R3959. FIG.3. DIAGRAMMATIC REPRESENTATION OF POSSIBLE SINGLE-AND DOUBLE-SCATTERING PROCESSES WHEN TWO PLANES SIMULTANEOUSLY SATISFY THE BRAGG CONDITION. THE INTENSITY RECORDED IN THE DIRECTION \vec{OP} IS ENHANCED BY THE DOUBLE-SCATTERING PROCESS A, \vec{OQ} TO \vec{QR} , AND REDUCED BY THE PROCESS B, \vec{OP} TO \vec{PR} .



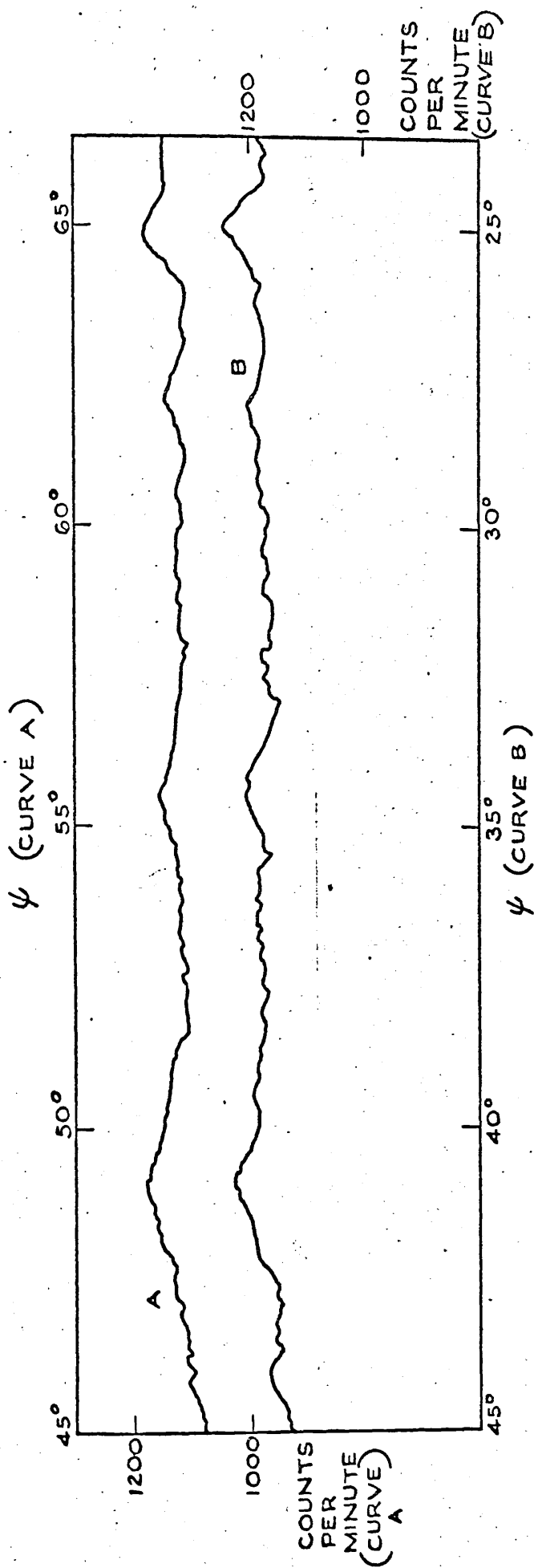
A.E.R.E.R.3959. FIG.4. DEPENDENCE OF INTENSITY
OF 200 REFLEXION FROM ThO_2 ON AZIMUTHAL
SETTING OF REFLECTING PLANE. ARROWS INDICATE
INTENSITY LEVEL IN THE ABSENCE OF MULTIPLE
SCATTERING. THE RENNINGER REFLEXIONS, LABELLED
 $a b c \dots$, ARE INDEXED IN TABLE I



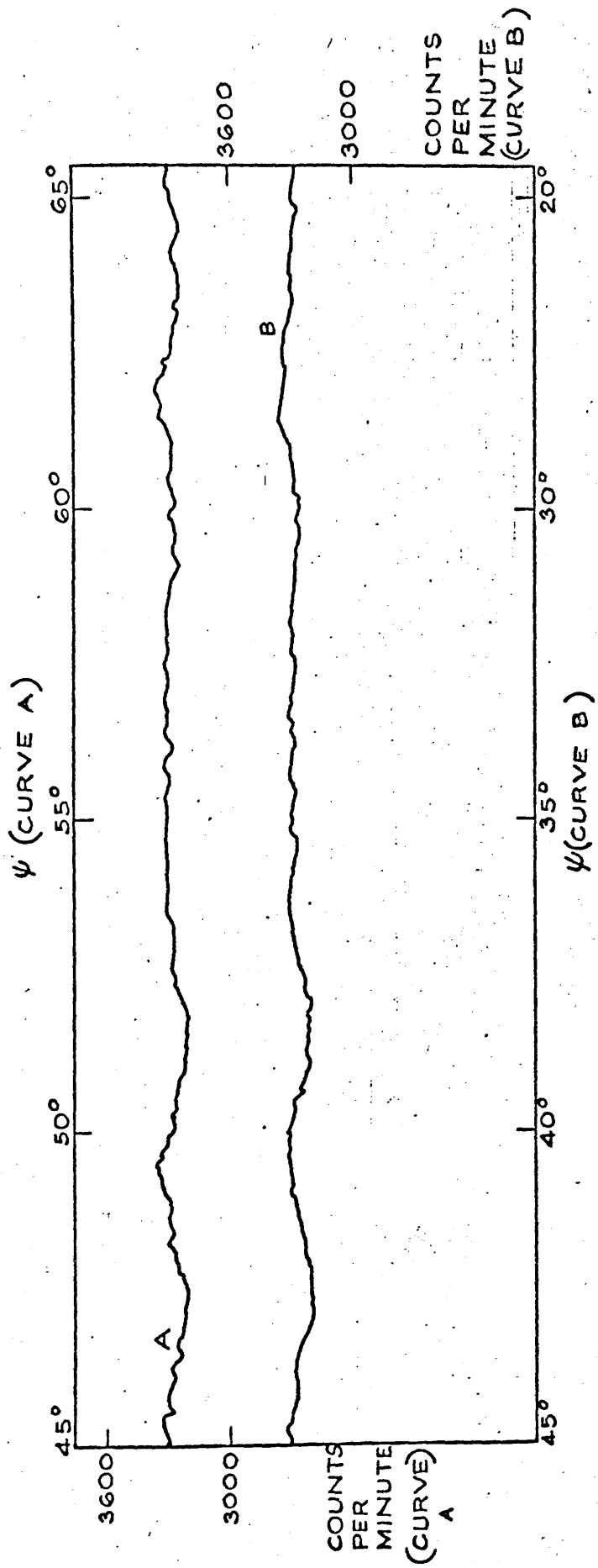
A.E.R.E. R.3959. FIG. 5. RECIPROCAL LATTICE AND EWALD
SPHERE OF REFLEXION FOR EXPERIMENTAL ARRANGEMENT
USED IN DERIVING FIG. 4.



A.E.R.E. R3959. FIG. 6. VARIATION OF INTENSITY OF 400 REFLEXION FROM ThO_2 WITH AZIMUTHAL SETTING OF REFLECTING PLANE. THE DIPS AT $\psi=37^\circ$ AND 53° ARE CAUSED BY SCATTERING OF THE ONCE-REFLECTED 400 BEAM BY THE (220) AND (202) PLANES



A.E.R.E. R3959. FIG. 7. RECORDER TRACE OF INTENSITY OF 200 REFLEXION OF UO_2 , TAKEN DURING CONTINUOUS ROTATION OF THE CRYSTAL ABOUT THE SCATTERING VECTOR. NOTE THE SYMMETRY OF THE TRACE ABOUT THE ORDINATE $\psi = 45^\circ$



A.E.R.E. R.3959 FIG. 8. RECORDER TRACE OF INTENSITY OF 511 REFLEXION OF UO_2 , TAKEN DURING CONTINUOUS ROTATION OF THE CRYSTAL ABOUT THE SCATTERING VECTOR.

*Reprinted without change of pagination from the
Proceedings of the Royal Society, A, volume, 274, pp. 122–133, 1963*

Neutron diffraction studies of the actinide oxides

I. Uranium dioxide and thorium dioxide at room temperature

BY B. T. M. WILLIS

Metallurgy Division, Atomic Energy Research Establishment, Harwell, Berks.

*(Communicated by R. Spence, F.R.S.—Received 13 December 1962
—Read 4 April 1963)*

Three-dimensional neutron structure factors have been measured on single crystals grown from the melt and from solution. The Bragg reflexions divide into three groups, strong, medium and weak: the strong and medium reflexions are affected by extinction, which is particularly severe for solution-grown crystals, and the weak reflexions by double Bragg scattering. Least-squares analysis of experimental data corrected for these systematic errors confirms that the oxides have the fluorite structure at room temperature and gives precise values for the Debye–Waller factors of the heavy-metal and oxygen atoms and for the ratios of their nuclear coherent scattering amplitudes.

1. INTRODUCTION

The crystal structures of the actinide oxides have been the subject of numerous X-ray investigations, but progress in this field has been restricted by the difficulty of locating with X-rays the relatively light atoms of oxygen. This difficulty is particularly severe with the uranium oxides, which exist in a multiplicity of stable states having complex phase relationships and wide ranges of non-stoichiometry. Under these circumstances it is necessary to make very precise diffraction measurements to determine, for instance, the positions of interstitial oxygen atoms present in only a small concentration, or the average (non-integral) occupation numbers of sites occupied by oxygen atoms.

In principle, direct location of the oxygen atoms can be carried out more easily by neutron diffraction. The slow-neutron coherent scattering cross-section of oxygen is between one-third and one-half of the scattering cross-sections of uranium and thorium, so that the oxygen atoms in UO_2 or ThO_2 contribute appreciably to the observed intensities. Moreover, the absorption cross-sections of these oxides for slow neutrons are four or five orders of magnitude less than for X-rays, so that single-crystal neutron intensities can be accurately corrected for the small effect of absorption and are representative of the whole crystal rather than of a surface layer a few microns deep, as in the X-ray case. On the other hand, to obtain adequate neutron intensities a single crystal measuring at least 1 mm across must be used, so that special precautions must be taken to avoid systematic errors in measuring the intensities, arising from secondary extinction and from double Bragg scattering (see §§ 4 and 5).

This paper (part I) describes neutron diffraction work at room temperature on single crystals of UO_2 and ThO_2 . The analysis of the experimental data indicates that the oxides have the fluorite-type structure, with isotropic atomic Debye–Waller factors, although at higher temperatures (see part II, Willis 1963, which

follows) this statement is no longer precisely true. A number of parameters are derived, including the ratio b_U/b_O of the nuclear coherent scattering amplitudes of uranium and oxygen, the corresponding ratio b_{Th}/b_O for thorium and oxygen, and the Debye–Waller factors of the metal and oxygen atoms at 20 °C.

2. THEORY

The aim is to determine that crystal structure which gives closest agreement between observed and calculated structure factors. In this section the structure factors are calculated for three cases, covering various possible configurations of the oxygen atoms in UO_2 and ThO_2 . Case (a) refers to the fluorite structure with the metal atoms at the 4-fold positions

$$4(a) = 000, \frac{1}{2}\frac{1}{2}0, \frac{1}{2}0\frac{1}{2}, 0\frac{1}{2}\frac{1}{2},$$

and the oxygen atoms at the 8-fold positions

$$8(c) = \frac{1}{4}\frac{1}{4}\frac{1}{4}, \frac{1}{4}\frac{1}{4}\frac{3}{4}, \frac{1}{4}\frac{3}{4}\frac{1}{4}, \frac{3}{4}\frac{1}{4}\frac{1}{4}, \\ \frac{3}{4}\frac{3}{4}\frac{1}{4}, \frac{3}{4}\frac{1}{4}\frac{3}{4}, \frac{1}{4}\frac{1}{4}\frac{3}{4}, \frac{1}{4}\frac{3}{4}\frac{3}{4}$$

of the cubic space-group $Fm\bar{3}m$ (see figure 1). X-ray work shows that these are

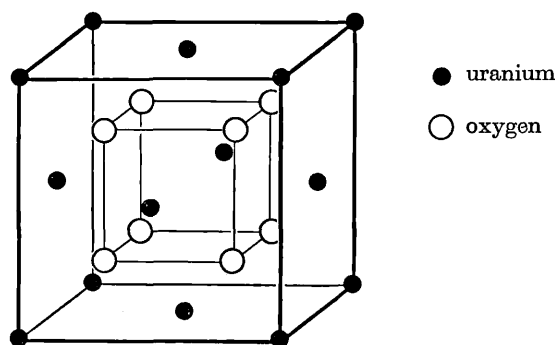


FIGURE 1. Unit cell of uranium dioxide (fluorite structure).

the correct positions for the metal atoms. In case (b) the space group remains $Fm\bar{3}m$ but the oxygen atoms occupy more general positions than 8(c) and in case (c) the lattice is no longer face-centred.

(a) Fluorite structure

The Bragg reflexions fall into three distinct groups. For $h+k+l = 4n$, where n is an integer, the metal and oxygen atoms scatter in-phase and the reflexion is strong; for $h+k+l = 4n+2$ they scatter out-of-phase and the reflexion is weak; and for $h+k+l = 4n+1$ the metal atoms only contribute to the scattering and the reflexion has medium intensity. The calculated structure factors F_c are:

$$\left. \begin{aligned} F_c^{4n} &= 4b_M \exp(-B_M \sin^2 \theta / \lambda^2) + 8b_O \exp(-B_O \sin^2 \theta / \lambda^2), \\ F_c^{4n+1} &= 4b_M \exp(-B_M \sin^2 \theta / \lambda^2), \\ F_c^{4n+2} &= 4b_M \exp(-B_M \sin^2 \theta / \lambda^2) - 8b_O \exp(-B_O \sin^2 \theta / \lambda^2). \end{aligned} \right\} \quad (1)$$

Here b_M and b_O are the nuclear coherent scattering amplitudes of the metal and oxygen atoms, B_M and B_O their 'temperature factors', θ the Bragg angle and λ the wavelength. Assuming that the lattice vibrations are harmonic these temperature factors are isotropic, as the atoms occupy sites with cubic point symmetry. A plot of $\ln F_c$ against $\sin^2 \theta / \lambda^2$ gives a straight line of slope $-B_M$ for the $4n \pm 1$ reflexions and two lines with slopes determined by both B_M and B_O for the $4n$ and $4n + 2$ reflexions. The intercepts of these three lines on the ordinate axis give F_c values in the arithmetic ratio $b_M + 2b_O : b_M : b_M - 2b_O$.

TABLE 1. NEUTRON STRUCTURE FACTORS CALCULATED FOR
 $u = 0.26$ IN SPACE GROUP $Fm\bar{3}m$

	hkl	F_c for UO_2	F_c for ThO_2
$h+k+l = 4n$	220	0.99	0.99
	440	0.97	0.97
	664	0.91	0.91
$h+k+l = 4n \pm 1$	111	1.00	1.00
	533	1.01	1.01
	755	0.94	0.95
$h+k+l = 4n + 2$	200	0.97	0.92
	600	0.74	0.46
	662	0.46	0.12

(b) *Face-centred (non-fluorite) structure*

If the eight oxygen atoms in the unit cell are statistically distributed about 16-fold or higher-fold positions of the $Fm\bar{3}m$ space-group, they can move away from the fluorite type $\frac{1}{4}\frac{1}{4}\frac{1}{4}$... sites. For example, the oxygen atoms could be statistically accommodated in one quarter of the 32-fold positions

$$32(f): (000, \frac{1}{2}\frac{1}{2}0, \frac{1}{2}0\frac{1}{2}, 0\frac{1}{2}\frac{1}{2}) \pm uuu, u\bar{u}\bar{u}, \bar{u}u\bar{u}, \bar{u}\bar{u}u$$

and, neglecting the effect of thermal vibration ($B_M = B_O = 0$), the structure-factor expression is then

$$F_c = 4b_M + 8b_O \cos 2\pi hu \cos 2\pi kv \cos 2\pi lu.$$

Table 1 lists F_c for the three groups of reflexions with $h+k+l = 4n, 4n \pm 1, 4n + 2$, as calculated for $u = 0.26$ and normalized to the value for $u = 0.25$, corresponding to the fluorite structure. The departure of F_c from unity in this table is caused by the oxygen atoms moving less than 0.1 Å from $u = 0.25$ to 0.26. The largest changes occur in the $4n + 2$ reflexions whose intensities, proportional to F_c^2 , are reduced at high scattering angles by a factor of four or more.

(c) *Non-face-centred lattice*

Extra reflexions of mixed indices will appear if the lattice is not face-centred. Table 2 gives a few structure factors calculated for these extra reflexions, assuming that the oxygen atoms occupy the 8-fold positions

$$8(g) = \pm uuu, u\bar{u}\bar{u}, \bar{u}u\bar{u}, \bar{u}\bar{u}u$$

of the $Pm\bar{3}m$ space-group, with $u = 0.26$. Again this only represents a small departure from the fluorite positions, but the strongest of these extra reflexions, whose F_c values are expressed in table 2 as a ratio of the scattering amplitude of oxygen, could be readily observed in a crystal weighing 10 mg.

We can now state in anticipation of results to be given later that case (a) applies to UO_2 at room temperature, (b) to UO_{2+x} at high temperatures, where $0 < x < 0.25$ and (c) to U_4O_9 . Thus, as interstitial oxygen atoms are added to UO_2 to form UO_{2+x} , the space-group remains $Fm\bar{3}m$ but the original oxygen atoms move away from fluorite 8(c) to more general positions; finally, at the approximate composition U_4O_9 ($x = 0.25$), the interstitial oxygen atoms assume an ordered configuration and the lattice becomes body-centred, space-group $I\bar{4}3d$.

TABLE 2. NEUTRON STRUCTURE FACTORS FOR REFLEXIONS WITH MIXED INDICES CALCULATED FOR $u = 0.26$ IN SPACE GROUP $Pm\bar{3}m$

hkl	F_c (normalized to b_0)
112	0.02
041	0.50
554	0.14
065	0.70
663	0.66

3. EXPERIMENTAL METHOD

Neutron intensities were measured by means of the single-crystal equipment described by Willis (1962*a*). Three-dimensional data were collected by adding a two-circle $\Phi - X$ attachment (Willis 1962*b*) to the base of the diffractometer, and with a neutron wavelength of 1.038 \AA all non-equivalent reflexions were measured out to $\sin \theta/\lambda = 0.92$. For each measurement the normal to the hkl plane was turned to the Bragg reflecting position in the equatorial plane and the integrated intensity ρ_{hkl} determined by the standard rotating-crystal method. Integrated intensities were reduced to observed structure factors $|F_o|$ by means of the formula

$$\rho_{hkl} = kA_{hkl}|F_o|^2 \operatorname{cosec} 2\theta_{hkl}, \quad (2)$$

where A_{hkl} is the absorption factor and k an unknown scale factor, which is the same for all reflexions. A_{hkl} was evaluated from the measured absorption coefficient and linear dimensions of the crystal; it was close to unity for all the crystals referred to below, except for the crystal of UO_2 enriched in the isotope $^{235}_{92}\text{U}$.

4. EXPERIMENTAL RESULTS ON URANIUM DIOXIDE

Single crystals were available which had been grown by three different techniques, from the melt, from the vapour and from solution. The fused crystals were selected from a batch supplied by Spencer Chemical Co., U.S.A. and the vapour-grown crystals were furnished by Dr S. Amelinekx (Van Lierde, Strumane, Smets & Amelinekx 1962). Crystals from both sources were of ample size for neutron diffraction and were cleaved or ground to shape. The solution-grown crystals were much smaller, weighing no more than 50 mg; they were provided by Dr R. G. Robins (Robins 1961).

(a) *Fused crystals*

Microscopic examination revealed that these contained 1 or 2% of polycrystalline U or UO_2 , segregated into small inclusions in the single-crystal matrix. The results given below refer to coherent scattering from the matrix only, whose composition was estimated by measuring the oxygen potential with a high temperature galvanic cell (Markin & Bones 1962) to be $\text{UO}_{2.000 \pm 0.004}$.

Figure 2 shows experimental results for two crystals, *A* and *B*: *A* was a fragment with {111} cleavage faces, weighing 170 mg, and *B* was a smaller crystal, cut into a pillar 1 mm \times 1 mm in cross-section and with its long axis along [110]. The reflexions are distributed about three curves, as predicted by equation (1) for the fluorite structure, but in both crystals the position of the intercept of the $4n$ curve

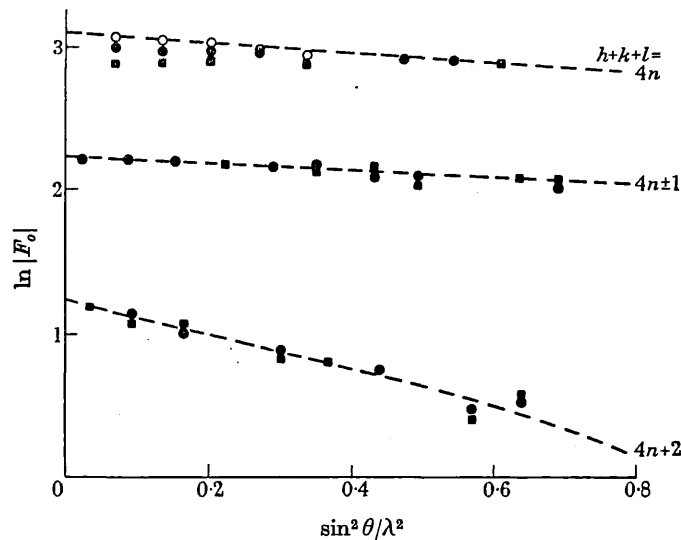


FIGURE 2. Experimental results for fused crystals of UO_2 . The broken lines represent the least-squares fit of equation (1) to the experimental points. $|F_o|$ is on an arbitrary scale. ■, Crystal *A*; ●, crystal *B*; ○, crystal *B*, corrected for extinction.

on the ordinate axis is lower than expected. The discrepancy between observed and calculated structure factors is more marked in the larger crystal and at small Bragg angles where the peak intensities are strongest. This behaviour is strongly suggestive of extinction.

The presence of secondary extinction in the smaller crystal *B* was confirmed by measuring the integrated intensities of several strong reflexions as a function of the path length of the neutron beam in the crystal. The path length was varied by rotating the crystal about the normal to the reflecting plane, use being made of the extra degree of rotational freedom available in a three-circle setting device (Willis 1962*b*). The secondary extinction factor E_{hkl}^s , defined as the proportional reduction in the integrated intensity due to secondary extinction, and the mosaic spread η were derived directly from the intensity measurements on each strong reflexion

(Willis 1962*c*) and are listed in table 3. The mean value of η is 4.3 minutes of arc and this will be compared later with the η values of crystals grown from solution and from the vapour.

To return now to the results given in figure 2, the $4n$ points for crystal *B* are shown as open circles after correction is made for extinction on the basis of an average mosaic spread of 4.3 minutes of arc. The intercept on the ordinate axis of the line through these corrected points is close to the theoretical position for the fluorite structure.

The structure-factor data for the $4n + 2$ and high-angle $4n \pm 1$ reflexions, which are unaffected by extinction, were analyzed by the least-squares method to obtain the best fit between $|F_o|$ and $|F_c|$ calculated from equation (1). Four parameters—overall scale factor k , ratio of scattering amplitudes of uranium and oxygen b_U/b_O , and temperature factors B_U , B_O —were determined on the Mercury computer, by means of a program which allows refinement of the scattering amplitudes

TABLE 3. ANALYSIS OF EXTINCTION MEASUREMENTS
ON FUSED URANIUM DIOXIDE

hkl	E_{hkl}^2	(minutes of arc)
220	0.85	5.1
400	0.88	4.3
422	0.91	3.7
440	0.93	3.9

of atoms in the space-group $Fm\bar{3}m$ as well as their positional co-ordinates and temperature factors. k and B_U were determined first from the $4n \pm 1$ reflexions, whose intensities are independent of the oxygen atoms. With k and B_U fixed, the values of b_U/b_O and B_O were then found from the $4n + 2$ data. Table 4 lists the computed values of B_U , B_O , b_U/b_O and their standard deviations, together with the number of reflexions used in the analysis and the residual $R_1 = \sum |F_o| - |F_c| / \sum |F_o|$ for the two crystals *A*, *B* and a third crystal *C* not included in figure 2. The residuals are larger for the $4n + 2$ reflexions than for $4n \pm 1$; this is probably due to double Bragg scattering (§ 5), which is more prominent for the weaker reflexions, and justifies the procedure of refining the data in two groups, assigning equal weight to each reflexion in a group. The amplitude of vibration of the oxygen atoms is greater than for uranium ($B_O > B_U$), a feature immediately apparent from figure 2 where the slope of the $4n + 2$ curve is greater than that of $4n \pm 1$. The average value of b_U/b_O in table 4 is 1.474 ± 0.010 , which compares with the most recently published value (Roof, Arnold & Gschneidner 1962) of 1.45 ± 0.09 . This ratio must be known to an accuracy of at least 1% to allow the determination by neutron diffraction of the occupation numbers of atomic sites in the non-stoichiometric uranium oxides.

It is estimated from the intensities of the $4n + 2$ reflexions, which are particularly sensitive to displacements of the oxygen atoms from the $\frac{1}{4}\frac{1}{4}\frac{1}{4} \dots$ positions (see table 1), that these atoms are within 0.02 Å of the fluorite positions. No extra neutron reflexions with mixed indices were observed, so that the lattice is face-centred as for the fluorite structure.

(b) Solution-grown crystals

A few single crystals, which had been grown by electro-deposition at 850 °C on a platinum cathode, were examined by neutron diffraction. They were of regular shape, bounded by {111} and {100} habit faces, with a maximum mass of about 50 mg. They contained no inclusions and the oxygen/uranium ratio was close to the stoichiometric value 2.000.

Figure 3 is a typical plot of $\ln |F_o|$ against $\sin^2 \theta / \lambda^2$ with the $|F_o|$'s uncorrected for extinction. The intensities of both $4n$ and $4n \pm 1$ reflexions, normalized to a standard

TABLE 4. LEAST-SQUARES ANALYSIS OF INTENSITY MEASUREMENTS ON URANIUM DIOXIDE

$4n \pm 1$ reflexions				
crystal	number of reflexions	B_U (\AA^2)	R_1 (%)	
A	13	0.29 ± 0.06	3.7	
B	13	0.42 ± 0.06	2.0	
C	7	0.23 ± 0.04	1.6	
average 0.31 ± 0.04				
$4n + 2$ reflexions				
crystal	number of reflexions	B_o (\AA^2)	$\frac{b_U}{b_o}$	R_1 (%)
A	7	0.44 ± 0.08	1.482 ± 0.014	4.8
B	10	0.56 ± 0.06	1.476 ± 0.011	2.8
C	4	0.46 ± 0.06	1.463 ± 0.010	2.6
average 0.49 ± 0.06 1.474 ± 0.010				

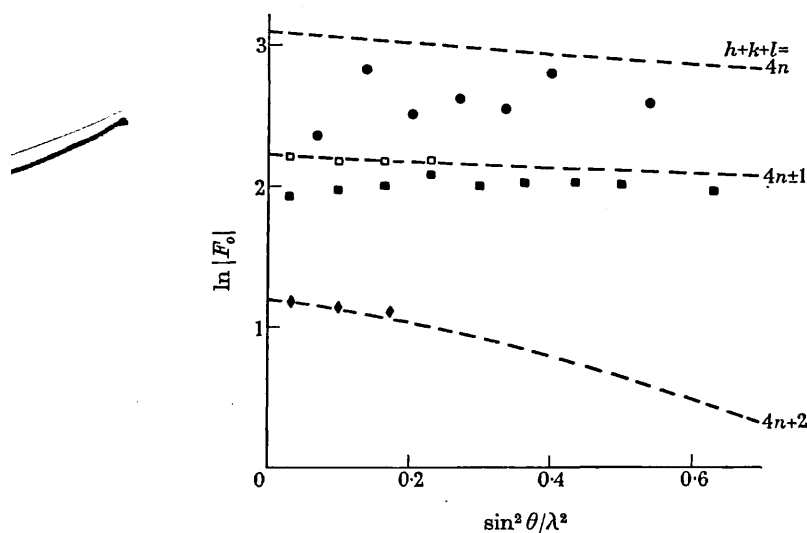


FIGURE 3. Experimental results for a solution-grown crystal of UO_2 . The broken lines are the theoretical curves for the fluorite structure. \bullet , $4n$; \blacksquare , $4n \pm 1$; \square , $4n \pm 1$, corrected for extinction; \blacklozenge , $4n + 2$.

mass and incident neutron flux, were less than for the fused crystals, whereas the $4n + 2$ reflexions were about the same. This discrepancy is due to secondary extinction, which is much more severe in solution-grown crystals in spite of their smaller size. Extinction of the $4n$ reflexions was too large to correct by measuring the intensity as a function of neutron path length, but the $4n \pm 1$ reflexions were corrected in this way and the analysis of the extinction results gave a mosaic spread η of 13 seconds of arc for the crystal to which figure 3 refers.

A small cubo-octahedral crystal of UO_2 containing 93% of ^{235}U was available, so that an attempt was made to measure the nuclear coherent scattering amplitude of ^{235}U from diffraction data. This quantity was not required for the present series of studies, but its value has not yet been recorded. The high fission cross-section of ^{235}U increases the linear absorption coefficient of the oxide; this was measured directly as 7.2 cm^{-1} , which compares with the measured value of 0.49 cm^{-1} for natural UO_2 . The absorption factor A_{hd} in equation (2) was computed for the $4n \pm 1$ and $4n + 2$ reflexions on the Mercury computer. The $|F_o|$ data were analyzed by least squares, keeping B_U and B_O fixed at the average values of table 4 and varying only the scale factor and the ratio b_U/b_O where b_U is the coherent scattering amplitude of ^{235}U . The analysis gave

$$b_U/b_O = 1.71 \pm 0.08,$$

and taking $b_O = 0.577 \pm 0.004 \times 10^{-12} \text{ cm}$ leads to the value

$$b_U = 0.99 \pm 0.05 \times 10^{-12} \text{ cm}.$$

The relatively large limits of error are due to the uncertainty in measuring the intensities arising from extinction.

(c) *Vapour-grown crystals*

These became available towards the end of the present investigation. No detailed intensity measurements were carried out, but it was clear that the Bragg reflexions were affected less by extinction than for either of the other kinds of crystal and that the mosaic spread η was at least 5 minutes of arc.

The differences in the neutron reflecting properties of the three kinds of crystal is brought out in a striking way in figure 4. This shows the rocking curve, relating the neutron intensity with rotation angle ω , of the 800 reflexion of each crystal. The 800 reflexion was chosen as this is near the 'focusing position', at which the reflected beam from the crystal is parallel to the direct beam striking the monochromator; for this position the rocking-curve width is a minimum and is independent of the collimation angle. The half-width Δ of the rocking curve is greatest for the vapour-grown crystal and least for that grown from solution. This order is that anticipated from the estimates of the mosaic spread given by the analysis of the extinction measurements. Figure 4 includes for each crystal the values of Δ , η and d : d is the maximum dislocation density estimated from the expression (Hirsch 1955)

$$d = \eta^2/9b^2,$$

where the magnitude of the Burgers vector b is taken as 3 \AA .

It appears, therefore, that crystals grown above 2000 °C from the vapour or the melt are more imperfect than those crystallizing from solution at 850 °C. Fused or vapour-grown crystals are more suitable for diffraction work as they approach more closely to the 'ideally imperfect crystal' of theoretical crystallography.

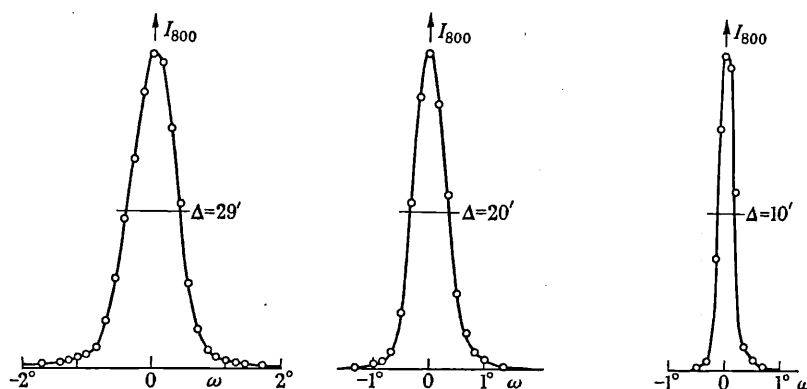


FIGURE 4. Rocking curves for the 800 reflexion: (a) refers to a crystal grown from the vapour, $\eta > 5'$, $d > 10^8 \text{ cm}^{-2}$; (b) from the melt, $\eta = 4.3'$, $d \doteq 10^8 \text{ cm}^{-2}$; and (c) from solution, $\eta = 0.22'$, $d \doteq 10^6 \text{ cm}^{-2}$. Δ is the half-width of the rocking curve, η the mosaic spread derived from extinction data and d the maximum dislocation density.

5. EXPERIMENTAL RESULTS ON THORIUM DIOXIDE

Figure 5 shows experimental results for two small single crystals *D* and *E*: *D* (90 mg) was grown from the melt and *E* (40 mg) by slowly cooling from 1500 to 800 °C a solution of ThO₂ in lead metaborate. The intensities of the $4n$ and $4n \pm 1$ reflexions are higher for the fused crystal; again this difference is due to extinction, which is less severe for the crystal grown at the higher temperature. No correction for extinction was attempted but it was estimated that the mosaic spreads were comparable for fused ThO₂ and UO₂ and for solution-grown ThO₂ and UO₂.

The experimental points for the $4n + 2$ reflexions in figure 5 are appreciably scattered about the broken line calculated for the fluorite structure. All the points except those marked by crosses were recorded at a fixed azimuthal position of the reflecting plane and the fluctuations about the broken line were reproducible with different crystals. The most anomalous reflexion was 10, 0, 0 whose intensity was twice that expected for both crystals *D* and *E*. No reflexions of mixed indices were observed, so that the lattice is face-centred and there is no reason to doubt the fluorite structure. The origin of the anomalous $|F_o|$ values for $4n + 2$ reflexions is, in fact, double Bragg scattering (Renninger 1937), which is more serious than in UO₂ as the scattering amplitude of thorium is greater than that of uranium and the $4n + 2$ reflexions are therefore much weaker in ThO₂. The points shown as crosses in figure 5 refer to $|F_o|$ values measured at different azimuthal orientations ψ , in 10° intervals of ψ , of the reflecting plane about its scattering vector. This rapid variation of $|F_o|$ with ψ is characteristic of double Bragg scattering.

A more detailed investigation of the double-scattering process was carried out on the 200 reflexion of crystal *D*. The peak intensity of 200 was measured at $\frac{1}{4}^\circ$

intervals of ψ and the results are plotted in figure 6 for the range $35^\circ < \psi < 65^\circ$. The most pronounced fluctuations in this curve are labelled *a, b, c...* and all these have been shown to be associated with double scattering from $(h'k'l')$ and $(2-h', k', l')$ planes. Successive scattering from planes with these indices simulates the single-scattering process from (200). Table 5 gives the $h'k'l'$ indices associated with each Renninger peak together with the observed and calculated values of ψ at which the peak occurs. $\psi_{\text{obs.}}$ and $\psi_{\text{calc.}}$ agree to within 15 minutes of arc; closer agreement cannot be expected as the neutron wavelength is not sufficiently well defined

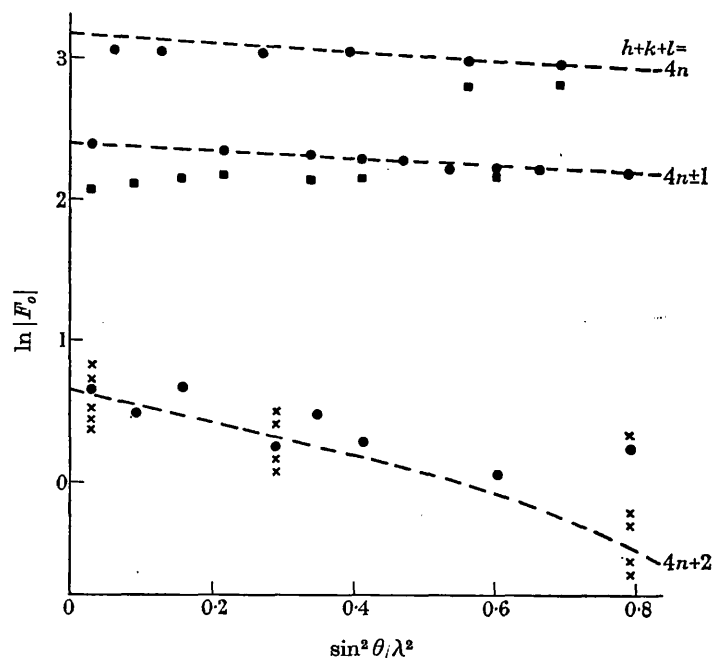


FIGURE 5. Experimental results for crystal *D* (●) of fused ThO_2 and crystal *E* (■) of ThO_2 grown from solution. The crosses refer to measurements of *D* taken at different azimuthal orientations of the reflecting plane. The broken lines are the theoretical curves for the fluorite structure.

($\lambda = 1.038 \pm 0.005 \text{ \AA}$). It is to be noted that figure 6 is symmetrical about the ordinate $\psi = 45^\circ$, corresponding to a symmetry position of the crystal, and that the indices $(h'k'l')$, $(2-h', k', l')$ are all odd. If either plane has even indices one of the planes is a $4n+2$ type, for which the structure factor is very small, so that the Renninger peak is relatively weak.

Table 6 gives the results of the least-squares analysis of the extinction-free $4n+1$ and $4n+2$ data from two fused crystals *D* and *F*. The $|F_0|$ values of the $4n+2$ reflexions were taken as the mean of those recorded at different settings of ψ ; it was probably more correct to use the minimum rather than the mean value but either choice gave similar values for the final parameters $b_{\text{Th}}/b_{\text{O}}$, B_{Th} and B_{O} . As for UO_2 the least-squares analysis was carried out in two stages and the high residual R_1 for the $4n+2$ reflexions reflects the influence of double Bragg scattering.

From table 6 $b_{\text{Th}}/b_{\text{O}}$ is 1.725 ± 0.016 , which compares with 1.69 ± 0.08 given by Roof *et al.* (1962). Table 7 summarizes the most recent determinations of the nuclear coherent scattering amplitudes of the actinide elements.

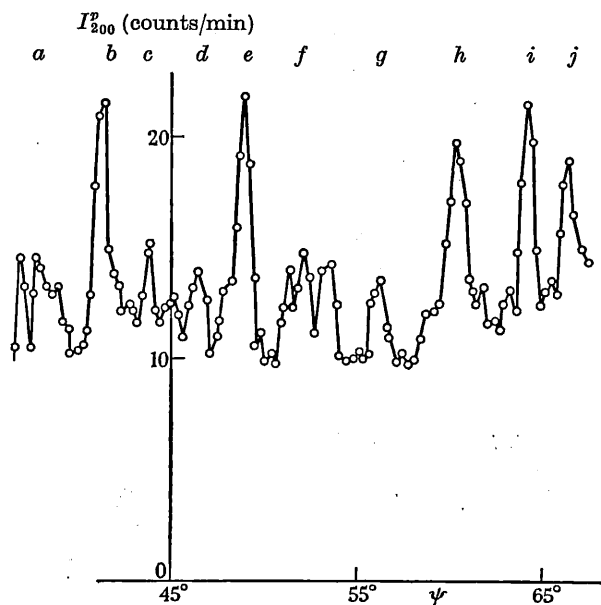


FIGURE 6. Dependence of peak intensity of 200 reflexion from ThO_2 on azimuthal orientation of (200) plane. The Renninger peaks are labelled a, b, c, \dots

TABLE 5. RENNINGER PEAKS ASSOCIATED WITH 200 REFLEXION OF THORIUM DIOXIDE

Renninger peak (figure 6)	$\psi_{\text{obs.}}$		$\psi_{\text{calc.}}^*$		$h'k'l'$
	deg	min	deg	min	
<i>a</i>	37	50	37	59	515
<i>b</i>	41	10	41	10	11 $\bar{1}$
<i>c</i>	43	35	43	46	1 $\bar{1}$ 5
<i>d</i>	46	25	46	14	15 $\bar{1}$
<i>e</i>	48	50	48	50	1 $\bar{1}$ 1
<i>f</i>	52	10	52	1	551
<i>g</i>	56	0	55	59	13 $\bar{1}$
<i>h</i>	60	15	60	11	331
<i>i</i>	64	15	64	29	1 $\bar{1}$ 1
<i>j</i>	66	30	66	41	313

* Calculated from $2k' \cos \psi + 2l' \sin \psi = \tan \theta_{200}(h'^2 + k'^2 + l'^2 - 2h')$.

6. CONCLUSIONS

The Bragg intensities of UO_2 and ThO_2 , measured by neutron diffraction, occur in three groups: strong, medium and weak, corresponding to $h + k + l = 4n$, $4n + 1$ and $4n + 2$, respectively. The strong and medium reflexions are affected by extinction, which is particularly severe for crystals grown from solution, and the weak reflexions by double Bragg scattering. Special precautions are therefore necessary

to obtain accurate structure-factor data. Least-squares analysis of three-dimensional data shows that the crystal structure is fluorite-type and gives the values of the isotropic Debye-Waller factors of the metal and oxygen atoms at 20 °C and the ratios of their nuclear coherent scattering amplitudes. The accurate measurement of these quantities is an essential preliminary step to the investigation, described in the next and subsequent parts, of UO_2 , ThO_2 and the non-stoichiometric uranium oxides at high temperature.

TABLE 6. LEAST-SQUARES ANALYSIS OF INTENSITY MEASUREMENTS ON THORIUM DIOXIDE

4n + 1 reflexions				
crystal	number of reflexions	B_{Th} (\AA^2)	R_1 (%)	
D	11	0.31 ± 0.03	0.9	
F	11	0.22 ± 0.04	2.1	
	average	0.27 ± 0.03		
4n + 2 reflexions				
crystal	number of reflexions	B_o (\AA^2)	b_{Th}/b_o	R_1 (%)
D	8	0.42 ± 0.05	1.715 ± 0.016	8.2
F	6	0.32 ± 0.05	1.736 ± 0.018	8.6
	average	0.37 ± 0.05	1.725 ± 0.016	

TABLE 7. SCATTERING AMPLITUDES OF ACTINIDE ELEMENTS

nuclide	b from Roof <i>et al.</i> (1962) (10^{-12} cm)	b* from present work (10^{-12} cm)
^{232}Th	0.98 ± 0.01	0.995 ± 0.009
^{235}U	—	0.98 ± 0.06
^{238}U	0.84 ± 0.02	0.850 ± 0.006

* Calculated on the assumption $b_o = 0.577 \times 10^{-12}$ cm.

The author is indebted to Messrs K. A. D. Lambe and T. M. Valentine for experimental assistance, to Mr K. D. Rouse for assistance in analyzing the results and to Dr J. S. Rollett of Oxford University for providing the least-squares Mercury program. Mr R. Bones of the Chemistry Division A.E.R.E. carried out the composition measurements.

REFERENCES

- Hirsch, P. B. 1955 *Progr. Metal Phys.* **6**, 281.
 Van Lierde, W., Strumane, R., Smets, E. & Amelinckx, S. 1962 *J. Nucl. Mater.* **5**, 250.
 Markin, T. L. & Bones, R. J. 1962 AERE unclassified report—R 4042.
 Renninger, M. 1937 *Z. Phys.* **106**, 141.
 Robins, R. G. 1961 *J. Nucl. Mater.* **3**, 294.
 Roof, R. B., Arnold, G. P. & Gschneidner, K. A. 1962 *Acta Cryst.* **15**, 351.
 Willis, B. T. M. 1962a *J. Sci. Instrum.* **39**, 590.
 Willis, B. T. M. 1962b *Brit. J. Appl. Phys.* **13**, 548.
 Willis, B. T. M. 1962c Pile neutron research in physics. *Proceedings of I.A.E.A. Conference, Vienna.*
 Willis, B. T. M. 1963 *Proc. Roy. Soc. A*, **274**, 134 (part II).

Reprinted without change of pagination from the
 Proceedings of the Royal Society, A, volume 274, pp. 134-144, 1963

Neutron diffraction studies of the actinide oxides

II. Thermal motions of the atoms in uranium dioxide and thorium dioxide between room temperature and 1100 °C

BY B. T. M. WILLIS

Metallurgy Division, Atomic Energy Research Establishment, Harwell, Berks.

(Communicated by R. Spence, F.R.S.—Received 13 December 1962

—Read 4 April 1963)

The mean-square thermal displacements of the atoms in UO_2 and ThO_2 have been determined as a function of temperature from the analysis of two-dimensional diffraction data. In the range investigated, 20 to 1100 °C, the oxygen atoms vibrate more strongly than the metal atoms and at each temperature the displacements of the metal and oxygen atoms are slightly less in ThO_2 than in UO_2 . The interpretation of these results gives a Debye characteristic temperature which is independent of temperature above 400 °C and equal to 377 °K for UO_2 and 393 °K for ThO_2 . As the temperature rises, the oxygen atoms tend to be displaced from the fluorite-type sites at $\frac{1}{4}\frac{1}{4}\frac{1}{4}\dots$ towards the large interstitial holes at $\frac{1}{2}\frac{1}{2}\frac{1}{2}\dots$. At 1000 °C the mean atomic co-ordinates of the oxygen atoms are $\frac{1}{4} + \delta\frac{1}{4} + \delta\frac{1}{4} + \delta\dots$, where $\delta = 0.016$ for UO_2 and $\delta = 0.014$ for ThO_2 . This relaxation effect indicates either that the oxygens are disordered or that they vibrate anharmonically across the $\frac{1}{4}\frac{1}{4}\frac{1}{4}\dots$ positions.

1. INTRODUCTION

The thermal agitation of the atoms in a crystal cause small and irregular displacements of the atoms from their mean positions. The atoms scatter slightly out-of-phase from those lying in an ideal set of equally spaced planes, and by studying the corresponding reduction in intensity of the Bragg reflexions as the temperature increases it is possible to determine the amplitudes of vibration of the atoms as a function of temperature. The intensity measurements must be made to a higher degree of accuracy than is normally required for the determination of atomic positions, and, because the presence of heavy atoms obscures the scattering from the lighter atoms and also requires large absorption corrections to be made to the measured intensities, there are probably no good X-ray measurements of the atomic vibration amplitudes in compounds of the heavy elements. An additional drawback of the X-ray method is that the atomic scattering factor f varies with scattering angle, so that one must assume either that f may be computed theoretically or that the temperature dependence of the Debye-Waller factor is known from theory.

The neutron diffraction method is free from these limitations: the absorption correction is almost negligible for UO_2 and ThO_2 , and the nuclear coherent scattering amplitudes are comparable in magnitude for the metal and the oxygen atoms and are independent of scattering angle. By measuring the intensities of the group of $M + 2O$ reflexions (with $h + k + l = 4n$) for which the metal and oxygen atoms scatter in-phase, and the group of M reflexions ($h + k + l = 4n \pm 1$) with contributions from the metal atoms only, the absolute mean-square displacements of the two kinds of atom can be found at each temperature.

The next section gives the basic formulae of the vibration theory, §3 describes the experimental technique, §4 the method of analyzing the data and §§5 to 7 the data from UO_2 and ThO_2 together with their interpretation in terms of the atomic vibration amplitudes and the characteristic temperatures of the oxides.

2. THEORY

Using the Debye approximation to describe the lattice vibrations of a cubic monatomic crystal, Weinstock (1944) showed that the vibrations reduce the intensities of the Bragg reflexions by the Debye-Waller factor $\exp(-2B \sin^2 \theta / \lambda^2)$, where B is the 'temperature factor', 2θ the scattering angle and λ the wavelength. The temperature factor is related to the absolute temperature T and the Debye characteristic temperature Θ by the equation

$$B = \frac{6h^2 T}{mk\Theta^2} [\phi(x) + \frac{1}{4}x]. \quad (1)$$

Here h and k are the Planck and Boltzmann constants, m the mass of the vibrating atom, $x = \Theta/T$ and $\phi(x)$ the tabulated integral

$$\frac{1}{x} \int_0^x \frac{\xi d\xi}{e^\xi - 1}.$$

The temperature factor is also related to the mean-square displacement $\overline{u_s^2}$ of the atom in a given direction and to the total mean-square displacement $\overline{u^2}$ from its equilibrium position by

$$B = 8\pi^2 \overline{u_s^2} = \frac{8}{3}\pi^2 \overline{u^2}. \quad (2)$$

For a simple ionic crystal containing several kinds of atom, each atom possesses its own temperature factor, but experiment shows that the differences between the individual B factors are not large, even when the atomic masses are very different (Lonsdale 1948). Under these circumstances equation (1) can still be used in an approximate form by replacing mB with

$$(1/n)(m_1 B_1 + m_2 B_2 + \dots + m_n B_n),$$

where n is the number of atoms in the unit cell and $m_1, B_1, m_2, B_2, \dots, m_n, B_n$ are their individual masses and temperature factors. Thus for UO_2 and ThO_2 we can write

$$\frac{1}{3}(m_M B_M + 2m_O B_O) = \frac{6h^2 T}{k\Theta^2} [\phi(x) + \frac{1}{4}x] \quad (3)$$

with the suffixes M, O referring to metal and oxygen atoms. Equation (3) will be used to derive the characteristic temperature Θ from the experimental quantities B_M and B_O ; this value of Θ is doubly approximate in the sense that the Debye theory is approximate and only applies to monatomic crystals. On the other hand, equation (2) is exact and gives the mean-square displacements of the metal and oxygen atoms in terms of their temperature factors:

$$\left. \begin{aligned} B_M &= \frac{8}{3}\pi^2 \overline{(u^2)}_M, \\ B_O &= \frac{8}{3}\pi^2 \overline{(u^2)}_O. \end{aligned} \right\} \quad (4)$$

and

One additional point must be mentioned in connexion with equations (1) and (3). It is assumed in the Debye-Waller-Weinstock theory that the volume of the

crystal remains constant as the temperature increases, whereas the pressure is normally constant during an experiment and the volume increases as a result of thermal expansion. The necessary modification of the theory has been discussed by Paskin (1957), who showed that for a crystal obeying Gruneisen's Law the absolute temperature in equations (1) and (3) must be replaced by the reduced temperature T' defined by

$$T' = T(V_T/V_{T_0})^{2\gamma}.$$

Here V_T and V_{T_0} are the volumes of the crystal at T and at the reference temperature T_0 (normally taken as room temperature) and γ is the Gruneisen constant, which is related to the atomic volume V , the specific heat C_v , the volume coefficient of expansion β and the compressibility κ by

$$\gamma = V\beta/C_v\kappa.$$

For UO_2 $C_v = 0.07 \text{ cal g}^{-1} \text{ deg}^{-1}$, $\kappa = 0.62 \times 10^{-12} \text{ cm}^2 \text{ dyne}^{-1}$, $V = 0.092 \text{ cm}^3 \text{ g}^{-1}$, $\beta = 3.24 \times 10^{-5} \text{ deg}^{-1}$, so that $\gamma = 1.7$. It will be assumed below that the same value of γ applies to ThO_2 : for UO_2 and ThO_2 the Paskin correction is only significant at high temperatures.

3. EXPERIMENTAL TECHNIQUE

A small single crystal of the sample was sealed in an evacuated silica tube and inserted inside a furnace mounted on goniometer arcs. The temperature was measured with a Pt/Pt-Rh thermocouple in contact with the crystal and was maintained constant to $\pm 2 \text{ deg C}$ by using a second thermocouple in the furnace windings to regulate the power supply. The integrated intensities of the (hkk) planes were measured in the temperature range 20 to 1100 °C with the DIDO single-crystal diffractometers (Willis 1962*a*).

Secondary extinction was observed in all crystals. It was present in the strongest reflexions only of UO_2 , namely, 220, 400, 422, 440 and 111, and these reflexions were omitted in the least-squares analysis. Extinction was more troublesome in ThO_2 , as it affected all the $M + 20$ reflexions of the two crystals examined. It was corrected in two ways:

(i) by using a three-circle goniometer to determine the mosaic spread and the extinction coefficients at room temperature (see part I, Willis 1963*b*);

(ii) by assuming a correction of the form

$$\rho' = \rho \exp(-g\rho't),$$

where ρ' and ρ are the uncorrected and corrected integrated intensities, t the path length and g a constant. The values of B_{Th} and B_0 at 20 °C were already known (see part I), and g was empirically adjusted to give the correct room-temperature values. Both methods gave similar corrections.

The $M - 20$ reflexions (with $h + k + l = 4n - 2$) were appreciably affected by double Bragg scattering, particularly in the case of ThO_2 , and these reflexions were omitted from the analysis. Small double-scattering effects were observed in the M reflexions, with odd indices, and so more of these were measured at each temperature than the $M + 20$ reflexions.

A third source of error is the inclusion of inelastic phonon scattering, which peaks at the centre of the Bragg reflexion and leads to an overestimate of the elastic

scattering above the background on either side of the reflexion. With a two-axis diffractometer, as used in this work, it is not possible to separate the elastic and inelastic scattering contributions but with a triple-axis instrument this separation is feasible (Brockhouse & Stewart 1958).

4. METHOD OF ANALYSIS

The structure factors F_{hkk} are given by

$$F_{hkk} = 4b_M \exp(-B_M \sin^2 \theta / \lambda^2) + 8b_O \exp(-B_O \sin^2 \theta / \lambda^2) \quad (5)$$

for the $M + 2O$ reflexions, and by

$$F_{hkk} = 4b_M \exp(-B_M \sin^2 \theta / \lambda^2) \quad (6)$$

for the M reflexions. b_M and b_O are the nuclear scattering amplitudes; their ratio is accurately known as 1.474 for UO_2 and 1.725 for ThO_2 (see part I). The M reflexions can be considered as fixing the overall scale factor and the temperature factor of the metal atom, and the $M + 2O$ reflexions the remaining quantity B_O . In principle, the $M + 2O$ reflexions determine both B_M and B_O but the standard deviations of the estimated temperature factors are much reduced by including the M reflexions as well.

Between ten and twenty independent values of F_{hkk} were measured at each temperature and the quantities B_M , B_O determined by least-squares analysis. After a few cycles of refinement the residual $R_1 = \sum ||F_o| - |F_c|| \div \sum |F_o|$ was reduced to less than 5%; it could be reduced further, particularly at high temperatures, by relaxing the oxygen atoms, as discussed in the next section.

5. EXPERIMENTAL RESULTS AND THEIR INTERPRETATION: UO_2

(a) Interpretation assuming fluorite structure

Table 1 lists the observed values of F_{hkk} for a small crystal G of fused UO_2 weighing 93 mg. The oxygen/uranium ratio was measured as 2.000 ± 0.005 ; additional evidence for its being close to the stoichiometric composition was given by microscopic examination, which gave no indication of a second U_4O_9 phase. All the figures in table 1 are on the same scale.

Least-squares analysis of these data, using equations (5) and (6) which apply to the fluorite structure with the oxygen atoms at $\frac{1}{4}\frac{1}{4}\frac{1}{4} \dots$, gave the temperature factors listed in table 2. The figures in brackets are the standard deviations derived from the least-squares refinement procedure. These temperature factors, also expressed as mean-square thermal displacements, are plotted against temperature in figure 1 (curves 1 and 3). The scaling factor was the same at each temperature to within 1%.

(b) Relaxation of oxygen atoms

The intensity of the 933 reflexion was less than 755 for all temperatures at which they were both measured (see table 1): these reflexions occur at the same Bragg angle and, from equation (6), should have equivalent intensities. Similar systematic discrepancies were observed in other reflexions, particularly those measured at the

higher temperatures. A careful series of measurements carried out on a crystal *H* of fused UO_2 at 1000 °C showed that these variations were reproducible on a second crystal.

TABLE 1. UO_2 : RELATIVE VALUES OF F_{hkl} FOR *M* AND *M* + 20 REFLEXIONS

tem- perature (°C)	F_{333}	F_{533}	F_{155}	F_{355}	F_{555}	F_{733}	F_{933}	F_{177}
20	171	160	153	156	143	144	139	141
213	161	148	150	147	126	145	118	124
325	—	140	—	—	123	131	111	111
455	152	137	133	133	111	125	95	102
608	—	125	—	118	101	—	91	91
763	—	119	121	—	94	111	84	75
908	143	113	108	112	83	102	68	68
995	143	108	—	—	76	108	59	69
1087	136	106	99	99	71	94	59	60

tem- perature (°C)	F_{755}	F_{444}	F_{800}	F_{066}	F_{822}	F_{466}	F_{844}
20	140	366	332	324	—	301	299
213	121	—	294	283	277	260	253
325	114	303	268	268	—	—	226
455	107	290	255	245	240	208	205
608	—	260	227	219	—	—	177
763	93	242	208	200	—	—	154
908	78	229	188	176	176	145	128
995	—	221	183	165	—	—	120
1087	74	207	169	156	—	123	102

TABLE 2. UO_2 (CRYSTAL *G*): TEMPERATURE FACTORS OF URANIUM AND OXYGEN ATOMS

temperature (°C)	B_U (Å ²)	B_O (Å ²)	δ
20	0.31 (0.04)	0.49 (0.06)	—
213	0.38 (0.02)	0.75 (0.03)	—
325	0.51 (0.02)	0.88 (0.03)	0.007 (0.008)
455	0.61 (0.02)	1.05 (0.03)	0.010 (0.002)
608	0.79 (0.02)	1.26 (0.03)	0.011 (0.002)
763	0.85 (0.03)	1.55 (0.07)	0.013 (0.001)
908	1.02 (0.03)	1.78 (0.06)	0.014 (0.001)
995	1.13 (0.05)	1.86 (0.10)	0.015 (0.001)
1087	1.21 (0.05)	2.09 (0.10)	0.016 (0.001)

Figure 2 is a plot of the structure factor F_{hkl} against $h^2 + k^2 + l^2$ for the *M*-type reflexions of crystal *H* at 1000 °C; each value of F_0 corresponds to the mean of several measurements made on at least two equivalent reflexions. The broken curve is the least-squares fit to the experimental points of equation (6), and it can be seen that several points deviate appreciably from this curve.

Much better agreement between observed and calculated intensities is achieved by allowing the oxygen atoms to relax along $\langle 111 \rangle$. If we write the oxygen

co-ordinates as $\frac{1}{2} + \delta \frac{1}{4} + \delta \frac{1}{4} + \delta \dots$, the structure factor expression becomes (ignoring thermal vibration)

$$F = 4b_U + 8b_O \cos 2\pi h(\frac{1}{2} + \delta) \cos 2\pi k(\frac{1}{2} + \delta) \cos 2\pi l(\frac{1}{2} + \delta).$$

For the M -type reflexions with h, k, l odd this gives

$$F_{4n\pm 1} = 4b_U + 8b_O \times 8\pi^3 \delta^3 (\pm h) (\pm k) (\pm l), \quad (7)$$

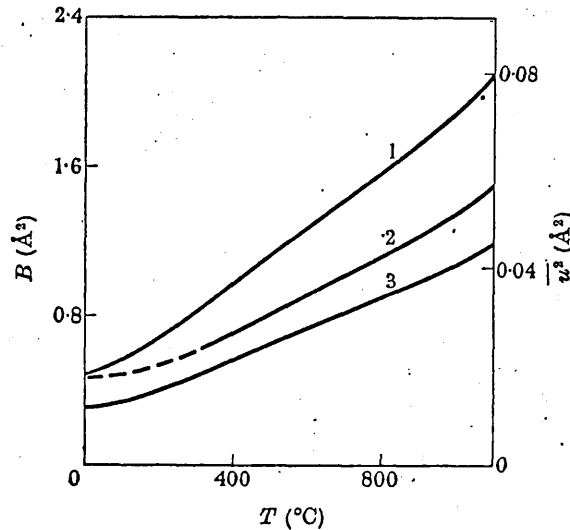


FIGURE 1. Variation with temperature of mean-square displacements and isotropic temperature factors of uranium and oxygen atoms in UO_2 . Curve 1 for oxygen was derived on the assumption of no relaxation and curve 2 on the assumption of relaxation of the oxygen atoms along $\langle 111 \rangle$. Curve 3 for uranium is the same for both models.

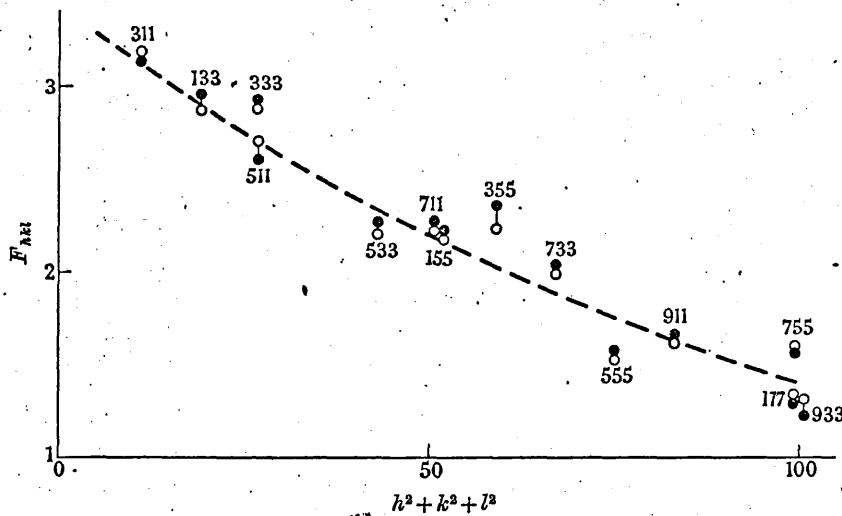


FIGURE 2. Structure factors of M -type reflexions of UO_2 at 1000°C . Full circles are observed values F_o , and open circles F_c , calculated on the assumption of relaxation along $\langle 111 \rangle$. Broken curve is calculated for fluorite structure with isotropic temperature factors. F is in arbitrary units.

where $\delta \ll 1$. The indices have positive signs for $h, k, l = 3, 7, 11, \dots$ and negative signs for $h, k, l = 1, 5, 9, \dots$. In particular, for the three high-angle reflexions 755, 177, 933 occurring at the same Bragg angle, equation (7) gives

$$F_{755} = 4b_U + 8b_O \times 8\pi^3\delta^3 \times 175,$$

$$F_{177} = 4b_U - 8b_O \times 8\pi^3\delta^3 \times 49,$$

$$F_{933} = 4b_U - 8b_O \times 8\pi^3\delta^3 \times 81.$$

Thus the calculated order for the intensities is $755 > 177 > 933$, which agrees with the observed order. Figure 2 shows that the other deviations from equation (6) can be explained in the same way.

TABLE 3. UO_2 (CRYSTAL *H*) AT 1000°C

<i>hkk</i>	F_o	F_c	<i>hkk</i>	F_o	F_c
200	109	-109	800	352	357
311	314	317	733	202	202
222	81	-77	066	350	336
133	296	287	822	338	328
511	260	270	555	156	154
333	298	286	911	165	163
044	512	540	466	274	281
533	227	219	844	251	255
444	457	445	933	121	135
711	221	211	177	127	137
155	227	221	755	156	159
355	236	222			

TABLE 4. UO_2 (CRYSTAL *H*): ANALYSIS OF DATA AT 1000°C

	B_U (\AA^2)	B_O (\AA^2)	δ	R_1 (%)
with relaxation	1.07 (0.05)	1.26 (0.10)	0.016 (0.001)	3.3
without relaxation	1.07 (0.07)	1.87 (0.12)	0	4.5

Table 3 lists the observed structure factors (arbitrary units) for crystal *H*: only those reflexions are included which were considered to be free from extinction and double-scattering effects. These F_o values are probably accurate to within 2 to 3%. The values of F_c in the table were calculated by a least-squares analysis using oxygen co-ordinates $\frac{1}{4} + \delta\frac{1}{4} + \delta\frac{1}{4} + \delta\dots$ and the space-group *Fm 3m*. The adjustable parameters in this calculation were the scale factor, the thermal parameters B_U and B_O , and the relaxation parameter δ . The final values of B_U , B_O , and δ are given in table 4, which also includes the calculated values of B_U and B_O assuming the fluorite structure (see § 5 (a)). The figures in brackets are the estimated standard deviations.

A systematic search for reflexions with mixed indices gave negative results. If the space-group changes from *Fm 3m* to *Pm 3m* on raising the temperature, the high-angle reflexions 770 and 655, contributed by the oxygens only, should be readily observable at 1000°C (see § 2, part I). The absence of these and other reflexions with mixed indices shows that the space-group remains *Fm 3m*. This implies that the observed relaxation can be interpreted in one of two ways. In the first the

oxygen atoms assume statistically four positions, which are displaced a little from the $\frac{1}{4}\frac{1}{4}\frac{1}{4}$ position along the tetrahedral directions joining this position with the large interstitial holes at $\frac{1}{2}\frac{1}{2}\frac{1}{2}$ It is only necessary that a proportion p of the atoms are displaced in this way (see figure 3), but the present data are not sufficiently

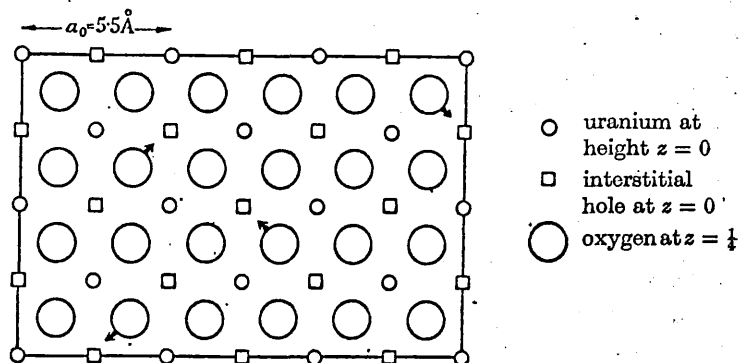


FIGURE 3. Possible structure of UO_2 at high temperature viewed along $[001]$. Arrows indicate relaxation of oxygen atoms towards interstitial holes.

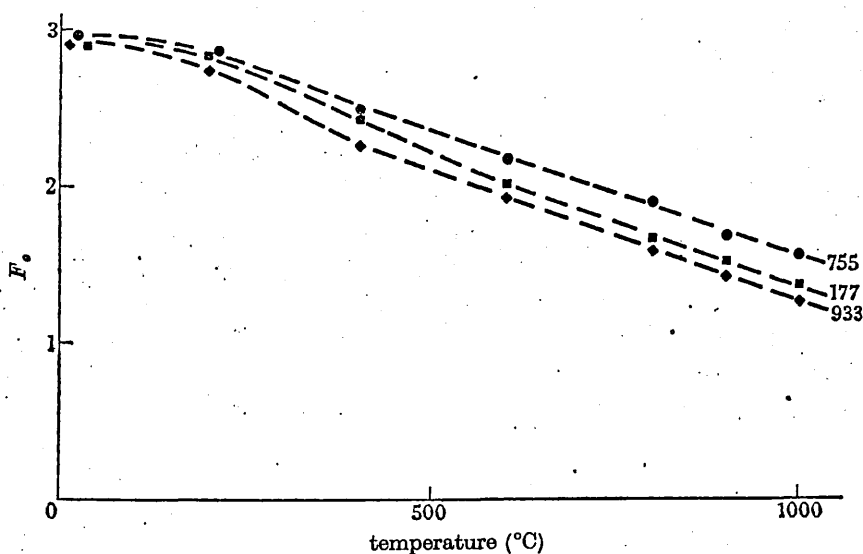


FIGURE 4. Observed structure factors of 755, 177 and 933 reflexions of UO_2 as a function of temperature. For the fluorite structure with isotropic temperature factors these should be equivalent at any one temperature.

accurate to allow a determination of p . The second interpretation is based on the assumption of asymmetric *anharmonic* vibrations of the oxygen atoms. Each oxygen atom is in a non-centrosymmetrical field surrounded tetrahedrally by four interstitial holes and it is conceivable that the oxygen atom vibrates asymmetrically across the normal position and towards the four holes. A clear distinction between these two interpretations can only be made from studies of diffuse scattering.

The three reflexions 755, 177 and 933 give a very sensitive indication of the degree of relaxation, and figure 4 shows the temperature variation of these reflexions, as

measured on crystal *H*. At room temperature the intensities are equivalent, as required by the fluorite structure with isotropic temperature factors, but they become progressively different as the temperature rises.

(c) *Interpretation assuming relaxation*

We must now return to the analysis of the data in table 1 and consider, in particular, the effect of relaxation in the derivation of the temperature factors. Table 4 shows that the temperature factor of uranium is unaffected by the oxygen relaxation but that there is a strong correlation between δ and the temperature factor of oxygen. This correlation is due to the shift of the oxygens along the four equivalent $\langle 111 \rangle$ directions; in the least-squares analysis with $\delta = 0$ this spreading of the oxygens is simulated by increasing the isotropic temperature factor. The final

TABLE 5. ThO_2 : TEMPERATURE FACTORS OF THORIUM AND OXYGEN ATOMS

crystal	temperature (°C)	B_{Th} (\AA^2)	B_{O} (\AA^2)	δ
I	20	0.20 (0.03)	0.37 (0.04)	—
	298	0.39 (0.04)	0.72 (0.04)	0.006 (0.004)
	573	0.65 (0.03)	1.09 (0.04)	0.009 (0.001)
	781	0.81 (0.06)	1.38 (0.07)	0.012 (0.001)
	1020	1.05 (0.06)	1.68 (0.07)	0.014 (0.001)
J	20	0.20 (0.04)	0.37 (0.05)	—
	137	0.26 (0.04)	0.40 (0.05)	—
	442	0.55 (0.06)	0.94 (0.07)	0.008 (0.003)
	890	0.99 (0.07)	1.45 (0.08)	0.013 (0.002)

column of table 2 gives the values of δ derived from the analysis with relaxation, and curve 2 in figure 1 shows the corresponding values of B_{O} plotted against temperature. The broken portion of curve 2 is extrapolated from higher temperatures; it could not be determined directly as the computer program for the least-squares calculation was invalid at very small δ ($\delta < 0.005$).

The following general conclusions can be derived from figure 1:

(i) The amplitude of vibration of the oxygen atoms exceeds that of uranium at all temperatures up to 1100 °C. The r.m.s. thermal displacement of oxygen is 50 % greater at room temperature but the ratio is less at higher temperatures.

(ii) At intermediate temperatures the mean-square displacements of uranium and oxygen are proportional to the absolute temperature. The departure from linearity at low temperatures is due to zero-point motion, and the small departure at high temperatures is to be ascribed to the Paskin effect. (The plot is linear at high temperatures if T is replaced by the reduced temperature T' , as discussed in § 2.)

6. EXPERIMENTAL RESULTS AND THEIR INTERPRETATION: ThO_2

The Bragg reflexions of two crystals of fused thoria were measured at various temperatures in the range 20 to 1020 °C. Again systematic differences occurred between the reflexions with the same values of $h^2 + k^2 + l^2$, and these differences could be satisfactorily explained in terms of the relaxation of oxygen atoms along

$\langle 111 \rangle$. The degree of relaxation is slightly less than in UO_2 at any given temperature: thus at 1000°C the mean value of δ is 0.014 ± 0.001 in ThO_2 as compared with 0.016 ± 0.001 in UO_2 .

The temperature factors calculated without relaxation are given in table 5 and the final column of the table lists the values of δ calculated assuming relaxation. The temperature factor of oxygen is plotted against temperature in figure 5, curve 1 being derived for the fluorite structure and curve 2 assuming relaxation. Curve 3

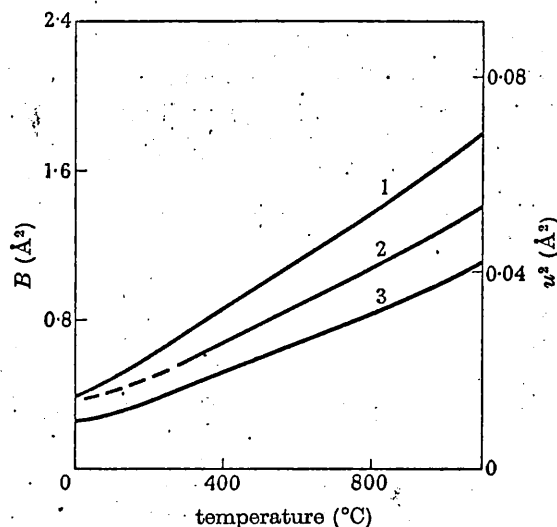


FIGURE 5. Variation with temperature of mean-square displacements and temperature factors of thorium and oxygen atoms in ThO_2 . Curve 1 for oxygen was derived assuming no relaxation and curve 2 with relaxation. Curve 3 refers to thorium.

shows the variation with temperature of the temperature factor of thorium. Figure 5 is very similar to figure 1 for UO_2 , but the amplitudes of vibration of both metal and oxygen atoms are slightly less at all temperatures in ThO_2 .

7. CHARACTERISTIC TEMPERATURES OF UO_2 AND ThO_2

The characteristic temperature Θ has been determined as a function of temperature using equation (3) with T replaced by the reduced temperature T' . Figure 6 gives the results for both UO_2 and ThO_2 : at low temperatures, where the mean-square atomic displacements are too small to measure with sufficient accuracy, the value of Θ is uncertain, but above 400°C it can be determined to at least $\pm 10^\circ\text{K}$. To within these limits it is constant and equal to 377°K for UO_2 and 393°K for ThO_2 .

These Θ values are comparable with the X-ray estimate of $\Theta = 415^\circ\text{K}$ for the isomorphous oxide PuO_2 (Roof 1960), although there are reasons to believe that the X-ray value is 30° or 40°K too high (Willis 1962*b*). Widely varying estimates of Θ for UO_2 are obtained by other methods: the analysis of specific heat data gives $\Theta = 160^\circ\text{K}$ at 20°K and $\Theta > 300^\circ\text{K}$ at high temperatures (Belle 1961), whereas thermal conductivity measurements give $\Theta = 870^\circ\text{K}$ (Tennery 1959).

The concept of a single characteristic temperature for these actinide oxides is clearly imprecise. It would appear that a better interpretation of the diffraction data would be in terms of a Debye model representing the vibrations of the heavy metal atoms, and an Einstein model characterizing the vibrations of the oxygen atoms. The vibrations of the heavy atoms are determined principally by the acoustic modes and the oxygen vibrations by the optical modes: as the mass ratio is 15:1 the frequency range of the modes in each optical branch is very small and, to a good

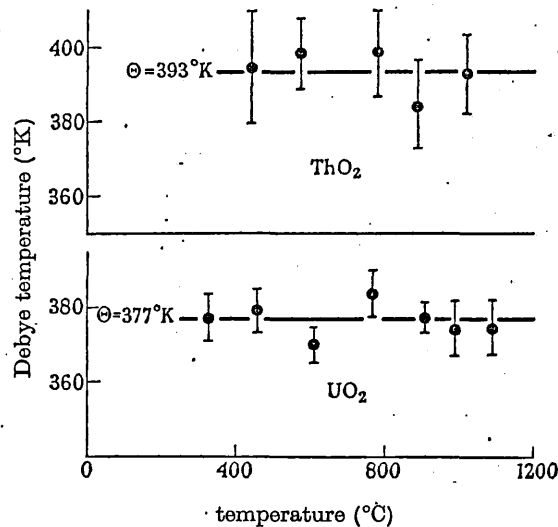


FIGURE 6. Temperature dependence of Debye characteristic temperature of UO_2 and ThO_2 . The vertical lines indicate the estimated standard deviations of Θ .

approximation, the oxygens vibrate at a single frequency ν_E . This interpretation gives a Debye temperature of 242 °K for UO_2 (from equation (3) with the left-hand side replaced by $m_{\text{O}} B_{\text{O}}$) and an Einstein frequency $\nu_E = 1.7 \times 10^{13} \text{ s}^{-1}$.

The author is deeply indebted to Mr K. A. D. Lambe for experimental assistance and to Dr J. S. Rollett for writing the least-squares computer program.

REFERENCES

- Belle, J. 1961 *Uranium dioxide; properties and nuclear applications*. U.S.A.E.C., pp. 190-192.
 Brockhouse, B. N. & Stewart, A. J. 1958 *Rev. Mod. Phys.* **30**, 236.
 Lonsdale, K. 1948 *Acta Cryst.* **1**, 142.
 Paskin, A. 1957 *Acta Cryst.* **10**, 667.
 Roof, R. B. 1960 *J. Nucl. Mat.* **2**, 39.
 Tennery, V. J. 1959 *Oak Ridge Rep.* ORNL-2656.
 Weinstock, R. 1944 *Phys. Rev.* **65**, 1.
 Willis, B. T. M. 1962a *J. Sci. Instrum.* **39**, 590.
 Willis, B. T. M. 1962b *Harwell Rep.* A.E.R.E.-R. 4001.
 Willis, B. T. M. 1963a *Nature, Lond.*, **197**, 755.
 Willis, B. T. M. 1963b *Proc. Roy. Soc. A*, **274**, 122 (part I).

UNCLASSIFIED

AERE - R 4939

(Approved for Publication)

A NEUTRON DIFFRACTION STUDY OF CERIUM DIOXIDE AT ROOM TEMPERATURE

by

T. M. Valentine

B. T. M. Willis

ABSTRACT

The basic structural parameters have been determined, viz. the nuclear coherent scattering cross-section of cerium and the Debye-Waller factors of the cerium and oxygen atoms. There is some evidence for a small anharmonic contribution to the Debye-Waller factor of the oxygen atoms.

Metallurgy Division,
U.K.A.E.A. Research Group,
Atomic Energy Research Establishment,
HARWELL

July, 1965

/DB.

HL65/4116 (C.16)

CONTENTS

	<u>Page</u>
1. Introduction	1
2. Lattice Parameter and Density Measurements	1
3. Experimental Technique	1
4. Analysis of Data	2
5. Effect of Extinction	2
6. Anharmonic Contribution to Debye-Waller Factors	3
References	4

TABLES

Table

1	Lattice Parameter Data for CeO ₂ Crystals	5
2	Density Data for CeO ₂ Crystals	5
3	Neutron Diffraction Data for Crystal D	6

ILLUSTRATIONS

Fig.

- 1 Crystal D. Variation of width of Bragg reflexion at half-height with $h^2 + k^2 + l^2$.
- 2 Structure factor data for crystal D. The lines represent the theoretical curves assuming no extinction. The points are observed values.

1. Introduction

Cerium dioxide, CeO_2 , crystallizes with the fluorite structure and has a wide range of non-stoichiometry which arises by the removal of oxygen atoms from the anion sub-lattice. This is in direct contrast with UO_2 where departure from the stoichiometric fluorite arrangement is achieved by adding oxygen atoms interstitially to the oxygen sub-lattice. A comparison between the crystal structures of CeO_{2-x} and UO_{2+x} is of interest, therefore, in understanding the properties of defect fluorite-type compounds. This report covers the initial work that has been necessary to determine the basic structural parameters of the stoichiometric oxide, CeO_2 : these parameters will be needed in the analysis of the non-stoichiometric data, to be reported later.

Cerium atoms scatter X-rays much more strongly than oxygen. For this reason, and because of the large absorption, X-ray diffraction is less suitable than neutron diffraction for obtaining good diffraction data.

2. Lattice Parameter and Density Measurements

Several single crystals of near-stoichiometric CeO_2 were obtained from G.E.C. Ltd., Wembley, and X-ray powder photographs were taken of a small quantity of powder from each sample. The lattice parameters are listed in Table 1, together with the oxygen/cerium ratio derived from lattice parameter versus composition data published by Bevan⁽¹⁾.

This ratio can also be derived from density measurements. The density of each sample is given in Table 2, together with the composition calculated from the relationship:

$$\rho = \frac{4[m_{\text{Ce}} + (2-x)m_{\text{O}}]}{a_0^3} \quad \dots (1)$$

Here ρ is the observed density, m_{Ce} and m_{O} the atomic masses of cerium and oxygen, a_0 the lattice parameter and $2-x$ the required oxygen/cerium ratio.

The discrepancy between the two sets of estimated compositions can be accounted for by assuming the presence of closed pores, which would have no effect on the lattice parameters but would make the observed densities lower than those given by equation (1). It seems, therefore, that better estimates of the oxygen/cerium ratio are given by the first method.

Crystal D was selected for the neutron diffraction study, because its composition was very nearly stoichiometric and its X-ray powder photograph showed no traces of impurities.

3. Experimental Technique

Crystal D, a cube 1.5 mm on edge and weighing 40.6 mgms, was mounted on the Mk.I Automatic Diffractometer⁽²⁾ and three-dimensional intensity

data at room temperature were collected from twenty-eight independent hkl reflexions up to $h^2 + k^2 + l^2 = 68$, using a neutron wavelength of 1.032 Å. The relative structure factors (F_{obs}) were calculated from the average of at least four of the equivalent reflexions of each hkl group (Table 3). The reflexions can be classified into strong, medium-strong and medium, depending on whether $h + k + l = 4n$, $4n + 2$ or $4n \pm 1$ respectively. The $4n + 2$ reflexions with metal and oxygen atoms scattering out of phase are stronger than the $4n \pm 1$ contributed by cerium atoms alone, as the scattering amplitude of cerium is less than that of oxygen. (In UO_2 the $4n \pm 1$ reflexions are stronger as b_{U} is greater than b_{O}).

4. Analysis of Data

The observed structure factors were analysed on the I.B.M. 7030 computer using the Oak Ridge OR-FLS program.⁽³⁾ In the least-squares refinement, the scale factor, isotropic temperature factors for cerium and oxygen (B_{Ce} , B_{O}) and the coherent scattering amplitude for cerium (b_{Ce}) were treated as variable parameters. It was apparent that the strong reflexions, $h + k + l = 4n$, and also the 200 and 222 reflexions were reduced by secondary extinction (see below), and so these were left out of the final cycles of least-squares.

The analysis of the remaining eighteen independent F values gave an R-index ($= \frac{\sum |F_{\text{obs}} - F_{\text{calc}}|}{\sum F_{\text{obs}}}$) of 1.0 per cent. The adjustable parameters attained the following values:

$$\begin{aligned} B_{\text{Ce}} &= 0.25 \pm 0.03 \text{ \AA}^2 \\ B_{\text{O}} &= 0.47 \pm 0.02 \text{ \AA}^2 \\ \text{and } b_{\text{Ce}} &= 0.479 \pm 0.002 \times 10^{-12} \text{ cm.} \end{aligned}$$

This value for b_{Ce} assumes $b_{\text{O}} = 0.577 \times 10^{-12}$ and an oxygen/cerium ratio of 2.00. For the ratio O/Ce = 1.99 b_{Ce} must be revised to the value of $b_{\text{Ce}} = 0.481 \times 10^{-12}$ cm. The figures after \pm are standard deviations.

5. Effect of Extinction

The widths at half-height were measured for each reflexion and these are plotted versus $h^2 + k^2 + l^2$ in Figure 1. At the focusing position of the Mk.I instrument, near $2\theta = 90^\circ$ or $h^2 + k^2 + l^2 = 52$, the half-width is $0^\circ 8'$. From the formula⁽⁴⁾

$$\Delta = 2(\eta_s^2 + \eta_m^2)^{\frac{1}{2}}$$

where Δ is the half width at the focusing position and η_s and η_m are the mosaic spread of sample and monochromator respectively, the value of η_s must be less than $0^\circ 12'$.

This low value suggests that secondary extinction is probably severe. This is confirmed by Figure 2, which is a plot of $\ln F_{\text{obs}}$ versus $\sin^2 \theta$. The figure shows a large discrepancy between F_{obs} and F_{calc} for the strong reflexions with $h + k + l = 4n$: similarly there is some extinction at the low-angle end of the $h + k + l = 4n + 2$ line.

6. Anharmonic Contribution to Debye-Waller Factors

The least-squares analysis described in section 4 assumed isotropic thermal motion of the atoms, in which case reflexions that occur at the same Bragg angle θ will have the same intensity. This is because the isotropic Debye-Waller factor, $\exp(-B \sin^2 \theta / \lambda^2)$, varies with θ only.

However, even at room temperature there is a difference in F_{obs} between the components of the three pairs of reflexions with equal values of $h^2 + k^2 + l^2$ (that is, equal θ). Thus $F_{333} > F_{511}$, $F_{711} > F_{511}$ and $F_{553} > F_{731}$. Similar differences occur in CaF_2 , UO_2 and ThO_2 (5). Each of these pairs of reflexions is of the $4n \pm 1$ type, with a calculated structure factor given by

$$F_{\text{calc}} = 4b_{\text{Ce}} \exp(-B_{\text{Ce}} \sin^2 \theta / \lambda^2).$$

Closer agreement between observed and calculated intensities is achieved by modifying the isotropic fluorite model to allow the oxygen atoms at $\frac{1}{4} \frac{1}{4} \frac{1}{4} \dots$ etc. to be displaced to $\frac{1}{4} + \delta, \frac{1}{4} + \delta, \frac{1}{4} + \delta \dots$ etc. where δ is a displacement parameter. The modified structure factor formula for $4n \pm 1$ type reflexions is then

$$F_{\text{calc}} = 4b_{\text{Ce}} \exp(-B_{\text{Ce}} \sin^2 \theta / \lambda^2) + 8b_{\text{O}} \times 8\pi^3 \delta^3 \times (\pm h)(\pm k)(\pm l) \exp(-B_{\text{O}} \sin^2 \theta / \lambda^2),$$

where the positive sign is associated with h, k, l , values = 3, 7, 11 ... and the negative sign with $h, k, l = 1, 5, 9 \dots$. This formula gives

$$\begin{aligned} F_{333} &= A + C(+27) \\ \text{and } F_{511} &= A + C(-5); \\ F_{551} &= A + C(-25) \\ \text{and } F_{711} &= A + C(7); \\ F_{553} &= A + C(75) \\ \text{and } F_{731} &= A + C(-21), \end{aligned}$$

where $A = 4b_{\text{Ce}}$ and $C = 8b_{\text{O}} \times 8\pi^3 \delta^3$. Thus the formula predicts the correct relative magnitudes of the three pairs of reflexions.

References

1. Bevan, D. J. M. (1955) *J. Inorg. Nucl. Chem.* 1, 49.
2. Arndt, U. W. and Willis, B. T. M. (1963) *Rev. Sci. Instrum.* 34, 224.
3. Busing, W. R., Martin, K. O. and Levy, H. A. (1962) ORNL-TM-305.
4. Willis, B. T. M. (1960) *Acta Cryst.* 13, 763.
5. Willis, B. T. M. (1963) *Proc. Roy. Soc. A* 274, 122, 134; (1965) *Acta Cryst.* 18, 74.

TABLE 1

Lattice Parameter Data for CeO₂ Crystals

Crystal	Lattice Parameter (Å)	Oxygen/Cerium Ratio
A	5.415 ± 0.001	1.988 ± 0.002
B	5.420 ± 0.001	1.978 ± 0.002
C	5.412 ± 0.001	1.994 ± 0.002
D	5.412 ± 0.001	1.994 ± 0.002

TABLE 2

Density Data for CeO₂ Crystals

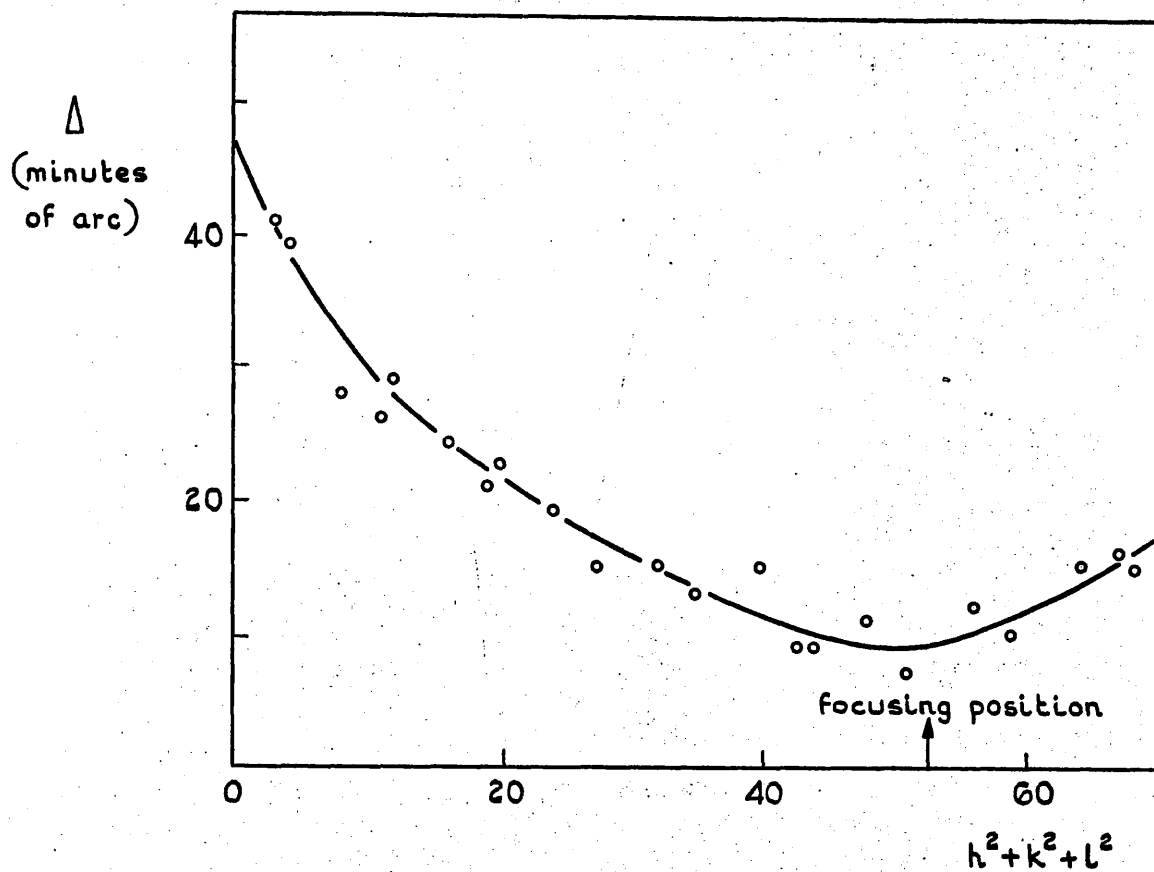
Crystal	Observed Density (gms/cc)	Oxygen/Cerium Ratio
A	7.160 ± 0.005	1.976 ± 0.002
B	7.123	1.962 ± 0.002
C	7.116	1.960 ± 0.002
D	7.184	1.986 ± 0.002

TABLE 3

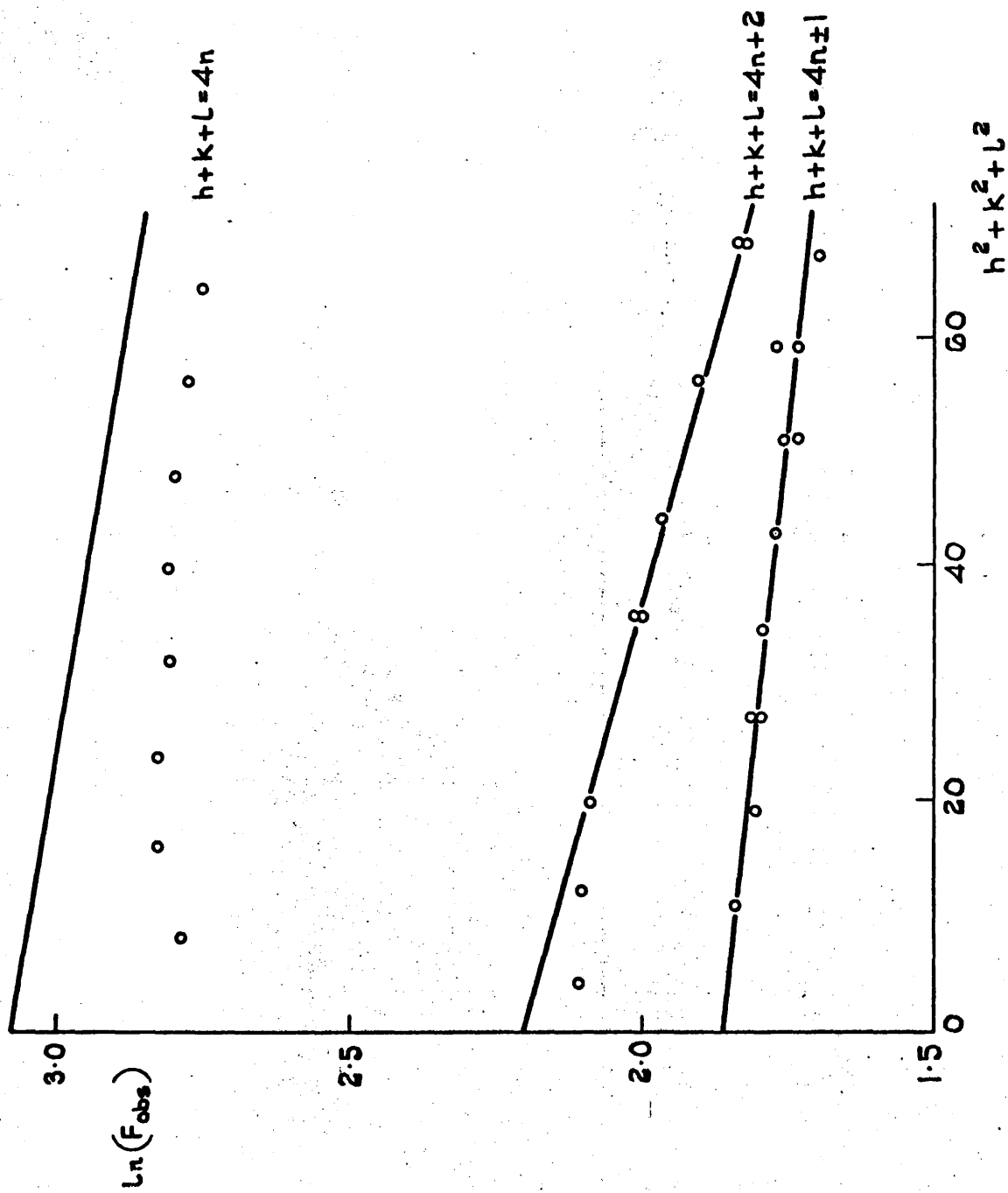
Neutron Diffraction Data for Crystal D

Type of Reflexion	hkl	F _{obs}	F _{calc}	F _{obs} - F _{calc}
h + k + l = 4n	220	269	350	- 81
	400	278	341	- 63
	422	278	332	- 54
	440	274	323	- 49
	620	274	314	- 40
	444	271	305	- 34
	642	264	297	- 33
	800	257	289	- 32
	200	136	146	- 10
	222	135	140	- 5
	h + k + l = 4n + 2	420	133	134
600		124	122	2
442		123	122	1
622		118	117	1
640		110	112	- 2
820		102	102	0
644		103	102	1
311		104	103	1
331		100	101	- 1
511		99	100	- 1
333		101	100	1
531		99	98	1
533		95	96	- 1
711		96	95	1
551		93	95	- 2
731	93	93	0	
553	97	93	4	
733	90	92	- 2	

The reflexions have been divided into their three types. The reflexions above the broken line are those suffering from secondary extinction; only those below the line were used in the least-squares refinement. Pairs of reflexions occurring at the same Bragg angle are bracketed together.



A.E.R.E. R4939. FIG.1. CRYSTAL D. VARIATION OF WIDTH OF BRAGG REFLEXION AT HALF HEIGHT WITH $h^2+k^2+l^2$.



A.E.R.E. R4939. FIG.2. STRUCTURE - FACTOR DATA FOR CRYSTAL D. THE LINES REPRESENT THE THEORETICAL CURVES ASSUMING NO EXTINCTION. THE POINTS ARE OBSERVED VALUES.

STRUCTURES OF UO_2 , UO_{2+x} AND U_4O_9 BY NEUTRON DIFFRACTION

By B. T. M. WILLIS,

Metallurgy Division, A. E. R. E., Harwell, Didcot, Berks., England.

Résumé. — Des monocristaux ont été étudiés par diffraction neutronique entre 20 °C et 1 100 °C et dans l'intervalle de composition UO_2 à U_4O_9 . Les recherches se divisent en trois groupes se rapportant à UO_2 , UO_{2+x} (où $0 < x < 0,25$) et U_4O_9 . UO_2 a la structure fluorine à la température ambiante, avec un facteur de Debye-Waller isotrope. A haute température l'arrangement atomique ne peut plus être décrit exactement par la structure fluorine idéale avec des vibrations thermiques harmoniques. Le meilleur accord entre les intensités observées et calculées est obtenu en donnant aux atomes d'oxygène des positions de coordonnées « relaxées » $1/4 + \delta$, $1/4 + \delta$, $1/4 + \delta$ dans le groupe d'espace Fm3m où δ vaut 0,016 à 1 000 °C. L'effet de relaxation peut être interprété en termes soit de désordre, soit d'agitation thermique anharmonique.

En oxydant UO_2 en UO_{2+x} , on forme une solution solide, contenant 3 sortes d'atomes d'oxygène, O, O' et O". Les atomes O occupent les sites de type fluorine de UO_2 mais une partie de ces sites est vide dans UO_{2+x} . Les atomes O' et O" occupent des positions interstitielles qui sont déplacées le long de $[110]$ pour O' et de $[111]$ pour O" à partir des grands vides de la structure fluorine. Les vides eux-mêmes ne sont pas occupés.

A la composition $UO_{2,25}$, les atomes d'oxygène sont ordonnés pour former une nouvelle phase U_4O_9 . Les principales réflexions de neutrons de U_4O_9 , correspondant aux raies de type fluorine de UO_2 sont plus fortes que les réflexions de surstructure qui proviennent de l'ordre des atomes d'oxygène interstitiels au sein de la charpente fluorine. L'examen des intensités des principales réflexions montre qu'il y a deux sortes de sites interstitiels, comme dans UO_{2+x} : les atomes O' sont placés le long de la direction $[110]$ à 0,85 Å du centre des grandes lacunes, et les atomes O" à 1,05 Å le long de $[111]$. On trouve des lacunes sur les sites d'oxygène du type fluorine (O), mais non pas sur les sites d'uranium, et la formule chimique $UO_{2,25}$ est exprimée plus complètement par $U_{1,00} O_{1,77} O'_{0,29} O''_{0,19}$.

On en conclut que les atomes d'oxygène ne peuvent pas entrer dans la structure fluorine individuellement mais sont incorporés en petits groupes contenant des atomes O' et O" et des lacunes O. Pour une détermination complète de la structure de U_4O_9 , il faut attendre l'analyse des réflexions de surstructure.

Abstract. — Single crystals have been examined by neutron diffraction in the range of temperatures 20 °C to 1 100 °C and of compositions UO_2 to U_4O_9 . The investigations divide into three groups, relating to UO_2 , UO_{2+x} (where $0 < x < 0,25$) and U_4O_9 .

UO_2 has the fluorite structure at room temperature, with isotropic Debye-Waller factors. At high temperatures the atomic arrangement can no longer be described exactly in terms of the ideal fluorite structure with harmonic thermal vibrations. Better agreement between observed and calculated intensities is obtained by allowing the oxygen atoms to relax to positions with coordinates $1/4 + \delta$, $1/4 + \delta$, $1/4 + \delta$... in the Fm3m space group, where δ is 0.016 at 1.000 °C. The relaxation effect can be interpreted in terms of either disorder or anharmonic thermal motion.

On oxidising UO_2 to UO_{2+x} a solid solution is formed, containing three kinds of oxygen atom, O, O' and O". The O atoms occupy the fluorite-type sites of UO_2 , but a proportion of these sites is empty in UO_{2+x} . The O' and O" atoms occupy interstitial positions, which are displaced along $\langle 110 \rangle$ (for O') and along $\langle 111 \rangle$ (for O") from the large interstices in the fluorite structure. The interstices themselves are not occupied.

At the composition $UO_{2,25}$ the oxygen atoms are ordered to form the new phase U_4O_9 . The "main" neutron reflexions of U_4O_9 , corresponding to the fluorite-type peaks of UO_2 , are much stronger than the superlattice reflexions, which arise from the ordering of the interstitial oxygen atoms within the fluorite framework. The analysis of the intensities of the main reflexions shows that there are two kinds of interstitial sites, as in UO_{2+x} : the O' atoms are located 0.85 Å along the $\langle 110 \rangle$ directions from the centres of the large interstices, and the O" atoms 1.05 Å along $\langle 111 \rangle$. Vacancies occur in the fluorite-type oxygen sites (O) but not in the uranium sites, and the chemical formula $UO_{2,25}$ is expressed more fully as $U_{1,00} O_{1,77} O'_{0,29} O''_{0,19}$. It is concluded that oxygen atoms cannot enter the fluorite structure individually but are incorporated in small groups containing O' and O" atoms and O vacancies. A complete structure determination of U_4O_9 must await the analysis of the superlattice reflexions.

1. INTRODUCTION.

In recent years there have been many fundamental studies of the oxides UO_2 , UO_{2+x} and U_4O_9 [1], and the aim of the present work was to

determine their crystal structures. The interpretation of thermodynamic and diffusion data, in particular, is critically dependent on knowing the positions of the oxygen atoms, and this knowledge is best gained from neutron diffraction work.

The structures of the three oxides are inter-related, and so it will be convenient to describe all three here. However, the bulk of the paper concerns U_4O_{10} only, as the work on UO_2 and UO_{2+x} has already been described elsewhere.

2. UO_2 .

At room temperature UO_2 has the fluorite structure (fig. 1), as originally proposed by Goldschmidt in 1923 [2]. The uranium atoms are at the $000\dots$ positions of the cubic cell (space group $Fm\bar{3}m$) and the oxygen atoms at $\frac{1}{4}\frac{1}{4}\frac{1}{4}, \frac{3}{4}\frac{3}{4}\frac{3}{4}, \dots$. These sites have cubic point symmetry, and the temperature factors B in the Debye-Waller expression $\exp(-B \sin^2 \theta / \lambda^2)$ are isotropic. Neutron data on single crystals give $B_U = 0.25 \text{ \AA}^2$, $B_O = 0.43 \text{ \AA}^2$ [3].

Above room temperature the atomic arrangement can no longer be described exactly in terms of the ideal fluorite structure with harmonic thermal vibrations [4]. For Bragg reflexions with $h + k + l$ odd the intensities calculated with this model are proportional to F^2 , where

$$F = 4b_U \exp(-B_U \sin^2 \theta / \lambda^2). \quad (1)$$

b_U is the nuclear scattering amplitude of uranium, B_U the isotropic temperature factor of uranium, 2θ the scattering angle and λ the wavelength. Equation (1) predicts equal intensities for independent reflexions occurring at the same scattering angle, whereas this is not confirmed by observation. Thus the 711 reflexion is stronger than 551, 751 is stronger than 555, and the three reflexions 755, 177, 933 have intensities in the order $755 > 177 > 933$. Better agreement between observed and calculated intensities is obtained by allowing the oxygen atoms to relax to positions with co-ordinates $\frac{1}{4} + \delta, \frac{1}{4} + \delta, \frac{1}{4} + \delta \dots$ in the $Fm\bar{3}m$ space group. The "relaxation parameter" δ increases steadily with temperature and is equal to 0.016 ± 0.001 at 1000°C .

There are two alternative explanations of this relaxation effect. In the first, the oxygen atoms are located statistically at the displaced positions, which are four times more numerous than the available number of oxygen atoms. These displaced positions lie along the $\langle 111 \rangle$ directions joining the $\frac{1}{4}\frac{1}{4}\frac{1}{4}$ position with the four adjacent interstices at $\frac{1}{2}\frac{1}{2}\frac{1}{2}, \frac{1}{2}00, 0\frac{1}{2}0$ and $00\frac{1}{2}$ (fig. 1). The second interpretation is based on the assumption of asymmetric anharmonic vibration of the oxygen atom. Each oxygen atom has a non-

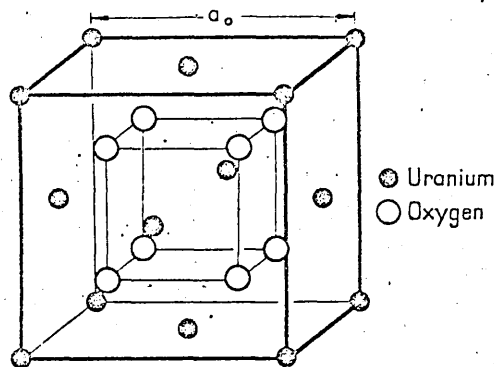


FIG. 1. — Unit cell of UO_2 (fluorite-type structure).

centrosymmetric cubic environment, and it is possible that the atom vibrates asymmetrically across its normal position and towards the adjacent interstices (fig. 2). In this case the vibration is anhar-

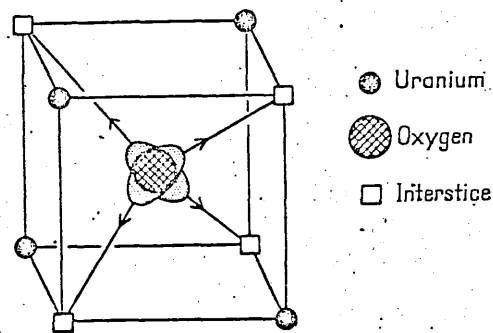


FIG. 2. — Diagram showing extension of the oxygen atom, under the influence of thermal vibration, along $\langle 111 \rangle$.

monic and cannot be described by the conventional vibration ellipsoid, specified by six parameters B_{ij} , which degenerate to a single B_0 for cubic symmetry.

3. UO_{2+x} .

When UO_2 is oxidised at high temperatures a disordered solid solution UO_{2+x} is formed. The additional oxygen atoms are incorporated at interstitial sites of two kinds, O' and O'' ; the O' atoms are displaced along $\langle 110 \rangle$ from the centres of the large interstices in the fluorite structure and the O'' atoms along $\langle 111 \rangle$. Vacancies exist in the fluorite-type positions, and the interstices themselves are not occupied. These conclusions were derived from the analysis of two-dimensional F_{hkl} data, collected from a crystal of $UO_{2.13}$ at 800°C [5], and were later confirmed by a three-dimensional study [15].

4. U_4O_9 : ANALYSIS OF MAIN BRAGG REFLEXIONS.

4.1. Introduction. — Alberman and Anderson [6] first recognised the existence of a phase of uranium oxide, whose structure is closely related to that of UO_2 but which has higher oxygen content. Héring and Péro [7] showed that the composition of this phase is close to $\text{UO}_{2.25}$, but more recent work [8, 9] has shown that there is a composition range from $\text{UO}_{2.23}$ to $\text{UO}_{2.25}$ at high temperatures, with the possibility of a narrower range at room temperature. Thus the phase U_4O_9 should be designated U_4O_{9-y} ; it will be referred to below simply as U_4O_9 , except where the precise composition is discussed.

Belbeoch, Piekarski and Péro [10] have interpreted the oxidation of UO_2 to U_4O_9 in the following way. At high temperatures oxygen atoms enter the UO_2 structure interstitially and in a statistically disordered fashion; the process continues up to the limiting composition $\text{UO}_{2.25}$, and then on cooling the interstitial oxygens are redistributed to form an ordered U_4O_9 phase at room temperature with an enlarged unit cell. This interpretation is supported by density measurements, which rule out the existence of vacancies in the uranium sub-lattice, and by X-ray diffraction data. The X-ray examination of U_4O_9 shows that the fluorite-type reflexions of UO_2 remain after oxidation, with a slight increase in the scattering angles, and that very weak superlattice lines appear. Belbeoch *et al.* found that the crystal system remains cubic on oxidation, with a reduction in space-group symmetry from $Fm\bar{3}m$ (UO_2) to $I43d$ (U_4O_9) and with an increase in the size of the unit cell to 21.8 Å for U_4O_9 , four times the cell size for UO_2 . They proposed a complete structure for the 21.8 Å cell, without using the conventional method of measuring structure factors. This structure is not compatible with the neutron diffraction results described below.

The neutrons reflexions divide into two groups: the very weak and numerous superlattice reflexions and the "main" or fluorite-type reflexions. Broadly speaking, the main reflexions represent scattering from all the atoms in the unit cell, whereas the superlattice reflexions are contributed by interstitial oxygen atoms alone. Apart from the determination of space group, which requires identifying all kinds of reflexion, this paper is concerned only with the measurement and interpretation of the main reflexions.

4.2. Space group of unit cell. — A single crystal, A, weighing 520 mg was prepared from a single crystal of UO_2 by heating for one month at 1450 °C in the presence of powdered U_3O_8 . The UO_2 crystal was placed in one arm of an evacuated

silica H-tube and the powder in the other arm, so that oxidation occurred *via* the vapour phase. Measurement of the oxygen potential with a high-temperature galvanic cell [11] showed that crystal A was single-phase, within the narrow homogeneity range of the U_4O_{9-y} phase, at temperatures above 650 °C. The composition is thus close to $\text{UO}_{2.25}$.

The crystal was mounted on a three-circle neutron diffractometer and reciprocal space was scanned in lines through the origin along [100], [010], [001], [110] ..., [111] ..., [211] ..., [321] ..., where the indices refer to the orthogonal axes of the 21.8 Å cell. Forty-six main reflexions and over one hundred superlattice reflexions were observed. All these reflexions indexed satisfactorily on a cubic $4a_0$ cell, with $a_0 = 5.44$ Å. For a given set of indices $\{hkl\}$, the superlattice reflexions with different signs and order of indices were equivalent in intensity: this indicates that the unit cell is cubic with Laue symmetry $m\bar{3}m$. $h + k + l$ was even for all observed reflexions, so that the lattice is body-centred. Because of their weak intensity, only one in ten of the superlattice reflexions for a body-centred $4a_0$ cell were detected, but the indices of all observed reflexions were consistent with the $I43d$ space group.

This space group and cell size of $4a_0$ are in accordance with the X-ray results of Belbeoch *et al.* [10] and will be adopted below. They are in disagreement with the conclusions of Steeb [12] based on the electron diffraction examination of a thin film of U_4O_9 .

4.3. Space group of composite cell. — The nuclear density $\rho(XYZ)$ at any point XYZ in the unit cell can be computed from the neutron structure factors F_{hkl} using the equation:

$$\rho(XYZ) = \frac{1}{V} \sum_h \sum_k \sum_l F_{hkl} \exp[-2\pi i(hX + kY + lZ)], \quad (2)$$

where V is the volume of the unit cell. For the main reflexions h, k, l are all multiples of four, and if the summation in (2) is restricted to *all* indices divisible by four, the computed density $\rho'(XYZ)$ is:

$$\rho'(XYZ) = \frac{1}{V} \sum_h \sum_k \sum_l F_{hkl} \exp[-2\pi i(hX + kY + lZ)] \quad (3)$$

$\rho'(XYZ)$ is derived from $\rho(XYZ)$ by superimposing the contents of the sixty-four subcells, each of side a_0 , contained in the unit cell of side $4a_0$. Expressed formally:

$$\rho'(XYZ) = \frac{1}{64} \left[\rho(XYZ) + \rho\left(X + \frac{1}{4}, Y, Z\right) + \rho\left(X + \frac{1}{2}, Y, Z\right) + \rho\left(X + \frac{3}{4}, Y, Z\right) \right]$$

$$\begin{aligned}
& + \rho\left(X, Y + \frac{1}{4}, Z\right) + \rho\left(X + \frac{1}{4}, Y + \frac{1}{4}, Z\right) \\
& + \rho\left(X + \frac{1}{2}, Y + \frac{1}{4}, Z\right) + \rho\left(X + \frac{3}{4}, Y + \frac{1}{4}, Z\right) \\
& + \dots\dots\dots \\
& + \rho\left(X, Y + \frac{3}{4}, Z + \frac{3}{4}\right) + \rho\left(X + \frac{1}{4}, Y + \frac{3}{4}, Z + \frac{3}{4}\right) \\
& + \rho\left(X + \frac{1}{2}, Y + \frac{3}{4}, Z + \frac{3}{4}\right) \\
& + \rho\left(X + \frac{3}{4}, Y + \frac{3}{4}, Z + \frac{3}{4}\right),
\end{aligned}$$

an equation in 64 terms which is readily derived from equations (2) and (3). $\rho'(XYZ)$ represents the contents of the "composite cell" of side a_0 .

It is found experimentally that only one or two very weak superlattice reflexions with $h, k, l = 4n$ can be detected. ρ' in equation (3) can be approximated, therefore, by a summation, which includes the main reflexions, only:

$$\rho'(XYZ) = \frac{1}{V} \sum_{\substack{\text{main} \\ \text{reflexions}}} \sum \sum F_{hkl} \exp[-2\pi i(hX + kY + lZ)]. \quad (4)$$

If the indices hkl in (4) are replaced by $h'k'l'$, where $h' = h/4$, $k' = k/4$, $l' = l/4$, the co-ordinates XYZ represent fractional lengths of the axes of the composite cell.

The space group for the distribution $\rho(XYZ)$ is $I\bar{4}3d$. In reducing the cell edge from $4a_0$ for the true cell to a_0 for the composite cell, I (body-centred) is transformed to P (primitive) and the diagonal glide d is changed to m (mirror plane). Thus the space group of the composite cell is $P\bar{4}3m$. However, $h'k'l'$ reflexions of mixed indices are either absent or only barely detectable, so that the lattice type is approximately F (face-centred) and the space group for ρ' , as defined by equation (4), is $F\bar{4}3m$. This space group will be used to analyse the main reflexions.

4.4. Experimental data. — The intensities of the main reflexions of crystal A were measured with a three-circle diffractometer. Forty-six independent reflexions were measured up to

$$h'^2 + k'^2 + l'^2 = 100$$

with a neutron wavelength of 1.04 Å. As in the case of UO_2 , these reflexions can be classified into three groups, which are weak, medium or strong depending on whether $h' + k' + l' = 4n + 2, 4n \pm 1$ or $4n$. Previous experience [3] suggested that the strong reflexions are subject to systematic errors from secondary extinction, and the weak reflexions to errors from double Bragg scattering. Fortunately, both errors proved to be small. Examination of the intensities from crystal A, varying both the

incident wavelength and the path length of the beam inside the crystal, showed that there was no appreciable extinction and that multiple scattering was less pronounced than for UO_2 . The widths of the rocking curves of crystal A were greater than for the UO_2 crystal from which it was prepared: this indicates that the entry of interstitial oxygen atoms strains the crystal and increases its mosaic spread to a point at which the two systematic errors referred to above are no longer significant.

A second crystal, B, weighing 490 mg and with the same composition as A, was examined also. The structure factors $|F|$ for the two crystals agreed to within a few per cent. Later, crystal A was re-measured with the Harwell Mark I automatic diffractometer [13], the observations being repeated for eight equivalent reflexions of each $\{h'k'l'\}$ set. Table I lists the observed values of F , averaged for the measurements on both crystals, together with the standard deviations $\sigma(F)$ of F . These σ 's were estimated from the variations in the individual measurements; they are appreciably greater than the random errors from the statistics of pulse counting, and represent uncertainties arising from other sources, such as non-uniformity of the incident neutron beam.

4.5. Analysis of data. — The similarity of the X-ray patterns of UO_2 and U_4O_9 [10] suggests that the fluorite structure can be adopted as the first model in refining the data in Table I by least-squares methods. For the space group $F\bar{4}3m$ this model requires placing the uranium atoms at the (d) positions (International Tables, Volume I) of four fold multiplicity

$${}_4(d) = \frac{333}{444}, \quad \frac{311}{444}, \quad \frac{131}{444}, \quad \frac{113}{444},$$

half the oxygen atoms at

$${}_4(a) = 000, \quad 0\frac{11}{22}, \quad \frac{1}{2}0\frac{1}{2}, \quad \frac{11}{22}0,$$

and the other half at

$${}_4(b) = \frac{111}{222}, \quad \frac{1}{2}00, \quad 0\frac{1}{2}0, \quad 00\frac{1}{2}.$$

The origin of the cell is occupied by an oxygen atom, although in the fluorite structure it is more usual to choose the origin at a uranium atom (fig. 1). In the least-squares refinement the scale factor and the individual isotropic temperature factors of uranium and oxygen (B_U, B_O) were treated as adjustable parameters. The results are presented under model 1 in Table II, which shows that the reliability factor

$$R = \frac{\sum |F_o| - |F_c|}{\sum |F_o|}$$

is already less than 16%. The Least Squares programme of Busing, Martin and Levy [14] was used for this and later calculations.

TABLE I

NEUTRON DIFFRACTION DATA FOR U_4O_9 . MAIN REFLEXIONS ONLY.

hkl	$h'k'l'$	$ F_{\text{obs}} $	$ F_{\text{calc}} $	$ F_{\text{obs}} - F_{\text{calc}} $	$\sigma(F_{\text{obs}})$
008	002	57	38	19	6
0, 0, 16	004	650	658	8	21
0, 0, 24	006	76	49	27	16
0, 0, 32	008	513	519	6	6
0, 0, 40	0, 0, 10	108	113	5	4
444	111	323	324	1	7
4, 4, 12	113	364	382	18	5
4, 4, 20	115	355	350	5	7
4, 4, 28	117	269	266	3	10
4, 4, 36	119	207	231	24	7
880	220	780	773	7	7
888	222	49	52	3	10
8, 8, 16	224	648	655	27	5
8, 8, 24	226	70	56	14	7
8, 8, 32	228	445	438	7	10
12, 12, 4	331	352	340	12	6
12, 12, 12	333	333	321	12	6
12, 12, 20	335	308	294	14	5
12, 12, 28	337	273	265	8	4
12, 12, 36	339	207	229	22	6
16, 8, 0	420	46	24	22	5
16, 16, 0	440	628	635	7	5
16, 16, 8	442	70	46	24	3
16, 16, 16	444	554	550	4	4
16, 16, 24	446	113	98	15	4
16, 16, 32	448	375	366	9	7
20, 12, 4	531	324	316	8	5
20, 20, 4	551	280	292	12	5
20, 20, 12	553	279	269	10	5
20, 20, 20	555	239	248	9	7
20, 20, 28	557	221	227	6	4
24, 8, 0	620	573	575	2	6
24, 16, 0	640	56	48	8	12
24, 16, 8	642	521	502	19	6
24, 24, 0	660	452	436	16	6
24, 24, 8	662	106	93	13	8
24, 24, 16	664	384	385	1	12
28, 12, 4	731	278	295	17	4
28, 20, 4	751	258	270	12	4
28, 20, 12	753	242	246	4	5
28, 28, 4	771	215	215	0	12
32, 8, 0	820	89	93	4	10
32, 16, 0	840	396	384	12	5
32, 16, 8	842	87	91	4	7
32, 24, 0	860	99	114	15	7
36, 12, 4	931	235	246	11	4

In model 2 another adjustable parameter was introduced, viz. the "occupation number" p_a of the atoms in the 4(a) sites. For $p_a = 1$ the fluorite positions are fully occupied, as in UO_2 , but for p_a less than unity a fraction $1 - p_a$ of the 4(a) sites is empty. R improved slightly (Table II).

TABLE II

LEAST-SQUARES REFINEMENT (MODELS 1 AND 2)

	TYPE OF ATOM	SITE OCCUPATION NUMBER, p	TEMPERATURE FACTOR (\AA^2)	R FACTOR
Model 1	U	1.00	0.52	—
	O ^a	1.00	1.54	
	O ^b	1.00	1.54	
Model 2	U	1.00	0.60	0.159
	O ^a	0.65	1.57	
	O ^b	1.00	1.57	

and p_a was reduced to 0.65. As the 4(a) and 4(b) sites are equivalent in the fluorite structure, model 2 can be used to refine $p_a + p_b$ only and not p_a , p_b independently. Thus the same results are obtained in model 2 with $p_a = 1$ and $p_b = 0.65$.

For the next calculation the ninth oxygen atom in the formula unit U_4O_9 , ignored in models 1 and 2, was placed at the position:

$$4(c) = \frac{111}{444}, \frac{133}{444}, \frac{313}{444}, \frac{331}{444}$$

of the composite cell. These are the sites of the large interstices in the fluorite structure, and were assumed by Belbeoch *et al.* [10] to be occupied by the interstitial oxygen atoms. However, no satisfactory refinement of the neutron data was possible with this model. All attempts at refinement led to the rejection of the ninth atom from the 4(c) position.

At this stage it was decided to carry out a three-dimensional Fourier synthesis, of the type described by equation (4), in the hope of locating the lost oxygen atoms. The phases of the observed structure factors F_{obs} were taken as those calculated for model 2. The nuclear density plot was dominated by strong peaks due to the oxygen and uranium atoms at fluorite positions, but there was no indication of other peaks which could be ascribed definitely to oxygen.

The interstitial oxygen atoms were finally located by difference Fourier syntheses. Figure 3 is a section of the difference map at height $Z = 3/8$ of the composite cell; the coefficients in the Fourier summation were derived from the observed structure factors and those calculated for model 2. The atoms at fluorite positions were not present on the difference map, and the peaks, labelled h and e in figure 3, represent interstitial oxygen atoms at two

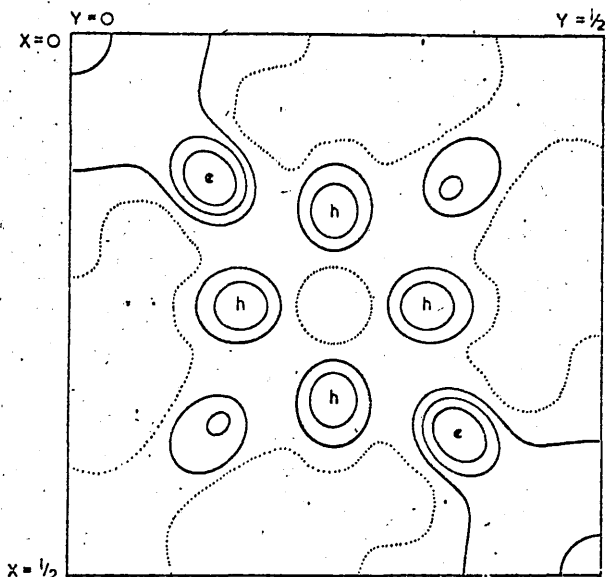


Fig. 3. — Section of Fourier difference map at height $Z = 3/8$ of composite cell, with uranium and fluorite-type oxygens removed. The peaks h are interstitial oxygens O' at 48(h) sites and e are interstitial oxygens O'' at 16(e) sites. Zero contour shown dotted.

kinds of crystallographic site. O' atoms are at positions:

$$48(h) = \left(000, 0\frac{11}{22}, \frac{1}{2}0\frac{1}{2}, \frac{11}{22}0 \right) + \left(\frac{1}{4} + \epsilon', \frac{1}{4} + \epsilon', \frac{1}{4} \right), \left(\frac{1}{4} + \epsilon', \frac{1}{4} + \epsilon', \frac{1}{4} + \epsilon' \right) \dots$$

and O'' atoms at:

$$16(e) = \left(000, 0\frac{11}{22}, \frac{1}{2}0\frac{1}{2}, \frac{11}{22}0 \right) + \left(\frac{1}{4} + \epsilon'', \frac{1}{4} + \epsilon'', \frac{1}{4} + \epsilon'' \right), \left(\frac{1}{4} + \epsilon'', \frac{3}{4} - \epsilon'', \frac{3}{4} - \epsilon'' \right) \dots$$

where

$$|\epsilon'| \approx |\epsilon''| \approx \frac{1}{8}.$$

Figure 4 is a drawing showing the relation of the 48(h) and 16(e) sites to the cube of eight fluorite-type oxygens.

The difficulty of locating the ninth oxygen atom in the full Fourier synthesis can be ascribed now to the large number of equivalent O' and O'' sites. This atom is distributed statistically in sites of eight-fold and sixteen-fold multiplicity, whereas the remaining oxygens occupy fluorite positions of only four-fold multiplicity.

The interstitial oxygens were placed at 48(h) and 16(e) sites for the least-squares refinement with model 3 (see Table III). Seven parameters were

TABLE III

LEAST-SQUARES REFINEMENT (MODEL 3)

TYPE OF ATOM	ATOMIC CO-ORDINATES IN COMPOSITE CELL	SITE OCCUPATION NUMBER, p	NUMBER OF ATOMS IN 21.8 Å CELL
U	$\frac{1}{4} \frac{1}{4} \frac{1}{4}$	1.00	256
O^a	0 0 0	0.81 ± 0.22	} 453 ± 5
O^b	$\frac{1}{2} \frac{1}{2} \frac{1}{2}$	0.96 ± 0.24	
O'	$\frac{1}{4} + \epsilon'$ $\frac{1}{4} + \epsilon'$ $\frac{1}{4}$	0.024 ± 0.004	73 ± 11
O''	$\frac{1}{4} + \epsilon''$ $\frac{1}{4} + \epsilon''$ $\frac{1}{4} + \epsilon''$	0.016 ± 0.003	48 ± 8

$$\epsilon' = 0.128 \pm 0.005, \quad \epsilon'' = 0.122 \pm 0.005, \quad R = 0.037.$$

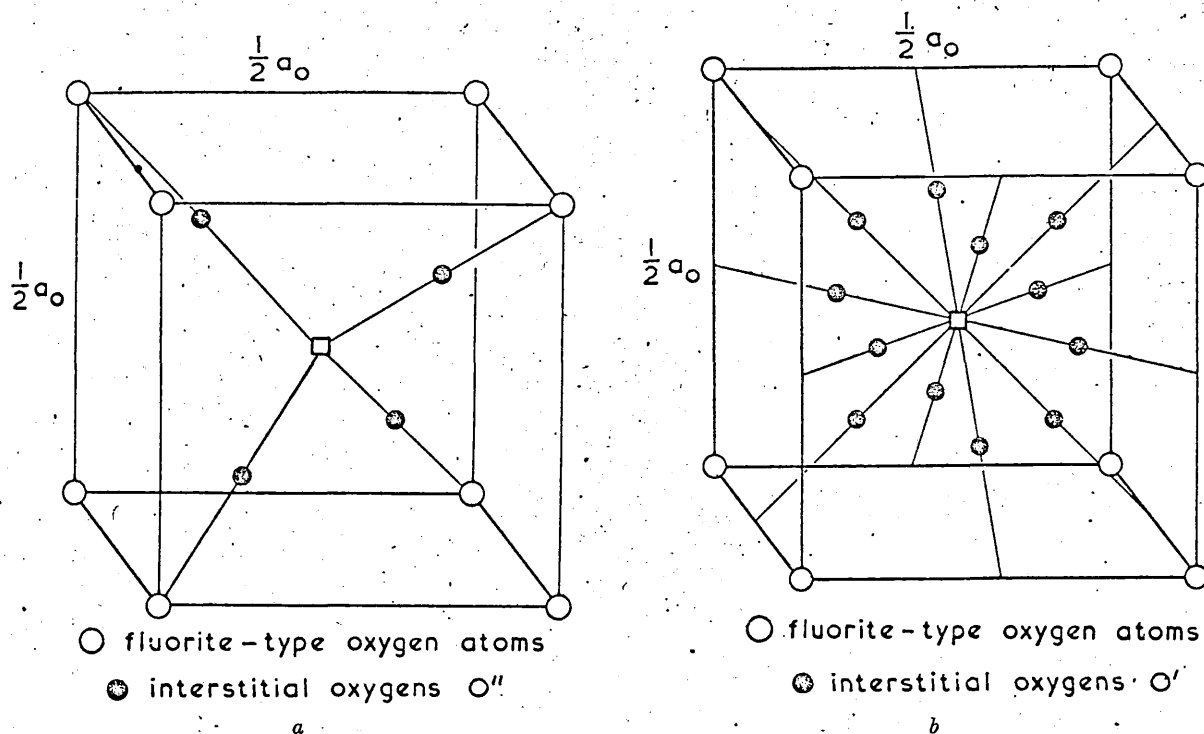


FIG. 4. — Composite cell of U_4O_9 showing interstitial oxygen atoms at a) O' sites, b) O'' sites. The large interstice is at the centre of the cube of fluorite-type oxygens. The O' oxygens are half way between the interstice and the mid-point of the cube edges; the O'' oxygens are half way from the interstice to the cube corners.

refined: the two positional co-ordinates, ϵ' and ϵ'' , the occupation numbers of the 4(a) sites (normal oxygen O^a), 4(b) (normal oxygen O^b), 48(h) (interstitial oxygen O') and 16(e) (interstitial oxygen O''), and the overall scale factor.

The temperature factors were kept fixed at the values given by model 2. Table III gives the results of the calculation, together with the estimated standard errors of the refined parameters. These parameters gave the F_{calc} column in Table I.

Later, separate refinement of the temperature factors gave no significant changes from $B_{\text{U}} = 0.60 \text{ \AA}^2$ and $B_{\text{O}} = 1.57 \text{ \AA}^2$.

The following features of the oxidation process, UO_2 to U_4O_9 , can be deduced from the refinement of model 3:

(1) The isotropic temperature factor at 20 °C increases from 0.25 \AA^2 for UO_2 [3] to 0.60 \AA^2 for U_4O_9 . If the whole of this increase, ΔB , is attributed to displacements of the uranium atoms

from the fluorite positions, the r. m. s. displacement in any direction is $\sqrt{\Delta B/8\pi^2} = 0.06 \text{ \AA}$.

(2) Oxidation proceeds by the incorporation of interstitial oxygen atoms at O' and O'' sites. O' atoms are located $0.86 \text{ \AA} (= \sqrt{2}\epsilon' a_0)$ along the $\langle 110 \rangle$ directions from the centres of the large interstices at $4(c)$; O'' atoms occupy positions $1.05 \text{ \AA} (= \sqrt{3}\epsilon'' a_0)$ along the $\langle 111 \rangle$ directions from $4(c)$ (see fig. 4).

(3) The incorporation of interstitial atoms is accompanied by the ejection of oxygen atoms from fluorite positions. Approximately one in ten of the normal oxygens are displaced to O' or O'' sites.

5. CONCLUSIONS.

The atomic arrangement in the composite cell of U_4O_9 is similar to that in the average cell of the disordered oxide $UO_{2.13}$ [5]. In both cases interstitial oxygen atoms occupy O' and O'' sites and vacancies occur in the fluorite sites of the normal oxygens. This suggests that oxygen atoms cannot be incorporated singly in the fluorite structure, but only in groups containing O' and O'' atoms and O vacancies.

There are two important differences between $UO_{2.13}$ and U_4O_9 . First, the normal oxygen atoms in U_4O_9 show little tendency to relax along $\langle 111 \rangle$ towards the centres of the large interstices. This relaxation effect in $UO_{2.13}$ can be attributed (as for UO_2 at high temperatures [4]) to disorder or to anharmonic thermal motion. Second, the space-group symmetry ($F43m$) of the composite cell of U_4O_9 is lower than the symmetry ($Fm3m$) of UO_{2+x} , so that the two interpenetrating sub-lattices, O^a and O^b , can be distinguished in U_4O_9 . However, there is a very high correlation between the occupation numbers p_a and p_b for model 3, and this is reflected in the high standard errors of these quantities.

Assuming that the fluorite positions $4(d)$ of the uranium atoms are fully occupied, the unit cell of the crystal with the exact composition U_4O_9 contains 256 uranium and 576 oxygen atoms. The results in Table III show that the unit cell contains 256 uranium and 572 oxygen atoms, and that the chemical formula is expressed more fully as

$$U_{1.00} O_{0.81 \pm 0.22} O_{0.90 \pm 0.24} O'_{0.29 \pm 0.05} O''_{0.19 \pm 0.04}$$

Because of the high correlation between p_a and p_b the least-squares refinement for model 3 was repeated with p_a fixed at the value given in Table III. This led to a reduction in the standard error for p_b (see last column of Table III) and the chemical formula worked out as:

$$U_{1.00} O_{1.77 \pm 0.02} O'_{0.29 \pm 0.04} O''_{0.19 \pm 0.03}$$

where O represents O_a and O_b atoms together.

The standard errors in the occupation numbers p are quite high, and the close agreement with the chemical composition $UO_{2.25}$ may be fortuitous. Clearly, extremely accurate intensity data are required to determine the p 's precisely.

- ⊙ uranium atoms at $Z = \frac{1}{4}a_0$
- interstices at $Z = \frac{1}{4}a_0$
- fluorite-type oxygens at $Z = 0$
- interstitial oxygen O

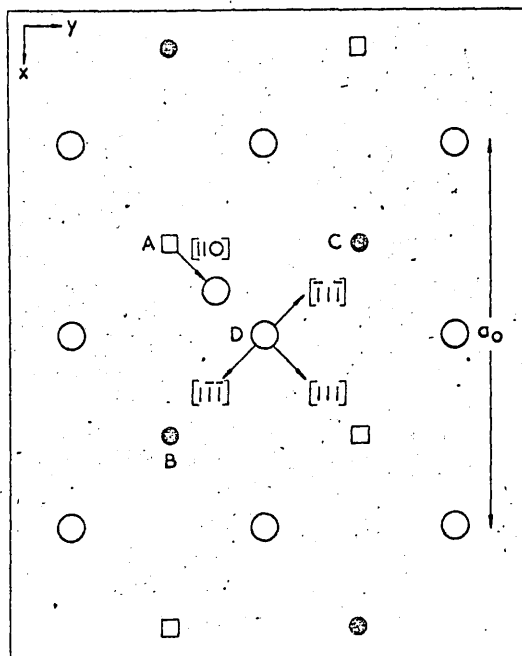


Fig. 5. — Possible mechanism for "polarisation" of interstitial oxygen atoms in UO_{2+x} and U_4O_9 . The interstitial oxygen enters the structure at A but is pulled along $[110]$ by the electrostatic force from uranium atoms B, C, which are converted from U^{4+} to U^{5+} to maintain charge balance. The fluorite-type oxygen at D is displaced, in turn, along one of the $\langle 111 \rangle$ directions shown.

Figure 5 is a diagram illustrating a possible mechanism for the preference of the interstitial atoms in UO_{2+x} and U_4O_9 for O' and O'' sites. The oxygen enters the fluorite structure at A but is pulled along $[110]$ by the electrostatic force from uranium atoms B, C, which are converted from U^{4+} to U^{5+} to maintain charge balance. The normal oxygen D is then ejected from its fluorite position in the directions $\langle 111 \rangle$ towards the adjacent interstices. This interpretation accounts for the presence of both O' and O'' atoms, and predicts that the numbers of O vacancies and O'' atoms are equal, in agreement with the figures quoted in Table III. Any further speculation must await the determination of the full structure of U_4O_9 from the measurement of the superlattice reflexions.

Acknowledgements. — The author wishes to acknowledge the discussion of this work with Dr. J. Williams and Dr L. E. J. Roberts. He is indebted to Dr M. H. Rand for preparing the U_4O_9 crystals and to Dr T. L. Markin for measuring their composition.

Discussion

Pr WATANABE. — N'avez-vous pas examiné une structure basée sur celle de la fluorine et en enlevant des atomes d'uranium de ses positions sans remplir d'oxygène les interstices ?

Dr WILLIS. — Le remplissage complet des sites du type fluorine par les atomes d'uranium est indiqué par des mesures de densité et par la comparaison des intensités avec celles d'un cristal de UO_2 placé dans le même faisceau de neutrons. Cependant, un travail supplémentaire est nécessaire pour établir une conclusion définitive.

Pr Post. — La maille U_4O_9 offre un volume d'approximativement 18 \AA^3 à chaque atome d'oxygène (en négligeant les atomes d'uranium). Ceci semble plutôt faible. Avez-vous calculé les distances O-O et certaines sont-elles anormalement courtes ?

Dr WILLIS. — Il n'est pas possible de calculer les distances O-O, car les résultats exposés sont relatifs à une maille moyenne, obtenue en superposant le continu de 64 mailles de la véritable maille élémentaire.

Dr ANDRESEN. — J'aimerais faire une remarque concernant la surstructure. En 1956, le Dr Frazer et moi-même avons enregistré quelques diagrammes de U_4O_9 sur le spectromètre de Corliss et Hastings. Nous avons trouvé que les raies de surstructure ne

pouvaient être indexées en système cubique, même en quadruplant la maille dans toutes les directions. Les raies de surstructures pouvaient au mieux être indexées dans une maille 16 fois plus grande avec un paramètre de $2a_0\sqrt{2}$ dans le plan de base et une hauteur de $2a_0$. Depuis nous avons pensé à plusieurs modèles pour placer les oxygènes supplémentaires mais aucun n'a pleinement réussi. C'est le manque de données suffisantes sur le monocristal qui, apparemment, laisse le problème encore sans solution.

Dr WILLIS. — Toutes les réflexions, à la fois principales et de surstructure, observées dans la présente étude pouvaient être indexées dans une maille de $4a_0$. Il est possible que d'autres réflexions, nécessitant une plus grande maille n'ont pas été enregistrées, malgré le soin et le temps employé à explorer l'espace réciproque.

Dr ROTH. — Observe-t-on une quelconque diffusion à la température ambiante ?

Dr WILLIS. — A la température ambiante, UO_2 et U_4O_9 sont tous deux des structures ordonnées. Aussi ne s'attend-on pas à une diffusion due aux défauts. Elle existe probablement à haute température, mais aucune tentative n'a été faite pour l'observer.

Dr ABRAHAMS. — Les écarts standard pour les facteurs d'occupation de O' et O'' sont de l'ordre du 1/60 de celles de O. Y a-t-il une normalisation spéciale pour ces « sigmas » sinon, pourquoi ces erreurs seraient-elles si petites ?

Dr WILLIS. — La corrélation entre les facteurs d'occupation de O^a et O^b est responsable de leurs grands écarts standard. Le tableau III montre que l'écart standard pour l'ensemble O^a et O^b est comparable à celui pour O' et pour O'' .

REFERENCES

- [1] BELLE (J.), Uranium dioxide : properties and nuclear applications (U. S. A. E. C.), 1961.
- [2] GOLDSCHMIDT (V. M.) and THOMASSEN (L.), Viden-skap. Skrift I. Mat.-Nat. Klasse; 1923, p. 1.
- [3] WILLIS (B. T. M.), *Proc. Roy. Soc.*, London, 1963, A 274, 122.
- [4] WILLIS (B. T. M.), *Proc. Roy. Soc.*, London, 1963, A 274, 134.
- [5] WILLIS (B. T. M.), *Nature*, 1963, 197, 755.
- [6] ALBERMAN (J. K.) and ANDERSON (J. S.), *J. Chem. Soc.*, Suppl., 1949, p. 5303.
- [7] HERING (J.) and PERIO (P.), *Bull. Soc. Chim. Fr.*, 1952, 19, 351.
- [8] BLACKBURN (P. E.), *J. Phys. Chem.*, 1958, 62, 897.
- [9] ROBERTS (L. E. J.) and WALTER (A. J.), *J. Inorg. Nucl. Chem.*, 1961, 22, 213.
- [10] BELBROCH (B.), PIEKARSKI (C.) and PERIO (P.), *Acta Cryst.*, 1961, 14, 837.
- [11] MARKIN (T. L.) and ROBERTS (L. E. J.), Thermodynamics of nuclear materials. I. A. E. A., Vienna, 1962, p. 693.
- [12] STEEB (S.), *Naturwiss.*, 1960, 47, 465.
- [13] ARNDT (U. W.) and WILLIS (B. T. M.), *Rev. Sc. Instr.*, 1963, 34, 224.
- [14] Busing (W. R.), MARTIN (K. O.) and LEVY (H. A.), Oak Ridge Report ORNL-TM-305, 1962.
- [15] WILLIS (B. T. M.), *J. Brit. Ceram. Soc.*, 1964, to be published.

The Anomalous Behaviour of the Neutron Reflexions of Fluorite

By B. T. M. WILLIS

Metallurgy Division, Atomic Energy Research Establishment, Harwell, Berks., England

(Received 30 December 1963)

At room temperature the neutron intensities of the Bragg reflexions of CaF_2 cannot be interpreted satisfactorily by the ideal fluorite model, with calcium atoms at the 000 , $\frac{1}{2}\frac{1}{2}0$, $\frac{1}{2}0\frac{1}{2}$, $0\frac{1}{2}\frac{1}{2}$ positions of the cubic cell, fluorine atoms at $\frac{1}{4}\frac{1}{4}\frac{1}{4}$, $\frac{1}{4}\frac{1}{4}\frac{3}{4}$... etc. and with all atoms executing isotropic thermal motion. Closer agreement with the observed data is obtained by assuming that the fluorine atoms are displaced slightly towards the centres of the interstices, which surround each fluorine tetrahedrally. This displacement can be ascribed to the anharmonic vibration of the fluorine atoms about their ideal positions. A similar effect has been reported previously for UO_2 and ThO_2 at high temperatures.

In cubic calcium fluoride, with calcium atoms at 000 +face-centred positions and fluorine atoms at $\frac{1}{4}\frac{1}{4}\frac{1}{4}$, $\frac{3}{4}\frac{3}{4}\frac{3}{4}$ +face-centred positions, the calculated neutron structure factors can be expressed in the form:

$$\left. \begin{aligned} F_c &= 4b_{\text{Ca}} + 8b_{\text{F}} \dots h+k+l = 4n \\ &= 4b_{\text{Ca}} \dots h+k+l = 4n+1 \\ &= 4b_{\text{Ca}} - 8b_{\text{F}} \dots h+k+l = 4n+2 \end{aligned} \right\} (1)$$

where the nuclear scattering amplitudes are $b_{\text{Ca}} = 0.49 \times 10^{-12}$ cm and $b_{\text{F}} = 0.55 \times 10^{-12}$ cm (Bacon, 1962). To account for the effect of thermal motion, b_{Ca} in (1) must be multiplied by the Debye-Waller factor $\exp(-B_{\text{Ca}} \sin^2 \theta/\lambda^2)$ and b_{F} by $\exp(-B_{\text{F}} \sin^2 \theta/\lambda^2)$. The calcium and fluorine atoms both occupy sites with cubic point symmetry ($m\bar{3}m$ for calcium and $\bar{4}3m$ for fluorine), so that, provided the thermal motion can be treated in terms of harmonic interatomic forces, the temperature factors B_{Ca} , B_{F} are independent of direction in the crystal.

The purpose of this paper is to point out that neutron diffraction measurements on single crystals of CaF_2 indicate that equations (1), modified to include isotropic Debye-Waller factors, do not account satisfactorily for the magnitudes of the observed structure factors F_o , particularly at high temperatures.

Fig. 1 shows the dependence on temperature of F_o for the three reflexions 755, 771 and 933. As these reflexions have equal values of $h^2+k^2+l^2$, they occur at the same value of $\sin^2 \theta/\lambda^2$, and $F_c = b_{\text{Ca}} \exp(-B_{\text{Ca}} \sin^2 \theta/\lambda^2)$ is the same for all three reflexions at any given temperature. However, the magnitudes of the observed structure factors are in the order $F_{755} > F_{771} > F_{933}$: at 20°C F_{755} is 12% greater than F_{933} and at 500°C the proportion is 40%, representing nearly a twofold increase in intensity of 755 compared with 933. Curves closely similar to Fig. 1 have also been obtained with UO_2 and ThO_2 (Willis, 1963), both of which have the fluorite structure.

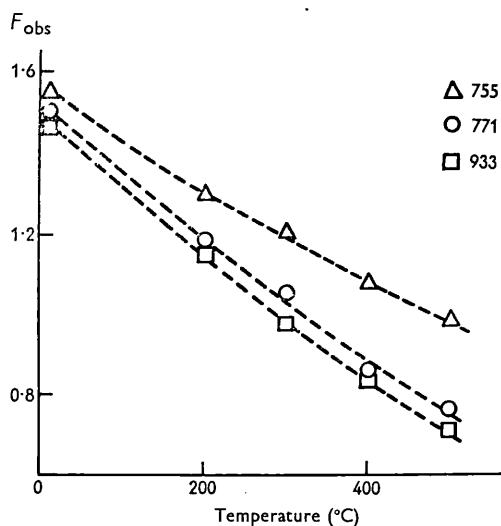


Fig. 1. Observed neutron structure factors for 755, 771 and 933 reflexions, as a function of temperature.

Closer agreement between F_o and F_c is obtained by allowing the fluorine atom at $\frac{1}{4}\frac{1}{4}\frac{1}{4}$ to move along the four tetrahedral directions joining the $\frac{1}{4}\frac{1}{4}\frac{1}{4}$ site with the adjacent holes or interstices at $\frac{1}{2}\frac{1}{2}\frac{1}{2}$, $\frac{1}{2}00$, $0\frac{1}{2}0$, and $00\frac{1}{2}$. Table 1 lists F_o for several high-angle reflexions together with the calculated structure factors determined for the fluorite arrangement, F_c , and for the modified arrangement, F'_c , with the fluorine atoms distributed at positions $\frac{1}{4} + \delta$, $\frac{1}{4} + \delta$, $\frac{1}{4} + \delta$... in the $Fm\bar{3}m$ space group. The structure factors were calculated by a least-squares analysis (Busing, Martin & Levy, 1962) of the observed data, using three adjustable parameters (B_{Ca} , B_{F} and scale factor) for F_c and a fourth adjustable parameter (δ) for F'_c . The refined values of B_{Ca} , B_{F} and δ are listed in Table 2, where the figures in brackets represent estimated standard deviations. By introducing the extra parameter δ , the discrepancy index $R =$

$\Sigma|F_o| - |F_c|/\Sigma|F_o|$ has fallen from 3.6% to 1.9%, a drop of nearly one-half. No further reduction in R was obtained by allowing displacement of the calcium atoms, and, indeed, difference Fourier syntheses, using coefficients $F_o - F_c$ with phases derived from F_c (ideal fluorite model), indicated that the displacement effect was restricted to the anion sub-lattice.

Table 1. Neutron diffraction data for CaF_2 at 20 °C

hkl	F_o	F_c	F_c'
733	1.626	1.535	1.580
644	1.652	1.642	1.651
555	1.440	1.496	1.417
662	1.571	1.571	1.578
911	1.329	1.458	1.454
933	1.341	1.384	1.337
771	1.402	1.384	1.357
755	1.500	1.384	1.492
10,0,0	1.368	1.376	1.363

F_c : Ideal fluorite model.

F_c' : Fluorite model with displacement of fluorine atoms.

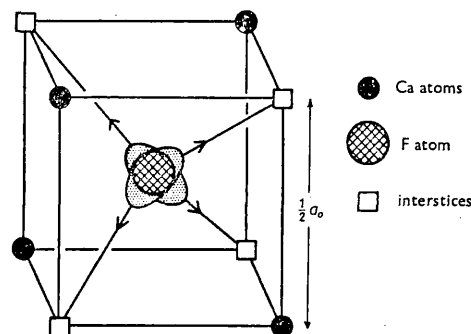
Table 2. Least-squares refinement of CaF_2 data at 20 °C

Model	B_{Ca} (Å ²)	B_{F} (Å ²)	δ	R
Ideal fluorite	0.39 (0.17)	0.53 (0.18)	0	0.036
Fluorite with displacement	0.39 (0.13)	0.32 (0.14)	0.009 (0.001)	0.019

Careful checks showed that the observed data in Table 1 were free from systematic errors due to extinction or multiple scattering. Moreover, if the displacement effect were associated with either of these errors, the effect would diminish with increasing temperature: the opposite is the case (Fig. 1). Most of the reflexions included in the least-squares analysis were those with odd indices, as (a) these reflexions are most sensitive to changes in δ and (b) the strong reflexions with even indices are not entirely extinction-free.

There are, at least, two alternative interpretations of the displacement effect: the fluorite structure is disordered, with some or all of the fluorine atoms displaced at random intervals towards the adjacent interstices at $\frac{1}{2}\frac{1}{2}\frac{1}{2}$... (Willis, 1963), or each fluorine atom vibrates in an asymmetric manner across the $\frac{1}{4}\frac{1}{4}\frac{1}{4}$ position. The second case is illustrated by Fig. 2, showing the fluorine atom drawn out along the four

tetrahedral directions while retaining the $\bar{4}3m$ point symmetry. Such an asymmetrical vibration must arise from anharmonic contributions to the Debye-Waller factor: when these contributions are included the Debye-Waller factor for an atom is no longer isotropic in the components of the scattering vector, even though it occupies a site of cubic symmetry (Maradudin & Flinn, 1963). A clear distinction between the two interpretations cannot be made from an analysis of the Bragg reflexions alone, although the general occurrence of the effect in CaF_2 , UO_2 and ThO_2 , and its moderate dependence on temperature, favour the anharmonic interpretation.

Fig. 2. Anharmonic vibration of the fluorine atom, leading to displacements along the four $\langle 111 \rangle$ directions shown.

The displacement effect was not observed by Weiss, Witte & Wölfel (1957), who carried out a careful X-ray investigation of CaF_2 single crystals at room temperature, using a counter diffractometer. This apparent discrepancy with the present results may be due to the greater precision of the neutron data, which require no correction for absorption.

References

- BACON, G. E. (1962). *Neutron Diffraction*. Oxford Univ. Press.
- BUSING, W. R., MARTIN, K. O. & LEVY, H. A. (1962). Oak Ridge National Laboratory, Tennessee. Report ORNL-TM-305.
- MARADUDIN, A. A., & FLINN, P. A. (1963). *Phys. Rev.* **129**, 2529.
- WEISS, A., WITTE, H. & WÖLFEL, E. (1957). *Z. Phys. Chem.* **10**, 98.
- WILLIS, B. T. M. (1963). *Proc. Roy. Soc. A*, **274**, 134.

NEUTRON DIFFRACTION STUDY OF ANTIFERROMAGNETISM IN UO_2

B. T. M. WILLIS and R. I. TAYLOR

*Metallurgy Division, Atomic Energy Research Establishment,
Harwell, Berks., England*

Received 16 June 1965.

Henshaw and Brockhouse [1] have studied anti-ferromagnetic ordering in approximately stoichiometric UO_2 by the neutron powder diffraction method. We have repeated the diffraction measure-

ments using single crystals of UO_2 and describe in this letter the results, some of which differ from those of Henshaw and Brockhouse. The new results are in broad agreement with those ob-

tained recently in a similar investigation of single-crystal UO_2 by Frazer et al. [2].

UO_2 crystallizes with the cubic calcium-fluoride structure, $a_0 = 5.47 \text{ \AA}$, and undergoes antiferromagnetic ordering below 30°K . Two crystals, weighing approximately 600 mg and 100 mg and with an oxygen/uranium ratio between 2.000 and 2.002, were examined at 4.2°K with 1.05 \AA neutrons. Magnetic reflexions appeared which could be indexed as 100, 110, 210, 211 ... on the basis of the normal cell; all the magnetic reflexions were present with indices consisting of a mixture of even and odd integers, and no additional reflexions were observed with fractional indices, $\frac{1}{2}00$, $\frac{1}{2}\frac{1}{2}0$...

The integrated intensities of sixteen hkk magnetic reflexions and eighteen hkk nuclear reflexions were measured by aligning the crystals with a [110] direction along the rotation axis. By comparing the magnetic and nuclear intensities of both the large and the small crystal it was possible both to correct for extinction, which amounted to no more than a few per cent for the strongest magnetic reflexions, and to place the magnetic intensities on an absolute scale.

All the intensity data were interpreted satisfactorily assuming a magnetic structure consisting of ferromagnetic (200) planes of uranium atoms, with antiferromagnetic coupling of the magnetic moments in adjacent (200) planes. Because of the cubic symmetry the normal to the

ferromagnetic sheet has an equal chance of coinciding with any of the three cubic axis, so that each crystal is divided into three types of domain with the ferromagnetic sheets parallel to (200), (020) and (002) planes. The observed equality of the intensity of symmetry-related reflexions showed that the domains were present in approximately equal proportions.

The magnetic moments lie within the ferromagnetic sheets and not along a [111] direction, as stated by Henshaw and Brockhouse. Thus the observed ratio of the intensities of the magnetic reflexions 221 and 300 is $I_{221}/I_{300} = 0.59$; the calculated ratio is independent of the nature of the form factor, as both reflexions occur at the same value of $\sin \theta/\lambda$, and is equal to 0.55 for the spin vector in the ferromagnetic sheet and 1.00 for the spin vector along [111]. Similarly, I_{100}/I_{110} is observed as 3.13, which is much closer to the calculated value for the first model (3.07) than for the second (1.56). In the absence of a single-domain sample it is not possible to determine the azimuth of the spin vector in the (200) ferromagnetic plane. However, if we assume that the spin sites use the highest possible point symmetry, the spin vector is either at 0° or 45° to a cube-axis direction within the (200) plane.

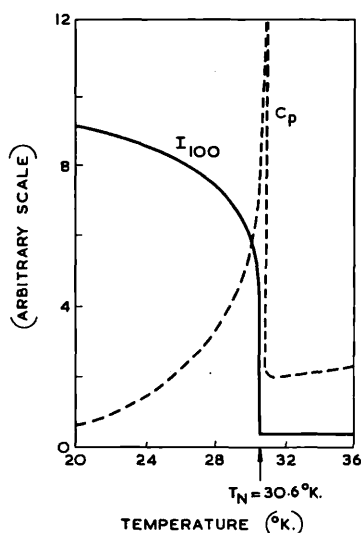


Fig. 1. Variation with temperature of intensity of magnetic reflexion 100 (this work) and of specific heat (Westrum).

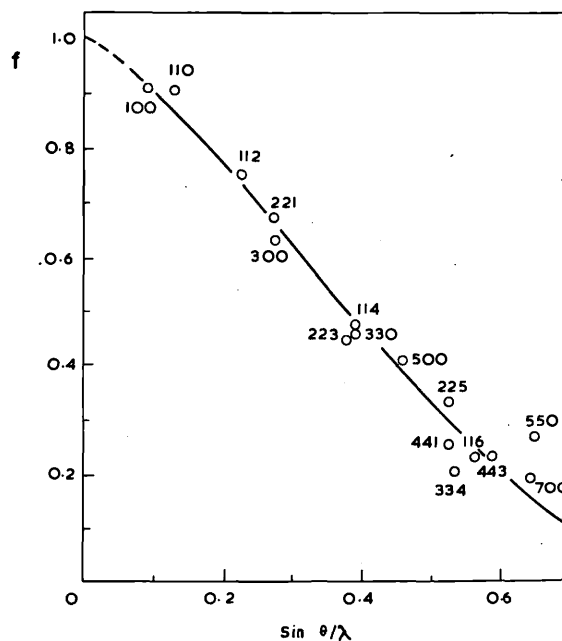


Fig. 2. Magnetic form factor for uranium atoms in UO_2 .

Just below the Néel point the temperature dependence of the 100 reflexion (see fig. 1) follows a very steeply falling curve: more than half the fall of intensity from 4.2°K occurs in the last degree before the transition temperature of 30.6°K. This value of the transition temperature is very close to the temperature, 30.4°K, of the specific heat anomaly observed by Westrum [3], and it would appear that the earlier value of $T_N = 28^\circ\text{K}$ [4] is definitely too low for stoichiometric UO_2 .

The magnetic form-factor curve for the uranium atoms is shown in fig. 2. The shape of this curve, which is related to the electronic configuration of the uranium atoms in UO_2 , is not greatly different from the form-factor curve for the uranium atoms in uranium nitride, UN, examined by Curry [5] using neutron diffraction. The experimental points in fig. 2 show systematic de-

partures from a smooth curve at high values of $\sin \theta/\lambda$, and this may be due to anisotropy of the form factor.

We should like to express our gratitude to Dr. G. G. Low for very helpful discussions.

References

1. D. G. Henshaw and B. N. Brockhouse, *Bull. Amer. Phys. Soc.* 2 (1957) 9.
2. B. C. Frazer, G. Shirane, D. E. Cox and C. E. Olsen, to be published.
3. E. Westrum, reported in "Thermodynamic and transport properties of uranium dioxide and related phases" (I.A.E.A., Vienna, 1965).
4. W. M. Jones, J. Gordon and E. A. Long, *J. Chem. Phys.* 20 (1952) 695.
5. N. Curry, private communication.

* * * * *

(Reprinted from Nature, Vol. 214, No. 5084, pp. 129-133, April 8, 1967)

Structure of a Monocarboxylic Acid Derivative of Vitamin B₁₂

One particular monocarboxylic acid derived from cyanocobalamin can be grown in very large crystals on which both X-ray and neutron diffraction measurements have been made. Calculations lead to the placing of some 205 atoms in the crystal asymmetric unit, including 98 hydrogen atoms, and thus to the detailed definition of the chemical structure of the molecule.

Crystal and Molecular Structure from X-ray Analysis

THE mild acid hydrolysis of cyanocobalamin gives rise to a mixture of mono- and di-carboxylic acids and one tri-carboxylic acid, a finding consistent with the view that the propionamide side chains on the molecule are the first objects of attack. The exact structure of one of these acids, which has particularly interesting properties, is the subject of the present investigation. This acid, first called *E*₂, constitutes more than 90 per cent of the monocarboxylic acid fraction of the B₁₂ hydrolysate¹; it crystallizes in large monoclinic crystals, easily separated by fractional crystallization from the isomeric acids. It also occurs as a natural product in the fermentation liquors of *Propionibacterium shermanii* (CMS₁², CMS-*e*³; Zone 1⁴) where it behaves as an intermediate in the biosynthesis of the B₁₂ vitamins⁵. It has antimetabolite activity compared with B₁₂ in *Escherichia coli* and *Ochromonas malhamensis*⁵.

The very large size of the crystals of the acid prompted an attack on its structure by a combination of X-ray and neutron diffraction. It was hoped by such measurements to define the crystal structure of the acid itself, to place the acid group on the molecule and to add the details of the arrangement of the hydrogen atoms to the structure of vitamin B₁₂. The X-ray analysis began on the air dried crystals because particularly perfect specimens of these, several mm on edge, had already been given to us by Dr. E. Lester Smith. Later, as experience with neutron diffraction indicated that the more stable crystals in their mother liquor should be the main subject of attack, wet crystals were also investigated by X-rays. Preliminary data on the crystals are given in Table 1.

Table 1. PRELIMINARY DATA ON THE B₁₂ MONOACID, C₁₂H₁₇O₁₁N₁₂PCo

	Unit cell dimensions			β	Space group	Density	Probable No. of water molecules
	a	b	c				
Air dried	14.51	17.09	16.85	103°	P2 ₁	1.335	13
Wet	14.915	17.486	16.409	104.11°	P2 ₁	1.339	16
σ	0.009	0.009	0.007	0.047			

The preferred values for the wet crystals were derived by neutron diffraction.

The air dried crystals of the acid gave very good X-ray data, extending to the limit of the copper sphere and showing marked Bijvoet differences due to anomalous dispersion at the cobalt atom. A total of 6,323 individual *hkl* and $\bar{h}\bar{k}\bar{l}$ reflexions were measured visually. Average F^2 values were derived and used for the initial three-dimensional Patterson calculations to place the cobalt atom. Two alternative phase angles were then calculated by the expressions given by Ramachandran and Raman⁶. Trials of a number of functions and variations of their expressions were made which will be described elsewhere. Evidence for the correct atomic arrangement was most

easily obtained from an electron density distribution calculated with 2,567 terms phased from the Bijvoet differences, with α chosen as the alternative nearest the cobalt atom contribution. The structure was, in fact, solved first from a less favourable approximation and the atomic positions improved in successive electron density distributions and least squares calculations. The present reliability index is 0.142; the average standard deviation in the carbon-carbon single bonds is 0.04. Fig. 1 shows the agreement at this stage between α_c , calculated on the present atomic parameters, and α_a , the phase angles derived from the Bijvoet effect. The curve shows that for 72 per cent of the reflexions, the first phase angle chosen was within 45° of the final value.

Once the structure of the air dried crystals was known, it was easy to derive that of the wet crystals, starting from a cobalt atom phased map alone, and sorting out the correct mirror image atoms by inspection of the three dimensional distribution. This route was followed at Harwell (F. M. M.). An alternative route using Bijvoet pairs of reflexions measured on oscillation photographs was taken at Auckland (T. N. M. W., J. M. W.). This alternative has some general interest as a possible method for deriving rapidly the general atomic distribution within a molecule in the correct absolute configuration.

The crystal structure of the air dried monoacid is illustrated in Fig. 2. It shows no resemblances to that of cyanocobalamin, wet or dry^{7,8}, nor to that of 5'-deoxyadenosylcobalamin⁹. The molecules are arranged in broad layers within which the planes of the corrin rings are inclined at about 80° to one another. Between the layers there is a marked cleavage; contact is made across the

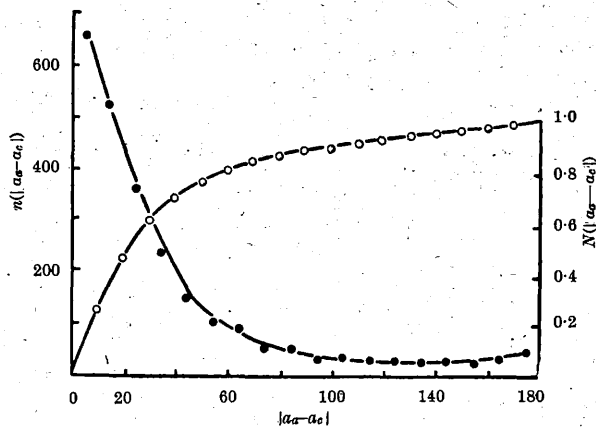


Fig. 1. Phase analysis. Here n is the number of reflexions in each 10° range and $N(a_a - a_c)$ is the normalized cumulative function for each value of $|a_a - a_c|$, where a_a is the phase from the Bijvoet effect, a_c the final phase calculated.

gap through hydrogen bonds between water molecules and the active groups at the ends of the side chains. The terminating atoms of two of the acetamide groups occupy alternative disordered sites and many of the water molecule positions also show disorder. There does not appear to be any obvious feature of the molecular arrangement that would suggest the position of the carboxylic acid groups among the amides. Direct observation of the electron density maps favours a definite orientation of

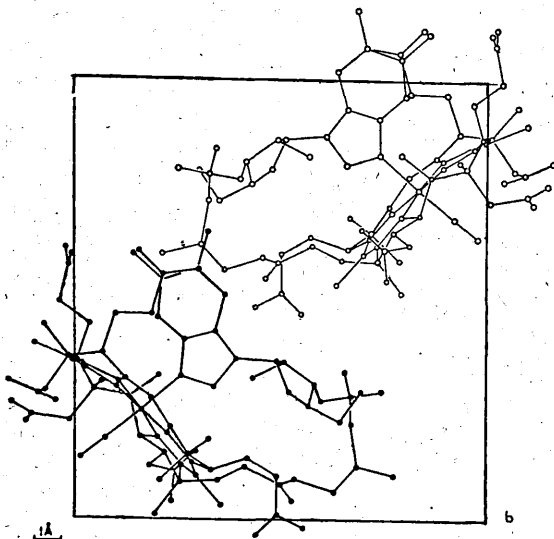
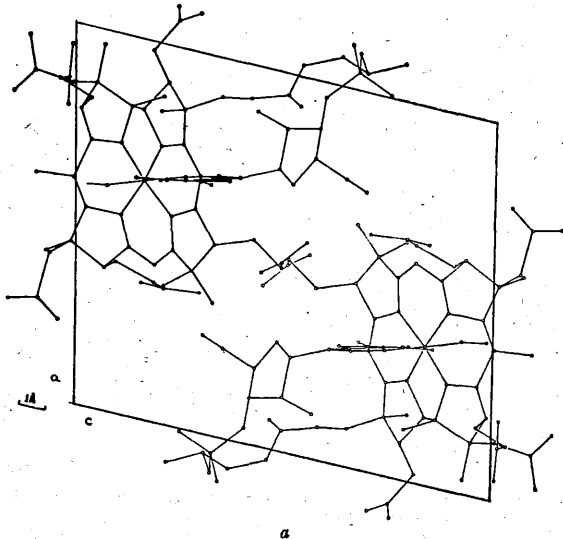


Fig. 2. Projection of the atomic positions found in air dried crystals of the B_{12} monoacid: *a*, along [010]; *b*, along [100]. Filled circles represent atoms at y , open circles at $y + \frac{1}{2}$.

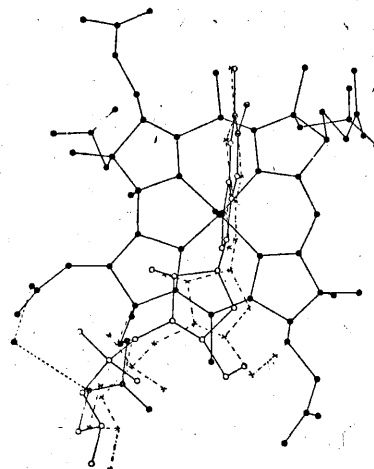


Fig. 3. Projection of atomic positions on the least squares plane through cobalt, N21, N22, N23 and N24. Solid line, B_{12} monoacid; dotted line, cyanocobalamin (both air dried).

each of the three acetamide groups in agreement with the neutron diffraction data below; the longer side chains, however, are less well defined in position and conclusions from the peak heights or interatomic distances are unreliable here.

The general atomic distribution in the molecule is closely similar to that in cyanocobalamin with one quite interesting difference. This is illustrated by Fig. 3, which shows a projection of the atomic positions on to a calculated least squares plane passing through the cobalt and four inner nitrogen atoms. When the corresponding projection of cyanocobalamin is compared with this, it is clear that there is a variation in the position of the nucleotide-like side chains in the two molecules. The phosphate and sugar group particularly have moved about 1 Å relative to the positions they occupy in cyanocobalamin. The benzimidazole, sugar, phosphate, and propanolamine groups are rather flexible and the new positions may represent no more than an adjustment to new packing conditions within the present crystal structure. They do not seem to be connected specifically with the position of the acid group.

We thank Dr. E. Lester Smith, Professor Bernhauer, Dr. Beisbarth and Dr. Wagner for crystals used in this research and for interesting discussions. Computing was carried out on the *KDF9* computer, University of Oxford. One of us (S. R.) thanks the Science Research Council for the award of a senior research fellowship.

C. K. NOCKOLDS T. N. M. WATERS
S. RAMASESHAN J. M. WATERS
DOROTHY CROWFOOT HODGKIN

Chemical Crystallography Laboratory,
University of Oxford.

Crystal and Molecular Structure from Neutron Diffraction Analysis

The distinction between an amide and a carboxylic acid can be made more easily by neutron diffraction than by X-ray diffraction. In contrast to X-ray scattering, the coherent neutron scattering lengths of nitrogen ($b = 9.4f^*$) and of oxygen ($b = 5.8f$) are widely different and in addition the coherent neutron scattering length of hydrogen ($b = 3.8f$), although negative, has a magnitude approximately equal to that of other atoms. Consequently it has been possible by neutron diffraction to define in detail the structure of the monocarboxylic acid derivative of cyanocobalamin.

described using the numbering system given in II. Contours are drawn at intervals of 1 fermi/Å³ and hydrogen atoms which have a negative scattering length are represented by broken contours.

Fig. 4 shows a composite Fourier map over the corrin nucleus. In contrast with the X-ray case, the central cobalt atom ($b = 2.5f$) is the "lightest" atom in the molecule and the nitrogen atoms, ($b = 9.4f$) the "heaviest". Of particular interest are the hydrogen atoms bonded to carbon atoms 3, 8, 10, 13, 18 and 19 and the absence of hydrogen atoms at positions 1, 4, 5, 6, 9, 11, 14, 15 and 16. These demon-

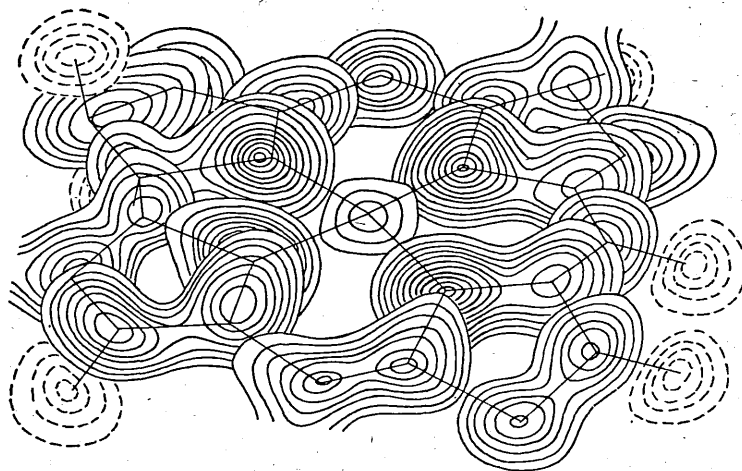


Fig. 4. Neutron scattering density over the corrin nucleus.

The neutron diffraction data for this purpose were measured using a wet crystal of weight 11 mg and density 1.339 g/c.c. All unique reflexions from planes with interplanar spacings, $d > 1.3 \text{ \AA}$, were investigated and 1,531 reflexions were classed as observable. The mean peak (including background) to background ratio for the observable reflexions was 1.3 : 1, but the count rate was sufficient to give a fractional standard deviation $\sigma(f)/F \sim 8$ per cent for the structure amplitudes after counting for 30 min equally divided between peak and background.

The structure analysis is summarized in the flow sheet. The neutron Patterson synthesis first calculated proved, as expected, to be uninterpretable because there are many atoms present in the unit cell, scattering with both positive and negative phase and no heavy atom dominating in neutron scattering power. First atomic co-ordinates were therefore derived from the parallel X-ray investigation and used to obtain approximate initial phases for the first neutron Fourier synthesis. This synthesis was used solely to refine the co-ordinates of the eighty-four non-hydrogen atoms used in the initial phasing. Subsequent neutron Fourier and difference Fourier maps were used to obtain further atomic positions and to refine the structure. Of the 228 atoms in the crystal asymmetric unit, of formula $C_{63}H_8O_{15}N_{13}PCo16H_2O$, the co-ordinates of all the atoms in the acid molecule have been determined and fourteen water oxygen atoms and eleven water hydrogen atoms have been located. Because 820 parameters have been determined using 1,531 observations, the standard deviations of these parameters are large and the analysis has been terminated at the seventh Fourier synthesis while further data are being collected.

The accompanying diagrams, of the nuclear scattering density over different parts of the molecule, illustrate various features emerging from the analysis. These will be

strate clearly that a conjugated single-bond/double-bond sequence extends from atom N21, through atoms 4, 5, 6, N22, 9, 10, 11, N23, 14, 15 and 16 to atom N24, and does not extend beyond atoms N21 and N24.

The methyl group C53, 53H₁, 53H₂ and 53H₃ bonded to C15 is illustrated in Fig. 5. As with all the other methyl groups in the molecule, the analysis has shown that the group does not have a range of orientations corresponding to free rotation about the C15-C53 single bond. This is shown by the definite peaks corresponding to the hydrogen atoms 53H₁, 53H₂ and 53H₃. It is doubtful whether the elongation of the hydrogen peaks corresponds to a small degree of rotational freedom about the C15-C53 bond; the effect is observed on all hydrogen peaks in the Fourier maps and probably arises from the low resolution obtainable from the data.

Figs. 6a and b illustrate the chemical assignment of the atoms in the acetic group bonded to atom C7 of ring B. Fig. 6a is a composite Fourier map phased with atoms 39 and 40 as oxygen atoms and without hydrogen atoms. The peak corresponding to atom 40 is significantly higher than that corresponding to atom 39 and there are also two negative peaks corresponding to hydrogen atoms bonded to

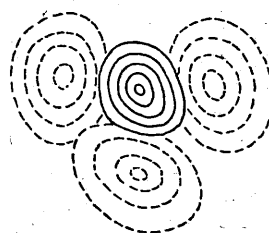
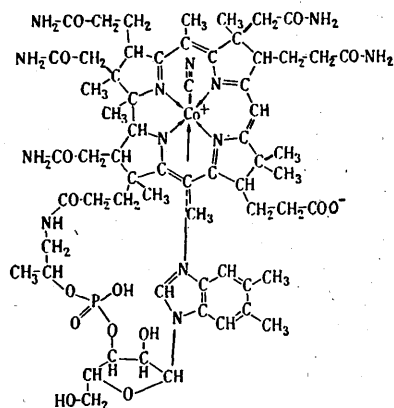
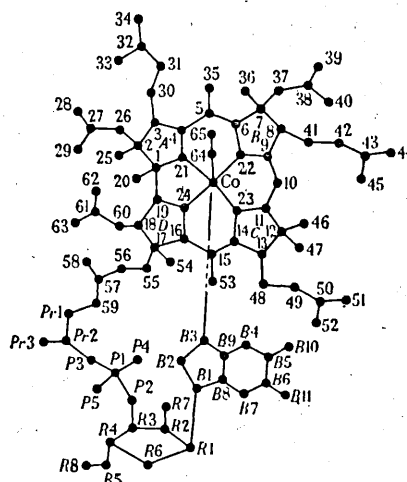


Fig. 5. Neutron scattering density over methyl group centred on C53.

* $f = 10^{-18} \text{ cm}$ (fermi unit).



I. Structure found for B_{12} monoacid E2.



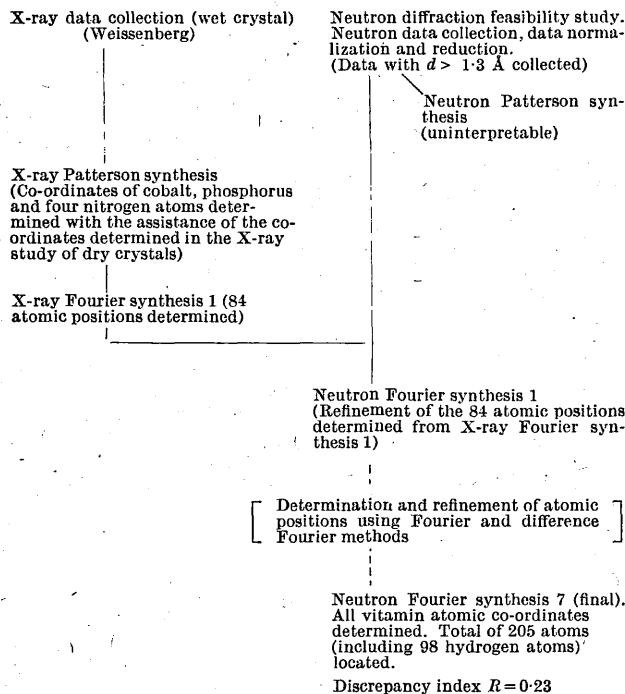
II. Numbering scheme used.

atom 40. The group was therefore assigned as an amide

group $\left(\begin{array}{c} \text{NH}_2 \\ | \\ -\text{C} \\ || \\ \text{O} \end{array} \right)$ with atom 40 as the nitrogen atom.

Fig. 6b is a composite Fourier map phased using all atoms of the group with their appropriate scattering lengths.

Flow sheet. STRUCTURE DETERMINATION FROM NEUTRON DIFFRACTION DATA



Although all the acetic groups were readily assigned as being acetamide groups, the assignment of the propionic groups was not definite until the structure had been refined considerably. Fig. 7 gives contour maps from the seventh Fourier synthesis. Figs. 7a-c correspond to composite Fourier maps over the propionic groups bonded to rings A, B and C respectively. In the phase calculations for the Fourier synthesis, the terminal non-hydrogen atoms of each group were given the scattering length of oxygen and the terminal hydrogen atoms were not included.

In the Fourier map over the propionic group bonded to ring A (Fig. 7a), the peak corresponding to atom 34 is

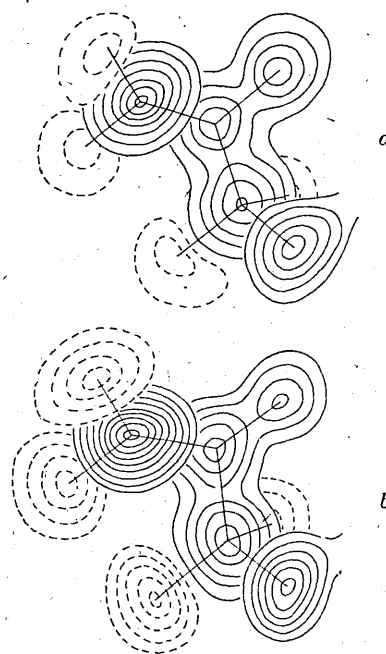


Fig. 6. Neutron scattering density over acetamide group attached to C7: a, phased with 39 and 40 as oxygen atoms and with no hydrogen atoms included; b, phased with all atoms given appropriate scattering lengths.

stronger than that corresponding to atom 33 and has two negative peaks corresponding to two feasible hydrogen atom positions near it. This group is therefore a propionamide group.

The Fourier map over the propionic group bonded to ring B (Fig. 7b) indicates that there is disorder of the terminal atoms between their respective positions. The peaks corresponding to atoms 44 and 45 are both higher than expected for an oxygen atom and lower than expected for a nitrogen atom. In addition there are hydrogen peaks near both of the positions 44 and 45. Again a propionamide group is indicated. It seems likely that the disorder is due to the position of this group between two negative atoms which do not bear hydrogen atoms, the cyanide nitrogen atom and an oxygen atom of the remaining side chain; the two alternative positions for the amide nitrogen atoms permit different types of hydrogen bonded contact.

The evidence from the Fourier map over the propionic group bonded to ring C (Fig. 7c) indicates that this group is a propionate ion. Both terminal peaks are only slightly

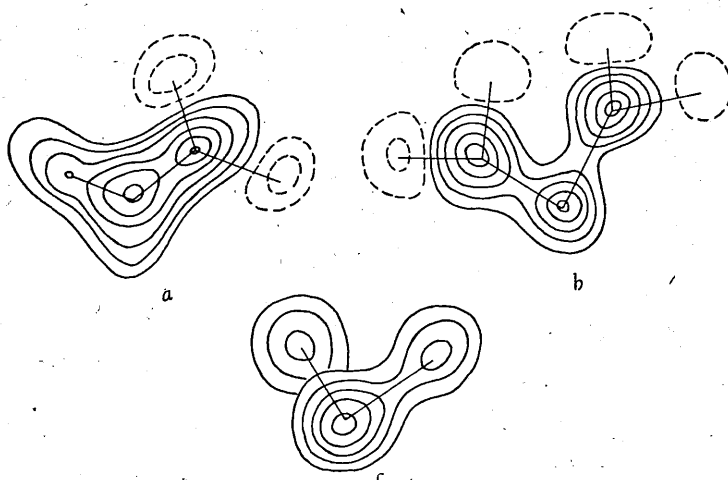


Fig. 7. Neutron scattering density over propionamide and propionate groups attached to: *a*, ring A; *b*, ring B; and *c*, ring C.

lower than expected for oxygen atoms and there is no evidence for terminal hydrogen atoms. On the other hand, a peak of height $-2.3f$ appears in the neighbourhood of the phosphate oxygen atom, P5, together with a smaller one, height $-1.8f$, near P4, which indicates that the

phosphate group here is uncharged $\text{>P} \begin{matrix} \text{=O} \\ \text{<OH} \end{matrix}$ and again

there may be some disorder between $=\text{O}$ and $-\text{OH}$.

That the propionate group on ring C is the acid group in our monocarboxylic acid as in Formula I is in agreement with the view recently expressed by Bernhauer *et al.*³ This view was based on observations of reactions of the monocarboxylic acid which appear to involve interaction between the phosphate group and the acid group within the molecule. Thus the acid, left in aqueous solution, is slowly hydrolysed with loss of the nucleotide-like group to give incomplete corrinoid compounds, whereas cyanocobalamin and the isomeric acid, E_1 , are quite unchanged under these conditions.

One of us (F. M. M.) was on attachment to Harwell from the University of Oxford during the course of this work and received a research grant from the Medical Research

Council. The computing was carried out on the Science Research Council ATLAS computer, Chilton.

F. M. MOORE
B. T. M. WILLIS

Ceramics Division,
Atomic Energy Research Establishment,
Harwell.

DOROTHY CROWFOOT HODGKIN
Chemical Crystallography Laboratory,
University of Oxford.

Received February 13, 1967.

¹ Armitage, J. B., Cannon, J. R., Johnson, A. W., Parker, L. F. W., Smith, E. Lester, Stafford, W. H., and Todd, A. R., *J. Chem. Soc.*, 3849 (1953).

² Bernhauer, K., Muller, O., and Wagner, F., *Adv. Enzymol.*, **26**, 274 (1964).

³ Bernhauer, K., Wagner, F., Beisbarth, H., Rietz, P., and Vogelmann, H., *Biochem. Zeit.*, **344**, 289 (1966).

⁴ Keemen, A. M., Czanyi, E., and Simon, A., *Acta Physiol. Acad. Sci. Hung.*, **21**, 177 (1962).

⁵ Ford, J. E., *J. Gen. Microbiol.*, **21**, 693 (1959).

⁶ Ramachandran, G. N., and Raman, S., *Curr. Sci., India*, **25**, 348 (1956).

⁷ Hodgkin, D. C., Lindsey, J., Sparks, R. A., Trueblood, K. N., and White, J. G., *Proc. Roy. Soc., A*, **266**, 494 (1962).

⁸ Brink-Shoemaker, C., Cruickshank, D. W. J., Hodgkin, D. C., Kamper, M. J., and Pilling, D., *Proc. Roy. Soc., A*, **278**, 1 (1966).

⁹ Lenhart, P. G., and Hodgkin, D. C., *Nature*, **192**, 937 (1961).

*Reprinted without change of pagination from the
Proceedings of the Royal Society, A, volume 298, pp, 307-315, 1967*

Anharmonic vibration and forbidden reflexions in
silicon and germanium

BY B. DAWSON AND B. T. M. WILLIS

Anharmonic vibration and forbidden reflexions in silicon and germanium

BY B. DAWSON

*Division of Chemical Physics, C.S.I.R.O. Chemical Research Laboratories,
Melbourne, Australia*

AND B. T. M. WILLIS

*Atomic Energy Research Establishment,
Harwell, Berkshire, England*

*(Communicated by W. Cochran, F.R.S.—Received 3 February 1966—
Revised 22 September 1966)*

An appraisal is given of antisymmetric features of vibrational anharmonicity in Ge and Si which could be manifested by Bragg reflexions in neutron diffraction studies conducted at elevated temperatures. The discussion is based on the generalized structure factor and the implications of effective one-particle potentials of the form

$$V_j(\mathbf{r}) = V_{0,j} + \frac{1}{2}\alpha_j(x^2 + y^2 + z^2) + \beta_jxyz$$

required to satisfy the T_d symmetry of the atomic sites. Values of the α -parameter, derived from the characteristic temperatures Θ_M of Ge and Si, are similar to the results for α_0 and α_F found in the vibration analysis of neutron data for the fluorite structures UO_2 and CaF_2 (Dawson, Hurley & Maslen 1967). This α -similarity is used to develop a 'fluorite-like' appraisal of possible vibrational anharmonicity in Ge and Si by assuming a β -parameter which satisfies the ratio $|\beta|/\alpha \sim 1.3 \text{ \AA}^{-1}$ found earlier for both UO_2 and CaF_2 . The resultant predictions for Bragg scattering at temperatures in excess of Θ_M are examined for the conditions relevant to both mosaic and perfect crystal specimens. It is shown that the two types of specimen offer different opportunities for detecting anharmonic phenomena, and that the perfect specimen could manifest strong scattering associated with the 'forbidden' reflexions 666 and 864 in experiments conducted at high temperatures.

1. INTRODUCTION

Two applications of the generalized structure factor (Dawson 1967*a*) have yielded new information on structural details in systems of quite different type. In diamond (Dawson 1967*b*: hereafter I), the appropriate X-ray version of the structure factor permits a detailed study of the electronic charge distribution associated with covalent bonding in that structure. In UO_2 and CaF_2 (Dawson, Hurley & Maslen 1967: hereafter II), the version relevant to neutron diffraction allows us to resolve important anharmonic parameters in the effective one-particle potentials experienced by the anions (of T_d site symmetry) in these ionic structures.

In this paper, we begin the extension of the results obtained in I and II by examining features of vibrational anharmonicity in silicon and germanium that could be manifested in high-temperature neutron studies of these covalent systems. The atomic sites have T_d symmetry, and, following II, we explore the consequences of effective one-particle anharmonic potential fields of the form

$$V_j(\mathbf{r}) = V_{0,j} + \frac{1}{2}\alpha_j(x^2 + y^2 + z^2) + \beta_jxyz \quad (1)$$

which satisfies this site symmetry. Values of the α parameter for both Si and Ge (available from determinations of Θ_M , the Debye characteristic temperature for diffraction studies) are numerically similar to the results found for α_O and α_F in II, so that the combination of these α parameters with the β information in II provides a 'fluorite-like' basis from which to judge results given by Si and Ge in appropriate high-temperature neutron experiments. A feature of special interest in these structures is that significant vibrational anharmonicity implies the generation of the 'forbidden' series $(h+k+l) = 4n+2$ (with no zero index). This is the neutron counterpart of the X-ray situation where only 222 occurs, and it is useful at this stage to assess what conditions should be satisfied if these reflexions are to be found. The appraisal which we give below considers both mosaic and perfect crystal specimens.

2. THEORETICAL

Using the notations of I and II, the neutron structure factors for diamond structures can be written in condensed form (see I) as

$$F(\mathbf{S}) = K(ab_{\mathbf{A}}T_{c,\mathbf{A}}(\mathbf{S}) + cb_{\mathbf{A}}T_{a,\mathbf{A}}(\mathbf{S})). \quad (2)$$

The A subscript denotes the A type atoms of Si or Ge in accord with figure 1 of I. Since nuclear scattering amplitudes are involved, $b_{\mathbf{A}} \equiv b_{\mathbf{B}}$ so that we now drop the subscript from this quantity. The Bragg reflexions fall into three distinct categories, with (2) having the forms

$$\left. \begin{aligned} \text{(i)} \quad F(\mathbf{S}) &= K_1 b T_{c,\mathbf{A}}(\mathbf{S}) && \text{for } (h+k+l) = 4n, \\ \text{(ii)} \quad F(\mathbf{S}) &= K_1 b T_{a,\mathbf{A}}(\mathbf{S}) && \text{for } (h+k+l) = 4n+2, \text{ no index zero,} \\ \text{(iii)} \quad F(\mathbf{S}) &= K_2 b (T_{c,\mathbf{A}}(\mathbf{S}) + T_{a,\mathbf{A}}(\mathbf{S})) && \text{for } (h+k+l) = 4n+1 (a), \\ &= K_2 b (T_{c,\mathbf{A}}(\mathbf{S}) - T_{a,\mathbf{A}}(\mathbf{S})) && \text{for } (h+k+l) = 4n-1 (b), \end{aligned} \right\} \quad (3)$$

where $|K_1| = 8$ and $|K_2| = 4\sqrt{2}$ (see table 1 of I). In terms of (1), we have (from II) that, at temperatures (T) in excess of Θ_M ,

$$\left. \begin{aligned} T_{c,\mathbf{A}}(\mathbf{S}) &\equiv \bar{T}_{c,\mathbf{A}}^h(\mathbf{S}) = \exp\left\{-\frac{1}{4}\bar{B}_{\mathbf{A}}S^2\right\}, \\ T_{a,\mathbf{A}}(\mathbf{S}) &= (\bar{B}_{\mathbf{A}}/4\pi a)^3 \exp\left\{-\frac{1}{4}\bar{B}_{\mathbf{A}}S^2\right\} (\beta_{\mathbf{A}}/kT) hkl, \end{aligned} \right\} \quad (4)$$

where
$$\bar{B}_{\mathbf{A}} = 8\pi^2 kT / \alpha_{\mathbf{A}} \equiv 8\pi^2 \langle u_S^2 \rangle_{\mathbf{A}}, \quad (4a)$$

the k in (4a) and the denominator of $T_{a,\mathbf{A}}(\mathbf{S})$ being the Boltzmann constant. Further from II, $\alpha_{\mathbf{A}} = \alpha_{\mathbf{B}}$ but $\beta_{\mathbf{A}} = -\beta_{\mathbf{B}}$, so that we can also drop the A subscript from quantities dependent only on the α parameter. Since the orientation of the A type tetrahedron here is equivalent to that involved in the Y' subset of II (compare figures 1 of I and II), $\beta_{\mathbf{A}}$ of (1) is a positive quantity.

The end result is that (3) predicts anharmonic features in the odd index reflexions which follow the pattern observed in the fluorite systems: at any value of S ($= 2 \sin \theta / \lambda$), the $(4n+1)$ members should be stronger than the $(4n-1)$ members, the differences depending on the sizes of the index-product hkl involved in each case. In addition, (3) also predicts a $(4n+2)$ series associated solely with the anharmonic vibrational motion implied by the T_d site symmetry: again, the members

of this series are governed by the index-product, from which it follows that only members with no zero index can arise. This series describes 'forbidden' aspects of neutron diffraction here since, with the customary assumption of harmonic vibration, (3) is replaced by the simpler predictions

$$\left. \begin{aligned} \text{(i)} \quad F(\mathbf{S}) &= K_1 b \bar{T}_c^{\text{har.}}(S), \\ \text{(iii)} \quad F(\mathbf{S}) &= K_2 b \bar{T}_c^{\text{har.}}(S), \end{aligned} \right\} \quad (5)$$

where $\bar{T}_c^{\text{har.}}(S)$ is equivalent to $\bar{T}_c^h(S)$ in (4), the different superscript being used (as in II) to underline the harmonic basis of (5). The neutron prospects for diamond structures are closely analogous to the X-ray possibilities which were exploited in I. The most notable difference is for the 'forbidden' neutron reflexions: the dependence on the index-product means that it is higher members of this class, rather than 222 itself, which are more likely to be detected at elevated temperatures.

The α parameters of (1) for Si and Ge can be derived from the X-ray studies of Batterman & Chipman (1962) who obtained, over the temperature range 300–1100 °K, Θ_M values (independent of temperature) of 543 ± 8 °K for Si and 290 ± 5 °K for Ge. Their results are averaged over measurements made on either even index planes or odd index planes whose index-products are small: 531 alone for Si, and 531 together with the doublet 511–333 for Ge. We therefore ignore the antisymmetric implications of (3)(iii) for these latter planes and relate Θ_M to α by recalling that Debye–Waller theory expresses the variation of $\langle u_S^2 \rangle$ with temperature by the equation

$$\langle u_S^2 \rangle = (3h^2T/4\pi^2mk\Theta_M^2) \{ \Phi(x) + \frac{1}{4}x \}, \quad (6)$$

where h and k are the Planck and Boltzmann constants, m is the mass of the vibrating atom, T is the absolute temperature (or, perhaps the reduced temperature (Paskin 1957) concerned with making Θ_M invariant with temperature as the theory specifies), $x = \Theta_M/T$, and the term in curly brackets is the Debye function as given in table V. 1 of James (1948). Since the value of the Debye function rapidly approaches unity for temperatures in excess of Θ_M , which is simply to say that the vibration problem can be treated classically at such temperatures, we have the 'high temperature' relation that

$$\alpha = 4\pi^2mk^2\Theta_M^2/3h^2 \quad (7)$$

(see Debye 1914). The values of α for the two structures are then found to be

$$\left. \begin{aligned} \alpha_{\text{Si}} &= 7.85 (0.23) \times 10^{-12} \text{ erg}/\text{\AA}^2, \\ \alpha_{\text{Ge}} &= 5.79 (0.20) \times 10^{-12} \text{ erg}/\text{\AA}^2. \end{aligned} \right\} \quad (8)$$

Since these α parameters are numerically similar to the results in II for α_0 and α_F (as we must expect from the general similarity of the four Θ_M values), a suitable starting point for studying the β_j in (1) is to assume values which satisfy the ratio $|\beta|/\alpha \sim 1.3 \text{ \AA}^{-1}$ found in II. This will provide a 'fluorite-like' basis for appraising possible anharmonic phenomena in Bragg scattering, against which we can judge results of actual experiment. For convenience, we adopt the common value $\beta_A = +1.0 \times 10^{-11} \text{ erg}/\text{\AA}^3$ for Si and Ge even though this gives $|\beta|/\alpha = 1.7 \text{ \AA}^{-1}$ for Ge. The effect of reducing the β estimate will emerge below.

For the cell dimension in (4), we take $a(\text{Si}) = 5.445 \text{ \AA}$ and $a(\text{Ge}) = 5.678 \text{ \AA}$: these are the results obtained, at 700 and 600 °C respectively, on using the room temperature data given by Swanson & Fuyat (1953) and Swanson & Tatge (1953). For the neutron wavelength, we retain the value $\lambda = 1.038 \text{ \AA}$ employed earlier (Willis 1963*a*). The coherent nuclear scattering amplitudes are $b_{\text{Si}} = 0.42 \times 10^{-12} \text{ cm}$ and $b_{\text{Ge}} = 0.84 \times 10^{-12} \text{ cm}$ (Bacon 1962).

Finally, we limit considerations to temperatures above 400 °C so as to satisfy the classical origins of (4) and (4*a*) (see II). The melting points of Si and Ge are, respectively, approximately 1420 and 960 °C, so we still have a wide range of potential observation with experimental facilities extending up to 1100 °C (Willis 1963*b*).

3. ESTIMATES OF BRAGG SCATTERING FROM Si AND Ge AT HIGH TEMPERATURES

(a) Mosaic crystal scattering

The Bragg intensities are related to the quantities

$$I'_m(\mathbf{S}) = |F(\mathbf{S})|^2 \operatorname{cosec} 2\theta, \quad (9)$$

where θ is the Bragg angle. Consider first the odd index structure factors of (3) in the form

$$F(\mathbf{S}) = \bar{F}_c(\mathbf{S}) + \Delta F_a(\mathbf{S}), \quad (10)$$

using $\Delta F_a(\mathbf{S})$ to denote the component involving the T_a factor of (4) and $\bar{F}_c(\mathbf{S})$ as an alternative expression for (5) to emphasise the isotropic centrosymmetric nature of the harmonic version of the structure factor. To first order, we then have

$$I'_m(\mathbf{S}) = \bar{I}'_m(\mathbf{S}) + 2\bar{F}_c(\mathbf{S})\Delta F_a(\mathbf{S}) \operatorname{cosec} 2\theta \quad (11)$$

and
$$\Delta I'_m(\mathbf{S}) = (I'_m(\mathbf{S}) - \bar{I}'_m(\mathbf{S})) / \bar{I}'_m(\mathbf{S}) = 2\Delta F_a(\mathbf{S}) / \bar{F}_c(\mathbf{S}), \quad (12)$$

where $\bar{I}'_m(\mathbf{S})$ is the \bar{F}_c analogue of (9). Hence, the measurement of intensities rather than structure factors for these odd index reflexions enhances twofold the chances of detecting the presence of vibrational anharmonicity in Bragg scattering at higher temperatures.

'Mosaic' results for Ge at 600 and 800 °C are shown in figure 1 for both odd-index and $(4n+2)$ reflexions. The \bar{B} factors at these temperatures are (using (6) and (4*a*) with θ_M of Ge) 1.65 and 2.02 Å² respectively, and the resultant variations of odd index \bar{I}'_m values with $\sin \theta / \lambda$ are shown by the broken lines in figure 1*a*. The discrete points scattered about these lines are the anharmonic I'_m values which follow our choice of β , and there are considerable departures from the harmonic values. Figure 1*c* displays the resultant $\Delta I'_m$ values, and the general dependence on temperature and $\sin \theta / \lambda$, and the explicit dependence on the index-product hkl , are evident: the overall pattern for these reflexions is similar to that discussed in II for fluorite structures.

The I'_m values of the $(4n+2)$ reflexions are shown in figure 1*b*, and a notable feature is their numerical smallness. Here, there is the problem that the square of a

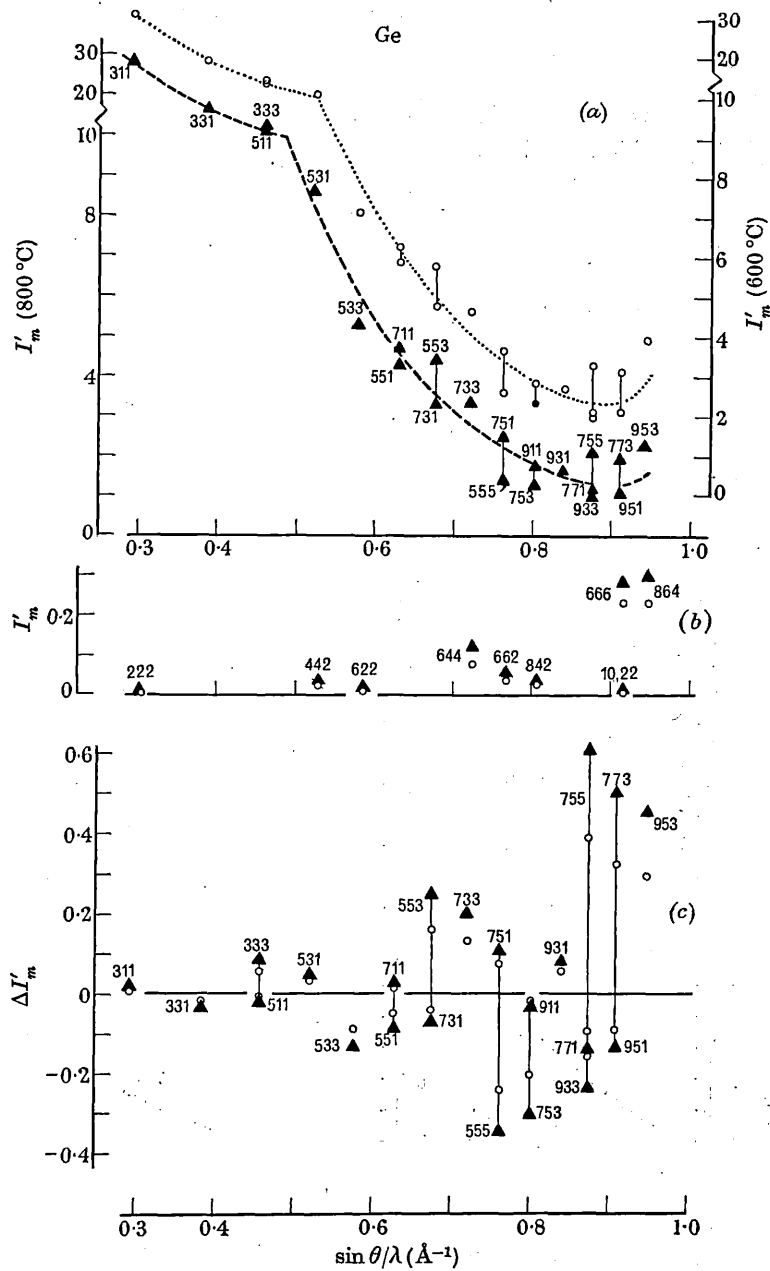


FIGURE 1. I'_m data for Ge at 600 °C (○) and at 800 °C (▲). (a) Comparison of I'_m data with \bar{I}'_m data (broken lines) for isotropic vibration for odd-index reflexions. (b) The I'_m data for the 'forbidden' reflexions. (c) The ratios $\Delta I'_m$ for the various reflexions of (a).

small quantity is a much smaller quantity, and the advantages of mosaic scattering summarized in (11) and (12) no longer apply. The only 'forbidden' which are at all experimentally attractive are the two with large index-products: 666 at $\sin \theta = 0.9151$ and 864 at $\sin \theta = 0.9484$ (for the subsidiary parameters in §2). For these two, the

ratio R_m of their I'_m values to the \bar{I}'_m value of the adjacent (in $\sin \theta/\lambda$) trio of conventional reflexions 755 etc. is approximately 20 and 10% at 800 and 600 °C respectively.

Figure 2 compares results for Si and Ge which follow the common β -assumption. For the high angle trio of odd index reflexions, figure 2c shows how the $\Delta I'_m$ ratios

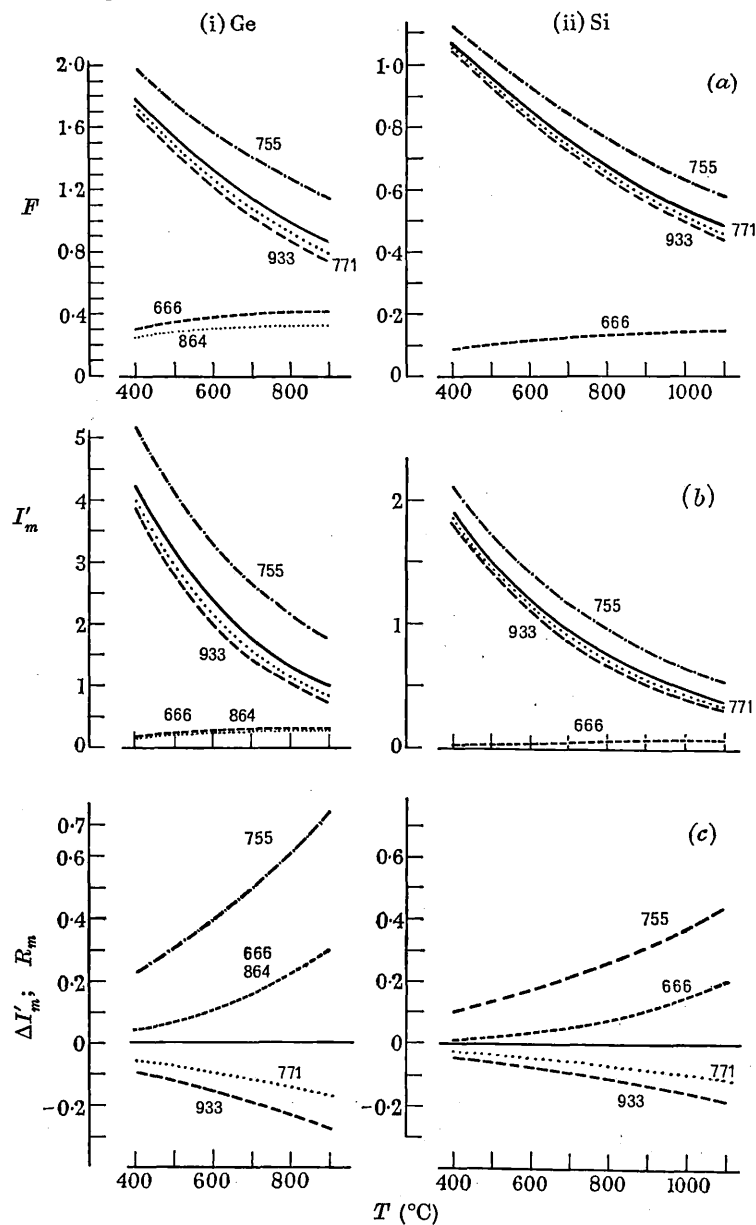


FIGURE 2. The variations with temperature of anharmonic phenomena for high-angle data in (i) Ge, (ii) Si. (a) The upper curves show the deviations of F values for 755, 771 and 933 from the common \bar{F} value (full line). The lower curves show $F(666)$ and $F(864)$ for Ge and $F(666)$ for Si. (b) Corresponding results for I'_m values. (c) The ratios $\Delta I'_m$ for 755, 771 and 933, and the ratios R_m for 666, 864.

are markedly dependent on temperature. The greater splittings shown for Ge are largely a consequence of using there the $|\beta|/\alpha$ ratio of 1.7 \AA^{-1} instead of 1.3 \AA^{-1} as in Si. Using the smaller ratio for Ge (by reducing β to $\beta(\text{Ge}) = 7.5 \times 10^{-12} \text{ erg/\AA}^3$) reduces the features in figure 2c by about one quarter, so the 'fluorite-like' predictions for these reflexions in both structures are quite similar.

For the $(4n+2)$ data of figure 2, their intensities depend only weakly on temperature, but now there is a strong dependence on the value assumed for β . A twofold reduction in this parameter means a fourfold reduction in the I'_m values of these reflexions, so that the results shown for Ge in figures 2b and 2c are halved on using the $\beta(\text{Ge})$ value above. Although this change has the effect of making the present predictions more similar in the two structures, the major point of note is the smallness of the quantities involved. With their strong β dependence, it is clear that experimental resolution of these reflexions in mosaic scattering must be a difficult technical problem. The advantages of using high temperatures lie mainly in the way the temperature-sensitive conventional reflexions are reduced to the point where their intensities are no longer grossly different from the 'forbidden' ones. This is shown by the R_m curves of figure 2c: for Si, $R_m(666)$ varies from 1 to 20% in the range 400–1100°C. With this reflexion, there is the subsidiary problem that $\sin \theta = 0.9906$ for $\lambda = 1.038 \text{ \AA}$, and this region may not be accessible experimentally: this can be overcome by using a shorter wavelength, thereby making 864 for Si also accessible. The general conclusion remains, however: while mosaic scattering, particularly at high temperatures, favours the detection of anharmonicity in the odd index reflexions, success in detecting the most favourable 'forbidden' will depend critically on the β -value responsible for their origin.

(b) *Perfect crystal scattering*

Here, the Bragg intensities are related to the quantities

$$I'_p(\mathbf{S}) = |F(\mathbf{S})| \operatorname{cosec} 2\theta, \quad (13)$$

and the possibilities of measuring vibrational anharmonicity are now rather different.

For the odd index reflexions, we have $\Delta I'_p$ analogues of (12) which are only half as large, since now

$$\Delta I'_p(\mathbf{S}) = \Delta F_a(\mathbf{S})/\bar{F}_c(S). \quad (14)$$

At any temperature, the result of (14) is that the $\Delta I'_p$ estimates are similar to the earlier $\Delta I'_m$ estimates *appropriate to a temperature about 300 to 400 deg. C lower*. From the discussion in (a), the operation of (13) thus demands that such reflexions be studied at as high a temperature as possible.

The advantage of (13) shows itself in the $(4n+2)$ reflexions. Although the intensities of *all* reflexions from a perfect specimen are much smaller than those from the mosaic specimen, we now have a situation where the 'forbidden' reflexions constitute an appreciably larger fraction of the total scattering that can be studied. In contrast to the temperature-variation of the R_m ratio quoted in (a) for 666 in Si, the R_p analogue here varies from 18 to 67%. Again this variation is due primarily to the reduction in the odd index scattering with temperature, but the much

larger proportion of 'forbidden' scattering is a favourable feature to balance against the problems posed by the overall weakness of scattering from a perfect specimen. Moreover, the effects of β -change on the magnitudes of the $(4n+2)$ reflexions are now linear rather than quadratic as in (a). Judged in these terms, the perfect crystal is potentially much more favourable for seeing the 'forbidden' aspects of anharmonic vibration. While keeping in mind the need for a high degree of experimental sensitivity, it is clear that the search for the strongest members, 666 and 864, can now tolerate quite a large departure of β from the value which satisfies the $|\beta|/\alpha$ -data of II.

4. DISCUSSION

It will be interesting to compare these anharmonic predictions with accurate experimental results at elevated temperatures. Preliminary studies of perfect crystal specimens which we have made to date are still inconclusive because of technical difficulties of experimentation which we have encountered. We therefore defer discussion of experimental results until such difficulties have been resolved.

Our purpose here has been to assess anharmonic possibilities in these covalent diamond structures on the basis of the results in II for ionic fluorite structures. To this end, we have used the β -information from II in the manner discussed above, and this involves an extrapolation of the present information to systems of totally different bonding character. We have seen that the α parameters here and in II are numerically similar, so the main concern is whether the β assumptions here are reasonable in the light of other physical evidence for Si and Ge compared with CaF_2 and UO_2 .

One useful qualitative guide on this point is provided by the linear expansion coefficients, χ , of these systems, and we can invoke these in terms of the anharmonic effective one-particle potentials in the following way: the approach is a novel one, but it gives results similar to those provided by standard simple treatments of thermal expansion based on vibration in a diatomic molecule (see Kittel (1960) and Fermi (1966)). In the directions $\langle 111 \rangle$, the T_d symmetry of the $V_j(\mathbf{r})$ (we consider only the anions in the fluorite structures) gives the result

$$V_j(111) = V_{0,j} + \frac{3}{2} \alpha_j x^2 + \beta_j x^3, \quad (15)$$

and we are interested in $\langle x \rangle_j$, the average displacement of the atom, along each axis, from its equilibrium position as a function of temperature. At high temperatures where classical statistical mechanics is valid,

$$\langle x \rangle_j = \int_{-\infty}^{+\infty} x \exp\{-V_j(111)/kT\} dx / \int_{-\infty}^{+\infty} \exp\{-V_j(111)/kT\} dx. \quad (16)$$

For small displacements we then have, approximately,

$$|\langle x \rangle_j| = |\beta_j| kT / 3\alpha_j^2, \quad (16a)$$

and the atoms move preferentially, in the $\langle 111 \rangle$ directions, towards the 'holes' in the fluorite and diamond structures: there are four 'holes' per unit cell in the former, each bounded by eight anions in cubic coordination, and eight per unit cell

in the latter, each of which is surrounded tetrahedrally by adjacent atoms. In both structures, the equilibrium distance ($\sqrt{3}a/4$) between 'hole-centre' and neighbours is thus diminished by $\sqrt{3}|\langle x \rangle_j|$, and, if we interpret this diminution as forcing an equivalent expansion of the unit cell, then the linear expansion coefficient can be written as

$$\chi = 4|\beta_j|k/3\alpha_j^2 a, \quad (17)$$

so that

$$|\beta_j|/\alpha_j = 3a\chi\alpha_j/4k. \quad (17a)$$

Using the χ -data for Si and Ge given by Straumanis & Aka (1952) and the a and α parameters listed earlier, (17a) predicts the average $|\beta|/\alpha$ ratio for these two structures as $1.03(0.05) \text{ \AA}^{-1}$, where the figure in brackets is the departure of the individual ratios from this mean. The approximate nature of (17a) is evident in the fact that the corresponding result for CaF_2 and UO_2 is $2.58(0.34) \text{ \AA}^{-1}$, so we use it only to compare its predictions for the two systems of such different character. The χ -evidence used in the form of (17a) thus suggests a roughly twofold difference in the anharmonic features of the two systems, while (17) shows how the harmonic aspects of (15) are involved in χ . Analogous relations and results arise in the customary (diatomic potential) interpretations of expansion noted above,† and there is no change in the qualitative conclusion that the adoption here of the 'fluorite-like' basis is unlikely to be in error by much more than a factor of two.

Detailed evidence of the actual $|\beta|/\alpha$ ratios in Si and Ge must await experimental studies. The importance of these systems lies in their covalent character, and their examination will provide a valuable complement to the anharmonic information available in II.

REFERENCES

- Bacon, G. E. 1962 *Neutron diffraction*. Oxford University Press.
 Batterman, B. W. & Chipman, D. R. 1962 *Phys. Rev.* **127**, 690.
 Dawson, B. 1967a *Proc. Roy. Soc. A*, **298**, 255.
 Dawson, B. 1967b *Proc. Roy. Soc. A*, **298**, 264. (Paper I.)
 Dawson, B., Hurley, A. C. & Maslen, V. W. 1967 *Proc. Roy. Soc. A*, **298**, 289. (Paper II.)
 Debye, P. 1914 *Ann. Physik* **43**, 49.
 Fermi, E. 1966 *Molecules, crystals, and quantum statistics*. New York: Benjamin.
 James, R. W. 1948 *The optical principles of the diffraction of X-rays*. London: Bell.
 Kittel, C. 1960 *Introduction to solid state physics*, 2nd ed. New York: Wiley.
 Paskin, A. 1957 *Acta crystallogr.* **10**, 667.
 Straumanis, M. E. & Aka, E. Z. 1952 *J. Appl. Phys.* **23**, 330.
 Swanson, H. E. & Fuyat, R. K. 1953 *N.B.S. Circ.* no. 539, **2**, 6.
 Swanson, H. E. & Tatge, E. 1953 *N.B.S. Circ.* no. 539, **1**, 18.
 Willis, B. T. M. 1963a *Proc. Roy. Soc. A* **274**, 122.
 Willis, B. T. M. 1963b *Proc. Roy. Soc. A* **274**, 134.

† Although the present approach to thermal expansion of cubic structures appears inapplicable when all atoms have $V_j(\mathbf{r})$ of O_h rather than T_d symmetry, this is not so. Then, however, it does imply that the anharmonic $V_j(\mathbf{r})$ must be anisotropic, but this is quite consistent with O_h symmetry.

PRINTED IN GREAT BRITAIN AT THE UNIVERSITY PRINTING HOUSE, CAMBRIDGE

UNCLASSIFIED



United Kingdom Atomic Energy Authority

RESEARCH GROUP

Report

SOLUTION OF THE PHASE PROBLEM
IN NEUTRON DIFFRACTION
BY THE ANOMALOUS DISPERSION METHOD

D. H. DALE B. T. M. WILLIS

Metallurgy Division,
Atomic Energy Research Establishment,
Harwell, Berkshire.

1966

© - UNITED KINGDOM ATOMIC ENERGY AUTHORITY - 1966

Enquiries about copyright and reproduction should be addressed to the
Scientific Administration Office, Atomic Energy Research Establishment,
Harwell, Didcot, Berkshire, England.

U.D.C.
548.78

SOLUTION OF THE PHASE PROBLEM IN NEUTRON
DIFFRACTION BY THE ANOMALOUS DISPERSION METHOD

by

D.H. Dale and B.T.M. Willis

ABSTRACT

The anomalous dispersion method (well established in X-ray work for determining the phases of X-ray reflexions) can be used to solve the phase problem in neutron diffraction. Relatively few isotopes have resonances close to the thermal neutron region (wavelength $\sim 1\text{\AA}$), but of these Cd^{113} and Sm^{149} show a pronounced dispersion effect, much stronger than the dispersion effect in X-ray diffraction. Measurements at two different wavelengths, preferably on different sides of the resonance, can be used to resolve the phase ambiguity associated with the anomalous dispersion method. The size of the unit cell of a non-centro symmetrical structure which can be solved by the neutron method lies within a range limited on the lower side by absorption and on the upper side by the observable intensity difference of the hkl , \overline{hkl} pairs of reflexions. The range is about 600 - 3,000 atoms per unit cell (P1 symmetry) for a 50% deuterated crystal containing one Cd^{113} atom per cell, and is above 3,000 atoms per cell for a 50% deuterated crystal containing one Sm^{149} atom per cell. For undeuterated crystals the range is narrower and the counting statistics less favourable. The solution of the crystal structure of rhombohedral insulin, of molecular weight equal to 6,000 and containing 2 or 4 Cd^{113} atoms and 6 molecules per unit cell, using the neutron anomalous dispersion method is a definite possibility.

Metallurgy Division,
U.K.A.E.A. Research Group,
Atomic Energy Research Establishment,
HARWELL.

April 1966

CONTENTS

	<u>Page No.</u>
1. Introduction	1
2. Phase determination in X-ray diffraction by the anomalous dispersion method	1
3. Anomalous scattering of neutrons	3
4. Phase determination by neutron anomalous dispersion	5
5. Anomalous dispersion method using Cd ¹¹³ at $\lambda = 1.0\text{\AA}$	6
(a) $\Delta I/I$, and upper limit on cell size	
(b) Absorption, and lower limit on cell size	7
(c) Statistics of counting. Time to measure $\Delta I/I$ for each reflexion	9
6. Anomalous dispersion method using Sm ¹⁴⁹ at $\lambda = 0.02\text{\AA}$ (resonance)	10
(a) $\Delta I/I$, and upper limit on cell size	
(b) Absorption, and lower limit on cell size	
(c) Statistics of counting. Time to measure $\Delta I/I$ for each reflexion	11
(d) Resolution of phase ambiguity using $\lambda = 0.92\text{\AA}$ and 1.12\AA	
Acknowledgements	12
References	

TABLES

Table

I Resonance wavelengths and $\Delta b''$ values for various elements	4
II Atomic absorption cross sections (at 1\AA)	8

ILLUSTRATIONS

Fig.

1. Wavelength dispersion of $\Delta f'$ and $\Delta f''$ for X-rays near a K absorption edge. λ is the incident wavelength and λ_K the wavelength of the K edge.

ILLUSTRATIONS (Contd)

Fig.

2. Amplitude-phase diagram for hkl and \overline{hkl} reflexions. F_R is the structure amplitude for the R atoms alone and F_A the amplitude for the anomalously scattering atom A. F_A has a real part F_A' , and an imaginary part F_A'' . \overline{F} denotes the F value for the inverse reflexion \overline{hkl} .
3. Harker diagram showing derivation of two possible phase angles for hkl and \overline{hkl} reflexions. The two phase angles for hkl are marked α_1 and α_2 .
4. Determination of mean phase angle α of hkl and \overline{hkl} .
5. Dispersion curves for Cd^{113} .
6. Dispersion curves for Sm^{149} .
7. Harker diagram for neutron wavelengths λ_0 (at resonance), λ_1 and λ_2 . λ_1 and λ_2 are the turning points of the anomalous dispersion curve for $\Delta b'$. All six circles (of radii determined by the experimental intensities) pass through the same point O, allowing an unambiguous determination of the phase of F.
8. Resolution of phase ambiguity in worst possible case. The two circles for $\lambda = \lambda_0$ intersect in O and O', and the two circles for $\lambda = \lambda_2$ in O and O''.

1. Introduction

A major limitation of neutron diffraction as applied to the determination of crystal structures is the difficulty of determining the phases of the neutron reflexions. Nearly all the neutron studies reported so far have been restricted to crystals for which the main features of the structure were already known from X-ray work. After application of approximate phases, calculated from the X-ray structure, refinement of the neutron structure, including the location of light atoms such as hydrogen, would follow.

In this report we show that the anomalous dispersion method could be used, in certain cases, to determine the phases of the neutron reflexions ab initio, without having recourse to the results of a prior X-ray structure determination.

The theory of the anomalous dispersion method is described in the first part of this paper, and in the second part the theory is applied to the solution of hypothetical structures containing either Cd¹¹³ or Sm¹⁴⁹ as anomalous scatterers of slow neutrons.

2. Phase determination in X-ray diffraction by the anomalous dispersion method

Ramaseshan⁽¹⁾ has reviewed the use of anomalous dispersion in X-ray diffraction. We shall describe here the principle of the anomalous dispersion method for determining the phase angles of the X-ray reflexions from non-centrosymmetric crystals.

The atomic scattering factor for X-radiation close to an absorption edge of the scattering atom can be expressed as

$$f = f_0 + \Delta f' + i\Delta f'', \quad \dots(1)$$

where f_0 is the normal scattering factor for wavelengths very far from the absorption edge, and $\Delta f'$ and $\Delta f''$ are the real and imaginary dispersion correction terms arising from dispersion effects. The variation of $\Delta f'$ and $\Delta f''$ with wavelength λ is shown in figure 1; the precise form of these curves varies with the wavelength λ_K of the absorption edge and with the nature of the scattering atom, but the figure is roughly correct for any K

absorption edge. Thus $\Delta f'$, the real dispersion component, is negative for $\lambda > \lambda_K$ and is either negative or only slightly positive for $\lambda < \lambda_K$. The imaginary component, $\Delta f''$, is phased 90° ahead of the real part of $f (= f_0 + \Delta f')$ and is positive for $\lambda < \lambda_K$ and zero for $\lambda > \lambda_K$. Near an absorption edge ($\lambda = \lambda_K$) the magnitudes of $\Delta f'$ and $\Delta f''$ are about equal, each contributing approximately twenty per cent to the magnitude of the total scattering factor f . We shall see later that, although neutron anomalous scattering can be expressed by an equation of the same form as equation (1), the relative magnitudes of the anomalous dispersion coefficients are usually much larger for neutron scattering close to resonance.

Let us suppose that the asymmetric unit of a crystal contains one anomalous scatterer, atom A, and the remaining atoms, R, scatter the radiation normally. If A and R are arranged acentrically in the unit cell the structure amplitude-phase diagram for the hkl reflection, and for its inverse \overline{hkl} , is as represented in figure 2. The contribution of A alone to \tilde{F}_{hkl} is $\tilde{F}_A = \tilde{F}'_A + \tilde{F}''_A$ where \tilde{F}'_A and \tilde{F}''_A are the real and imaginary parts of \tilde{F}_A . Since \tilde{F}''_A is phased 90° ahead of \tilde{F}'_A the intensities of hkl and \overline{hkl} , proportional to $|\tilde{F}_{hkl}|^2$ and $|\tilde{F}_{\overline{hkl}}|^2$, are not equal (Bijvoet effect). Provided the position of the single atom A is known, the phase of hkl (and \overline{hkl}) can be determined by measuring the quantities $|\tilde{F}_{hkl}|^2$ and $|\tilde{F}_{\overline{hkl}}|^2$ experimentally. The principle of this phase determination is best illustrated by constructing the so-called Harker diagram.

The basic equation to be solved is the vector relationship

$$\tilde{F}_{hkl} - \tilde{F}_{\overline{hkl}} = 2\tilde{F}''_A$$

where \tilde{F}''_A and the magnitudes but not phases of \tilde{F}_{hkl} and $\tilde{F}_{\overline{hkl}}$ are known. Two circles are drawn (figure 3), one with radius \tilde{F}_{hkl} and with the end-point of the vector $2\tilde{F}''_A$ as centre, and the other with radius $\tilde{F}_{\overline{hkl}}$ and with the starting-point of $2\tilde{F}''_A$ as centre. The points of intersection of these two circles define two possible phases for hkl (and \overline{hkl}), and one of the two phases is the correct one. Ramaseshan⁽¹⁾ has discussed possible ways of resolving this ambiguity: one way is to make a third intensity measurement with the anomalously scattering atom replaced by a normal atom.

We can derive an analytical expression for the phase angle of hkl using figure 4, which is equivalent to figure 2 with the lower half reflected across the Ox axis. Let θ be the angle between the vectors \vec{OP} and \vec{F}_A'' . Then

$$|F_{hkl}|^2 = OP^2 + |F_A''|^2 + 2OP \cdot |F_A''| \cos \theta$$

and ...(2)

$$|\overline{F_{hkl}}|^2 = OP^2 + |F_A''|^2 - 2OP \cdot |F_A''| \cos \theta,$$

so that

$$\cos \theta = \frac{|F_{hkl}|^2 - |\overline{F_{hkl}}|^2}{4 OP F_A''} = \frac{\Delta F^2}{4F' F_A''} \quad \dots(3)$$

The numerator is equal to the difference in the absolute intensities of the hkl and \overline{hkl} reflexions, after correcting for the Lorentz-polarisation factor. F' is the real part of the structure amplitude, represented by \vec{OP} .

Where anomalous scatterers are centrosymmetrically related the two possible values of the phase angle are given by

$$\alpha_{1,2} = \alpha_A + 90^\circ \pm \theta, \quad \dots(4)$$

the alternative signs of θ arising from the cosine form of θ in equation (3). If the position of the anomalous scatterer A in the unit cell is known, α_A can be calculated and the phase determined from (3) and (4).

3. Anomalous scattering of neutrons

X-ray anomalous scattering is electronic in origin, whereas the anomalous scattering of neutrons involves nuclear interactions. The single-level Breit-Wigner dispersion relation⁽²⁾ gives the nuclear scattering amplitude in the form

$$b = b_0 + \Delta b' + i\Delta b''.$$

The term b_0 is independent of the energy E of the incoming neutron and represents potential or hard-sphere scattering. The remaining terms $\Delta b'$,

$\Delta b''$ are the dispersion terms, whose variation with energy is very small except in the neighbourhood of a resonance (i.e. near $E = E_0$, where E_0 is the resonance energy, or the neutron energy required to excite a single level of the compound nucleus). The only elements of interest are those with resonances near the thermal energy region and are listed in Table I (after Peterson & Smith⁽²⁾). Of these elements, cadmium and samarium only will be discussed below, as experimental data relating the variation of $\Delta b'$ and $\Delta b''$ with wavelength are lacking for europium and gadolinium.

The dispersion curves for Cd^{113} and Sm^{149} are shown in figures 5 and 6. $\Delta b'$, the real component, is greatest at $\lambda_{19}\lambda_2$ and it is positive on the low wavelength side of resonance, goes through zero at resonance and is negative at high wavelengths. The imaginary component $\Delta b''$ is always positive and is greatest at resonance.

Table I

Resonance wavelengths and $\Delta b''$ values for various elements

element	wavelength at resonance	$\Delta b''$ at resonance
natural Cd ₁₁₃ Cd	0.68 Å	0.58 x 10 ⁻¹² cm. 4.70
natural Sm ₁₄₉ Sm	0.92	0.88 6.30
natural Eu ₁₅₁ Eu	~0.6	1.31 2.74
natural Gd ₁₅₇ Gd	~1.8	1.26 6.60

There are a number of important differences between the X-ray dispersion curves, figure 1, and the neutron dispersion curves, figure 5 and 6. Whereas with X-rays, the ratios $\Delta f'/f_0$ and $\Delta f''/f_0$ never exceed -0.20 and 0.32 at $\sin \theta/\lambda = 0$ (although the contribution of anomalous scattering gradually increases as a function of θ), the ratios $\Delta b'/b_0$ and $\Delta b''/b_0$ for neutrons can be at least twenty times greater. For example Cd^{113} shows values of $\Delta b'/b_0$ equal to 2.8 at $\lambda = 0.55$ Å and -3.3 at 0.80 Å, and $\Delta b''/b_0$ is 7.6 at resonance ($\lambda = 0.68$ Å). The much larger anomalous scattering effect with neutrons leads to the possibility of determining

crystal structures of large molecules by the neutron anomalous dispersion method. This particular fact was first pointed out by one of us⁽³⁾ in 1964 although Peterson and Smith⁽²⁾ made it clear that anomalous neutron scattering effects could readily be applied to solving problems of structure and of absolute configuration.

Note that $\Delta b'/b_0$ can be both strongly negative and positive with neutrons, but not with X-rays. This characteristic of neutrons is important in resolving the phase ambiguity in equation (4).

4. Phase determination by neutron anomalous dispersion

Exactly the same theory as that described in section 2 applies to phase determination by neutron anomalous dispersion. It is only necessary to replace the X-ray scattering factors f by the neutron scattering amplitudes b .

The Harker diagram corresponding to figure 3 is drawn in figure 7 for the three neutron wavelengths $\lambda = \lambda_0, \lambda_1$ and λ_2 . λ_0 is the resonance wavelength and λ_1, λ_2 are the maximum and minimum positions of the real part of the dispersion curve. The proportional change $\Delta I/I$ in the intensities of hkl and \overline{hkl} is usually greatest for $\lambda = \lambda_0$, but the resolution of the phase ambiguity is accomplished most readily by working at the two wavelengths λ_1, λ_2 on either side of resonance. All six circles in figure 7, corresponding to the measured values of $|F_{hkl}|$ and $|F_{\overline{hkl}}|$ at the three different wavelengths, pass through the single point 0; clearly, only three circles are required to locate 0 and to resolve the phase ambiguity.

We have assumed, of course, that the position of the anomalous scattering atom A in the unit cell is known. This point is discussed very clearly by Ramaseshan⁽⁴⁾, who describes two methods for locating A. In the first method, a wavelength is used for which the real part of the scattering factor of A is five to ten times the scattering factor of the remaining atoms. A is then effectively a 'heavy' atom and it can be readily located by a Patterson synthesis. The second method requires the combination of intensity measurements on either side of the resonance wavelength.

5. Anomalous dispersion method using Cd¹¹³ at $\lambda = 1.0 \text{ \AA}$

With conventional neutron diffraction apparatus, using a crystal-monochromatized beam, the useful wavelength range is 0.75 to 1.8 \AA . The range can be extended below 0.75 \AA by using a hot source of neutrons, and the upper limit of 1.8 \AA can be extended with mechanical velocity selectors (which eliminate higher-order contamination of the monochromatic beam).

The range 0.75 - 1.8 \AA considered in this report lies outside the resonance wavelength of Cd¹¹³ but includes the resonance wavelength of Sm¹⁴⁹.

Unfortunately, the ideal situation depicted in figure 7, in which $\Delta I/I$ is measured at all three wavelengths $\lambda = \lambda_0, \lambda_1$ and λ_2 , applies only in the case of Sm¹⁴⁹.

(a) $\Delta I/I$, and upper limit on cell size

At 1.0 \AA the anomalous scattering amplitudes are

$$\Delta b' = -1.9 \times 10^{-2} \text{ cm.}$$

and $\Delta b'' = 1.2 \times 10^{-2} \text{ cm.,}$

giving the ratios ($b_0 = 0.62 \times 10^{12} \text{ cm}$) :

$$\frac{\Delta b'}{b_0} = -3.1, \quad \frac{\Delta b''}{b_0} = 1.9 \quad \dots(5)$$

Suppose we have a unit cell containing one anomalously scattering atom (A) and N normal atoms. The symmetry of the cell is P1. We shall attempt to answer the question: what value of N corresponds to an average $\Delta I/I$ value of 10 per cent? 10 per cent is chosen as the minimum value of $\Delta I/I$ which can be measured conveniently: this criterion sets an upper limit on the value of N.

From equation (3) $|F_{hkl}|^2 - |\overline{F_{hkl}}|^2$ lies between zero and $4 |F'_{hkl}| F_A''$, dependent on the value of θ . The average value of $|F_{hkl}|^2 - |\overline{F_{hkl}}|^2$ is $\frac{8}{\pi} |F'_{hkl}| F_A''$, or

$$\frac{|F_{hkl}|^2 - |\overline{F_{hkl}}|^2}{|F'_{hkl}|^2} = \frac{8}{\pi} \frac{F_A''}{|F'_{hkl}|} \quad \dots(6)$$

The left-hand side of (6) is effectively $\Delta I/I$, and putting $\Delta I/I = \frac{1}{10}$ gives

$$\frac{F_A''}{|F_{hkl}'|} = \frac{1}{25.5} \quad \dots(7)$$

Now the mean value of $|F_{hkl}'|$ for N randomly distributed atoms ($N \gg 1$) of scattering amplitude b_o' is $\sqrt{N} b_o'$. b_o' is equal to 0.38, 0.66 and 0.58×10^{-12} cm. for hydrogen, carbon, oxygen respectively; we will assume an average b_o' value of 0.55. Substituting in equation (7):

$$\frac{F_A''}{0.55 \sqrt{N}} = \frac{1}{25.5}$$

But $\Delta b'' = 1.2$ at 1.0 \AA (F_A'')

hence $\sqrt{N} = 56$

or $N_{\text{max}} = 3,000$ atoms.

We can check that the reasoning above is approximately correct by referring to the work of Dale and Peterson⁽⁵⁾ on the determination of the structure of cadmium bromate dihydrate by the anomalous neutron scattering method. $\Delta b''$ for cadmium at 1.44 \AA , the wavelength used in the experiment, is 0.083×10^{-12} cm. The molecule contains one cadmium atom, two bromines, eight oxygens and four hydrogens. Thus $N = 15$, the average value of b_o' is 0.53×10^{-12} cm., and

$$F' \text{ average} = \sqrt{15} \times 0.53 \times 10^{-12}$$

Substituting in equation (6):

$$\frac{\Delta I}{I} = \frac{8}{\pi} \cdot \frac{\Delta b''}{F'} = \frac{8 \times 0.083}{\pi \times \sqrt{15} \times 0.53} = 0.104.$$

This estimated value of 10.4% compares very well with the experimentally determined value. For example, of the 54 strongest intensities observed in the $[2k1]$ zone (orthorhombic cell, $P2_12_12_1$) 28 show a $\Delta I/I$ ratio greater than and 26 less than 10.4%.

(b) Absorption, and lower limit on cell size

The resonance scattering process is accompanied by resonance absorption

and this absorption sets a lower limit on cell size (i.e. an upper limit on the density of anomalous scattering centres). The incident beam flux is very low in neutron diffraction and the linear absorption coefficient μ must not be so high that absorption appreciably reduces the overall scattering amplitude of the hkl reflexion. Using a spherical crystal of radius R, and assuming a maximum permissible intensity reduction of two-fold by absorption, we have

$$\mu R \approx 0.5 \quad \text{or} \quad \mu = 5 \text{ cm.}^{-1} \quad \dots(8)$$

for a crystal of 1 mm. radius.

Table II lists the atomic absorption cross-sections for a crystal containing one atom of Cd¹¹³, $\frac{1}{2}$ N hydrogen and $\frac{1}{2}$ N non-hydrogen atoms. The net value of μ is equal to $\sum N_o \sigma$ summed over all the atoms, where N_o is the number of each kind of atom 1 cc.

Thus from Table II

$$\mu = \frac{1}{N} \times 2.3 \times 10^3 + 2.1 \quad \dots(9)$$

and equating this to 5 cm.⁻¹ from equation (8) gives

$$\frac{1}{N} \times 2.3 \times 10^3 = 2.9, \quad \text{or} \quad \underline{N_{\min} = 800 \text{ atoms.}}$$

Table II

Atomic absorption cross sections (at 1Å)

atom	absorption cross-section, σ	number of atoms/cc., N_o	$N_o \sigma$
Cd ¹¹³	$2.3 \times 10^{-20} \text{ cm.}^2$	$\frac{1}{N} \times 10^{23} \text{ cm.}^{-3*}$	$\frac{1}{N} \times 2.3 \times 10^3 \text{ cm.}^{-1}$
hydrogen	40×10^{-24}	5.10^{22}	2.0
(deuterium)	6×10^{-24}		
non-hydrogen (carbon, oxygen, nitrogen...)	$\approx 2 \times 10^{-24}$	5.10^{22}	0.1

*We assume approximately 10^{23} atoms of all kinds per cc.

If half the hydrogen in the crystal is replaced by deuterium, the absorption cross-section for hydrogen drops from 40 barns/atom to 23 barns/atom and the second term of equation (9) is reduced to 1.25. In this case the minimum value of N is about 600 atoms.

The conclusion from sections 5 (a) and 5(b) is that for a 1 mm. radius crystal the optimum value of N is around 1,500 atoms: higher values of N give $\Delta I/I$ values which are very difficult to observe, and lower values of N give I values which are reduced too much by absorption.

(c) Statistics of counting. Time to measure $\Delta I/I$ for each reflexion

The statistics of counting is much more favourable if the crystal is deuterated. 'Absorption' of the beam by hydrogen is not true absorption, i.e. neutron capture by an n- γ process: the 'absorption' arises from isotropic incoherent scattering. Each Bragg reflexion is observed on a background of this incoherent scattering, which will be much larger than the coherent Bragg scattering for large molecules. Thus the average signal-to-background ratio for reflexions from a vitamin B₁₂ monoacid crystal⁽⁶⁾, observed at a flux of 2.7×10^6 neutrons cm.⁻² sec.⁻¹ in the θ range 0-30° was 1.4:1; the background count (incoherent scattering) was 400 counts per minute and the average coherent intensity was 150 counts per minute. Now for this crystal $N \sim 400$, and if N is increased from 200 to 2,000 the background count rate for the same size of crystal remains 400 c.p.m. whereas the coherent count rate is $\frac{1}{5} \times 150 = 30$ c.p.m. With such poor signal-to-noise ratios the statistics of counting is extremely unfavourable: hence the need to deuterate the sample, if at all possible.

To estimate the time to measure $\Delta I/I$ we shall assume a fifty per cent deuterated sample with a background count rate of 200 c.p.m. We require to measure $\Delta I/I$ values of around 10 per cent, and so the counting statistics must be good enough to give I accurate to better than 10 per cent - say, five per cent.

In order to resolve adjacent Bragg reflexions, it is necessary to tighten the collimation of the neutron beam as the value of N rises. If the longest cell edge is doubled between $N = 400$ (vitamin B₁₂) and $N = 2000$ the collimation angle must be reduced accordingly. This will cause a drop

of about 2 in the neutron flux but is partly compensated for by improved resolution of the peaks. We can say, therefore, that I is about 20 c.p.m. for a molecule examined under the same conditions (regarding resolution and primary neutron intensity) as in the case of vitamin B₁₂. A total of 4,000 counts must be accumulated on the peak to obtain a statistical uncertainty not exceeding 5%. The total counting time required per reflexion is 4000/20 minutes or about 3½ hours. This counting time is fairly reasonable, and in fact is about six times that adopted in the B₁₂ work. This assumes that peak count rates, and not integrated intensities, are used to determine ΔI/I.

6. Anomalous dispersion method using Sm¹⁴⁹ at λ = 0.92 Å (resonance)

The situation here is more favourable than for Cd¹¹³, as we can measure ΔI/I close to resonance. We sketch below the results of calculations of the same type as those given in section 5, and also discuss the possibility of resolving the phase ambiguity by measuring ΔI/I at two wavelengths, λ = λ₀ (0.92 Å) and λ = λ₂ (1.12 Å).

(a) ΔI/I, and upper limit on cell size

For N randomly distributed atoms (hydrogen, carbon ...) the mean value of F'_{hkl} is $\sqrt{N} \times 0.55 \times 10^{-12}$ cm., and so

$$\frac{\Delta I}{I} = \frac{8}{\pi} \cdot \frac{\Delta b''}{F'_{hkl}} = \frac{8}{\pi} \times \frac{6.6}{\sqrt{N} \times 0.55} \quad \dots(10)$$

Choosing ΔI/I = 10%, as before, equation (10) gives

$$\underline{N_{\max} = 90,000 \text{ atoms.}}$$

Thus the anomalous dispersion effect is so strong that there is virtually no upper limit to the size of cell which can be examined. For a cell containing 4,000 atoms the expected average value of ΔI/I is 50%.

(b) Absorption, and lower limit on cell size

The atomic absorption cross-section of Sm¹⁴⁹ at resonance is 11.4 x 10⁻²⁰ cm². This gives (of equation (9))

$$\mu = \frac{1}{N} \times 11.4 \times 10^3 + 2.1$$

and $\underline{N_{\min} = 4,000}$ for an undeuterated sample.

For N less than this, the reduction in intensity by absorption is greater than two-fold and is unacceptable. If the sample is half deuterated N_{\min} falls to 3,000 atoms.

We conclude from sections 6 (a) and 6 (b) that the permissible range of N is roughly 3,000-90,000 atoms. The abundance of the resonant isotope Sm^{149} is 14%, and we would expect to lower the value of N_{\min} in the same proportion by using natural samarium.

(c) Statistics of counting. Time to measure $\Delta I/I$ for each reflexion

The situation is more favourable than for Cd^{113} , because the anomalous dispersion effect is stronger. Thus for a 50% deuterated crystal containing 2,000 atoms per unit cell, plus one atom of Cd^{113} , a counting time on the peak of $3\frac{1}{2}$ hours per reflexion is necessary to measure I to an uncertainty not exceeding 5%. For the same crystal, containing Sm^{149} rather than Cd^{113} , $\Delta I/I$ is considerably larger, and so I need only be measured to much lower precision.

(d) Resolution of phase ambiguity using $\lambda = 0.92 \text{ \AA}$ and 1.12 \AA

This can be done by combining measurements of $\Delta I/I$ at two different wavelengths, $\lambda = \lambda_0$ and $\lambda = \lambda_2$. The amplitude-phase (Harker) diagram is drawn in figure 8 for the worst possible case, where the ambiguity in phase is such that there is a maximum difference of 180° between the two possible phase solutions. To resolve the ambiguity the ratio PQ/OP should not exceed the uncertainty in determining the radii of the various circles. Thus for a 5% uncertainty in measuring I , or a 2.5% uncertainty in F ,

$$\frac{PQ}{OP} < 0.025 \quad \dots(11)$$

With $\text{Sm}^{149} \Delta b' = 0$ for $\lambda = \lambda_0$ and -3.3×10^{-12} cm. for $\lambda = \lambda_2$, so that PQ is 3.3×10^{-12} cm. The magnitude of OP is $\sqrt{N} \times 0.55 \times 10^{-12}$ cm. Substituting in (11):

$$\frac{3.3}{\sqrt{N} \times 0.55} < 0.025$$

or $N_{\max} \sim 50,000$ atoms.

If the precision in measuring I is lowered from 5% to 15%, N_{\max} is still as high as 2,800 atoms. It would appear, therefore, that the resolution of the phase ambiguity by the two-wavelength method is quite feasible.

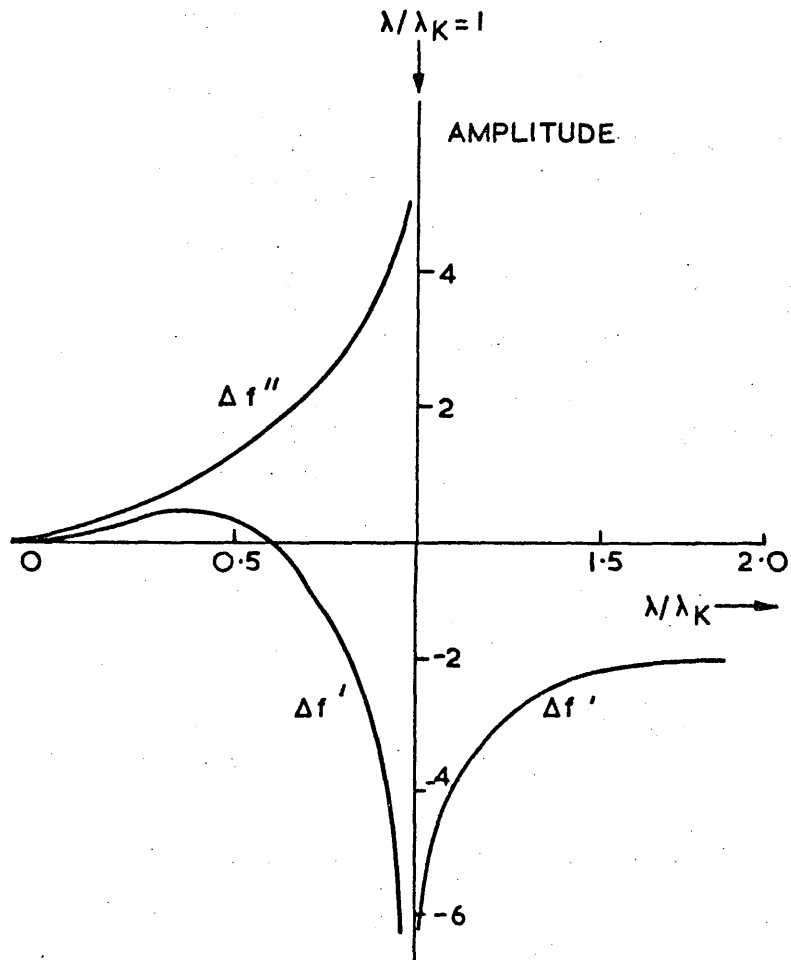
Acknowledgements

The authors have profitted from many discussions with colleagues at Harwell, Oxford University and elsewhere: they are especially grateful to Professors D.C. Hodgkin, S. Ramaseshan and S.W. Peterson, Dr. K. Venkatesan and Mr. F.H. Moore. One of us (D.D.) is indebted to the Australian Institute of Nuclear Science and Engineering for a Fellowship held during the early part of the work.

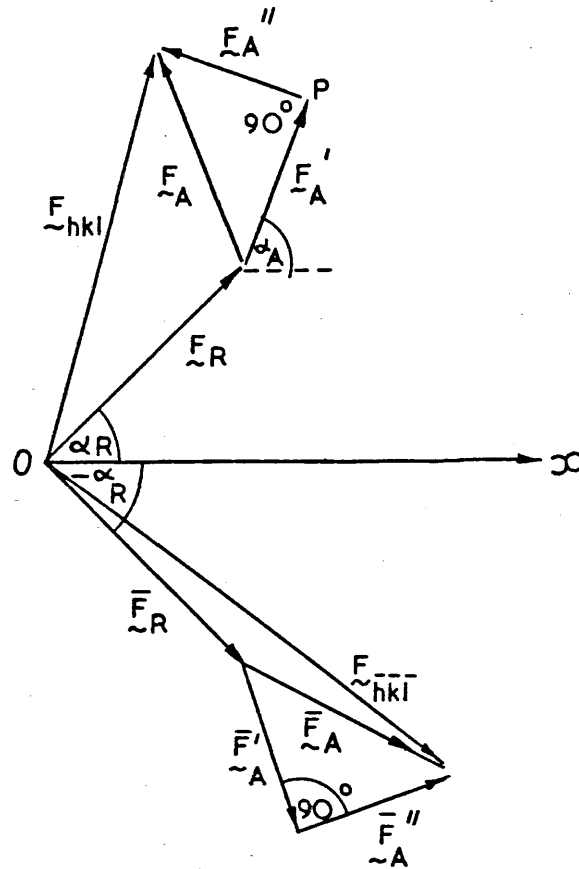
References

- (1) RAMASESHAN, S. (1964). In "Advanced Methods of Crystallography": Academic Press, p. 67.
- (2) PETERSON, S.W. and SMITH, H.G. (1962). Jour. Phys. Soc. Japan, 17, Supplement BII, p. 335.
- (3) DALE, D.H. (1964). Australian Institute of Nuclear Science and Engineering Annual Report. (A.I.N.S.E., P.O. Sutherland, N.S.W., Australia).
- (4) RAMASESHAN, S. (1966). Current Science, 35, p. 87.
- (5) DALE, D.H. and PETERSON, S.W. (Private communication).
- (6) MOORE, F.H. (Private communication).

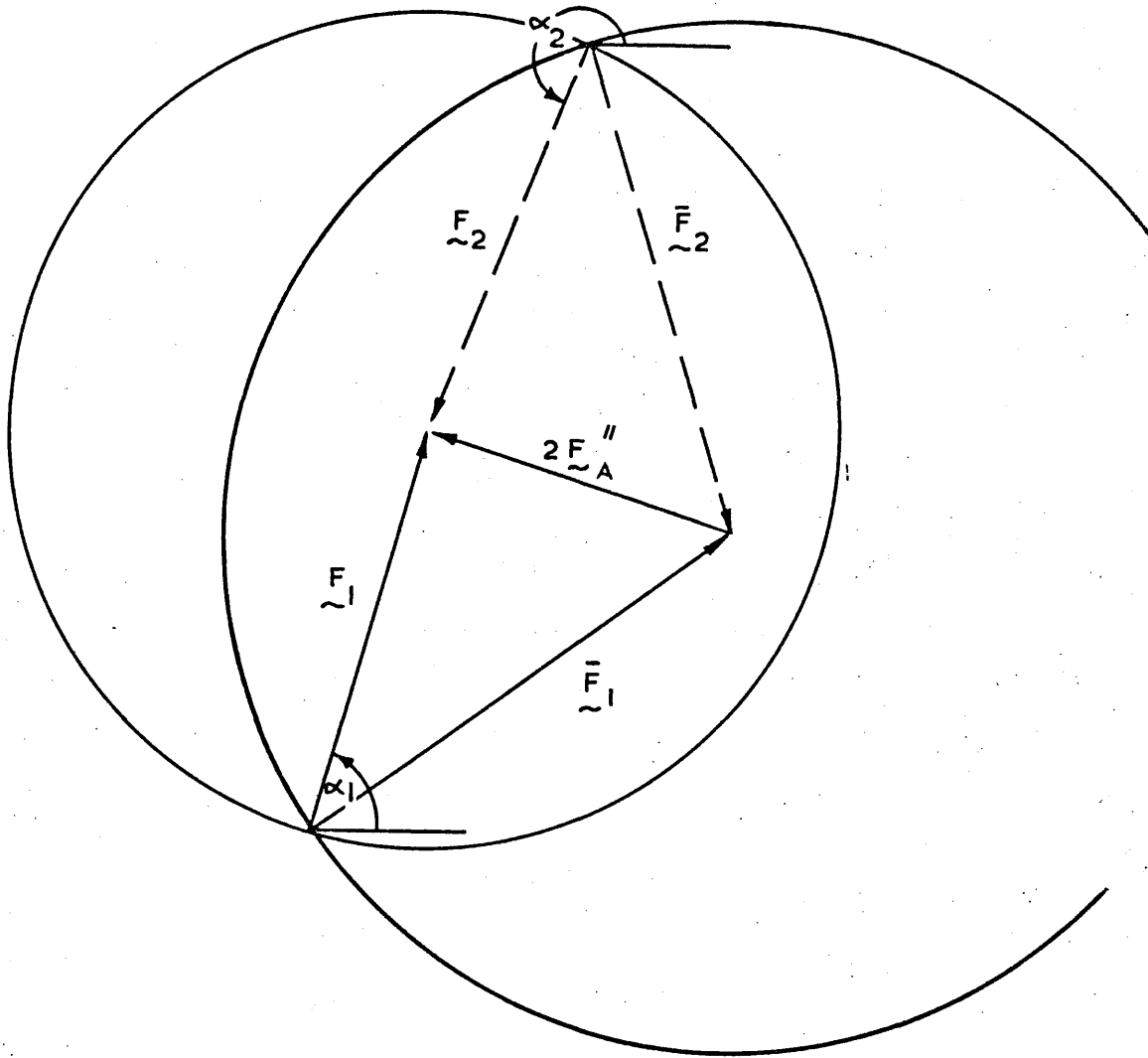
No standard distribution except to Authority
Libraries



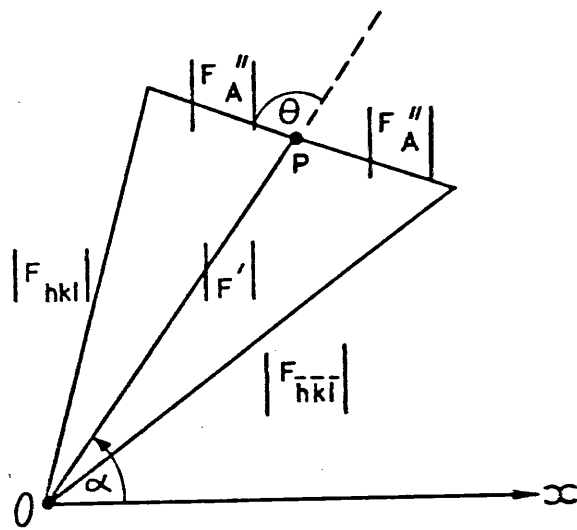
A.E.R.E R 5195 FIG 1. WAVELENGTH DISPERSION OF $\Delta f'$ AND $\Delta f''$ FOR X-RAYS NEAR A K ABSORPTION EDGE. λ IS THE INCIDENT WAVELENGTH AND λ_K THE WAVELENGTH OF THE K EDGE.



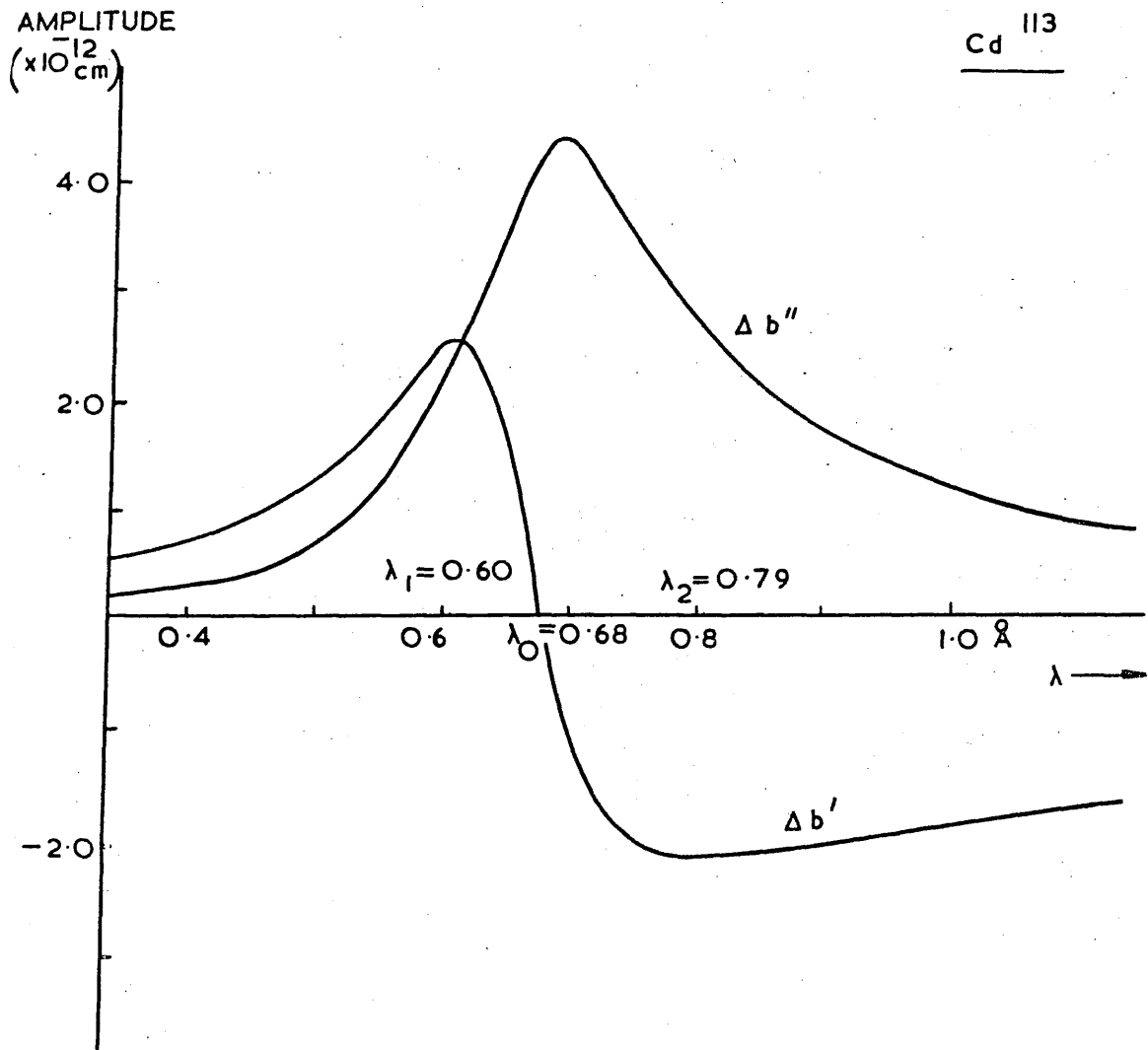
A.E.R.E. R 5195 FIG. 2 AMPLITUDE-PHASE DIAGRAM FOR hkl AND $\bar{h}\bar{k}\bar{l}$ REFLEXIONS. F_R IS THE STRUCTURE AMPLITUDE FOR THE R ATOMS ALONE AND F_A THE AMPLITUDE FOR THE ANOMALOUSLY SCATTERING ATOM A. F_A HAS A REAL PART F_A' AND AN IMAGINARY PART F_A'' . \bar{F} DENOTES THE F VALUE FOR THE INVERSE $\bar{h}\bar{k}\bar{l}$.



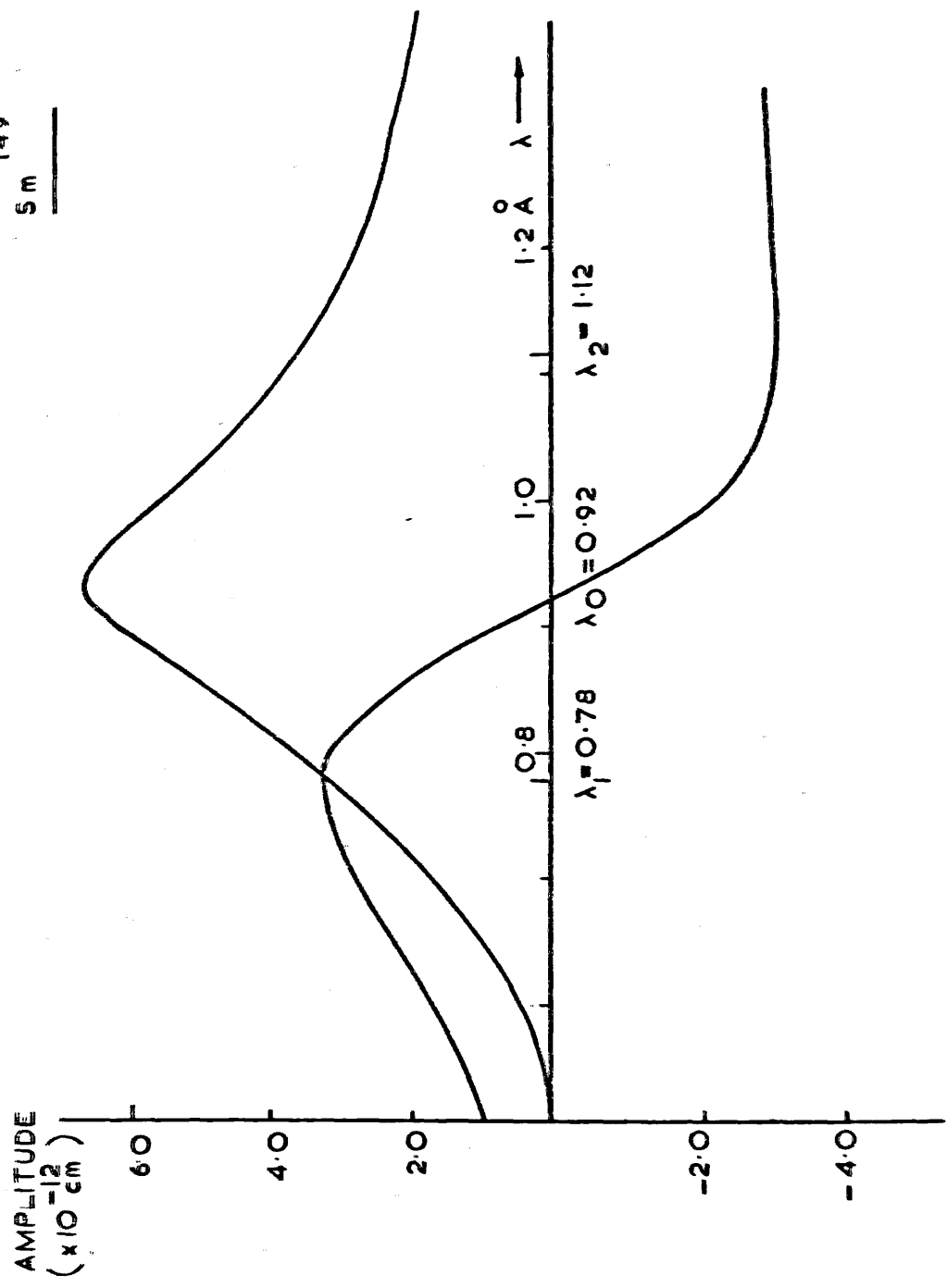
A.E.R.E.R 5195 FIG. 3 HARKER DIAGRAM SHOWING DERIVATION OF TWO POSSIBLE PHASES FOR hki AND $\bar{h}\bar{k}\bar{i}$ REFLEXIONS . THE TWO PHASE ANGLES FOR hki ARE MARKED α_1 AND α_2 .



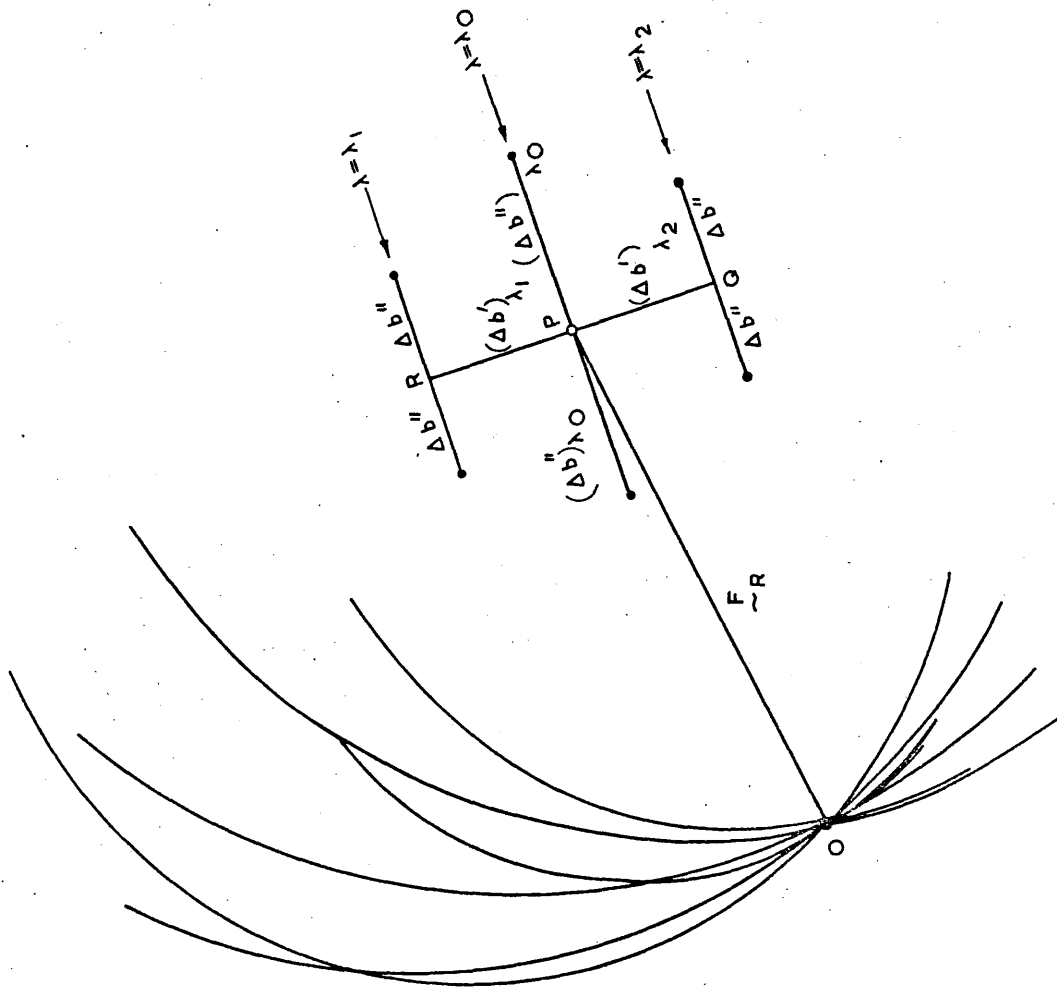
AE.R.E.R 5195 FIG 4 DETERMINATION OF MEAN PHASE ANGLE α OF hkl AND $\bar{h}kl$.



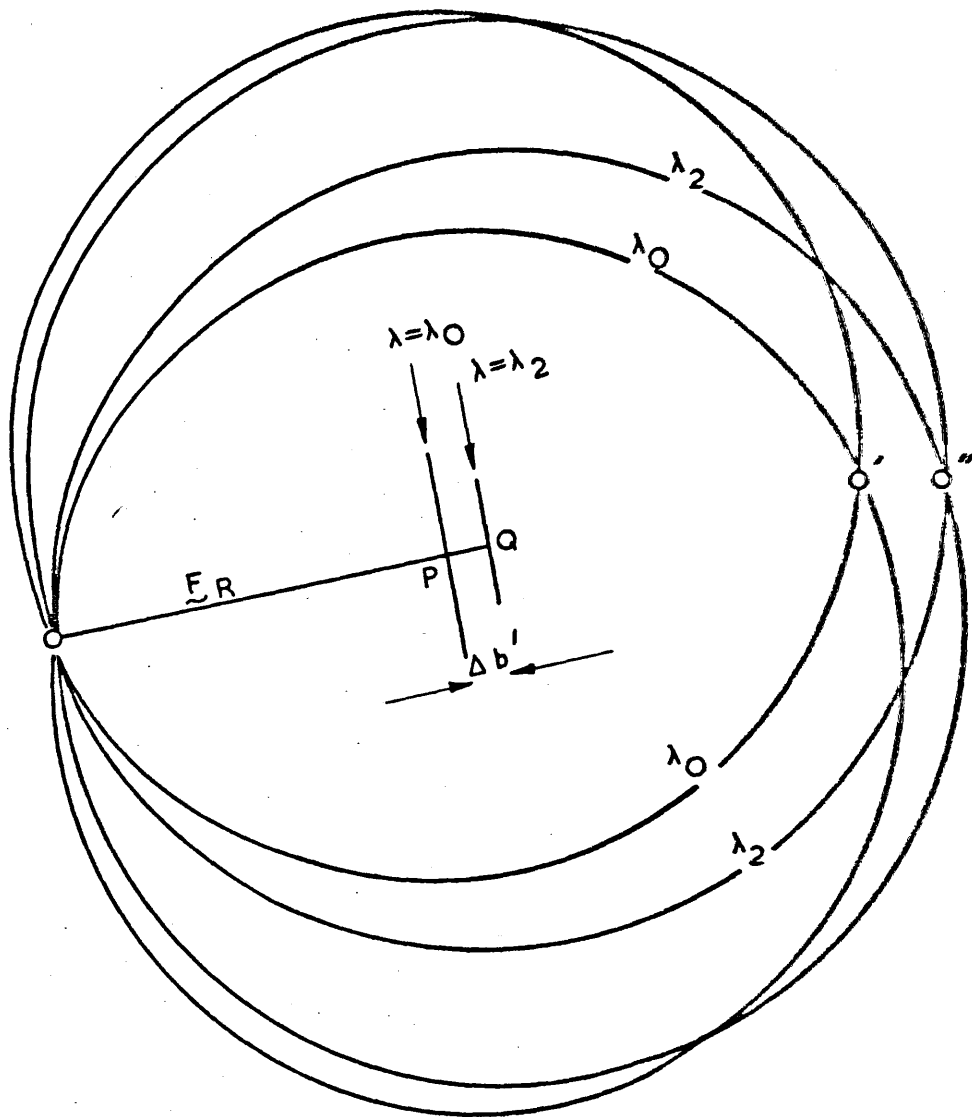
A.E.R.E.R. 5195. FIG 5 DISPERSION CURVES FOR Cd 113



A.E.R.E.R. 5195 FIG 6. DISPERSION CURVES FOR 5 m 149 .



A.E.R.E. 5195 FIG 7 HARKER DIAGRAM FOR NEUTRON WAVELENGTHS λ_0 (AT RESONANCE), λ_1 AND λ_2 . λ_1 AND λ_2 ARE THE TURNING POINTS OF THE ANOMALOUS DISPERSION CURVE FOR Δb^i . ALL SIX CIRCLES (OF RADII DETERMINED BY THE EXPERIMENTAL INTENSITIES) PASS THROUGH THE SAME POINT O, PERMITTING AN UNAMBIGUOUS DETERMINATION OF THE PHASE OF \bar{F} .



A.E.R.E.R 5195 FIG 8. RESOLUTION OF PHASE AMBIGUITY IN WORST POSSIBLE CASE. THE TWO CIRCLES FOR $\lambda = \lambda_0$ INTERSECT IN O AND O', AND THE TWO CIRCLES FOR $\lambda = \lambda_2$ IN O AND O''.

ANHARMONIC CONTRIBUTIONS TO THE DEBYE-WALLER FACTORS OF UO_2 *

BY

K. D. ROUSE AND B. T. M. WILLIS

Atomic Energy Research Establishment, Harwell, Didcot, England.

AND A. W. PRYOR

A.A.E.C. Research Establishment, Lucas Heights, N.S.W., Australia.

Abstract

The integrated intensities of UO_2 , with the cubic fluorite-type structure, have been measured at $20^\circ C$ by neutron diffraction. If structure factors are calculated assuming harmonic temperature factors for the uranium and oxygen atoms, there are systematic differences between the observed and calculated intensities of odd-index reflexions, whereas good agreement is obtained for even-index reflexions.

These results can be explained as the effect of anharmonicity on the temperature factor of the oxygen atoms, which occupy non-centrosymmetric sites. The introduction of one additional parameter to describe this anharmonic effect leads to good agreement ($R \sim \frac{1}{2}\%$) for all measured reflexions.

* Paper published in January 1968 issue of Acta Crystallographica, Section A ('Ewald Festschrift')

1. Introduction

The atoms of a thermally agitated crystal may be described as smeared out by a function, the smearing function $t(\underline{r})$, defined as the probability of finding the atom at a distance r from its equilibrium position. In calculating the intensity of a Bragg diffraction peak, the scattering amplitude of the j^{th} atom in the unit cell is multiplied by the Fourier transform, $T_j(\underline{S})$, of $t_j(\underline{r})$, where \underline{S} is the 'scattering vector' ($|\underline{S}| = 2 \sin\theta/\lambda$). One can properly base a discussion of Bragg intensities on functions $T_j(\underline{S})$, each pertaining to one atom: correlations between the motions of the atoms, so crucial in understanding thermal diffuse scattering, are irrelevant.

For any crystal with harmonic interatomic forces, T_j is Gaussian in form and can be written

$$T_j = \exp - (b_{11}h^2 + b_{22}k^2 + b_{33}l^2 + b_{12}hk + b_{23}kl + b_{13}hl) \dots (1)$$

where the constants b_{11} etc. are the six anisotropic temperature factors, defining the size and orientation of the thermal vibration ellipsoid.

If the atoms occupy sites with cubic point symmetry, the ellipsoid degenerates into a sphere and T_j is characterised by a single isotropic temperature factor B_j , where

$$T_j = \exp(- B_j \sin^2\theta/\lambda^2) = \exp(- \frac{1}{4} B_j S^2) \dots (2)$$

This spherical symmetry is a consequence of the invariance of quadratic forms under transformations of a cubic point group. When the atomic interactions are anharmonic (i.e. the force on an atom is no longer proportional to its relative displacement) then T is not Gaussian and

In this paper, we shall refer to T_j as the 'temperature factor' of the atom j , and to B_j as its 'B-factor'. The term 'Debye-Waller factor' refers to a reflexion (in reciprocal space), rather than to an atom (in direct space): it will be used to denote the reduction in intensity of a reflexion caused by thermal vibration.

so, even in a cubic crystal, departures from spherical symmetry are allowable.

Anisotropy in the temperature factors of a cubic crystal, with atoms at sites of cubic symmetry, was first observed by Willis (1963) in a high-temperature neutron diffraction study of UO_2 . He showed that some reflexions with the same $|S|$, but belonging to different scattering vectors S , were not equal in intensity, as they should be on the harmonic theory. Anharmonic effects were also observed in CaF_2 (Willis, 1965) and in UO_{2+x} (Willis, 1964).

To account for the effect of anharmonicity, Willis adopted a generalized fluorite arrangement, where each anion is replaced by four $\frac{1}{4}$ -anions set down at the corners of a small tetrahedron at the anion sites (see figure 1). This artifice simulated the tetrahedral distortion of the smearing function of the anion, caused by the anharmonic interactions of the anion with its tetrahedral frame of cations. It predicted the presence of anharmonic contributions to the structure factors of odd-index reflexions, such that reflexions with $h + k + l = 4n + 1$ possess intensities exceeding the harmonically-calculated values, whereas those with $h + k + l = 4n - 1$ have intensities lower than the harmonic values. These predictions accorded qualitatively with the observations.

Willis' procedure was criticized by Hamilton (1965), who showed that it gave a displacement parameter δ ^{(see section 3(a))} of marginal statistical significance, at least in the case of the CaF_2 data at 20°C . It is unfortunate that Hamilton failed to extend his analysis to the higher temperature range for CaF_2 and UO_2 , where the anharmonic effects were much stronger. The force of Hamilton's remarks led Ladell (1965) to suggest that the neutron measurements on CaF_2 were unsound, and that there was no evidence for anharmonic behaviour.

The original interpretation of Willis was also criticized by Pryor (1966) on the grounds that the hypothetical displacements of the anions in the Willis theory are much larger than the usual expressions for interatomic potentials would lead one to expect.

The objections to the validity of the experimental results and to their interpretation are answered in the present paper. In the next section, we present further experimental data on UO_2 at 20°C . These results are more accurate and extend to longer scattering vectors (i.e. higher values of $|S|$) than before. In the third section, we outline the Willis theory of accounting for anharmonic effects, and its relation to a more complete and satisfactory theory proposed by Dawson (1967). In section 4, we describe the interpretation of the new UO_2 results by the Dawson theory, deriving a value for the 'anharmonic parameter' β_0 of oxygen (replacing the parameter δ in the Willis theory), which agrees with that deduced by Dawson, Hurley and Maslen (1967). We discuss briefly, in the final section, proposals for experimental work which would subject Dawson's theory to a more critical examination than that described here.

2. Structure Factors of UO_2 at 20°C : interpretation by harmonic model

A spherical crystal of radius 1.6mm was chosen for the investigation: it had been examined earlier and was known to be free of extinction for reflexions of medium intensity (with $h + k + l = 4n + 1$) and for weak reflexions ($h + k + l = 4n + 2$). Three dimensional measurements were made with the Hilger and Watts/Ferranti automatic neutron diffractometer. As far as possible, measurements of each reflexion were taken on 12 "variants", defined as symmetrically-equivalent but distinct hkl planes (i.e. permutations of hkl not including both hkl and $\bar{h}\bar{k}\bar{l}$). Because of the lower multiplicity, only three variants of 006 and four variants of 333 and 555 were measured; apart from these exceptions the

F_{obs} values in Table I and II are averaged over twelve variants. 10-20,000 neutron counts were recorded for each variant, and the standard deviation of the distribution of measurements over twelve variants was usually fractionally larger than the standard deviation calculated from the counting statistics for a single observation. For example, the standard deviation from counting statistics was typically 1.0%, and that from the distribution was 1.0 to 1.7%.

An important source of error in accurate Bragg intensity measurements is double-Bragg scattering. It is well known that this will cause the intensity to vary with the azimuthal setting ψ (angle of rotation about the normal) of the reflecting plane. We checked for this effect by rotating about the scattering vector for several reflexions, but could never detect it. As an extra precaution, however, we measured each of the twelve variants of a reflexion at different values of ψ , incrementing ψ by 2.0° between each individual measurement.

The peaks were scanned in an ω -2 θ mode using a counter aperture 1.2cm square at a distance of 25 cm from the crystal. Background was counted on either side of the Bragg peak; it was subtracted from the peak counts to give the integrated intensity, uncorrected for the thermal diffuse scattering, which rises to a maximum at the centre of the Bragg peak.

The neutron measurements were made in two groups:

- (i) 9 odd-index ($4n + 1$) reflexions and 5 even-index ($4n + 2$), measured at a wavelength of 1.038\AA ;
- (ii) 17 odd-index reflexions, at higher $\sin\theta/\lambda$ than in (i), measured at a wavelength of 0.866\AA .

These results are listed in Table I ($\lambda = 1.038\text{\AA}$) and Table II ($\lambda = 0.866\text{\AA}$). All observations at a given wavelength were made on the same relative scale: no attempt was made to determine intensities

Table I. Structure factors for UO_2 : measurements at $\lambda = 1.038\text{\AA}$

hkl	$h^2+k^2+l^2$	F_{obs}	$\sigma(F_{obs})$	F_{calc}^{harm}	$F_{obs} - F_{calc}^{harm}$	F_{calc}^{anh}	$F_{obs} - F_{calc}^{anh}$
<u>$h+k+l = 4n+1$</u>							
133	19	3.216	0.006	3.220	-0.004	3.215	+0.001
333	27	3.181	0.003	3.176	+0.005	3.178	+0.003
115	27	3.166	0.007	3.176	-0.010	3.172	-0.006
135	35	3.128	0.004	3.132	-0.004	3.132	-0.004
335	43	3.082	0.006	3.088	-0.006	3.078	+0.004
117	51	3.050	0.006	3.046	+0.004	3.046	+0.004
155	51	3.033	0.007	3.046	-0.013	3.040	-0.007
355	59	3.015	0.007	3.003	+0.012	3.016	-0.001
137	59	3.002	0.005	3.003	-0.001	2.999	+0.003
<u>$h+k+l = 4n+2$</u>							
024	20	-1.085	0.005	-1.088	+0.003	-1.088	+0.003
006	36	-0.921	0.012	-0.937	+0.016	-0.937	+0.016
244	36	-0.946	0.005	-0.937	-0.009	-0.937	-0.009
226	44	-0.860	0.011	-0.865	+0.005	-0.865	+0.005
046	52	-0.793	0.006	-0.797	+0.004	-0.797	+0.004

absolutely, nor to determine experimentally the scale factor relating the two sets of observations. The two scale factors were obtained from a least-squares analysis, as described below, and the results quoted in the tables have been multiplied by the appropriate scale factor to bring them to an absolute scale. F_{obs} is the observed structure factor, derived from the mean of the intensity measurements on the variants. $\sigma(F_{obs})$ is the standard error of F_{obs} , calculated from

Table II. Structure factors for UO_2 : measurements at $\lambda = 0.866\text{\AA}$

hkl	$h^2+k^2+l^2$	F_{obs}	$\sigma(F_{obs})$	F_{calc}^{harm}	$F_{obs} - F_{calc}^{harm}$	F_{calc}^{anh}	$F_{obs} - F_{calc}^{anh}$
	$\frac{h+k+l}{4n+1} = \frac{4n-1}{4n-1}$						
733	67	2.997	0.020	2.981	+0.016	2.982	+0.015
751	75	2.934	0.020	2.940	-0.006	2.936	-0.002
	555	2.918	0.023	2.940	-0.022	2.904	+0.014
	911	2.896	0.012	2.897	-0.001	2.888	+0.008
	753	2.879	0.012	2.897	-0.018	2.869	+0.010
755		2.845	0.005	2.816	+0.029	2.845	0.000
	771	2.788	0.007	2.816	-0.028	2.804	-0.016
	933	2.797	0.007	2.816	-0.019	2.798	-0.001
773	107	2.793	0.025	2.776	+0.017	2.801	-0.008
	591	2.754	0.025	2.776	-0.022	2.767	-0.013
11,1,1	123	2.723	0.024	2.698	+0.025	2.703	+0.020
	775	2.684	0.023	2.698	-0.014	2.660	+0.024
971		2.674	0.010	2.660	+0.014	2.675	-0.001
	11,3,1	2.669	0.009	2.660	+0.009	2.659	+0.010
	955	2.631	0.010	2.660	-0.029	2.628	+0.003
11,3,3	139	2.645	0.012	2.622	+0.023	2.645	0.000
	973	2.591	0.012	2.622	-0.031	2.599	-0.008

$$\sigma^2(F_{obs}) = \frac{\sum_{m=1}^{m=n} (F_m - F_{obs})^2}{n(n-1)}$$

where F_m is the F-value of an individual variant and the total number of variants, n , is normally 12.

The fourth column in Tables I and II gives F_{calc}^{harm} , the structure factor calculated within the limits of the harmonic approximation.

The effect of thermal vibration of the atoms is represented by terms of the type given by equation (2), so that

$$\begin{aligned}
 F_{\text{calc}}^{\text{harm}} &= 4b_{\text{U}} \exp(-B_{\text{U}} \sin^2 \theta / \lambda^2) \\
 &\quad \dots h+k+l = 4n \pm 1 \\
 &= 4b_{\text{U}} \exp(-B_{\text{U}} \sin^2 \theta / \lambda^2) - 8b_{\text{O}} \exp(-B_{\text{O}} \sin^2 \theta / \lambda^2) \\
 &\quad \dots h+k+l = 4n \pm 2
 \end{aligned}
 \quad \left. \dots (3) \right.$$

b_{U} and b_{O} are the coherent nuclear scattering amplitudes of uranium and oxygen, and B_{U} and B_{O} are the isotropic (harmonic) temperature factors. Values of the ratio $b_{\text{U}}/b_{\text{O}}$, and of B_{U} and B_{O} , were derived from a least-squares analysis of the 1.038\AA data based on equations (3), treating these three quantities and an overall scale factor as adjustable parameters. Table III gives the values of $b_{\text{U}}/b_{\text{O}}$, B_{U} and B_{O} , with the estimated standard deviations in brackets. For the analysis of the odd-index reflexions in Table II, there were only two adjustable parameters, the scale factor and B_{U} : it is encouraging that the two values of B_{U} in Table III, derived from two independent sets of data over different ranges of $\sin^2 \theta / \lambda^2$, overlap. The computer program used for the least-squares harmonic analysis was that of Busing, Levy and Martin (1962); individual F_{obs} 's were weighted by the reciprocal of the σ -values in Tables I and II, but the results were only marginally altered by replacing these individual weights by unit weights.

In spite of the apparently good agreement between F_{obs} and $F_{\text{calc}}^{\text{harm}}$, a number of the differences $F_{\text{obs}} - F_{\text{calc}}^{\text{harm}}$ in Table II are 3 to 4 times the standard error of F_{obs} . Furthermore, for those groups of either two or three reflexions appearing at the same $h^2 + k^2 + l^2$ in both Tables I and II, the observed F tends to be larger than the calculated F for the member of the group with $h+k+l = 4n+1$ and smaller than the calculated F for the member with $h+k+l = 4n-1$. (For the harmonic model the calculated F is invariant within each group). On the other

Table III. Results of harmonic analysis

Wavelength (\AA)	Number of F_{obs} 's	$\frac{b_U}{b_0}$	B_U (\AA^2)	B_0 (\AA^2)
1.038	14	1.440(5)	0.209(11)	0.428(11)
0.866	17	-	0.214(14)	-

hand, the $4n+2$ reflexions in Table I have $F_{\text{obs}} - F_{\text{calc}}^{\text{harm}}$ values which are less than twice the standard error of F_{obs} , and the harmonic model explains adequately the observed intensities of even-index reflexions.

These systematic discrepancies in the observed intensities are similar to those reported previously in UO_2 , ThO_2 and CaF_2 at high temperature (Willis 1963, 1965), and can be explained in terms of anharmonic contributions to the Bragg intensities. In the next section we shall describe briefly the methods used by Willis and ^{by} Dawson for including these contributions in the analysis of the experimental data.

3. Extension of conventional vibration theory to include anharmonic effects

a. Willis treatment

The anharmonic contributions to the temperature factors are calculated by imagining each anion as being replaced by four $\frac{1}{4}$ -anions; the distortion of the spherical smearing function, $t(r)$, arising from anharmonic interactions, is then simulated by allowing the $\frac{1}{4}$ -anions to move slightly along the four tetrahedral directions in figure 1(b). In this way, the requirements of $\bar{4}3m$ point symmetry are satisfied, and one extra parameter δ is introduced into the structure refinement, where $\frac{1}{4} + \delta$, $\frac{1}{4} - \delta$, $\frac{1}{4} + \delta$... are the atomic co-ordinates of the $\frac{1}{4}$ -anions in the $\text{Fm}\bar{3}m$ space group. The individual $\frac{1}{4}$ -anions retain spherical symmetry, so that the

temperature factors for these $\frac{1}{2}$ -anions are still isotropic. For $\delta = 0$, the $\frac{1}{2}$ -anions coalesce into whole ions occupying the $\frac{111}{244}$... positions.

The expression for the calculated structure factor, for reflexions with $h+k+l = 4n+1$, is:

$$F_{\text{calc}}^{\text{anh}} = 4b_U \exp(-B_U \sin^2 \theta / \lambda^2) \pm 8b_0 \cos 2\pi h(\frac{1}{2} + \delta) \cos 2\pi k(\frac{1}{2} + \delta) \cos 2\pi l(\frac{1}{2} + \delta) \exp(-B_0 \sin^2 \theta / \lambda^2) \dots (4)$$

The + sign in equation (4) is associated with $4n+1$ and the - sign with $4n-1$. B_0 is the isotropic temperature factor of the $\frac{1}{2}$ -ion. The displacement δ is small, $\delta \ll 1$, and so (4) can be rewritten

$$F_{\text{calc}}^{\text{anh}} = 4b_U \exp(-B_U \sin^2 \theta / \lambda^2) \pm 8b_0 \cdot 8\pi^3 \delta^3 \cdot hkl \cdot \exp(-B_0 \sin^2 \theta / \lambda^2) \dots (5)$$

In the same way, the expression for the structure factor of even-index reflexions with $h+k+l = 4n+2$ is

$$F_{\text{calc}}^{\text{anh}} = 4b_U \exp(-B_U \sin^2 \theta / \lambda^2) - 8b_0 \exp(-B_0 \sin^2 \theta / \lambda^2) + 8b_0 \cdot 2\pi^2 \delta^2 \cdot (h^2 + k^2 + l^2) \cdot \exp(-B_0 \sin^2 \theta / \lambda^2) \dots (6)$$

All terms of higher power than δ^3 are ignored in deriving (5) and (6). For $\delta = 0$, (5) and (6) reduce to the harmonic expressions, equation (3).

From equation (4), there is a difference in the calculated F values of odd-index reflexions occurring at the same θ . The presence of the second term in (4) accounts for the $4n+1$ intensities exceeding the harmonic values, and for the $4n-1$ intensities being smaller. For the even-index reflexions at the same θ (e.g. 600 and 422) equation (6) predicts the same intensity: this, too, is supported by the observations. We can summarise the situation by stating that the Debye-Waller factors are isotropic (i.e. depend on

the magnitude but not the orientation of the scattering vector S) for even-index reflexions, and are anisotropic for odd-index reflexions.

This distinction between the two types of reflexion is also predicted by the Dawson theory.

b. Dawson treatment

In the Willis treatment, the distortion of the spherical smearing function is simulated by an atomic displacement from $\frac{111}{444}$ to $\frac{1}{4}+\delta$, $\frac{1}{4}+\delta$, $\frac{1}{4}+\delta$. Clearly, a more satisfactory procedure is to retain $\frac{111}{444}$ as the mean position of the anion, and to modify the smearing function directly in accordance with the local site symmetry. ^{(See figure (10)).} This procedure is adopted by Dawson, who has developed a theory based on general symmetry arguments (Dawson, 1967), which can be applied to any kind of crystal structure. Here we shall only discuss its application to the fluorite structure of UO_2 .

We start with the concept of a single-particle potential $V(\underline{r})$: $V(\underline{r})$ gives the variation, with displacement \underline{r} from the mean atomic position, of the overall potential between the atom and the surrounding ~~lattice~~ ^{array}. In a crystal with harmonic forces, and with atoms at sites of cubic symmetry, $V(\underline{r})$ could only be

$$V(\underline{r}) = V_0 + \frac{1}{2} \alpha (r_x^2 + r_y^2 + r_z^2) \quad \dots (7)$$

where α is a constant depending in a complex way on the interatomic potentials. (The relation between α and the Born-von Karman force constants is obtained from a detailed sum over the normal modes of vibration). Employing classical statistics, the smearing function $t(\underline{r})$ is

$$t(\underline{r}) = N \exp [-(V(\underline{r}) - V_0)/k_B T]$$

where k_B is Boltzmann's constant and the normalizing constant N is

$$N = (2\pi k_B T/a)^{-3/2}$$

The limitation to classical statistics implies that T exceeds the Debye temperature Θ . ~~For UO_2 , $\Theta = 460^\circ K$ (Hillis, 1962) and so the high-temperature approximation is adequate.~~ The temperature factor $T(S)$ is the Fourier transform of $t(\underline{r})$:

$$T(S) = \exp(-\frac{1}{2} S^2 k_B T/a)$$

so that $k_B T/a$ can be identified with the mean-square atomic displacement $\langle r^2 \rangle_{av}$ or with $B/8\pi^2$.

In a cubic crystal with anharmonic forces; the form of $V(\underline{r})$ depends on the site symmetry. For the anion in UO_2 , occupying a site of tetrahedral $\bar{4}3m$ symmetry, the next term after the quadratic (harmonic) term in (7) is a third-order term containing $r_x r_y r_z$. There is no third-order term for the cation, as the centre of symmetry associated with $m\bar{3}m$ symmetry requires that all odd-index terms in the potential expansion are identically zero; the next terms after the harmonic term are two quartic terms, describing the e_g and t_{2g} modifications of the spherical smearing function. We expect, therefore, that the principal anharmonic correction to the structure factor comes from the $\beta_0 r_x r_y r_z$ term of the anion, where β_0 is the coefficient of the third-order term in the expansion of $V(\underline{r})$ for oxygen. If this is the only correction, the expressions for F_{calc} are (Dawson, 1967):

$$F_{calc}^{anh} = 4b_U \exp(-B_U \sin^2 \theta / \lambda^2) \pm 8b_O \exp(-\beta_0 \sin^2 \theta / \lambda^2) \left(\frac{\beta_0}{4\pi a_O} \right)^3 \frac{hkl}{K_B T} \beta_0 \dots (8)$$

$$\text{for } h+k+l = 4n \pm 1,$$

and

$$F_{\text{calc}}^{\text{anh}} = 4b_U \exp(-B_U \sin^2 \theta / \lambda^2) - 8b_O \exp(-B_O \sin^2 \theta / \lambda^2) \quad \dots (9)$$

$$\text{for } h+k+l = 4n + 2,$$

where B_U , B_O are the isotropic temperature factors for uranium, oxygen, and a_0 is the edge of the unit cell. It is straightforward to extend (8) and (9) to include higher-order anharmonic corrections, but the experimental data for all fluorite systems which have been examined to date do not support this extension.

In the refinement of the UO_2 data based on equations (8) and (9), β_0 must be treated as an adjustable quantity, in addition to the quantities B_U and B_O . For a lattice with no thermal expansion, β_0 is independent of temperature for all temperatures exceeding the Debye temperature Θ . To within the same limitations, the harmonic parameters

$$\alpha_U = 8\pi^2 k_B T / B_U \quad \text{and} \quad \alpha_O = 8\pi^2 k_B T / B_O$$

are also independent of temperature.

If we identify the 'displacement parameter', δ , of the Willis theory with the quantity

$$\frac{B_O}{8\pi^2} \cdot \frac{1}{a_0} \left(\frac{\beta_0}{k_B T} \right)^{\frac{1}{3}}$$

of the Dawson theory, equations (5) and (8) for the odd-index reflexions are identical in the two theories. However, the two expressions for the even-index reflexions (equations (6) and (9)) are not the same, although both predict no intensity splitting of reflexions occurring at a common θ . The Dawson treatment is based on sounder physical assumptions, and will be used in the next section for the re-interpretation of the UO_2 data.

4. Re-interpretation of Bragg intensities using Dawson (anharmonic) theory

A full-matrix least-squares computer program based on equations (8)

and (9) was kindly written for us by Dr. E. H. Bracher. The program allows variation of any combination of the five parameters b_U/b_0 , B_U , B_0 , β_0 and overall scale factor. The last two columns of Tables I and II list the quantities $F_{\text{calc}}^{\text{anh}}$ and $F_{\text{obs}} - F_{\text{calc}}^{\text{anh}}$, where $F_{\text{calc}}^{\text{anh}}$ is the structure factor calculated with this program. For the 1.038Å data in Table I, all five parameters were varied. For the 0.866Å data, b_U/b_0 and B_0 were fixed at the values given by the 1.038Å analysis, and only three parameters (B_U , β_0 and scale factor) were varied: this procedure was necessary because no even-index reflexions were measured at 0.866Å. Table IV gives the final values, with estimated standard deviations in brackets, of b_U/b_0 , B_U , B_0 and β_0 for the 1.038Å data, and of B_U and β_0 for the 0.866Å data.

Table IV. Results of anharmonic analysis

Wavelength (Å)	Number of F_{obs} 's	$\frac{b_U}{b_0}$	B_U (Å ²)	B_0 (Å ²)	β_0 (10 ¹² erg Å ⁻³)
1.038	14	1.440(3)	0.206(6)	0.426(9)	-8.0(3.0)
0.866	17	-	0.202(5)	-	-9.6(1.0)

We note first that the introduction of the β_0 parameter leads to an appreciable improvement in the agreement between observed and calculated structure factors. This can be expressed in terms of the R-factor, defined by $R = \frac{\sum_{hkl} \omega_{hkl} \left| |F_{\text{obs}}| - |F_{\text{calc}}^{\text{anh}}| \right|}{\sum_{hkl} \omega_{hkl} |F_{\text{obs}}|}$, where the weights ω_{hkl} are the reciprocals of $\sigma(F_{\text{obs}})$ in Tables I and II. The R-factors for the anharmonic analysis, and for the harmonic analysis ($\beta_0 = 0$) described in section 2, are listed in Table V. The R-factor ratio, defined as the harmonic R-factor divided by the anharmonic R-factor, is $\frac{1.33}{1.27}$ for the 1.038Å measurements and $\frac{1.12}{1.05}$ for the 0.866Å measurements.

Table V. R-factors

Wavelength (Å)	Anharmonic analysis	Harmonic analysis	R-factor ratio
1.038	0.21%	0.29%	1.35
0.866	0.32%	0.68%	2.12

The significance of these R-factor ratios can be evaluated by applying the procedure described by Hamilton (1965). We wish to test the hypothesis H_0 : The oxygen atoms have anisotropic (anharmonic) temperature factors.

One extra parameter (β_0) is included in the anharmonic model, and so the dimension of the hypothesis is 1. There are fourteen measurements at 1.038 Å and five variable parameters, giving nine degrees of freedom. From Hamilton's table

$$R_{1, 9, 0.010} = 1.47$$

and

$$R_{1, 9, 0.025} = 1.34$$

The observed R-factor ratio is 1.35 so that we can accept the hypothesis at the 25% level but reject it at the 1% level. The 1.038 Å results, therefore, do not show conclusively the need to refine the data with the anharmonic model: this is also suggested by Table IV where the value of β_0 , $-8.0 (3.0) \times 10^{-12}$ erg Å⁻³, differs from zero by less than three standard deviations.

The 0.866 Å measurements are more conclusive. Here the number of observations is 17 and the number of adjustable parameters (B_U , β_0 and scale factor) is 3, giving 14 degrees of freedom. Hamilton's table gives

$$R_{1, 14, 0.005} = 1.34$$

the observed R-factor ratio is 2.12, so that we can readily accept the hypothesis H_0 at the 0.5% level. This again is reflected in the more

precise estimate of β_0 , $-9.6 (1.0) \times 10^{-12}$ erg \AA^{-3} , obtained from the 0.866\AA data.

Returning to Table IV, we note that the values of b_U/b_O , B_U and B_O are different from those published earlier (Lipson and Cochran, 1956):

$$b_U/b_O = 1.474 (10), \quad B_U = 0.31 (0.04)\text{\AA}^2, \quad B_O = 0.49 (0.06)\text{\AA}^2.$$

These earlier values must be considered as superseded by the figures in Table IV. The β_0 value in the Table agrees satisfactorily with the value

$$\beta_0 = -9.4 (1.5) \times 10^{-12} \text{ erg } \text{\AA}^{-3},$$

deduced by Dawson, Hurley and Maslen (1967) from the analysis of the high-temperature UO_2 data of Willis (1963).

There are at least three possible sources of systematic error, whose presence would not be revealed by the least-squares anharmonic analysis, and which would cause errors in the parameters listed in Table IV. A very small degree of extinction, amounting to a reduction in intensity of the low-angle reflexions by one per cent, cannot be ruled out: this would be compensated in the analysis by an artificial reduction of B_U and B_O . Second, the neglect of thermal diffuse scattering, which rises to a maximum at the Bragg position, has the opposite effect, leading to an over-estimate of the B-factors (Pryor, 1966). A third source of error is the assumption of an incorrect neutron wavelength λ , which can be determined to $\pm 0.004\text{\AA}$. We have re-determined F_{obs} in Table II, assuming $\lambda = 0.870\text{\AA}$ instead of $\lambda = 0.866\text{\AA}$, and have re-analysed the data by means of the anharmonic model: the β_0 value was unchanged from the figure given in Table IV, but B_U increased from $0.202(0.005)$ to $0.227(0.005)\text{\AA}^2$.

A simple relation between B_U and B_O follows from the assumption that the single-particle potentials of uranium and oxygen include nearest neighbour interactions only. The α -parameter in equation (7)

is then derived by adding eight interatomic potentials for the uranium atom and four interatomic potentials for oxygen. Thus $a_U = 2a_O$. But $a = k_B T/B$, so that

$$B_U = \frac{1}{2} B_O.$$

This relationship is obeyed quite well by the figures in Table IV.

5. Conclusions

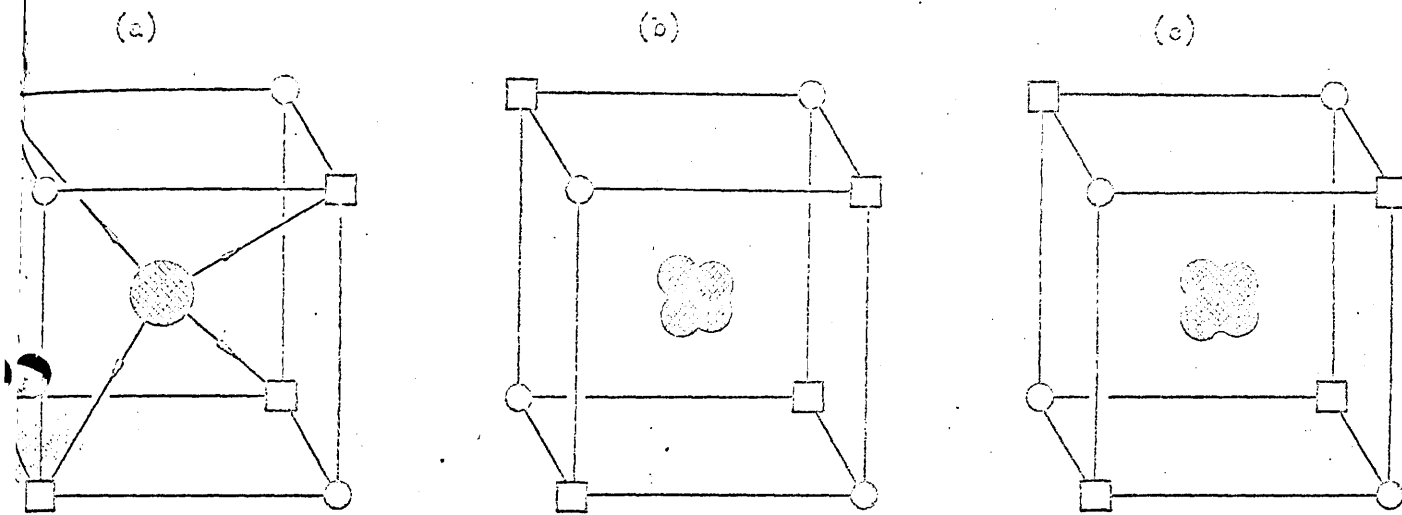
In the case of UO_2 at $20^\circ C$, anharmonic effects are very small: the changes in intensity are not much more than one per cent, even for the most sensitive reflexions. The anharmonic parameter β_0 was derived from the 0.866\AA measurements with an estimated fractional standard deviation of 10%. For the measurements at 1.038\AA , the anharmonic effects were barely significant: this is not surprising, since few reflexions in these data possessed high index-products, $h \times k \times l$. The purpose of the higher-wavelength measurements was to define B_O and the ratio of the scattering lengths b_U/b_O , so that these values could then be used in the analysis of the lower-wavelength, odd-index data. The values of B_U are the same for both sets of data, within the estimated limits of error, but the B-factors may possess other sources of error not apparent in a least-squares analysis (see section 4).

We have shown that it is possible to measure neutron structure factors with an estimated error not larger than $\frac{1}{2}\%$. It is tedious to do this -- the F_{obs} 's represent the mean of twelve independent measurements of the hkl variants -- but it is not particularly difficult.

The results demonstrate the presence of anharmonic effects and their dependence on the index-product. Further points in the theory can only be verified by taking measurements over a range of temperatures. It is more profitable to do this on other fluorite-type systems, such as BaF_2 , SrF_2 and CaF_2 , where the scattering length ratio (anion versus cation) is more favorable: neutron studies of these crystals will be reported separately.

References

- Busing, W. R., Levy, H. and Martin, K. O. (1962). "ORFLS: A FORTRAN Crystallographic Least-Squares Program". ORNL-TM-305.
- Dawson, B. (1967). Proc. Roy. Soc. In the press.
- Dawson, B., Hurley, A. C. and Maslen, V. W. (1967). Proc. Roy. Soc. In the press.
- Hamilton, W. C. (1965). Acta Cryst. 18, 502.
- Hamilton, W. C. (1965). Transactions of the American Crystallographic Association, 1, 17.
- Lipson, H. and Cochran, W. (1966). "The determination of crystal structures", p.372. London: Bell.
- Ladell, J. (1965). Transactions of the American Crystallographic Association, 1, 31.
- Pryor, A. W. (1965). J. Phys. Chem. Solids 26, 2045.
- Pryor, A. W. (1966). Acta Cryst. 20, 318.
- Willis, B. T. M. (1963). Proc. Roy. Soc. A274, 122 and 134.
- Willis, B. T. M. (1964). Jour. de Physique et le Rad. 25, 431.
- Willis, B. T. M. (1965). Acta Cryst. 18, 75.






-  anion
-  cations
-  vacant sites

Figure 1 Anion in the fluorite structure vibrates preferentially along the four tetrahedral directions shown by arrows (a). This aspherical motion is represented by four $1/4$ -anions in the Willis treatment (b), and by a tetrahedrally-distorted smearing function in the Dawson theory (c).